The
University
Of
Sheffield.

Transition metal complexes as chromophores and catalysts for artificial photosynthesis

James David Shipp

A thesis submitted to the University of Sheffield in partial fulfilment of the requirements for the degree of Doctor of Philosophy

November 2021

Department of Chemistry – University of Sheffield

Acknowledgement of collaborative work within the thesis

The candidate confirms that the work submitted is their own, except where work that has formed part of jointly authored publications has been included. The contribution of other authors to this work has been stated explicitly below. All data analysis and interpretation has been performed by the candidate. The candidate confirms that appropriate credit has been given within the thesis where reference has been made to the work of others.

- Dr. Andrew Sadler – Synthesis of [Re(mesBIAN)$(CO)_3$Cl], [Re(mesBIAN-N_3)$(CO)_3$Cl] (Chapter 4), and the Pt(II) donor-bridge-acceptor complexes (Chapter 5).
- Dr. Simon Parker – Synthesis of [ZnTMPyP]Cl_4 and [Mn(phos-bpy)$(CO)_3$Br], as well as preliminary catalytic experiments monitored by NMR spectroscopy (Chapter 3).
- Dr. Steven Spall – Previous work on catalytic and electrochemical studies of [Mn(HPEAB)$(CO)_3$Br], [Re(HPEAB)$(CO)_3$Cl], and [Mn(phos-bpy)$(CO)_3$Br] (Chapter 2, 3).
- Heather Carson – DFT calculations on [Mn(HPEAB)$(CO)_3$Br], [Re(HPEAB)$(CO)_3$Cl], [Re(mesBIAN)$(CO)_3$Cl], [Re(mesBIAN-N_3)$(CO)_3$Cl], and the Pt(II) donor-bridge-acceptor complexes (Chapter 2 – 5).
- Prof. Anthony Meijer – DFT calculations on [Mn(HPEAB)$(CO)_3$Br], [Re(HPEAB)$(CO)_3$Cl], [Re(mesBIAN)$(CO)_3$Cl] and [Re(mesBIAN-N_3)$(CO)_3$Cl]] and the Pt(II) donor-bridge-acceptor complexes (Chapter 2 – 5).
- Dr. Ricardo Fernández-Terán – Anharmonic DFT calculations on [Re(HPEAB)$(CO)_3$Cl], [Re(mesBIAN)$(CO)_3$Cl] and [Re(mesBIAN-N_3)$(CO)_3$Cl] (Chapter 4).
- Prof. Mike Towrie – Recording of time domain 2DIR data for the Pt(II) donor-bridge-acceptor complexes (Chapter 5).
- Dr. Milan Delor – Recording of TRIR and frequency domain 2DIR data on [Re(HPEAB)$(CO)_3$Cl], [Re(mesBIAN)$(CO)_3$Cl] and [Re(mesBIAN-N_3)$(CO)_3$Cl] (Chapter 4).
- Dr. Igor Sazanovich – Recording of TRIR and frequency domain 2DIR data on [Re(HPEAB)$(CO)_3$Cl], [Re(mesBIAN)$(CO)_3$Cl] and [Re(mesBIAN-N_3)$(CO)_3$Cl] (Chapter 4).
- Dr. Craig Robertson – Recording of single crystal X-ray diffraction data, and crystal structure refinement.

Abstract

This thesis contributes to the growing field of artificial photosynthesis, with a focus on developing our understanding of photo- and electrocatalytic CO_2 reduction in artificial systems. Such systems rely on transition metal complexes to act as catalysts, photosensitisers, or both. The key aspects of this project were to (i) understand the activation mechanism for Mn(I), and Re(I) CO_2 reduction catalysts through electrochemical studies; (ii) understand the ultrafast relaxation processes of Re(I) photocatalysts and Pt(II) chromophores following visible light excitation; and (iii) further develop Re(I) photocatalysts and Zn(II) photosensitisers that can effectively harvest red light.

In chapters two and three, a series of novel CO_2 reducing systems were developed, using Mn(I) or Re(I) complexes with the general structure $[M(L_2)(CO)_3(X)]$ (L_2 = 2,2′-bipyridyl derivative, M/X = Re/Cl or Mn/Br). The capacity of these complexes to reduce CO_2 to CO following electrolysis or photosensitisation from a Zn(II) porphyrin was established through electrochemical, catalytic, and photophysical studies. CO_2 reduction catalysis was also demonstrated in aqueous solution under red light irradiation which selectively produced CO as the product. The recyclability of the Mn(I) catalysts – an important criterion for practical application – was demonstrated through successive catalytic experiments.

The efficiency of photocatalysis is partially controlled by the excited state dynamics of the catalyst. In chapter four, these dynamics were probed on the ultrafast timescale with time-resolved IR spectroscopy, which was used to study three Re(I) tricarbonyl diimine complexes. The first complex was functionalised with sterically hindering amide groups in the 6,6′-position of $[Re(bpy)(CO)_3Cl]$ (bpy = 2,2′-bipyridine). As well as providing steric protection of the metal centre, this was found to significantly reduce the excited state lifetime ($\tau = 2.9$ ns) when compared to the unfunctionalised complex. The short lifetime prevented application of the sterically hindered complex as a CO_2 reduction photocatalyst. Typically, Re(I) complexes do not absorb light at the wavelengths longer than 450 nm, limiting their potential to harvest solar radiation. Thus, new complexes were studied which incorporate the bis(mesitylimino)acenaphthene (mesBIAN) ligand, this is a much stronger electron acceptor than 2,2′-bipyridine, where the MLCT absorption band is shifted toward lower energies, up to 650 nm. The $[Re(mesBIAN)(CO)_3Cl]$ complexes form multiple triplet excited states following visible light excitation into an MLCT excited state. However, the small energy gap between the excited state and the ground state resulted in a triplet state lifetime that was too short (< 5 ns) for application in bimolecular photocatalysis. Vibrational excitation of the triplet excited states was found to promote interconversion, resulting in equilibration of the excited state population between lowest triplet states, T_1 and T_2.

In a multicomponent system in solution the rate of electron transfer is limited by diffusion. This can be circumvented through construction of a covalent donor-bridge-acceptor complex. It has been shown that the rate of electron transfer in these systems can be influenced by mode-specific IR excitation of a transient excited state as the excited state landscape evolves towards charge separation. However, this effect is not yet fully understood. To this end, vibrational energy transfer in a Pt(II) donor-bridge-acceptor complex was studied by two-dimensional IR spectroscopy, revealing how the molecular vibrations are coupled, and how vibrational energy is redistributed from the bridge to the donor and acceptor ligands. In chapter five, a mechanism of vibrational energy redistribution was proposed, providing new information on how molecular vibrations may influence the rate of charge separation within the donor-bridge-acceptor complex.

Acknowledgements

Firstly, I would like to express my gratitude to my supervisor, Professor Julia Weinstein, for providing me with the opportunity to carry out my PhD in her research group. Julia's continuous support of my research goals, careful attention to detail, and willingness to teach me about the intricacies of catalysis, electrochemistry, and spectroscopy has been invaluable. I would also like to thank Dr. Peter Portius, for his encouragement and insightful advice on inorganic chemistry, catalytic studies, and approaches to research at the postgraduate level. I would also like to thank my co-supervisors, Dr. Alistair Buckley and Professor Tao Wang, for their advice on CO_2 reduction catalysis and approaches to artificial photosynthesis. Furthermore, I would like to thank the Grantham Centre for Sustainable Futures for funding my PhD research and for providing a comprehensive and interesting training course in sustainability outreach and activism. Also, I would like to thank the Royal Society of Chemistry, and EPSRC for additional funding.

I am grateful to the Central Laser Facility and its staff for their advice and support in the collection and analysis of time-resolved spectroscopic data. I would like to thank Dr. Igor Sazanovich, Dr. Paul Donaldson, Dr. Greg Greetham, and Professor Mike Towrie for sharing their expertise with me in the fields of Raman, TRIR, and 2DIR spectroscopy. Furthermore, I would like to thank Dr. Dimitri Chekulaev, for his patience and support of my research in the Lord Porter laser laboratory. Dimitri's willingness to answer my many questions and guide my development of the time domain 2DIR spectrometer at Sheffield has been invaluable.

Throughout my time as a PhD student, I have been extremely fortunate to have the support of my fellow researchers. First and foremost, I would like to express my thanks to Dr. Simon Parker, Dr. Andy Sadler, Dr. Steven Spall, Dr. George Farrow, and Dr. Alex Auty for their support, advice, patience, and advice during the early stages of my research project, and for teaching me the vital skills I needed to perform my research. I have been incredibly fortunate to work in a welcoming and supportive research group, the friendship of Heather, Simon, Alex, Martin, Guanzhi, Isuru, Callum, Catherine, Samantha, Marta, Tao, Ricardo, Rory, and Iona has been very welcome. I would like to extend a special thank you to those members of the group who have collaborated with me in the pursuit of my research goals.

I would also like to thank my close friends, Josh, Chris, Ben, and Callum for their support, advice, and company over the past eight years at Sheffield. Finally, I would like to express my gratitude to my family, especially my Mum and Dad, without whom I would not be where I am today.

Table of Contents

Chapter 1. Introduction

1.1 Research motivation

Since the industrial revolution, modern society has depended on the burning of fossil fuels for power generation. In recent years, more than 80% of our energy was provided by the combustion of coal, oil, or gas.[1] Whilst these are highly energy dense, they do present significant drawbacks. The first of these is that fossil fuels are finite, hence new energy sources will be required as they are depleted. Another major issue is the release of CO_2 as a product of combustion. Anthropogenic CO_2 release is one of the most significant driving forces of both global warming and climate change.[2]

A promising alternative are renewable energy sources, which do not emit greenhouse gases during their operation. Wind, wave, and solar power are the most promising replacements for fossil fuels. These energy generators are not carbon neutral as they do not uptake CO_2 during operation and a significant amount of greenhouse gases are released during production and maintenance of the system. However, this CO_2 release can be offset through emergent technologies, such as carbon capture, storage, and utilisation. Renewable energy sources do have disadvantages, such as their intermittent power production. For example, at night or during poor weather, little to no power is generated from a solar panel. Some renewable energy technologies, such as tidal power stations, do regularly produce large amounts of power; however, these power sources have their own problems, such as the limited number of coastal sites suitable for these stations. The ideal solution is to store the excess power generated when the generators are active, and then allow the grid to deplete this energy from storage when the renewables are not producing electricity. In practice this is very difficult to accomplish as modern batteries have high capacitance but a limited lifetime, and supercapacitors have a long lifetime but a low capacitance. Currently, there are no energy storage devices which could store the required amount of energy for a sufficiently long working lifetime. In addition, the required storage devices would likely be extremely costly to produce and maintain.

Solar fuels

What is required is a method of storing the energy derived from renewable power sources for an extended period. A proposed way of achieving this is the conversion of solar energy to chemical energy, in the form of storable molecular fuels. An existing example of this technology is the electrolysis of water to form hydrogen and oxygen utilising energy produced from photovoltaics (Eq. 1.1).[3]

$$\mathrm{H_2O} \rightarrow \mathrm{H_2} + 0.5\ \mathrm{O_2} \qquad \Delta G^\circ = -1.23\ \mathrm{V} \qquad \text{Eq. 1.1}$$

Unlike electrical power, ‘solar fuels’, such as hydrogen gas, are cost effective to store and transport.[4] When the energy is needed, the hydrogen can be combusted to release the stored energy whilst converting some of it back into electrical power. There are several examples of chemical reactions capable of producing hydrogen, and other solar fuels. Many of which rely on the use of rare earth and precious metal elements such as Pt, Ru, or Re. For practical large-scale application, it is imperative that solar fuel producing devices only use abundant elements to allow for their widespread use as energy storage systems. Elements such as Mn are over one million times more abundant than Re, hence provide opportunities for industrial scale applications (Elemental abundances: Mn – 0.1 wt%, Re – $7x10^{-8}$ wt%).[5]

The ideal energy source for solar fuel production is sunlight. Many of the desired reactions, such as the conversion of CO_2 to CH_4, can be photoinduced following excitation of a suitable catalyst. The use of sunlight as a power source would also allow for the construction of integrated devices, which require no external power supplies or generators. Many electrochemical methods of producing solar fuels have also been found. In principle, these could be powered with the energy from the grid, or with a dedicated generator, such as a solar panel. A system such as this could prove to be carbon neutral, as over time it converts the equivalent amount of CO_2 used to produce and operate the system.

Natural and artificial photosynthesis

Charge separation in natural photosynthesis is extremely efficient, and the resulting anionic and cationic charges are used to drive water splitting and CO_2 reduction to produce oxygen and glucose. Therefore, nature is a key source of inspiration for photocatalysis and solar fuel production. In plants, carbon dioxide and water are converted to glucose and O_2 in a sunlight-driven process. Natural photosynthesis can be subdivided into three sections: light capture, H_2O oxidation, and CO_2 reduction. These processes are linked through electron transport chains, which facilitate charge separation and prevent unproductive back electron transfers. Whilst natural photosynthesis is a highly complex and specialised process, it can be simplified to a ‘Z-scheme’ to highlight the key features.

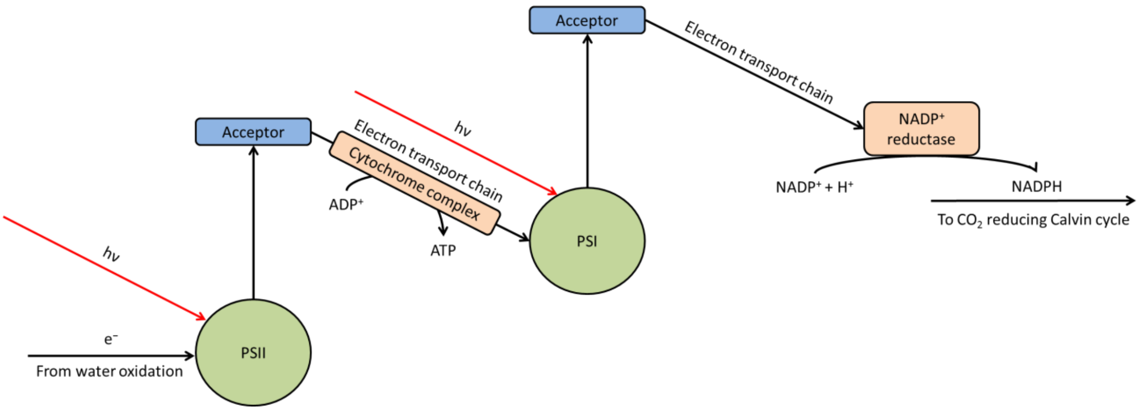

Figure 1.1 – A simplified diagram of the 'Z-scheme' for natural photosynthesis in plants.

The light harvesting component consists of two photosystems, largely constructed of biological porphyrin derivatives such as chlorophyll a. All chlorophyll structures contain the magnesium chlorin group, which is the site of light absorption. Chlorin molecules, such as chlorophyll, are porphyrin derivatives which are ideal for light harvesting as they absorb strongly across the visible spectrum. H_2O oxidation takes place at photosystem II, where two H_2O molecules are oxidised to produce four protons and one molecule of oxygen. The electrons produced by H_2O oxidation are used to restore the oxidised light absorbing pigments following electron transfer.

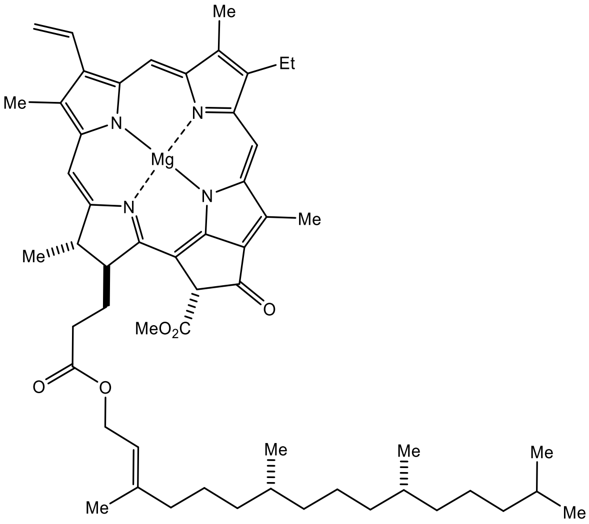

Figure 1.2 – The structure of chlorophyll a.

The electron transport chains which connect the reaction centres facilitate the reduction of $NADP^+$ to NADPH by the enzyme $NADP^+$ reductase. From this point, the reactions in natural photosynthesis are 'light independent'. The NADPH is transported to the Calvin cycle, where CO_2 reduction takes place. This is an enzyme-catalysed process which utilises the protons, ATP, and NADPH produced in the light-dependent reaction to complete the photosynthetic reaction by reducing CO_2 to glucose. Natural photosynthesis can be approximated to a donor-chromophore-acceptor system which artificial catalysts can be modelled on.

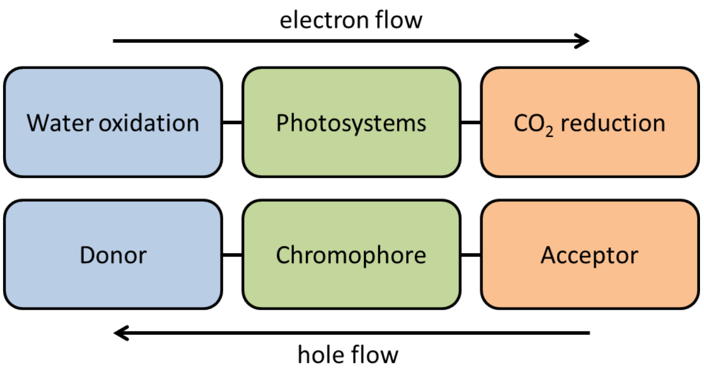

Figure 1.3 – A simple donor-chromophore-acceptor system, which approximates the key components of natural photosynthesis.

Artificial photosynthetic systems aim to replicate this carbon fixation process. The overarching aim of the field is to use sunlight to convert CO_2 and H_2O to solar fuels and industrial feedstocks through proton-coupled oxidation and reduction processes. Due to the complexity of this task, most current artificial photosynthetic systems only replicate one half of the process, either CO_2 reduction or water oxidation. In place of water oxidation, many CO_2 reducing systems employ sacrificial compounds to replenish the oxidised chromophore. To date, no artificial photosynthetic systems have been developed which are robust and efficient enough for large scale CO_2 utilisation.[6]

CO_2 as a source of fuels and chemical feedstocks

The reduction of CO_2 is a promising candidate for solar fuel synthesis. However, direct electrochemical reduction of CO_2 is extremely energy intensive. This is a result of the required linear to non-linear geometry change that occurs upon reduction. The non-linear $CO_2^{\cdot-}$ product is unstable and is readily re-oxidised to neutral CO_2. A multi-step reaction utilising catalysts is a more promising method of reducing CO_2 to desirable products. Through successive proton coupled two-electron reduction processes it is possible to convert CO_2 to CO (carbon monoxide), $^{-}CO_2H/H_2CO_2$ (formate/formic acid), H_2CO (formaldehyde), H_3COH (methanol), and CH_4 (methane). These reductions are more thermodynamically favourable than direct reduction, as shown by the standard electrochemical potentials (Eq. 1.2 – 1.7) (Standard electrochemical potentials are reported against the standard hydrogen electrode in water at pH 7).[7] The ideal proton source for these reactions is water, although organic reagents such as trifluoroacetic acid (TFA) or triethanolamine (TEOA) can be used.

$$CO_2 + e^- \rightarrow CO_2^{\cdot -} \qquad \Delta G^\circ = -1.90\ \mathrm{V} \qquad \text{Eq. 1.2}$$

$$CO_2 + 2H^+ + 2e^- \rightarrow CO + H_2O \qquad \Delta G^\circ = -0.53\ \mathrm{V} \qquad \text{Eq. 1.3}$$

$$CO_2 + 2H^+ + 2e^- \rightarrow H_2CO_2 \qquad \Delta G^\circ = -0.61\ \mathrm{V} \qquad \text{Eq. 1.4}$$

$$CO_2 + 4H^+ + 4e^- \rightarrow H_2CO + H_2O \qquad \Delta G^\circ = -0.48\ \mathrm{V} \qquad \text{Eq. 1.5}$$

$$CO_2 + 6H^+ + 6e^- \rightarrow H_3COH + H_2O \qquad \Delta G^\circ = -0.38\ \mathrm{V} \qquad \text{Eq. 1.6}$$

$$CO_2 + 8H^+ + 8e^- \rightarrow CH_4 + 2H_2O \qquad \Delta G^\circ = -0.24\ \mathrm{V} \qquad \text{Eq. 1.7}$$

This approach to CO_2 reduction has been widely demonstrated, where transition metal complexes and semiconductive materials have been used to reduce CO_2 to each one of these reduction products. There are, however, significant challenges which must be overcome. For example, semiconductor catalysts can perform the eight-electron reduction of $CO_2 \rightarrow CH_4$, but with poor selectivity. In contrast, molecular transition metal complexes are often only able to produce the two-electron reduction products, CO or $^{-}CO_2H$, but with high selectivity. This limitation in the extent of reduction is a result of the stability of the catalytic intermediates. For example, the CO bound complex which forms following two-electron reduction of CO_2 is often unstable, resulting in rapid dissociation of the CO ligand before it can be further reduced. Molecular catalysts with specialised ligands have been able to produce small quantities of H_2CO, H_3COH, and CH_4. From a kinetic standpoint the reduction of CO_2 is further complicated as it requires successive diffusion-controlled reactions which limit the rate of catalysis. Therefore, catalysts which are specialised for each reaction are required to maximise the rate of catalysis. In an idealised artificial photosynthetic system, these specialised catalysts could operate in sequence as CO_2 is reduced to CH_4 by each complex in a stepwise fashion.

Benchmarking molecular CO_2 reduction catalysts

There are several requirements of a CO_2 reduction catalyst before its application to large-scale catalysis can be considered. The first requirement is the viability of preparing the catalyst for industrial chemistry. If the synthesis of the catalyst requires high-cost reagents or difficult multi-step reactions, then the feasibility of industrial application is reduced. The second requirement is that the catalyst must selectively reduce CO_2 to a desirable product. If the catalyst is non-selective the products must be separated, decreasing the viability of the artificial photosynthetic reaction. Although some product mixtures, such as CO/H_2 synthesis gas (syngas), are desirable. The third requirement is that the catalysis is both fast and efficient, where unproductive reactions of the catalyst are minimised, and the turnover number (TON), turnover frequency (TOF), and Faradaic efficiency (or quantum yield) are high. The final requirement is that the catalyst is stable under catalytic conditions for an extended period and can be recycled for long-term usage.

Table 1.1 – Catalytic benchmarks for quantification of CO_2 reduction performance (TON – turnover number; n – number of moles; TOF – turnover frequency; FE – Faradaic efficiency; N_{e^-} - number of electrons transferred in each catalytic reduction; CS – catalytic selectivity; φ_{cat} – quantum yield of photocatalysis; k_{cat} – rate of catalysis; k_r – rate of radiative excited state relaxation; k_{nr} – rate of non-radiative excited state relaxation.

Turnover number	$\mathrm{TON} = \frac{\mathrm{n_{product}}}{\mathrm{n_{catalyst}}}$	Eq. 1.8
Turnover frequency	$\mathrm{TOF} = \frac{\mathrm{TON}}{\text{reaction time}}$	Eq. 1.9
Faradaic efficiency	$\mathrm{FE} = \frac{\mathrm{n_{product}}}{\mathrm{n_{electrons}}} \cdot \mathrm{N}_{e^-}$	Eq. 1.10
Catalytic selectivity	$\mathrm{CS} = \frac{\mathrm{n_{desired\ product}}}{\mathrm{n_{undesired\ product(s)}}}$	Eq. 1.11
Quantum yield of catalysis	$\varphi_{\mathrm{cat}} = \frac{\mathrm{k_{cat}}}{\mathrm{k_{cat}} + \mathrm{k_r} + \mathrm{k_{nr}}}$	Eq. 1.12

Evaluation of catalytic performance by electrochemical methods

The electrochemical properties of a CO_2 reduction catalyst play a key role in determining its catalytic performance. Cyclic voltammetry (CV) is used to measure these properties, such as oxidation and reduction potentials, electrochemical reversibility, and stability under electrolysis. CV is performed in a three-electrode electrochemical cell with a working electrode, counter electrode, and reference electrode. In this work these are glassy carbon, Pt wire, and Ag wire in an aqueous 3 mol dm^{-3} KCl solution saturated with AgCl, respectively. The analyte is dissolved in anhydrous solvent with an electrolyte, $[NBu_4][PF_6]$, which increases the solution conductivity. The three electrodes are connected to a potentiostat which allows for application of a potential difference across the cell and subsequent measurement of the current flowing between the working and counter electrodes. The applied potential difference is measured relative to the reference electrode, where different reference electrodes result in different measured redox potentials for the analyte. To standardise the measured potentials within this thesis, all electrochemical redox potentials are quoted relative to the ferrocene/ferrocenium redox couple (Fc/Fc^+). In the CV experiment, the potential difference is first scanned from 0 V toward positive potential, after reaching the selected maximum potential difference, the scan direction changes toward negative potential. The scan direction changes again at the selected minimum potential difference, and scans back to the start point, completing the cycle. A plot of the measured current against the applied potential then produces the cyclic voltammogram.

If the analyte has a redox process within the scanned range, a redox couple is observed in the cyclic voltammogram. Under ideal conditions, the redox process follows the Nernst equation (Eq. 1.13), which relates the potential of the electrochemical cell to the ratio of oxidised and reduced species in solution.

$$E = E^0 - \frac{RT}{nF} \cdot ln \frac{a_{red}}{a_{ox}} \qquad \text{Eq. 1.13}$$

$$E = E^{\frac{1}{2}} - \frac{RT}{F} \cdot ln \frac{[Red]}{[Ox]} \qquad \text{Eq. 1.14}$$

In the Nernst equation, E is the potential of the electrochemical cell, E^0 is the standard electrochemical potential for the reaction, R is the gas constant, T is the temperature, n is the number of electrons transferred, F is the Faraday constant, and the $\ln(a_{red}/a_{ox})$ term gives the relative activities of the oxidised and reduced species in solution. For a one-electron reduction, the activities can be replaced with concentrations, where ln([Red]/[Ox]) gives the ratio of oxidised and reduced molecules. This ratio determines the probability of a molecule being oxidised or reduced at a given cell potential. Under equilibrium conditions, ln([Red]/[Ox]) is equal to the equilibrium constant (K). Furthermore, the standard electrochemical potential can be replaced with the formal electrochemical potential (defined as the potential where [Red]/[Ox] = 1.00), which is well estimated by the experimentally determined electrochemical half-potential ($E^{1/2}$) (Eq. 1.14, Figure 1.4).

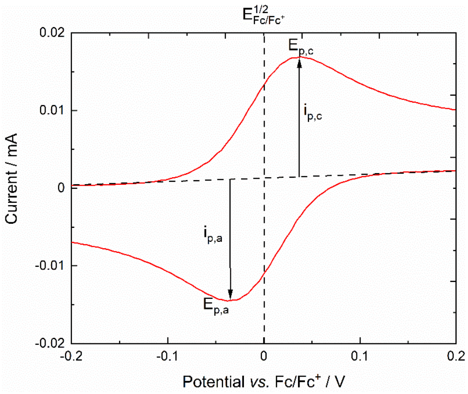

Figure 1.4 – Cyclic voltammogram of the reversible Fc/Fc^+ redox couple, the electrochemical half-potential of which is defined as 0 V ($i_{p,a}$: Peak current of anodic oxidation process, $i_{p,c}$: Peak current of cathodic reduction process, $E_{p,a}$: peak potential of anodic oxidation process, $E_{p,c}$: peak potential of cathodic reduction process, $E^{1/2}$: Electrochemical half-potential of the Fc/Fc^+ redox couple).

If a redox process is fully chemically reversible, the peak-to-peak separation of the reductive and oxidative processes is 57 mV under ideal conditions. Additionally, the forward and return (e.g. Fc → Fc^+, Fc^+ → Fc) peaks will have the same integrated current, and the ratio of measured current $i_{p,c}$ or

$i_{p,a}$ to the square root of the scan rate (v) will be linear. The magnitude of the measured current is proportional to the number of electrons transferred between the electrode surface and the analyte; hence a two-electron process will have twice the integrated current of a one-electron process. Many redox processes are only quasi-reversible, which results in increased separation between the anodic and cathodic peak potentials ($E_{p,a}$ and $E_{p,c}$). Redox processes can also be completely irreversible, where no peak is observed in the reverse scan. Quasi-reversible and irreversible reduction or oxidation processes are very common in CO_2 reduction catalysis, where the catalyst reacts to form a different species following one or two electron reduction. The electrochemical half-potential ($E^{1/2}$) of the first and second reduction processes of a CO_2 reduction catalyst are key parameters which determine the energy required to initiate the catalytic reaction.

CV data also allows for estimation of the rate of electrocatalytic CO_2 reduction through calculation of the TOF and required overpotential (η). The overpotential is defined as the difference in electrochemical potential between the standard potential of the catalytic reaction and the applied potential required to achieve the maximum turnover frequency (TOF_{max}). One method of doing this is to increase the scan rate to a point at which diffusion of the CO_2 substrate to the electrode surface becomes the rate-limiting step. At this point the CV has a characteristic S-shape, and further increases to the scan rate will not change the data. The TOF and η can then be obtained from this curve.[8] In cases where it is not possible to increase the CV scan rate to this point, the electrochemical performance of the catalysts can be estimated by foot-of-the-wave (FOTW) analysis. This technique analyses the onset region (the 'foot') of the catalytic reduction potential. This is also useful for catalysts which undergo undesirable side-reactions or decompose during catalysis. A summary of the FOTW method used here is presented in Appendix B, detailed explanations of the theoretical and kinetic background to the method are available elsewhere.[9]

Whilst CV is a versatile technique for analysis of electrocatalytic performance, it does have limitations. To obtain the TON, TOF, and faradaic efficiency under catalytic conditions, controlled potential electrolysis (CPE) must be used instead. This technique is similar, utilising a three-electrode electrochemical cell, however it operates on a larger scale. Typical electrodes for CPE are a large Pt mesh working electrode, a large Pt wire counter electrode and an Ag wire pseudoreference electrode. In a CPE experiment, the electrochemical potential is held at a particular value, ideally the optimum overpotential found by CV analysis. The CO_2 reduction performance is then quantified through measurement of product formation yield, as described below. From this data, the TON, TOF, and Faradaic efficiency can be calculated.

Whilst CV and CPE are valuable tools for quantification of catalytic performance, they do not provide information on the catalytic mechanism or the chemical reactions which are initiated by the one and two-electron reduction processes. Spectroelectrochemistry (SEC) can be used for this purpose, where the spectral changes in the analyte solution are monitored following application of an electrochemical potential. This experiment is performed in an optically transparent thin-layer electrochemical (OTTLE) cell, which is equipped with Pt minigrid working and counter electrodes, and an Ag wire pseudoreference electrode.[10] IR-SEC provides vital information about the chemical changes a CO_2 reduction catalyst undergoes following reduction and allows for definitive assignment of the redox couples observed in CV and CPE.

Quantification of CO_2 reduction product formation

The quantification of CO_2 reduction performance requires reliable methods of measuring the yield of each reduction product. Gas chromatography (GC) is used to measure the formation of CO, CH_4 as well as the H_2 which can result from undesirable proton reduction. The product formation is quantified with reference mixtures of the analyte with an inert gas, such as argon. GC is a simple, fast, and versatile method of quantifying gaseous product evolution. However, there are limitations of this technique. For example, optimised detection of H_2 and CO requires different conditions for each analyte. For example, the optimum setup for CO detection uses H_2 as a carrier gas – hence the selectivity for CO_2 reduction over proton reduction cannot be quantified in a single experiment. A second disadvantage is that GC experiments can be adversely affected by CO_2, which strongly binds to the chromatography column. Finally, GC cannot report on the contents of the liquid phase due to the presence of water in the catalytic reaction, as such the quantity of gaseous products dissolved in the reaction mixture is difficult to obtain.

Determination of liquid product formation is commonly done by either ion chromatography, for HCO_2^- production, or NMR spectroscopy for non-ionic products. Quantification of product formation by ^1H NMR spectroscopy can be difficult due to overlap of the product spectrum with ^1H NMR resonances of other species present in solution, such as the catalyst, photosensitiser, sacrificial donor, organic solvent, and water. However, isotopic labelling experiments with $^{13}CO_2$ have been used to overcome this problem with proton decoupled carbon-13 ($^{13}C\{^1H\}$) NMR spectroscopy. FTIR can also be used for liquid product formation monitoring. However, this is also limited by overlap of the IR-absorption bands of the product with that of the IR absorption bands of other species in solution.

1.2 The dynamics of electronic excited states

As a light driven process, photochemical CO_2 reduction is dependent on the excited state dynamics of the catalysts and photosensitisers involved. Therefore, to understand the factors underlying the catalytic performance of photochemical system, an understanding of the relevant photophysical and photochemical process is required.

Absorption

The first step in any photocatalytic reaction is the absorption of a photon, which results in the promotion of a molecule from the ground state to an electronic excited state. The absorption of light is governed by the Beer-Lambert law (Eq. 1.13, 1.14), where the absorbance is given by the difference in incident light intensity (I_0) and transmitted light intensity (I). This is equal to the extinction coefficient (σ – molecular extinction coefficient; ε – molar extinction coefficient) multiplied by the sample concentration (c) and path length (l). The excited states of molecules are quantised with discrete energy levels, however, the absorption bands of molecules are not observed at a single transition energy. Instead, they extend over a range of energies. This broadening is described with the full width at half maximum (FWHM) of the absorption band. Line broadening is caused by several effects, such as the natural broadening arising from the Heisenberg uncertainty principle. In electronic transitions, line broadening is also attributed to molecular vibration and rotation, where the population is distributed over many vibrational and rotational states. This results in a statistical distribution of electronic absorption energies, broadening the absorption band. Due to these broadening effects, it is not possible to resolve the individual vibrational and rotational transitions for an analyte molecule in solution, hence a continuous band, centred on the main transition, is usually observed. The distribution of solvent geometries around the analyte complex also results in line broadening, where different solvent orientations also shift the electronic and/or vibrational transition energies.

$$-\frac{\mathrm{dI}}{\mathrm{dx}} = \sigma_\nu \mathrm{cI} \qquad \text{Eq. 1.13}$$

$$\mathrm{A} = -\ln\left(\frac{\mathrm{I}}{\mathrm{I_0}}\right) = \sigma_\nu \mathrm{cl} \qquad \text{Eq. 1.14}$$

Visible light absorption often results in the formation of an electronic excited state which is also highly vibrationally excited. This is a result of the Frank-Condon principle for vibronic (vibrational / electronic) transitions. The Frank-Condon principle states that vibronic transitions must be vertical relative to the reaction coordinate. This means that no changes in nuclear geometry can take place during the electronic transition. This is a product of the Born-Oppenheimer approximation, which states that the motion of the nuclei and electrons is separable due to the vastly different timescales of their motion. In this situation the shift of electron density will be completed first, resulting in an unfavourable nuclear geometry for the new electron density distribution. As a result, the product of the electronic transition is a vibrationally excited electronic state. To reach the most stable molecular geometry for the excited state, the molecule vibrationally relaxes until the $\nu = 0$ level is reached. This process is known as vibrational cooling. In some cases, the electron density distribution of both electronic states is very similar, it is possible to promote a molecule to the lowest vibrational level of the electronic excited state, where no vibrational cooling is observed.

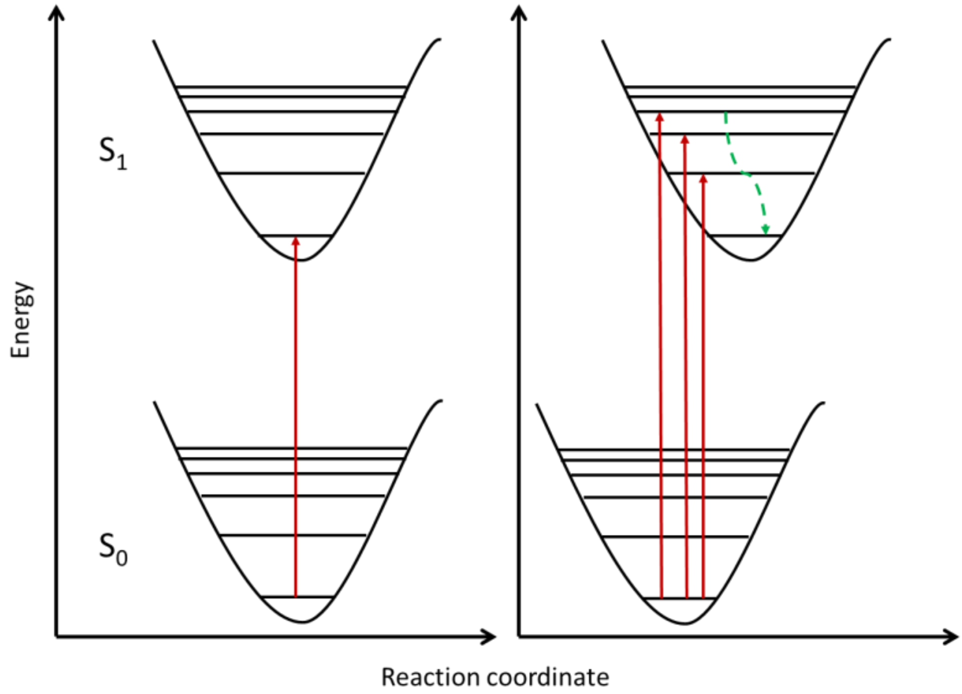

Figure 1.5 – Vertical vibronic transitions enforced by the Frank-Condon principle, shown for a change in equilibrium bond length of x = 0 (left) and x > 0 (right) for a model two-dimensional potential energy surface.

Relaxation of electronic excited states

Once a molecule is in an electronic excited state, there are several possible deactivation processes which allow it to return to the ground state electronic configuration.[11]

Internal conversion (IC) is a non-radiative intramolecular relaxation process which conserves the electron spin (s). For example, a molecule in the second singlet (s = 0, S = 1 {S = 2s+1}) excited state (S_2) could relax to the first singlet excited state (S_1) by IC. This cannot take place between states of different multiplicities. If a molecule is excited to a higher level than S_1, internal conversion from the optically prepared singlet state to S_1 will typically be the first step of the excited state relaxation mechanism. Internal conversion is also possible within other multiplicities, such as conversion between triplet states (e.g. $T_2 \rightarrow T_1$, where s = 1, S = 3).

Fluorescence is the spontaneous emission of a photon during relaxation between states of the same multiplicity (e.g. $S_1 \rightarrow S_0$). Whereas radiative decay between states of different multiplicities (e.g. $T_1 \rightarrow S_0$) is referred to as phosphorescence. These processes can be measured through emission spectroscopy. It is typical that the emitted photons are of lower energy than the absorbed photons, a phenomenon known as Stokes shift. This arises due to the Frank-Condon effect, where the vertical transition from the ν = 0 level of the excited state results in the formation of a vibrationally excited ground state, for example. It is also possible to observe negative Stokes shifts, where the fluorescence wavelength is shorter than the absorption wavelength. This is caused by the absorption of light from a higher vibrational energy level in the ground state than the energy level produced after fluorescence. However, this is a rare occurrence as usually most of the population is in the ν_0 vibrational level under equilibrium conditions at room temperature. Consequently, the vibrational progressions commonly observed in emission spectra correspond to vibrational energy differences in the ground state; whilst vibrational progression in the absorption spectra corresponds to the vibrational energy levels in the excited state.

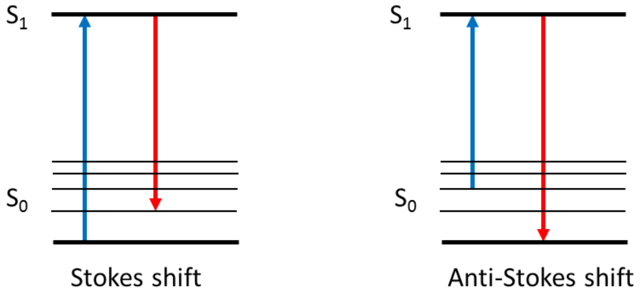

Figure 1.6 – Example Jablonski energy level diagrams showing absorption and emission processes which produce Stokes and anti-Stokes shifts.

It is possible for an excited molecule to convert between states of different multiplicity (e.g. $S_1 \rightarrow T_1$). This process is known as intersystem crossing (ISC), a non-radiative, spin-forbidden transition where an electron in the initial state changes in spin to form the product state.[12] A change in multiplicity during an electronic transition is forbidden by the mutually exclusive electronic and magnetic selection rules for electronic transitions; the Laporte rule states that a change in parity is required, whilst the magnetic selection rule states that the two states must have the same parity before and after the transition. Normally, it is not possible to satisfy both of these conditions – hence ISC is forbidden. However, these spin selection rules can be circumvented through spin-orbit coupling.

Spin-orbit coupling is the interaction of the spin magnetic moment with the magnetic field arising from the orbital angular momentum. These two magnetic moments can be aligned either parallel or perpendicular to one another, resulting in the orbital energy splitting into two further energy levels, one where the electron is spin-up (α) and a second where the electron is spin-down (β). As a result of spin-orbit coupling, the electrons in each orbital no longer have a well-defined spin and the states are no longer pure singlets or triplets, for example. The overall effect of this mixing is that transitions between states of different multiplicities are now weakly allowed. Spin-orbit coupling is a relativistic effect and is enhanced by the presence of atoms in the molecule with large numbers of electrons, such as the transition metals. This 'heavy-atom effect' enables interconversion of singlets and triplets in transition metal complexes, but not in organic compounds containing only light elements.

ISC also is facilitated by the manifold of vibrational levels associated with the singlet and triplet states, as an overlap in the vibrational wavefunctions of the singlet and triplet is required to allow ISC to take place. The degree of overlap between these wavefunctions is also a factor in determining the rate of a non-radiative transition, such as ISC or IC. This overlap is inversely proportional to the energy spacing between the initial and final energy levels. Therefore, the closer the singlet and triplet excited states are in energy, the greater the rate of ISC will be. This is an example of the 'energy gap law', where the rate of radiationless interconversion of two states is enhanced by smaller energy separations. This increased rate of IC or ISC results from the greater wavefunction overlap integral between initial and final states with small energy separations, which is known as the Franck-Condon factor.[13]

Photochemical processes

Excited states can also be deactivated by photochemical processes, such as photolysis of the chromophore, electron transfer, or emission quenching (Figure 1.7). There are three general laws of photochemistry which can be used to predict the outcome of these light-driven processes.[12,14]

- Grotthuss-Draper Law – only absorbed light can initiate a photochemical reaction.
- Stark-Einstein Law – only one molecule is activated by one absorbed photon.
- Kasha's rule – Due to the slow rate of emission compared to internal conversion, the emissive energy level of a given multiplicity is typically the lowest excited level of that multiplicity.

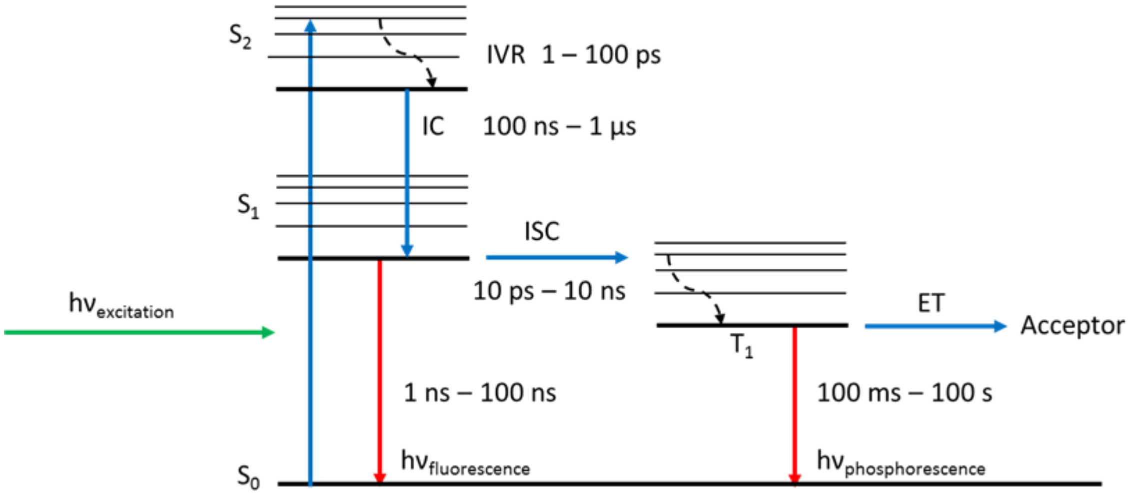

Figure 1.7 – A summary of the deactivation processes for electronic excited states. Example lifetimes are given for the photophysical processes.[15]

Emission quenching

The transfer of an electron from an emissive excited state species to a donor molecule results in a decrease in the emission quantum yield. This is known as emission quenching and is relevant to studies of photochemical CO_2 reduction, where the photocatalyst or photosensitiser are quenched during each electron transfer step of the catalytic reaction. Quenching is a process that leads to a reduction in the excited state population of a molecule, this is normally intermolecular, but in some cases a chromophore can self-quench through intramolecular processes. There are two mechanisms for emission quenching: static and dynamic (Figure 1.8). Static quenching takes place in the ground state, where the quencher forms a complex with the chromophore. This changes the absorption properties of the chromophore, preventing it from reaching the emissive state. Static quenching is not useful for photocatalytic CO_2 reduction. Dynamic quenching is an excited state process where the electronically excited molecule interacts with the quencher, becoming deactivated in the process. This interaction can be done through either electron transfer, or energy transfer.

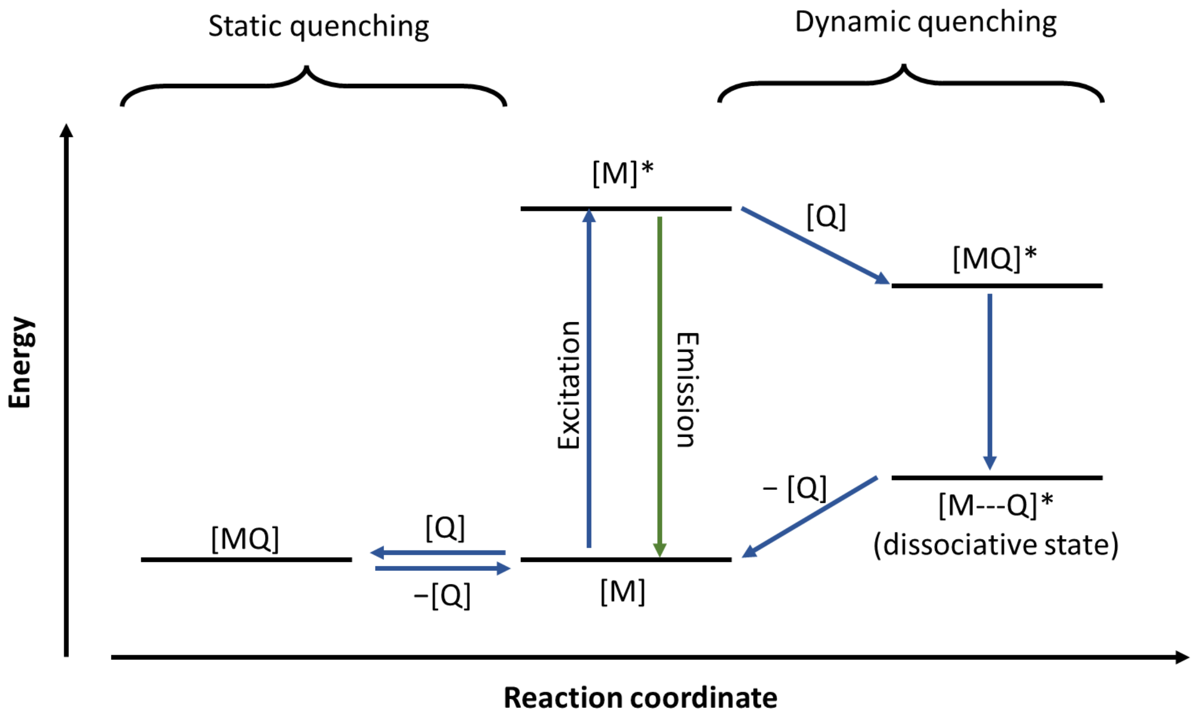

Figure 1.8 – Energy level diagram for intermolecular static and dynamic quenching of an emissive molecule (M) by a quencher (Q).

Emission quenching can be quantitatively studied with the Stern-Volmer relationship (Eq. 1.15, 1.16). In the Stern-Volmer equation, I_0 is the emission intensity in the absence of any quencher, I is the emission intensity, K_s is the equilibrium constant for interaction of the emissive molecule and the quencher in the ground state, [Q] is the quencher concentration, τ_0 is the excited state lifetime of the emissive molecule in the absence of quencher, τ is the excited state lifetime, and k_q is the rate constant for the excited state quenching reaction (Figure 1.9).

If an emissive molecule undergoes static quenching only, then a linear relationship between I_0/I and [Q] (Eq 1.15) is expected, where increasing the quencher concentration results in a decrease in emission intensity. In this situation, no change in the excited state lifetime is expected, hence the plot of τ_0/τ (Eq. 1.16) will have a gradient of 1. If the emissive molecule undergoes only dynamic quenching, both Stern-Volmer relationships (Eq 1.15, 1.16) would have linear gradients. Therefore, the Stern-Volmer equation can be used to distinguish if the emissive molecule undergoes static or dynamic quenching. If both quenching mechanisms are available, the relationship of τ_0/τ (Eq. 1.16) with [Q] is unchanged compared to pure dynamic quenching, as the static quenching contribution has no effect on the observed emission lifetime. Thus, this Stern-Volmer plot can still be used to obtain k_q. However, the relationship of I_0/I with [Q] is now non-linear, and a quadratic dependence of [Q] on the emission intensity is observed (Eq. 1.17).

$$\frac{I_0}{I} = 1 + K_s[Q] \qquad \text{Eq. 1.15}$$

$$\frac{\tau_0}{\tau} = 1 + \tau_0 k_q[Q] \qquad \text{Eq. 1.16}$$

$$\frac{I_0}{I} = (1 + K_s[Q])(1 + \tau_0 k_q[Q]) \qquad \text{Eq. 1.17}$$

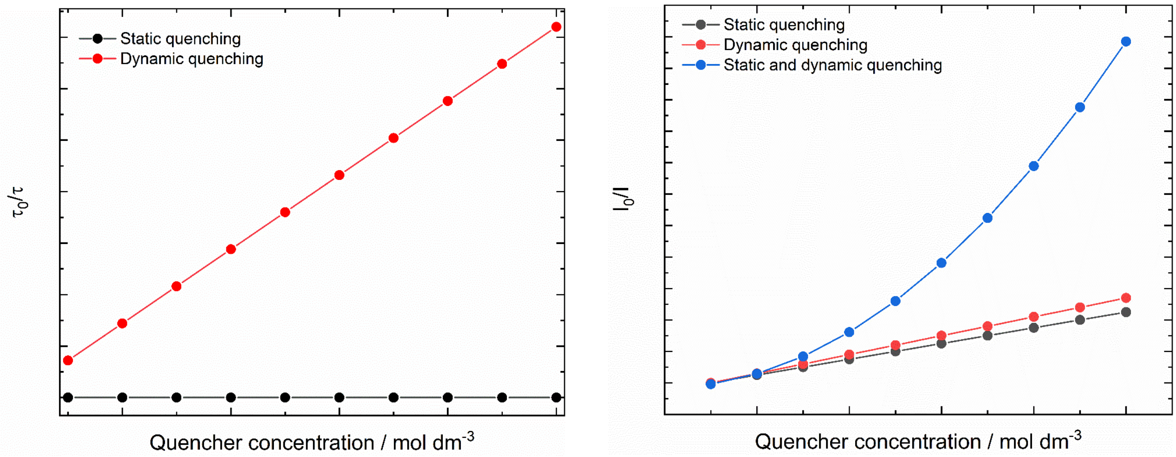

Figure 1.9 – Example Stern - Volmer plots for static and dynamic quenching of emission.

In static quenching, the lifetime of the analyte is not changed whilst emission intensity is reduced. However, dynamic quenching processes lead to changes in both the emission intensity and the excited state lifetime. The Stern-Volmer equation (Eq 1.15, 1.16) allows the quenching mechanisms to be characterised. In the plot of I_0/I *vs.* [Q], a linear gradient indicates static or dynamic quenching is occurring, and a non-linear gradient indicates both static and dynamic quenching are taking place. In the plot of τ_0/τ *vs.* [Q], the quenching mechanisms be individually identified – where a gradient of zero indicates static quenching and a linear gradient indicates dynamic quenching. There are two dynamic quenching mechanisms relevant to CO_2 reduction catalysis, oxidative and reductive quenching. Both mechanisms are suitable for photosensitisation of a catalyst and the mechanism a photosensitiser-catalyst system will undergo is dependent on the redox potentials of the photosensitiser, sacrificial donor, and catalyst.

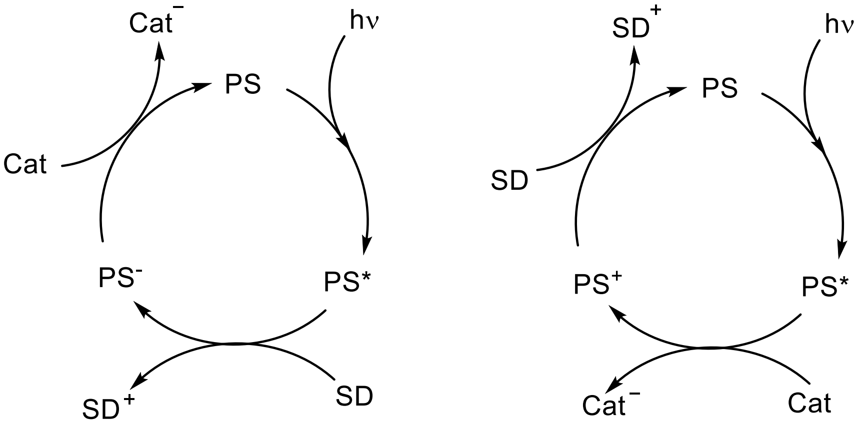

Figure 1.10 – Reaction cycles for reductive (left) and oxidative (right) quenching (PS – photosensitiser; SD – sacrificial donor; Cat – catalyst).

Photoinduced electron transfer

A key step in any photosynthetic system is electron transfer. The product of which is a charge-separated state that performs the oxidative and reductive catalytic reactions. It is for this reason that the study of electron transfer is of great importance to the fields of artificial photosynthesis, solar fuels, and photocatalysis. For a catalytic system to perform as required it is imperative that the initial electron transfer is fast and efficient, and that back-electron transfer to reform the initial state of the system is minimised. The rate constant of electron transfer can be calculated from the Arrhenius equation (Eq. 1.18). Here, k_{et} is the rate of electron transfer, A is the Arrhenius pre-exponential factor, $\Delta G^‡$ is the Gibbs energy of activation, R is the gas constant and T is the system temperature.

$$k_{et} = Ae^{-\frac{\Delta G^‡}{RT}} \quad \text{Eq. 1.18}$$

This equation shows that k_{et} is dependent on the Gibbs energy of activation, hence any effects that lead to changes in $\Delta G^‡$ will result in changes in the rate of electron transfer. For example, solvent effects can significantly influence $\Delta G^‡$. For example, polar solvents will stabilise the anion and cation formed following an electron transfer, reducing the activation energy. Conversely, non-polar solvents such as hexane have no ability to stabilise the charges. In this case the activation energy is likely too high for charge-separated state formation. Whilst the value $\Delta G^‡$ is difficult to calculate, the thermodynamic Gibbs free energy of electron transfer can be estimated with the Rehm-Weller equation (Eq. 1.19). This uses the electrochemical redox potentials of the electron donor (D) and acceptor (A) as well as the $\nu_0 - \nu_0$ emission energy (E_{00}) of the chromophore to determine ΔG_{et}. The value of E_{00} can be determined experimentally by recording the emission spectrum of the chromophore at 77 K, where vibrational excitation in the ground state is minimised. The coulombic attraction term is often assumed to be zero for systems where the donor and acceptor are initially neutral (e – elementary charge; ξ – electrical permittivity of vacuum; d – distance between anionic and cationic charges).

$$\Delta G_{et} = E^{\frac{1}{2}}(D/D^{+}) - E^{\frac{1}{2}}(A/A^{-}) - E_{00} - \frac{e^2}{\xi d} \qquad \text{Eq. 1.19}$$

1.3 The dynamics of vibrational excited states

Infrared (IR) light can be used to produce vibrational excited states if the IR light is resonant with a vibrational transition. As with electronic transitions, vibrational transitions are also subject to selection rules. Firstly, the vibration must involve a change in transition dipole moment. For example, symmetric molecules such as H_2 do not have ‘IR-active’ vibrational modes, whilst asymmetric molecules such as HCl do. Secondly, the vibrational transition must involve an integer change in vibrational quantum number (ν, $\Delta\nu = \pm1, \pm2, \ldots$). The ν_0-ν_1 transition is known as the fundamental vibration, and higher $\Delta\nu$ transitions correspond to overtone vibrations, where the intensity of the absorption band decreases as $\Delta\nu$ increases. For non-linear polyatomic molecules, there are 3N-6 normal vibrational modes, where N is the number of atoms. Each normal mode is comprised of local modes, such as the stretching of an individual bond, and is associated with a vibrational wavefunction, each contributing to the total vibrational wavefunction. There are multiple types of normal mode, common forms are symmetric and antisymmetric stretching modes, as well as bending modes. Combination modes are also possible, for example simultaneous bending and stretching motions. These combination bands are observed at the sum frequency between the two contributing normal modes. Example vibrational transitions for the fundamental, overtone, and combination transitions of two coupled vibrational modes are shown in Figure 1.11.

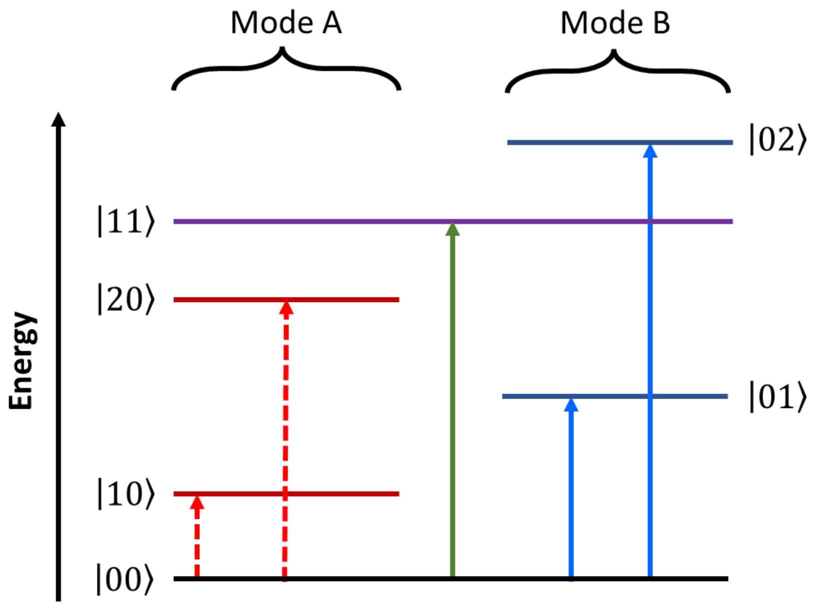

Figure 1.11 – Energy level diagram for two coupled molecular vibrations, illustrating the fundamental (00 → 01), overtone (00 → 20) and combination (00 → 11)) transitions for a system with two coupled vibrational modes. The numbers in bra-ket notation give the vibrational quanta for the excited states, where the left number refers to mode A and the right number refers to mode B. For example, |10⟩ is the product of the fundamental transition of A following a single excitation.

Vibrational energy redistribution

The vibrational dynamics of artificial photosynthetic systems is a fundamental, yet important, aspect of study into photocatalytic reactions, as molecular vibrations have been shown to influence excited state relaxation dynamics of transition metal complexes.[16] Therefore, a detailed understanding of how vibrational modes interact with each other, and with electronic excited states is required. Several of the excited state relaxation processes described above rely on these vibronic coupling interactions. For example, ISC is facilitated by vibronic coupling between the triplet and singlet energy levels, and IC occurs by relaxation of an electronic excited state through the vibrational energy levels of the complex. Absorption and emission also involve the vibrational energy levels of the ground and excited states, as evidenced by the Frank-Condon effect. Vibronic coupling interactions have been used to manipulate electron transfer, which demonstrates the strong influence that molecular vibrations have over the charge separation processes required for artificial photosynthesis.[17–24] Typically, there are three mechanisms of vibrational energy redistribution available to polyatomic molecules in solution.[25–28] The terminology for the relaxation processes used in this thesis is defined below.

(i) Intramolecular vibrational relaxation (IVR)

IVR takes place following the relaxation of a vibrationally excited state to low frequency modes ($\nu < 1000$ cm^{-1}) of the molecule. This energy then cascades through the low-frequency modes in a through-bond process from the initially perturbed group to the terminal ends of the molecule.[29,30] The rate of IVR is dependent on the frequencies and distribution of the low-frequency modes in the molecule under study.[31,32]

(ii) Intra- and intermolecular vibrational energy transfer (VET).

VET is a through space or through bond transfer of vibrational population between modes. VET processes between functional groups can be solvent assisted in the condensed phase. Intermolecular VET from the excited molecule to the continuum of low-frequency solvent modes is typically the final step in vibrational relaxation of a molecule in the condensed phase.[31] This rate of VET is highly dependent on the system temperature as well as the anharmonic coupling strength between the solute and solvent modes.[33,34] VET to the solvent returns the excited molecule to the vibrational ground state, the vibrational energy is then dissipated by the solvent, which acts as a thermal bath.

(iii) Coherent dynamic processes, such as coherence transfer, quantum beating, and coherence-to-population transfer.

Vibrational excitation with a short laser pulse can result in the formation of an oscillating quantum superposition of states, known as a vibrational coherence. The coherence oscillates with a sine function, where the ensemble of molecules which are excited initially oscillate synchronously, creating a macroscopic polarisation (P(t)) within the sample (Eq. 1.20). In this equation c_0 and c_1 are coefficients which give the probability a molecule will be found in ν_0 or ν_1, μ_{01} is the transition dipole moment for the transition, ω_0 is the frequency of the vibrational transition, and t is the time delay between measurement and excitation.

$$P(t) = c_0 c_1 \cdot \mu_{01} \cdot \sin(\omega_0 t) \qquad \text{Eq. 1.20}$$

As the molecules which have formed coherences oscillate, an infrared light field is emitted. Over time, the macroscopic polarisation resulting from coherences is lost by dephasing, where the oscillations of the individual molecules become out of phase as a result of fluctuations in their local environment.[35] The coherent oscillations of the individual molecules are damped over time, a process known as decoherence. In certain cases, a coherence can be transferred between two modes which are mutually coupled by a low-frequency bath mode. This allows for the transfer of vibrational energy between modes. Previously, coherent oscillations have been used to characterise the coherence transfer processes between high-frequency modes, including transfer to dark excited states.[36–41]

These vibrational energy redistribution mechanisms are mediated by the coupling interactions of the vibrational modes. An important interaction is anharmonic coupling, which arises from the interaction of at least two vibrational modes. As a result of this coupling interaction, excitation of one of the modes results in changes to the vibrational transition energy of the coupled mode(s). This induces a response of the other modes within the molecule, which can be measured by 2DIR spectroscopy (see section 1.4). Under the harmonic approximation, such anharmonic coupling interactions are not possible.

Electrical and mechanical effects also contribute to vibrational coupling, which result from the motion of the atoms involved in the vibration. In electrical coupling effects, such as dipole-dipole interactions, the displacement of atomic δ^+ and δ^- partial charges induces motion of neighbouring atoms and groups due to the electrostatic interactions between them. Mechanical coupling effects are similar, where the motion of atoms and groups during a vibration induces motion of neighbouring groups through the covalent bond framework of the molecules.

1.4 Experimental techniques for the study of ultrafast dynamics

To study the excited state and vibrational dynamics of coordination complexes, high time-resolutions are required to adequately measure the ultrafast photophysical processes. This is achieved through the use of pulsed laser spectroscopies. A key technique utilising pulsed lasers is pump-probe spectroscopy, where a narrowband excitation (pump) pulse is used to form an initial ‘optically prepared’ excited state. A broadband probe pulse is then used to monitor the spectral changes in the sample as the excited state relaxes back to the ground state. As the pump and probe pulses are synchronised by the laser system, the pump – probe time delay is introduced with an optical delay stage of variable path length. The optical delay stage can be introduced into the path of either the pump or probe pulses.

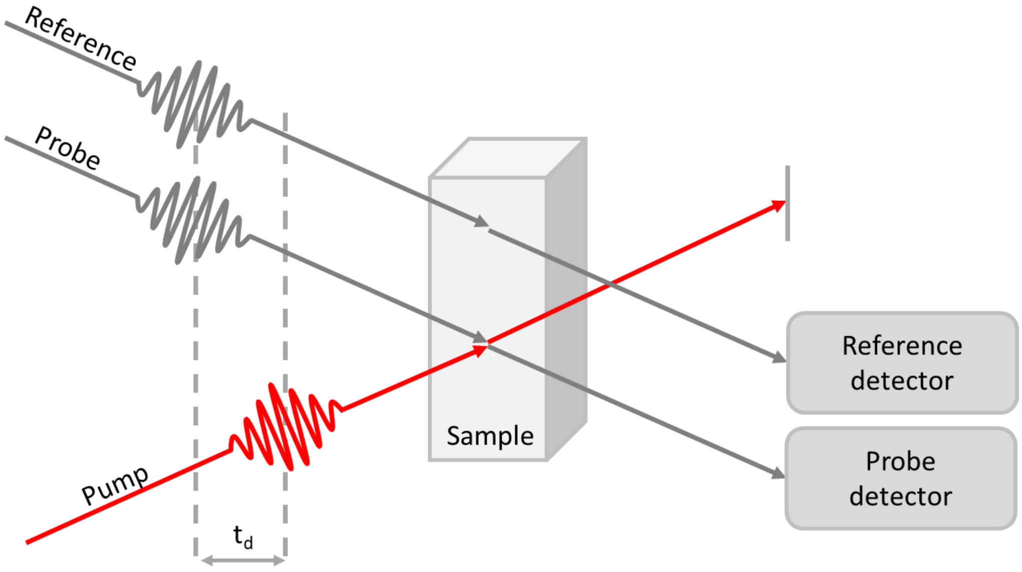

Figure 1.12 – Example beam geometry of a referenced pump – probe transient absorption measurement at the sample position (t_d: pump – probe/reference time delay)

In a pump-probe measurement, the repetition rate of the narrowband excitation pulses is reduced to half of the repetition rate of the probe with an optical chopper. This results in a pump on / pump off pulse sequence, which allows for recording of the probe pulse with and without the excitation pulse. These 'pump on' and 'pump off' spectra are then used to calculate differential absorption (ΔA) spectra (Eq. 1.19). The data reported herein are exclusively differential absorption spectra, where excited state transient absorption bands have positive intensity, and ground state bleaches have negative intensity.

$$\Delta A = -\log\left(I^{Probe}_{(Pump\ on)} \div I^{Probe}_{(Pump\ off)}\right) \qquad \text{Eq. 1.21}$$

In pump – probe spectroscopy, the delay time is scanned through three regions. At 'negative time', the probe pulse arrives at the sample before the pump pulse. Therefore, no differential absorption signal is observed. As the time delay is scanned from negative to positive time, the pump pulse approaches the probe until a point at which they are simultaneously passing through the sample. Here, grow-in of the transient signal is observed during the 'instrument response'. The length of the instrument response function (IRF) in time is given by convolution of the pump and probe pulse lengths. A typical IRF for femtosecond transient absorption spectroscopy utilising 40 fs pulses is 150 fs. The delay time at which 50% of the maximum signal intensity is observed during this grow in is defined as 'time zero'. After time zero, the pump – probe delay increases to 'positive time' and relaxation of the excited state is observed.

The signal-to-noise ratio is often a limiting factor in pump – probe spectroscopy. This can be improved by increasing the sample concentration or increasing the excitation power. However, for very weak transient signals a reference pulse can be used to improve the signal-to-noise. A reference pulse is a copy of the broadband probe, often produced with a 50% beamsplitter, that is not overlapped with the pump pulse. The reference pulse is used to calculate a second ΔA spectrum, which in the absence of noise will not deviate from the spectral baseline. If there are changes in the ΔA spectrum which are not attributed to the pump, these will be observed in both the probe and reference spectra. Therefore, these undesirable deviations can be corrected out of the data, improving the signal-to-noise ratio during the calculation of the ΔA spectra. An example beam geometry of a referenced pump – probe spectrometer at the sample position is shown in Figure 1.12.

Pump – probe spectroscopies are typically defined by the region of the electromagnetic spectrum the pump and probe fall within. The relevant examples for this thesis are:

- Transient absorption (TA)

  UV-vis pump (267 – 800 nm), UV-vis-NIR probe (340 – 1500 nm)

- Time-resolved infrared (TRIR)

  UV-vis pump (267 – 800 nm), mid-IR probe (4000 – 1000 cm^{-1})

- Frequency domain two-dimensional infrared (FD-2DIR)

  Narrow-band mid-IR pump (4000 – 1000 cm^{-1}), mid-IR probe (4000 – 1000 cm^{-1})

- Time domain two-dimensional infrared (TD-2DIR)

  Broad-band mid-IR pump (4000 – 1000 cm^{-1}), mid-IR probe (4000 – 1000 cm^{-1})

TA and TRIR spectroscopies are used to monitor the relaxation of electronic excited states following visible light excitation. The spectrum of the ground state species is 'bleached' following excitation and is observed as a negative ΔA signal. The transient species are observed as positive ΔA signals. The change in the ΔA spectra with increasing delay time report on how the optically prepared excited state relaxes to the ground state.

2DIR spectroscopy in the frequency domain (FD-2DIR), also known as pump – probe 2DIR, utilises a narrow-band IR pulse to selectively excite a vibrational transition. A broad-band probe pulse is then used to measure the transient spectrum with increasing delay time, analogous to transient absorption spectroscopy. This technique reports on the relaxation of vibrational excited states. In 2DIR spectra the vibrational modes of the ground state which are perturbed following IR excitation are bleached. This bleach is overlapped with stimulated emission from the vibrational excited state to the ground state. Each of these modes has a corresponding transient absorption band shifted to higher frequency. The difference in centre frequency between the transient and bleach is defined as the anharmonic shift (Δ). In transition metal complexes, the anharmonic shift is typically small (10 – 30 cm^{-1}), hence 2DIR signals are observed as transient/bleach peak pairs. The transient absorption frequencies and anharmonicities contain information on vibrational coupling within the complex, and the change in the 2DIR spectrum over time provides the vibrational relaxation mechanism. In principle, the structure of the analyte complex can be determined from these vibrational coupling interactions, however this is very difficult to achieve in practice.

More complex three-pulse sequences can be used for specialised experiments, for example 2DIR spectroscopy can be done following visible light excitation. These excited state 2DIR (ES-2DIR) measurements allow for interrogation of the vibrational properties of electronic excited states. In three pulse ES-2DIR experiments, with a probe/reference repetition rate of 10 kHz, the IR pump is chopped to 5 kHz and the visible pump is chopped to 2.5 kHz. As a result, it is possible to simultaneously collect ground state 2DIR (GS-2DIR), TRIR, and excited state (ES-2DIR) ΔA spectra (Figure 1.13).

Note that the reverse arrangement, where the IR pump is chopped to 2.5 kHz, and the UV pump is chopped to 5 kHz is also possible and can be used for the collection of the same data.

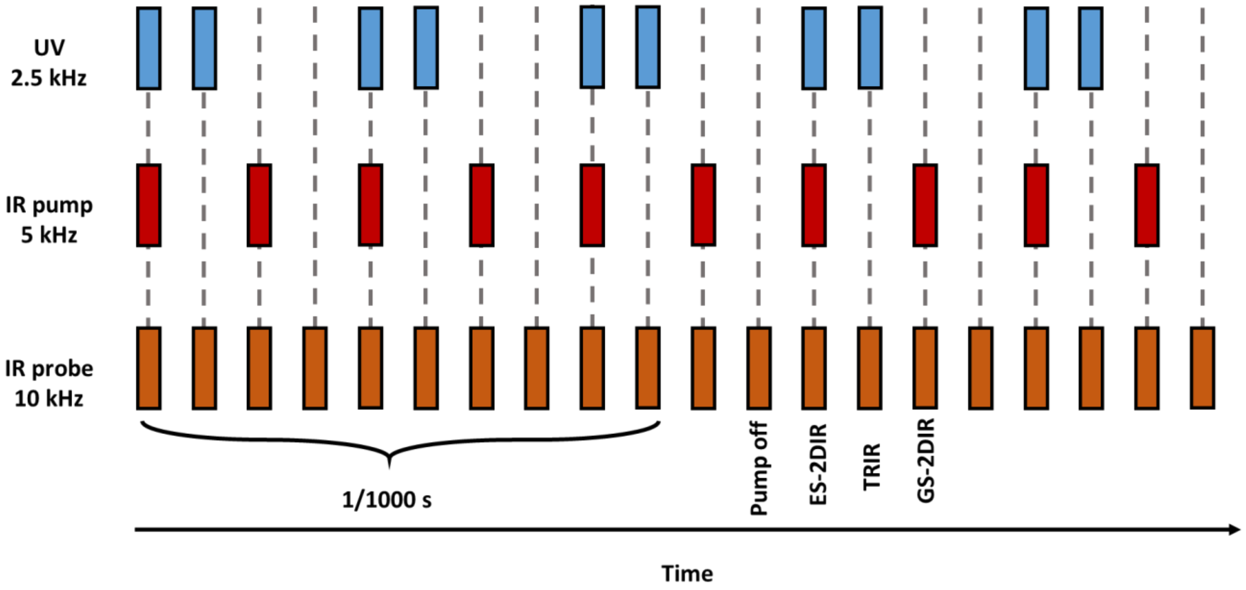

Figure 1.13 – Pulse sequences obtained by optical chopping of an electronic excitation pulse to 2.5 kHz and a mid-IR excitation pulse to 5 kHz with a 10 kHz probe pulse.

The time resolution of pump – probe 2DIR spectroscopy is limited by the requirements of the IR pump, which must be sufficiently narrowband to allow for selective excitation of a single vibration. As a result of the Heisenberg uncertainty principle the smaller the spectral FWHM of the pump pulse, the greater the temporal FWHM will be, and *vice versa*. For example, an IR pump with a 15 cm^{-1} spectral FWHM has a temporal FWHM greater than 1 ps. As such, the IR pump significantly limits the time resolution of GS-2DIR and ES-2DIR pump – probe measurements, especially in experiments utilising probe pulses with a temporal FWHM under 100 fs. To overcome the time resolution limits of FD-2DIR, we can instead utilise third order 2DIR spectroscopy, also known as Fourier transform or time domain 2DIR (TD-2DIR). Time domain 2DIR uses two broadband excitation pulses separated by a variable time delay which is scanned during the measurement (Figure 1.14). After the two pump pulses, a broadband probe pulse is used to monitor the spectral changes after excitation. The two pump pulses can be produced by a beamsplitter, in which case the t_1 delay is created by an additional optical delay line. Alternatively, the double pump can be produced by a mid-IR pulse shaper, where the t_1 delay is electronically controlled with the pulse shaper. The broadband pump pulses allow for a very short temporal FWHM, resulting in large improvements in time resolution compared to FD-2DIR.

Figure 1.14 – Pulse sequences for pump – probe frequency domain (left) and time domain 2DIR (right).

The three pulses have specific roles in producing the desired third-order signal (Figure 1.15). As the first pulse passes through the sample, vibrational coherences are created between the vibrational ground state (ν_0) and the first vibrational excited state (ν_1) for all modes which are resonant with the broadband IR pump. These oscillating coherences generate a macroscopic polarisation, resulting in the emission of an oscillating electromagnetic field. This field decays over time as the coherences undergo dephasing and decoherence. The second excitation pulse is separated by a variable time delay (t_1), this pulse converts the coherences produced by the first pulse into vibrational population states. Depending on the value of t_1, the coherences will be converted to either a ν_0 or a ν_1 population. Hence t_1 is scanned during the measurement to produce different combinations of states. The probe pulse is separated by a second variable time delay (t_2), known as the population time, and interacts with the ν_0 and ν_1 populations to produce new quantum coherences between ν_0-ν_1 and ν_1-ν_2. A second electromagnetic field is emitted by these oscillating coherences which contains the desired third order 2DIR signal.

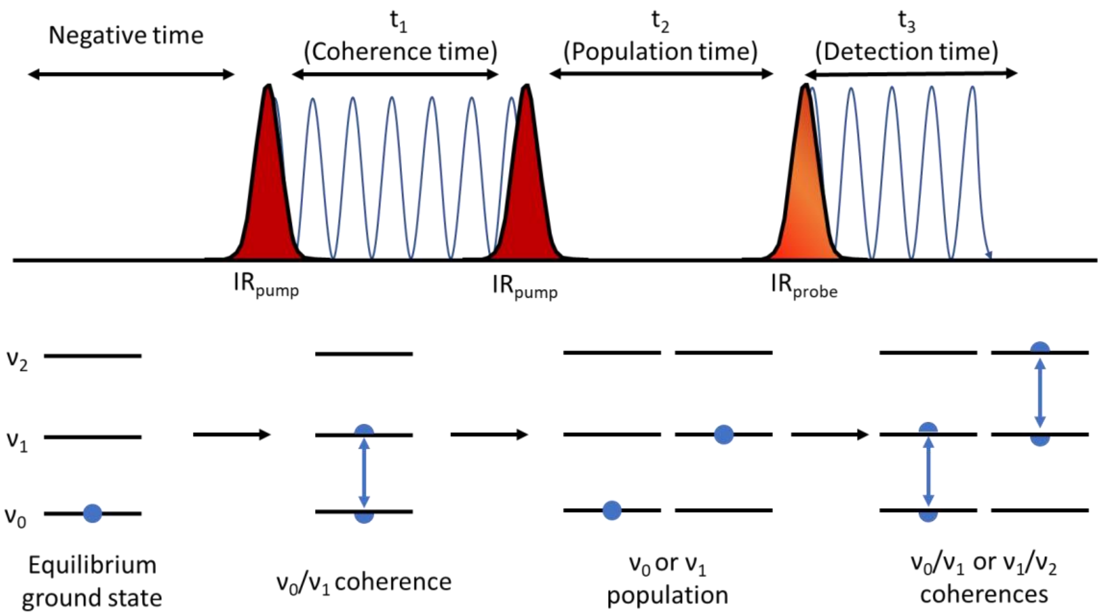

Figure 1.15 – Illustration of the time domain 2DIR pulse sequence for the partially colinear geometry, showing the coherence, population, and detection time periods, as well as the vibrationally excited coherence and population states produced by the IR pump and probe pulses.

The collection of the emitted signal field is either done with a heterodyne or homodyne technique. In homodyne detection the signal field constructively and deconstructively interferes with the probe pulse that created the quantum coherences. A liquid nitrogen cooled MCT detector is then used to record the probe spectrum and calculation of the ΔA spectra provides the third-order signal. In a heterodyne detection system, the emitted signal field is directly recorded with the MCT detector. However, this field only contains amplitude data, to obtain the phase component of the signal, a fourth 'local oscillator' pulse, typically an 800 nm pulse sourced from the laser system, is used. The local oscillator pulse interferes with the emitted signal field at the detector, providing the heterodyned 2DIR signal. The local oscillator pulse is separated by a third time delay, the detection time (t_3). Heterodyne detection is required in the BOXCARS beam geometry commonly used for TD-2DIR, where the emitted signal field is not emitted co-linearly with the probe pulse (Figure 1.16). In contrast, the partially co-linear pump – probe geometry naturally provides homodyne detection, eliminating the need for a local oscillator pulse. The simplicity of the partially-colinear beam geometry does not allow for more advanced data acquisition techniques, such as the separate recording of non-rephasing and rephasing components of the third order 2DIR signal. Use of a pulse shaper to produce the 1st and 2nd pump pulses enforces the partially-colinear beam geometry, and only absorptive 2DIR spectra can be recorded as a result. Furthermore, homodyne detection means that t_3 is always zero, further limiting the experiments that can be run.

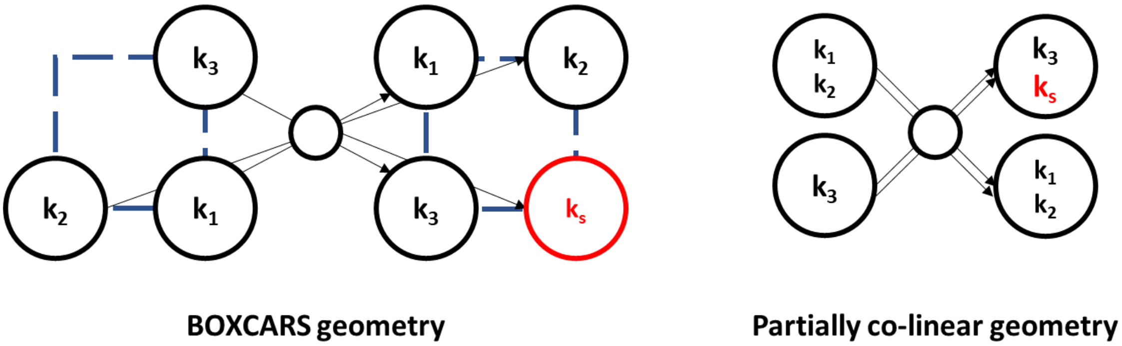

Figure 1.16 – BOXCARS (left) and pump – probe (right) beam geometries at the sample positions for time-domain 2DIR experiments (k_1: 1st pump vector, k_2: 2nd pump vector, k_3: probe vector, k_s: emitted signal vector).

At a particular value of t_2, the third order 2DIR signal is a function of t_1 and probe frequency. A cross-section of the data along t_1 contains a free induction decay, Fourier transformation of which then provides the oscillation frequency of the v_0-v_1 and v_1-v_2 coherences produced by the probe pulse (Figure 1.17). Therefore, the Fourier spectrum provides the frequencies of the vibrational modes which respond to different pump energies. If the Fourier transformation is applied to every probe frequency, a contour map is produced as a function of pump frequency and probe frequency. In this contour map diagonal signals where $\nu_{pump} = \nu_{probe}$ represent the self-response of a vibrational mode after excitation. Off-diagonal signals where $\nu_{pump} \neq \nu_{probe}$ correspond to the response of non-resonant vibrations to excitation of the mode(s) resonant with the pump frequency (Figure 1.17). The diagonal anharmonic shifts (Δ_{ii}) for 2DIR self-response signals are typically larger than the off-diagonal anharmonic shifts (Δ_{ij}) of cross-peaks. The magnitude of Δ_{ii} is a measure of the anharmonicity of the vibrational potential energy surface for the pumped mode. The magnitude of Δ_{ij} is a measure of the coupling strength between the diagonal and off-diagonal mode.

TD:2DIR can be also adapted for specific purposes. One example is the study of long-range vibrational coupling interactions in a 'relaxation-assisted 2DIR' experiment.[42] This can been used to study the role of low-frequency modes in vibrational energy redistribution following ultrafast relaxation of a coupled high frequency mode.[31,43]

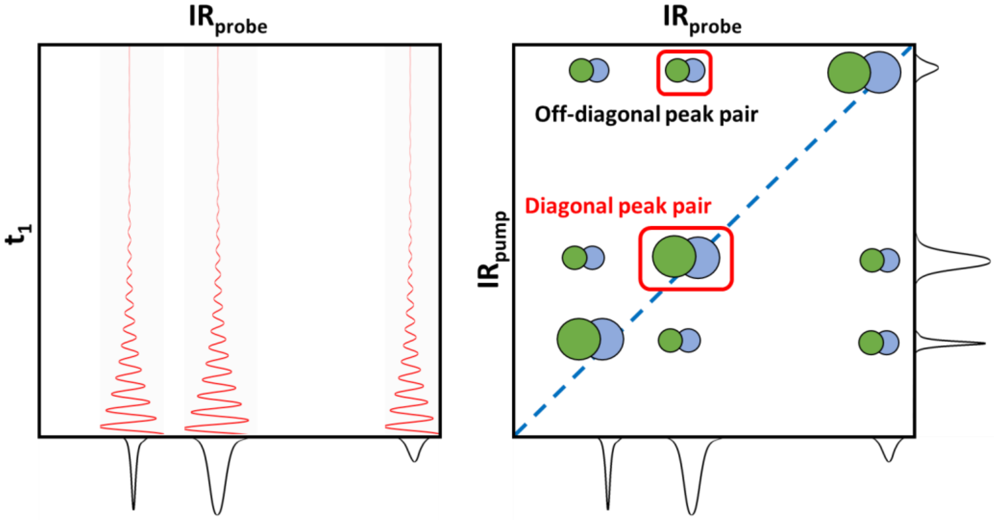

Figure 1.17 – Representative diagrams of the time domain (left) and frequency domain (right) data obtained after Fourier transformation over t_1. Examples of diagonal and off-diagonal signals are highlighted, example FTIR spectra are shown along the pump and probe axes.

In TD-2DIR, the pump resolution is often less than the FWHM of a vibrational lineshape, a typical value is 2 cm^{-1}. Therefore, at $t_2 = 0$ ps, only a subset of the microstates which comprise the vibrational lineshape are excited (Figure 1.18). The result of this is the self-response peak pair is elongated along the diagonal axis. As t_2 increases, the excited molecules re-sample their available frequency space through conformational changes (rotation, torsional motion) as well as rearrangement of the surrounding solvent molecules. This causes the 2DIR lineshape to change from elliptical to circular, a process known as spectral diffusion. During spectral diffusion the 2DIR line shape is dependent on the pump frequency, this correlation becomes weaker over time as the frequency fluctuations scramble the excited population amongst the vibrational microstates, such that when the process is complete the 2DIR line shape no longer has any dependence on the pump frequency. This process is attributed to the frequency-frequency correlation function (FFCF), which reports on the rate of spectral diffusion (Eq. 1.22).

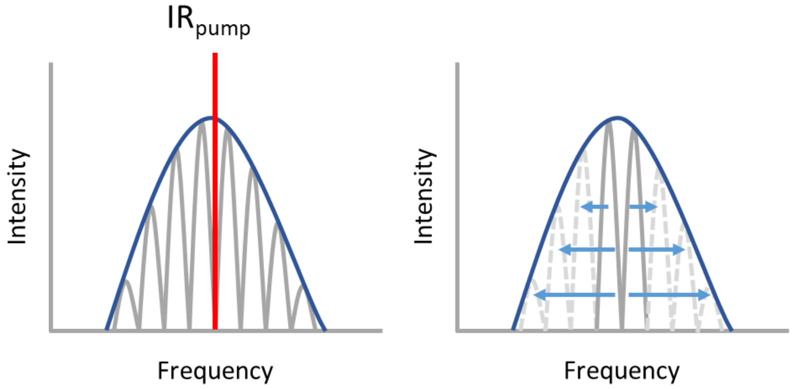

Figure 1.18 – Representation of excitation of a subset of the available frequencies of a molecule in solution, and subsequent spectral diffusion as the molecule resamples its available configurations.

The FFCF can be obtained from the TD-2DIR data in two ways, either following the change in the gradient of the nodal plane between the $\nu_{1\text{-}2}$ and $\nu_{0\text{-}1}$ bands or following the change in ellipticity of either the $\nu_{1\text{-}2}$ or $\nu_{0\text{-}1}$ bands, both of which approach zero as spectral diffusion occurs.[44] The resulting plot of nodal plane gradient or ellipticity against population time approximates the FFCF and gives information about the correlation of the 2DIR line shape with the pump frequency. The FFCF can be fit with an exponential function (Eq. 1.21) to obtain the fluctuation amplitude ($\Delta\omega^2$) and the correlation time (τ_c), which reveal the magnitude and timescale of the frequency fluctuations. Typically, these functions are biexponential with an inertial component (*ca.* 100 fs), and a slower diffusive component on the picosecond timescale. The inertial component is often not detectable by TD-2DIR due to convolution with the IRF. This causes the FFCF to begin below 1.0 at time zero, after the majority of the inertial spectral diffusion has taken place.

$$FFCF = \langle \delta\omega(t)\delta\omega(0)\rangle = \Delta\omega^2 \cdot e^{-\frac{t}{\tau_c}} \qquad \text{Eq. 1.22}$$

1.5 Kinetic and spectral analysis of time-resolved data

Analysis of time resolved spectroscopy data is done with the objective of proposing a kinetic mechanism for the excited state relaxation of the analyte complex. This analysis is typically done in stages, the first of which is single-point exponential fitting, which allows for measurement of the time constants for the grow in or decay of the transient signal at a single wavelength. These time constants provide a foundation for the development of a global analysis model. The second foundation for global analysis is obtained through deconvolution of the time-resolved spectra at select pump – probe delay times. This deconvolution is typically done with pseudo-Voigt profiles, a convolution of a Lorentzian and a Gaussian function that is well suited for fitting UV-vis and IR absorption spectra.

This deconvolution allows for identification of individual absorption bands and is especially useful in congested spectra where multiple bands are overlapped. If each spectrum is deconvoluted in this way, a plot of peak area against pump – probe delay time gives the pure kinetic trace for that absorption band.

Whilst spectral deconvolution by peak fitting is an effective method of obtaining the grow in and decay time constants of individual absorption bands, it is a time intensive process. Global lifetime analysis (GLA) presents an alternative option for deconvolution of time-resolved data. GLA software typically uses singular value decomposition (SVD) to identify the key kinetic components in a time-resolved dataset. The kinetic components are then used to construct a simultaneous or sequential kinetic model from first order differential rate equations. Additional components are added to the kinetic model to account for the IRF and group velocity dispersion within the time-resolved data, improving the accuracy of the GLA results. Initial values for the kinetic rate constants are input and then simultaneously fit to every kinetic trace in the dataset, the value of the rate constants is then optimised by least squares analysis.[45]

GLA links these rate constants to the spectral features of the time-resolved dataset. This is done by plotting the exponential amplitude of the fit data for each kinetic trace against the wavelength that trace corresponds to – this plot is known as a decay associated spectrum (DAS). The DAS shows which spectral features grow in or decay with a particular rate constant. Positive amplitude in the DAS indicates decay of the transient signal, negative amplitude shows growth of the transient signal. GLA also outputs evolution associated spectra (EAS). Unlike the DAS, the EAS are affected by the kinetic mechanism input into the GLA parameters, and each EAS represents the transient spectrum of a kinetic component. If the input mechanism is accurate, then the EAS become species associated spectra (SAS), which are the true transient spectra of each excited state species.[45]

GLA is a robust and powerful method of analysing time-resolved data, although it does have limitations. For example, the necessity of enforcing a kinetic mechanism on the fitting procedure can result in undesirable errors in the obtained rate constants and DAS/EAS if that mechanism does not adequately describe the data. Furthermore, the global fitting algorithm often cannot model complex excited state dynamics involving equilibria, branching states, or manifolds of states. In these situations, lifetime density analysis (LDA) can be a viable alternative option.[46] LDA is not reliant on a kinetic mechanism, and instead fits a distribution of time constants to the data. The DAS for each time constant in the distribution is then calculated. To distinguish these spectra from the DAS obtained by GLA or global target analysis (GTA) they are herein referred to as lifetime density traces (LDT). The LDTs are commonly assembled into a contour map to visualise the data in an effective manner. The LDA maps can be interpreted to suggest a kinetic mechanism for the excited state dynamics, which can then be tested through global target analysis (GTA) models. Further details on the mathematical background to LDA will not be discussed further here and are available in the literature.[47]

Global target analysis is a more specific form of GLA, where a pre-determined kinetic model is applied to the time resolved data. GTA models are typically more complex than the simultaneous or sequential mechanisms used in GLA, often containing branch points or equilibria. GTA outputs the same data as GLA; rate constants, DAS, EAS, and SAS.

1.6 A review of Re and Mn molecular catalysts bearing diimine ligands for electro- and photochemical CO_2 reduction

A previous version of section 1.6 was published as part of the following book chapter, the following text was written entirely by J.D.S.

Simon C. Parker, Andrew J. Sadler, James D. Shipp, and Julia A. Weinstein, "*Photochemical reduction of* CO_2 *with metal-based systems*" in "*Transformations Vol. 2*", De Gruyter, 2019, ISBN: 9783110665147, DOI: 10.1515/9783110665147-030.

The selected CO_2 reduction catalysts for study in this thesis are Mn and Re Lehn-type catalysts, which have the general structure $[M(L_2)(CO)_3X]$, where M = Mn or Re, L_2 is a diimine chelate ligand, and X is a halide or pseudohalide. This review summarises the key developments in the field of CO_2 reduction with Mn and Re catalysts, providing the background for the research project.

Rhenium catalysts

The earliest artificial CO_2 reduction catalysts were developed by Lehn *et al*. These 'Lehn-type' catalysts were Re diimine tricarbonyl halides, such as $[Re(bpy)(CO)_3Cl]$ (bpy = 2,2′-bipyridine). These complexes are prepared from $[Re(CO)_5Cl]$ by ligand substitution; as such, they are easily modifiable by altering the diimine ligand (Figure 1.19). The synthesis is simple, fast, and selective, hence is suitable for large-scale preparative chemistry. Lehn demonstrated the ability of $[Re(bpy)(CO)_3Cl]$ to reduce CO_2 to CO following electron transfer from a $[Ru(bpy)_3]^{2+}$ photosensitiser following broadband white light irradiation.[48] It was later discovered that direct excitation of the catalyst led to catalytic activity, eliminating the need for the photosensitiser.[49] In these catalytic reactions, the electrons were ultimately supplied by sacrificial donors, such as triethylamine (TEA) or triethanolamine (TEOA).

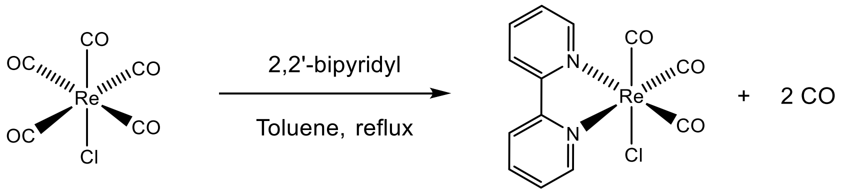

Figure 1.19 – The synthesis of [Re(bpy)(CO)$_3$Cl] from [Re(CO)$_5$Cl] and 2,2'-bipyridine.

CO_2 reduction with Lehn-type catalysts can also be initiated by electrochemical methods. The reduction of CO_2 to form CO and $^{-}CO_2H$ was performed by CPE of [Re(bpy)(CO)$_3$Cl] at −1.12 V *vs.* NHE.[50] It was initially proposed that an equatorial carbonyl ligand dissociates from the reduced complex to allow the coordination of carbon dioxide. The coordinated CO_2 ligand is then converted into CO and H_2O by reaction with two equivalents of H^+. However, it was later discovered that it is not the carbonyl ligand that dissociates from the complex, it is the halide. This was determined through infrared-spectroelectrochemical (IR-SEC) analysis of the [Re(bpy)(CO)$_3$Cl] reduction processes.[51]

It is now accepted that the active catalyst is [Re(bpy)(CO)$_3$]$^-$, which forms following two-electron reduction of [Re(bpy)(CO)$_3$Cl] (Figure 1.20), coordinates to CO_2 to initiate the catalytic cycle. In the presence of a coordinating solvent, such as MeCN, the vacant coordination site is transiently occupied by solvent molecules until either CO_2 or the free halide coordinates to the Re centre.[52] Alternate active catalyst formation mechanisms involving [Re(L$_2$)(CO)$_3$]$_2$ have also been proposed. However, these are less thermodynamically favourable due to instability of the neutral five-coordinate Re species required for dimerisation.[53,54]

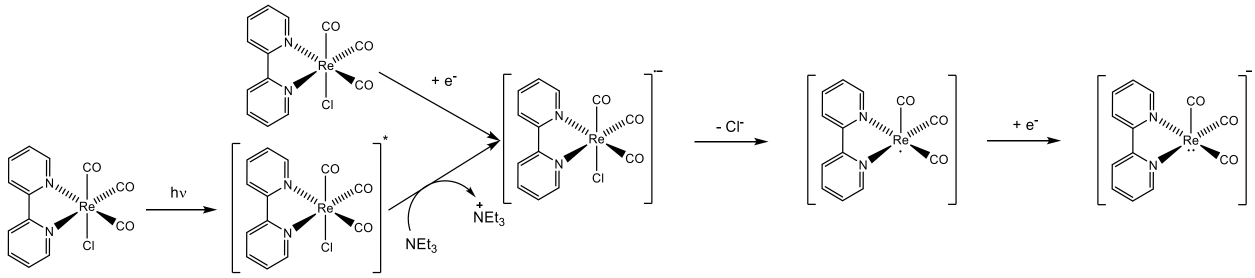

Figure 1.20 – A possible mechanism of [Re(bpy)(CO)$_3$]$^-$ formation, following electrochemical or photochemical reduction in the presence of TEA.

The mechanism for CO_2 reduction with Re Lehn-catalysts is still under study. The catalytic cycle is generally accepted to start from the coordination of CO_2 and then proceed by protonation of [Re(L$_2$)(CO)$_3$(CO$_2$)]$^-$ to form [Re(L$_2$)(CO)$_3$(CO$_2$H)]. A second protonation then results in the elimination of H_2O to produce [Re(L$_2$)(CO)$_4$]$^+$. The active catalyst is then reformed upon reduction of this complex, liberating CO as the product.[55,56] This mechanism is known as the 'protonation first' pathway. A 'reduction first' pathway is also possible, where [Re(L$_2$)(CO)$_3$(CO$_2$H)] is first reduced, and then protonated. In this mechanism the final intermediate is a neutral tetracarbonyl complex,

$[Re(L_2)(CO)_4]$.[57] In both mechanisms, the rate limiting step of catalysis is the protonation/H_2O elimination reaction.[58] This is in agreement with the widely reported finding that the rate of CO_2 reduction catalysis with Re Lehn-type catalysts is enhanced by addition of a weak Brønsted acid, such as water.[59] In non-sterically hindered catalysts, dimeric intermediates where two Re centres are bridged by a CO_2 ligand are also proposed intermediates in the catalytic cycle.[60,61] Re hydride intermediates, which undergo CO_2 insertion into the R-H bond to form Re-CO_2H, have also been suggested.[62] Computational studies have supported the role of Re-H complexes in the CO_2 to $^{-}CO_2H$ reduction mechanism.[63]

Since their discovery, there has been significant interest in the development of novel Re Lehn-type complexes. New catalysts with functionalised bipyridyl ligands have been proven to be effective CO_2 reduction catalysts. This functionalisation allows for adaptation and optimisation of the Lehn-type catalyst for a particular purpose. For example, 4,4′-dipyrenyl-2,2′-bipyridine been used to enhance visible light absorption of the complex, thus improving the photocatalytic performance.[64] Other light-harvesting moieties have been covalently bound to the diimine ligand for the same purpose, such as anthracene,[65] ruthenium complexes,[66] porphyrins,[67] and napthalimide.[68] Covalent binding to the Re centre is desirable as the rate of electron transfer from chromophore to catalyst is much faster than diffusion controlled intermolecular electron transfer. However, facile back-electron transfer from the reduced catalyst to the oxidised sensitiser is a problem. In a napthalimide/Re dyad, this back electron transfer has been prevented by introducing an anthracene electron acceptor between the chromophore and the catalyst in a molecular triad (Figure 1.21).[69,70]

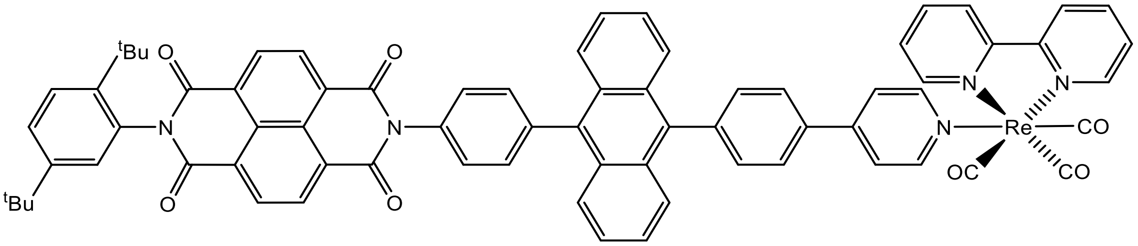

Figure 1.21 – The [NDI-anthracene-Re(bpy)(CO)$_3$] triad used for intramolecular photosensitisation of a CO_2 reduction catalyst.[69]

Incorporation of groups which change the electron density of the bipyridyl ligand is also common. This results in changes to the redox potentials, required overpotential, and catalytic performance.[71] For example, the addition of tertiary butyl groups to the bipyridyl 4,4′-positions was found to increase the selectivity for CO_2 reduction over proton reduction.[58] In some cases, changes to the electron density of the bipyridyl ligand can alter the catalytic mechanism or render the catalyst unstable.[59]

Functional groups which can interact with the catalytic reaction are also used. For example, hydrogen bond donor groups, such as arylamines, have been added to the 6,6′-position of the bipyridyl ring. This was found to enhance the TOF and lower the overpotential required for electrocatalytic CO_2 reduction.[72] It has also been shown that the presence of hydrogen bond donor groups, such as aniline groups to the 6,6′-positions of the bipyridyl ring, can increase the Faradaic efficiency of electrocatalysis.[73] The mechanism for this increase in catalytic performance has been attributed to hydrogen bond formation between the Ar-NH_2 group and the oxygen atom of coordinated CO_2. However, this functionalisation can adversely affect catalytic performance if the amine group is close enough to the metal centre to form a coordination bond. These secondary sphere amine groups can also alter the selectivity for CO or $^{-}CO_2H$ formation following two-electron CO_2 reduction.[74] Proton responsive groups can also act as a 'proton relay' to promote the rate of catalysis.[73] This has been demonstrated for bipyridyl catalysts with pendant amino acid chains,[75] as well as simpler functional groups such as amines, alcohols, carboxylic acids, and phosphonates. The magnitude of this effect is dependent on the pK_a and position of the proton responsive group relative to the metal centre.[76] These groups facilitate the required protonation steps of the catalytic cycle by increasing the effective H^+ concentration at the catalyst active site, promoting the rate of catalysis.

Functional group addition can also be used to modify the solubility of a CO_2 reducing complex. For example, hydroxymethyl groups have been used to solubilise an Re catalyst in water, allowing for CO_2 reduction in an aqueous electrochemical cell.[77] It is also possible to replace the bipyridyl ligand with other chelate ligands, such as 1,10′-phenanthroline, N-heterocyclic carbenes (NHCs),[78] meso-ionic carbenes (MICs),[79] imidazolates,[80] and terpyridyls.[81] An additional example which is particularly relevant for chapter 4 of this thesis is the use of bis(arylimino)acenaphthene (Ar-BIAN) ligands, where [Re(Ar-BIAN)$(CO)_3$Cl] has strong visible light absorption up to 600 nm and good electrocatalytic activity.[82]

Bimetallic complexes, where two Re centres are present in the same molecule have also been reported as active CO_2 reduction catalysts. For example, two [Re(bpy)$(CO)_3$Cl] centres have been covalently bound to a xanthene bridge. It was found that the two metal centres cooperate to enhance the catalytic rate; one Re centre acted as a photosensitiser whilst the other performed the catalytic reaction. This cooperativity was evidenced by a significantly higher TOF for the bimetallic complex compared to [Re(bpy)$(CO)_3$Cl] in DMF.[83] Dinuclear Re complexes have also been incorporated into carbon nanotube electrode surfaces. This hybrid catalyst was able to reduce CO_2 and H_2O to syngas. However problems with desorption of the catalyst in organic solution were reported during catalysis.[84]

Re Lehn-type catalysts have almost exclusively been shown to form either CO and/or $^{-}CO_2H$ as CO_2 reduction products with high selectivity. Whilst this selectivity is an advantage, catalysts which can produce more highly reduced products are also desirable. Three Re complexes which are able to perform the eight-electron reduction of CO_2 to form CH_4 have recently been reported.[58] These catalysts incorporate asymmetric diimine ligands such as 2-(isoquinolin-1-yl)-4,5-dihydrooxazole (Figure 1.22), which are able to stabilise the catalytic intermediates through intramolecular interactions. This allowed for further reduction of the axial carbonyl ligand in $[Re(L_2)(CO)_4]$. The ligand also donates a hydride ion during the reduction of CO to CH_4. This work highlighted the key role of the chelate ligand in determining the catalytic activity of the Re catalyst.

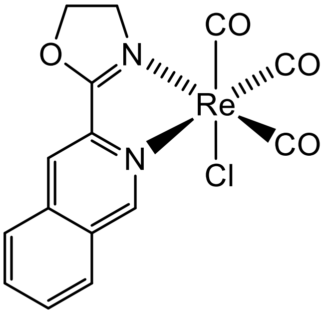

Figure 1.22 – The structure of [Re(2-(isoquinolin-3-yl)-4,5-dihydrooxazole)$(CO)_3Cl$], the first molecular Re catalyst capable of electrochemically reducing CO_2 to CH_4.[58]

To eliminate the need for a sacrificial donor, $[Re(bpy)(CO)_3Cl]$ has been used in conjunction with a water oxidation catalyst, $[Cr(Cp)(CO)_3]$ and a tetraphenylporphyrin zinc(II) chromophore to produce CO with only CO_2 and H_2O as reagents. The three components for this system were carefully selected so that the Zn chromophore was able to reduce the Re catalyst, and then be regenerated by the water oxidation catalyst. This demonstrated that true artificial photosynthetic catalysis is possible in organic solution.[86]

Photophysical studies of Re CO_2 reduction catalysts

The excited state dynamics of $[Re(L_2)(CO)_3Cl]$ catalysts play an important role in light-driven artificial photosynthesis. Numerous studies have been carried out using time-resolved spectroscopy to elucidate the photophysical and photochemical process these Re complexes undergo, and how it could affect their function as catalysts.

The ultrafast dynamics of $[Re(bpy)(CO)_3Cl]$ are well known.[26,87–90] At 400 nm excitation, the pump light is typically resonant with the MLCT transition. The optically prepared ^{1}MLCT excited state undergoes rapid ISC to form a ^{3}MLCT state, which is commonly the lowest energy excited state in the complex. Initially, the triplet states are highly vibrationally excited, and cool to the v_0 level on a 10 – 20 ps timescale concurrently with a shift in the vibrational transient absorption bands to higher frequency.[91] The ^{3}MLCT state relaxes to the equilibrium ground state by phosphorescence with a time constant of 25 ns.[92] At higher excitation energies, other excited states can also play a role in the dynamics, such as intraligand (IL) or ligand field (LF) states.[93]

Replacement or functionalisation of the bipyridyl ligand can have a large effect on the excited state dynamics of the complex.[94] For example, the lowest energy excited state in the dipyridophenazine (dppz) complex, $[Re(dppz)(CO)_3Cl]$, is a triplet intraligand charge transfer (^{3}ILCT) state in equilibrium with a ^{3}MLCT state.[95] More complex ligand functionalisation, such as the introduction of a boron dipyrrin (bodipy) complex covalently bound to the bipyridyl ring, has been found to significantly increase the triplet state lifetime.[96] In some cases, the ILCT states have a larger role in the excited state dynamics than MLCT states. This can result in slower ISC and an increased triplet state lifetime as a result of the smaller influence of the heavy Re centre on the ILCT state.[97] The electron density of the chelate ligand also plays a role in the ^{3}ILCT lifetime. For example, electron withdrawing groups have a stabilising effect on the ^{3}ILCT state, reducing the energy. The decreased separation between the triplet state and the ground state upon functionalisation with an electron withdrawing group can lead to a decreased excited state lifetime, which is a result of the energy gap law.[98]

The charge transfer absorption envelope in the UV-vis spectrum of the Re catalysts is described as having mixed MLCT/XLCT character. As a result, the excited state dynamics are sensitive to the halide ion. It has been demonstrated that exchange of Cl for Br or I in $[Re(L_2)(CO)_3X]$ complexes results in an increase to the triplet state lifetime. This has been attributed to increasing the extent of mixing between the $d_\pi(Re)$ and $p_\pi(X)$ orbitals from Cl > Br > I.[99] TRIR studies of $[Re(L_2)(CO)_3(NCS)]$ (L_2 = 2,2′-bipyridyl or *N,N′*-diisopropyl-1,4-diazabutadiene) also suggested a mixed MLCT/XLCT character of the lowest energy triplet state, which can be visualised as an electron density transfer from the entire $\{Re(CO)_3(NCS)\}$ moiety to the ligand π^* orbital.[100] These studies involving exchange of the halide ligand are potentially relevant to initial photochemical activation of the $[Re(L_2)(CO)_3X]$ pre-catalyst. However, these effects are not relevant to catalytic performance once the active catalyst has formed due to the necessary dissociation of the axial (pseudo)halide.

It is also possible to replace the axial halide with an electron donor or electron acceptor.[93,101,102] In such complexes, a ligand-to-ligand charge transfer (LL′CT) state can form from the ^{3}MLCT state following electron transfer from the diimine ligand to the acceptor. The charge transfer from one ligand to the other is facilitated by electronic coupling of the two ligands through the Re d-orbitals. The formation of LL′CT states is also evidenced by the quenching of ^{3}MLCT emission.[103] Controlled switching between LL′CT and MLCT formation has been demonstrated. This was achieved with an azacrown substituted axial ligand, where the binding of Ba^{2+} to the crown has been shown to switch the preferentially formed excited state from ^{3}LL′CT to ^{3}MLCT.[104]

It has been suggested that molecular vibrations of the complex can play a significant role in promoting the rate of electron transfer between the diimine and axial ligands. This has been demonstrated in [Re(bpy-ester)$(CO)_3$(3-dimethylaminobenzonitrile)] (bpy-ester = 4,4′-diethylester-2,2′-bipyridyl) (Figure 1.23), where IR excitation of the bipyridyl ring stretching modes resulted in significant modulation of the LL′CT formation rate. It was thought that the vibrational relaxation of the bipyridyl ring mode played an important role in this electron transfer rate modulation effect.[19,105] Further exploration of the role of vibrational dynamics in such effects is a key area in the design of molecular complexes where it is possible to control the rate and direction of electron transfer.[106]

The vibrational dynamics of $[Re(L_2)(CO)_3(X)]$ complexes have been well studied by ground and excited state 2DIR spectroscopy. In addition to the three-pulse experiments used to study electron transfer rate modulation, ES-2DIR has been used to definitively assign the ^{3}MLCT transient absorption bands in the mid-IR region.[107] These experiments used a ‘labelling’ pulse sequence which tracks the vibrational modes of the ‘reagent’ and ‘product’ complexes during electronic excitation. Importantly, this study revealed that the frequency order of the a″ and a′(2) modes switches upon electronic excitation. In addition, it was found that the character of the three ν(CO) group vibrations was similar between the ground and ^{3}MLCT states.

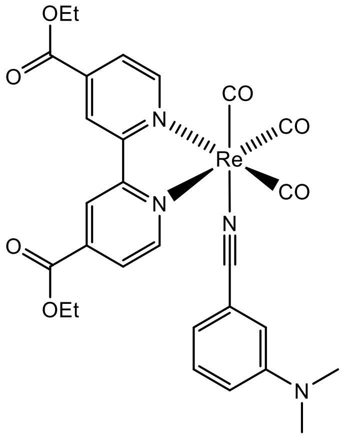

Figure 1.23 – The structure of [Re(bpy-ester)$(CO)_3$(3-dimethylaminobenzonitrile)].[19]

The dynamics of $[Re(L_2)(CO)_3Cl]$ catalysts following IR excitation have been studied by 2DIR spectroscopy. The IVR process for these complexes is assigned to relaxation of the excited ν(CO) vibrations relax to low-frequency modes of the complex. Then, the vibrational energy propagates from the low-frequency modes of the $\{Re(CO)_3Cl\}$ centre to the diimine ligand. Once the vibrational energy is equilibrated within the low-frequency modes of the complex, it is transferred to low-frequency solvent modes, returning the complex to its vibrational ground state. It was found that vibrational energy redistribution in the triplet excited state took place by the same mechanisms, but significantly faster. It was proposed that this rate increase was a result of cationic and anionic charges which form within the ^{3}MLCT excited state.[25] The presence of the charged moieties polarises the solvent molecules around them to a greater extent than the ground state complex. This reduces the ‘dielectric friction’ of the solvent molecules, which has a promoting effect on the rate of intermolecular VET.

The carbonyl group vibrations of $[Re(L_2)(CO)_3Cl]$ catalysts are an excellent probe for study of these vibrational dynamics. For example, an area of interest in recent years has been the effect of electronic excitation and molecular structure on the rate of complex-solvent interactions. To understand these effects, 2DIR spectroscopy has been applied to obtain the rates of spectral diffusion.[108–110] In addition, these spectral diffusion dynamics have been used to identify how molecular geometry fluctuations and dipole moments within the complex affect the vibrational dynamics.[26] Of particular interest to CO_2 reduction, the vibrational dynamics of electrochemically reduced species can be analysed through time-resolved vibrational spectroscopy, providing important insights into the dynamics of the catalytic intermediates through time-resolved 2DIR spectroelectrochemistry.[111]

Manganese catalysts

Whilst Re Lehn catalysts are effective at performing CO_2 reduction, they are not practical for large scale application. Re has an abundance of 0.0026 ppm, with a total industrial production per year of 47.2 tonnes, as such it is one of the rarest elements on Earth. Whilst Re is used in the petroleum industry for the catalytic reforming of naptha, its abundance is not sufficiently high to support multiple industrial processes.[112] Therefore, earth-abundant catalysts are required for CO_2 reduction to be industrially relevant. Applicable elements for this are the first-row transition metals, such as Mn. Due to the ease of synthesis from $[Mn(CO)_5Br]$, and large abundance of Mn (950 ppm), significant research interest has been devoted to Mn Lehn-type catalysts. There are also efforts to develop CO_2 reduction catalysts based on other earth-abundant elements, such as Mo, Ni, Co, and Fe, which have been extensively reviewed elsewhere.[113,114]

Initially perceived to be inactive, $[Mn(bpy)(CO)_3Br]$ was first used to reduce CO_2 to CO by controlled potential electrolysis in 2011. The required overpotential was decreased by 0.40 V compared to the Re analogue, whilst preserving the selectivity for CO over H_2CO_2 and high Faradaic efficiency. A key difference between Re and Mn is that $[Mn(bpy)(CO)_3Br]$ requires the presence of a weak Brønstead acid, such as water, for catalysis to take place.[115] The redox properties of this catalyst were studied by CV and UV-vis spectroelectrochemistry to elucidate the CO_2 reduction mechanism. It was determined that a key intermediate was a Mn-Mn dimer, which forms from the five-coordinate radical anion, $[Mn(bpy)(CO)_3]^{\cdot -}$.

Active catalyst formation from a Mn Lehn-type catalyst is different to Re catalysts (Figure 1.24). After one-electron reduction to form $[Mn(bpy)(CO)_3Br]^{\cdot -}$, the Br^- ligand dissociates to produce $[Mn(bpy)(CO)_3]$. In coordinating solvents, such as MeCN, the solvent will transiently coordinate to the Mn centre. This five-coordinate complex then dimerises, which is generally considered to be an unproductive reactive step. After a second reduction, the Mn-Mn dimer iscleaved to produce one equivalent of the active catalyst, $[Mn(bpy)(CO)_3]^-$.

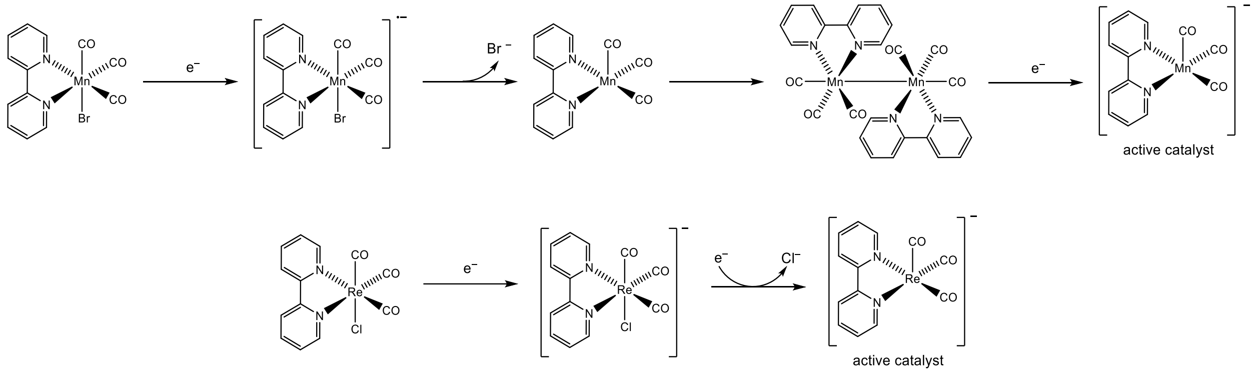

Figure 1.24 – The thermodynamically preferred reduction pathways for $[Re(bpy)(CO)_3Cl]$ and $[Mn(bpy)(CO)_3Br]$ to form the active catalyst, as evidenced by spectroelectrochemical studies. The solvated complexes $[M(L_2)(CO)_3(sol)]$ are not shown.

Whilst both the Re and Mn catalysts can form the M-M dimer, $[Re(bpy)(CO)_3]_2$ is not an active CO_2 reduction catalyst. However $[Mn(bpy)(CO)_3]_2$ has been shown to reduce CO_2 when photosensitised by $[Ru(dmbpy)_3]^{2+}$ (dmbpy = 4,4′-dimethyl-2,2′-bipyridyl).[116] DFT calculations and TRIR experiments have shown that the rate of dimer formation is significantly higher for the Mn species compared to Re, a result of the thermodynamic instability of $[Re(L_2)(CO)_3]^{\cdot -}$.[117]

The CO_2 reduction mechanism with $[Mn(L_2)(CO)_3Br]$ is generally accepted to start from the active catalyst $[Mn(L_2)(CO)_3]^-$ which coordinates to CO_2. The CO_2 ligand is then protonated by the Brønstead acid to form a formate ligand. From this point, two mechanistic pathways are possible. The ‘protonation first’ route involves protonation of the $^-CO_2H$ ligand and subsequent elimination of H_2O to produce $[Mn(L_2)(CO)_4]^+$ (Figure 1.25). This complex then undergoes two successive reductions to reform the active catalyst and eliminate CO as the product.[118] In most Mn catalysts, the tetracarbonyl complexes are unstable, hence it is not possible to reduce the CO ligand to HCOH, MeOH, or CH_4. The second ‘reduction first’ pathway differs in the order of the reaction steps. In this case, the $[M(L_2)(CO)_3(CO_2H)]$ intermediate is first reduced, and then protonated. The subsequent elimination of water produces $[Mn(L_2)(CO)_4]$, which reforms the active catalyst and eliminates CO after one-electron reduction.[119] The ‘reduction first’ pathway is more thermodynamically demanding, requiring more overpotential, hence catalysts which preferentially take the 'protonation first' route are desirable. Functionalisation of the bipyridyl ligand with bis(methoxy)phenyl groups has been shown to increase the preference for 'protonation first' route, lowering the required overpotential for catalytic turnover.[120] The elimination of $^{-}CO_2H$ from $[Mn(L_2)(CO)_3(CO_2H)]$ is the source of the formate product. Any observed preference for formate elimination or CO formation is often a result of the reaction conditions. For example, CO_2 reduction catalysis is often more selective for formate in DMF, and CO in MeCN.

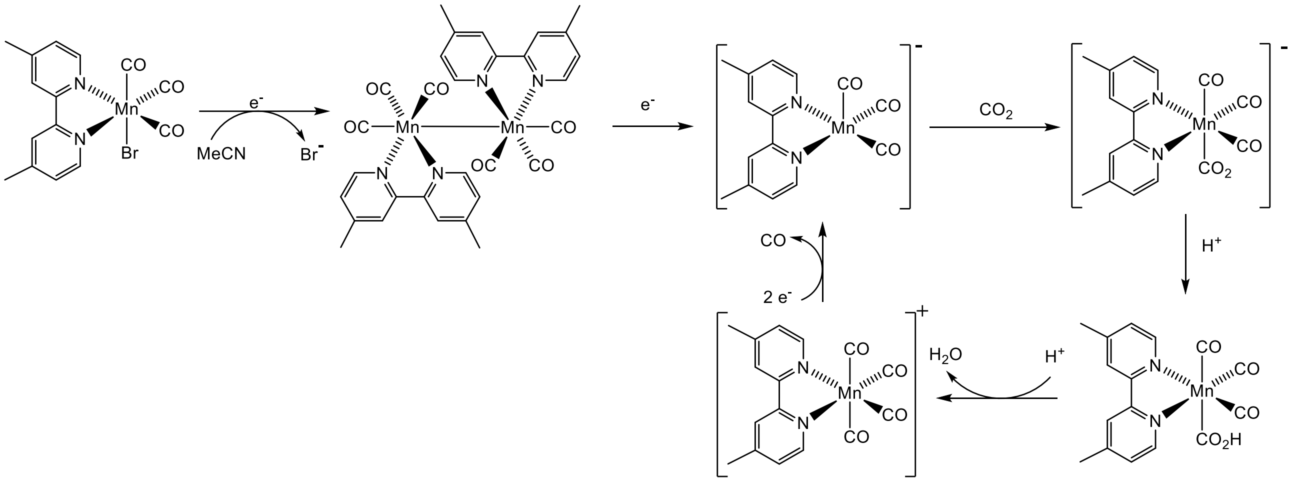

Figure 1.25 – The 'protonation first' CO_2 reduction mechanism with a $[Mn(L_2)(CO)_3Br]$ catalyst.

The reactivity of the pre-catalyst, active catalyst, and catalytic intermediates toward CO_2 is not yet fully understood and advanced spectroscopic techniques are utilised to develop knowledge about the CO_2 reduction mechanism. For example, vibrational sum-frequency generation (VSFG) spectroscopy has been used to study the reactivity of the Mn-Mn dimer at an electrode surface, which revealed that this dimer does interact with CO_2 in the presence of acid at the surface.[121] Another time-resolved spectroscopy technique which has been used to understand the catalytic mechanism is pulse radiolysis coupled with time-resolved infrared spectroscopy (PR-TRIR). PR-TRIR was used to observe all intermediate species in the conversion of the $[Mn(^{t}Bu\text{-}bpy)(CO)_3Br]$ (^{t}Bu-bpy = 4,4′-bis(tertiary-butyl)-2,2′-bipyridyl) pre-catalyst to the active catalyst.[117]

As with Re, a significant number of investigations into Mn Lehn-type catalysts involve the use of substituted diimine ligands.[122] These substituents have been used to alter the electronic and steric properties of the complex. One example is $[Mn(mes\text{-}bpy)(CO)_3Br]$ (mes-bpy = 6,6′-bis(mesityl)-2,2′-bipyridine) (Figure 1.27). The bis(mesityl)bipyridyl ligand is very sterically hindering, which prevented unproductive dimerisation of the five-coordinate anion. As a result, the first and second electrochemical reduction processes merged into a single two-electron reduction peak, as shown by cyclic voltammetry.[123] The active catalyst $[Mn(mes\text{-}bpy)(CO)_3]^{-}$ was formed at 300 mV less overpotential than $[Mn(bpy)(CO)_3]^{-}$. This showed that preventing the dimerisation step significantly reduced the potential required to produce the active catalyst. However, no catalytic activity was observed until an additional 400 mV of overpotential was applied. IR-SEC indicated that this additional overpotential was required to reduce the $[Mn(mes\text{-}bpy)(CO)_3(CO_2H)]$ intermediate. This demonstrated how functionalisation of the bipyridyl ligand can significantly alter the CO_2 reduction catalysis. $[Mn(mes\text{-}bpy)(CO)_3Br]$ was also used to determine the effect of adding Lewis acids to the reaction mixture.[124] The addition of $Mg(OTf)_2$ resulted in the formation of CO and $MgCO_3$ in a reductive disproportionation reaction (Figure 1.26). The Mg^{2+} interacted with the coordinated CO_2 ligand, stabilising the anionic charge on the complex, reducing the required overpotential. This Lewis acid assisted catalysis was studied by DFT calculations to confirm the proposed mechanism and suggest new ligand designs to further reduce the required overpotential.[125]

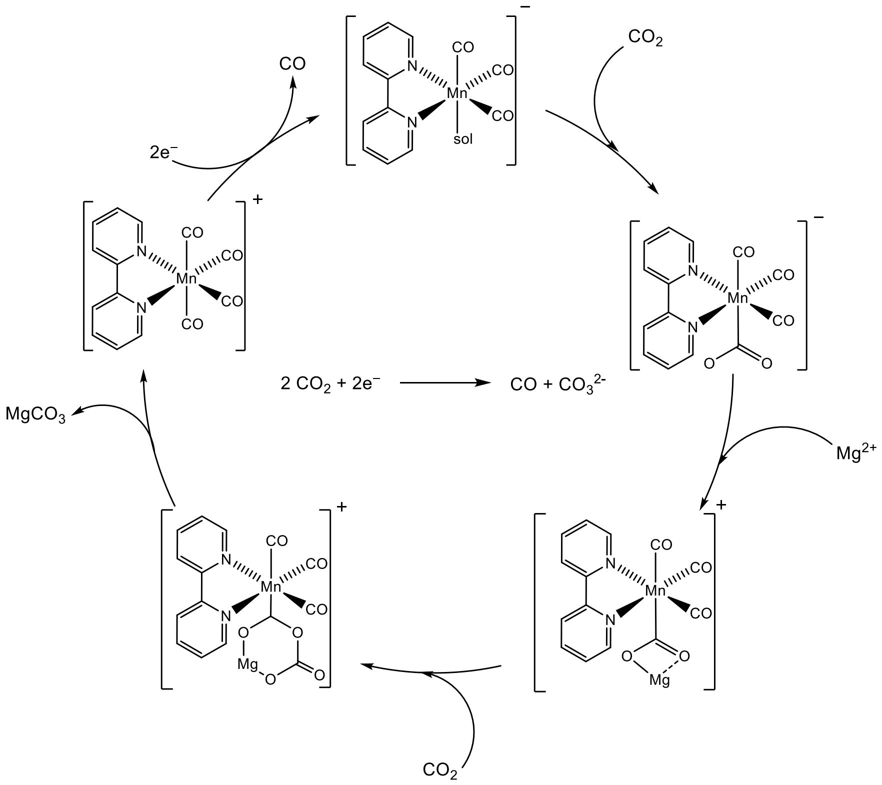

Figure 1.26 – The reductive disproportionation mechanism for CO_2 reduction catalysed by $[Mn(mes\text{-}bpy)(CO)_3Br]$ in the presence of a Lewis acid, $[Mg(OTf)_2]$.

This process is an example of a bimetallic catalytic system where the Mn centre initiates CO_2 reduction, and the Mg^{2+} facilitates C-O bond cleavage. An issue with this system is that the Mg^{2+} cation binds very strongly to the carbonate ion and the magnesium cation is not regenerated. Hence, the $[Mg(OTf)_2]$ acts as a co-substrate in this system, rather than as a co-catalyst.

As with Re Lehn-type catalysts, hydrogen bond donor groups have been incorporated into Mn bipyridyl complexes.[76] Bipyridyl ligands bearing phenol or methoxyphenyl groups were found to form hydrogen bonds with the coordinated CO_2 ligand (Figure 1.27), stabilising the carboxylate complex and facilitating C-O bond cleavage. This resulted in significant catalytic current enhancement for [Mn(6-(o-hydroxyphenyl-2,2′-bipyridyl)(CO)$_3$Br] over [Mn(bpy)(CO)$_3$Br] in CV experiments.[126] Addition of an aniline group to the 6-position of the bipyridyl ring has also been found to significantly enhance the turnover frequency of catalysis with high Faradaic efficiencies and lower required overpotential.[127] The introduction of amine groups into the secondary coordination sphere of a Mn catalyst has also been shown to influence the product selectivity. This effect has a dependence on the relative positions of the amine and the Mn centre. The amine group can also act as a proton relay, assisting the formation of Mn-H complexes. CO_2 can then insert into the metal-hydride bond to produce the $^{-}CO_2H$ ligand.[128]

Asymmetric diimine ligands have also used in Mn Lehn-type catalysts (Figure 1.27). A range of phenylimino-pyridyl (IP) ligands were used to identify how steric and electronic effects can alter the catalytic mechanism. IR-SEC experiments showed that sterically demanding substituents on the IP ligand resulted in the direct formation of the five-coordinate anion [Mn(CO)$_3$(IP)]$^-$, consistent with [Mn(mes-bpy)(CO)$_3$Br]. Whereas less sterically demanding IP ligands allowed for dimerisation to take place. An IP ligand with ‘moderate’ steric bulk and electron density was found to have an intermediate behaviour, where both the anion and the Mn-Mn dimer were detected simultaneously. A repeat of these experiments under CO_2 atmosphere revealed that for most of the complexes the CO_2 coordination outcompetes the dimerisation pathway, and the Mn-Mn dimer was not detected.[129]

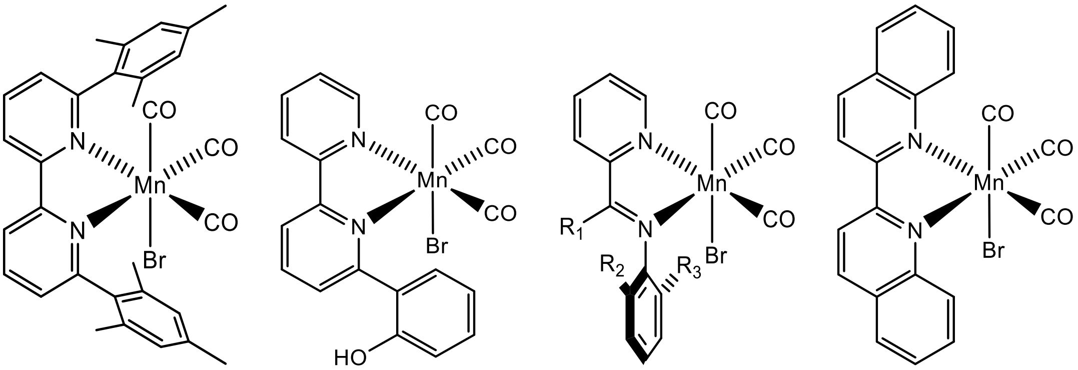

Figure 1.27 – The chemical structures of four reported CO_2 reduction catalysts; [Mn(mes-bpy)(CO)$_3$Br],[124] [Mn(6-(o-hydroxyphenyl-2,2′-bpy)(CO)$_3$Br],[126] [Mn(R,R′-IP)(CO)$_3$Br] (R_1, R_2, R_3¸= H),[129] and [Mn(biq)(CO)$_3$Br].[130]

Other chelate ligands have also been used to prepare Mn CO_2 reduction catalysts. For example, replacement of bipyridine for biquinoline (biq) (Figure 1.27) has been shown to suppress dimerisation of the catalyst and allow for formation of [Mn(biq)(CO)$_3$]$^-$ by a concerted two-electron reduction process, similar to [Mn(mes-bpy)(CO)$_3$Br]. However, this five-coordinate anion was not able to reduce CO_2 and a third reduction was required to form the active catalyst and initiate catalysis.[130] NHC complexes have also been prepared, which are highly effective CO_2 reduction catalysts.[131,132]

Alongside the study of Mn Lehn-type catalysts for electrochemical CO_2 reduction, there are efforts to develop photocatalytic systems. However, this is complicated by the photosensitivity of $[Mn(L_2)(CO)_3(X)]$ complexes. Excitation of the MLCT or XLCT absorption bands results in photolysis of a Mn-CO bond and dissociation of a carbon monoxide ligand. Whilst useful for targeted carbon monoxide therapy,[133,134] this photosensitivity prevents initiation of CO_2 reduction by light absorption. Therefore, if a photosensitiser is used, it must absorb at wavelengths the catalyst does not. The Mn-Br bond can also be photolysed, which results in dimerisation to produce $[Mn(L_2)(CO)_3]_2$. Whilst this could be potentially be used for preparation of the active catalyst by one-electron reduction, it is not possible to control which of the CO or Br ligands will dissociate first. Whilst the photosensitivity of the Mn catalysts is generally undesirable, it has been utilised in CO_2 reduction catalysis. Photolysis of the electrochemically prepared Mn-Mn dimer has been used in a hybrid electro/photochemical catalytic system in place of the second electrochemical reduction. This photolysis results in the homolytic cleavage of the dimer, producing the active catalyst.[135] The photolysis mechanisms of $[Mn(L_2)(CO)_3Br]$ are not fully understood, and further opportunities to utilise visible light absorption in Mn(I) catalysed CO_2 reduction may present themselves in future research.

There are several examples of photochemical CO_2 reduction which utilise photosensitisers such as $[Ru(bpy)_3]^{2+}$, or $[Ru(dmbpy)_3]^{2+}$.[116] However, there is only a single example of a photocatalytic CO_2 reducing system employing only earth-abundant elements, where tetraphenylporphyrin zinc(II) (ZnTPP) was used to photosensitise $[Mn(phen)(CO)_3Br]$ in the presence of a triethylamine sacrificial donor.[136] The porphyrin complex was selected as the Q-bands of ZnTPP are well separated from the XLCT/MLCT absorption bands of $[Mn(phen)(CO)_3Br]$. The proposed mechanism for this catalysis (Figure 1.28) is subtly different from the generally accepted mechanism described above (Figure 1.25). This illustrates the continuing debate over the catalytic mechanism in the literature.

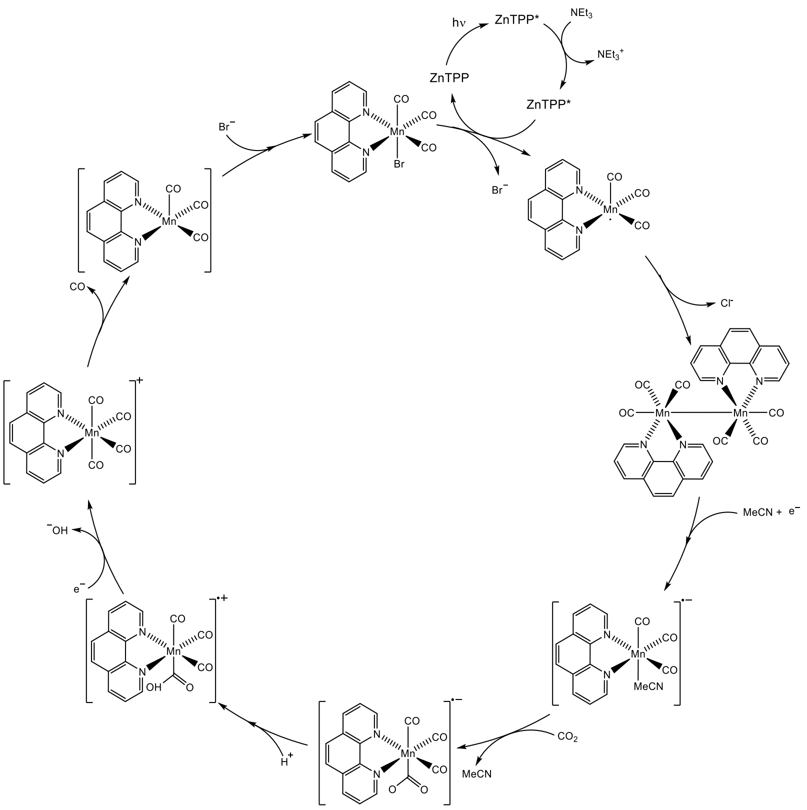

Figure 1.28 – The proposed catalytic cycle for CO_2 to CO reduction catalysed by [Mn(phen)$(CO)_3$Br], which was photosensitised by ZnTPP. Addition of e^- represents electron transfer from the photoreduced Zn porphyrin.

It is possible to substitute the axial halide ligand of a Lehn-catalyst to further functionalise or modify the catalyst and alter its reactivity. For example, Br^- has been replaced with $PhCC^-$, which significantly altered the photochemistry of the complex. [Mn(bpy)$(CO)_3$(CCPh)] does not undergo photolysis and instead a facial to meridional isomerisation takes place.[137]

In another example, the substituted cyanide complex, [Mn(bpy)$(CO)_3$(CN)] was been used for CO_2 reduction when photosensitised by $[Ru(dmbpy)_3]^{2+}$. The Ru photosensitiser was excited with monochromatic 470 nm light for 15 hours, leading to the production of both CO and $^-CO_2H$ by the Mn catalyst. The product selectivity was solvent dependent, with CO as the major product in MeCN and $^-CO_2H$ as the major product in DMF. This solvent dependence was a result of the differing stabilities of the catalytic intermediates in MeCN and DMF.[138] The exchange of Br^- for the CN^- ligand had two key effects on the CO_2 reduction process. Firstly, it removed the XLCT absorption band from the Lehn catalyst absorption spectrum, allowing for a wider range of visible light harvesting. This was advantageous as many photosensitisers do not absorb at wavelengths greater than 500 nm. Secondly, the exchange resulted in a change of reaction mechanism. According to the spectrochemical series, the CN^- ligand is more strongly binding than Br^-. Therefore, axial ligand dissociation is less thermodynamically favourable and more energy is required to remove the ligand. Therefore, upon reduction of the complex, the axial ligand does not immediately dissociate. Instead the active catalyst was generated by disproportionation of two equivalents of $[Mn(bpy)(CO)_3(CN)]^{\bullet-}$ to form $[Mn(bpy)(CO)_3]^-$, $[Mn(bpy)(CO)_3(CN)]$, and free CN^- (Figure 1.29), as determined through CV and IR-SEC analysis.[139]

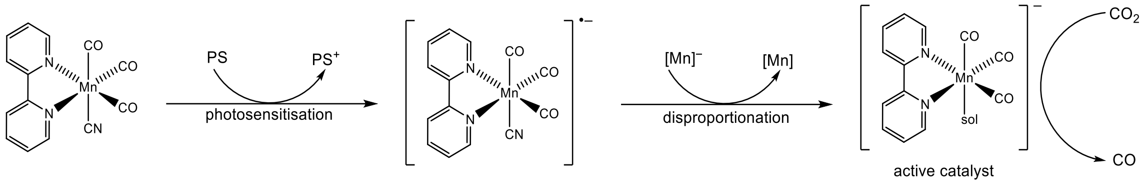

Figure 1.29 – The formation of the active catalyst, $[Mn(bpy)(CO)_3(sol)]^-$, from $[Mn(bpy)(CO)_3(CN)]$.

The cyanide ligand has also been used to prepare a bimetallic bridged complex, $[(OC)_3(L_2)Mn\text{-}CN\text{-}Mn(L_2)(CO)_3]$. Unlike all previously reported Mn(I) diimine catalysts, this complex can reduce CO_2 electrochemically and photochemically. This cyanide-bridged complex is photostable, and reduces CO_2 under 355 nm irradiation, unlike the precursor complexes $[Mn(L_2)(CO)_3(CN)]$ and $[Mn(L_2)(CO)_3Br]$.[140]

To reduce the environmental impact of the process, the development of water-soluble CO_2 reducing catalysts is highly desirable. The sole example of a molecular Mn Lehn-type complex which operates in aqueous solution is $[Mn(bpy\text{-}acid)(CO)_3Br]$ (bpy-acid = 4,4′-biscarboxy-2,2′-bipyridyl).[141,142] This complex was found to produce CO with high selectivity over proton reduction at −1.40 V *vs*. Ag/AgCl in aqueous electrolyte solution. CO_2 reduction in water has additional thermodynamic considerations. For example, the pH of the reaction mixture can influence the value of the reduction potentials, or alter the proton reduction *vs*. CO_2 reduction selectivity.[7] Currently there are no reported molecular $[Mn(L_2)(CO)_3Br]$ catalysts which reduce CO_2 photochemically in aqueous solution.

Typically, Mn catalysts are only capable of reducing CO_2 to CO and $^-CO_2H$, and further reduction has not yet been demonstrated with a $[Mn(L_2)(CO)_3(X)]$ complex. However, there are examples of CO_2 reduction by more than two-electrons with other Mn complexes. For example, Mn P-N-N pincer complexes have been shown to reduce CO_2 to both formate,[143] and methanol.[144] Mn corrole complexes have been able to reduce CO_2 to acetic acid in acidified water (pH 6).[145]

Heterogenisation of molecular catalysts – hybrid catalytic systems

A significant disadvantage of the homogeneous catalysts discussed herein is the difficulty in recovering the catalyst from the reaction mixture. A potential solution to this is attachment of the molecular catalyst to a solid support, electrode surface, or nanoparticle surface to form a hybrid catalyst. The support can be inert or play a role in the reduction, for example, TiO_2 semiconductors could be used as both an electron relay and solid support in a photoelectrochemical cell. The heterogenised catalyst can then be separated from the reaction mixture by filtration or centrifugation. There have been several examples of hybrid catalysts which are formed from binding a molecular catalyst to an inorganic semiconductor. These materials are potentially good photosensitisers as they can absorb light to promote an electron to the conduction band, which can then be donated to a molecular catalyst. This section provides a non-comprehensive overview of heterogenisation methods which are applicable for CO_2 reduction catalysis.

There are many options for the semiconductive material, such as metal oxides (TiO_2, ZrO_2), metal sulphides (cadmium sulphide, CdS), and carbon-based materials such as graphene and its derivatives.[146] The selection of the semiconductive material is key to ensuring the hybrid catalyst is stable under irradiation, able to absorb a sufficiently wide range of wavelengths, and is able to efficiently transfer electrons from the conduction band to the catalyst.[147] The catalyst must also be strongly bound to the semiconductor, preferably through covalent linkage. This minimises leaching of the catalyst into solution, which results in a decrease in catalytic activity over subsequent reactions. An example of a suitable covalent linkage is through a triazole ring, prepared by an alkyne-nitrile cycloaddition reaction between nitrile groups on the surface, and an ethynyl group on the catalyst.[148]

Mn Lehn catalysts have been photosensitised in this manner. For example, the phosphonate acid functionalised catalyst $[Mn(4,4'\text{-bis}[\{HO\}_2OPCH_2]_2\text{-}2,2'\text{-bipyridyl})(CO)_3Br]$ was immobilised on a mesoporous TiO_2 electrode and utilised for electrochemical CO_2 reduction.[149] It is not possible to use TiO_2 to photosensitise the Mn catalyst, as the required irradiation wavelength (*ca.* 350 nm) would lead to catalyst photolysis. Instead, a photoanode, such as CdS, can be added to the system to act as a chromophore. The excited electrons are then transferred to the TiO_2 through a circuit to be injected into the catalyst.[150] Immobilisation of a Mn catalyst in this manner can also prevent dimerisation of the complex if the surface concentration is sufficiently low.

The semiconductive material does not have to be a bulk solid, it is possible to bind molecular catalysts to nanoparticles and quantum dots (Figure 1.30).[151–153] Systems such as these act in a similar fashion to a chromophore-catalyst dyad, where the nanomaterial chromophore is regenerated by a sacrificial donor after the electron transfer is complete. This approach has been demonstrated with other types of earth-abundant catalyst, such as $[Ni(terpy)_2]^{2+}$ and $[Ni(cyclam)]^{2+}$ (Figure 1.30).

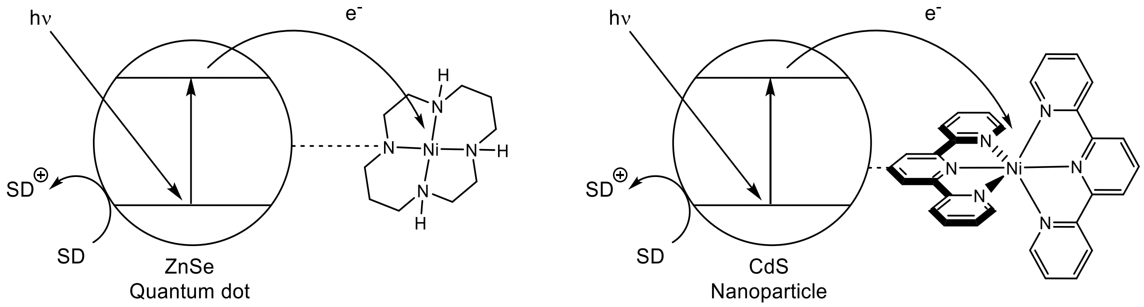

Figure 1.30 – The photosensitisation of a CO_2 reducing electrocatalyst with a nanoparticle or quantum dot (SD: sacrificial donor).

Carbon based electrodes, such as functionalised graphene, have also been used as photosensitisers and electrodes. For example, Re catalysts have also been bound to colloidal nanographene.[154] Graphitic carbon nitride (gC_3N_4) is also a common solid support which can also act as a photosensitiser. For example, gC_3N_4 has been used to sensitise a Ru-Ru dyad CO_2 reduction catalyst. The Ru catalyst was bound to the electrode with a bipyridyl ligand functionalised with $-CH_2PO_3^{2-}$ groups. The sp^3 carbon acts as a spacer, electronically decoupling the bipyridyl ring from the gC_3N_4 surface.[155] The phosphonate acid moiety is an effective linkage group as it forms strong binding interactions with the surface. gC_3N_4 electrodes have also been used to photosensitise an earth-abundant cobalt porphyrin complex.[156] Recently, $[Mn(bpy\text{-}acid)(CO)_3Br]$ has been covalently bound to gC_3N_4 through a carboxylate linkage group. The gC_3N_4 support enhanced the catalytic activity of the Mn catalyst, as well as increased the selectivity for CO formation.[157] It is also possible to use functionalised silica as a solid support for catalysis. Mesoporous silica is photochemically inert but can be used as a photosensitiser if it is doped with a chromophore, such as acridone.[158]

Supramolecular materials, such as metal-organic frameworks (MOFs), are also useful for heterogenisation of CO_2 reduction catalysts. For example, diimine ligands with amine groups in the 5,5′-position have also been used to incorporate Re Lehn-type catalysts into covalent organic frameworks (COFs) and MOFs.[159] In another example, $[Mn(bpy\text{-}acid)(CO)_3Br]$ was bound to a Zr(IV) MOF with 5,5′-dicarboxylate-2,2′-bipyridyl linking groups. $[Ru(dmbpy)_3]^{2+}$ was used to photosensitise the catalyst. The Mn-bound MOF had a greater turnover compared to free $[Mn(bpy\text{-}acid)(CO)_3Br]$, which was attributed to the prevention of dimerisation and presence of the Ru photosensitiser within the pores of the MOF. This hybrid MOF was prone to decomposition under catalytic conditions, therefore more stable supramolecular materials are required.[160,161]

Photoelectrochemical cells

The development of hybrid catalysts is an important aspect in the development of photoelectrochemical cells, where the reductive CO_2 reduction process is coupled to a water oxidation catalyst through a circuit (Figure 1.31). The development of photoelectrochemical cells is highly desirable as a replacement for the use of sacrificial donors. In a photoelectrochemical cell, the CO_2 reduction catalyst is bound to the photoanode, and the water oxidation catalyst is bound to the photocathode. The electrodes are then immersed in aqueous solvent purged with CO_2. The catalysis is then initiated by light absorption by the photoanode and subsequent donation of an electron to the CO_2 reduction catalyst. This electron is then replenished through the circuit by the cathodic water oxidation reaction, completing the cycle. This water oxidation process can also be light assisted by a photoactive cathode (photocathode) The electrodes are separated by a semi-permeable membrane which allows proton diffusion from the water oxidation compartment to the CO_2 reduction reaction.[162] The design of an effective photoelectrochemical cell requires a detailed understanding of the individual catalysts, as well as the electrodes themselves. These devices are the peak of current artificial photosynthetic technology and will likely be the target of future research for practical application of CO_2 reduction catalysis.

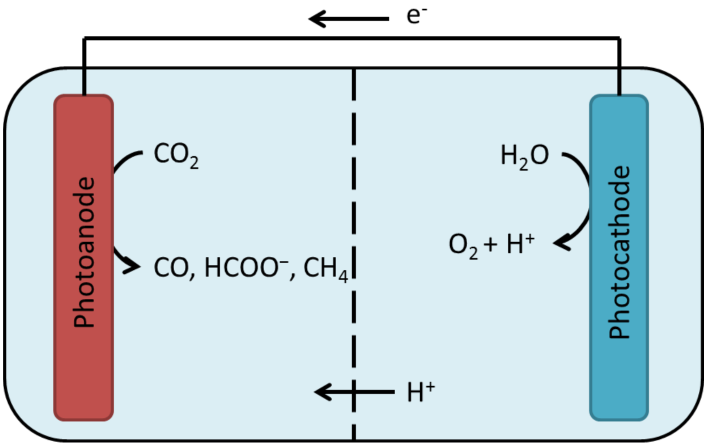

Figure 1.31 – A schematic for a photoelectrochemical cell, illustrating how CO_2 reduction and water oxidation reactions can be coupled through an electric circuit.

1.7 Research objectives and aims

The overarching aim of this thesis is to determine how the structure of the light harvesting and CO_2 reducing components of an artificial photosynthetic system can affect its capability to perform catalytic reactions. To fulfil this objective, several research questions have been proposed. The first chapters of this work aim to develop an understanding of the capacity of functionalised Re(I) and Mn(I) CO_2 reduction catalysts to selectively reduce CO_2 to CO through electrochemical and catalytic studies. The design of the CO_2 reducing system will have an emphasis on the use of earth-abundant catalysts and photosensitisers, and efforts will be made to modify the catalyst and photosensitiser to allow for CO_2 reduction in water. This is an important aspect of the proposed research, as the design of effective noble-metal and organic solvent free methods of catalytic CO_2 reduction would be highly beneficial to modern science and industry.

The thesis will then move on to the study of three Re(I) CO_2 reduction catalysts by time-resolved laser spectroscopy, the aim of which was to understand how use of either a functionalised bipyridyl or red-light absorbing bis(mesitylimino)acenaphthene ligand in an $[Re(L_2)(CO)_3Cl]$ complex changes its excited state relaxation mechanism following visible light excitation. These results will be expanded on through multidimensional IR spectroscopy in the ground and excited states of the complex. The aim of this is to discover how the vibrational energy redistribution within the complex can be altered through electronic excitation or structural modifications. Whilst these studies are more fundamental, they will contribute to a growing field that is relevant to the development of novel photocatalysts for CO_2 reduction under visible light irradiation.

The final proposed project investigates the rates and mechanism of vibrational energy transfer in a model donor-bridge-acceptor complex bearing a naphthalene monoimide electron acceptor and phenothiazine electron donor, connected by a Pt(II) *trans*-acetylide bridge. To investigate the vibrational dynamics of each acetylide group, the complex has been isotopically labelled with carbon-13, allowing for individual perturbation of either the donor or acceptor ligand with time domain 2DIR spectroscopy. The results of this work will be used to develop our understanding of the influence molecular vibrations have over electronic excited state relaxation.

Five research questions have been proposed, which form the structure of the thesis. The proposed methodology that will be used to answer each question is detailed below.

1) How does the catalytic activity of a Re or Mn Lehn-type catalyst change if dimerisation is inhibited by introduction of sterically hindering groups? (Chapter 2)

- Characterise the structure and spectroscopic properties of the Re(I) and Mn(I) analogues of a sterically hindered CO_2 reduction catalyst bearing a bipyridyl ligand functionalised with N-(p-hexylphenyl)-N-ethyl-amide groups in the 6,6′ positions.
- Evaluate the electrochemical properties of the Re and Mn catalysts to determine the effect of functionalisation on the redox chemistry of the catalysts.
- Estimate the rate of electrochemical CO_2 reduction with the Foot-of-the-Wave analysis technique.
- Evaluate the electrocatalytic performance of the Re(I) and Mn(I) catalysts with controlled potential electrolysis, monitored by gas chromatography.
- Evaluate the photocatalytic performance of the Re catalyst under visible light irradiation in the presence of a sacrificial donor.
- Evaluate the photocatalytic performance of the Mn catalyst following photosensitisation with an Earth-abundant light harvesting complex in the presence of a sacrificial donor.
- Compare the catalytic performance of the Re(I) and Mn(I) catalysts with previously reported CO_2 reduction catalysts.

2) Can we introduce new functionality to Mn Lehn-type catalysts without affecting their ability to perform electro- or photochemical CO_2 reduction? (Chapter 3)

- Characterise the structure and spectroscopic properties of a Mn catalyst, bearing a bipyridyl ligand functionalised in the 4,4′ positions with phosphonate ester groups separated by a methylene spacer, and evaluate how the functionalisation affects the optical properties of the complex.
- Evaluate the electrochemical properties of the Mn catalyst to determine the effect of functionalisation on the redox chemistry of the catalyst.
- Estimate the rate of electrochemical CO_2 reduction with the Foot-of-the-Wave technique.
- Evaluate the photocatalytic performance of the Mn catalyst following photosensitisation with an Earth-abundant light harvesting complex in the presence of a sacrificial donor.
- Determine the water solubility of the Mn(I)-phosphonate catalyst and determine its capacity to reduce CO_2 to CO in aqueous solution.

- Compare the catalytic performance of the Mn catalyst with previously reported CO_2 reduction catalysts.

3) How effective are earth-abundant Zn porphyrin complexes at photosensitising Mn Lehn-type catalysts in aqueous and organic solution? (Chapters 2 and 3)

- Evaluate the capacity of tetraphenylporphyrin zinc(II) to act as an earth-abundant red light absorbing photosensitiser for Mn Lehn-type catalysts in organic solution.
- Evaluate the capacity of tetra(N-methyl-4-pyridyl)porphyrin zinc(II) to act as an earth-abundant red light absorbing photosensitiser for Mn Lehn-type catalysts in aqueous solution.
- Evaluate the stability of the porphyrin photosensitisers under catalytic conditions.

4) Is there a link between the structure of a $[Re(L_2)(CO)_3Cl]$ CO_2 reduction catalyst and its excited state and vibrational dynamics? (Chapter 4)

- Characterise the steady-state spectroscopic properties of three Re(I) catalysts which are effective CO_2 reduction electrocatalysts.
- Analyse and interpret the ultrafast TRIR data recorded for these catalysts, proposing a mechanism for the excited state dynamics of each complex.
- Analyse and interpret the ultrafast frequency domain 2DIR data recorded for these catalysts in the electronic ground state, proposing a mechanism for vibrational energy redistribution within each complex.
- Analyse and interpret the ultrafast frequency domain 2DIR data recorded for these catalysts in the excited state, comparing the vibrational dynamics in the ground and excited states.
- Compare the observed vibrational and electronic dynamics to previously reported Re(I) photocatalysts, such as $[Re(bpy\text{-}ester)(CO)_3Br]$ to identify any effects of structural modification of the excited state dynamics.

5) How do the coupling interactions between high-frequency acetylide vibrations affect the redistribution of vibrational energy in a Pt(II) donor-bridge-acceptor complex? (Chapter 5)

- Characterise the vibrational absorption spectrum of a series of four *trans*-acetylide Pt(II) donor-bridge-acceptor complexes where the acetylide groups have been systematically labelled with carbon-13.
- Propose mechanisms for vibrational energy redistribution following IR excitation of the acetylide bridge in the unlabelled, donor-side labelled, acceptor-side labelled, and fully labelled D-B-A complexes.

- Compare the vibrational energy redistribution mechanisms of the complexes to understand the effect of isotopic substitution of the vibrational dynamics of these complexes.

References

1 L. Hammarström, *Acc. Chem. Res.*, 2009, **42**, 1859–1860.

2 R. Lal, *Energy Environ. Sci.*, 2008, **1**, 86.

3 X. Zou and Y. Zhang, *Chem. Soc. Rev.*, 2015, **44**, 5148–5180.

4 S. C. Roy, O. K. Varghese, M. Paulose and C. A. Grimes, *ACS Nano*, 2010, **4**, 1259–1278.

5 A. A. Yaroshevsky, *Geochemistry Int.*, 2006, **44**, 48–55.

6 D. Gust, T. A. Moore and A. L. Moore, *Acc. Chem. Res.*, 2009, **42**, 1890–1898.

7 D. C. Grills, M. Z. Ertem, M. McKinnon, K. T. Ngo and J. Rochford, *Coord. Chem. Rev.*, 2018, **374**, 173–217.

8 C. Costentin, M. Robert and J.-M. M. Savéant, *Chem. Soc. Rev.*, 2013, **42**, 2423–2436.

9 C. Costentin, S. Drouet, M. Robert, J. Save and J. M. Savéant, *J. Am. Chem. Soc.*, 2012, **134**, 11235–11242.

10 M. Krejčik, M. Daněk and F. Hartl, *J. Electroanal. Chem. Interfacial Electrochem.*, 1991, **317**, 179–187.

11 A. Vlček, *Coord. Chem. Rev.*, 2000, **200**–**202**, 933–977.

12 H. Kriegsmann, *Encyclopedia of Spectroscopy*, Wiley-VCH, Weinheim, 1996, vol. 195.

13 J. S. Wilson, N. Chawdhury, M. R. A. Al-mandhary, M. Younus, M. S. Khan, P. R. Raithby, A. Ko and R. H. Friend, *J. Am. Chem. Soc.*, 2001, **123**, 9412–9417.

14 S. Seiffert and J. Sprakel, *Physical chemistry of supramolecular polymer networks*, Oxford University Press, Oxford, 2012, vol. 41.

15 C. A. Royer, *Fluorescence spectroscopy.*, Wiley-VCH, Weinheim, 1995, vol. 40.

16 J. D. Gaynor, J. Sandwisch and M. Khalil, *Nature Commun.*, 2019, **10**, 5621.

17 I. V. Rubtsov, *Nature Chem.*, 2015, **7**, 683–684.

18 Z. Lin, C. M. Lawrence, D. Xiao, V. V. Kireev, S. S. Skourtis, J. L. Sessler, D. N. Beratan and I. V. Rubtsov, *J. Am. Chem. Soc.*, 2009, **131**, 18060–18062.

19 Y. Yue, T. Grusenmeyer, Z. Ma, P. Zhang, R. H. Schmehl, D. N. Beratan and I. V. Rubtsov, *Dalton Trans.*, 2015, **44**, 8609–8616.

20 P. A. Scattergood, M. Delor, I. V. Sazanovich, O. V. Bouganov, S. A. Tikhomirov, A. S. Stasheuski, A. W. Parker, G. M. Greetham, M. Towrie, E. S. Davies, A. J. H. M. H. M. Meijer and J. A. Weinstein, *Dalton Trans.*, 2014, **43**, 17677–17693.

21 M. Delor, P. A. Scattergood, I. V. Sazanovich, A. W. Parker, G. M. Greetham, A. J. H. M. Meijer, M. Towrie and J. A. Weinstein, *Science*, 2014, **346**, 1492–1495.

22 M. Delor, T. Keane, P. A. Scattergood, I. V. Sazanovich, G. M. Greetham, M. Towrie, A. J. H. M. Meijer and J. A. Weinstein, *Nature Chem.*, 2015, **7**, 689–695.

23 P. A. Scattergood, M. Delor, I. V. Sazanovich, M. Towrie and J. A. Weinstein, *Faraday Discuss.*, 2015, **185**, 69–86.

24 M. Delor, S. A. Archer, T. Keane, A. J. H. M. H. M. Meijer, I. V. Sazanovich, G. M. Greetham, M. Towrie and J. A. Weinstein, *Nature Chem.*, 2017, **9**, 1099–1104.

25 M. Delor, I. V. Sazanovich, M. Towrie, S. J. Spall, T. Keane, A. J. Blake, C. Wilson, A. J. H. M. Meijer and J. A. Weinstein, *J. Phys. Chem. B*, 2014, **118**, 11781–11791.

26 L. M. Kiefer, J. T. King and K. J. Kubarych, *Acc. Chem. Res.*, 2015, **48**, 1123–1130.

27 C. R. Baiz, P. L. McRobbie, J. M. Anna, E. Geva and K. J. Kubarych, *Acc. Chem. Res.*, 2009, **42**, 1395–1404.

28 I. V. Rubtsov and A. L. Burin, *J. Chem. Phys.*, 2019, **150**, 020901.

29 Z. Wang, *Science*, 2002, **296**, 2201–2203.

30 J. T. King, J. M. Anna and K. J. Kubarych, *Phys. Chem. Chem. Phys.*, 2011, **13**, 5579–5583.

31 V. M. Kasyanenko, Z. Lin, G. I. Rubtsov, J. P. Donahue and I. V. Rubtsov, *J. Chem. Phys.*, 2009, **131**, 154508.

32 S. L. Tesar, V. M. Kasyanenko, I. V. Rubtsov, G. I. Rubtsov and A. L. Burin, *J. Phys. Chem. A*, 2013, **117**, 315–323.

33 P. Moore, A. Tokmakoff, T. Keyes and M. D. Fayer, *Phys. Fluids*, 1967, **10**, 3325–3334.

34 R. Zwanzig, *J. Chem. Phys.*, 1961, **34**, 1931–1935.

35 P. Hamm and M. Zanni, *Concepts and Methods of 2D Infrared Spectroscopy*, Cambridge University Press, Cambridge, 2011.

36 T. L. C. Jansen, S. Saito, J. Jeon and M. Cho, *J. Chem. Phys.*, 2019, **150**, 100901.

37 C. R. Baiz, K. J. Kubarych and E. Geva, *J. Phys. Chem. B*, 2011, **115**, 5322–5339.

38 S. Rafiq and G. D. Scholes, *J. Am. Chem. Soc.*, 2019, **141**, 708–722.

39 D. Kumar Das, K. Makhal and D. Goswami, *Phys. Chem. Chem. Phys.*, 2018, **20**, 13400–13411.

40 P. A. Eckert and K. J. Kubarych, *J. Chem. Phys.*, , DOI:10.1063/1.5111016.

41 M. J. Nee, C. R. Baiz, J. M. Anna, R. McCanne and K. J. Kubarych, *J. Chem. Phys.*, 2008, **129**, 084503.

42 I. V. Rubtsov, *Acc. Chem. Res.*, 2009, **42**, 1385–1394.

43 V. M. Kasyanenko, S. L. Tesar, G. I. Rubtsov, A. L. Burin and I. V. Rubtsov, *J. Phys. Chem. B*, 2011, **115**, 11063–11073.

44 D. G. Osborne and K. J. Kubarych, *J. Phys. Chem. A*, 2013, **117**, 5891–5898.

45 I. H. M. van Stokkum, D. S. Larsen and R. van Grondelle, *Biochim. Biophys. Acta - Bioenerg.*, 2004, **1657**, 82–104.

46 C. Ruckebusch, M. Sliwa, P. Pernot, A. de Juan and R. Tauler, *J. Photochem. Photobiol. C Photochem. Rev.*, 2012, **13**, 1–27.

47 C. Slavov, H. Hartmann and J. Wachtveitl, *Anal. Chem.*, 2015, **87**, 2328–2336.

48 J. Hawecker, J.-M. Lehn and R. Ziessel, *J. Chem. Soc., Chem. Commun.*, 1983, 536–538.

49 J. Hawecker, J.-M. Lehn and R. Ziessel, *Helv. Chim. Acta*, 1986, **69**, 1990–2012.

50 J. Hawecker, J.-M. Lehn and R. Ziessel, *J. Chem. Soc., Chem. Commun.*, 1984, 328–330.

51 J. M. Smieja and C. P. Kubiak, *Inorg. Chem.*, 2010, **49**, 9283–9289.

52 A. J. Morris, G. J. Meyer and E. Fujita, *Acc. Chem. Res.*, 2009, **42**, 1983–1994.

53 C. W. Machan, M. D. Sampson, S. A. Chabolla, T. Dang and C. P. Kubiak, *Organometallics*, 2014, **33**, 4550–4559.

54 C. Riplinger, M. D. Sampson, A. M. Ritzmann, C. P. Kubiak and E. A. Carter, *J. Am. Chem. Soc.*, 2014, **136**, 16285–16298.

55 Y. Kuramochi, O. Ishitani and H. Ishida, *Coord. Chem. Rev.*, 2018, **373**, 333–356.

56 B. Kumar, M. Llorente, J. Froehlich, T. Dang, A. Sathrum and C. P. Kubiak, *Annu. Rev. Phys. Chem.*, 2012, **63**, 541–569.

57 T. W. Schneider, M. Z. Ertem, J. T. Muckerman and A. M. Angeles-Boza, *ACS Catal.*, 2016, **6**, 5473–5481.

58 J. M. Smieja, E. E. Benson, B. Kumar, K. A. Grice, C. S. Seu, A. J. M. Miller, J. M. Mayer and C. P. Kubiak, *Proc. Natl. Acad. Sci.*, 2012, **109**, 15646–15650.

59 M. L. Clark, P. L. Cheung, M. Lessio, E. A. Carter and C. P. Kubiak, *ACS Catal.*, 2018, **8**, 2021–2029.

60 J. Agarwal, E. Fujita, H. F. Schaefer and J. T. Muckerman, *J. Am. Chem. Soc.*, 2012, **134**, 5180–5186.

61 Y. Hayashi, S. Kita, B. S. Brunschwig and E. Fujita, *J. Am. Chem. Soc.*, 2003, **125**, 11976–11987.

62 B. P. Sullivan and T. J. Meyer, *Organometallics*, 1986, **5**, 1500–1502.

63 J. Agarwal, R. P. Johnson and G. Li, *J. Phys. Chem. A*, 2011, **115**, 2877–2881.

64 L. Q. Qiu, K. H. Chen, Z. W. Yang and L. N. He, *Green Chem.*, 2020, **22**, 8614–8622.

65 N. P. Liyanage, W. Yang, S. Guertin, S. Sinha Roy, C. A. Carpenter, R. E. Adams, R. H. Schmehl, J. H. Delcamp and J. W. Jurss, *Chem. Commun.*, 2019, **55**, 993–996.

66 B. Gholamkhass, H. Mametsuka, K. Koike, T. Tanabe, M. Furue and O. Ishitani, *Inorg. Chem.*, 2005, **44**, 2326–2336.

67 Y. Kuramochi and A. Satake, *Chem. Eur. J.*, 2020, **26**, 16365–16373.

68 D. R. Case, A. Spear, A. F. Henwood, M. Nanao, S. Dampf, T. M. Korter, T. Gunnlaugsson, J. Zubieta and R. P. Doyle, *Dalton Trans.*, 2021, **50**, 3479–3486.

69 J. F. Martinez, N. T. La Porte, C. M. Mauck and M. R. Wasielewski, *Faraday Discuss.*, 2017, **198**, 235–249.

70 J. F. Martinez, N. T. La Porte, S. Chaudhuri, A. Sinopoli, Y. J. Bae, M. Sohail, V. S. Batista and M. R. Wasielewski, *J. Phys. Chem. C*, 2019, **123**, 10178–10190.

71 B. Kumar, J. M. Smieja, A. F. Sasayama and C. P. Kubiak, *Chem. Commun.*, 2012, **48**, 272–274.

72 K. Talukdar, S. Sinha Roy, E. Amatya, E. A. Sleeper, P. Le Magueres and J. W. Jurss, *Inorg. Chem.*, 2020, **59**, 6087–6099.

73 A. N. Hellman, R. Haiges and S. C. Marinescu, *ChemElectroChem*, 2021, **8**, 1864–1872.

74 M. R. Madsen, J. B. Jakobsen, M. H. Rønne, H. Liang, H. C. D. Hammershøj, P. Nørby, S. U. Pedersen, T. Skrydstrup and K. Daasbjerg, *Organometallics*, 2020, **39**, 1480–1490.

75 S. A. Chabolla, C. W. Machan, J. Yin, E. A. Dellamary, S. Sahu, N. C. Gianneschi, M. K. Gilson, F. A. Tezcan and C. P. Kubiak, *Faraday Discuss.*, 2017, **198**, 279–300.

76 J. Mukherjee and I. Siewert, *Eur. J. Inorg. Chem.*, 2020, **2020**, 4319–4333.

77 A. Nakada and O. Ishitani, *ACS Catal.*, 2018, **8**, 354–363.

78 C. Carpenter, P. Brogdon, L. McNamara, G. Tschumper, N. Hammer and J. Delcamp, *Inorganics*, 2018, **6**, 22.

79 L. Suntrup, F. Stein, J. Klein, A. Wilting, F. G. L. Parlane, C. M. Brown, J. Fiedler, C. P. Berlinguette, I. Siewert and B. Sarkar, *Inorg. Chem.*, 2020, **59**, 4215–4227.

80 S. Sinha, E. K. Berdichevsky and J. J. Warren, *Inorganica Chim. Acta*, 2017, **460**, 63–68.

81 S. Sinha, A. Sonea, C. A. Gibbs and J. J. Warren, *Dalton Trans.*, 2020, **49**, 7078–7083.

82 E. Portenkirchner, E. Kianfar, N. S. Sariciftci and G. Knör, *ChemSusChem*, 2014, **7**, 1347–1351.

83 R. Giereth, P. Lang, E. McQueen, X. Meißner, B. Braun-Cula, C. Marchfelder, M. Obermeier, M. Schwalbe and S. Tschierlei, *ACS Catal.*, 2021, **11**, 390–403.

84 L. A. Paul, S. Rajabi, C. Jooss, F. Meyer, F. Ebrahimi and I. Siewert, *Dalton Trans.*, 2020, **49**, 8367–8374.

85 J. K. Nganga, L. M. Wolf, K. Mullick, E. Reinheimer, C. Saucedo, M. E. Wilson, K. A. Grice, M. Z. Ertem and A. M. Angeles-Boza, *Inorg. Chem.*, 2021, **60**, 3572–3584.

86 N. La Porte, D. Moravec, M. Hopkins, *PNAS*, 2014, **111**(27), 9745-9750.

87 S. Sato, Y. Matubara, K. Koike, M. Falkenström, T. Katayama, Y. Ishibashi, H. Miyasaka, S. Taniguchi, H. Chosrowjan, N. Mataga, N. Fukazawa, S. Koshihara, K. Onda and O. Ishitani, *Chem. - A Eur. J.*, 2012, **18**, 15722–15734.

88 J. B. Asbury, Y. Wang and T. Lian, *Bull. Chem. Soc. Jpn.*, 2002, **75**, 973–983.

89 K. Koike, N. Okoshi, H. Hori, K. Takeuchi, O. Ishitani, H. Tsubaki, I. P. Clark, M. W. George, F. P. A. Johnson and J. J. Turner, *J. Am. Chem. Soc.*, 2002, **124**, 11448–11455.

90 J. R. Schoonover and G. F. Strouse, *Chem. Rev.*, 1998, **98**, 1335–1355.

91 D. J. Liard, M. Busby, P. Matousek, M. Towrie and A. Vlček, *J. Phys. Chem. A*, 2004, **108**, 2363–2369.

92 D. R. Striplin and G. A. Crosby, *Chem. Phys. Lett.*, 1994, **221**, 426–430.

93 A. Vlček and M. Busby, *Coord. Chem. Rev.*, 2006, **250**, 1755–1762.

94 A. El Nahhas, C. Consani, A. M. Blanco-Rodríguez, K. M. Lancaster, O. Braem, A. Cannizzo, M. Towrie, I. P. Clark, S. Záliš, M. Chergui and A. Vlček, *Inorg. Chem.*, 2011, **50**, 2932–2943.

95 J. Dyer, W. J. Blau, C. G. Coates, C. M. Creely, J. D. Gavey, M. W. George, D. C. Grills, S. Hudson, J. M. Kelly, P. Matousek, J. J. McGarvey, J. McMaster, A. W. Parker, M. Towrie and J. A. Weinstein, *Photochem. Photobiol. Sci.*, 2003, **2**, 542–554.

96 F. Zhong, X. Yuan, J. Zhao and Q. Wang, *Sci. China Chem.*, 2016, **59**, 70–77.

97 A. M. Blanco-Rodríguez, H. Kvapilová, J. Sýkora, M. Towrie, C. Nervi, G. Volpi, S. Záliš and A. Vlček, *J. Am. Chem. Soc.*, 2014, **136**, 5963–5973.

98 G. E. Shillito, T. B. J. Hall, D. Preston, P. Traber, L. Wu, K. E. A. Reynolds, R. Horvath, X. Z. Sun, N. T. Lucas, J. D. Crowley, M. W. George, S. Kupfer and K. C. Gordon, *J. Am. Chem. Soc.*, 2018, **140**, 4534–4542.

99 B. D. Rossenaar, D. J. Stufkens and A. Vlček, *Inorg. Chem.*, 1996, **35**, 2902–2909.

100 A. M. Blanco Rodríguez, A. Gabrielsson, M. Motevalli, P. Matousek, M. Towrie, J. Šebera, S.

Záliš and A. Vlček, *J. Phys. Chem. A*, 2005, **109**, 5016–5025.

101 M. Busby, A. Gabrielsson, P. Matousek, M. Towrie, A. J. Di Bilio, H. B. Gray and A. Vlček, *Inorg. Chem.*, 2004, **43**, 4994–5002.

102 Y. Yue, T. Grusenmeyer, Z. Ma, P. Zhang, T. T. Pham, J. T. Mague, J. P. Donahue, R. H. Schmehl, D. N. Beratan and I. V. Rubtsov, *J. Phys. Chem. B*, 2013, **117**, 15903–15916.

103 Y. Yue, T. Grusenmeyer, Z. Ma, P. Zhang, R. H. Schmehl, D. N. Beratan and I. V. Rubtsov, *J. Phys. Chem. A*, 2014, **118**, 10407–10415.

104 J. D. Lewis, M. Towrie and J. N. Moore, *J. Phys. Chem. A*, 2008, **112**, 3852–3864.

105 A. Vlček, H. Kvapilová, M. Towrie, S. Záliš, H. Kvapilova and M. Towrie, *Acc. Chem. Res.*, 2015, **48**, 868–876.

106 Z. Ma, Z. Lin, C. M. Lawrence, I. V. Rubtsov, P. Antoniou, S. S. Skourtis, P. Zhang, D. N. Beratan, P. Zhang and D. N. Beratan, *Chem. Sci.*, 2018, **9**, 6395–6405.

107 J. Bredenbeck, J. Helbing and P. Hamm, *J. Am. Chem. Soc.*, 2004, **126**, 990–991.

108 L. M. Kiefer and K. J. Kubarych, *J. Phys. Chem. A*, 2015, **119**, 959–965.

109 C. M. Olson, A. Grofe, C. J. Huber, I. C. Spector, J. Gao and A. M. Massari, *J. Chem. Phys.*, 2017, **147**, 124302.

110 L. M. Kiefer, J. T. King and K. J. Kubarych, *J. Phys. Chem. A*, 2014, **118**, 9853–9860.

111 L. M. Kiefer, L. B. Michocki and K. J. Kubarych, *J. Phys. Chem. Lett.*, 2021, **12**, 3712–3717.

112 J. H. Gary and G. E. Handwerk, *Petroleum Refining*, Marcel Dekker, 2nd edn., 2001.

113 L. Rotundo, R. Gobetto and C. Nervi, *Curr. Opin. Green Sustain. Chem.*, 2021, **31**, 100509.

114 D.-C. Liu, D.-C. Zhong and T.-B. Lu, *EnergyChem*, 2020, **2**, 100034.

115 M. Bourrez, F. Molton, S. Chardon-Noblat and A. Deronzier, *Angew. Chemie - Int. Ed.*, 2011, **50**, 9903–9906.

116 H. Takeda, H. Koizumi, K. Okamoto and O. Ishitani, *Chem. Commun.*, 2014, **50**, 1491–1493.

117 D. C. Grills, J. A. Farrington, B. H. Layne, S. V. Lymar, B. A. Mello, J. M. Preses and J. F. Wishart, *J. Am. Chem. Soc.*, 2014, **136**, 5563–5566.

118 H. Kuo, S. E. Tignor, T. S. Lee, D. Ni, J. E. Park, G. D. Scholes and A. B. Bocarsly, *Dalton Trans.*, 2020, **49**, 891–900.

119 D. C. Grills, M. Z. Ertem, M. McKinnon, K. T. Ngo and J. Rochford, *Coord. Chem. Rev.*, 2018, **374**, 173–217.

120 K. T. Ngo, M. McKinnon, B. Mahanti, R. Narayanan, D. C. Grills, M. Z. Ertem and J. Rochford, *J. Am. Chem. Soc.*, 2017, **139**, 2604–2618.

121 G. Neri, P. M. Donaldson and A. J. Cowan, *Phys. Chem. Chem. Phys.*, 2019, **21**, 7389–7397.

122 A. Sinopoli, N. T. La Porte, J. F. Martinez, M. R. Wasielewski and M. Sohail, *Coord. Chem. Rev.*, 2018, **365**, 60–74.

123 M. D. Sampson, A. D. Nguyen, K. A. Grice, C. E. Moore, A. L. Rheingold, C. P. Kubiak and P. Kubiak, *J. Am. Chem. Soc.*, 2014, **136**, 5460–5471.

124 M. D. Sampson and C. P. Kubiak, *J. Am. Chem. Soc.*, 2016, **138**, 1386–1393.

125 X. Wang, H. Ma, C. Meng, D. Chen and F. Huang, *Phys. Chem. Chem. Phys.*, 2019, **21**, 8849–8855.

126 S. E. Tignor, T. W. Shaw and A. B. Bocarsly, *Dalton Trans.*, 2019, **48**, 12730–12737.

127 S. S. Roy, K. Talukdar and J. W. Jurss, *ChemSusChem*, 2021, **14**, 662–670.

128 M. H. Rønne, D. Cho, M. R. Madsen, J. B. Jakobsen, S. Eom, É. Escoudé, H. C. D. Hammershøj, D. U. Nielsen, S. U. Pedersen, M.-H. H. Baik, T. Skrydstrup and K. Daasbjerg, *J. Am. Chem. Soc.*, 2020, **142**, 4265–4275.

129 S. J. P. Spall, T. Keane, J. Tory, D. C. Cocker, H. Adams, H. Fowler, A. J. H. M. Meijer, F. Hartl and J. A. Weinstein, *Inorg. Chem.*, 2016, **55**, 12568–12582.

130 M. McKinnon, V. Belkina, K. T. Ngo, M. Z. Ertem, D. C. Grills and J. Rochford, *Front. Chem.*, 2019, **7**, 1–14.

131 T. H. T. Myren, A. M. Lilio, C. G. Huntzinger, J. W. Horstman, T. A. Stinson, T. B. Donadt, C. Moore, B. Lama, H. H. Funke and O. R. Luca, *Organometallics*, 2019, **38**, 1248–1253.

132 Y. Yang, Z. Zhang, X. Chang, Y.-Q. Q. Zhang, R.-Z. Z. Liao and L. Duan, *Inorg. Chem.*, 2020, **59**, 10234–10242.

133 E. Kottelat and Z. Fabio, *Inorganics*, 2017, **5**, 24.

134 J. Jimenez, I. Chakraborty and P. K. Mascharak, *Eur. J. Inorg. Chem.*, 2015, **2015**, 5021–5026.

135 J. O. Taylor, Y. Wang and F. Hartl, *ChemCatChem*, 2020, **12**, 386–393.

136 J. X. Zhang, C. Y. Hu, W. Wang, H. Wang and Z. Y. Bian, *Appl. Catal. A Gen.*, 2016, **522**, 145–151.

137 V. Yempally, S. Moncho, F. Hasanayn, W. Y. Fan, E. N. Brothers and A. A. Bengali, *Inorg. Chem.*, 2017, **56**, acs.inorgchem.7b01543.

138 P. L. Cheung, C. W. Machan, A. Y. S. Malkhasian, J. Agarwal and C. P. Kubiak, *Inorg. Chem.*, 2016, **55**, 3192–3198.

139 C. W. Machan, C. J. Stanton, J. E. Vandezande, G. F. Majetich, H. F. Schaefer, C. P. Kubiak and J. Agarwal, *Inorg. Chem.*, 2015, **54**, 8849–8856.

140 H.-Y. Y. Kuo, T. S. Lee, A. T. Chu, S. E. Tignor, G. D. Scholes and A. B. Bocarsly, *Dalton Trans.*, 2019, **48**, 1226–1236.

141 J. J. Walsh, G. Neri, C. L. Smith and A. J. Cowan, *Organometallics*, 2019, **38**, 1224–1229.

142 M. Hu, B. Zhu, H. Zhou, L. Qiao, J. Fan, Y. Du, F. Chang and S. Yu, *Inorg. Chem. Commun.*, 2020, **119**, 108093.

143 A. Kumar, P. Daw, N. A. Espinosa-Jalapa, G. Leitus, L. J. W. Shimon, Y. Ben-David and D. Milstein, *Dalton Trans.*, 2019, **48**, 14580–14584.

144 L. Zhang, M. Pu and M. Lei, *Dalton Trans.*, 2021, **50**, 7348–7355.

145 R. De, S. Gonglach, S. Paul, M. Haas, S. S. Sreejith, P. Gerschel, U. P. Apfel, T. H. Vuong, J. Rabeah, S. Roy and W. Schöfberger, *Angew. Chemie*, 2020, **132**, 10614–10621.

146 Y. Zhao and Z. Liu, *Chin. J. Chem*, 2018, **36**, 455–460.

147 J. Zhao, X. Wang, Z. Xu and J. S. C. Loo, *J. Mater. Chem. A*, 2014, **2**, 15228–15233.

148 A. Zhanaidarova, A. L. Ostericher, C. J. Miller, S. C. Jones and C. P. Kubiak, *Organometallics*, 2019, **38**, 1204–1207.

149 S.-J. J. Woo, S. Choi, S. Y. Kim, P. S. Kim, J. H. Jo, C. H. Kim, H. J. Son, C. Pac and S. O. Kang, *ACS Catal.*, 2019, **9**, 2580–2593.

150 T. E. Rosser, C. D. Windle and E. Reisner, *Angew. Chemie - Int. Ed.*, 2016, **55**, 7388–7392.

151 M. F. Kuehnel, K. L. Orchard, K. E. Dalle and E. Reisner, *J. Am. Chem. Soc.*, 2017, **139**, 7217–7223.

152 M. F. Kuehnel, C. D. Sahm, G. Neri, J. R. Lee, K. L. Orchard, A. J. Cowan and E. Reisner, *Chem. Sci.*, 2018, **9**, 2501–2509.

153 F. Arcudi, L. Đorđević, B. Nagasing, S. I. Stupp and E. A. Weiss, *J. Am. Chem. Soc.*, , DOI:10.1021/jacs.1c06961.

154 R. N. Schaugaard, K. Raghavachari and L. Li, *Inorg. Chem.*, 2018, **57**, 10548–10556.

155 R. Kuriki and K. Maeda, *Phys. Chem. Chem. Phys.*, 2017, **19**, 4938–4950.

156 G. Zhao, H. Pang, G. Liu, P. Li, H. Liu, H. Zhang, L. Shi and J. Ye, *Appl. Catal. B Environ.*, 2017, **200**, 141–149.

157 X. Ma, L. Zheng and Z. Bian, *Chem. Eng. Sci.*, 2021, **229**, 116042.

158 Y. Ueda, H. Takeda, T. Yui, K. Koike, Y. Goto, S. Inagaki and O. Ishitani, *ChemSusChem*, 2015, **8**, 439–442.

159 D. A. Popov, J. M. Luna, N. M. Orchanian, R. Haiges, C. A. Downes and S. C. Marinescu, *Dalton Trans.*, 2018, **47**, 17450–17460.

160 H. Fei, M. D. Sampson, Y. Lee, C. P. Kubiak and S. M. Cohen, *Inorg. Chem.*, 2015, **54**, 6821–6828.

161 S. Wannakao, W. Jumpathong and K. Kongpatpanich, *Inorg. Chem.*, 2017, **56**, 7200–7209.

162 N. Zhang, R. Long, C. Gao and Y. Xiong, *Sci. China Mater.*, 2018, **61**, 771–805.

Chapter 2. Sterically hindered Re- and Mn- CO_2 reduction catalysts for solar energy conversion

---

A previous version of this chapter was published in the following article:

James D. Shipp, Heather Carson, Steven J. P. Spall, Simon C. Parker, Dimitri Chekulaev, Natalie Jones, Mikhail Ya. Mel'nikov,[a] Craig C. Robertson, Anthony J. H. M. Meijer, Julia A. Weinstein, *Dalton Trans.* 2020, **49**, 4230-4243.

Abstract

Novel molecular Re and Mn tricarbonyl complexes bearing a bipyridyl ligand functionalised with sterically hindering substituents in the 6,6′-position, [M(HPEAB)$(CO)_3$(X)] (M/X = Re/Cl, Mn/Br; HPEAB = 6,6′-{N-(4-hexylphenyl)-N(ethyl)-amido}-2,2′-bipyridine) have been synthesised, fully characterised, including by single crystal X-ray crystallography, and their propensity to act as catalysts for the electrochemical and photochemical reduction of CO_2 established. Controlled potential electrolysis showed that the catalysts are effective CO_2 reduction electrocatalysts, yielding CO as the product (in acetonitrile for the Re-complex, in 95:5 (v/v) MeCN:H_2O mixture for the Mn-complex). The recyclability of the catalysts was demonstrated through replenishment of CO_2 within solution. The novel catalysts had similar reduction potentials to previously reported complexes of similar structure, and results of the foot-of-the-wave analysis showed comparable maximum turnover rates, too. It is shown that the typical dimerisation of the Mn-catalyst was prevented by incorporation of sterically hindering groups, whilst the Re-catalyst undergoes the usual mechanism following Cl^- loss. No photochemical CO_2 reduction was observed for the Re complex in the presence of a sacrificial donor, which was attributed to the short triplet excited state lifetime (3.6 ns), insufficient for diffusion-controlled electron transfer. Importantly, [Mn(HPEAB)$(CO)_3$Br] can act as a CO_2 reduction catalyst when photosensitised by a zinc porphyrin under red light irradiation ($\lambda > 600$ nm) in MeCN:H_2O (95:5). Thus, this work demonstrates the wide utility of sterically protected Re- and Mn-diimine carbonyl catalysts, where the rate and yield of CO production can be adjusted based on the metal centre and catalytic conditions, with the advantage of suppressing unwanted side-reactions through steric protection of the vacant coordination site.

2.1 Introduction

The goal of artificial photosynthesis is to create a carbon neutral system where the harvesting of sunlight is used to drive the reduction of CO_2 to either a combustible fuel (methane), or chemical feedstock (CO, formate, methanol).[1,2] Accordingly, there is significant research interest in the design, study, and optimisation of novel CO_2 reduction catalysts, which efficiently and selectively produce one of the CO_2 reduction products. A key example are group 7 catalysts that were first proposed in 1983, when it was found that $[Re(bpy)(CO)_3Cl]$ can effectively catalyse the reduction of CO_2 to CO under electrochemical or photochemical activation.[3,4] Since then, there has been much interest in $[Re(L_2)(CO)_3(X)]$ complexes as photosensitisers, photocatalysts, and producers of singlet oxygen,[5–7] owing primarily to their photostability, strong visible light absorption, and long-lived phosphorescent triplet charge-transfer excited states,[8,9] the latter also enabling participation in excited state intermolecular electron transfer reactions.[10,11] $[Re(L_2)(CO)_3(X)]$ complexes are easily functionalised by either modification of the diimine ligand or substitution of the halide, potentially enabling enhanced visible light harvesting following an extension of the aromatic ring system, or modification of the redox potentials to allow for less energy-intensive electrocatalysis.[11–17]

The mechanism for electro- and photocatalytic CO_2 reduction with $[Re(R_2\text{-bpy})(CO)_3(X)]$ (bpy = 2,2′-bipyridine) is generally accepted to proceed *via* the active catalytic species, $[Re(R_2\text{-bpy})(CO)_3]^-$. After one-electron reduction (by photochemical or electrochemical means), the one-electron reduced species (OERS), $[Re(R_2\text{-bpy})(CO)_3Cl]^{\cdot -}$, undergoes axial ligand dissociation to form a solvated neutral complex. Upon a second reduction, the transiently-coordinated solvent molecule dissociates, to form the active catalyst, $[Re(R_2\text{-bpy})(CO)_3]^-$. This species coordinates CO_2, starting the catalytic cycle.[18–20] Whilst the precise mechanism of catalysed CO_2 reduction catalysis is still under some debate, the mainly accepted mechanism first involves protonation of the coordinated CO_2 ligand to form a formate ligand, which is then protonated again followed by the rapid loss of water to yield $[Re(R_2\text{-bpy})(CO)_4]^+$.[21] Upon two-electron reduction of the latter, the CO is released and the active catalyst reformed.[22–28] Mechanisms involving dinuclear Re complexes have also been reported,[28–31] where the preference for reaction mechanism is dependent on catalyst concentration, proton concentration, and the irradiation wavelength.[32,33]

Replacing Re-based catalysts with their Mn-analogues would be a huge step towards more affordable and abundant catalysts. The studies into Mn-catalysts, originally perceived inactive, have intensified since 2011, when it was found that Mn-catalysts are electrocatalytically active, but, differently from their Re-analogues, require a weak Brønsted acid such as water for the catalytic process to occur. $[Mn(bpy)(CO)_3Br]$ was demonstrated to have electrocatalytic activity with significantly less overpotential than the Re analogue.[34] The key differences between the properties of the Re and Mn analogues include: (i) the propensity for dimerisation of the manganese solvent-coordinated OERS, which has been widely demonstrated by IR-spectroelectrochemistry. This Mn-Mn dimer is then cleaved following a second reduction process to produce one equivalent of

$[Mn(L_2)(CO)_3]^-$, the active catalyst; (ii) the Mn catalysts require the presence of a weak Brønsted acid, such as water, for catalytic activity to occur;[35] (iii) the Mn derivatives are photosensitive, undergoing decarbonylation after photoexcitation, and therefore cannot be photoactivated directly.

Using light instead of electricity to activate such Mn-catalysts would be highly beneficial but is precluded by photosensitivity of the $[Mn(L_2)(CO)_3(X)]$ complexes. Therefore, photosensitisers, such as $[Ru(bpy)_3]Cl_2$,[36] and, recently, photosensitisers which do not contain noble metals such as porphyrins, organic chromophores, and copper bis(phenanthroline) complexes have been tested.[37–40] Through modification of the chelate and ancillary ligands, the light-absorbing and electrochemical properties of Mn complexes can be tuned to optimise CO_2 reduction catalysis, as shown by recent work involving functionalised bipyridyl ligands and substitution of Br^- for CN^- or $PhCC^-$.[41–45] In some cases it has been possible to prepare functionalised Mn catalysts which are stable under visible light.[45,46] Photo-assisted CO_2 reduction catalysis under visible light irradiation was recently demonstrated, where photolysis of the electrochemically prepared Mn-Mn dimer with 405 or 365 nm light resulted in a 500 mV decrease in the catalytic overpotential.[47]

The focus of this work was to develop new CO_2 reduction catalysts bearing bulky substituents (Figure 2.1). The 6,6′-substituents introduced electron-withdrawing amide groups to reduce the required reduction potential, allowing for less energy-intensive electrocatalysis, and for the use of less strongly-reducing photosensitisers.[48] The bipyridyl ligand, 6,6′-{N(4-hexylphenyl)-N(ethyl)-amido}-2,2′-bipyridine (HPEAB), and its Re and Mn complexes have been synthesised, characterised, and their ability to reduce CO_2 in an electro- or a photo-chemical processes has been investigated experimentally and computationally.

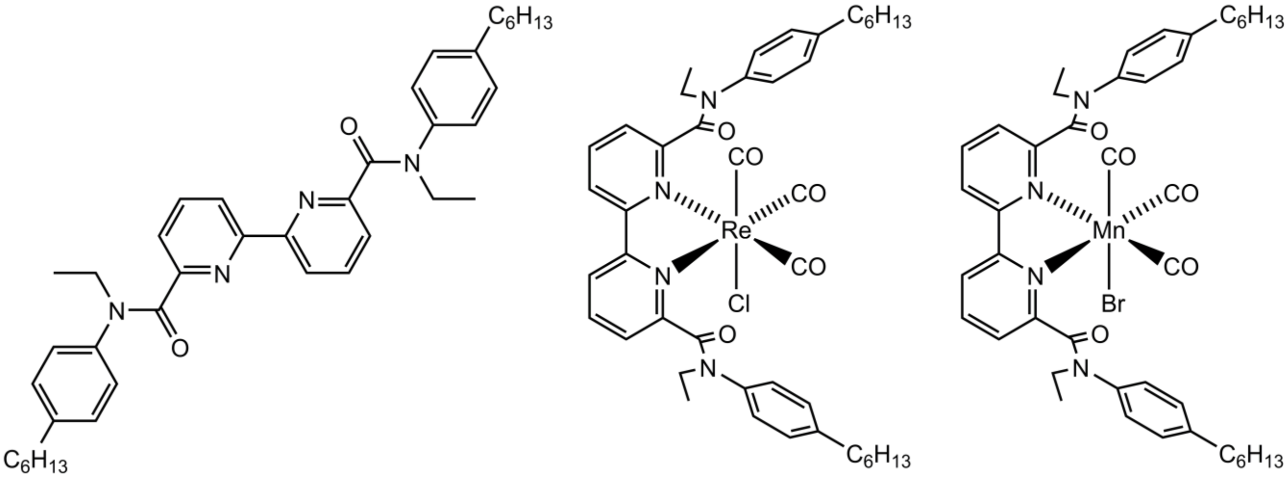

Figure 2.1 – The structures of HPEAB and the Re and Mn complexes used in this study.

2.2 Experimental

Chemical compounds and solvents were purchased from Sigma-Aldrich, Apollo Scientific, Fischer Scientific, and STREM and used as received unless stated otherwise. $[NBu_4][PF_6]$ was recrystallised from boiling ethanol prior to electrochemical measurements. Low chlorin zinc (II) tetraphenylporphyrin (ZnTPP) was supplied by Sigma-Aldrich and used for photocatalytic studies as received. Dry solvents were obtained from the University of Sheffield Grubbs solvent purification system. Ar, N_2, and CO_2 were supplied by BOC. 6,6′-{N-(4-hexylphenyl)-N(ethyl)-amido}-2,2′-bipyridine (HPEAB) was prepared as described previously.[49] UV-vis spectroscopy was performed with an Agilent Varian Cary 50 or Agilent Varian Cary 5000 spectrometer using quartz cuvettes of 10 mm path length. FT-IR spectroscopy was performed with a Perkin-Elmer Spectrum One spectrometer with a solution cell equipped with CaF_2 windows, set to a resolution of 2 cm^{-1}. ^1H and ^{13}C NMR spectra were recorded on a Bruker AVIIIHD 400 MHz spectrometer equipped with a 5 mm BBFO SmartProbe. High resolution mass spectra were recorded using the direct infusion ESI+ TOF method at the University of Sheffield mass spectrometry service. C, H, and N contents were determined using a Perkin-Elmer 2400 CHNS/O Series II Elemental Analyser, values were accurate to ± 0.3 %. Gas analysis was performed with a Perkin-Elmer Autosystem XL gas chromatograph equipped with a thermal conductivity detector (TCD) using He reference gas, on a Restek RT-M separation column of porous layer sieve (5 Å), 30 m long with a diameter of 0.53 mm. 100 µL gas samples were injected directly into the chromatography column. Single crystal X-ray crystallography was carried out in the following manner: Intensity data for $[Re(HPEAB)(CO)_3Cl]\cdot Et_2O$ (CCDC – 1953191) was collected at 100 K with a Bruker D8 Venture diffractometer equipped with a Photon 100 CMOS detector using a CuKα microfocus X-ray source. Intensity data for $[Mn(HPEAB)(CO)_3Cl]\cdot\frac{1}{2}Et_2O$ (CCDC – 1949135) was collected at 100 K on a Bruker SMART APEX-II CCD diffractometer operating with a MoKα sealed-tube X-ray source. Crystals were mounted in fomblin oil on a MiTiGen microloop and cooled in a stream of cold N_2.

Transient absorption spectroscopy was performed at the Lord Porter Laser Laboratory, University of Sheffield. A Ti:Sapphire regenerative amplifier (Spitfire ACE PA-40, Spectra-Physics) provided 800 nm pulses (40 fs FWHM, 10 kHz, 1.2 mJ). 400 nm pulses for excitation were generated by doubling a portion of the 800 nm output in a β-barium borate crystal within a commercially available doubler/tripler (TimePlate, Photop Technologies). White light super-continuum probe pulses in the range 340 – 790 nm were generated using 2 % of the Ti:Sapphire amplifier output, focused on a CaF_2 crystal. Detection was achieved using a commercial transient absorption spectrometer (Helios, Ultrafast Systems) using a CMOS sensor for the UV-vis spectral range. The relative polarisation of the pump and probe pulses was set to the magic angle of 54.7° for anisotropy free measurements. Samples were held in 2 mm path length quartz cells and were stirred during experiments. The optical density at the excitation wavelength was kept at approximately 0.5. The optical density across the probe range was kept below 1.0.

Cyclic voltammetry was carried out using either a Princeton Applied Research VersaSTAT 3, EmStat 3+, or Autolab 100 potentiostat, with a glassy carbon working electrode, a Pt wire counter electrode, and an Ag/AgCl (0.1 mol dm^{-3}) reference electrode. The analyte concentration was typically $2x10^{-3}$ mol dm^{-3}, in a 0.2 mol dm^{-3} solution of the $[NBu_4][PF_6]$ supporting electrolyte. The solutions were saturated with N_2 or CO_2 by bubbling the gas into solution for 30 minutes prior to the performing the measurements. All potentials were quoted relative to the ferrocene-ferrocenium couple (Fc/Fc^+). The individual redox processes were isolated and scanned at various rates (20, 50, 100, 200, and 500 mVs^{-1}) to determine if the redox processes were electrochemically reversible.

Controlled potential electrolysis was carried out in a custom-made glass reaction vessel equipped with a Pt mesh-working electrode, Pt wire counter electrode, and an Ag wire pseudo-reference electrode under CO_2 atmosphere. 0.2 mol dm^{-3} solutions of $[NBu_4][PF_6]$ in anhydrous MeCN were used as the supporting electrolyte. The composition of the gas headspace was monitored by gas chromatography. CO concentrations were calculated based on a calibration curve prepared with home-made reference gas mixtures.

Photocatalytic CO_2 reduction with $[Re(HPEAB)(CO)_3Cl]$ under 405 nm irradiation was conducted as follows. A solution of $[Re(HPEAB)(CO)_3Cl]$ ($1.6x10^{-6}$ mol) was prepared in MeCN:H_2O (95:5 v/v) (2 cm^3) in a 10 mm path length quartz cuvette equipped with a screw-cap Teflon septum seal. NEt_3 was then added (0.5 cm^3) and the solution purged with CO_2 for 30 minutes. The reaction mixture was then stirred and irradiated with 405 nm light supplied by a mounted LED diode (Thorlabs M405L4, 100 mW, 4 cm^2 focal area). The focal point of the light was set to the mid-point of the 10 mm path length cell. The composition of the gas headspace was monitored by gas chromatography.

Photosensitisation of $[Mn(HPEAB)(CO)_3Br]$ with ZnTPP under 625 nm irradiation was conducted as follows. A solution containing $[Mn(HPEAB)(CO)_3Br]$ ($1.5x10^{-6}$ mol) and ZnTPP ($1.9\ x10^{-6}$ mol) was prepared in MeCN:H_2O (95:5 v/v) (25 cm^3) in a custom-made cylindrical glass reaction vessel of 10 cm path length equipped with a collection bulb for gaseous products. NEt_3 was then added (5 cm^3) and the solution purged with CO_2 for 30 minutes. The reaction mixture was then stirred and irradiated with 625 nm light supplied by a mounted LED diode (Thorlabs M625L4, 200 mW, 4 cm^2 focal area). The focal point of the light was set to the mid-point of the 10 cm path length cell. The composition of the gas headspace was monitored by gas chromatography. Experiments were halted after the plateau in CO production was reached. Control experiments were carried out under Ar atmosphere to show that CO production was not a result of catalyst decomposition.

IR-Spectroelectrochemistry was performed using a Princeton Applied Research VersaSTAT 3 or EmStat 3+ Potentiostat. $4x10^{-3}$ mol dm^{-3} solutions of the analyte with 0.3 mol dm^{-3} $[NBu_4][PF_6]$ supporting electrolyte in anhydrous MeCN were prepared under Ar or CO_2 atmosphere. Measurements were performed in an optically transparent thin-layer electrochemical (OTTLE) cell equipped with Pt mesh working and counter electrodes, an Ag-wire pseudo-reference electrode, and CaF_2 windows. Spectral monitoring was done with a Perkin-Elmer Spectrum One FT-IR spectrometer. During IR-SEC, the applied potential was scanned toward negative potential until the onset of the 1st reduction was reached. At this point the scan was paused and the spectral changes in the mid-IR region monitored until the 1st reduction was complete. The potential scan was then resumed until the second reduction potential onset was reached, the scan was then paused and the electrolysis monitored until the 2nd reduction process was complete.

Photostability measurements were performed on a modified flash photolysis setup home-built at the University of Sheffield. A steady-state 150 W Xe arc lamp (Hamamatsu Photonics) was used as the irradiation source. Detection was achieved with a Spex Minimate monochromator and FEU0118 PMT. The detector current output was coupled into a Tektronix TDS 3032B digital oscilloscope. Analyte decomposition was measured by recording the increase in voltage in the PMT, and subsequent conversion to ΔOD at the MLCT maximum. Data were baseline-corrected to the signal obtained from pure dichloromethane (DCM). Samples were flown through a Harrick cell equipped with CaF_2 windows by a peristaltic pump.

Calculations were performed using the SMP version of the Gaussian09 package, revision D.01.[50] Gaussian was compiled using the Gaussian supplied version of BLAS and ATLAS on the EMT64 architecture.[51,52] The solvent, dichloromethane (DCM), was simulated using the integral equation formalism polarisable continuum model (IEFPCM) using parameters as implemented in Gaussian09.[53–55] All calculations utilized the PBE0 functional.[56] The Karlsruhe basis set, def2-SVP,[57,58] was employed for all atoms except Re and Mn. For these, the Dirac-Hartree-Fock basis set, dhf-SVP,[59] was used instead. Frequencies within the harmonic approximation were calculated for all optimised structures. The absence of imaginary frequencies confirmed that energy minima had been found. For all calculations, ultrafine integrals were used, and no symmetry constraints were applied. Calculated vibrational frequencies were scaled to account for the anharmonicity of the vibrational modes.[60–64] The applied scaling factors are provided in appendix B (Table B1).

Synthesis of [Re(HPEAB)(CO)$_3$Cl]

A solution of [Re(CO)$_5$Cl] (120 mg, 0.33 mmol) and HPEAB (200 mg, 0.32 mmol) was prepared in toluene (20 cm^3). The reaction mixture was heated to reflux for 16 hours, yielding a fine yellow/orange precipitate. The reaction mixture was cooled in a NaCl/H_2O bath and diethyl ether (100 cm^3) was added to induce further precipitation. The product was isolated by vacuum filtration and then re-dissolved in dichloromethane. The DCM was removed under reduced pressure, and then the product was purified by column chromatography on silica stationary phase (1:1 DCM: ethyl acetate). Crystals of the purified product were grown by vapour diffusion of Et_2O into a concentrated DCM solution of the complex to yield the pure product as a yellow crystalline solid (43 %).

Found: λ_{max} / nm (DCM, ε / dm^3 mol^{-1} cm^{-1}) 326 (15319), 407 (2999); υ_{max} / cm^{-1} (CaF_2 cell, DCM) 2026 (CO), 2016 (CO), 1919 (CO), 1908 (CO), 1655 (C=O), 1647 (C=O); δ_H (400 MHz, $CDCl_3$) 7.92 (d, J = 8.2 Hz, 2H), 7.59 (t, J = 7.6 Hz, 2H), 7.44 (d, J = 7.6 Hz, 4H), 7.07 (d, J = 7.7 Hz, 4H), 6.94 (d, J = 7.6 Hz, 2H), 4.14 (ddd, J = 20.3, 13.8, 7.1 Hz, 4H), 2.47 (t, J = 7.3 Hz, 4H), 1.67 – 1.38 (m, 10H), 1.24 (s, 12H), 0.86 (s, 6H); $\delta_C\{^1H\}$ (101 MHz, $CDCl_3$) 195.98, 165.47, 158.56, 157.17, 142.64, 138.99, 137.95, 129.64, 127.27, 125.84, 123.22, 44.62, 35.42, 31.74, 31.16, 28.98, 22.69, 14.20, 13.38; MS (TOF, AP+): m/z 924.5. Elemental analysis calc. for $C_{43}H_{50}ClN_4O_5Re$: C 55.86 %, H 5.45 %, N 6.06 %, Cl 3.86 %. Found: C 55.60 %, H 5.39 %, N 6.04 %, Cl 3.69 %. Crystal Data for $C_{47}H_{60}ClN_4O_6Re$ (M =998.64 g/mol): monoclinic, space group $P2_1/c$ (no. 14), a = 15.9608(5) Å, b = 16.3375(4) Å, c = 17.8363(5) Å, β = 107.5280(10)°, V = 4435.0(2) Å^3, Z = 4, T = 100.0 K, μ(CuKα) = 6.333 mm^{-1}, $Dcalc$ = 1.496 g/cm^3, 68588 reflections measured ($7.502° \leq 2\Theta \leq 133.708°$), 7875 unique ($R_{int}$ = 0.0690, R_{sigma} = 0.0336) which were used in all calculations. The final R_1 was 0.0413 ($I > 2\sigma(I)$) and wR_2 was 0.1069 (all data).

Synthesis of [Mn(HPEAB)(CO)$_3$Br]

A solution of [Mn(CO)$_5$Br] (66 mg, 0.24 mmol) and HPEAB (150 mg, 0.22 mmol) was prepared in Et_2O (20 cm^3). The reaction mixture was heated to reflux for three hours, yielding a fine orange precipitate. The precipitate was isolated by centrifugation and washed with Et_2O to yield the pure product, an orange powder (91 %). Single crystals for crystallographic study were grown by vapour diffusion of Et_2O into a DCM solution of the compound.

Found: λ_{max} / nm (DCM, ε / dm^3 mol^{-1} cm^{-1}) 326 (16587), 439 (2093) υ_{max} / cm^{-1} (CaF_2 cell, DCM) 2029 (CO), 2024 (CO), 1942 (CO), 1927 (CO), 1650 (C=O); δ_H (400 MHz, $CDCl_3$) 7.86 (d, J = 6.4 Hz, 2H), 7.62 – 7.48 (m, J = 38.1 Hz, 5H), 7.09 (d, J = 8.3 Hz, 4H), 6.94 (d, J = 7.6 Hz, 2H), 4.18 (ddd, J = 32.2, 13.8, 7.0 Hz, 5H), 2.60 – 2.32 (m, 4H), 1.57 – 1.46 (m, 5H), 1.40 (t, J = 7.2 Hz, 6H), 1.29 – 1.19 (m, 10H), 0.86 (t, J = 6.7 Hz, 6H); $\delta_C\{^1H\}$ (101 MHz, $CDCl_3$) 165.98, 159.65, 157.70, 142.45, 139.00, 137.01, 129.51, 127.25, 125.87, 44.55, 35.38, 31.68, 31.14, 28.90, 22.63, 14.14, 13.07; HRMS (TOF-ESI+): m/z ($M+Na^+$) Calc. for $C_{43}H_{50}N_4O_5NaMnBr$ 859.2243; Found 859.2267; Elemental analysis calc. for $C_{43}H_{50}N_4O_5BrMn$: Calc. 61.65 %, H 6.02 %, N 6.69 %, Br 9.54 %. Found: C 61.06 %, H 5.81 %, N 6.64 %, Br 10.09 %. Crystal Data for $C_{45}H_{55}BrMnN_4O_{5.5}$ (M =874.78 g/mol): monoclinic, space group $P2_1/c$ (no. 14), a = 15.8147(12) Å, b = 16.2939(11) Å, c = 17.9380(11) Å, β = 106.379(4)°, V = 4434.7(5) Å^3, Z = 4, T = 110.01 K, μ(MoKα) = 1.247 mm^{-1}, $Dcalc$ = 1.310 g/cm^3, 76332 reflections measured (2.684° ≤ 2Θ ≤ 55.286°), 10219 unique (R_{int} = 0.1106, R_{sigma} = 0.1125) which were used in all calculations. The final R_1 was 0.0947 (I > 2σ(I)) and wR_2 was 0.2798 (all data).

2.3 Results and Discussion

Synthesis and characterisation

X-ray crystallography

[Re(HPEAB)$(CO)_3$Cl] was crystallised by diffusion of Et_2O into a solution of the complex in DCM to yield yellow plate crystals of [Re(HPEAB)$(CO)_3$Cl]$\cdot Et_2O$. The crystals were monoclinic with the $P2_1/c$ space group. The complex formed the expected facial isomer of the octahedral complex (Figure 2.2). The ethyl and hexyl aliphatic chains were disordered, indicating that there were no intramolecular interactions involving the aliphatic groups in the crystal to fix their geometry. Et_2O sits within the hydrophobic pocket between hexyl chains. It was also disordered, indicating no intermolecular interactions between the Re complex and Et_2O. [Mn(HPEAB)$(CO)_3$Br] was crystallised through analogous methods, forming orange plate crystals of [Mn(HPEAB)$(CO)_3$Cl]$\cdot\frac{1}{2}Et_2O$. As with the Re analogue, the crystal system was monoclinic with the $P2_1/c$ space group.

Comparison of the average bond lengths within the octahedral unit showed that the metal-carbon bonds are longer in the Re complex compared with Mn, likely due to the difference in atomic radii of the two metal centres. The difference in C≡O bond length between the Re and Mn complexes was not statistically significant, hence the strength of the backbonding effect was similar in the solid-state crystal of each complex (Table 2.1).

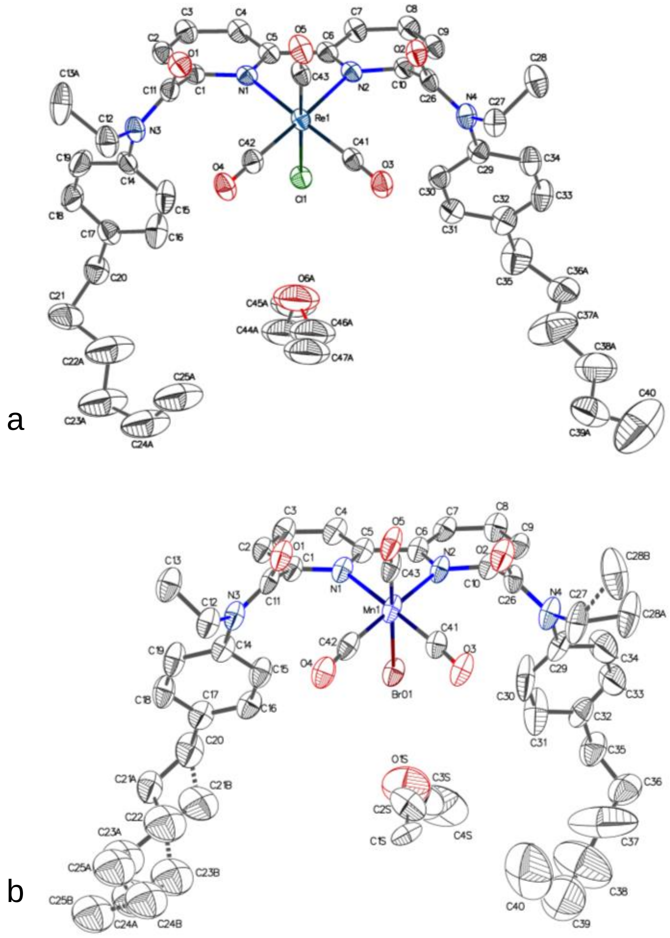

Figure 2.2 – Molecular structures of the $[Re(HPEAB)(CO)_3Cl]{\cdot}Et_2O$ *(a) and* $[Mn(HPEAB)(CO)_3Cl]{\cdot}\frac{1}{2}Et_2O$ *crystals (b), measured by single crystal X-ray diffraction, thermal ellipsoids are drawn at the 50% probability level. Selected bond distances are given in Table 2.1.*

Table 2.1 – Selected bond lengths for the crystal structures of $[Mn(HPEAB)(CO)_3Br]{\cdot}\frac{1}{2}Et_2O$ *and* $[Re(HPEAB)(CO)_3Cl]{\cdot}Et_2O$*.*

Parameter / Å	$[Re(HPEAB)(CO)_3Cl]{\cdot}Et_2O$	$[Mn(HPEAB)(CO)_3Cl]{\cdot}\frac{1}{2}Et_2O$
Average M-C	1.916(5)	1.794(8)
M-X	2.4968(11)	2.5487(12)
Average C-O	1.148(6)	1.151(8)
Average M-N	2.205(5)	2.0785(6)

UV-vis spectroscopy

The UV-vis absorption spectrum of each complex was consistent with similar compounds that have been reported previously (Figure 2.3a).[65] In both Re- and Mn- complexes, there are multiple intense absorptions at $\lambda < 400$ nm which correspond to π-π^* electronic transitions within the bipyridyl ligand. The broad absorption bands observed at lower energies were attributed to metal/halide-to-ligand charge transfer transitions, MLCT/XLCT. The MLCT/XLCT absorption envelope was shifted from 439 nm in the Mn-complex to 407 nm (ΔE = 1791 cm^{-1}) in the Re-complex, similar to the shift of the absorption maximum between [Mn(dmbpy)$(CO)_3$Br] and [Re(dmbpy)$(CO)_3$Cl] from 418 to 376 nm (ΔE = 2673 cm^{-1}) (Appendix B, fig. B2). For Re and Mn, the MLCT/XLCT absorption envelopes are red shifted when L_2 = HPEAB compared to L_2 = dmbpy. Whilst the effect was small compared to substitution with -CF_3 or -NO_2 groups, it showed that the π^* orbital within the aromatic ligand is stabilised by the introduction of the amide groups, as evidenced by the decrease in MLCT/XLCT transition energy.[42]

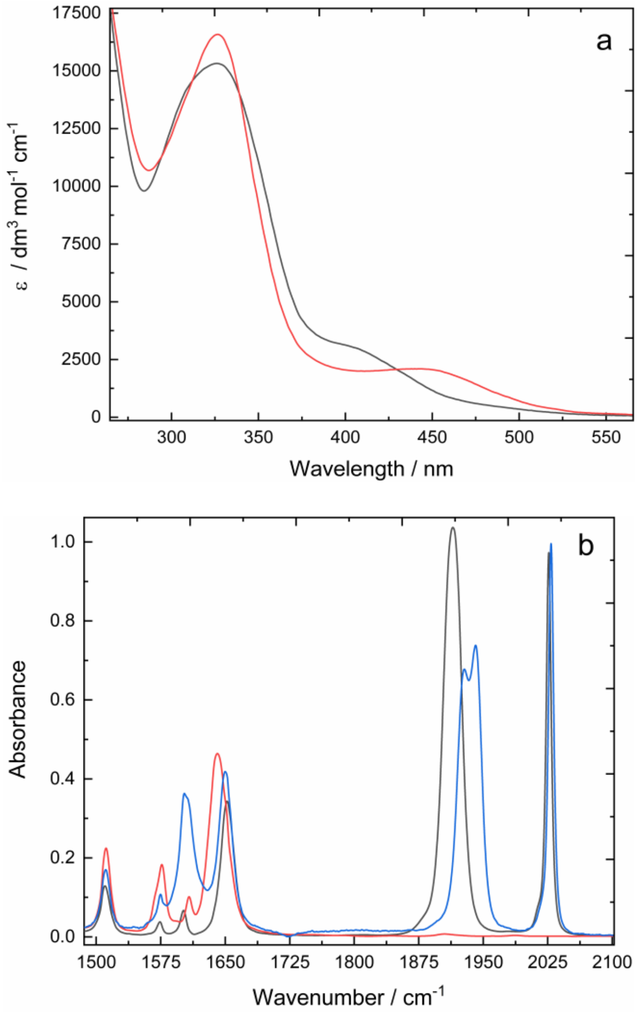

Figure 2.3 – a). Electronic absorption spectra for [Re(HPEAB)$(CO)_3$Cl] (black) and [Mn(HPEAB)$(CO)_3$Br] (red) in DCM at room temperature. b). IR vibrational absorption spectra for HPEAB (red), [Re(HPEAB)$(CO)_3$Cl] (black), and [Mn(HPEAB)$(CO)_3$Br] (blue) in DCM, the spectra of the complexes have been normalised to the a'(1) carbonyl ligand stretching vibrational mode. See Appendix B fig. B30 and B34 for the calculated IR spectra of the compounds.

FT-IR spectroscopy

The Re and Mn complexes, as well as the free HPEAB ligand, were studied by FT-IR spectroscopy in DCM (Figure 2.3b). In [Re(HPEAB)$(CO)_3$Cl] four absorption bands were observed in the 1850 – 2075 cm^{-1} region. The largest peaks correspond to the a′(1) (2026 cm^{-1}), a″ and a′(2) group vibrations of the carbonyl ligands. The a″ and a′(2) modes are very similar in energy, forming a single absorption envelope from 1880 – 1950 cm^{-1}. In contrast, the peak-to-peak separation of the analogous modes in [Re(bpy)$(CO)_3$Cl] is sufficient to resolve two peak centres. Deconvolution of the FT-IR spectrum of [Re(HPEAB)$(CO)_3$Cl] with pseudo-Voigt profiles revealed a shoulder at 2013 cm^{-1} that was assigned as a combination mode of the carbonyl ligands and a ligand centred mode (Appendix B, fig. B5, B6), as suggested previously through computation of the anharmonic vibrational potentials.[66] The 900 – 1700 cm^{-1} spectral region contained a large number of absorption bands which were associated with the ligand, including the amide C=O and C-N stretches, C=C stretch, in-plane C-H bending, and in-plane ring bending.[67] The absorption envelope for the C=O stretching vibration consists of two absorption bands, which were assigned as symmetric (the higher energy band) and antisymmetric stretching modes of the two C=O groups. This assignment was supported through visualisation of the calculated vibrational frequencies (Appendix B, fig. B30, B34).

The vibrational spectrum of [Mn(HPEAB)$(CO)_3$Br] was different to the Re analogue, where the a″ and a′(2) energies were influenced by the M-X moiety: the absorption bands of the two modes do not overlap to form a symmetric envelope in the Mn complex, with pseudo-Voigt deconvolution (Appendix B, Eq. B1) yielding a slightly different peak-to-peak separation (Re: 11 cm^{-1}, Mn: 13 cm^{-1}) (Appendix B, fig. B7, B8). Consistent with the less electron-rich metal centre, all of the carbonyl group vibrations are shifted to higher frequency in the Mn complex, albeit to a different extent; the a′(1), a″ and a′(2) modes were shifted by 3, 23, and 19 cm^{-1}, respectively. The additional combination mode observed at 2024 cm^{-1} in the Mn complex was found to have a 3.5x larger relative peak area than the same band in the Re complex, perhaps due to stronger coupling between the carbonyl and ligand modes which constitute this combination mode.[66] The energies of the ν(CO) group vibrations are consistent with both complexes being present in solution in their neutral form (without the loss of halogen).

Evaluation of catalytic performance by electrochemical methods

Cyclic voltammetry

The complexes [Re(HPEAB)$(CO)_3$Cl] and [Mn(HPEAB)$(CO)_3$Br] were studied by cyclic voltammetry to determine their potential to operate as CO_2 reduction electrocatalysts.

Under an inert atmosphere in anhydrous MeCN, three reduction processes were observed for [Re(HPEAB)$(CO)_3$Cl] (Figure 2.4a), similar to those observed in electrochemical measurements of [Re(dmbpy)$(CO)_3$Cl]. The potential of the first reduction of the HPEAB complex was shifted to a less negative value compared to that of [Re(bpy)$(CO)_3$Cl] and [Re(dmbpy)$(CO)_3$Cl]. This difference was attributed to reduced electron density within the bipyridyl π-system due to the electron withdrawing amide groups. The first reduction process was electrochemically reversible, as indicated by the linear relationship between the current and the square root of the scan rate (Appendix B fig. B19). The second reduction of the Re-complex was observed at potentials similar to that of bpy or dmbpy analogues, indicating little influence of the bipyridyl substituents on the reduction of [Re(HPEAB)$(CO)_3$(NCMe)]. The second reduction process was only partially electrochemically reversible, with a large peak-to-peak separation of 700 mV. The third reduction process was observed at −2.3 V. As this process is not related to the catalytic activity of the complex, it was not studied further.

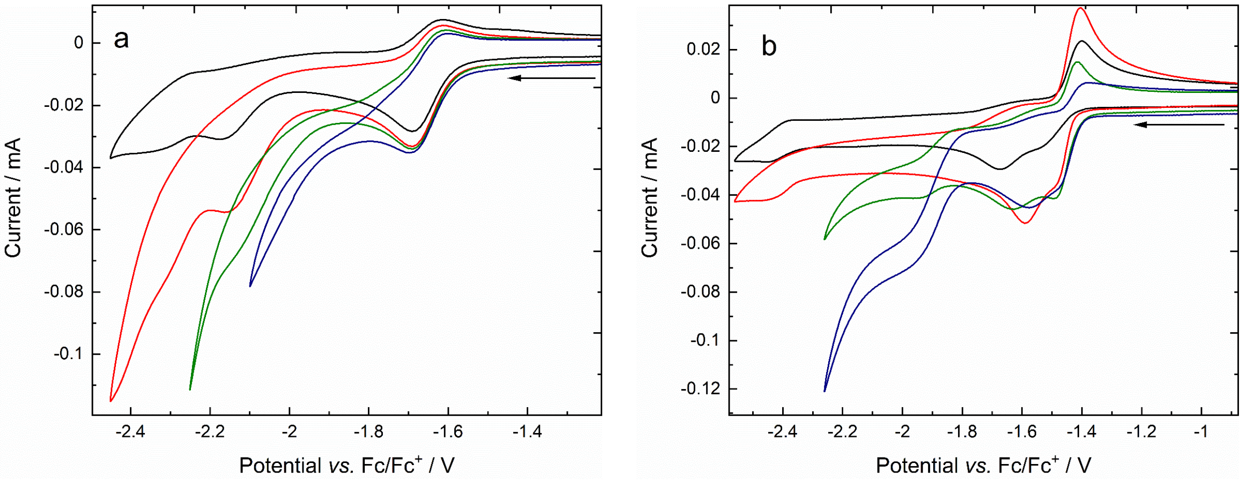

Figure 2.4 – Cyclic voltammograms of 2x10^{-3} mol dm^{-3} solutions of [Re(HPEAB)$(CO)_3$Cl] (a) and [Mn(HPEAB)$(CO)_3$Br] (b) in 0.2 mol dm^{-3} $[NBu_4][PF_6]$ supporting electrolyte at a scan rate of 100 mV s^{-1} under N_2 atmosphere in dry MeCN (black), CO_2 atmosphere in anhydrous MeCN (red), CO_2 atmosphere with 2% H_2O in MeCN (green), and CO_2 atmosphere with 5% H_2O in MeCN (blue). The arrow indicates the initial scan direction.

In the presence of CO_2, current enhancement at the second reduction process was observed, this effect was attributed to the catalytic reaction. The current enhancement was quantified through comparison of the peak potentials under inert (i_p) and catalytic (i_{cat}) conditions. Addition of water (to the concentration of 2% H_2O in MeCN) to the electrochemical cell resulted in a further increase in the current enhancement, as well as a reduction in the catalytic onset potential by 50 mV. The presence of a weak Brønsted acid is known to promote the rate of CO_2 reduction catalysis through protonation of $[Re(L_2)(CO)_3(CO_2)]^-$ to form the corresponding formate complex. A further increase of water concentration to 5% H_2O in MeCN led to the catalytic process in the CV being partially obscured by the reduction of water.

[Mn(HPEAB)$(CO)_3$Br] (Figure 2.4b) exhibited different electrochemical behaviour compared to both [Re(HPEAB)$(CO)_3$Cl] and [Mn(bpy)$(CO)_3$Br]. Under N_2 in dry MeCN, the first and second reduction processes are partially overlapped, with peak potentials of −1.48 and −1.74 V for the first and second reductions, respectively. The second reduction potential, which forms the active catalyst, was 510 mV lower than [Mn(bpy)$(CO)_3$Br]. This is partially a result of the electron withdrawing amide groups, which stabilise the anionic charge on the bipyridyl π*-orbital. However, with IR-spectroelectrochemical (IR-SEC) analysis also shows that dimerisation of the 5-coordinate anion was prevented, which further reduces the required reduction potential for active catalyst formation.

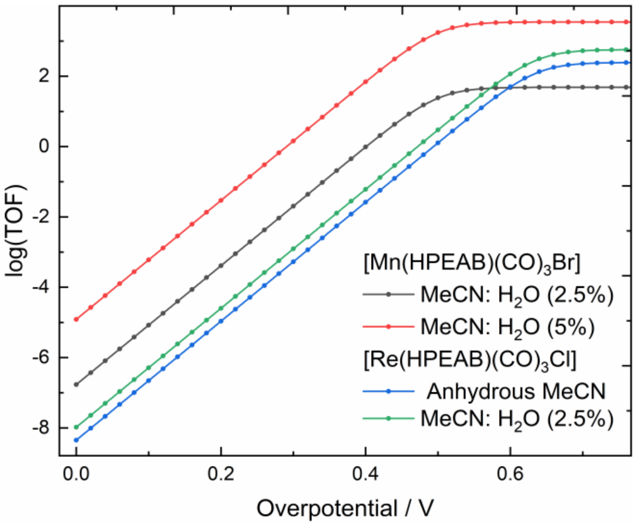

Figure 2.5 – Tafel plots for CO_2 reduction by [Mn(HPEAB)$(CO)_3$Br] or [Re(HPEAB)$(CO)_3$Cl] under various conditions, as stated on the graph. The plots are produced by the foot of the wave analysis of the cyclic voltammetry data.

The reduction processes for [Mn(HPEAB)$(CO)_3$Br] are similar to [Mn(mes-bpy)$(CO)_3$Br], (mes-bpy = 6,6′-bismesityl-2,2′-bipyridyl).[68] In this complex, the mesityl groups prevented dimerisation following reduction, and the active catalyst was produced following a single two-electron reduction centred at −1.60 V *vs.* Fc/Fc$^+$. Introduction of the mesityl groups also resulted in extension of the aromatic π-system, increasing the electron-accepting ability of the ligand and leading to a reduction in the required potential for electrocatalysis by *ca.* 300 mV.[68–70] These previous data support our conclusion from the IR-SEC experiments that the sterically-protecting amide groups in the 6,6′-positions prevent dimerisation of the one-electron reduction product, [Mn(HPEAB)$(CO)_3$], which instead forms a solvated complex, [Mn(HPEAB)$(CO)_3$(NCMe)]. This difference is attributable to the more facile reduction of the neutral 5-coordinate complex, [Mn(HPEAB)$(CO)_3$(NCMe)], compared to the dimeric [Mn(dmbpy)$(CO)_3$]$_2$.

In the presence of CO_2, no significant changes were observed in the redox chemistry of [Mn(HPEAB)$(CO)_3$Br]. After the addition of water, a new reduction process was observed 310 mV higher in energy than the second reduction. This corresponds to the potential required for the turnover of the catalytic cycle. Increasing the concentration of water resulted in enhancement of the measured current for this process, indicating a faster turnover of the cycle.

Table 2.2 – Electrochemical and electrocatalytic properties of [M(diimine)$(CO)_3$(X)] complexes measured by cyclic voltammetry and evaluated by foot-of-the-wave analysis.

Complex	**$E_{1/2}$ / V**	**$E_{1/2}$/ V**	**Conditions**	**E_{cat}, $E_0(CO_2/CO)$ / V**	**i_{cat} / i_p**	**Optimum overpotential (η) / V**	**log(TOF_0)**	**log(TOF_{max})**
[Re(bpy)$(CO)_3$Cl][16,76]	−1.72[b]	−2.11[a]	DMF, 2 M H_2O	−1.25, −1.33	-	0.41 - 0.56	−4.9	2.0 – 3.9
[Re(dmbpy)$(CO)_3$Cl][16]	−1.81[b]	−2.15[a]	-	-	-	-	-	-
[Re(HPEAB)$(CO)_3$Cl]	−1.65[b]	−2.17[a]	MeCN	−2.0, −1.40	1.8	0.74	−8.3	2.4
			MeCN, 2% H_2O	−2.0, −1.40	2.0	0.74	−8.0	2.8
[Mn(bpy)$(CO)_3$Br][34]	−1.65[a]	−1.89[a]	-	-	-	-	-	-
[Mn(dmbpy)$(CO)_3$Br][34,76]	−1.73[a]	−1.98	MeCN, 5% H_2O	−1.83, −1.29	-	0.51	−8.7	-0.4
[Mn(mes-bpy)$(CO)_3$Br][68]	−1.60[a]	-	MeCN, 0.1 M Mg^{2+}	−1.60, −1.40	-	0.30 - 0.45	−2.3 - −4.8	2.8
			MeCN, 0.3 M TFE	−1.60, −1.40	-	0.30 - 0.45	−7.0	3.7
[Mn(HPEAB)$(CO)_3$Br]	−1.48[a]	−1.74[a]	MeCN, 2% H_2O	−1.90, −1.40	1.4	0.62	−6.8	1.7
			MeCN, 5% H_2O	−1.90, −1.40	2.3	0.62	−4.9	3.5

(a) Potential given as cathodic peak potential ($E_{p,a}$), b) Potential given as the half-wave potential ($E_{1/2}$). Reduction potentials were recorded in anhydrous MeCN under inert atmosphere. Where required, literature data for redox potentials were converted to Fc/Fc^+ reference with the following conversion factors – $Fc/Fc^+ = 0$, NHE = −630 mV, SHE = −624 mV, Ag/AgCl = −450 mV, SCE = −380 mV[77]). DMF = dimethylformamide, TFE = trifluoroethanol. Optimum overpotential, log(TOF_0), and log(TOF_{max}) were estimated with the foot-of-the-wave method, where TOF_0 is turnover frequency at zero overpotential, and TOF_{max} is turnover frequency at the potential required for maximum catalytic rate.

To estimate the rate of electrocatalysis, foot-of-the-wave (FOTW) analysis (See Appendix B) was applied to estimate the turnover frequency (TOF) at zero overpotential (TOF_0), and at the overpotential required to maximise the rate of catalysis, TOF_{max} (Table 2.2).[71–74] FOTW analysis was required as it was not possible to increase the scan rate to the point at which substrate diffusion was rate limiting.[75] It was found that compared to [Re(bpy)$(CO)_3$Cl], [Re(HPEAB)$(CO)_3$Cl] required significantly higher overpotential (ca. 0.25 V) to maximise the rate of catalysis. In addition, the TOF values for this complex are similar to [Re(bpy)$(CO)_3$Cl]. Similarly, [Mn(HPEAB)$(CO)_3$Br] required higher overpotential compared to both [Mn(dmbpy)$(CO)_3$Br] and [Mn(mes-bpy)$(CO)_3$Br]. However, the TOF_0 was larger than for both [Mn(dmbpy)$(CO)_3$Br] and [Mn(mes-bpy)$(CO)_3$Br] (in the absence of a Mg^{2+} co-substrate). The increased overpotential requirement could be explained by the effect of the electron-withdrawing amide substituents, as more electron deficient diimine ligands have been demonstrated to negatively affect the catalytic performance of [Mn(R_2-bpy)$(CO)_3$(X)] complexes through stabilisation of the π^*-orbital, resulting in a decrease in the rates of halogen dissociation and CO_2 complexation.[43] At optimum overpotential the HPEAB catalyst performed better than [Mn(dmbpy)$(CO)_3$Br]. The performance was comparable to that of [Mn(mes-bpy)$(CO)_3$Br], with the added advantage of requiring milder conditions to achieve the same TOF_{max} value. A Tafel plot comparison of the catalytic performance of [Re(HPEAB)$(CO)_3$Cl] and [Mn(HPEAB)$(CO)_3$Br] under different conditions (Figure 2.5) shows that the Mn complex required significantly lower overpotential to reach TOF_{max} compared to Re. In addition, at higher water concentrations, [Mn(HPEAB)$(CO)_3$Br] had a larger TOF value for all overpotentials compared to [Re(HPEAB)$(CO)_3$Cl]. Results of the FOTW analysis are summarised in Table 2.2.

IR-spectroelectrochemistry

Spectral changes in the mid-IR region following electrochemical reduction of [Re(HPEAB)$(CO)_3$Cl] in MeCN were observed by IR-SEC (Figure 2.6). Prior to electrolysis, the IR-absorption bands of the starting complex were observed at 2024, 1912 and 1652 cm^{-1}. Upon application of the first reduction potential, a decrease in the absorbances of the starting complexes and the grow-in of new bands at 2004 and 1882 cm^{-1} was observed. These new absorbances were attributed to $[Re(HPEAB)(CO)_3Cl]^{\cdot-}$, the assignment of which was supported by DFT calculations (Appendix B fig. B31). The a′(1) vibration was shifted to lower frequency by 20 cm^{-1}, similar to the 23 cm^{-1} shift between [Re(bpy)$(CO)_3$Cl] and its radical anion.[17] Further spectral changes took place after the formation of $[Re(HPEAB)(CO)_3Cl]^{\cdot-}$, where the growth of additional bands at 1995 and 1975 cm^{-1} occurred concurrently with the broadening and shifting of the a″/a′(2) absorption envelope to 1860 cm^{-1}. These changes could correspond to dissociation of the axial chloride ligand to form [Re(HPEAB)$(CO)_3$] and subsequently [Re(HPEAB)$(CO)_3$(NCMe)], assignment of which were supported by DFT calculations (Appendix B fig. B32) and previous studies.[17] At potentials greater than −2.2 V, the formation of $[Re(HPEAB)(CO)_3]^-$ was observed, as evidenced by the growth of a new mode at 1959 cm^{-1}.

In the presence of CO_2, the initial spectral changes upon reduction were unchanged. $[Re(HPEAB)(CO)_3Cl]^{\cdot-}$ is formed, as evidenced by formation of the bands at 2004 and 1882 cm^{-1}. In contrast to the reduction under an argon atmosphere, the bands assignable to the 5-coordinate anion

$[Re(HPEAB)(CO)_3]^-$ were not detected. Instead, multiple new IR-absorption bands were observed: a broad envelope centred around 1896 cm^{-1}, and bands at 1682, 2013, and 2029 cm^{-1}. It is likely that $[Re(HPEAB)(CO)_3]^-$ was reacting rapidly with CO_2 to form $[Re(HPEAB)(CO)_3(CO_2)]^-$: the 1682 cm^{-1} could be assigned to the coordinated CO_2, 2013 cm^{-1} could be assigned as the a′(1), and the a″/a′(2) modes would account for two overlapping bands in the 1896 cm^{-1} absorption envelope. The remaining bands in the spectrum, at 1886, 1927, and 2030 cm^{-1} could be tentatively assigned to the species which comprise the catalytic cycle. For example, $[Re(HPEAB)(CO)_3(CO_2H)]$, where the carbonyl modes are shifted to higher energies due to a reduction in electron density following protonation of $[Re(HPEAB)(CO)_3(CO_2)]^-$ (Appendix B fig. B33). No evidence was observed for the formation of dinuclear or CO_2-bridged Re-catalysts, indicating that the sterically hindering substituents only allow for a mononuclear catalytic pathway to take place.[33]

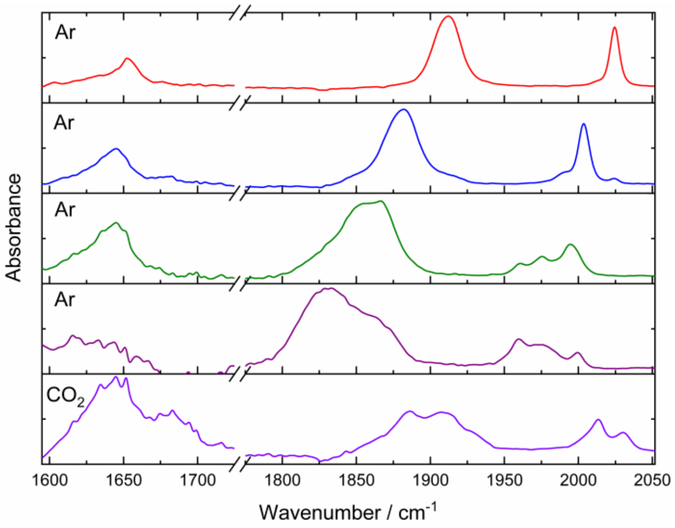

Figure 2.6 – Spectral changes in the mid-IR region following electrochemical reduction of $[Re(HPEAB)(CO)_3Cl]$ *at the first and second reduction potentials, IR-SEC spectra are displayed in increasing electrolysis time from top to bottom. The first four spectra were recorded under argon atmosphere, the final spectrum was recorded under* CO_2 *atmosphere in a separate experiment.*

$[Mn(HPEAB)(CO)_3Br]$ exhibited significantly different behaviour to that of $[Re(HPEAB)(CO)_3Cl]$ following electrochemical reduction (Figure 2.7). Firstly, the complex is prone to hydrolysis when held at low negative potentials, with the formation of $[Mn(HPEAB)(CO)_3(OH_2)]^+$ evidenced by the absorption bands at 1972 and 2050 cm^{-1} (Appendix B fig. B36).[78,12] At potentials lower than the onset of the first reduction, the IR-absorption bands of the parent complex at 2027, 1939 and 1922 cm^{-1} decay concurrently with the growth of multiple new absorbances. Tentative assignment of these new bands with the aid of DFT calculations (Appendix B fig. B35, B37) suggest formation of the singly reduced complex $[Mn(HPEAB)(CO)_3Br]^{\cdot-}$ and neutral five-coordinate species. This assignment was further supported by comparison with IR-SEC data previously reported for $[Mn(mes\text{-}bpy)(CO)_3Br]$.[69] It was clear from our experiments that the dimerisation commonly observed for non-sterically hindered Mn CO_2 reduction catalysts did not take place for [Mn(HPEAB)$(CO)_3$Br].[79]

At longer electrolysis times, absorbance bands were observed to form at 1811 and 1825 cm^{-1}. These correspond to the second reduction product, [Mn(HPEAB)$(CO)_3$]$^-$. These species already partially form at the first reduction potential, suggesting a strong overlap of the two reduction processes. At potentials below −2.0 V the [Mn(HPEAB)$(CO)_3$Br] selectively converts to [Mn(HPEAB)$(CO)_3$]$^-$, the proposed active CO_2 reduction catalyst (Appendix B fig. B36).

In the presence of CO_2, after formation of [Mn(HPEAB)$(CO)_3$]$^-$, an additional absorption band grows in at 1682 cm^{-1}, which was ascribed to the asymmetric stretching vibration of the CO_2 ligand, indicating formation of the Mn-CO_2 adduct. The frequency of the carbonyl modes of the complex were not significantly affected by CO_2 coordination, which indicated that the electron density of the Mn centre was unchanged by CO_2 complexation. Therefore, this suggests that the Mn-CO_2 bond is weak and the CO_2 ligand is only weakly coordinated (Appendix B fig. B38, B39). The proposed mechanism of interconversion between starting material and the active catalyst for [Re(HPEAB)$(CO)_3$Cl] and [Mn(HPEAB)$(CO)_3$Br] is summarised in Figure 2.8.

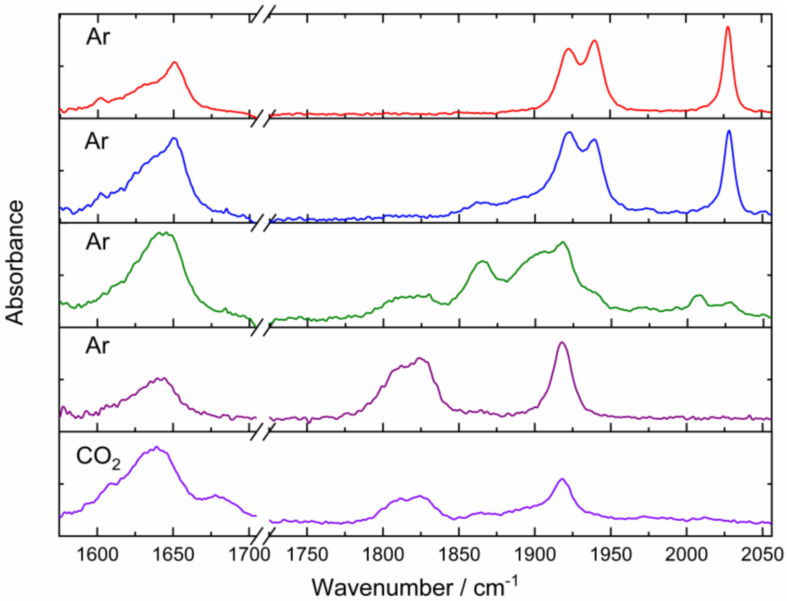

Figure 2.7 – Spectral changes in the mid-IR region following electrochemical reduction of [Mn(HPEAB)$(CO)_3$Br] at the first and second reduction potentials. IR-SEC spectra are displayed in increasing electrolysis time from top to bottom. The first four spectra were recorded under argon atmosphere, the final spectrum was recorded under CO_2 atmosphere in a separate experiment.

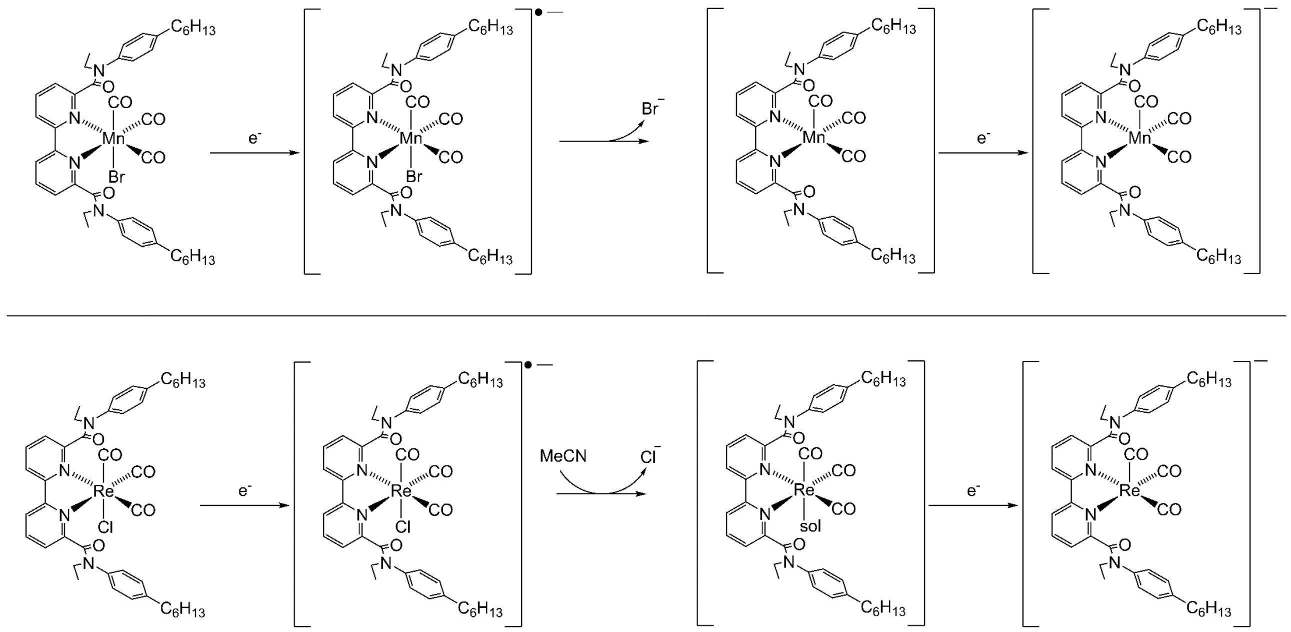

Figure 2.8 – Proposed mechanisms for electrochemical formation of the active CO_2 reduction catalyst for [Mn(HPEAB)$(CO)_3$Br] (top) and [Re(HPEAB)$(CO)_3$Cl] (bottom), suggested on the basis of species observed during IR-SEC measurements.

Table 2.3 – Experimental and calculated vibrational frequencies for species detected in situ during IR-spectroelectrochemical analysis of [Re(HPEAB)$(CO)_3$Cl] and [Mn(HPEAB)$(CO)_3$Br] in MeCN, scaling factors for anharmonic correction of calculated frequencies are given in Appendix B (Table B1).

Species	**Experimental vibrational frequencies / cm^{-1}**		**Calculated vibrational frequencies / cm^{-1}**
	C≡O	**C=O / CO_2**	
[Re(HPEAB)$(CO)_3$Cl]	2024, 1912	1652	1653, 1916, 1919, 2024
[Re(HPEAB)$(CO)_3$Cl]$^{\cdot -}$	2004, 1882	1645	1643, 1885, 1889, 2004
[Re(HPEAB)$(CO)_3$]	1995, 1867	1645	1642, 1857, 1862, 1993
[Re(HPEAB)$(CO)_3$(NCMe)]	1975, 1853	1645	1643, 1847, 1871, 1974
[Re(HPEAB)$(CO)_3$]$^{-}$	1959, 1831	1642	1641, 1852, 1863, 1960
[Re(HPEAB)$(CO)_3$$(CO_2)$]$^{-}$	2013, 1896	1645 / 1682	1643, 1704, 1893, 1894, 2012
[Mn(HPEAB)$(CO)_3$Br]	2027, 1939, 1922	1650	1650, 1926, 1937, 2013
[Mn(HPEAB)$(CO)_3$Br]$^{\cdot -}$	1865, 1953	1650	1644, 1864, 1875, 1957
[Mn(HPEAB)$(CO)_3$]	1903, 1919, 2008	1650	1648, 1902, 1920, 2005
[Mn(HPEAB)$(CO)_3$$(OH_2)$]$^{+}$	2051, 1973	1650	1652, 1949, 1974, 2050
[Mn(HPEAB)$(CO)_3$(NCMe)]	Not detected		
[Mn(HPEAB)$(CO)_3$]$^{-}$	1918, 1825, 1812	1640	1641, 1808, 1828, 1897
[Mn(HPEAB)$(CO)_3$$(CO_2)$]$^{-}$	1918, 1825, 1812	1640, 1678	1632, 1689, 1801, 1831, 1896

Catalytic activity

The results of electrocatalytic and photocatalytic studies are summarised in Table 2.4. Confirmation of CO_2 reduction by the complexes was done by controlled potential electrolysis (Appendix B fig. B40, B41). [Mn(HPEAB)$(CO)_3$Br] was reduced at −1.9 V vs. Ag^+, leading to the production of CO. The CO yield was compared to a standard, [Re(dmbpy)$(CO)_3$Cl], under identical conditions. The turnover number (TON) was found to be similar to the standard after *ca.* 40 min of electrolysis. This continued until 85 min, where the TON_{CO} maximises at 2.79. The CO concentration in the gas headspace decreased from this point, indicating catalysis had stopped. The initial TOF of the Mn catalyst was significantly higher than for [Re(dmbpy)$(CO)_3$Cl]. Replenishment of H_2O and CO_2 within the solution allowed for continuation of the CO_2 reduction catalysis. However, the yield of CO decreased by 97 %, potentially a result of decomposition of the active catalyst whilst electrolysis was paused to replenish H_2O and CO_2.

The [Re(HPEAB)$(CO)_3$Cl] catalyst also performed comparably to [Re(dmbpy)$(CO)_3$Cl]. However, the TON_{CO} after 40 min was less than the dmbpy complex, as was the initial TOF. This indicates that there was a lag-phase at the start of the catalysis which was longer for [Re(HPEAB)$(CO)_3$Cl]. A notable advantage of [Re(HPEAB)$(CO)_3$Cl] was the longevity of the catalytic activity, which showed no sign of decrease after 6 h of electrolysis, whereas the TON_{CO} reaches a plateau after 2.5 h with the [Re(dmbpy)$(CO)_3$Cl] catalyst. Furthermore, upon re-purging the solution with CO_2, the catalytic activity continued, with $TON_{CO} = 7.26$ after 3 h. This increase could be tentatively ascribed to a long catalytic lag-phase resulting from slow formation of the active catalyst from the hexacoordinate anion precursor. In contrast, for [Mn(HPEAB)$(CO)_3$Br] the initial TOF was greater than for [Re(HPEAB)$(CO)_3$Cl], but the longevity of the catalyst was much less.

Table 2.4 – Catalytic performance in electrochemical and photochemical CO_2 reduction studies, quantified by gas chromatography in either controlled potential electrolysis, or irradiation experiments, respectively.

Catalyst	**Reaction conditions**	**Maximum TON_{CO}**	**Initial rate**
[Re(dmbpy)$(CO)_3$Cl]	MeCN, −2.3 V *vs.* Ag^+	2.8	2.3
[Re(HPEAB)$(CO)_3$Cl]	MeCN, −2.0 V *vs.* Ag^+	8.4	1.3
[Mn(HPEAB)$(CO)_3$Br]	MeCN/H_2O, −2.0 V *vs.* Ag^+	2.8	11.6
[Mn(HPEAB)$(CO)_3$Br]	MeCN/H_2O, ZnTPP, NEt_3, 625 nm irradiation	0.30	0.75

The potential of these catalysts for photodriven reduction of CO_2 was investigated under visible light irradiation. $[Re(HPEAB)(CO)_3Cl]$ and NEt_3 were dissolved in 95:5 MeCN:H_2O under CO_2 atmosphere. After 3 h of 405 nm irradiation no CO was detected. This was likely a result of the short lifetime of the ^{3}MLCT state formed following photoexcitation. Indeed, femtosecond transient absorption studies revealed that the excited state of the Re complex had a lifetime of 3.6 ± 0.2 ns (Appendix B, fig. B27-B29), too short to engage in bimolecular reductive quenching by a sacrificial donor, the first step in the photocatalytic cycle (Figure 2.9). This is unlike the excited state dynamics of most reported $[Re(L_2)(CO)_3(X)]$ complexes, which typically have long-lived ^{3}MLCT states (*ca.* 60 ns).[8]

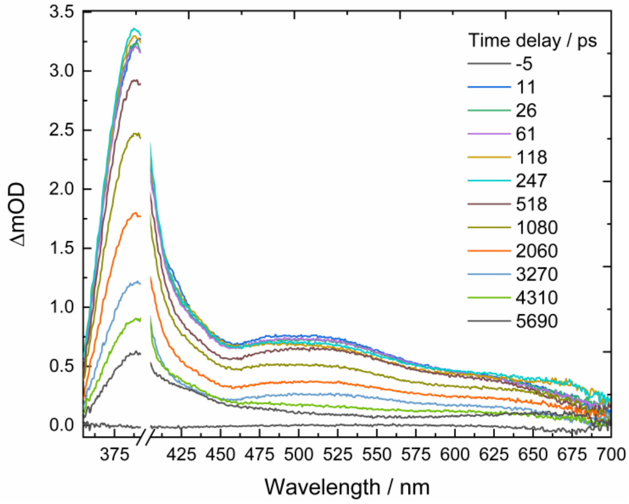

Figure 2.9 – Transient absorption spectra of $[Re(HPEAB)(CO)_3Cl]$ in DCM at various pump – probe time delays following 400 nm, 100 fs excitation.

In contrast to the $[Re(L_2)(CO)_3(X)]$ complexes that only photolyse under UV irradiation,[80] the Mn analogues are unstable under visible light irradiation, although there are several recent reports on the feasibility of photo-assisted activation of Mn CO_2 reduction catalysts, as well as catalysts which do not photodecompose.[45–47] The main photolysis pathway under these conditions is decarbonylation, caused by a weakening of the M-CO bonds by formal oxidation of the metal in the MLCT excited state.[81] The photostability of $[Mn(HPEAB)(CO)_3Br]$ was quantitatively studied through irradiation of an air-saturated MeCN solution with broadband white light from a high-pressure Xe lamp. By monitoring the decrease in optical density at the MLCT absorption maximum at 439 nm throughout the irradiation, it was found that the complex had a photolysis time constant of 48 minutes (Appendix B, fig. B16).

This photosensitivity clearly prohibited the use of $[Mn(HPEAB)(CO)_3Br]$ as a photocatalyst under direct photoactivation. Therefore, Zn(II) tetraphenylporphyrin (ZnTPP), a noble-metal free photosensitiser, was used under 625 nm irradiation in MeCN:H_2O (95:5 v/v) with NEt_3 as a sacrificial donor. The reaction proceeds through the following steps; the excitation of ZnTPP to ZnTPP*, reduction of ZnTPP* by NEt_3 to form $ZnTPP^-$, which in turn reduces $[Mn(HPEAB)(CO)_3Br]$ to its anion, initiating the catalytic cycle. During irradiation experiments of ZnTPP/Mn-complex/NEt_3 mixture under CO_2, gas evolution was observed which was shown to be CO by gas chromatography. Control experiments detected no CO formation upon irradiation of the reaction mixture under inert atmosphere (no CO_2), confirming photostability of the catalyst under these conditions. Quantification of the catalytic performance showed reduction by 90% when compared to electrochemical reduction (Appendix B, fig. B42). This low performance was likely due to inefficient reduction of the catalyst by the reduced porphyrin, as estimation of the Gibbs energy of electron transfer (ΔG_{et}) from $ZnTPP^-$ to $[Mn(HPEAB)(CO)_3Br]$ suggests that this process was only weakly thermodynamically favourable. This was quantified using the Rehm-Weller equation, as shown in Appendix B. Furthermore, the estimated ΔG_{et} showed that the reduction process needed for turnover of the catalytic cycle was thermodynamically unfavourable (See Appendix B). Overall, experiments with ZnTPP have shown the possibility of photoreduction of CO_2 using $[Mn(HPEAB)(CO)_3Br]$ as a catalyst.

2.4 Conclusions

Two group 7 complexes, $[Mn(HPEAB)(CO)_3Br]$ and $[Re(HPEAB)(CO)_3Cl]$, which include a bipyridyl ligand functionalised in the 6,6′-position with sterically hindering N-(4-hexylphenyl)-N(ethyl)-amido groups, have been developed, fully characterised, and shown to be effective CO_2 reduction catalysts. Single crystal X-ray crystallography established that the functionalised ligand did not significantly affect the structure of the octahedral complex. A change of the M-X centre from Re-Cl to Mn-Br results in a shift of the carbonyl group vibrations to higher frequencies. Both compounds absorb visible light, with the lowest excited state being an MLCT in nature. The MLCT transitions in the new complexes were shifted to lower energies compared to $[M(dmbpy)(CO)_3X]$. The introduction of sterically hindering substituents did not alter the redox chemistry of $[Re(HPEAB)(CO)_3Cl]$ in comparison to other Re(I) diimine complexes, as shown by CV and IR-SEC studies. However, an important change was invoked on the mechanism of reduction of the Mn complex – the sterically hindering substituents prevent the dimerisation commonly observed for $[Mn(diimine)(CO)_3]^{\cdot -}$ complexes, where the diimine is a non-sterically protecting ligand. Under CO_2 atmosphere, both complexes were able to reduce CO_2 to CO electrochemically. The TOF_{max} determined by the foot-of-the-wave analysis were comparable to those reported previously for other Re- and Mn-catalysts when analysed in the same way. However, for the complexes presented here, the same TOF_{max} values could be achieved using only water as the Brønsted acid, instead of an organic proton donor. Irradiation of $[Re(HPEAB)(CO)_3Cl]$ with 405 nm light in the presence of a sacrificial donor under CO_2 atmosphere did not lead to any catalytic activity, which was attributed to the short

(3.6 ns) lifetime of the ^{3}MLCT excited state, as measured by transient absorption spectroscopy. As with the majority of Mn(I) complexes of this type, it was not possible to employ [Mn(HPEAB)(CO)$_3$Br] as a photocatalyst directly, due to its rapid photodecomposition.

Importantly, [Mn(HPEAB)(CO)$_3$Br] can act as a CO_2 reduction catalyst when photosensitised by a zinc porphyrin under red light irradiation ($\lambda > 600$ nm) in MeCN:H_2O (95:5); there has been only one reported example of photoactivating Mn-catalysts with porphyrins in this manner. Thus, this work adds to the growing body of research on the wide utility of sterically protected Re- and Mn-diimine carbonyl catalysts, where the rate and yield of CO production can be adjusted based on the metal centre and catalytic conditions, with the advantage of suppressing unwanted side-reactions through steric protection of the vacant coordination site. Overall, the Mn-complex with sterically hindering ligands presents a platform for future study into CO_2 reduction catalysts which do not require expensive elements, and bypass unproductive dimerisation reactions in the catalytic cycle.

References

1 L. Hammarström and S. Hammes-Schiffer, *Acc. Chem. Res.*, 2009, **42**, 1859–1860.

2 S. C. Roy, O. K. Varghese, M. Paulose and C. A. Grimes, *ACS Nano*, 2010, **4**, 1259–1278.

3 J. Hawecker, J.-M. Lehn and R. Ziessel, *J. Chem. Soc. Chem. Commun.*, 1983, 536–538.

4 J. Hawecker, J.-M. Lehn and R. Ziessel, *J. Chem. Soc., Chem. Commun.*, 1984, 328–330.

5 A. Coleman, C. Brennan, J. G. Vos and M. T. Pryce, *Coord. Chem. Rev.*, 2008, **252**, 2585–2595.

6 A. J. Morris, G. J. Meyer and E. Fujita, *Acc. Chem. Res.*, 2009, **42**, 1983–1994.

7 H. Takeda, C. Cometto, O. Ishitani and M. Robert, *ACS Catal.*, 2017, **7**, 70–88.

8 L. M. Kiefer, J. T. King and K. J. Kubarych, *J. Phys. Chem. A*, 2014, **118**, 9853–9860.

9 S. Mai and L. González, *Chem. Sci.*, 2019, **10**, 10405–10411.

10 J. Hawecker, J.-M. Lehn and R. Ziessel, *Helv. Chim. Acta*, 1986, **69**, 1990–2012.

11 S. Ranjan, S. Y. Lin, K. C. Hwang, Y. Chi, W. L. Ching, C. S. Liu, Y. T. Tao, C. H. Chien, S. M. Peng and G. H. Lee, *Inorg. Chem.*, 2003, **42**, 1248–1255.

12 S. J. P. Spall, T. Keane, J. Tory, D. C. Cocker, H. Adams, H. Fowler, A. J. H. M. Meijer, F. Hartl and J. A. Weinstein, *Inorg. Chem.*, 2016, **55**, 12568–12582.

13 J. R. Wagner and D. G. Hendricker, *J. Inorg. Nucl. Chem.*, 1975, **37**, 1375–1379.

14 K. Kalyanasundaram, *J. Chem. Soc. Faraday Trans. 2 Mol. Chem. Phys.*, 1986, **82**, 2401–2415.

15 H. Takeda, K. Koike, H. Inoue and O. Ishitani, *J. Am. Chem. Soc.*, 2008, **130**, 2023–2031.

16 J. M. Smieja and C. P. Kubiak, *Inorg. Chem.*, 2010, **49**, 9283–9289.

17 F. P. A. Johnson, M. W. George, F. Hartl and J. J. Turner, *Organometallics*, 1996, **15**, 3374–3387.

18 A. Klein, C. Vogler and W. Kaim, *Organometallics*, 1996, **15**, 236–244.

19 T. Scheiring, A. Klein and W. Kaim, *J. Chem. Soc. Perkin Trans. 2*, 1997, 2569–2571.

20 M. D. Doherty, D. C. Grills, J. T. Muckerman, D. E. Polyansky and E. Fujita, *Coord. Chem. Rev.*, 2010, **254**, 2472–2482.

21 K. A. Grice, N. X. Gu, M. D. Sampson and C. P. Kubiak, *Dalton Trans.*, 2013, **42**, 8498.

22 H. Takeda and O. Ishitani, *Coord. Chem. Rev.*, 2010, **254**, 346–354.

23 M. Dunwell, Y. Yan and B. Xu, *ACS Catal.*, 2017, **7**, 5410–5419.

24 B. Kumar, M. Llorente, J. Froehlich, T. Dang, A. Sathrum and C. P. Kubiak, *Annu. Rev. Phys. Chem.*, 2012, **63**, 541–569.

25 G. Guisado-Barrios, J. Bouffard, B. Donnadieu and G. Bertrand, *Organometallics*, 2011, **30**, 6017–6021.

26 Y. Kou, Y. Nabetani, D. Masui, T. Shimada, S. Takagi, H. Tachibana and H. Inoue, *J. Am. Chem. Soc.*, 2014, **136**, 6021–6030.

27 D. C. Grills, M. Z. Ertem, M. McKinnon, K. T. Ngo and J. Rochford, *Coord. Chem. Rev.*, 2018, **374**, 173–217.

28 J. Agarwal, E. Fujita, H. F. Schaefer and J. T. Muckerman, *J. Am. Chem. Soc.*, 2012, **134**, 5180–5186.

29 B. P. Sullivan, C. M. Bolinger, D. Conrad, W. J. Vining and T. J. Meyer, *J. Chem. Soc. Chem. Commun.*, 1985, 1414–1416.

30 Y. Hayashi, S. Kita, B. S. Brunschwig and E. Fujita, *J. Am. Chem. Soc.*, 2003, **125**, 11976–11987.

31 E. E. Benson and C. P. Kubiak, *Chem. Commun.*, 2012, **48**, 7374–7376.

32 J. A. Keith, K. A. Grice, C. P. Kubiak and E. A. Carter, *J. Am. Chem. Soc.*, 2013, **135**, 15823–15829.

33 P. Lang, R. Giereth, S. Tschierlei and M. Schwalbe, *Chem. Commun.*, 2019, **55**, 600–603.

34 M. Bourrez, F. Molton, S. Chardon-Noblat and A. Deronzier, *Angew. Chemie - Int. Ed.*, 2011, **50**, 9903–9906.

35 C. Riplinger, M. D. Sampson, A. M. Ritzmann, C. P. Kubiak and E. A. Carter, *J. Am. Chem. Soc.*, 2014, **136**, 16285–16298.

36 P. L. Cheung, C. W. Machan, A. Y. S. Malkhasian, J. Agarwal and C. P. Kubiak, *Inorg. Chem.*, 2016, **55**, 3192–3198.

37 C. O. Dietrich-Buchecker, P. A. Marnot, J. P. Sauvage, J. R. Kirchhoff and D. R. McMillin, *J. Chem. Soc. - Chem. Commun.*, 1983, 513–515.

38 M. Sandroni, Y. Pellegrin and F. Odobel, *Comptes Rendus Chim.*, 2016, **19**, 79–93.

39 J. X. Zhang, C. Y. Hu, W. Wang, H. Wang and Z. Y. Bian, *Appl. Catal. A Gen.*, 2016, **522**, 145–151.

40 H. Takeda, H. Kamiyama, K. Okamoto, M. Irimajiri, T. Mizutani, K. Koike, A. Sekine and O. Ishitani, *J. Am. Chem. Soc.*, 2018, **140**, 17241–17254.

41 X. Wang, H. Ma, C. Meng, D. Chen and F. Huang, *Phys. Chem. Chem. Phys.*, 2019, **21**, 8849–8855.

42 W. C. Henke, C. J. Otolski, W. N. G. Moore, C. G. Elles and J. D. Blakemore, *Inorg. Chem.*,

2020, **59**, 2178–2187.

43 S. E. Tignor, H. Y. Kuo, T. S. Lee, G. D. Scholes and A. B. Bocarsly, *Organometallics*, 2019, **38**, 1292–1299.

44 V. Yempally, S. Moncho, F. Hasanayn, W. Y. Fan, E. N. Brothers and A. A. Bengali, *Inorg. Chem.*, 2017, **56**, 11244–11253.

45 B. J. Aucott, A. K. Duhme-Klair, B. E. Moulton, I. P. Clark, I. V. Sazanovich, M. Towrie, L. A. Hammarback, I. J. S. Fairlamb and J. M. Lynam, *Organometallics*, 2019, **38**, 2391–2401.

46 H. Y. Kuo, T. S. Lee, A. T. Chu, S. E. Tignor, G. D. Scholes and A. B. Bocarsly, *Dalton Trans.*, 2019, **48**, 1226–1236.

47 J. O. Taylor, Y. Wang and F. Hartl, *ChemCatChem*, 2020, **12**, 386–393.

48 K. S. Rawat, S. C. Mandal and B. Pathak, *Electrochim. Acta*, 2019, **297**, 606–612.

49 D. O. O. Kirsanov, N. E. E. Borisova, M. D. Reshetova, A. V. Ivanov, L. A. Korotkov, I. I. Eliseev, M. Y. Alyapyshev, I. G. Spiridonov, A. V. Legin, Y. G. Vlasov, V. A. Babain, I. Edition, R. Federation and R. Federation, *Russ. Chem. Bull.*, 2012, **61**, 881–890.

50 M. J. Frisch, G. W. Trucks, H. B. Schlegel, G. E. Scuseria, M. A. Robb, J. R. Cheeseman, G. Scalmani, V. Barone, G. A. Petersson, H. Nakatsuji, X. Li, M. Caricato, A. V. Marenich, J. Bloino, B. G. Janesko, R. Gomperts, B. Mennucci, H. P. Hratchian, J. V. Ortiz, A. F. Izmaylov, J. L. Sonnenberg, D. Williams-Young, F. Ding, F. Lipparini, F. Egidi, J. Goings, B. Peng, A. Petrone, T. Henderson, D. Ranasinghe, V. G. Zakrzewski, N. R. J. Gao, G. Zheng, W. Liang, M. Hada, M. Ehara, K. Toyota, R. Fukuda, J. Hasegawa, M. Ishida, T. Nakajima, Y. Honda, O. Kitao, H. Nakai, T. Vreven, K. Throssell, J. A. Montgomery, Jr., J. E. Peralta, F. Ogliaro, M. J. Bearpark, J. J. Heyd, E. N. Brothers, K. N. Kudin, V. N. Staroverov, T. A. Keith, R. Kobayashi, J. Normand, K. Raghavachari, A. P. Rendell, J. C. Burant, S. S. Iyengar, J. Tomasi, M. Cossi, J. M. Millam, M. Klene, C. Adamo, R. Cammi, J. W. Ochterski, R. L. Martin, K. Morokuma, O. Farkas, J. B. Foresman and D. J. Fox, 2016.

51 R. C. Whaley and A. Petitet, *Softw. - Pract. Exp.*, 2005, **35**, 101–121.

52 R. C. Whaley, A. Petitet and J. J. Dongarra, *Parallel Comput.*, 2001, **27**, 3–35.

53 J. L. Pascual-ahuir, E. Silla and I. Tuñon, *J. Comput. Chem.*, 1994, **15**, 1127–1138.

54 S. Miertuš, E. Scrocco and J. Tomasi, *Chem. Phys.*, 1981, **55**, 117–129.

55 S. Miertuš and J. Tomasi, *Chem. Phys.*, 1982, **65**, 239–245.

56 C. Adamo and V. Barone, *J. Chem. Phys.*, 1999, **110**, 6158–6170.

57 F. Weigend, F. Furche and R. Ahlrichs, *J. Chem. Phys.*, 2003, **119**, 12753–12762.

58 F. Weigend and R. Ahlrichs, *Phys. Chem. Chem. Phys.*, 2005, **7**, 3297–3305.

59 F. Weigend and A. Baldes, *J. Chem. Phys.*, 2010, **133**, 174102–174110.

60 A. P. Scott and L. Radom, *J. Phys. Chem.*, 1996, **100**, 16502–16513.

61 M. K. Kesharwani, B. Brauer and J. M. L. Martin, *J. Phys. Chem. A*, 2015, **119**, 1701–1714.

62 M. L. Laury, M. J. Carlson and A. K. Wilson, *J. Comput. Chem.*, 2012, **33**, 2380–2387.

63 M. D. Halls, J. Velkovski and H. B. Schlegel, *Theor. Chem. Acc.*, 2001, **105**, 413–421.

64 K. K. Irikura, R. D. Johnson and R. N. Kacker, *J. Phys. Chem. A*, 2005, **109**, 8430–8437.

65 R. Heydová, E. Gindensperger, R. Romano, J. Sýkora, A. Vlček, S. Záliš and C. Daniel, *J. Phys. Chem. A*, 2012, **116**, 11319–11329.

66 H. Kvapilová, A. Vlček, V. Barone, M. Biczysko and S. Záliš, *J. Phys. Chem. A*, 2015, **119**, 10137–10146.

67 T. P. Gerasimova and S. A. Katsyuba, *Dalton Trans.*, 2013, **42**, 1787–1797.

68 M. D. Sampson and C. P. Kubiak, *J. Am. Chem. Soc.*, 2016, **138**, 1386–1393.

69 M. D. Sampson, A. D. Nguyen, K. A. Grice, C. E. Moore, A. L. Rheingold, C. P. Kubiak and P. Kubiak, *J. Am. Chem. Soc.*, 2014, **136**, 5460–5471.

70 K. T. Ngo, M. McKinnon, B. Mahanti, R. Narayanan, D. C. Grills, M. Z. Ertem and J. Rochford, *J. Am. Chem. Soc.*, 2017, **139**, 2604–2618.

71 R. Francke, B. Schille and M. Roemelt, *Chem. Rev.*, 2018, **118**, 4631–4701.

72 C. Costentin, S. Drouet, M. Robert, J. Save and J. M. Savéant, *J. Am. Chem. Soc.*, 2012, **134**, 11235–11242.

73 C. Costentin, J. Savøant and J.-M. Savéant, *ChemElectroChem*, 2014, **1**, 1226–1236.

74 C. Costentin, G. Passard and J. M. Savéant, *J. Am. Chem. Soc.*, 2015, **137**, 5461–5467.

75 K. J. Lee, N. Elgrishi, B. Kandemir and J. L. Dempsey, *Nat. Rev. Chem.*, 2017, **1**, 1–14.

76 C. Costentin, M. Robert and J.-M. M. Savéant, *Chem. Soc. Rev.*, 2013, **42**, 2423–2436.

77 V. V. Pavlishchuk and A. W. Addison, *Inorganica Chim. Acta*, 2000, **298**, 97–102.

78 Q. Zeng, J. Tory and F. Hartl, *Organometallics*, 2014, **33**, 5002–5008.

79 B. D. Rossenaar, F. Hartl, D. J. Stufkens, C. Amatore, E. Maisonhaute and J. N. Verpeaux, *Organometallics*, 1997, **16**, 4675–4685.

80 J. Jimenez, I. Chakraborty, A. Dominguez, J. Martinez-Gonzalez, W. M. C. Sameera and P. K. Mascharak, *Inorg. Chem.*, 2018, **57**, 1766–1773.

81 E. Kottelat and Z. Fabio, *Inorganics*, 2017, **5**, 24.

Chapter 3. Photocatalytic reduction of CO_2 to CO in aqueous solution by a Noble-metal free system under red light irradiation

Abstract

This work demonstrates the first example of photocatalytic CO_2 to CO reduction in aqueous solution at wavelengths above 600 nm using a molecular Mn catalyst. To achieve this, a water soluble catalyst with the structure $[Mn(L_2)(CO)_3Br]$ has been synthesised and fully characterised. Water solubility was imparted through functionalisation of the bipyridyl ligand with phosphonate ester groups in the 4,4′-positions. To minimise any increase in the light harvesting ability of the photosensitive Mn complex above 500 nm, a $-CH_2-$ spacer was inserted between the phosphonate ester and pyridyl ring to electronically decouple the two groups. Electrochemical studies in acetonitrile-water mixtures established that the catalyst can reduce CO_2 to CO following two electron reduction. The maximum turnover frequency, estimated with the foot-of-the-wave method, was $\log(TOF_{max}) = 2.2$ at an overpotential of 0.84 V. The phosphonate catalyst was also able to reduce CO_2 to CO in aqueous solution following electron transfer to the Mn(I) catalyst from a Zn(II) porphyrin photosensitiser under 625 nm irradiation.

3.1 Introduction

The design of novel systems for the photochemical reduction of CO_2 to industrial feedstocks (CO, H_2CO_2, MeOH) or solar fuels, such as methane, is a key problem for modern chemistry.[1] As such, there have been significant efforts into the design of efficient and selective CO_2 reduction catalysts. Group 7 metal carbonyl complexes bearing diimine ligands, such as $[Re(bpy)(CO)_3Cl]$ (bpy = 2,2′-bipyridyl), have been well studied for this purpose, beginning with the photo- and electrochemical catalytic reduction of CO_2 to CO by Lehn *et al.*[2] Whilst many catalysts based on the $[Re(L_2)(CO)_3(X)]$ structure have been developed,[3–6] the scarcity of Re in the Earth's crust has prompted the development of earth-abundant catalysts. The Mn(I) analogues, $[Mn(L_2)(CO)_3Br]$[7,8] have been shown to be effective electrochemical CO_2 reduction catalysts in the presence of a weak Brønsted acid, such as water, and at lower overpotentials than their Re(I) predecessors.[9] In the past decade, many novel Mn(I) catalysts with substituted diimine ligands have been reported,[8] with different catalytic reaction mechanisms, product selectivity and stability.[10–18] One example of this ligand functionalisation is to incorporate an anchoring group, such as carboxylate or phosphonate substituents, which have been utilised to bind Mn catalysts onto semiconductor surfaces and metal-organic frameworks.[19–22]

The accepted mechanism for catalytic CO_2 reduction with $[Mn(L_2)(CO)_3Br]$ begins with two-electron reduction of the complex. The first reduction results in Br^{-} dissociation to form $[Mn(L_2)(CO)_3(sol)]^{\cdot -}$, which dimerises to form $[Mn(L_2)(CO)_3]_2$.[23] The formation of this Mn-Mn dimer is generally considered unproductive, and can be prevented by increasing the steric bulk around the Mn centre.[12,17,24] The second reduction process leads cleavage of the Mn-Mn bond which produces one equivalent of the active catalyst, $[Mn(L_2)(CO)_3]^{-}$. The catalytic cycle proceeds by coordination of CO_2 to the Mn centre, the coordinated CO_2 ligand is then protonated to form a formate complex, followed by a second protonation and the elimination of water to form $[Mn(L_2)(CO)_4]^{+}$.[25] A 'reduction first' mechanism resulting in formation of $[Mn(L_2)(CO)_4]$ is also possible, but is less desirable due to higher required overpotentials.[26] Upon reduction of the tetracarbonyl intermediate, CO is released, and the active catalyst is reformed.[27] Other catalytic processes have also been reported to occur simultaneously, such as proton reduction.[28]

Ideally, Mn-catalysed CO_2 reduction should operate photochemically, allowing the process to harness solar energy. However, this is often precluded by the photosensitivity of $[Mn(L_2)(CO)_3X]$ complexes. Excitation of the metal-to-ligand (MLCT) or halide-to-ligand (XLCT) charge transfer transitions results in decomposition of the complex through dissociation of the CO and/or Br^{-} ligands.[29,30] Photosensitisers that harvest light energy at wavelengths the Mn catalyst does not absorb are therefore required to initiate catalysis. Various compounds have been used to photosensitise Mn-catalysed CO_2 reduction, such as $[Ru(bpy)_3]Cl_2$,[31] as well as porphyrins, organic dyes, and copper bis(diimine) complexes.[32–35] Recently, a light-assisted electrocatalytic CO_2 reduction has been reported, where the Mn-Mn dimer was prepared electrochemically, and the metal-metal bond was then cleaved by photolysis to form the active catalyst, eliminating the need for a second electrochemical reduction.[36]

Most reported CO_2 reduction catalysts are only soluble in organic solvents, whilst the environmental cost of catalytic processes will be obviously reduced in aqueous solution. There have been several examples of electrochemical CO_2 reduction in water, but this often requires immobilisation of the catalyst on an electrode surface such as graphene,[37] TiO_2 nanoparticles, carbon nanotubes or graphitic carbon nitride. This is commonly achieved through the use of carboxylate or phosphonate anchoring groups.[19,20,38,39] It is also possible to introduce a $-CH_2-$ spacer group between the pyridyl ring and phosphonate group.[20] However, the effect of introducing the spacer group on the light harvesting or electrochemical properties of the Mn(I) catalyst has not yet been studied.

Only a few examples of electrocatalytic CO_2 reduction in aqueous solution with Mn-complexes have been reported: these include [Mn(bpy-acid)$(CO)_3$Br] (bpy-acid = 4,4′-dicarboxy-2,2′-bipyridyl), which electrochemically reduces CO_2 to CO with high selectivity,[40] and an Mn-corrole complex immobilised on carbon paper, which electrochemically reduces CO_2 to acetic acid with high TON in acidified water (pH 6).[41] Imparting aqueous solubility on Mn-catalysts requires the addition of a solubilising group, such as carboxylate or phosphonate groups. However, the addition of these electron withdrawing moieties results in a shift of the MLCT/XLCT absorption bands to lower energies. Whilst this can be an advantage in electrocatalysis by lowering the required reduction potential, the increased visible light absorption limits the choice of photosensitiser to those that strongly absorb at $\lambda > 500$ nm. As such, a careful balance must be considered in the design of the Mn catalysts to optimise the optical and electrochemical properties of the complex for either electrocatalysis or photocatalysis.[16,42]

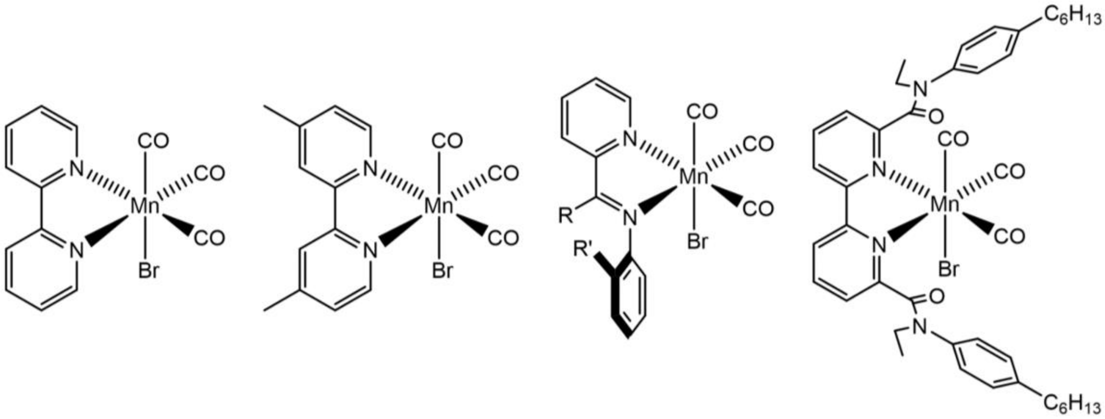

Figure 3.1 – Chemical structures of [Mn(bpy)$(CO)_3$Br],[7] [Mn(dmbpy)$(CO)_3$Br],[7] [Mn(R_2-IP)$(CO)_3$Br],[16] [Mn(HPEAB)$(CO)_3$Br],[17] and [Mn(mesbpy)$(CO)_3$Br],[12] four previously reported CO_2 reduction catalysts.

Currently, no catalytic systems utilising Mn(I) complexes which operate in aqueous solution under photochemical activation with an Earth-abundant photosensitiser have been reported. Here, we demonstrate such a system using an Mn(I) catalyst functionalised with pendant phosphonate ester groups (Figure 1). To prevent the effect of the phosphonate electron withdrawing groups from red-shifting the MLCT/XLCT absorption bands, the bipyridyl π-system and the phosphonate group were electronically decoupled by introducing a CH_2 spacer between them. The resulting catalyst [Mn(4,4′-$\{Et_2PO_3CH_2\}_2$-2,2′-bipyridyl)$(CO)_3$Br] (**1**) was photosensitised by a water-soluble porphyrin, tetra(N-methyl-4-pyridyl)porphyrin Zn(II) tetrachloride ([Zn(TMPyP)]Cl_4], **2**) under 625 nm irradiation. The ability of the Mn-catalyst to reduce CO_2 following both electro- or photochemical activation has been investigated through electrochemical and catalytic study in either an MeCN:H_2O mixture or pure water.

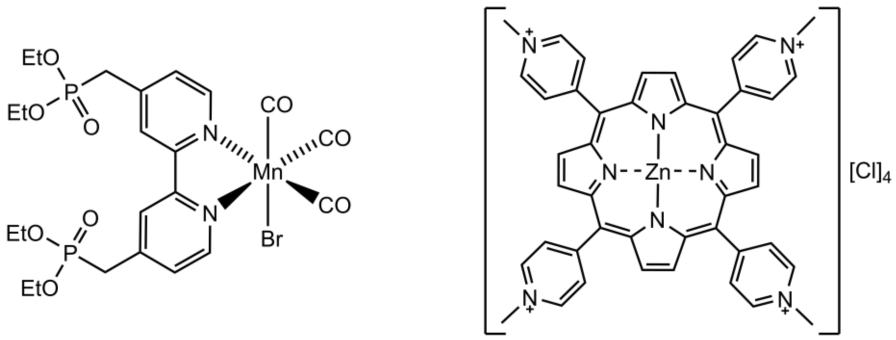

*Figure 3.2 – Chemical structures of [Mn(4,4′-{$Et_2PO_3CH_2$}-2,2′-bipyridyl)$(CO)_3$Br] (**1**) and [ZnTMPyP][Cl]$_4$ (**2**), the catalyst and photosensitiser used in this study.*

3.2 Experimental

Chemical compounds and solvents were purchased from Sigma-Aldrich, Apollo Scientific, Fischer Scientific, and STREM and used as received unless stated otherwise. [NBu_4][PF_6] was recrystallised from boiling ethanol prior to electrochemical measurements. Dry solvents were obtained from the University of Sheffield Grubbs solvent purification system. Ar, N_2, and CO_2 were supplied by BOC. Tetra(N-methyl-4-pyridyl)porphyrin zinc (II) tetrachloride ([ZnTMPyP]Cl_4) was prepared as described previously.[43] UV-vis spectroscopy was performed with an Agilent Varian Cary 50 spectrometer using quartz cuvettes of 10 mm path length. FTIR spectroscopy was performed with a Perkin-Elmer Spectrum One spectrometer with a solution cell equipped with CaF_2 windows. ^{1}H and ^{13}C NMR spectra were recorded on a Bruker AVIIIHD 400 MHz spectrometer equipped with a 5 mm BBFO SmartProbe. High resolution mass-spectra were recorded using the direct infusion ESI+ TOF method at the University of Sheffield mass spectrometry service. C, H, and N contents were determined using a Perkin-Elmer 2400 CHNS/O Series II Elemental Analyser, values were accurate to ± 0.3 %. Gas analysis was performed with a Perkin-Elmer Autosystem XL gas chromatograph equipped with a thermal conductivity detector (TCD) using He reference gas, on a Restek RT-M separation column of porous layer sieve (5 Å), 30 m long with a diameter of 0.53 mm. 100 µL gas samples were injected directly into the chromatography column. Single crystal X-ray crystallography intensity data for [Mn(4,4′-{$Et_2PO_3CH_2$}-2,2′-bipyridyl)$(CO)_3$Br] (CCDC – 2119883) was collected at 100 K with a Bruker D8 Venture diffractometer equipped with a Photon 100 CMOS detector using a CuKα microfocus X-ray source. Crystals were mounted in fomblin oil on a MiTiGen microloop and cooled in a stream of cold N_2.

Cyclic voltammetry was carried out using an Autolab 100 potentiostat, with a glassy carbon working electrode, a Pt wire counter electrode, and an Ag/AgCl (0.1 mol dm^{-3} in saturated KCl) reference electrode. The analyte concentration was 2×10^{-3} mol dm^{-3}, in a 0.2 mol dm^{-3} solution of the [NBu_4][PF_6] supporting electrolyte. The solutions were saturated with N_2 or CO_2 prior to performing the measurements. All potentials were quoted relative to the ferrocene-ferrocenium couple (Fc/Fc$^+$). The individual redox processes were isolated and scanned at various rates (20, 50, 100, 200, and 500 mVs^{-1}) to determine if the redox processes were electrochemically reversible. The working electrode was regularly repolished using an alumina-water slurry. Controlled potential electrolysis was carried out in a custom-made glass reaction vessel equipped with a Pt mesh-working electrode, Pt wire counter electrode, and an Ag wire pseudo-reference electrode under CO_2 atmosphere. 0.2 mol dm^{-3} solutions of $[NBu_4][PF_6]$ in anhydrous MeCN were used as the supporting electrolyte. The composition of the gas headspace was monitored by gas chromatography. CO concentrations were calculated based on a calibration plot constructed with home-made reference gas mixtures.

Photocatalytic CO_2 reduction experiments were conducted as follows: A solution containing **1** (1.5x10^{-6} mol) and **2** (1.9x10^{-6} mol) was prepared in deionised H_2O (2.5 cm^3) in a 10 mm path length quartz cuvette equipped with a septum seal. Ascorbic acid was then added (25 mg) and the solution purged with CO_2 for 30 minutes. The reaction mixture was then stirred and irradiated with 625 nm light supplied by a mounted LED diode (Thorlabs M625L4, 200 mW, 4 cm^2 focal area). The focal point of the light was set to the centre of the quartz cell. The composition of the gas headspace was monitored by gas chromatography. Experiments were halted after the plateau in CO turnover frequency was reached. Control experiments were carried out under Ar atmosphere to show that CO production was not a result of catalyst decomposition.

Monitoring of the reaction mixture composition was carried out by NMR spectroscopy. A solution containing **1** (4.9x10^{-6} mol), **2** (4.9 x10^{-6} mol), and ascorbic acid (5x10^{-4} mol) was prepared in either D_2O (5 cm^3) or D_2O: H_2O (90:10 v/v). The reaction mixture was then divided into five 1 cm^3 aliquots in NMR tubes equipped with septum seals. Tubes 1 – 4 were then purged with CO_2, and tube 5 was purged with Ar. Then, tubes 1,2,3, and 5 were irradiated with 625 nm light supplied by the mounted LED diode. The composition of the reaction mixture was monitored by ^1H and $^{13}C\{^1H\}$ NMR spectroscopy. The composition of the gas headspace was monitored by gas chromatography to confirm catalysis was taking place.

IR-spectroelectrochemistry was performed using an EmStat 3+ Potentiostat, where 4x10^{-3} mol dm^{-3} solutions of the analyte with 0.3 mol dm^{-3} $[NBu_4][PF_6]$ supporting electrolyte in anhydrous MeCN were prepared under either Ar or CO_2 atmosphere. Measurements were performed in an optically transparent thin-layer electrochemical (OTTLE) cell equipped with Pt mesh working and counter electrodes, an Ag-wire pseudo-reference electrode, and CaF_2 windows. Spectral monitoring was done with a Perkin-Elmer Spectrum One FTIR spectrometer. During IR-SEC, the applied potential was scanned toward negative potential until the onset of the 1st reduction was reached. At this point the scan was paused and the spectral changes in the mid-IR region monitored until the 1st reduction was complete. The potential scan was then resumed until the second reduction potential onset was reached, the scan was then paused and the electrolysis monitored until the 2nd reduction process was complete.

Transient absorption spectroscopy was performed at the Lord Porter Laser Laboratory, University of Sheffield. A Ti:Sapphire regenerative amplifier (Spitfire ACE PA-40, Spectra-Physics) provided 800 nm pulses (40 fs FWHM, 10 kHz, 1.2 mJ). 625 nm excitation pulses were generated from the 800 nm fundamental beam with a commercially available optical parametric amplifier (TOPAS, Light Conversion). White light super-continuum probe pulses in the range 340 – 790 nm were generated in situ using 2 % of the Ti:Sapphire amplifier output, focused on a CaF_2 crystal. Detection was achieved using a commercial transient absorption spectrometer (Helios, Ultrafast Systems) using a CMOS sensor for the UV-vis spectral range. The relative polarisation of the pump and probe pulses was set to the magic angle of 54.7° for anisotropy free measurements. Samples were held in 2 mm path length quartz cells and were stirred during experiments. The optical density at the excitation wavelength was kept at approximately 0.5. The optical density across the probe range was kept below 1.0.

Flash photolysis was performed on a home-built setup at the University of Sheffield. A steady-state 150 W Xe arc lamp (Hamamatsu Photonics) was used as the probe source. Sample excitation was achieved with a Nd:YAG laser (LOTIS TII), which provided 355 nm pulses that were then used in a commercially available optical parametric oscillator (LOTIS TII) to produce the 620 nm pulses for sample excitation. Detection was achieved with a Spex Minimate monochromator and FEU0118 PMT. The detector current output was coupled into a Tektronix TDS 3032B digital oscilloscope. The decay traces with the Xe lamp on and off were used to produce the kinetic trace for excited state relaxation in ΔOD.

Preparation of $[Mn(4,4'\text{-}\{Et_2O_3PCH_2\}\text{-}2,2'\text{-bipyridyl})(CO)_3Br]$

$[Mn(4,4'\text{-}\{Et_2O_3PCH_2\}_2\text{-}2,2'\text{-bipyridyl})(CO)_3(Br)]$ was prepared by literature proceedure.[7,20] The synthetic route for the 4,4′-bis(methyl-diethoxyphosphonato)-2,2′-bipyridine ligand is detailed in the Appendix C.

$[Mn(CO)_5Br]$ (300 mg, 1.09 mmol) and 4,4′-bis(methyl-diethoxyphosphonato)-2,2′-bipyridine (465 mg, 1.02 mmol) were dissolved in diethyl ether (50 cm^3) and then heated to reflux for four hours in the dark. The reaction vessel was left to cool to room temperature and then then further cooled in an ice-water bath to induce precipitation of the product remaining in solution. The precipitate was then isolated by vacuum filtration and washed with cold diethyl ether to yield the product as a yellow powder (582 mg, 79%).

υ_{max} / cm^{-1} (CH_2Cl_2, CaF_2 cell) 3689 (w, CH), 3601 (vw, CH), 2028 (vs, CO), 1938 (s, CO), 1923 (s, CO), 1620 (w, bpy), 1605 (w, bpy), 1051 (m, PO), 2024 (m, PO); λ_{max} (CH_2Cl_2 / nm 258 (π- π*), 296 (π- π*), 426 (MLCT); δ_H (400 MHz, $(CD_3)_2SO$) 9.13 (d, *J* = 5.5 Hz, 2H, Ar*H*), 8.45 (s, 2H, Ar*H*), 7.64 (s, 2H, Ar*H*), 4.03 (m, 8H, CH_3CH_2O), 3.59 (d, *J* = 22.6 Hz, 8H, PCH_2), 1.20 (t, *J* = 6.7 Hz, 12H, CH_3CH_2O); $\delta_C\{^1H\}$ (100 MHz, CD_2Cl_2) 155.97 (C), 153.67 (CH), 145.64 (*C*), 127.92 (*C*H), 124.33 (*C*H), 63.45 (CH_2), 34.07 (d, *J* = 136.3 Hz, CH_2), 16.77 (CH_3) (Not all quaternary carbons observed); $\delta_P\{^1H\}$ (162 MHz, CD_2Cl_2) 22.81 ($Et_2O_3PCH_2$); m/z (TOF MS ES+, Na^+ added) 457.3 ($\{Et_2O_3PCH_2\}_2C_{10}H_6N_2$), 479.3 ($\{Et_2O_3PCH_2\}_2C_{10}H_6N_2Na$), 511.2 (M-3CO-Br), 595.3 (M-Br), 697.2 (M+ Na^+); Elemental analysis calc. for $C_{23}H_{30}BrMnN_2O_9P_2$: C 40.91 %, H 4.48 %, Br 11.83 %, N 4.15 %, Found: C 40.18 %, H 4.35 %, Br 12.36 %, N 4.05 %; Crystal data for $C_{23}H_{30}BrMnN_2O_9P_2$ (*M* = 675.28 g mol^{-1}): triclinic, space group P-1 (no. 2), *a* = 11.2728(5) Å, *b* = 12.1366(6) Å, *c* = 12.4282(6) Å, *α* = 61.173(2)°, *β* = 72.144(2)°, *γ* = 74.311(2)°, *V* = 1402.48(12) Å^3, *Z* = 2, *T* = 100.0 K, μ(CuKα) = 6.333 mm^{-1}, *Dcalc* = 1.599 g cm^{-3}, 22074 reflections measured (1.91° ≤ 2Θ ≤ 27.55°), 6307 unique (R_{int} = 0.0621) which were used in all calculations. The final R_1 was 0.0500 (I > 2σ(I)) and wR_2 was 0.0980 (all data).

3.3 Results and Discussion

Electronic absorption spectra

The UV-vis absorption spectrum of **1** in DCM was similar to previously reported $[Mn(L_2)(CO)_3Br]$ catalysts. The electronic absorption bands observed at λ < 400 nm were assigned as bipyridyl π – π* transitions. At greater wavelengths, a broad absorption envelope was observed. Deconvolution of the UV-vis spectrum with pseudo-Voigt profiles reveals two absorption bands, assigned as the XLCT and MLCT transitions of the Mn complex. The absorption maxima for this envelope was found at 414 nm, very similar to $[Mn(dmbpy)(CO)_3Br]$ (Appendix C, fig. C1-C2). This indicated that the energy of the MLCT/XLCT excited state energy was not decreased by addition of the phosphonate ester groups, hence the phosphonate and bipyridyl moieties were electronically decoupled by the methylene spacer group. This contrasts with other reported catalysts bearing functionalised bipyridyl groups, where it has been shown that introduction of electron rich or electron deficient groups caused shifts in the energy of the electronic transitions in the complex.

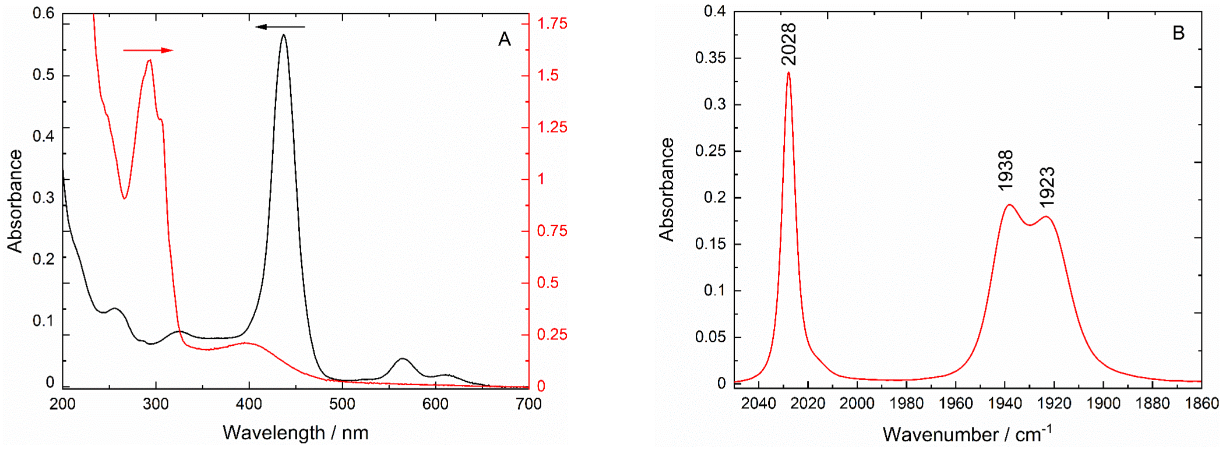

Figure 3.3 – A. UV-vis absorption spectrum of ***1*** *(red) and* ***2*** *(black) in H_2O, the arrows point toward the absorbance axis for the Mn-catalyst (red) and porphyrin (black). B. Vibrational absorption spectrum of* ***1*** *in DCM. Multi-peak deconvolution of the UV-vis and FTIR spectra of* ***1*** *are available in Appendix C.*

Vibrational absorption spectra

The vibrational absorption spectrum of **1** in DCM contains absorption bands corresponding to the a′(1), a″, and a′(2) carbonyl group vibrations in the 2035 – 1885 cm^{-1} region as is typical for $[Mn(L_2)(CO)_3Br]$ complexes. A shoulder observed at 2020 cm^{-1} was assigned as a CO/ligand group vibration, on the basis of previous observations.[44] The vibrational frequencies of these four group vibrations are within 5 cm^{-1} of those for $[Mn(dmbpy)(CO)_3Br]$ (Appendix C, fig. C3-C4), indicating the electron density on the Mn centre is very similar between the two complexes, confirming that the phosphonate ester and bipyridyl groups are electronically decoupled. The IR absorption bands observed at lower frequencies were associated with either the bipyridyl ligand, such as an aromatic overtone vibration at 1620 cm^{-1}, or with the $\{Et_2O_3P\text{-}CH_2\}$ groups from 1000 – 1100 cm^{-1}.

Electrocatalytic performance

The electrochemical properties of **1** were studied by cyclic voltammetry (CV) to determine its ability to reduce CO_2 upon application of an electric field (Figure 3.4). Under inert N_2 atmosphere, one oxidative and three reductive processes were observed in the CV in the range from −2.7 to 1.4 V *vs*. Fc/Fc^+ (Figure 3.4A); These processes were quasi-reversible, and repeated scans resulted in permanent changes in the CV, which resulted from deposition of the sample onto the electrode surface. This partial reversibility was further evidenced by the scan rate dependent peak potentials, although the relationship between the square root of the scan rate and the peak current was approximately linear (Appendix C, fig. C9-C14). The 1st and 2nd reduction potentials of **1** and $[Mn(dmbpy)(CO)_3Br]$ are very similar, and more negative than $[Mn(bpy)(CO)_3Br]$, indicating an increase of the electron density on the diimine ligand following functionalisation with the $-CH_3$ or

[Et_2O_3P-CH_2-] groups. This observation is consistent with the electronic decoupling of the bipyridyl and phosphonate groups, as was also evident in the UV-vis and FTIR data (Table 3.1).

Purging the solution of **1** with CO_2 resulted in subtle changes to the cyclic voltammogram (Figure 3.4B), where the reverse peaks for the 1st and 2nd reduction had a reduced peak intensity. The peak intensity of the 3rd reduction redox process was also significantly reduced: similar to what was observed in [Mn(bpy)$(CO)_3$Br].[7] This was attributed to the reaction of the active catalyst formed following two-electron reduction with CO_2, which prevented the 3rd reduction of **1** from taking place. Under anhydrous conditions without Brønsted acid, the catalytic cycle could not be initiated, and the CO_2 reduction process halts following formation of [Mn(phos-bpy)$(CO)_3(CO_2)]^-$. Addition of H_2O to the reaction mixture in the electrochemical cell containing **1** results in further changes to the cyclic voltammogram, where the 1st and 2nd reduction potentials of **1** were no longer observed, and instead new reduction peaks were found at more negative potentials. These new reduction processes were associated with the CO_2 reduction catalytic cycle. The first of these is associated with initiation of the catalytic reaction, and the second is the electrochemical potential required to ensure turnover of the catalytic cycle. This was evidenced by the enhancement of the measured current with increasing water concentrations for this catalytic reduction. The current enhancement quantified with the ratio of peak currents under catalytic and inert conditions (i_{cat}/i_p), reached 1.9 in a 95:5 MeCN:H_2O solvent mixture. The measured i_{cat}/i_p for **1** was less than the previously reported [Mn(HPEAB)$(CO)_3$Br] catalyst, which was attributed to the larger reduction potential required for electrochemical initiation of **1**.[17] The observation of current enhancement confirmed that **1** is able to electrochemically reduce CO_2.

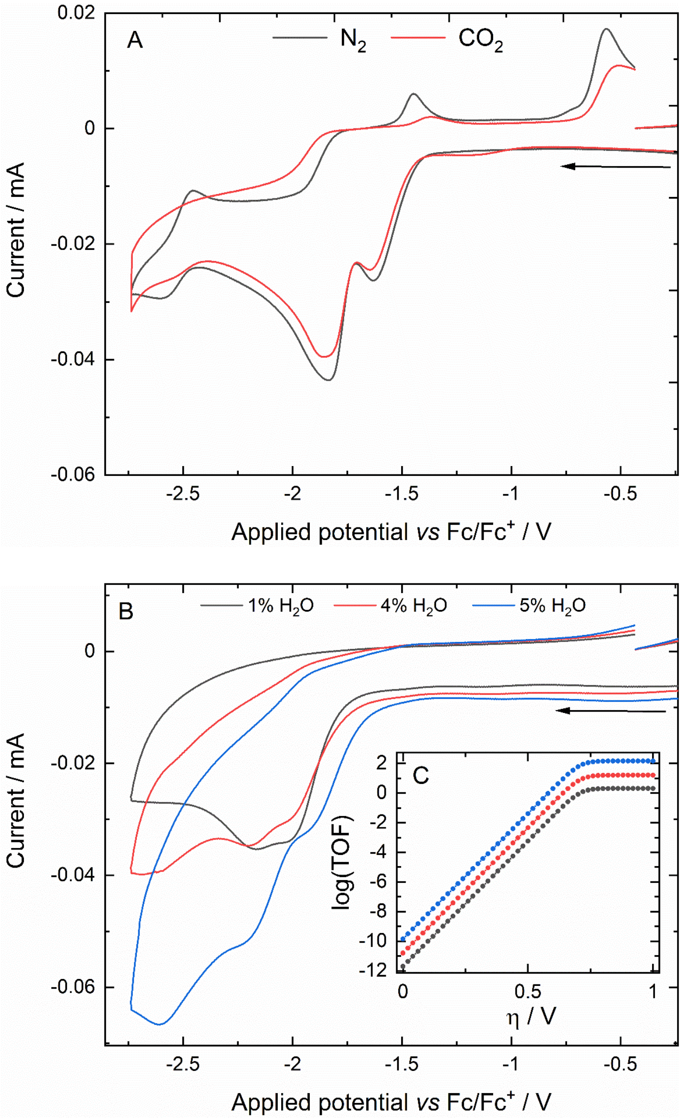

Figure 3.4 – A. Cyclic voltammograms of a 2 x 10^{-3} mol dm^{-3} solution of ***1*** *and 0.2 mol dm^{-3} [NBu$_4$][PF$_6$] supporting electrolyte at a scan rate of 100 mV s^{-1} under N$_2$ atmosphere in anhydrous MeCN (black) and CO$_2$ atmosphere in anhydrous MeCN (red). B. Cyclic voltammograms of the CO$_2$ purged solution in 1% H$_2$O:MeCN (black), 4% H$_2$O:MeCN (red), and 5% H$_2$O:MeCN (blue). C. Tafel plots corresponding to the catalytic CO$_2$ reduction, estimated by foot-of-the-wave analysis for 1% H$_2$O:MeCN (black), 4% H$_2$O:MeCN (red), and 5% H$_2$O:MeCN (blue). The arrow indicates the initial scan direction.*

The overpotential required to maximise the rate of electrocatalysis, as well as the turnover frequency for CO formation was estimated with the foot-of-the-Wave (FOTW) analysis procedure (Appendix B).[45–48] At an overpotential of 0 V, the value of log(TOF$_0$) was less than previously reported catalysts analysed by the FOTW method – indicating that **1** is intrinsically a less effective CO$_2$ reduction catalyst than [Mn(HPEAB)(CO)$_3$Br] and [Mn(mes-bpy)(CO)$_3$Br] under similar conditions (Table 3.1). However, the log(TOF$_{max}$) of **1** was greater than [Mn(dmbpy)(CO)$_3$Br] in 95:5 MeCN: H$_2$O. The trend in log(TOF$_{max}$) value follows the trend in the second reduction potential for these catalysts, where less negative potentials resulted in faster catalytic rates (Appendix C, fig. C17). Therefore, whilst the electronic decoupling of the phosphonate ester and bipyridyl groups does have the advantage of increasing the spectral range available for light harvesting without photolysis of the Mn catalyst, this was at the cost of the electrocatalytic performance. It was not possible to assess the catalytic performance in aqueous solution by electrochemical means, therefore it is assumed that the TOF is similar in MeCN:H_2O and pure H_2O. The ability of **1** to reduce CO_2 to CO in MeCN:H_2O was confirmed by controlled potential electrolysis, where reduction at −1.8 V *vs*. Ag^+ resulted in the formation of CO.

Table 3.1 – Light absorption, electrochemical and electrocatalytic properties of [Mn(L_2)($CO)_3$(Br)] complexes measured by cyclic voltammetry and evaluated by foot-of-the-wave analysis; all data in MeCN.

L_2	MLCT λ_{max} / nm	1st reduction / V	2nd reduction / V	Brønsted acid addition	E_{cat}, $E_0(CO_2/CO)$ / V	i_{cat} / i_p	Optimum overpotential (η) / V	log(TOF_0)	log(TOF_{max})
bpy[7]	416	−1.65^a	−1.89^a	-	-	-	-	-	-
dmbpy[7,49]	419	−1.73	−1.98	5% H_2O	−1.83, −1.29	-	0.51	−8.7	−0.4
mes-bpy[12]	-	−1.60^a	-	0.1 M Mg^{2+}	−1.60, −1.40	-	0.3 – 0.45	−2.3 – −4.8	2.8
				0.3 M TFE	−1.60, −1.40	-	0.3 – 0.45	−7.0	3.7
HPEAB[17]	442	−1.48^a	−1.74^a	2% H_2O	−1.90, −1.40	1.4	0.62	−6.8	1.7
				5% H_2O	−1.90, −1.40	2.3	0.62	−4.9	3.5
phos-bpy (**1**)	416	−1.73^a	−1.86	2% H_2O	−2.10, −1.40	1.2	0.84	−11.6	0.3
				5% H_2O	−2.10, −1.40	1.9	0.84	−9.8	2.2

(a) Potential given as cathodic peak potential ($E_{p,a}$). Reduction potentials were recorded in anhydrous MeCN under inert atmosphere. Where required, literature data for redox potentials were converted to Fc/Fc^+ reference with the following conversion factors: Fc/Fc^+ = 0, NHE = −630 mV, SHE = −624 mV, Ag/AgCl = −450 mV, SCE = −380 mV, $AgNO_3$ = −87 mV)).[50] TFE = trifluoroethanol. Optimum overpotential, log(TOF_0), and log(TOF_{max}) were estimated with the foot-of-the-wave method, where TOF_0 is turnover frequency at zero overpotential, and TOF_{max} is turnover frequency at the potential required for maximum catalytic rate. The FOTW method is detailed in the SI.

Mechanistic study of active catalyst formation by IR-SEC

To determine the effect of phosphonate ester addition to the bipyridyl ligand on the active catalyst formation mechanism, the spectral changes following electrochemical reduction were monitored with FTIR spectroscopy. Upon application of the first reduction potential (−1.1 V *vs*. Ag^+), the intensity of the a′(1), a″, and a′(2) absorption bands at 2027, 1935, and 1922 cm^{-1} decrease, concurrent with the formation of new absorption bands at 1885, 1880, 1933, and 1975 cm^{-1} (Figure 3.5). These spectral changes were consistent with the commonly reported dissociation of the Br^- ligand and subsequent dimerisation of the resulting $[Mn(L_2)(CO)_3]^{\cdot -}$ anion (Figure 3.5B).

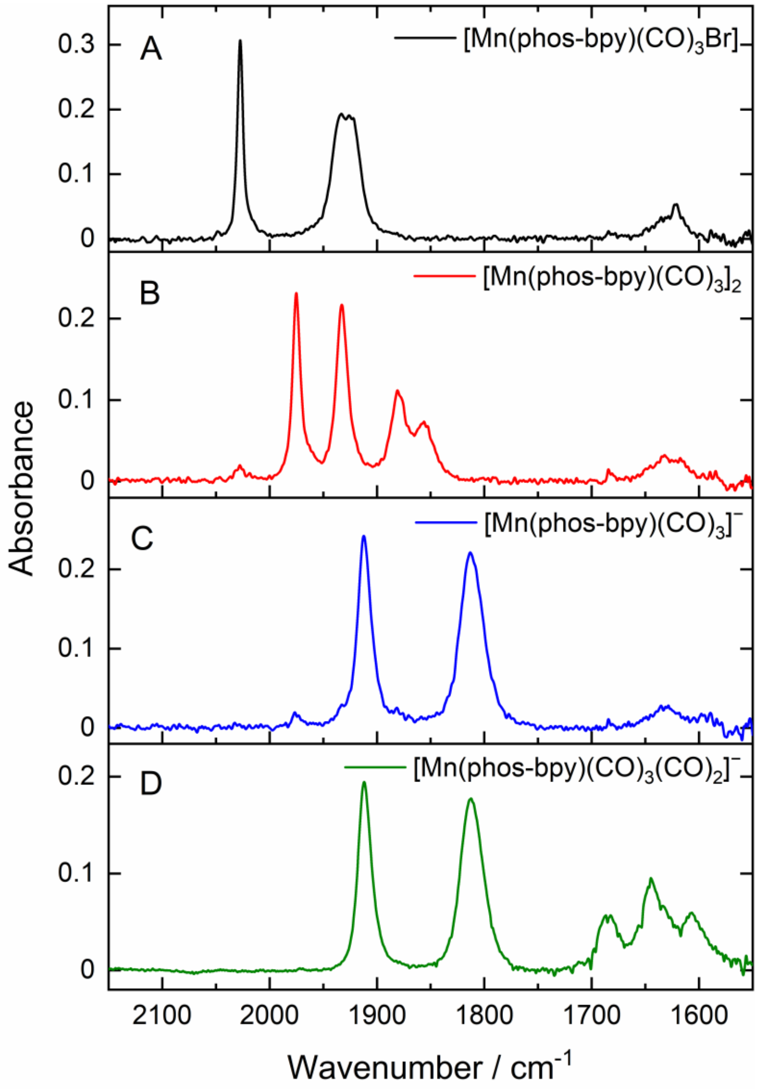

Figure 3.5 – Spectral changes in the 2150 – 1550 cm^{-1} *region of the IR spectrum of* ***1*** *following application of the 1*st *and 2*nd *reduction potentials. A. FTIR spectrum at no applied potential in Ar purged anhydrous MeCN. B. FTIR spectrum after electrolysis at −1.1 V vs Ag*$^+$ *in Ar purged anhydrous MeCN, which corresponds to the 1*st *reduction potential. C. FTIR spectrum after electrolysis at −1.6 V vs Ag*$^+$ *in Ar purged anhydrous MeCN, which corresponds to the 2*nd *reduction potential. D. FTIR spectrum after electrolysis at −1.6 V vs Ag*$^+$ *in* CO_2 *purged anhydrous MeCN, which corresponds to the 2*nd *reduction potential of* ***1****.*

After application of the second reduction potential (−1.6 V *vs*. Ag$^+$), the bands associated with the $[Mn(phos\text{-}bpy)(CO)_3]_2$ dimer decay, simultaneously with the grow-in of two bands centred at 1912 and 1812 cm^{-1}, which were ascribed to the $[Mn(phos\text{-}bpy)(CO)_3]^-$ anion (Figure 3.5C). This species is the active CO_2 reduction catalyst which coordinates to CO_2 to initiate the catalytic cycle. Upon application of a positive potential (0.1 V *vs*. Ag$^+$), the vibrational absorption bands of the starting complex did not completely reform, consistent with the partial reversibility observed in the cyclic voltammetry data. In CO_2 purged solution, the same spectral changes were observed during the two-electron reduction process. However, an additional step was now observed, with new bands formed from 1700 – 1650 cm^{-1} (Figure 3.5D). These were ascribed to formation of the CO_2 bound complex, [Mn(phos-bpy)$(CO)_3(CO)_2]^-$. Due to the lack of available protons, no further steps in the catalytic cycle were observed. The mechanism of catalytic activation, proposed on the basis of the IR-SEC data is summarised in Figure 3.6 and Table 3.2.

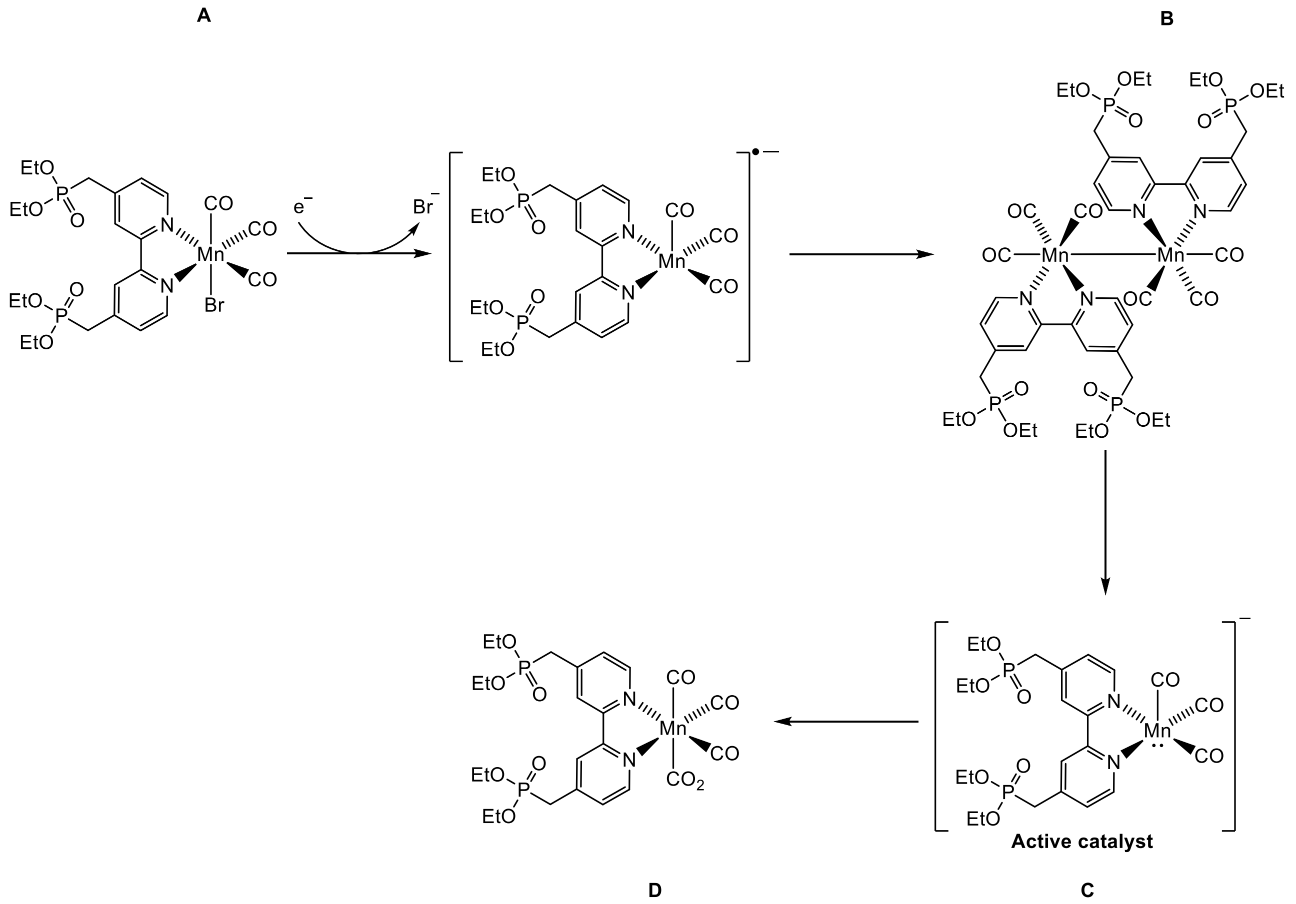

*Figure 3.6 – Active catalyst formation mechanism following two-electron reduction of **1** in CO_2 saturated anhydrous MeCN, proposed on the basis of IR-spectroelectrochemical data. See Table 3.2 and Figure 3.5 for IR-absorbances of A-D.*

*Table 3.2 – Vibrational frequencies for species A – D observed during IR-spectroelectrochemical measurements of solution of **1** in MeCN.*

Complex	**Vibrational frequencies / cm^{-1}**
[Mn(phos-bpy)$(CO)_3$Br] (A)	2027, 1935, 1922, 1631, 1625
[Mn(phos-bpy)$(CO)_3]_2$ (B)	1885, 1880, 1933, 1975, 1625, 1631
[Mn(phos-bpy)$(CO)_3]^-$ (C)	1912, 1812, 1631
[Mn(phos-bpy)$(CO)_3(CO_2)]^-$ (D)	1912, 1812, 1686, 1645, 1607

Photosensitisation of 1 with porphyrin 2 in aqueous solution

To evaluate the effectiveness of **1** as a CO_2 reduction catalyst in aqueous solution, a catalytic system was designed utilising a water-soluble porphyrin as a photosensitiser and ascorbic acid as the sacrificial electron donor. The selected porphyrin (**2**) was chosen for its high-water solubility and strong light absorption in the 575 – 650 nm region, where **1** has negligible absorption (Figure 3.3). To confirm that **2** has a sufficiently long lifetime to enable diffusion controlled electron transfer, the photophysical properties of the porphyrin photosensitiser following Q-band excitation were analysed by time-resolved transient absorption spectroscopy (Figure 3.7). A solution of **2** in water was excited with a 40 fs, 625 nm laser pulse and the spectral changes following excitation were monitored by a 420 – 780 nm white light probe. At very small time delays ($t < 150$ fs) two transient absorption bands were observed at 511 and 485 nm, corresponding to the singlet and triplet excited states, respectively. The spectral profile was consistent with previously reported data following Soret band excitation at 404 nm.[51] The 511 nm band fully decays within 0.5 ps, indicating intersystem crossing (ISC) from S_1 to T_1 was complete. Due to convolution with the instrument response function, it was not possible to obtain an exact time-constant for ISC. After 500 fs, no further spectral changes occur up to the longest available time delay of 7 ns. The lifetime of the T_1 state of **2** in aerated water, measured by microsecond flash photolysis experiments following 600 nm, ~12 ns excitation, was found to be 1.0 ± 0.013 μs, and is sufficient for diffusion-controlled electron transfer to take place. Hence **2** was used to photoreduce **1**, initiating CO_2 reduction catalysis.

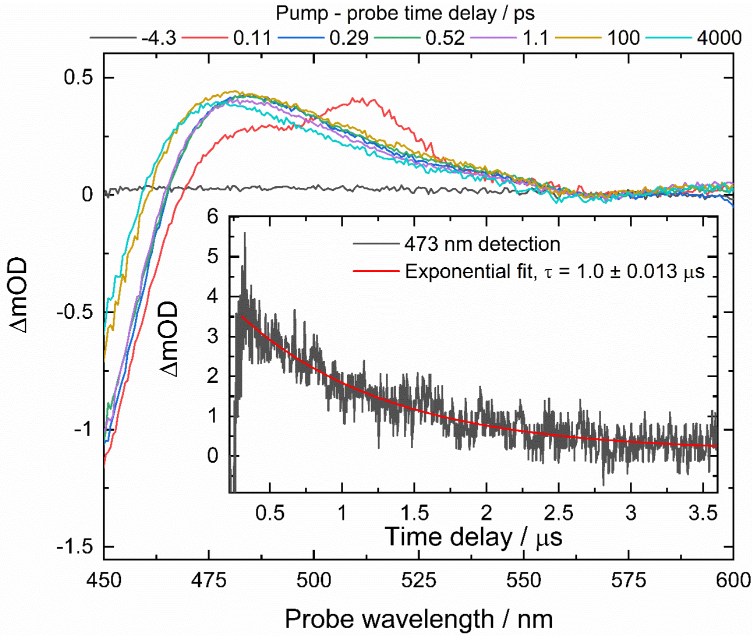

Figure 3.7 – Femtosecond transient absorption spectra of $[ZnTMPyP]Cl_4$ in H_2O following 40 fs, 625 nm excitation. Inset: Triplet excited state decay trace following 620 nm, 12 ns excitation during flash photolysis, and monitored at 473 nm.

Irradiation of an aqueous solution of **1** and **2** in the presence of ascorbic acid with 625 nm light resulted in the evolution of CO from the liquid phase. The rate of CO formation was monitored by gas chromatography and quantified with the turnover number and turnover frequency. The CO product was produced slowly at a continuous rate during the catalytic experiment. The initial TOF for the first 30 minute irradiation interval was significantly less than the electrochemical TOF$_{max}$ estimated by FOTW analysis, likely a result of inefficient photosensitisation. The photochemical TOF$_{max}$ was reached after 150 minutes of irradiation. To assess catalyst recyclability, the reaction mixture was purged with CO_2 after 250 minutes of irradiation, then the mixture was then irradiated for a further 110 minutes. The catalytic performance in this second cycle was very similar to the first cycle, indicating catalyst deactivation was not a significant problem during the reaction. A control experiment, carried out in the absence of CO_2, resulted in negligible CO formation (Appendix C, fig. C19), confirming that the CO observed during the catalytic experiment was produced by CO_2 reduction and not through decomposition of the Mn catalyst.

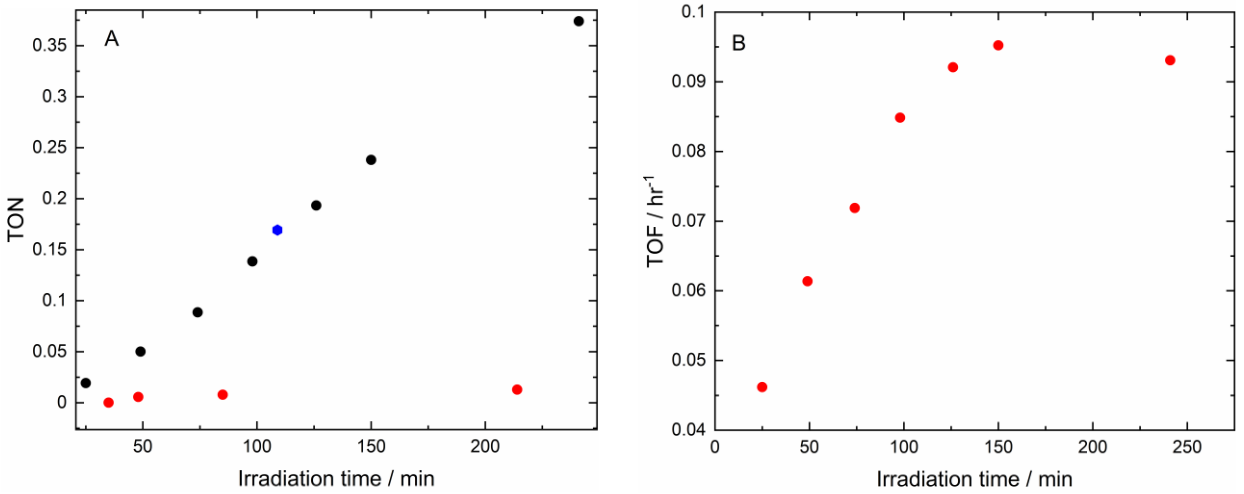

Figure 3.8 – A. Plot of turnover number versus irradiation time for the first cycle of the catalytic reaction (black). Also shown is the TON value following re-purging the reaction mixture with CO_2 (blue) and control experiment data with no porphyrin photosensitiser (red). B. Plot of turnover frequency against irradiation time for the catalytic reaction.

A solution of **1**, **2**, and ascorbic acid was prepared in D_2O to monitor changes in the reaction mixture composition during CO_2 reduction catalysis by NMR spectroscopy. Irradiation of this reaction mixture with 625 nm light resulted in the formation of four new resonances at 7.71, 8.27, 8.57, and 8.64 ppm, as well as other weak bands (Appendix C, fig. C20). These new signals were broad and structureless, hence were likely associated with multiple species.

The initial proton resonances of **2** were found to decay within one hour of irradiation, indicating that the porphyrin was permanently changed during catalysis. The resonance at 8.64 ppm was ascribed to the resulting porphyrin decomposition product. This was evidenced by a control experiment, where **2** was irradiated with 625 nm light in the presence of ascorbic acid (Appendix C, fig C25). The decomposition of the porphyrin under catalytic conditions was also evidenced by a solution colour change from dark to light green. UV-vis absorption spectra of the reaction mixture from this control experiment were recorded before and after the irradiation period. It was found that new absorption bands had formed at lower energies compared to the Q-bands of **2**. This can be attributed to the formation of a photoreduced porphyrin species, such as a chlorin, where one of the porphyrin C=C bonds has been hydrogenated following photoreduction (Appendix C, fig C26).[52] The rate of porphyrin photoreduction was significantly reduced in the absence of **1**, and the photoreduction product is seemingly stable under 625 nm irradiation. The photoreduced porphyrin is likely able to photosensitise **1**, as evidenced by the continuous CO evolution from the reaction mixture after 1 hour of irradiation.

In the absence of CO_2, the grow-in of resonances at 7.71, 8.57, and 8.64 ppm was also observed (Appendix C, fig. C20). As the resonance at 8.64 corresponds to the photoreduced porphyrin complex, the resonances at 7.71 and 8.57 are tentatively assigned as intermediate Mn species, such as the Mn-Mn dimer and active catalyst. The spectrum of the reaction mixture in the absence of CO_2 was effectively the same as when the irradiation was carried out under CO_2 atmosphere. This suggests it was not possible to initiate the catalytic cycle in D_2O. After 16 hours of irradiation with 625 nm light, the catalyst did not decompose in D_2O solution. In the presence of CO_2, but absence of light, no changes in the NMR spectrum were observed during the 16-hour experiment.

The catalytic studies were repeated in a 90:10 H_2O:D_2O mixture. The ^1H NMR spectra were baseline-corrected with a polynomial function to reduce the effect of the large H_2O resonance at 4.7 ppm and observe the aromatic proton environments. The NMR spectra were similar to CO_2 reduction in pure D_2O, where we again observe the formation of a photoreduced porphyrin resonance at 8.6 ppm. However, some differences were observed. For example, the resonances of the intermediate Mn-species at 7.71 and 8.57 ppm were much broader and weaker. The gas chromatography analysis show that catalysis does take place under these conditions. Therefore, the weak, broad resonances are a result of the catalytic turnover, where the steady-state concentration of each intermediate is not high enough for individual detection by NMR spectroscopy.

No evidence of $^{-}CO_2H$ was found in the ^1H NMR spectra, which has an expected ^1H chemical shift in H_2O:D_2O of 8.45 ppm. The absence of formate was confirmed by recording $^{13}C\{^1H\}$ NMR spectra of the catalytic reaction mixture in the presence of $^{12}CO_2$ or $^{13}CO_2$ (Appendix C, fig. C24). The only significant difference was observation of the $^{13}CO_2$ resonance at 125 ppm. Together, these NMR experiments suggest CO_2 reduction with **1** in water results in selective formation of CO as the product.

3.4 Conclusions

A water-soluble Mn(I) diimine complex [Mn(4,4′-{$Et_2O_3PCH_2$}$_2$-2,2′-bipyridyl)$(CO)_3Br$], where the bipyridyl ligand was functionalised with phosphonate ester groups has been prepared, fully characterised, and shown to be an effective CO_2 reduction catalyst in aqueous solution. The phosphonate ester group was incorporated into the diimine ligand to achieve significant water solubility of the Mn-catalyst. The electron density on the bipyridyl ring of the catalyst **1** was similar to [Mn(dmbpy)$(CO)_3Br$] due to the presence of a CH_2 spacer group, as evidenced by the electronic and vibrational absorption spectra, as well as the similar values of the 1st and 2nd reduction potentials of the two compounds. This was attributed to electronic decoupling of the electron-accepting phosphonate group from the bipyridyl ligand. As a result, the catalyst did not absorb at $\lambda > 500$ nm, allowing for a wider range of photosensitisers to be used in future applications of the light sensitive Mn-catalyst. Electrochemical two-electron reduction was found to result in the formation of a five coordinate anion, [Mn(phos-bpy)$(CO)_3]^-$. The mechanism for formation of this active catalyst is suggested on the basis of the IR-spectroelectrochemical studies to proceed through the usual Mn-Mn dimer complex. Foot-of-the-wave analysis estimated the maximum turnover frequency after electrochemical initiation as $\log(TOF_{max}) = 2.2$, which was larger than [Mn(dmbpy)$(CO)_3Br$] under identical conditions.[47] In the presence of a Zn-porphyrin photosensitiser and a sacrificial donor, the [Mn(phos-bpy)$(CO)_3Br$] complex selectively reduces CO_2 to CO in aqueous solution under 625 nm irradiation. Analysis of the catalytic reaction mixture composition by ^1H and ^{13}C NMR spectroscopy revealed the active catalyst was stable under catalytic conditions. After the TOF had reached a plateau, purging the reaction mixture with CO_2 allowed for catalysis to continue at its original rate, demonstrating the recyclability of the Mn-catalyst. Control experiments showed the observed CO formation was not a result of catalyst decomposition. This is only the third example of a Mn catalyst activated by a porphyrin photosensitiser, the first example of such a system operating in aqueous solution, and the first example of fully Noble-metal free photocatalytic CO_2 reduction in water with a molecular Mn(I) catalyst. Overall, this catalyst presents a promising platform for further development of Earth-abundant CO_2 reducing catalysis, where replacement of the Zn-porphyrin with a more effective photosensitiser could unlock the potential of [Mn(phos-bpy)$(CO)_3Br$] for larger scale CO_2 reduction catalysis in aqueous solution.

References

1 S. C. Roy, O. K. Varghese, M. Paulose and C. A. Grimes, *ACS Nano*, 2010, **4**, 1259–1278.

2 J. Hawecker, J.-M. Lehn and R. Ziessel, *J. Chem. Soc., Chem. Commun.*, 1984, 328–330.

3 L. M. Kiefer, J. T. King and K. J. Kubarych, *J. Phys. Chem. A*, 2014, **118**, 9853–9860.

4 S. Mai and L. González, *Chem. Sci.*, 2019, **10**, 10405–10411.

5 L. Rotundo, D. E. Polyansky, R. Gobetto, D. C. Grills, E. Fujita, C. Nervi and G. F. Manbeck, *Inorg. Chem.*, 2020, **59**, 12187–12199.

6 L. Rotundo, D. C. Grills, R. Gobetto, E. Priola, C. Nervi, D. E. Polyansky and E. Fujita, *ChemPhotoChem*, 2021, **5**, 526–537.

7 M. Bourrez, F. Molton, S. Chardon-Noblat and A. Deronzier, *Angew. Chemie - Int. Ed.*, 2011, **50**, 9903–9906.

8 A. Sinopoli, N. T. La Porte, J. F. Martinez, M. R. Wasielewski and M. Sohail, *Coord. Chem. Rev.*, 2018, **365**, 60–74.

9 C. Riplinger, M. D. Sampson, A. M. Ritzmann, C. P. Kubiak and E. A. Carter, *J. Am. Chem. Soc.*, 2014, **136**, 16285–16298.

10 D.-C. Liu, D.-C. Zhong and T.-B. Lu, *EnergyChem*, 2020, **2**, 100034.

11 M. D. Sampson, A. D. Nguyen, K. A. Grice, C. E. Moore, A. L. Rheingold, C. P. Kubiak and P. Kubiak, *J. Am. Chem. Soc.*, 2014, **136**, 5460–5471.

12 M. D. Sampson and C. P. Kubiak, *J. Am. Chem. Soc.*, 2016, **138**, 1386–1393.

13 J. Mukherjee and I. Siewert, *Eur. J. Inorg. Chem.*, 2020, **2020**, 4319–4333.

14 S. E. Tignor, T. W. Shaw and A. B. Bocarsly, *Dalton Trans.*, 2019, **48**, 12730–12737.

15 S. S. Roy, K. Talukdar and J. W. Jurss, *ChemSusChem*, 2021, **14**, 662–670.

16 S. J. P. Spall, T. Keane, J. Tory, D. C. Cocker, H. Adams, H. Fowler, A. J. H. M. Meijer, F. Hartl and J. A. Weinstein, *Inorg. Chem.*, 2016, **55**, 12568–12582.

17 J. D. Shipp, H. Carson, S. J. P. Spall, S. C. Parker, D. Chekulaev, N. Jones, M. Y. Mel’nikov, C. C. Robertson, A. J. H. M. Meijer and J. A. Weinstein, *Dalton Trans.*, 2020, **49**, 4230–4243.

18 C. W. Machan, C. J. Stanton, J. E. Vandezande, G. F. Majetich, H. F. Schaefer, C. P. Kubiak and J. Agarwal, *Inorg. Chem.*, 2015, **54**, 8849–8856.

19 T. E. Rosser, C. D. Windle and E. Reisner, *Angew. Chemie - Int. Ed.*, 2016, **55**, 7388–7392.

20 S.-J. J. Woo, S. Choi, S. Y. Kim, P. S. Kim, J. H. Jo, C. H. Kim, H. J. Son, C. Pac and S. O. Kang, *ACS Catal.*, 2019, **9**, 2580–2593.

21 X. Ma, L. Zheng and Z. Bian, *Chem. Eng. Sci.*, 2021, **229**, 116042.

22 D. A. Popov, J. M. Luna, N. M. Orchanian, R. Haiges, C. A. Downes and S. C. Marinescu, *Dalton Trans.*, 2018, **47**, 17450–17460.

23 G. Neri, P. M. Donaldson and A. J. Cowan, *Phys. Chem. Chem. Phys.*, 2019, **21**, 7389–7397.

24 Y. Yang, Z. Zhang, X. Chang, Y.-Q. Q. Zhang, R.-Z. Z. Liao and L. Duan, *Inorg. Chem.*, 2020, **59**, 10234–10242.

25 D. C. Grills, M. Z. Ertem, M. McKinnon, K. T. Ngo and J. Rochford, *Coord. Chem. Rev.*, 2018, **374**, 173–217.

26 K. T. Ngo, M. McKinnon, B. Mahanti, R. Narayanan, D. C. Grills, M. Z. Ertem and J. Rochford, *J. Am. Chem. Soc.*, 2017, **139**, 2604–2618.

27 H. Kuo, S. E. Tignor, T. S. Lee, D. Ni, J. E. Park, G. D. Scholes and A. B. Bocarsly, *Dalton Trans.*, 2020, **49**, 891–900.

28 A. J. Morris, G. J. Meyer and E. Fujita, *Acc. Chem. Res.*, 2009, **42**, 1983–1994.

29 D. C. Grills, M. Z. Ertem, M. McKinnon, K. T. Ngo and J. Rochford, *Coord. Chem. Rev.*,

2018, **374**, 173–217.

30 E. Kottelat and Z. Fabio, *Inorganics,* 2017, **5**, 24.

31 P. L. Cheung, C. W. Machan, A. Y. S. Malkhasian, J. Agarwal and C. P. Kubiak, *Inorg. Chem.*, 2016, **55**, 3192–3198.

32 C. O. Dietrich-Buchecker, P. A. Marnot, J. P. Sauvage, J. R. Kirchhoff and D. R. McMillin, *J. Chem. Soc. - Chem. Commun.*, 1983, 513–515.

33 M. Sandroni, Y. Pellegrin and F. Odobel, *Comptes Rendus Chim.*, 2016, **19**, 79–93.

34 J. X. Zhang, C. Y. Hu, W. Wang, H. Wang and Z. Y. Bian, *Appl. Catal. A Gen.*, 2016, **522**, 145–151.

35 H. Takeda, H. Kamiyama, K. Okamoto, M. Irimajiri, T. Mizutani, K. Koike, A. Sekine and O. Ishitani, *J. Am. Chem. Soc.*, 2018, **140**, 17241–17254.

36 J. O. Taylor, Y. Wang and F. Hartl, *ChemCatChem*, 2020, **12**, 386–393.

37 J. Wang, L. Gan, Q. Zhang, V. Reddu, Y. Peng, Z. Liu, X. Xia, C. Wang and X. Wang, *Adv. Energy Mater.*, 2019, **9**, 1803151.

38 X. Ma, C. Hu and Z. Bian, *Inorg. Chem. Commun.*, 2020, **117**, 107951.

39 A. Zhanaidarova, S. C. Jones, E. Despagnet-Ayoub, B. R. Pimentel and C. P. Kubiak, *J. Am. Chem. Soc.*, 2019, **141**, 17270–17277.

40 J. J. Walsh, G. Neri, C. L. Smith and A. J. Cowan, *Organometallics*, 2019, **38**, 1224–1229.

41 R. De, S. Gonglach, S. Paul, M. Haas, S. S. Sreejith, P. Gerschel, U. P. Apfel, T. H. Vuong, J. Rabeah, S. Roy and W. Schöfberger, *Angew. Chemie*, 2020, **132**, 10614–10621.

42 J. M. Smieja and C. P. Kubiak, *Inorg. Chem.*, 2010, **49**, 9283–9289.

43 V. Penicaud, F. Odobel and B. Bujoli, *Tetrahedron Lett.*, 1998, **39**, 3689–3692.

44 H. Kvapilová, A. Vlček, V. Barone, M. Biczysko and S. Záliš, *J. Phys. Chem. A*, 2015, **119**, 10137–10146.

45 R. Francke, B. Schille and M. Roemelt, *Chem. Rev.*, 2018, **118**, 4631–4701.

46 C. Costentin, S. Drouet, M. Robert, J. Save and J. M. Savéant, *J. Am. Chem. Soc.*, 2012, **134**, 11235–11242.

47 C. Costentin, J. Savøant and J.-M. Savéant, *ChemElectroChem*, 2014, **1**, 1226–1236.

48 C. Costentin, G. Passard and J. M. Savéant, *J. Am. Chem. Soc.*, 2015, **137**, 5461–5467.

49 C. Costentin, M. Robert and J.-M. M. Savéant, *Chem. Soc. Rev.*, 2013, **42**, 2423–2436.

50 V. V. Pavlishchuk and A. W. Addison, *Inorganica Chim. Acta*, 2000, **298**, 97–102.

51 M. Enescu, K. Steenkeste, F. Tfibel and M.-P. Fontaine-Aupart, *Phys. Chem. Chem. Phys.*, 2002, **4**, 6092–6099.

52 D. Mauzerall, *J. Am. Chem. Soc.*, 1962, **84**, 2437–2445.

Chapter 4. The excited state and vibrational dynamics of functionalised Re(I) CO_2 reduction catalysts

Abstract

The dynamics of the electronic and vibrational excited states of three Re(I) CO_2 reduction catalysts have been studied by time resolved infrared and two-dimensional infrared spectroscopy. A sterically hindered catalyst, $[Re(HPEAB)(CO)_3Cl]$ (HPEAB = 6,6′-{*N*-(4-hexylphenyl)-*N*-(ethyl)-amido}-2,2′-bipyridine) was found to form a singlet metal/halide-to-ligand charge transfer state following 400 nm excitation, which then undergoes intersystem crossing to a triplet state. Multidimensional IR spectroscopy was used to show that the amide and carbonyl vibrations are coupled through low-frequency modes, with no through-space dipole-dipole coupling. The rate limiting step of intramolecular vibrational relaxation from the $\{Re(CO)_3Cl\}$ moiety to the ligand was found to be energy transfer from the high frequency carbonyl modes to low frequency modes. Vibrational relaxation was faster in the triplet state, attributed to the different charge density distribution of the excited state compared to the ground state. Overall, 6,6′-substitution of the bipyridyl ring leads to similar electronic and vibrational dynamics to 4,4′-substitution. A red-light harvesting complex $[Re(mesBIAN)(CO)_3Cl]$ (mesBIAN = bis(mesitylimino)acenaphthene) was also studied, where the excited state dynamics following 400 nm excitation were significantly altered compared to previously reported bipyridyl catalysts. A highly excited singlet state was produced, which intersystem crosses to form multiple triplet states that initially equilibrate, and then relax independently on the nanosecond timescale. Functionalisation of the mesBIAN ligand with an azide group was found to significantly alter the excited state absorption spectrum, but not the excited state dynamics. Vibrational coupling between the mesBIAN aromatic ring modes and the carbonyl ligands was very weak. The mesBIAN → CO coupling was enhanced by addition of an azide group. This results from a new population transfer pathway from the high frequency azide stretching vibration to the lower frequency carbonyl modes. Preliminary analysis of the excited state 2DIR data suggests vibrational excitation of the triplet excited state induces internal conversion between two triplet states with a small energy separation, which was not possible in the vibrationally relaxed triplet states.

4.1 Introduction

The mechanism of excited state relaxation, and the rates of vibrational energy redistribution are fundamental, yet important, aspects of CO_2 reduction photocatalysis. Studies of the dynamics following visible light excitation give critical information about the suitability of a photocatalyst for

CO_2 reduction catalysis. For example, the excited state lifetime of the photocatalyst must be longer than the timescale of diffusion, otherwise intermolecular electron transfer is not possible and photocatalysis cannot take place. Furthermore, these studies give information about the energies of the excited states, which must be in the correct range to be able to reduce CO_2, and then be regenerated by the sacrificial donor.

The study of molecular vibrations, their coupling strengths, and their relaxation following excitation with an infrared pulse is another important field for fundamental studies of CO_2 reduction photocatalysts. Molecular vibrations been shown to influence other photophysical processes, such as internal conversion between triplet states or electron transfer.[1–7] The redistribution of vibrational energy throughout a coordination complex takes place on a range of timescales: from ultrafast coherence transfer on the femtosecond timescale, to slow intermolecular vibrational energy transfer on the 10-50 ps timescale.[8] The overlap of vibrational wavefunctions also plays a role in determining the rate of non-radiative decay processes. For example, intersystem crossing (ISC) and internal conversion (IC) are mediated by vibrational modes. Therefore, to understand how molecular vibrations can influence the rate of excited state relaxation, a detailed understanding of vibrational energy redistribution is required.[9,10] This level of understanding is highly desirable, as the ultrafast photophysical processes which take place following visible light excitation are the first steps of photochemical CO_2 reduction, where electron transfer reactions between the photosensitiser, catalyst, and sacrificial donor initiate the catalytic reaction. The role of vibrational relaxation may be especially important in intramolecular electron transfer, which is required for catalyst-photosensitiser dyads.

An effective class of CO_2 reduction catalysts which are ideally suited for study by vibrational spectroscopy are the group 7 tricarbonyl complexes, such as $[Re(bpy)(CO)_3Cl]$ (bpy = 2,2′-bipyridine). These complexes are able to efficiently reduce CO_2 to useful products, such as CO, with high turnover and selectivity. The carbonyl ligands have strong vibrational absorption bands in the 1850 – 2150 cm^{-1} region of the electromagnetic spectrum. Therefore, IR spectroscopy is ideal for study of these catalysts, their redox processes, and the CO_2 reduction catalytic cycle.[11,12] Linear IR spectroscopy has been used to characterise the one and two-electron reduction products of $[Re(L)_2(CO)_3Cl]$ catalysts, allowing for definitive assignment of the catalytic activation mechanism. This was further advanced by pulse radiolysis coupled with time-resolved infrared (TRIR) spectroscopy, which provided rates of reaction for the catalyst activation steps.[13–15]

For *fac*-$[Re(L_2)(CO)_3X]$ complexes with the C_s point group there are typically three major absorption bands for the carbonyl ligands. These are vibrations with symmetry labels a′(1), a″, and a′(2), which correspond to symmetric stretching of all three carbonyls, antisymmetric stretching of the equatorial carbonyls, and antisymmetric stretching of all three carbonyls, respectively.[16]

Time-resolved infrared (TRIR) spectroscopy following visible light excitation has also been used for the study of Re(I) CO_2 reduction catalysts.[17–22] In [Re(bpy)$(CO)_3$Cl] (bpy = 2,2′-bipyridyl), the relaxation of the singlet metal-to-ligand charge transfer (^{1}MLCT) excited state has been shown to take place by ultrafast intersystem crossing to the ^{3}MLCT state, which then cools to the thermally equilibrated vibrational level on the 10 – 20 ps timescale.[22] In most cases, the ^{3}MLCT state is long lived and relaxes directly to the ground state by phosphorescence on the 10 – 100 nanosecond timescale.[23,24] Alternate mechanisms have also been reported that involve halide-to-ligand charge transfer (XLCT), intraligand charge transfer (ILCT), ligand-to-ligand charge transfer (LLCT) and metal-centred (MC) excited states, which can be introduced into the excited state relaxation mechanism through functionalisation of the diimine or axial ligands.[25–31] Introduction of electron donor or electron acceptor groups can also lead to the formation of charge separated excited states (CSS), allowing for intramolecular photosensation of the catalyst.[25,32–34] It has also been shown that the vibrational modes of the Re(I) complex can influence the rate of electron transfer between imidazolate and bipyridyl ligands. This process forms the CSS state, where the positive charge is on the axial imidazole and the negative charge is in the bipyridyl π^* orbital. This demonstrates the importance of a strong understanding of vibrational dynamics in the design of novel catalytic complexes.[1,10,35,36]

Two-dimensional infrared (2DIR) spectroscopy is used to study the vibrational dynamics of coordination complexes. In this work we utilise 2DIR in the frequency domain, with a narrow-band IR pump (*ca.* 1.5 ps, 15 cm^{-1}) and broadband IR probe (*ca.* 100 fs, 100 cm^{-1}).[37,38] This technique has been implemented previously to study the rates of vibrational relaxation in the ground and ^{3}MLCT excited states of [Re(bpy-ester)$(CO)_3$Cl] (bpy-ester = 4,4′-diethylester-2,2′-bipyridine).[39] This was used to show that the carbonyl ligands and ester groups are vibrationally coupled, and excitation of one mode results in a response of the other due to the intramolecular vibrational coupling. This occurs by intramolecular vibrational energy redistribution (IVR) through the low-frequency modes of the complex, which are populated from the initially excited high-frequency mode. IVR is an equilibration process, where vibrational energy is rapidly transferred between low energy modes with small energy and spatial separation until the terminal ends of the complex are reached.[40–42] After IVR is complete, the complex relaxes to the vibrational ground state by intermolecular vibrational energy transfer (VET) to the continuum of low frequency solvent modes.

There are several other studies of [Re$(L_2)(CO)_3$X] catalysts in solution which instead utilise time domain 2DIR, a Fourier transform technique which provides a much higher time resolution than the frequency domain method. The time domain studies of Re(I) photocatalysts typically focus on determining the rates of spectral diffusion; providing information on the electrostatic interactions between the complex and the solvent molecules.[21,43–45] It has been shown that the rate of spectral diffusion is greater in the excited state compared to the ground state, a result of the decreased dielectric friction between the ^{3}MLCT state and the solvent. Time domain excited state 2DIR has also been used to definitively characterise the vibrational absorption bands of the MLCT state with a ‘labelling’ pulse sequence, where the complex was vibrationally excited prior to electronic excitation. This revealed that the frequency order of the a′(2) and a″ modes is reversed in the excited state.[46] Advanced techniques for the study of CO_2 reduction catalysts are under continuous development. For example, surface sensitive techniques such as vibrational echo spectroscopy,[47] 2DIR-ATR,[48] and vibrational sum-frequency generation,[49] have been recently demonstrated, as well as 2DIR of electrochemically reduced catalysts.[50]

This study is divided into two parts, part I focusses on the electronic and vibrational excited state dynamics of a recently reported CO_2 reduction catalyst, which incorporates sterically hindering groups in the 6,6′-position of the bipyridyl ring, [Re(HPEAB)(CO)$_3$Cl] (HPEAB = 6,6′-{*N*-(4-hexylphenyl)-*N*-(ethyl)-amido}-2,2′-bipyridine) (Figure 4.1). The amide functional group which links the phenyl and bipyridyl rings acts as an IR-reporter, allowing for study of the vibrational energy redistribution rates in the complex. The excited state dynamics are analysed by TRIR spectroscopy following 400 nm excitation, with the aim of increasing our understanding of the demonstrated lack of photocatalytic activity following excitation, which is uncommon for [Re(L$_2$)(CO)$_3$(X)] catalysts. The vibrational dynamics of the ^{3}MLCT excited state will also be studied to determine how the rate of vibrational energy transfer in the complex is affected by electronic excitation. The results will be compared to the previously reported complex, [Re(bpy-ester)(CO)$_3$Cl] (bpy-ester = 4.4′-diethylester-2,2′-bipyridine), to determine if the choice of 4,4′- or 6,6′-functionalisation of the bipyridyl ring has any significant effects on the electronic and vibrational dynamics of the CO_2 reduction catalyst.

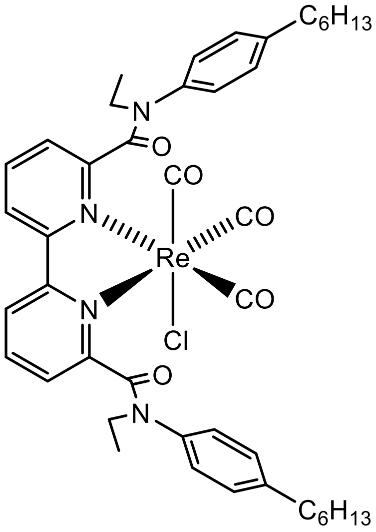

Figure 4.1 – Chemical structure of [Re(HPEAB)(CO)$_3$*Cl] (**1**).*

In part II, the electronic and vibrational excited state dynamics of two Re(I) complexes, where the bipyridyl ligand is replaced for a bis(mesitylimino)acenaphthene (mesBIAN) ligand. The electronic and vibrational dynamics of these complexes are of significant interest, as [Re(Ar-BIAN)(CO)$_3$Cl] (Ar = phenyl, mesityl, diisopropylphenyl (dpp)) complexes have been investigated previously as electrocatalysts for CO_2 reduction. It was found that when the Ar group is a phenyl ring, the Re complex has no electrocatalytic activity. However, when the Ar group was mesityl or diisopropylphenyl, catalytic current enhancement was observed.[51] These results suggested the steric bulk of the aryl substituents had a large influence on the electrocatalytic activity. This was later expanded on, where further electrochemical studies have showed that the sterically hindering dpp-BIAN ligand prevents dimerisation of the [Re(Ar-BIAN)(CO)$_3$]$^{\cdot-}$ intermediate.[52] The photocatalytic activity of the Ar-BIAN complexes has not been reported in the literature. The Ar-BIAN ligands have been suggested as potential 'electron reservoirs', where they could be highly reduced to allow for CO_2 reduction beyond CO or H_2CO_2. However, a study utilising spectroelectrochemistry and density functional theory (DFT) calculations has showed that whilst the Ar-BIAN ligand is a good π-acceptor, it cannot be reduced by more than two electrons.[53] It was also shown that the LUMO of the complex is a low-energy, highly stabilised state. The capacity of the [Re(Ar-BIAN)(CO)$_3$Cl] complexes to perform photochemical CO_2 reduction has not yet been reported. However, it has been shown in the Weinstein group that irradiation of a CO_2 saturated solution of [Re(mesBIAN)(CO)$_3$Cl] with broadband white light in the presence of a triethanolamine sacrificial donor did not result in CO_2 reduction.[54] Currently there are no studies of the excited state or vibrational dynamics of a [Re(Ar-BIAN)(CO)$_3$Cl] complex following visible light excitation.

The two mesBIAN complexes studied here differ in the substituent on the 4-position of the acenaphthene ring, which is either a hydrogen atom or an azide group (Figure 4.2). The azide group was selected as it can act as an IR-reporter for vibrational spectroscopy. Here, the excited state dynamics of these complexes are analysed following 400 nm excitation to determine if the use of the mesBIAN ligand has a significant effect on the capacity of the Re(I) complex to harvest solar energy for the purposes of CO_2 reduction. Infrared excitation of both the carbonyl and azide groups will also be used to probe the intramolecular vibrational coupling between the $\{Re(CO)_3\}$ and N_3 moieties. This will then be extended to study of the vibrational dynamics within the triplet electronic excited states formed following 400 nm excitation.

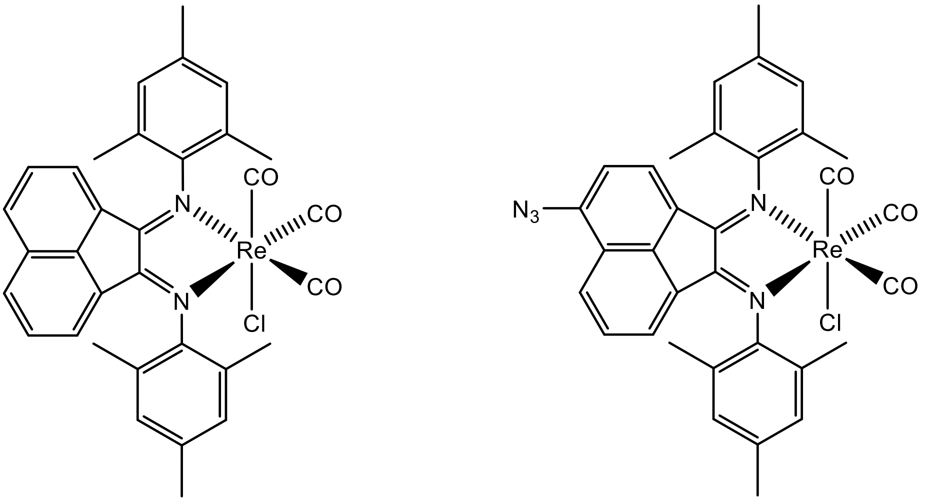

2 **3**

*Figure 4.2 – Chemical structures of [Re(mesBIAN)(CO)$_3$Cl] (**2**), and [Re(4-N$_3$-mesBIAN)(CO)$_3$Cl] (**3**).*

4.2 Experimental

[Re(HPEAB)(CO)$_3$Cl], was prepared and characterised as described previously.[55] [Re(mesBIAN)(CO)$_3$Cl] and [Re(4-mesBIAN-N$_3$)(CO)$_3$Cl] were synthesised by Dr. Andrew Sadler.[54] The complex was dissolved in spectroscopic grade dichloromethane (DCM) for all experiments. TRIR and 2DIR data were analysed in Glotaran, OPTIMUS, and OriginPro by conventional global analysis techniques.[56] TRIR and 2DIR experiments were performed on the ULTRA setup at the Central Laser Facility, Rutherford Appleton Laboratory, Harwell.[57] Three-pulse experiments used optical choppers to set the repetition rate of the UV pump to 5 kHz, and the IR pump to 2.5 kHz. The probe and reference pulses had repetition rates of 10 kHz. This allowed for the simultaneous collection of UV_{pump}–IR_{probe} (TRIR), IR_{pump}–IR_{probe} (GS-2DIR) and UV_{pump}-IR_{pump}-IR_{probe} (ES-2DIR) data. The IR_{pump} bandwidth was approximately 15 cm^{-1} and the IR_{probe} bandwidth was approximately 400 cm^{-1}. The pulses used for 2DIR spectroscopy were generated by two optical parametric amplifiers pumped by synchronized Ti:sapphire regenerative amplifiers with picosecond and femtosecond pulse durations. The 400 nm pump beam was generated from the second harmonic of the femtosecond laser. The probe spectrum was recorded with two liquid nitrogen cooled HgCdTe array detectors that yielded a spectral resolution of 2 cm^{-1}. For the data shown in the text, pulse energies were approximately 0.5 μJ for both UV and IR pumps, with spot sizes of approximately 80, 100, and 150 μm for IR_{probe}, IR_{pump}, and UV_{pump}, respectively. In TRIR experiments the relative polarisation of the pump and probe pulses was set to the magic angle of 54.7° for anisotropy free measurements. In GS-2DIR and ES-2DIR experiments, the UV and IR pumps were set parallel to each other, and the probe beam was set at magic angle with respect to these pumps. Samples were flowed and rastered through Harrick cells by a peristaltic pump. Optical densities at the excitation wavelength (400 nm) were kept at approximately 0.5.

4.3 Results and Discussion

Part I: Vibrational energy transfer in the ground and excited states of a sterically protected CO_2 reduction catalyst

Electronic and vibrational absorption spectra

The UV-vis absorption spectrum of **1** was recorded in DCM, and is similar to [Re(bpy)$(CO)_3Cl$], consistent with other functionalised bipyridyl complexes (Figure 4.3).[55] The vibrational absorption spectrum of **1** in the 1480 – 2100 cm^{-1} region of the spectrum is primarily comprised of seven absorption bands. These are assigned as the a′(1), a″, and a′(2) group vibrations of the carbonyl ligands at 2025, 1920, and 1910 cm^{-1}. Unlike most other [Re$(L_2)(CO)_3Cl$] catalysts, the a″ and a′(2) bands are close in energy and are observed as a single absorption envelope. At lower frequencies, the stretching vibrations of the amide C=O group are observed (1652 cm^{-1}) as a single convoluted absorption band. This band is comprised of symmetric and asymmetric combination modes of the local amide C=O stretching modes. The overtone bands of the aromatic groups (1573, 1600 cm^{-1}), and the C-N stretching mode of the amide group are found at lower frequencies, assigned on the basis of the calculated harmonic IR spectrum. There are additional weak features in the IR spectrum, such as shoulders on the low frequency side of the a′(1) and a′(2) bands. These are possibly attributed to the presence of a second conformer of **1** present in DCM solution. This was further evidenced by the ground state 2DIR measurements described herein (see below). Additionally, the shoulder on the a′(1) mode likely has some contribution from the anharmonic combination mode described previously.[58]

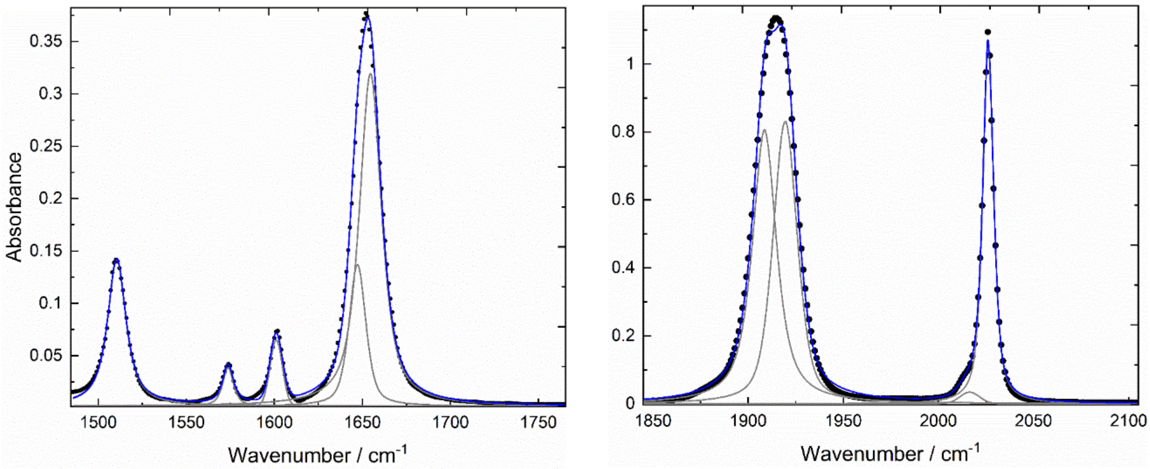

*Figure 4.3 – Vibrational absorption spectra of **1** in the 1490 – 1760 and 1850 – 2100 cm^{-1} regions of the IR spectrum, recorded in DCM and deconvoluted with pseudo-Voigt profiles. The fitting equation used for this deconvolution is provided in appendix B, Eq. B1.*

Excited state dynamics of [Re(HPEAB)(CO)$_3$Br]

The excited state dynamics of **1** have previously been characterised by UV-vis transient absorption spectroscopy, which found that the excited state lifetime was 3.6 ± 0.2 ns.[55] Thus, the lifetime was too short for use of **1** as a photosensitiser or photocatalyst. Here we expand on these results with TRIR spectroscopy (Figure 4.4), which is more structurally sensitive than TA and provides more information on the excited state relaxation mechanism. TRIR data of **1** were recorded following 400 nm excitation. This pump wavelength was resonant with a mixed halide-to ligand (XLCT) and metal-to-ligand charge transfer (MLCT) transition, as characterised by TD-DFT calculations (Appendix D, fig. D2) ($S_0 \rightarrow S_2$, centred at 420 nm), where an electron is transferred from the Re d-orbitals and Cl p-orbitals to the ligand π* orbital. The pump was likely also resonant with a pure MLCT transition ($S_0 \rightarrow S_3$, centred at 395 nm). An intraligand charge transfer (ILCT) transition ($S_0 \rightarrow S_4$, centred at 385 nm) was also found at slightly higher energies, which corresponds to electron transfer from the amide and phenyl groups to the bipyridyl ring. However, the $S_0 \rightarrow S_4$ transition was not resonant with the pump. The lowest singlet excited state (S_1) was characterised as ^{1}MLCT/XLCT. The $S_0 \rightarrow S_1$ transition was also non-resonant with the 400 nm pump.

400 nm excitation of **1** resulted in a single fluorescence emission band, centred at 481 nm (Appendix D, fig. D7). The emission intensity was very weak, with a lower intensity than the Raman scattering signal from the DCM solvent. The peak maximum was found at a shorter wavelengths compared to fluorescence of [Re(bpy)(CO)$_3$Cl] following 400 nm excitation.[26] In aerated DCM, no phosphorescence signal was detected, indicating that the major ^{3}MLCT relaxation pathway was non-radiative. No changes in the emission spectrum were observed upon removing oxygen from the

solution, as the excited state lifetime is too short to participate in diffusion-controlled emission quenching.

TRIR data of a solution of **1** in DCM were recorded following 400 nm excitation (Figure 4.4). The transient absorption bands formed immediately after excitation were shifted to higher frequency by 37 – 69 cm^{-1} compared to the ground state absorption bands. The peak centres of the transient absorption bands at a time delay of 100 fs were at 1947, 1989, and 2067 cm^{-1}, which correspond to the a″, a′(2), and a′(1) modes, respectively.[46] The separation between a″ and a′(2) ν(C≡O) modes is significantly larger in the excited state compared to the ground state. The increase in the ν(C≡O) frequencies indicates that the Re centre is formally oxidised in the initial excited state, consistent with assignment of the transition at 400 nm as an MLCT. The oxidation of the metal centre resulted in decreased d(Re) → π*(C≡O) back donation, leading to an increase in C≡O bond strength, decrease in bond length, and increase in vibrational frequency. The transient absorption of the amide ν(C=O) stretching mode was found at lower frequencies than the ground state bleach. This shows the C=O bond is longer and weaker following the charge transfer, indicating the electron acceptor is a conjugated π* orbital involving the bipyridyl and amide π-systems. Weak transient signals which correspond to the aromatic overtone vibrations of the excited state were also observed. These bands are very broad and are overlapping, preventing accurate assignment.

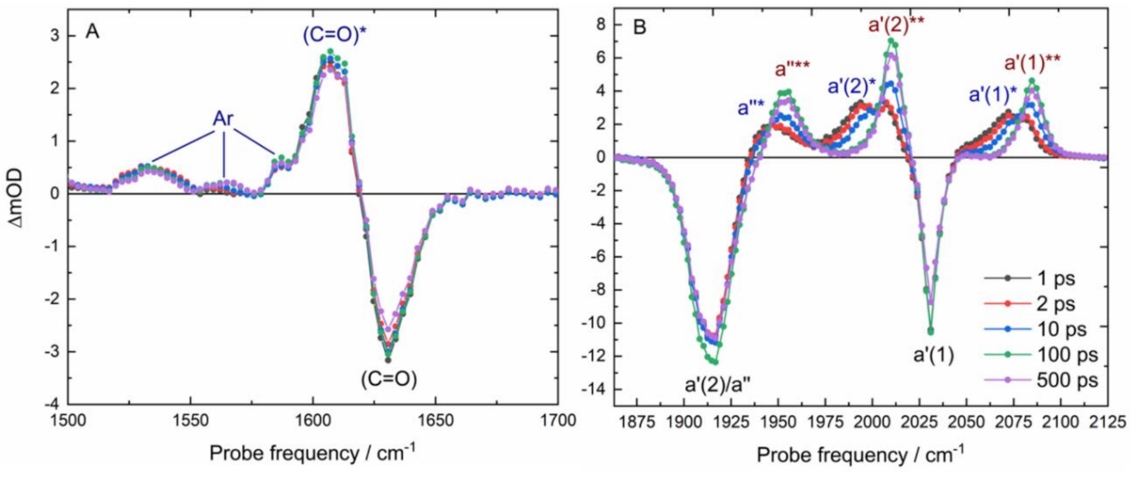

Figure 4.4 – TRIR spectra of ***1*** *in dichloromethane following 400 nm, 40 fs excitation in the 1520 – 1690 (A) and 1875 – 2120 cm*$^{-1}$ *(B) regions of the IR spectrum. The pump – probe time delays are shown, as well as assignments of the transient absorption and ground state bleach bands, the vibrationally hot bands are noted with an asterisk (*), the thermally equilibrated bands are noted with a double asterisk (**).*

Intersystem crossing (ISC) in Re(I) transition metal complexes is ultrafast,[59] hence no transient absorptions of the optically prepared singlet states were detected by TRIR. It is probable that the optically prepared ^{1}MLCT and ^{1}MLCT/XLCT states rapidly internally converted to the lowest energy singlet state prior to ISC. The TRIR spectra suggest only a single triplet state was formed following

400 nm excitation, this state was assigned as ^{3}MLCT/XLCT on the basis of the harmonic IR spectrum of the thermally relaxed T_1 state.

From 1 – 2 ps, the ν(C≡O) transient absorption bands begin to shift to higher frequencies (Figure 4.4B) , which is attributed to vibrational cooling of the ^{3}MLCT/XLCT state. During this time, no shift in the position of the amide ν(C=O) transient absorption was observed (Figure 4.4A). This suggests the vibrational cooling was largely associated with the high frequency ν(C≡O) modes. The vibrational relaxation continues until 10 ps after excitation, forming three transient absorption bands at 1953, 2009, and 2084 cm^{-1}. The magnitude of the blue shift from 1 – 10 ps was approximately 15 cm^{-1}, very similar to the anharmonic shifts of the a″, a′(2), and a′(1) modes obtained from excited state 2DIR experiments (Figure 4.5) where the ν = 1 level of the vibrational modes is directly populated. This lends further support to the assignment of the spectral evolution between 1 – 10 ps as vibrational relaxation. These bands of the thermally equilibrated triplet state did not undergo any further frequency shifts or line narrowing, confirming the equilibrium molecular geometry had been formed. The average magnitude of the ν(C≡O) blue shift in the vibrationally cooled excited state is a measure of the Re → bpy charge separation. For **1**, Δν was 64 cm^{-1} at 500 ps. Comparison with previously reported Re-complexes suggests the lowest energy triplet in **1** has a greater Re → bpy charge separation than [Re(dmbpy)(CO)$_3$(Etpy)], (Etpy = 4-ethylpyridine, Δν = 50 cm^{-1}), and [Re(bpy)(CO)$_3$Cl] (Δν = 55 cm^{-1}).[22] The charge separation character was similar to [Re(bpy-ester)(CO)$_3$(Etpy)][PF$_6$] (Δν = 63 cm^{-1}), indicating the amide and ester complexes have similar electron densities on the Re centre in the thermally equilibrated triplet state.[60]

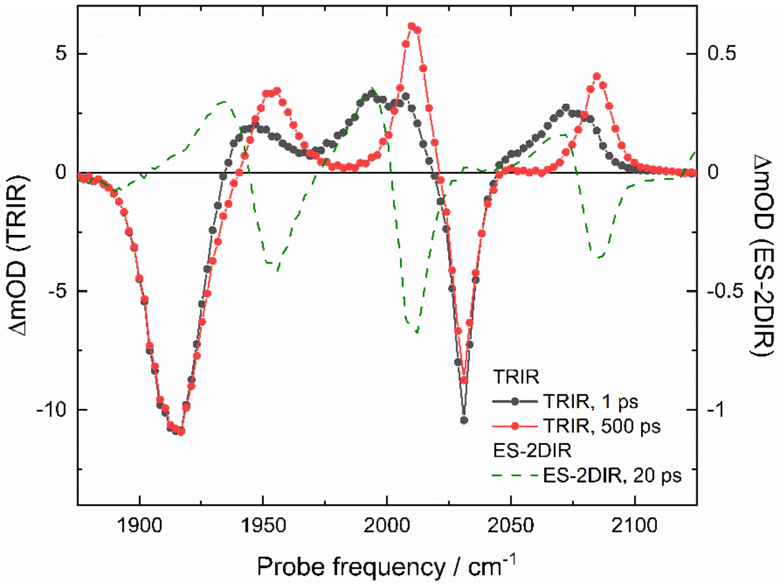

*Figure 4.5 – Comparison of the TRIR spectra of **1** at time delays of 1 and 500 ps after 400 nm excitation, overlaid with excited state 2DIR spectrum of **1** 500 ps after 400 nm excitation, and 20 ps after excitation of the ν[a'(1)] mode with a narrowband IR pump centred at 1995 cm^{-1}).*

The decay of the excited state to the ground state was observed from 10 – 3000 ps for the ν(C≡O), ν(C=O), and ν(Ar) modes. During this time no further changes to the spectral profile were observed. This confirmed that the excited state species were in the lowest energy triplet state and no other photophysical processes took place on the 500 – 3000 ps timescale.

The TRIR data were further analysed with lifetime density analysis (LDA). A distribution of 200 time constants between 0.1 – 4000 ps were fit to the data, the L-curve for this LDA analysis is shown in Appendix D, figure D5. The LDA traces were used to identify the key time constants involved in the excited state relaxation of **1** (Figure 4.6). Three regions of interest were found which correspond to the IRF convoluted ultrafast processes (including ISC), vibrational cooling, and triplet state decay. The ultrafast region contained spectral components associated with the grow in of the transient signals, convoluted with the initial relaxation processes such as ISC. The LDA bands in this time region were maximised at a time constant of 0.27 ps. The vibrational cooling region was found from 10 – 50 ps. These time constants are associated with the shifting of the transient absorption bands to higher frequency with increasing population time. The median time constant for the cooling process was 12 ps. The final region contained LDA components corresponding to the decay of the transient signals and ground state recovery, which occurred at time constants from 3000 ps. The LDA traces allowed for complete deconvolution of each photophysical process, and bleach recovery was only observed in the final triplet state decay.

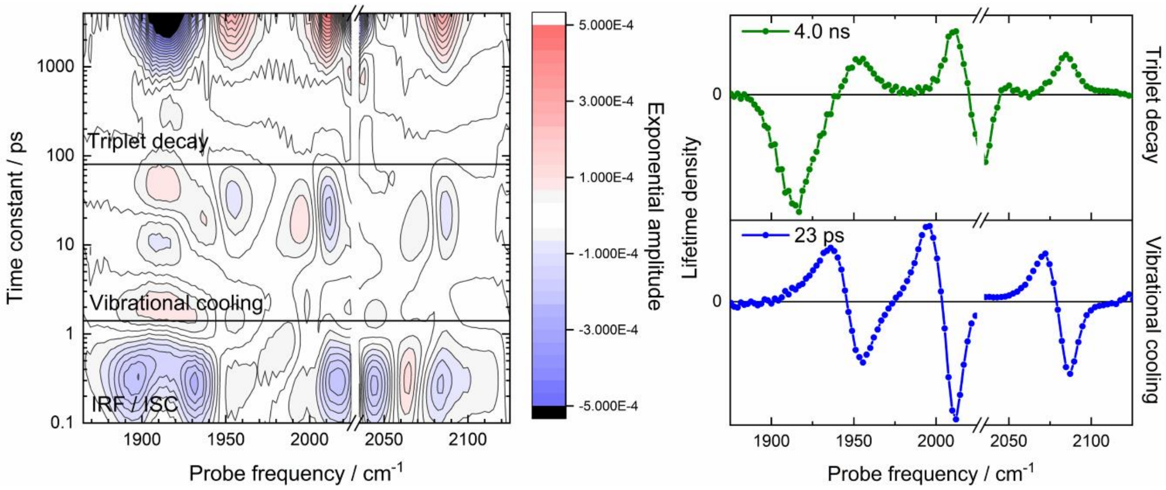

*Figure 4.6 – Lifetime density map for a distribution of 200 time constants from 0.1 – 4000 ps fit to the TRIR data of **1**, the time constants are divided into three regions corresponding to the key photophysical processes in the excited state relaxation. Key lifetime density traces from the LDA contour data are also shown. In both diagrams, positive intensity corresponds to transient decay or bleach grow in. Negative intensity corresponds to transient grow in or bleach recovery. The 'L-curve' and regularisation parameter are provided in Appendix D, fig. D5. Note than an artifact is present in the experimental data at 2030 cm^{-1} that is imprinted onto the LDA traces which has been cropped out of the graphs.*

The LDA results were used to propose a kinetic model for the excited state dynamics of **1** (Figure 4.7), where the rates of ISC, vibrational cooling, and ground state recovery were optimised through global lifetime analysis (GLA). A three-component sequential model was required to adequately model the experimental TRIR data (Appendix D, fig. D4). Good agreement was found between the model and experimental data, with no spectral or kinetic components remaining in the residual data. Due to convolution with the instrument response function (IRF), it was not possible to obtain an accurate time constant for the ISC process. The rate of vibrational cooling was modelled as 12 ps, identical to the median time constant obtained from LDA. However, the 12 ps time constant will be associated with a large uncertainly, as sequential GLA is not suitable for modelling of vibrational cooling, which occurs over a range of timescales as the transient absorption bands shift to higher frequency, as shown in the LDA contour map. The ground state recovery time constant provided by GLA was 2.9 ns.

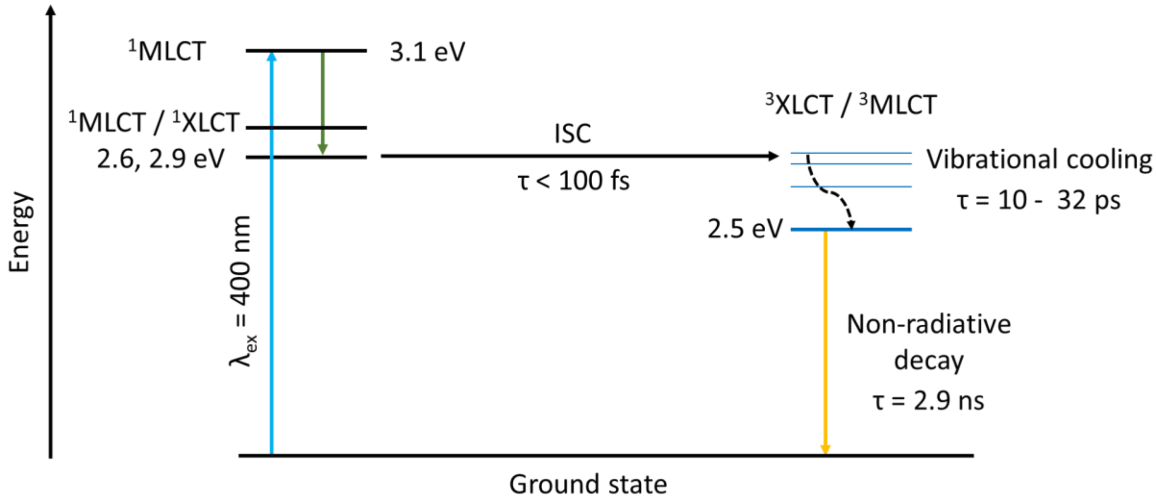

Figure 4.7 – Proposed Jablonski energy level diagram for the excited state relaxation of ***1*** *following 400 nm, 40 fs excitation of the* $S_0 \rightarrow S_2$ *transition. For clarity, vibrational relaxation of the optically prepared Frank-Condon singlet state(s) is not shown.*

The initial dynamics of **1** are similar to previously reported [Re(L$_2$)(CO)$_3$X] catalysts, where the initially formed singlet state undergoes intersystem crossing to the ^{3}MLCT/XLCT state. However, after vibrational cooling the spectral profile of the lowest energy triplet state in **1** is quite different to these previously reported Re complexes. The transient absorption bands have significantly smaller linewidths than [Re(bpy)(CO)$_3$Cl],[46] [Re(bpy-ester)(CO)$_3$Cl],[39] [Re(phen)(CO)$_3$(4-etpy)],[32] and [Re(bpy)(CO)$_3$(NCS)][61] in the thermally equilibrated triplet state. This is tentatively ascribed to the steric protection of the {Re(CO)$_3$Cl} centre by the bipyridyl ligand, which reduces interactions between the vibrational modes and the solvent. Therefore, solvent induced line broadening effects within the thermally equilibrated triplet state are reduced compared to these previously reported catalysts. In future, this could be investigated further through spectral diffusion studies of the ν(C≡O) modes, which would provide an estimate for the rate of solute-solvent interactions.

Vibrational dynamics of [Re(HPEAB)(CO)$_3$Cl] in the ground state

The vibrational dynamics of the electronic ground state were studied with frequency domain 2DIR spectroscopy (Figure 4.8). Excitation of the a′(1) mode with a picosecond IR pulse centred at 2026 cm^{-1} resulted in initial formation of a transient/bleach peak pair corresponding to the a′(1) self-response, as well as a convoluted off-diagonal peak pair assigned to the a″/a′(2) bands. At 1 ps, the intensity of the self-response was greater than the off-diagonal signal. From 1 – 2 ps, the off-diagonal intensity increases concurrently with an increase in the off-diagonal anharmonic shift (Δ_{ij}), reaching the maximum at 2.3 ps. This was ascribed to equilibration of vibrational energy between the ν = 1 levels of the a′(1), a″, and a′(2) modes, facilitated by ultrafast mechanical coupling interactions. The increase in Δ_{ij} was a result of vibrational population transfer from the initially populated ν_1[a′(1)] level to the ν_1[a″] and ν_1[a′(2)] levels, which results in an increase in the off-diagonal anharmonic shift as the ν = 1 levels of these modes are populated. The time constant for this equilibration process, obtained by single point exponential fitting was 1.7 ± 0.10 ps (Figure 4.9B). After equilibration of the high frequency ν(C≡O) modes was complete, the 2DIR signal intensity decreases as the ground state recovery takes place (Figure 4.9B). The first step in this relaxation is the transfer of vibrational energy from the high frequency ν_1(C≡O) energy levels to low-frequency modes of the complex. This step was associated with a decrease in Δ_{ij} of the a″ and a′(2) transient absorption band during the ground state recovery process, which is evidence of depopulation of the ν_1[a″] and ν_1[a′(2)] levels (Figure 4.8B). This decrease was not evident until large delay times, hence IVR to low-frequency modes proceeded slowly. Considering the dynamics observed following amide excitation, it is probable that IVR from the ν_1[a′(1)], ν_1[a″], and ν_1[a′(2)] energy levels to low-frequency modes was the rate-limiting step in the ground state recovery mechanism. Once the energy transfer to low frequency modes was complete, vibrational energy then cascaded through the low-frequency mode continuum until an equilibrium state is reached, from which the vibrational energy is then transferred to the continuum of solvent modes. The average time constant for intermolecular VET from the {Re(CO)$_3$Cl} moiety to the solvent was 39 ± 0.64 ps. This process returns the excited complex to its thermally equilibrated vibrational ground state (Figure 4.9B).

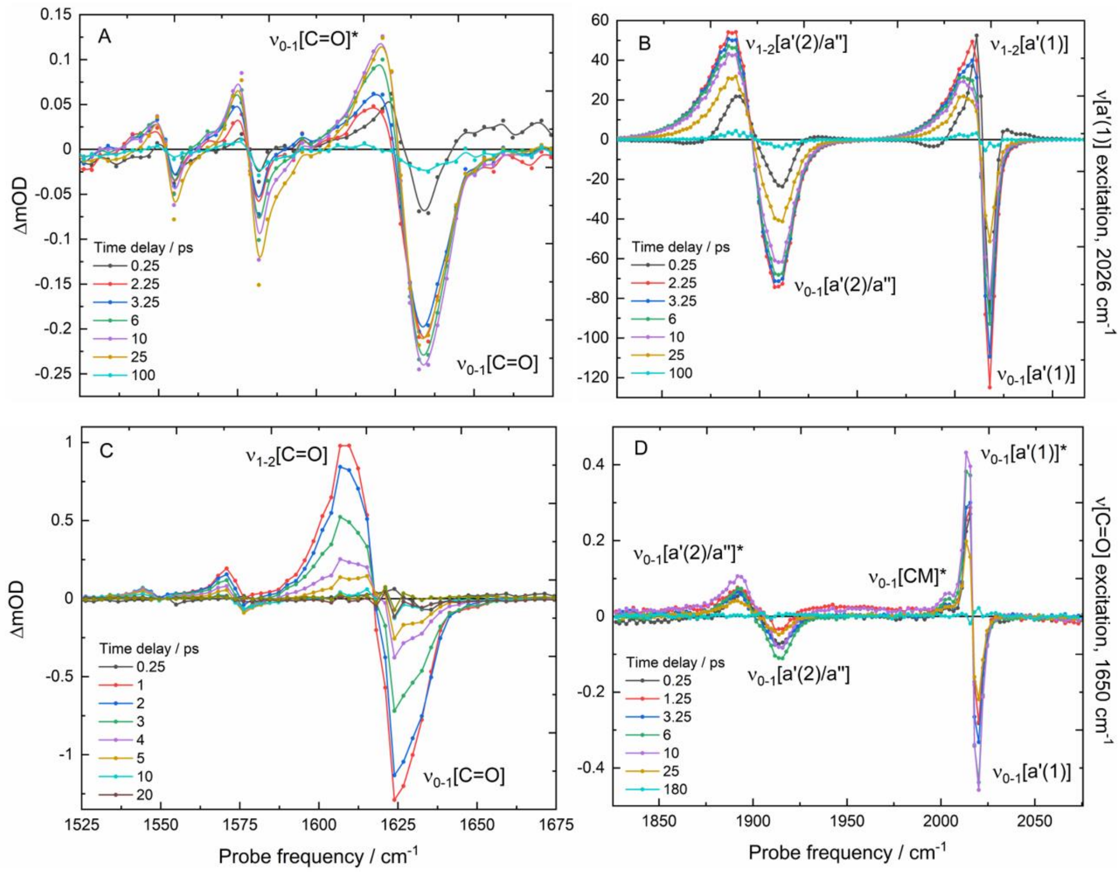

*Figure 4.8 – Ground state 2DIR spectra of **1** in the 1520 – 1670 (A,C) and 1830 – 2065 (B,D) cm^{-1} regions of the IR spectrum following excitation of the carbonyl a'(1) (A,B) or amide C=O (C,D) stretching vibrations with a 2022 or 1950 cm^{-1} IR pump, respectively. The IR_{pump} – IR_{probe} delays and assignments of transient absorption and ground state bleach bands are shown in the legends.*

The propagation of vibrational energy from the Re centre to the bipyridyl ligands through low-frequency modes results in off-diagonal signal formation in the 1500 – 1700 cm^{-1} region of the spectrum (Figure 4.8A). Therefore, the ν(C≡O) modes are vibrationally coupled to the modes of the bipyridyl ligand. The off-diagonal signals for the aromatic overtone modes reached their maximum intensity 24 ps after excitation. The amide ν(C=O) peak pair had a faster grow in rate, reaching maximum intensity 14 ps after excitation (Figure 4.9A). DFT calculations of the anharmonic coupling constants suggests that despite their close spatial proximity, dipole-dipole coupling interactions between the $\{Re(CO)_3Cl\}$ moiety and the amide groups were not a significant vibrational energy transfer pathway in **1** (Appendix D, fig. D3).

As a result, the mechanism of off-diagonal signal formation is assigned as IVR through low-frequency modes following relaxation of the ν(C≡O) high frequency modes. The slow formation of the off-diagonal peak pairs was ascribed to the presence of the heavy metal Re centre, which can act as a vibrational bottleneck to decrease the rate of IVR between functional groups. The off-diagonal anharmonicity is less than the observed Δ_{ii} for the diagonal ν(C=O) mode. Therefore, the ν_1(C=O) level is not populated following excitation of the ν(C≡O) groups. Instead, the transient signal forms from distortion of the vibrational potential energy surface by thermal population of the low-frequency modes anharmonically coupled to the ν(C=O) vibration. The time constant for decay of the off-diagonal amide and bipyridyl signals is significantly larger than what is observed following direct amide excitation. This is due to the slow relaxation of the high-frequency modes in the $\{Re(CO)_3Cl\}$ moiety, which continuously populate the low-frequency modes of the bipyridyl ligand during their relaxation.

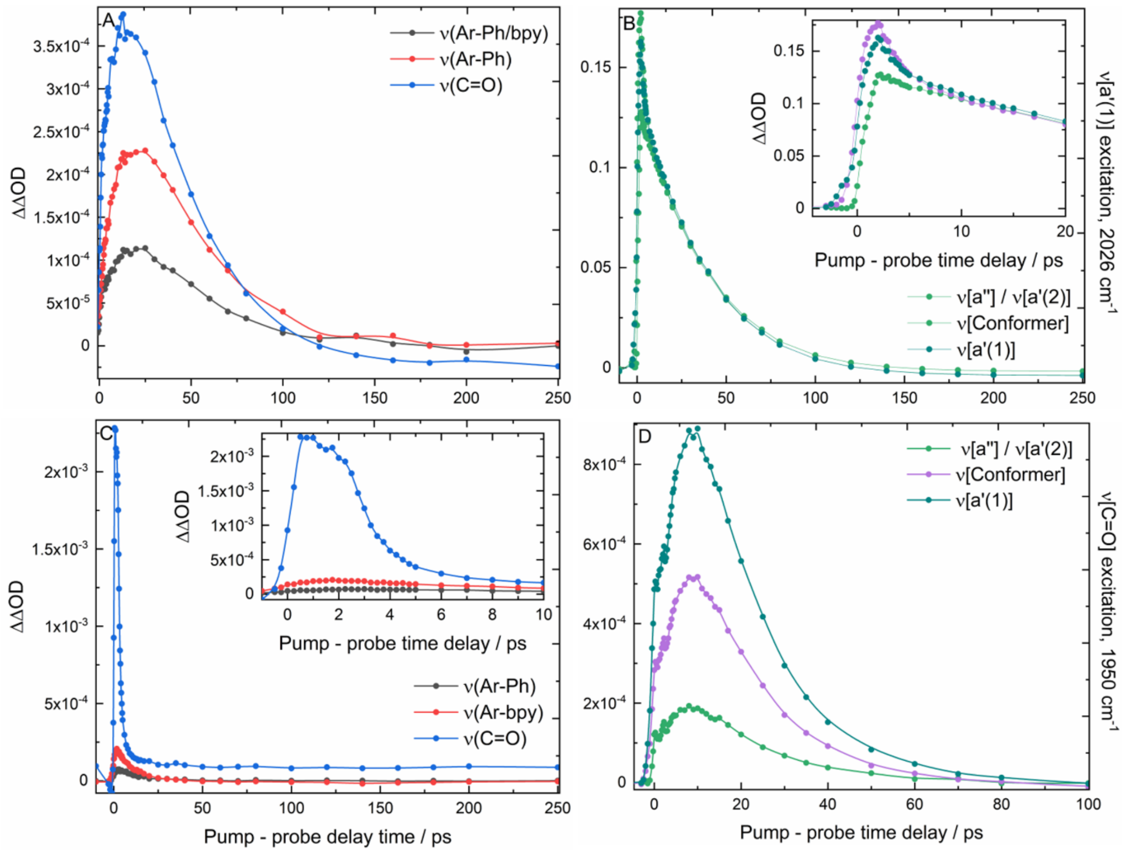

Figure 4.9 – Kinetic traces for the 2DIR peak pairs observed in the electronic ground state of [Re(HPEAB)(CO)$_3$Cl] following either ν[a'(1)] or ν(C=O) excitation with a 1.5 ps, 15 cm^{-1} infrared pump pulse centred at 1950 or 2022 cm^{-1}. The kinetic traces are calculated through subtraction of the ν$_{0-1}$ peak intensity from the ν$_{1-2}$ peak intensity at each time delay.

Excitation of the amide ν(C=O) stretching vibration results in the formation of a strong diagonal peak pair in the 1500 – 1650 cm^{-1} region of the 2DIR spectrum, ascribed to the self-response of the amide group (Figure 4.8C). The diagonal anharmonic shift (Δ_{ii}) for this mode was 17 cm^{-1}. This peak pair corresponds to vibrational population of the ν$_1$(C=O) level. The diagonal amide peak pair decayed monoexponentially with a 2.6 ± 0.18 ps time constant (Figure 4.9C). This was too fast to be assigned as intermolecular VET, thus this was attributed with IVR to low frequency modes. The rapid IVR results in fast formation of off-diagonal signals corresponding to the aromatic stretching vibrations of the bipyridyl and phenyl groups. The aromatic transient absorption at 1570 cm^{-1} reached its maximum intensity 1.75 ps after excitation, significantly faster than the transient at 1544 cm^{-1} (t_{max}

= 3.0 ps). The difference between t_{max} for these modes is possibly due to their different spatial localisations. The aromatic off-diagonal signals relax by intermolecular VET to solvent modes with very similar time constants of 12 ± 0.76 and 11 ± 0.28 ps.

Off-diagonal peak pairs corresponding to the ν(C≡O) modes also form following excitation of the amide ν(C=O) vibration (Figure 4.8D). The value of Δ_{ij} was significantly less than Δ_{ii} for the carbonyl ligand vibrations, indicating the ν=1 levels of the a′(1), a′(2), and a″ modes were not populated following amide excitation. The FWHM of the off-diagonal transient absorption bands were approximately the same as the ground state bleaches, indicating the vibrational potential energy surface was only weakly perturbed. The off-diagonal signal intensity for the a′(1), a″, and a′(2) modes reached their maximum intensity 8.6 ps after excitation (Figure 4.9D). This was faster than the off-diagonal ν(C=O) grow in rate by a factor of 1.6. Thus, the rate of IVR between the amide group and {$Re(CO)_3Cl$} centre was dependent on which mode is first excited. As the rate of IVR through the low-frequency modes is likely extremely similar in both directions, the differences in off-diagonal peak pair grow in rate are a result of the different IVR rates from the ν_1(C=O) and ν_1(C≡O) energy levels to the low-frequency modes.

The decay of the off-diagonal ν(C≡O) modes is slow compared to the decay of the diagonal amide peak pair, with time constants of 18 and 22 ps. This shows that VET from the {$Re(CO)_3Cl$} centre to the solvent modes is slow compared to VET from the bipyridyl ligand to the solvent. This was thought to be due to the restricted amount of solvent around the sterically protected metal centre, which inhibits the rate of VET. Further evidence of the sterically hindering ligand restricting the VET process is given by the 1.4x slower VET rate for the off-diagonal ν[a′(1)] mode of **1** when compared to the non-sterically hindered [Re(4,4′-bpy-ester)$(CO)_3Br$].

The off-diagonal transient absorption of the a′(1) mode was paired with another transient absorption at 2003 cm^{-1} (Figure 4.10). This additional transient absorption band was not a result of vibrational population of the ν_1[a′(1)] level, as the required energy could not be provided by the environment. For example, the endothermic $\nu_1(C{=}O) \rightarrow \nu_1[a'(1)]$ energy transfer would require 373 cm^{-1} of energy, and the available thermal energy at 298 K is only ≈ 200 cm^{-1}. Instead, the additional transient was tentatively assigned as the distorted a′(1) mode within different conformers of **1** present in solution. These conformers differ in the relative orientation of the p-hexylphenyl and ethyl groups around the nitrogen centre of the amide group, of which there are three unique combinations. In the 2DIR experiment, all three conformers are vibrationally excited as the frequency separation between the conformers is close enough such that the narrowband IR pump is resonant with all three species. The observation of this off-diagonal transient absorption band shows that the different conformations of **1** are slow to interconvert, such that they can be independently detected. This slow interconversion also introduces planar chirality to the complex which results in splitting of the ^{1}H NMR resonance for the ethyl CH_2 groups.[55] The origin of this restricted rotation is electron delocalisation of the lone pair on the nitrogen atom toward the amide carbon. The transient absorption bands of the conformers were not observed for the a′(2)/a″ convoluted peaks due to the low signal intensity of this peak pair. Furthermore, the overlap of the peak pairs in the 1525 – 1650 cm^{-1} region prevents accurate assignment of the transient absorption bands associated with other conformers of **1**. There are other possible explanations to account for the observed transient absorption band at 2003 cm^{-1}. For example, it could be argued that this band corresponds to the transient absorption of the anharmonic combination mode which is observed in the FTIR spectrum. However, the combination mode is ubiquitous in $[Re(L_2)(CO)_3Cl]$ complexes, whilst the off-diagonal transient at 2003 cm^{-1} has not been observed previously. Thus the assignment of this band as the perturbed a′(1) vibration of a conformer of **1** is the most reasonable assignment when considering the available experimental data.

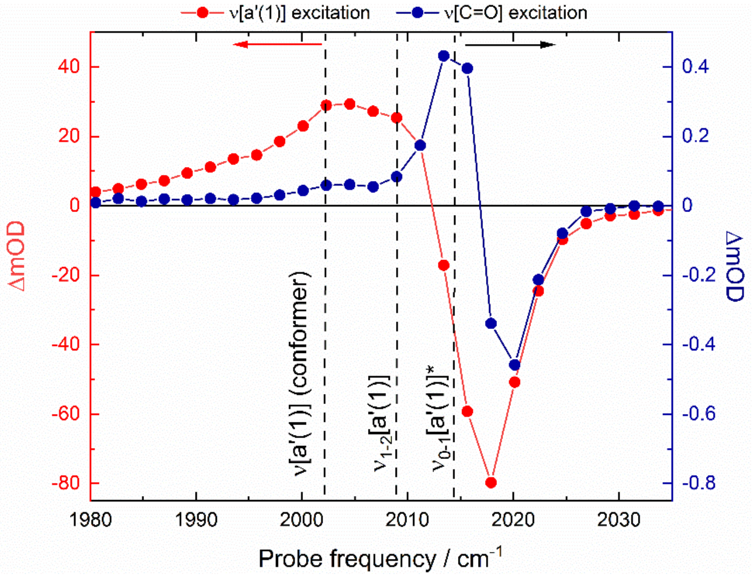

Figure 4.10 – 2DIR spectra of ***1*** *in the 1980 – 2035 cm^{-1} region following IR excitation (1.5 ps, 15 cm^{-1}) of either the a′(1) (red) or amide C=O stretching vibrations. The transient absorption maxima of the $\nu_{0\text{-}1}$[a′(1)]*, $\nu_{1\text{-}2}$[a′(1)], of the major and minor conformers (2003 cm^{-1}) are shown with the dashed lines.*

The vibrational relaxation dynamics of **1** are similar to the reported dynamics of $[Re(bpy\text{-}ester)(CO)_3Cl]$. However, some differences were found. For example, the relaxation of the amide mode self-response to low-frequency modes in **1** was slower than the previously reported ester vibration. However, vibrational energy transfer from the low-frequency modes of the L_2 ligand to the solvent was the same, as evidenced by the similar off-diagonal signal ν(C=O) decay lifetime. Furthermore, the time taken for the ester and amide off-diagonal signals to reach their maximum intensity following ν(C≡O) excitation was approximately the same. This showed that intramolecular coupling between substituents in the 4,4′ or 6,6′ positions of a bipyridyl ring with the $\{Re(CO)_3Cl\}$

moiety is very similar. This also supports the proposal that through-space vibrational energy transfer does not take place between the carbonyl ligands and amide group. If this were a vibrational energy transfer pathway, an increased rate of off-diagonal signal formation would be expected. Together, these results show that IVR between the bipyridyl ligand substituents and the carbonyl ligands was not significantly affected by replacement of a 4,4′-ester substituted bipyridyl ligand for a 6,6′-amide substituted ligand.

Vibrational relaxation in the ^{3}MLCT/XLCT electronic excited state

A three-pulse experiment was used to study the rates of vibrational energy redistribution in the thermally equilibrated excited state, which has primarily ^{3}MLCT/XLCT character (Figure 4.11). The time delay between the 400 nm and mid-IR excitation pulse was fixed to 500 ps, when the complex is in the lowest energy triplet state, and then the time delay between the IR_{pump} and IR_{probe} was scanned. Excitation of the a′(1) mode in the ^{3}MLCT/XLCT state results in the formation of three peak pairs, corresponding to the, a″, a′(2), and a′(1) modes. The diagonal anharmonic shifts were larger in the excited state compared to the ground state, which indicated that the difference between the energies of the $\nu_0 \rightarrow \nu_1$ and $\nu_1 \rightarrow \nu_2$ transitions was larger.

The early time 2DIR spectra did not show the increase in off-diagonal anharmonic shift of the a″, and a′(2) modes, as was observed following a′(1) excitation of the electronic ground state (Figure 4.11A). However, differences in the grow in rate of the a″, and a′(2) and a′(1) peak pairs were found, which reached their maximum intensities following a′(1) excitation at 6.0, 3.0, and 1.0 ps, respectively. This suggests the coupling interaction between a′(1) and a′(2) modes was stronger than a′(1) and a″.

The decay time constant for the three peak pairs is shorter in the ^{3}MLCT/XLCT state compared to the ground state, with time constants of 24 – 30 ps (Figure 4.11C). This shows that VET to the solvent is faster, similar to the previously reported dynamics of [Re(bpy)(CO)$_3$Cl] and [Re(bpy-ester)(CO)$_3$Cl].[39,45] This was thought to be due to the formation of anionic and cationic charges upon electronic excitation. Whilst this decreases the permanent dipole moment of the complex, changes in the intramolecular electrostatic environment have an effect on the interactions between the complex and the solvent. Similar effects have been demonstrated previously, where the rate of solvent induced vibrational frequency fluctuation is significantly decreased in the ^{3}MLCT state of [Re(bpy)(CO)$_3$Cl] compared to the ground state.[45] The decrease in the spectral diffusion rate was rationalised as a change in the ‘dielectric friction’ within the system, which results from changes in the solvent polarisability when the charge density within a solute molecule is changed. The changes in dielectric friction result in changes to the intermolecular dipole-dipole interaction strength, and the rate of VET as a result.

Overall, the vibrational dynamics of the {Re(CO)$_3$Cl} moiety in the excited state are very similar between **1** and [Re(bpy-ester)(CO)$_3$Cl]. This shows that changing the molecular structure of the complex from 4,4′- to 6,6′-functionalised does not significantly affect the rate of vibrational energy redistribution in the charge transfer excited state.

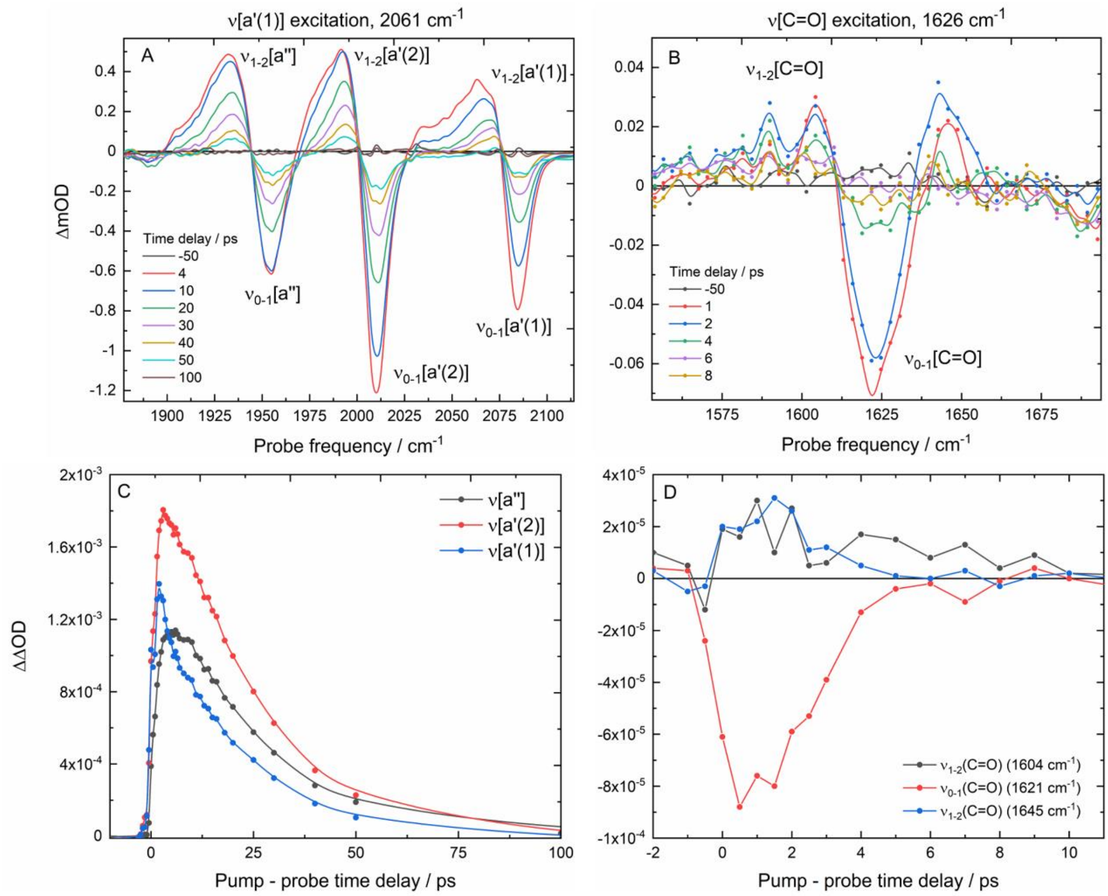

*Figure 4.11 – A) Excited state 2DIR spectra of **1** in the 1880 – 2115 cm^{-1} region of the spectrum following excitation of the a′(1) mode in the ^{3}MLCT/XLCT state (2061 cm^{-1}). B) Excited state 2DIR spectra of **1** in the 1510 – 1690 cm^{-1} region of the spectrum following excitation of the amide C=O stretching vibration (1626 cm^{-1}). The UV$_{pump}$ – IR$_{pump}$ delay time was 500 ps for all data points, the IR$_{pump}$ – IR$_{probe}$ delays are shown on the graphs. C,D) Kinetic traces for the 2DIR peak pairs observed in the ^{3}MLCT/XLCT excited state of [Re(HPEAB)(CO)$_3$Cl] following either ν[a′(1)] (C) or ν(C=O) (D) excitation with a 1.5 ps, 15 cm^{-1} infrared pump pulse. For C, the kinetic traces are calculated through subtraction of the ν$_{0-1}$ peak intensity from the ν$_{1-2}$ peak intensity at each time delay.*

Excitation of the amide group in the ^{3}MLCT state results in the formation of a weak, short-lived bleach at 1623 cm^{-1}, overlapped with a very broad transient centred at higher frequency (Figure 4.11B). Accurate determination of Δ_{ii} was not possible due to the poor spectral definition of the transient absorption band. The origin of this broadening effect is currently unknown. The decay time constant for the amide bleach was similar to the electronic ground state (2 ps). Whilst this indicates the anionic charge in the bipyridyl π* orbital did not significantly promote VET from the amide group to the solvent, the convolution of this decay with the IRF makes accurate comparisons difficult. It was not possible to observe the low intensity peak pairs of the aromatic ring modes due to their low intensity, as well as their overlap with the broad ν_{1-2}(C=O) transient absorption band. In the 1750 – 2150 cm^{-1} region of the 2DIR spectrum, no off-diagonal signals were observed following amide excitation. This suggests that vibrational coupling between the amide C=O and C≡O ligands is weaker in the excited state, such that if any off-diagonal signals are formed they are not distinguishable from the spectral noise.

Part II. The influence of azide group addition on the electronic and vibrational dynamics of a red-light harvesting Re(I) bis(mesitylimino)acenapthene complex.

Electronic and vibrational absorption spectra

The UV-vis absorption spectra of **2** and **3** were recorded in dichloromethane (Figure 4.12A). Both complexes have broad visible light absorption up to 625 nm. This enhanced visible light harvesting capability compared to bipyridyl catalysts is a result of the extended π-system within the mesBIAN ligand. The addition of an azide group to the acenaphthene ring results in broadening of the metal-to-ligand charge transfer (MLCT)/halide-to-ligand charge transfer (XLCT) absorption envelope compared to the unfunctionalised mesBIAN ligand. Calculation of the electronic transitions for both complexes suggests this broadening was due to the introduction of additional electronic transitions involving the azide group, which can act as an electron acceptor.

DFT calculations were used to visualise the charge density differences upon electronic excitation from the ground state to a singlet excited state. For **2**, S_1 – S_3 were all characterised as ^{1}MLCT/XLCT transitions and are associated with the broad absorption band observed at 500 nm. In these transitions, electron density is donated from the Re d-orbitals and Cl p-orbitals to the diimine (mes-N=C(R)-C(R)=N-mes) moiety. The calculated oscillator strength of the $S_0 \rightarrow S_1$ transition was negligible. S_4 was assigned as an ILCT transition, corresponding to the donation of electron density from the mesityl rings to the naphthene group. The next two transitions, forming S_9 and S_{10}, were assigned as MLCT and correspond to electron density transfer from the Re d-orbitals to the naphthene ring. Electronic transitions at higher energy were not characterised. In **3**, the electronic transitions were similar, however differences were found. S_1 and S_2 again correspond to MLCT/XLCT transitions, but S_3 was now a mixed MLCT/ILCT state. $S_0 \rightarrow S_4$ was an ILCT transition, similar to **2**. The S_{10} and S_{11} states, were characterised as MLCT character, where the azide group also acts as an electron acceptor, in addition to the naphthene ring. Electronic transitions at higher energies were not characterised. Typically, highly excited states, such as S_3 – S_{11} are not characterised, but for **2** and **3** this was necessary due to the choice of excitation wavelength for TRIR and ES-2DIR experiments, where the 400 nm pump was resonant with the $S_0 \rightarrow S_{10}$ electronic transition in both complexes.

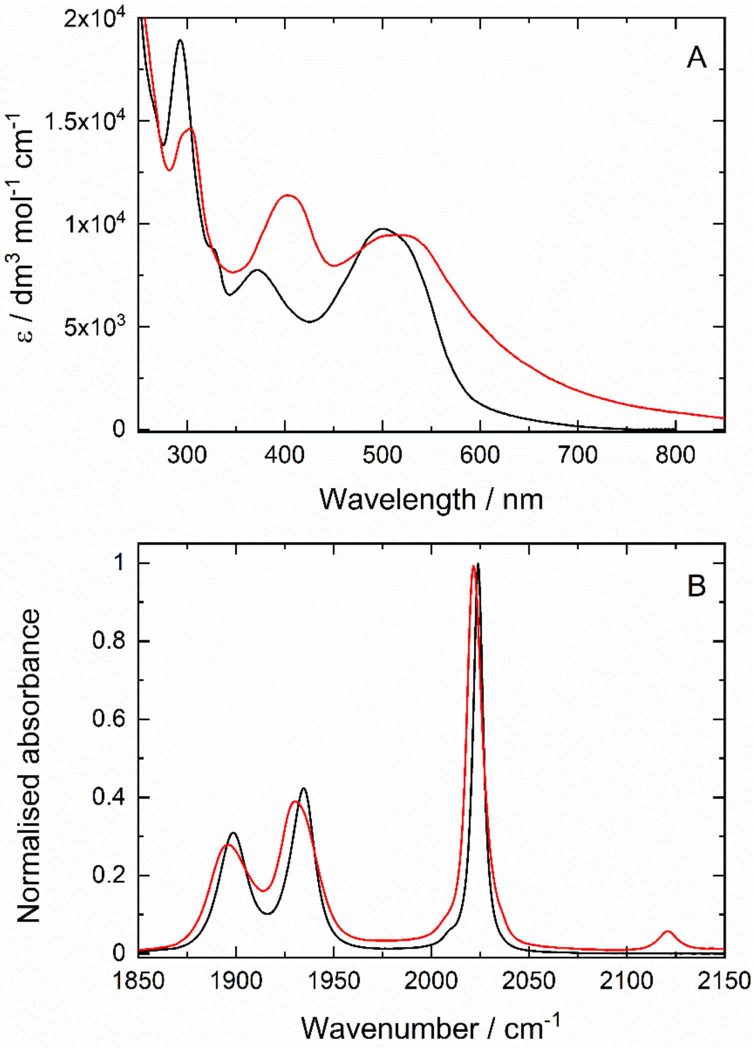

Figure 4.12 – Absorption spectra of ***2*** *(black) and* ***3*** *(red) in the UV-vis (A) and mid-IR (B) spectral regions in DCM solution. The UV-vis spectra are plotted as the molar extinction coefficient versus wavelength, the FTIR spectra are plotted as normalised absorbance versus wavenumber.*

The IR spectra of **2** and **3** are similar to [Re(bpy)$(CO)_3$Cl], where three distinct ν(C≡O) absorption bands were observed in the 1850 – 2100 cm^{-1} region of the spectrum (Figure 4.12B). These bands correspond to excitation of the a′(2), a″, and a′(1) vibrational modes, which are assigned as asymmetric stretching of the three CO ligands, asymmetric stretching of the equatorial CO ligands, and symmetric stretching of the three CO ligands, respectively. The symmetry point group of the mesBIAN complexes is C_s. The vibrational absorption bands in the azide-functionalised complex were broadened and shifted to lower frequency by 2 – 4 cm^{-1} compared to **1**. These subtle changes were due to a small increase in the electron density within the mesBIAN π-system through electron resonance with the azide group. This in turn increases the electron density on the Re(I) centre, causing a red-shift in ν(CO) frequency. The asymmetric stretching vibration of the azide group in **2** was found at 2121 cm^{-1}. In both complexes weak absorption bands corresponding to the aromatic overtone vibrations of the mesBIAN ligand are observed in the 1480 – 1900 cm^{-1} region. As is typical for [Re(L$_2$)(CO)$_3$Cl] complexes, a weak shoulder was found on the a′(1) absorption band, ascribed to an anharmonic combination mode.

Excited state dynamics of [Re(mesBIAN)(CO)$_3$Cl] and [Re(4-azido-mesBIAN)(CO)$_3$Cl]

The ultrafast excited state dynamics of **2** and **3** were studied with TRIR spectroscopy following 400 nm excitation (Figure 4.13). This pump wavelength is resonant with the pure MLCT absorption band in both complexes. The excited electronic transition was not the lowest energy absorption band in either complex. Therefore, the first step in electronic excited state relaxation was likely rapid internal conversion to the lowest energy singlet state accessible to the optically prepared state. The time resolution of the TRIR data presented here was not sufficiently high to observe this process, hence the singlet states will be treated as a single ‘manifold’ of excited states in this analysis. After initial relaxation of the optically prepared singlet states by IC, the complex will undergo ISC to form a triplet state. The ISC process also could not be resolved within the TRIR data.

The vibrational transient absorption bands observed immediately after 400 nm excitation of **1** in the 1850 – 2120 cm^{-1} region are assigned to the high-frequency carbonyl vibrations of a triplet excited state. The transients were shifted to higher frequency relative to the ground state bleaches. This is consistent with the proposed MLCT character of the excited state and occurs due to the formal oxidation of the Re centre in the MLCT state. The decrease in electron density on the Re centre decreases d(Re) → π*(CO) back-bonding strength, resulting in an increase in ν(CO) vibrational frequency. When comparing the profile of the TRIR spectrum to previously reported catalysts, it was clear that additional dynamics were occurring following excitation of **1**. For example, from 1 – 10 ps the a′(1) and a″ bleaches increase in intensity, commensurate with a rise in transient absorption intensity at 1980 and 2050 cm^{-1}. Note that the intensity of the a′(2) bleach did not change during this period. These observations show that additional transient absorption bands are present which are overlapped with the a′(1) and a″ bleaches, where the observed intensity increase of the bleaches was a result of the decay of the overlapped transient absorption bands. It could be argued that these dynamics only correspond to vibrational cooling, similar to what was observed following 400 nm excitation of **1**. However, both the initial transients and those which grow in on the 10 ps timescale persist on the nanosecond timescale. This is not possible for the vibrationally excited state, as confirmed by ES-2DIR experiments, where an approximate vibrational lifetime of 28 ps was found. Therefore, these dynamics indicate that two triplet excited states are present following 400 nm excitation, and that these states can interconvert on the 1 – 10 ps timescale. As complete conversion from one triplet to the second was not observed, it is tentatively proposed that the two triplets are in equilibrium with one another whilst they are vibrationally excited. The observed shift in the transient absorption frequency is thus a result of both vibrational cooling of the triplet states, and internal conversion between the two states.

To identify the triplet states present after 400 nm excitation, DFT was used to optimise the geometry of the T_1 state, characterised as ^{3}MLCT/XLCT. The resulting harmonic IR spectrum of T_1 was found to correspond to the initial transient absorption bands which are overlapped with the ground state bleaches. Therefore, the remaining transient absorption bands which grow in with the IC process are ascribed to a higher energy triplet state. Thus, the observed dynamics correspond to internal conversion from T_1 to this second triplet state. This is most likely the T_2 state, which is higher in energy by 979 cm^{-1}. If the T_1 state were vibrationally excited such that the ν(CO) modes are populated, it is feasible that the $T_1 \rightarrow T_2$ transition is energetically favourable. The T_3 state is 2870 cm^{-1} higher in energy than T_1, hence the $T_1 \rightarrow T_3$ transition was not possible. The populated T_2 state does not spontaneously convert back to T_1 on the ps – ns timescale, which supports the notion that the two states are only able to equilibrate whilst vibrationally excited.

After 10 ps, the observed bleach intensity increase stops, as does the growth of the transient signal at 1980 and 2050 cm^{-1}, hence the internal conversion pathway between states is no longer accessible. This is on the same timescale as vibrational cooling in $[Re(L_2)(CO)_3Cl]$ complexes, thus, it is proposed that the IC pathway from ^{3}MLCT/XLCT to T_2 is only open whilst the states are vibrationally hot. During this time, the 979 cm^{-1} energy barrier for internal conversion is overcome, allowing for equilibration of the two triplet states. Once the complex has vibrationally cooled, the equilibration process halts, and the two triplet states independently decay to the ground state. Vibrational cooling is typically associated with a shift in the transient absorption bands to higher frequencies, however this was not distinguishable from the blue-shift associated with IC in the TRIR data of **2**. Hence a time constant for vibrational cooling could not be provided.

As discussed in part I, the magnitude of the shift in carbonyl stretching frequency upon formation of a CT state is a measure of the degree of charge separation between the Re centre and the diimine acceptor. In **2**, the ν(CO) shift in the T_1 state, obtained from the decay associated spectra, was 4 cm^{-1}. This suggests that the degree of charge separation is small, and the electron involved in the charge transfer is still largely localised around the Re-Cl moiety. In the T_2 state, the magnitude of the ν(CO) shift is significantly greater, 24 cm^{-1}, suggesting the charge separation degree is larger. However, this shift is significantly less than bipyridyl Re complexes ($[Re(bpy)(CO)_3Cl]$ $\Delta\nu = 55$ cm^{-1}) in the lowest energy ^{3}MLCT/XLCT state.

After 10 ps, no further excited state dynamics are observed with the exception of ground state recovery on the nanosecond timescale. It was found that the relative intensities of the transient absorption bands slowly change with increasing delay time. The bands of the ^{1}MLCT/XLCT state (T_1) appear to decay more slowly than T_2, resulting in an apparent decrease in the T_1/T_2 ratio. This further supports the argument that the triplet states cannot equilibrate once vibrational cooling is complete. From 50 ps onward, the intensity ratio of the ground state bleaches closely matched that of the FTIR spectrum, hence the intensity of the T_1 absorption bands overlapped with the bleaches was small, and T_2 is the major contributor to the transient spectrum at late time delays, as further evidenced by preliminary analysis of the ES-2DIR data (see below).

The change in the relative intensity of the T_1 and T_2 absorption bands was quantified by the ratio of peak areas, obtained through spectral deconvolution of the TRIR dataset (Figure 4.14). It was found that the peak area ratio (2037 cm^{-1} / 2046 cm^{-1}) increased from 200 – 3000 ps, showing that the 2037 cm^{-1} band has a slower decay time constant than the band at 2046 cm^{-1}. The effect of this ratio change is most prominent at time delays greater than 1 ns. As the maximum possible time delay was 3 ns, it was not possible to fully sample the triplet state decay process. As such, the rates of ground state recovery for the two triplet states could not be distinguished from one another. This problem was exacerbated by the limited number of data points between 500 ps and 3 ns, as evidenced through single-point fitting of the kinetic trace of the a′(2) bleach at 1897 cm^{-1}. If TRIR spectra were recorded on longer timescales (1 – 20 ns), a biexponential ground state recovery time constant would be expected if this model of the excited state dynamics is accurate.

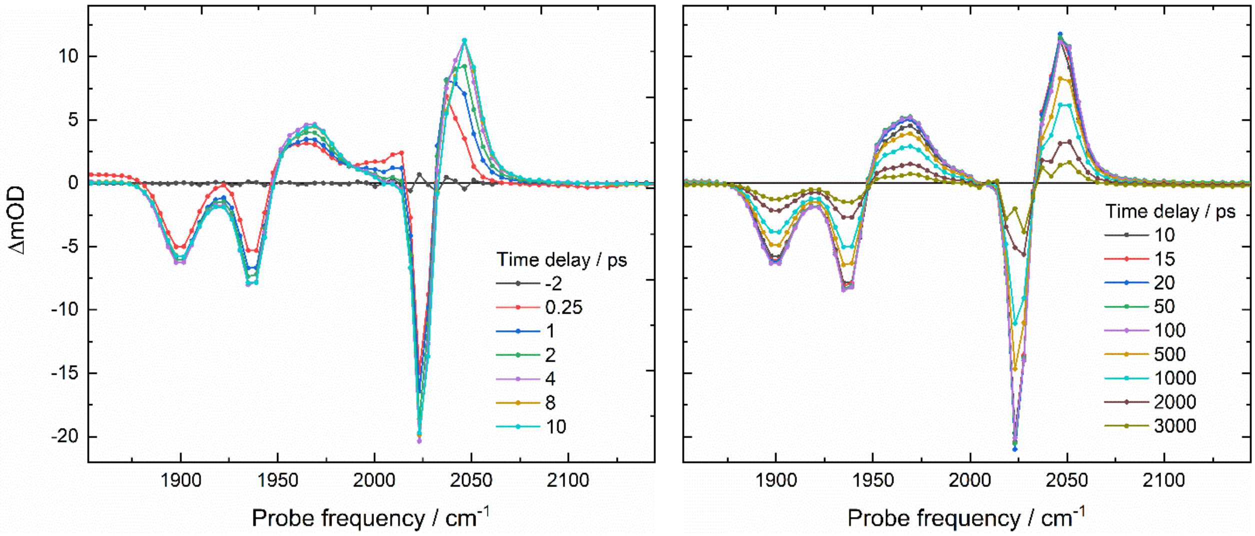

*Figure 4.13 – TRIR spectra of **2** following 400 nm, 40 fs excitation in the 1850 – 2150 cm^{-1} region of the IR spectrum. The pump – probe delays are shown in the graph legends. To enable comparison, the y-axis scale is identical in both plots.*

To further analyse the excited state dynamics, the TRIR spectrum at a time delay of 500 ps was deconvoluted with pseudo-Voigt profiles (Appendix B, Eq. B1), where ten fit peaks were required to adequately model the spectrum (Figure 4.14). Four of the bands model the ground state bleaches and were obtained from the FTIR spectrum. The remaining six bands were ascribed to the transient absorption bands. Note that these fit peaks do not necessarily represent the true FWHM and intensity of the transient absorption bands, especially for those which are largely overlapped with a negative bleach. Instead, they model the positive intensity which remains following calculation of the ΔA (Pump on – pump off) spectrum. A selection of TRIR spectra from 5 – 3000 ps were deconvoluted with the fitting model. The change in the peak area with increasing delay time was then analysed to provide an estimate of the excited state relaxation lifetime of each state. The four bleaches (p1 – p4) behave synchronously, with a recovery on the nanosecond timescale with time constants of 2.1 ± 0.39 ns. The three most prominent transient absorption bands are assigned to the a″ (p7), a′(2) (p5) and a′(1) (p6) modes of the T_2 state. These grow in on the 20 ps timescale and relax on the nanosecond timescale with a model time constant of 1.9 ± 0.31 ns. The residual positive intensity following cancellation of the transient absorption band overlapped with the a′(1) bleach (p10) decayed biexponentially, with time constants of 17 ± 0.0062 ps and 1.5 ± 0.27 ns. However, the uncertainty in these time constants is large, due to the overlap of the fit peaks. This was assigned as the a′(1) mode of the ^{3}MLCT/XLCT (T_1) state. The other bands which are attributed to this state are overlapped with the a″ bleach and could not be deconvoluted. Peaks 8 and 9 were low intensity bands with a large FWHM, which were used to account for the broad absorption tails on the high-frequency side of the MLCT absorption envelopes. It is likely these do not correspond to a third triplet excited state that is formed following 400 nm excitation.

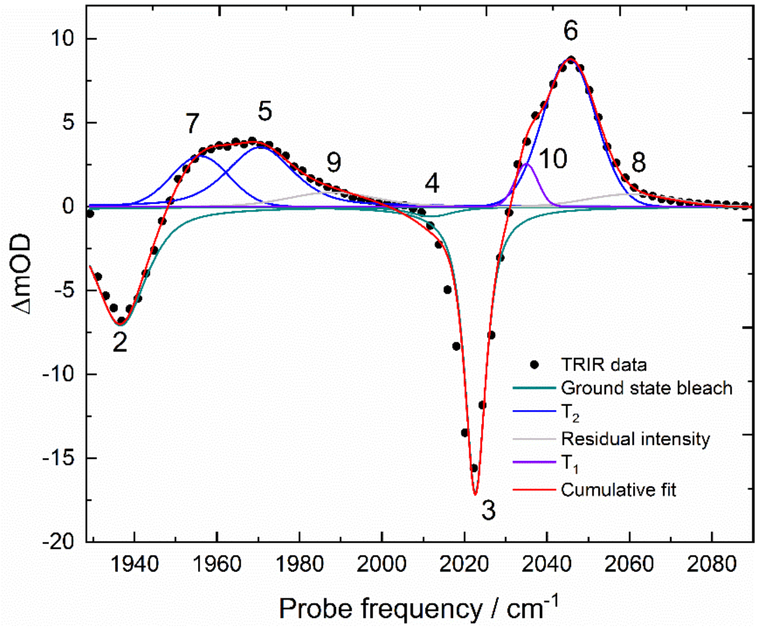

Figure 4.14 – TRIR spectrum of ***2*** *at a UV$_{pump}$ – IR$_{probe}$ time delay of 500 ps (dots), deconvoluted with 10 pseudo-Voigt profiles. The fit peaks are grouped based on their assignment, as shown on the graph legend.*

The excited state relaxation mechanism following 400 nm excitation of **2** was further studied with global lifetime analysis, where three kinetic components in a sequential model were required to adequately fit the experimental data. The first component, with a time constant of 100 fs, was assigned to ultrafast processes that were convolved with the instrument response function (IRF), such as relaxation within the manifold of singlet states and intersystem crossing. The second time constant, 1.44 ps, was associated with the bleach deepening process, and internal conversion of the vibrationally hot T_1 state to T_2, as well as vibrational cooling of both triplet states. The decay associated spectrum of this component showed a synchronous decay of the T_1 transient absorption bands with grow in of the T_2. It was not possible to deconvolute the IC and vibrational cooling processes, as both occur simultaneously and result in a blue-shift of the transient absorption bands. It was not possible to model a kinetic component for vibrational cooling, if constraints were used to introduce a component with a time constant between 10 – 50 ps, the resulting DAS and EAS were very similar to the final ground state recovery component. The final time constant, 1.7 ns, was associated with decay of the triplet excited states to the ground state. It is probable that the vibrational cooling of **1** occurs simultaneously with IC between T_1 and T_2.

Lifetime density analysis confirmed the GLA model was accurate, no other significant time constants were found that could account for additional spectral evolution not accounted for by a three-component sequential model.

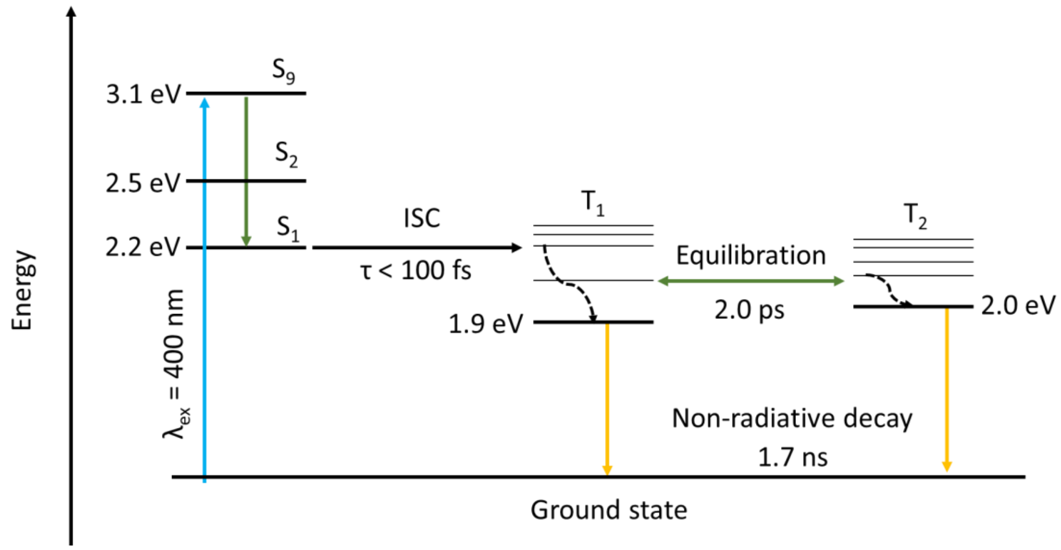

*Figure 4.15 – Proposed Jablonski energy level diagram for the excited state relaxation mechanism of **2** following 400 nm, 40 fs excitation. For clarity, vibrational relaxation of the optically prepared Frank-Condon singlet state(s) is not shown.*

The substitution of the proton in the 4-position of the mesBIAN ligand for an azide group has a significant effect on the profile of the TRIR spectra following 400 nm excitation (Figure 4.16). The most prominent absorption bands were found from 1945 – 2020 cm^{-1}, between the a″ and a′(1) ground state absorption bands. Unusually, no transient absorption bands associated with the carbonyl vibrations was detected at higher frequencies than the a′(1) bleach.

As with **2**, the limited time resolution of the TRIR measurement prevented observation of relaxation within the singlet manifold or intersystem crossing to the triplet manifold. As a result, the initial transient absorption bands are ascribed to triplet states. The a′(1) transient absorption band is not shifted to higher frequencies than the a′(1) bleach, unlike other reported [Re(L$_2$)(CO)$_3$Cl] complexes. Instead, the transient spectrum is similar to what was observed at early time delays in **1**, where the magnitude of Δν(CO) is small. Therefore, the electron involved in the MLCT/XLCT charge transfer is likely primarily localised around the {Re(CO)$_3$Cl} moiety in the initial triplet state, and the degree of Re → mesBIAN charge separation is small.

The harmonic IR spectrum of T$_1$, provided by DFT calculations only had partial agreement with the experimental TRIR spectrum, and could not account for all of the transient absorption bands present following 400 nm excitation, suggesting a second excited state is also formed, similar to **2**. The T$_1$ state is characterised as an ^{3}MLCT/XLCT state, similar to **2**. The higher energy triplet states was not characterised computationally, and may correspond to either ^{3}MLCT/XLCT, ^{3}ILCT, or ^{3}MLCT. The spectral profile indicates that the degree of charge Re → diimine separation of this second triplet state is less than or equal to that of T$_1$, therefore the character of the two states is likely similar.

The transient absorption band associated with the azide asymmetric stretching vibration was shifted to lower frequencies relative to the ground state band. The red-shift of $\nu_{as}(N_3)$ indicates the conjugated π*-orbitals of the acenaphthene-azide moiety have been populated following excitation, which results in a decrease in N=N=N bond strength and vibrational frequency. Therefore, this group has been formally reduced following 400 nm excitation, consistent with assignment of T_1 and T_2 as ^{3}MLCT/XLCT. The positive peak appears to be made up of two contributing transient absorption bands. However, the spectral resolution was not sufficient to accurately deconvolute the transient absorption envelope. Similar to the ν(CO) modes, the shift between the transient and bleach centres of the $\nu_{as}(N_3)$ mode is a measure of the degree of charge separation in the complex. Initially the transient absorption centre of the $\nu_{as}(N_3)$ mode was shifted 16 cm^{-1} to lower frequency compared to the bleach. During the first 30 ps after excitation, the magnitude of this shift decreased to 11 cm^{-1}, which may be attributed to vibrational cooling. This assignment is supported by the long lifetime of the $\nu_{as}(N_3)$ vibrational excited state, as determined by ground state 2DIR spectroscopy. Determining the magnitude of Δν(CO) was not possible in **3**, as it was not possible to adequately deconvolute the transient spectra of T_1 and T_2 by pseudo-Voigt fitting, GLA, or LDA.

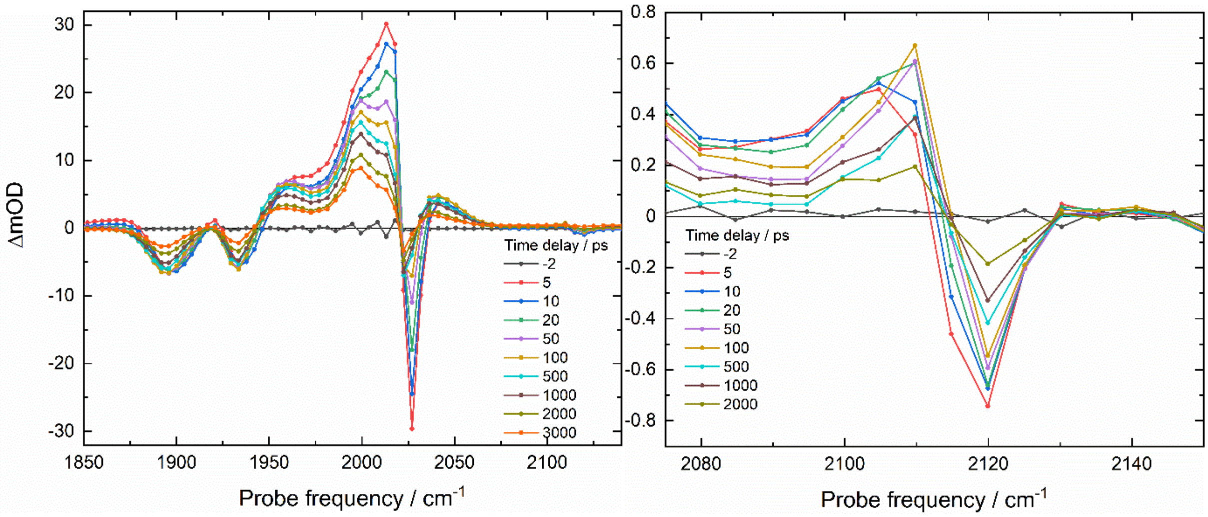

*Figure 4.16 – TRIR spectra of **3** following 400 nm, 40 fs excitation in the 1850 – 2150 cm^{-1} region of the IR spectrum. The pump – probe delays are shown in the graph legends.*

Unlike **1**, no increases in the intensity of the ground state bleaches were found during the first 10 ps after excitation, hence the transient absorption bands which are overlapped with the bleaches were not decaying without bleach recovery also taking place. The convoluted transient absorption envelope changes in shape during the 1 – 10 ps time period, which is tentatively ascribed to vibrational cooling of the two triplet states. The pronounced synchronous decay and formation of bands observed in **2** was not observed here. Whilst this suggests that a one-way IC process does not occur in **3**, it is possible the IC process between triplets does not result in a significant change in the convoluted transient absorption envelope. Therefore, it cannot be definitively stated if IC between T_1

and T_2 occurs from the TRIR data alone. From the TD-DFT calculations, the T_1 – T_2 energy separation in **3** was 1405 cm^{-1}, and the T_2 – T_3 separation was 2942 cm^{-1}. These were larger than the analogous values from **2** by 426 and 71 cm^{-1}, respectively. These values suggest that $T_1 \rightarrow T_2$ internal conversion is possible in the vibrationally excited T_1 state of **3**. However, further experiments are required to understand the nature of the excited states present after 400 nm excitation before any definite conclusions can be made on the assignments and dynamics of these triplet species.

From 10 – 3000 ps, the ratio of the transient absorption bands at 1999 and 2013 cm^{-1} changes, similar to what was observed in **2**. This suggests that the two triplet states formed following 400 nm excitation have different relaxation time constants, which results in a change in the peak area ratio over time. However, it was not possible to obtain individual decay time constants for each triplet state due to the limited number of data points from 1 – 3 ns and incomplete collection of the triplet decay kinetic trace.

GLA was used to model the excited state dynamics of **3** following 400 nm excitation. A three-component sequential model was required to adequately model the experimental data, and addition of a fourth component did not improve the fitting model. These components with time constants of 100 fs, 19 ps, and 2.9 ns, were ascribed to ultrafast IRF convoluted processes, vibrational cooling of the triplet excited states, and ground state recovery, respectively. LDA of the time-resolved data suggested the GLA model was adequate, and no additional kinetic components were required. The dynamics of the manifold of singlet states could not be determined from the TRIR data, hence it is assumed that the excited complex rapidly internally converts to the lowest energy single state accessible following 400 nm excitation.

The key difference between the excited state dynamics of **2** and **3** was the degree of charge separation within the triplet states formed following 400 nm excitation. The smaller magnitude of $\Delta\nu(CO)$ in **3** suggests that the electron density is more strongly localised around the Re-Cl moiety as a result of introducing the azide group to the mesBIAN ligand. This was likely a result of the electron density donation from the azide group to the conjugated π-system of the acenaphthene ring by resonance, which slightly decreases the electron accepting ability of the diimine ligand. Considering this, introduction of an electron withdrawing substituent, such as an ester group, is expected to increase the degree of Re → diimine charge separation. This complex, [Re(4-mesBIAN-CO_2Et)$(CO)_3$Cl] will be the focus of future research. A second difference in the excited state dynamics is the observed internal conversion between triplet states in **2**, which could not be confirmed for **3**. As a result, it was possible to obtain an estimated time constant for vibrational cooling in **3**, which was not resolvable from IC in **2**.

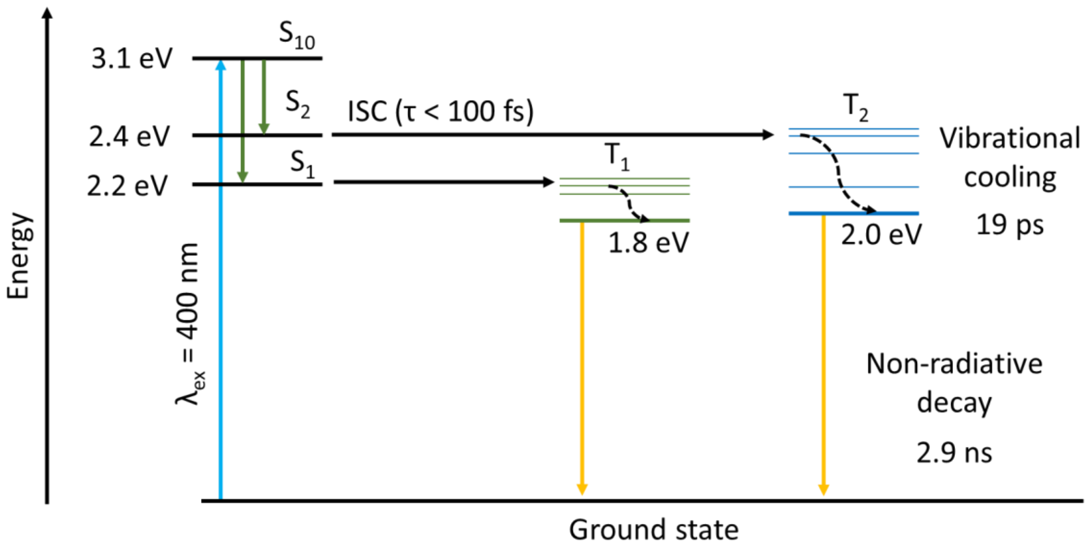

Figure 4.17 – Proposed Jablonski energy level diagram for the excited state relaxation mechanism of ***3*** *following 400 nm, 40 fs excitation. For clarity, vibrational relaxation of the optically prepared Frank-Condon singlet state(s) is not shown.*

Vibrational dynamics in the electronic ground state

The vibrational dynamics of **2** were probed following excitation with a narrowband (FWHM = 15 cm^{-1}) IR pump pulse centred at 2025, 1940, 1890, and 1605 cm^{-1} (Figure 4.18). This allowed for the vibrational energy redistribution mechanism within the complex to be determined. Excitation of the a′(1) vibration in the electronic ground state resulted in formation of three peak pairs corresponding to the ν(CO) vibrational modes. As is typical for $[Re(L_2)(CO)_3Cl]$ complexes, vibrational energy redistribution between the carbonyl vibrations was rapid due to the strong mechanical coupling of the modes. The transient absorption envelope corresponding to the $\nu_{1\text{-}2}$[a′(1)] mode was split into two bands, which likely occurs due to overlap of the self-responses of the a′(1) mode and the anharmonic combination mode. The a′(1) peak pair relaxes biexponentially, with an initial 1.7 ± 0.085 ps time constant. This is ascribed to vibrational equilibration between the three ν(CO) group vibrations. The equilibration time constant is convoluted with the IRF, hence the evolution of the off-diagonal a′(2) and a″ peak pairs during equilibration could not be resolved. As a result, all peak pairs in the 1840 – 2050 cm^{-1} region reach their maximum intensity 1.7 ps after excitation. After equilibration was complete, the anharmonic shift for the a′(2), a″, and a′(1) modes was 20, 17, and 14 cm^{-1} respectively, similar to previously reported $[Re(L_2)(CO)_3Cl]$ complexes. The average vibrational relaxation lifetime for these peak pairs was 34 ± 0.74 ps, which corresponds to vibrational energy transfer from the complex to the continuum of low-frequency solvent modes. A time constant for IVR to low-frequency modes of the $\{Re(CO)_3Cl\}$ moiety was not distinguishable from the VET relaxation. The fast equilibration between the ν(CO) group vibrations was further evidenced through excitation of the a′(2) and a″ vibrational modes, which resulted in very similar dynamics to a′(1) excitation. The only significant difference upon excitation of each ν(CO) mode was the relative intensity of the three peak pairs, where the excited mode more intense at early delay times. However, after vibrational energy equilibration between modes is completed, the relative intensity of the a′(2), a″, and a′(1) modes was the same for each ν(CO) excitation frequency.

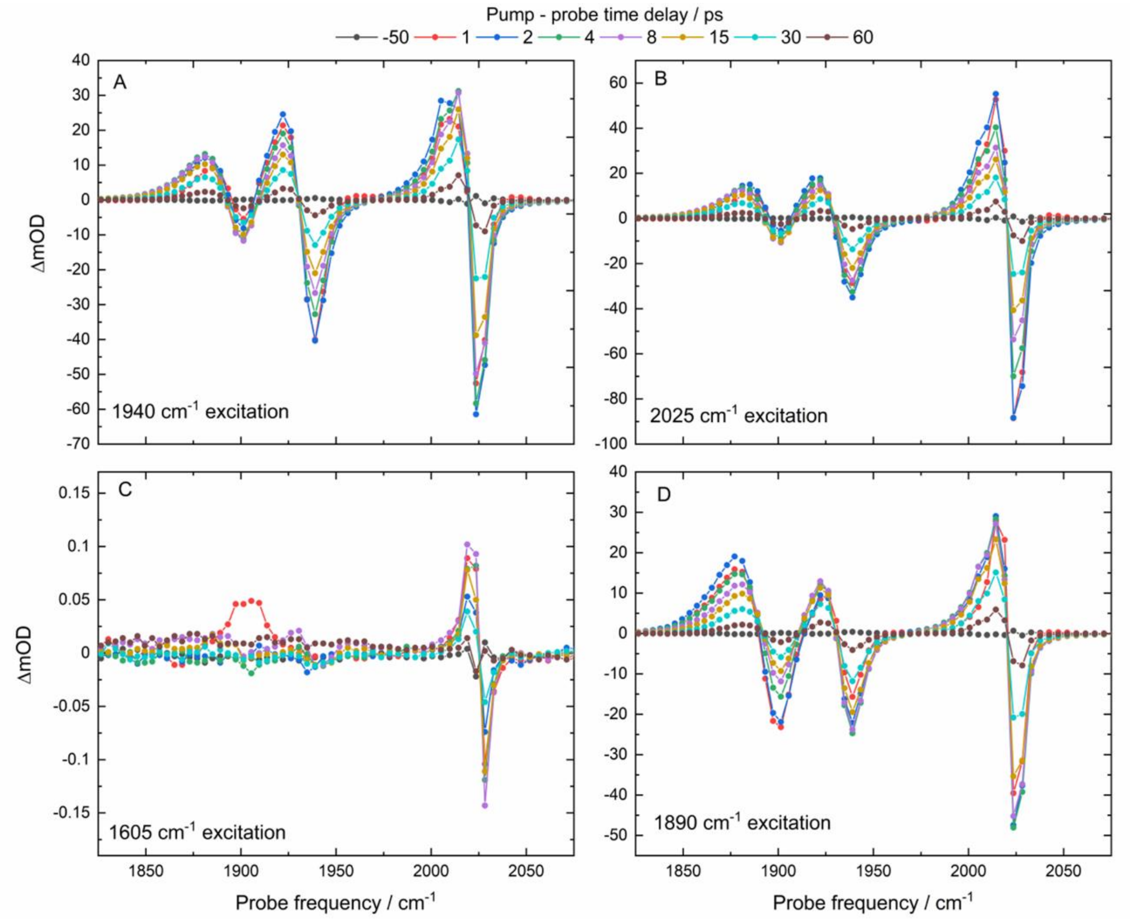

*Figure 4.18 – Frequency domain 2DIR spectra of **2** following excitation with a narrowband IR pulse centred at 1605, 1890, 1940, or 2025 cm^{-1}, as stated on the graph. The pump – probe delay times for all spectra are shown at the top.*

Excitation of the aromatic stretching vibrations of the mesBIAN ligand at 1605 cm^{-1} was found to result in the formation of very weak off-diagonal peak pairs corresponding to the ν(CO) modes. The a′(1) peak pair was the only one of the three which was completely distinguishable from the spectral noise, and was found to grow in with an 8.5 ± 1.7 ps time constant. The a″ and a′(2) off-diagonal peak pairs were only observed at short delay times, with very low signal intensities. The weak off-diagonal signal intensity and slow rate of grow in indicated that the vibrational coupling between the carbonyl modes and the aromatic modes was weak, which was further evidenced by the small off-diagonal anharmonic shift (Figure 4.19). This is a result of the large spatial (through-bond) separation between the acenaphthene and mesityl rings and the CO ligands, as well as the presence of the heavy metal Re centre, which acts as a vibrational energy transfer bottleneck. This coupling was likely mediated through low-frequency modes of the complex following vibrational relaxation of the ν = 1 level of the excited aromatic modes. The off-diagonal peak pair for the aromatic vibrations following ν(CO) excitation was not studied.

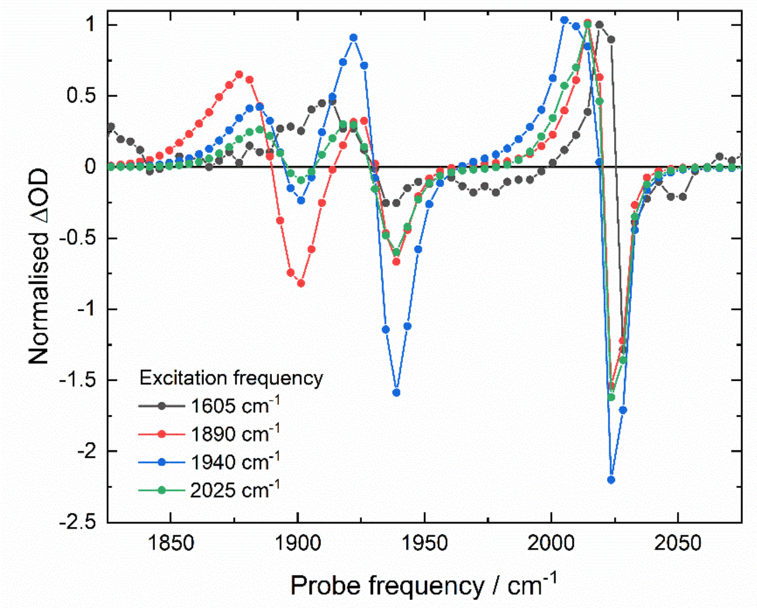

Figure 4.19 – Normalised 2DIR spectra recorded at a time delay of 1.5 ps following narrowband IR excitation, as stated in the figure legend.

In **3**, the introduction of an azide group to the acenaphthene ring does not significantly alter the vibrational coupling interactions between the ν(CO) modes. For example, excitation of the a′(1) mode results in ultrafast grow in of off-diagonal peak pairs corresponding to the a′(2) and a″ vibrations due to the strong mechanical coupling interactions between the carbonyl modes. The relaxation of the a″ and a′(1) modes was biexponential, whilst the a′(2) mode decays monoexponentially (Figure 4.20). The initial time constant for the a″ and a′(1) modes was 2.1 ± 0.31 ps, which corresponds to the equilibration between carbonyl modes. The time constant for VET from the {$Re(CO)_3Cl$} moiety to the continuum of solvent modes takes place with an average time constant of 34 ± 1.0 ps. The off-diagonal peak pair of the azide group following ν(CO) excitation was found to grow in slowly. This shows that ν(CO) → $\nu_{as}(N_3)$ coupling was weak, similar to the aromatic vibrations of **2**. The $\nu_{as}(N_3)$ peak pair reached its maximum intensity 13 ps after excitation of the a′(1) mode, and 17 ps after excitation of the a″ mode (Figure 4.20). These differences in observed off-diagonal signal formation rate can be rationalised in terms of the frequency separation between modes, where a larger difference in ν_{0-1} transition energy between the diagonal mode and the off-diagonal mode decreases the vibrational energy transfer rate.[62] The relaxation of the off-diagonal $\nu_{as}(N_3)$ peak pair was found to be slow, with a lifetime in excess of 50 ps. A more accurate time constant could not be determined due to the very low signal intensity of the off-diagonal mode, as well as the limited spectral resolution of the 2DIR data.

Vibrational energy transfer from $\nu_{as}(N_3)$ to the a′(2), a″, and a′(1) modes was probed following 2126 cm^{-1} excitation of **3**. Following excitation, a strong diagonal peak pair was observed for the $\nu_{as}(N_3)$ mode, the anharmonic shift of which was 26 cm^{-1}. The relaxation of this diagonal mode was biexponential, with time constants of 1.3 ± 0.04 and 35 ± 5.8 ps. Off-diagonal signals corresponding to the carbonyl modes were found to form within 2 ps, suggesting that $N_3 \rightarrow CO$ coupling is strong despite the large spatial separation of the modes. Notably, this was significantly faster than the observed rate of acenaphthene → CO vibrational energy transfer observed in **2** (Figure 4.20). This suggests than an additional vibrational redistribution mechanism is present in **3**, as well as IVR through low-frequency modes. As the $\nu_{as}(N_3)$ mode is found at higher frequency than the ν(CO) modes, it is possible that a spontaneous population transfer from $\nu_{as}(N_3) \rightarrow \nu(CO)$ takes place. In this mechanism, the excess energy released by the exothermic population transfer is absorbed by the DCM solvent. This process results in formation of the $\nu = 1$ excited states of the carbonyl vibrations, hence it is expected the anharmonic shifts and vibrational lifetimes would be similar to direct excitation of the a′(2), a″, and a′(1) modes. This was the case, where off-diagonal shifts of 14, 17, and 24 cm^{-1} were observed, with an average vibrational relaxation time constant of 33 ± 6.2 ps.

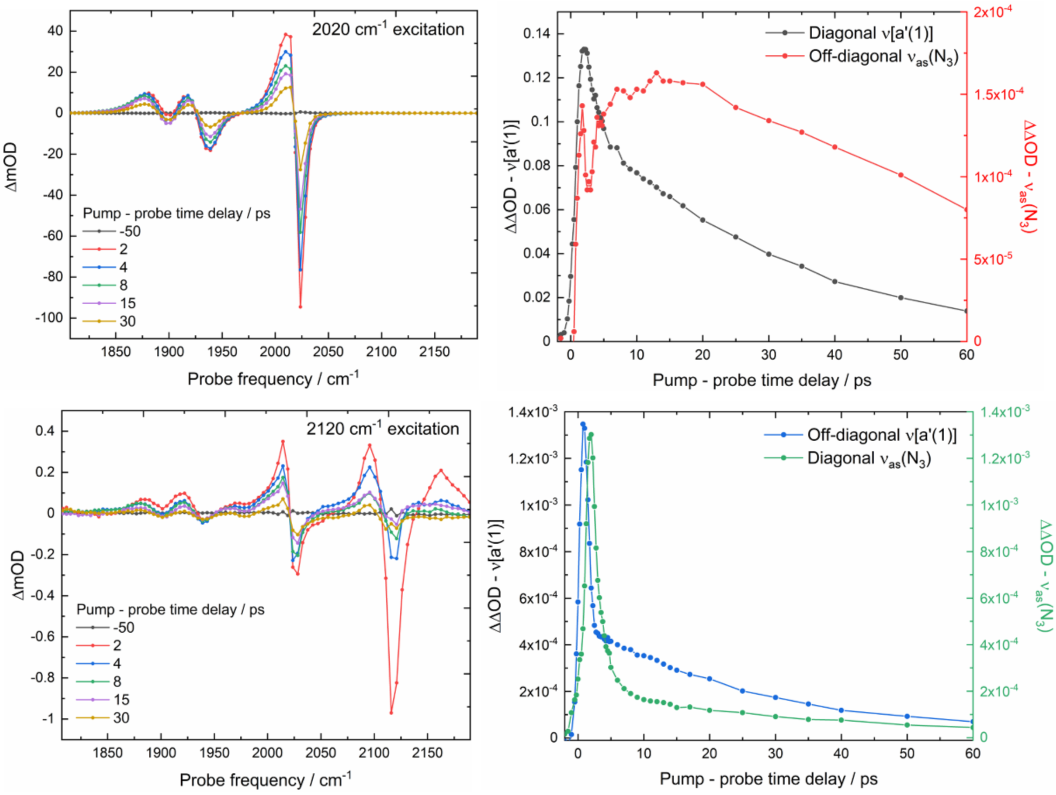

*Figure 4.20 – Kinetic traces for the diagonal and off-diagonal ν[a′(1)] and $\nu_{as}(N_3)$ peak pairs and corresponding ground state 2DIR spectra following excitation of **3** with a narrowband pulse centred at either 2026 (a′(1) diagonal) or 2126 cm^{-1} (N_3 diagonal), demonstrating the difference in vibrational energy transfer rate depending on which mode is excited. 2DIR spectra focussing on the low intensity $\nu_{as}(N_3)$ off-diagonal peak pair are available in Appendix D, fig. D16.*

Vibrational dynamics following 400 nm excitation

To provide further insight into the dynamics of the triplet states present after 400 nm, excited state 2DIR spectra of **2** and **3** were recorded. In these experiments, the $UV_{pump} – IR_{pump}$ delay was fixed to 500 ps, and then the $IR_{pump} – IR_{probe}$ delay was scanned. This allowed for study of the vibrational dynamics of the thermally equilibrated triplet states. In **2**, at an $IR_{pump} – IR_{probe}$ delay of 2 ps, two prominent peak pairs were observed, as well as other weaker absorbance bands, following excitation at 2050 cm^{-1} (Figure 4.21A,B). This narrow-band IR pump pulse was resonant with the a′(1) modes of both the T_1 and T_2 states. The two strongest peak pairs, which had transient absorption frequencies of 1940 and 2030 cm^{-1} were ascribed to the T_2 state on the basis of the spectral assignment of the TRIR data. The other three observable peak pairs had a significantly lower intensity and were tentatively associated with the T_1 state (Figure 4.21). However, accurate assignment of these peak pairs is difficult due to the significant overlap of the absorption bands. These observations were consistent with assignment of T_2 as the major product of 400 nm excitation at 500 ps.

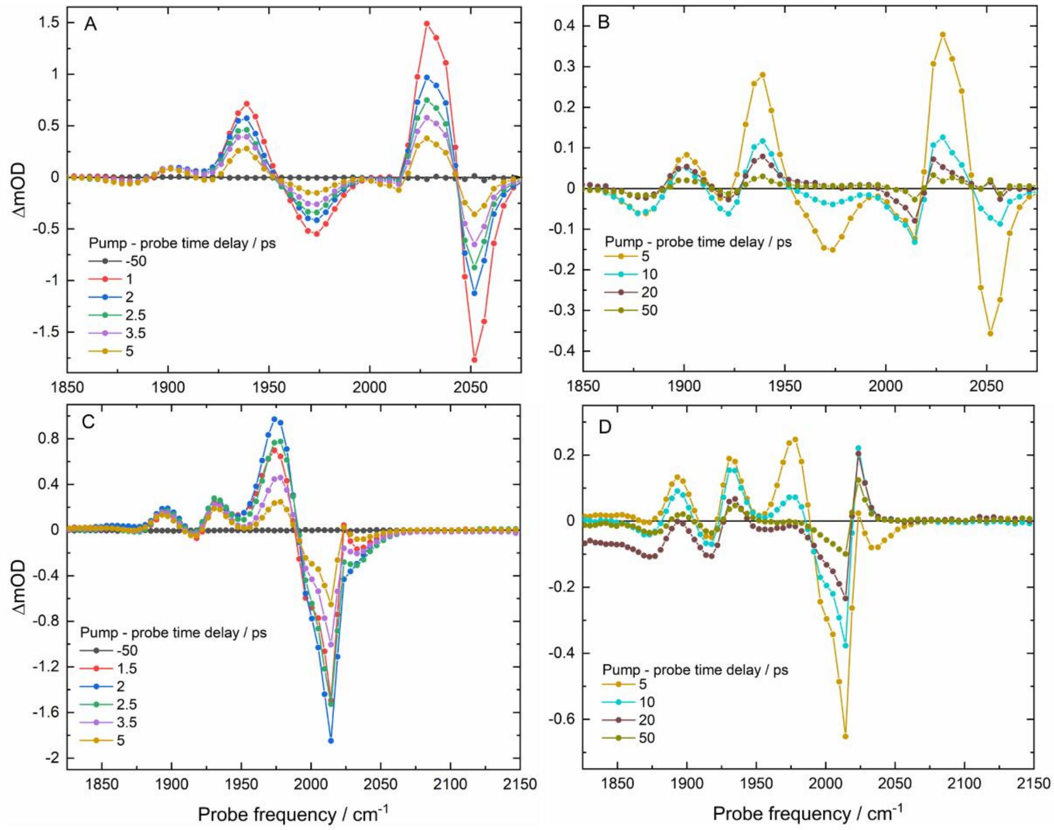

*Figure 4.21 – Excited state 2DIR traces of **2** (A,B) and **3** (C,D), recorded following IR excitation of the a'(1) transient absorption band found 500 ps after 400 nm excitation. The $IR_{pump} – IR_{probe}$ delay times are shown in the graph legends.*

Over time, the transient absorption bands of T_2 decay, concomitant with an apparent intensity increase of the second set of peak pairs, ascribed to T_1. The increase in intensity of the T_1 bands suggests that vibrational excitation of the a′(1) mode in T_2 allows $T_2 \rightarrow T_1$ internal conversion to take place, similar to what was observed in the TRIR data whilst the complex is vibrationally hot. These observations further suggest that the two triplets formed following 400 nm excitation of **2** are very close in energy, such that vibrational excitation can overcome the activation barrier of internal conversion, resulting in re-equilibration of the triplet states. The 2DIR spectrum is highly convoluted, hence accurate characterisation of the transient absorption bands, anharmonic shifts, and decay time constants is difficult. To aid analysis, the data was studied by GLA.

A two-component sequential model was used to model the vibrational dynamics. Whilst this model provided a good multiexponential fit of the time-resolved data, it is unlikely that a sequential model accurately describes the vibrational dynamics of the excited T_1 and T_2 states. The first component, which had a time constant of 2.45 ps, was ascribed to the initial decay of the T_2 bands. Tentatively, the DAS and EAS for this component suggest that the 2DIR peak pairs of the T_1 state increase in intensity with this time constant (Appendix D, fig. D16, D17). Furthermore, this time constant was similar to the $T_1 \rightarrow T_2$ internal conversion time constant found in the TRIR data of **1**. Thus it is possible that vibrational excitation of the T_1 and/or T_2 a′(1) modes results in re-equilibration of the excited state population between T_1 and T_2. However, this cannot be stated for definite from this ES-2DIR data alone. The second GLA component had a time constant of 28 ps, which was assigned as relaxation of the vibrationally excited states to the equilibrium vibrational ground state. This was faster than the vibrational relaxation time constant observed in the ground state 2DIR data, indicating that VET to the solvent is faster in the triplet excited state, consistent with previous studies of $[Re(L_2)(CO)_3Cl]$ complexes. The DAS for this component accounts for the decay of the T_1 and T_2 peak pairs, suggesting they decay synchronously to their vibrational ground states.

To fully understand the vibrational dynamics of these triplet states, additional ES-2DIR experiments are required. Firstly, TRIR data should be collected following lower energy visible light excitation, where S_2 is formed instead of S_9/S_{10}. Furthermore, the ES-2DIR data could be collected in the time domain, where the pump resolution is sufficiently high for selective excitation of either T_1 or T_2. Ideally these experiments would confirm the possibility of IC between the vibrationally hot T_1 and T_2 states.

In the excited state 2DIR spectra of **3**, very similar observations were found for **2**, where the initial transient spectrum changes as one set of bands converts to a second. As with **2**, this suggests that vibrational excitation of the majority triplet state present at a UV_{pump} – IR_{pump} time delay of 500 ps results in population re-equilibration with a second triplet state with a small energy separation. GLA modelling estimated the grow-in of the second triplet state occurs with a 1.90 ps time constant, and vibrational relaxation takes place with a 44 ps time constant. As with **2**, the 2DIR spectrum is highly convoluted, and to fully understand the observed vibrational dynamics, a more accurate model of the transient spectrum is required. This can be achieved through additional TRIR and excited state 2DIR experiments which utilise a low energy visible pump (*ca.* 650 nm) to selectively produce the S_1 or S_2 states. Furthermore, additional DFT calculations of the triplet excited states of **3** may allow for more accurate characterisation of the excited state dynamics.

4.4 Conclusions

Part I

The electronic and vibrational excited state dynamics of a sterically hindered CO_2 reduction catalyst have been studied by TRIR and 2DIR spectroscopies to determine if 6,6′-functionalisation of the bipyridyl ring has any effect on the excited state relaxation mechanism compared to the more commonly studied 4,4′-functionalised catalysts. On the ultrafast timescale, the complex undergoes internal conversion from $S_3 \rightarrow S_2 \rightarrow S_1$, and then intersystem crosses to form the lowest triplet excited state, ^{3}MLCT/XLCT. This state then vibrationally cools until the equilibrium bond geometry at room temperature is reached. The excited state lifetime of ^{3}MLCT/XLCT is short, only 3 ns. This accounts for the observed inability of [Re(HPEAB)(CO)$_3$Cl] to reduce CO_2 following visible light excitation. The vibrational lineshapes of the ^{3}MLCT/XLCT state were narrow when compared to previously reported Re tricarbonyl complexes, ascribed to steric protection of the carbonyl ligands, which inhibits the solvent-solute interactions that contribute to vibrational line broadening.

Vibrational energy redistribution between the carbonyl ligands, aromatic rings, and amide groups was studied with 2DIR spectroscopy. In the electronic ground state, the a′(1), a″, and a′(2) high frequency modes equilibrate following excitation of the a′(1) mode. This redistributes the vibrational energy amongst the three $\nu = 1$ levels and was facilitated by strong mechanical coupling of the modes. The vibrational energy was then slowly transferred to low-frequency modes of the {Re(CO)$_3$Cl} moiety, which was the rate-limiting step of the vibrational energy redistribution following a′(1) excitation. The vibrational energy then equilibrates within the low-frequency modes of the complex, perturbing the potential energy surfaces of other coupled modes. This resulted in off-diagonal signal formation for the amide and aromatic modes of the bipyridyl ligand. The complex returns to its equilibrium ground state by vibrational energy transfer from the low-frequency modes to the continuum of solvent modes. The rate of intermolecular VET was fast for the bipyridyl ligand modes, and slow for the {Re(CO)$_3$Cl} modes, as shown through comparison of amide C=O and C≡O excitation data. The rate of VET from the {Re(CO)$_3$Cl} moiety to the DCM solvent was 1.4x slower than that of the previously reported [Re(4,4′-bpy-ester)(CO)$_3$Cl] complex, which was ascribed to restricted complex-solvent interactions around the sterically protected metal centre.

Intermolecular vibrational energy transfer from the ^{3}MLCT excited state to the solvent was faster than in the electronic ground state, which was attributed to the formation of charges within the complex, consistent with previous studies. However, intramolecular vibrational coupling was weaker, evidenced by the lack of off-diagonal carbonyl modes following amide C=O excitation.

This work builds on our understanding of vibrational energy transfer within metal complexes, it is shown that a $[Re(L_2)(CO)_3Cl]$ complex which is functionalised in the 6,6′-positions has very similar vibrational dynamics to the more common 4,4′-substituted complexes. In future, this study could be further developed through use of time domain 2DIR techniques, which give access to the ultrafast spectral diffusion processes. This would allow for comparison of the solvation dynamics of the $[Re(HPEAB)(CO)_3Cl]$ complex with the well-studied $[Re(bpy)(CO)_3Cl]$ compound. Furthermore, this work could be expanded upon by studying the electrochemically reduced catalyst by spectroelectrochemistry, revealing additional information about the vibrational and excited state dynamics of CO_2 reduction catalytic intermediates in solution.

Part II

The excited state dynamics of two $[Re(L_2)(CO)_3Cl]$ complexes, where L_2 was bis(mesityimino)acenaphthene or bis(mesitylimino)(4-azido-acenapthene) were studied by TRIR spectroscopy following 400 nm excitation. This pump wavelength was resonant with electronic transitions from the ground states to highly excited singlet states, such as S_9 and S_{10}. For both complexes, the optically prepared singlet states were of MLCT character, as shown by preliminary DFT calculations. In the unfunctionalised mesBIAN complex (**2**), the excited complex relaxes to the lowest excited state of the singlet manifold on the ultrafast timescale, and then undergoes intersystem crossing to form a vibrationally hot MLCT/XLCT triplet state, assigned as T_1 by DFT calculations. Whilst the ^{3}MLCT/XLCT state is vibrationally excited, internal conversion could take place to form the T_2 state, 979 cm^{-1} higher in energy. Preliminary excited state 2DIR experiments provided further support for the presence of an internal conversion pathway which results in re-equilibration of the excited state population between the vibrationally hot triplet states. After vibrational cooling is complete, the T_1 and T_2 states are no longer in equilibrium. From this point the two triplet states cannot interconvert and decay to the ground state independently of one another. Addition of an azide group to the 4-position of the acenaphthene ring results in changes to the spectral profile of the TRIR spectrum. This was tentatively ascribed to an increase in electron density within the acenaphthene ring upon azide addition, which alters the character of the triplet states. Results of the excited state 2DIR experiments also tentatively suggest that vibrational excitation of the triplet states also results in internal conversion between T_1 and T_2.

The vibrational dynamics of [Re(mesBIAN)$(CO)_3$Cl] were found to be similar to previously reported complexes, where vibrational energy is equilibrated between the a′(2), a″, and a′(1) modes on the ultrafast timescale. Excitation of the acenaphthene aromatic stretching vibration at 1615 cm^{-1} results in slow formation of off-diagonal peaks corresponding to the carbonyl vibrations, which was attributed to IVR through low-frequency modes of the mesBIAN ligand. Introduction of the azide group in [Re(4-azido-mesBIAN)$(CO)_3$Cl] does not change the relaxation of the carbonyl ligands. However, excitation of the asymmetric azide stretching vibration at 2126 cm^{-1} results in fast formation of carbonyl off-diagonal peak pairs. Thus, vibrational coupling between the mesBIAN-N_3 ligand and carbonyl ligands is significantly strengthened by substitution of the hydrogen atom with the azide group. This was attributed to direct vibrational population transfer from the azide $\nu = 1$ level to the ν(CO) $\nu = 1$ levels, which results in fast formation of the carbonyl off-diagonal signals within 2 ps after IR excitation.

This study of the mesBIAN and mesBIAN-N_3 complexes promotes our understanding of red-light harvesting CO_2 reduction catalysts, where excitation of the complex with 400 nm light results in preparation of a highly excited singlet state. Such insights into the dynamics of Re(I) complexes bearing non-bipyridyl ligands is highly informative and may be used to guide the design of novel catalysts which are active for both electro- and photochemically active CO_2 reduction. To further elucidate the excited state dynamics of the [Re(mesBIAN)$(CO)_3$Cl] complexes, further experiments are required. Firstly, TRIR spectra should be recorded following 600 nm excitation. Ideally, this should result in direct formation of S_1 and T_1 following visible light excitation, significantly simplifying analysis of the transient spectra. Furthermore, the selective formation of T_1 with the visible light excitation pulse will also simplify the excited state 2DIR data, allowing for more accurate determination of the vibrational dynamics, and how vibrational excitation of the excited state can promote internal conversion between triplet states. Finally, the series of complexes could be expanded, where the N_3 substituent is replaced with an electron withdrawing group, such as an ester. This would allow for further characterisation of the vibrational coupling mechanism within the electronic ground state Re(I) complex. Furthermore, as the oscillator strength of the C=O stretching vibration (expected at 1720 cm^{-1}) would be significantly higher than that of the aryl-N_3 group, it would likely be possible to probe the vibrational dynamics of the ester ligand in the excited state. Additionally, excitation of this ester vibration could also allow for induced re-equilibration of the triplet excited states, provided the T_1 / T_2 energy separation is less than 1700 cm^{-1}.

References

1 Y. Yue, T. Grusenmeyer, Z. Ma, P. Zhang, R. H. Schmehl, D. N. Beratan and I. V. Rubtsov,

Dalton Trans., 2015, **44**, 8609–8616.

2 P. Antoniou, Z. Ma, P. Zhang, D. N. Beratan and S. S. Skourtis, *Phys. Chem. Chem. Phys.*, 2015, **17**, 30854–30866.

3 D. Xiao, S. S. Skourtis, I. V. Rubtsov and D. N. Beratan, *Nano Lett.*, 2009, **9**, 1818–1823.

4 Z. Lin, C. M. Lawrence, D. Xiao, V. V. Kireev, S. S. Skourtis, J. L. Sessler, D. N. Beratan and I. V. Rubtsov, *J. Am. Chem. Soc.*, 2009, **131**, 18060–18062.

5 M. Delor, P. A. Scattergood, I. V. Sazanovich, A. W. Parker, G. M. Greetham, A. J. H. M. Meijer, M. Towrie and J. A. Weinstein, *Science*, 2014, **346**, 1492–1495.

6 M. Delor, S. A. Archer, T. Keane, A. J. H. M. H. M. Meijer, I. V. Sazanovich, G. M. Greetham, M. Towrie and J. A. Weinstein, *Nature Chem.*, 2017, **9**, 1099–1104.

7 I. V. Rubtsov, *Nature Chem.*, 2015, **7**, 683–684.

8 T. Elsaesser and W. Kaiser, *Annu. Rev. Phys. Chem.*, 1991, **42**, 83–107.

9 J. D. Gaynor, J. Sandwisch and M. Khalil, *Nature Commun.*, 2019, **10**, 5621.

10 Z. Ma, Z. Lin, C. M. Lawrence, I. V. Rubtsov, P. Antoniou, S. S. Skourtis, P. Zhang, D. N. Beratan, P. Zhang and D. N. Beratan, *Chem. Sci.*, 2018, **9**, 6395–6405.

11 L. J. G. W. Van Wilderen and J. Bredenbeck, *Angew. Chemie - Int. Ed.*, 2015, **54**, 11624–11640.

12 J. F. Cahoon, K. R. Sawyer, J. P. Schlegel and C. B. Harris, *Science*, 2008, **319**, 1820–1823.

13 D. C. Grills, J. A. Farrington, B. H. Layne, S. V. Lymar, B. A. Mello, J. M. Preses and J. F. Wishart, *J. Am. Chem. Soc.*, 2014, **136**, 5563–5566.

14 D. C. Grills, M. Z. Ertem, M. McKinnon, K. T. Ngo and J. Rochford, *Coord. Chem. Rev.*, 2018, **374**, 173–217.

15 K. T. Ngo, M. McKinnon, B. Mahanti, R. Narayanan, D. C. Grills, M. Z. Ertem and J. Rochford, *J. Am. Chem. Soc.*, 2017, **139**, 2604–2618.

16 K. T. Oppelt, L. Sevéry, M. Utters, S. D. Tilley and P. Hamm, *Phys. Chem. Chem. Phys.*, 2021, **23**, 4311–4316.

17 S. Sato, Y. Matubara, K. Koike, M. Falkenström, T. Katayama, Y. Ishibashi, H. Miyasaka, S. Taniguchi, H. Chosrowjan, N. Mataga, N. Fukazawa, S. Koshihara, K. Onda and O. Ishitani, *Chem. - A Eur. J.*, 2012, **18**, 15722–15734.

18 J. B. Asbury, Y. Wang and T. Lian, *Bull. Chem. Soc. Jpn.*, 2002, **75**, 973–983.

19 K. Koike, N. Okoshi, H. Hori, K. Takeuchi, O. Ishitani, H. Tsubaki, I. P. Clark, M. W. George, F. P. A. Johnson and J. J. Turner, *J. Am. Chem. Soc.*, 2002, **124**, 11448–11455.

20 J. R. Schoonover and G. F. Strouse, *Chem. Rev.*, 1998, **98**, 1335–1355.

21 L. M. Kiefer, J. T. King and K. J. Kubarych, *Acc. Chem. Res.*, 2015, **48**, 1123–1130.

22 D. J. Liard, M. Busby, P. Matousek, M. Towrie and A. Vlček, *J. Phys. Chem. A*, 2004, **108**, 2363–2369.

23 D. R. Striplin and G. A. Crosby, *Chem. Phys. Lett.*, 1994, **221**, 426–430.

24 B. D. Rossenaar, D. J. Stufkens and A. Vlček, *Inorg. Chem.*, 1996, **35**, 2902–2909.

25 A. Vlček and M. Busby, *Coord. Chem. Rev.*, 2006, **250**, 1755–1762.

26 A. El Nahhas, C. Consani, A. M. Blanco-Rodríguez, K. M. Lancaster, O. Braem, A. Cannizzo, M. Towrie, I. P. Clark, S. Záliš, M. Chergui and A. Vlček, *Inorg. Chem.*, 2011, **50**, 2932–2943.

27 J. Dyer, W. J. Blau, C. G. Coates, C. M. Creely, J. D. Gavey, M. W. George, D. C. Grills, S. Hudson, J. M. Kelly, P. Matousek, J. J. McGarvey, J. McMaster, A. W. Parker, M. Towrie and J. A. Weinstein, *Photochem. Photobiol. Sci.*, 2003, **2**, 542–554.

28 F. Zhong, X. Yuan, J. Zhao and Q. Wang, *Sci. China Chem.*, 2016, **59**, 70–77.

29 A. M. Blanco-Rodríguez, H. Kvapilová, J. Sýkora, M. Towrie, C. Nervi, G. Volpi, S. Záliš and A. Vlček, *J. Am. Chem. Soc.*, 2014, **136**, 5963–5973.

30 G. E. Shillito, T. B. J. Hall, D. Preston, P. Traber, L. Wu, K. E. A. Reynolds, R. Horvath, X. Z. Sun, N. T. Lucas, J. D. Crowley, M. W. George, S. Kupfer and K. C. Gordon, *J. Am. Chem. Soc.*, 2018, **140**, 4534–4542.

31 A. M. Blanco Rodríguez, A. Gabrielsson, M. Motevalli, P. Matousek, M. Towrie, J. Šebera, S. Záliš and A. Vlček, *J. Phys. Chem. A*, 2005, **109**, 5016–5025.

32 M. Busby, A. Gabrielsson, P. Matousek, M. Towrie, A. J. Di Bilio, H. B. Gray and A. Vlček, *Inorg. Chem.*, 2004, **43**, 4994–5002.

33 Y. Yue, T. Grusenmeyer, Z. Ma, P. Zhang, T. T. Pham, J. T. Mague, J. P. Donahue, R. H. Schmehl, D. N. Beratan and I. V. Rubtsov, *J. Phys. Chem. B*, 2013, **117**, 15903–15916.

34 J. F. Martinez, N. T. La Porte, S. Chaudhuri, A. Sinopoli, Y. J. Bae, M. Sohail, V. S. Batista and M. R. Wasielewski, *J. Phys. Chem. C*, 2019, **123**, 10178–10190.

35 Y. Yue, T. Grusenmeyer, Z. Ma, P. Zhang, R. H. Schmehl, D. N. Beratan and I. V. Rubtsov, *Dalton Trans.*, 2015, **44**, 8609–8616.

36 A. Vlček, H. Kvapilová, M. Towrie, S. Záliš, H. Kvapilova and M. Towrie, *Acc. Chem. Res.*, 2015, **48**, 868–876.

37 V. Cervetto, J. Helbing, J. Bredenbeck and P. Hamm, *J. Chem. Phys.*, 2004, **121**, 5935–5942.

38 J. Bredenbeck, J. Helbing, C. Kolano and P. Hamm, *ChemPhysChem*, 2007, **8**, 1747–1756.

39 M. Delor, I. V. Sazanovich, M. Towrie, S. J. Spall, T. Keane, A. J. Blake, C. Wilson, A. J. H. M. Meijer and J. A. Weinstein, *J. Phys. Chem. B*, 2014, **118**, 11781–11791.

40 I. V. Rubtsov, *Acc. Chem. Res.*, 2009, **42**, 1385–1394.

41 V. M. Kasyanenko, Z. Lin, G. I. Rubtsov, J. P. Donahue and I. V. Rubtsov, *J. Chem. Phys.*, 2009, **131**, 154508.

42 V. M. Kasyanenko, S. L. Tesar, G. I. Rubtsov, A. L. Burin and I. V. Rubtsov, *J. Phys. Chem. B*, 2011, **115**, 11063–11073.

43 L. M. Kiefer and K. J. Kubarych, *J. Phys. Chem. A*, 2015, **119**, 959–965.

44 C. M. Olson, A. Grofe, C. J. Huber, I. C. Spector, J. Gao and A. M. Massari, *J. Chem. Phys.*, 2017, **147**, 124302.

45 L. M. Kiefer, J. T. King and K. J. Kubarych, *J. Phys. Chem. A*, 2014, **118**, 9853–9860.

46 J. Bredenbeck, J. Helbing and P. Hamm, *J. Am. Chem. Soc.*, 2004, **126**, 990–991.

47 D. E. Rosenfeld, Z. Gengeliczki, B. J. Smith, T. D. P. Stack and M. D. Fayer, *Science*, 2011, **334**, 634–639.

48 J. P. Kraack and P. Hamm, *Chem. Rev.*, 2017, **117**, 10623–10664.

49 G. Neri, P. M. Donaldson and A. J. Cowan, *Phys. Chem. Chem. Phys.*, 2019, **21**, 7389–7397.

50 L. M. Kiefer, L. B. Michocki and K. J. Kubarych, *J. Phys. Chem. Lett.*, 2021, **12**, 3712–3717.

51 E. Portenkirchner, E. Kianfar, N. S. Sariciftci and G. Knör, *ChemSusChem*, 2014, **7**, 1347–

1351.

52 P. A. Abramov, A. A. Dmitriev, K. V. Kholin, N. P. Gritsan, M. K. Kadirov, A. L. Gushchin and M. N. Sokolov, *Electrochim. Acta*, 2018, **270**, 526–534.

53 I. Löw, M. Bubrin, A. Paretzki, J. Fiedler, S. Záliš and W. Kaim, *Inorganica Chim. Acta*, 2017, **455**, 540–548.

54 A. J. Sadler, The University of Sheffield, 2018.

55 J. D. Shipp, H. Carson, S. J. P. Spall, S. C. Parker, D. Chekulaev, N. Jones, M. Y. Mel'nikov, C. C. Robertson, A. J. H. M. Meijer and J. A. Weinstein, *Dalton Trans.*, 2020, **49**, 4230–4243.

56 I. H. M. van Stokkum, D. S. Larsen and R. van Grondelle, *Biochim. Biophys. Acta - Bioenerg.*, 2004, **1657**, 82–104.

57 G. M. Greetham, P. Burgos, Q. Cao, I. P. Clark, P. S. Codd, R. C. Farrow, M. W. George, M. Kogimtzis, P. Matousek, A. W. Parker, M. R. Pollard, D. A. Robinson, Z.-J. Xin and M. Towrie, *Appl. Spectrosc.*, 2010, **64**, 1311–1319.

58 H. Kvapilová, A. Vlček, V. Barone, M. Biczysko and S. Záliš, *J. Phys. Chem. A*, 2015, **119**, 10137–10146.

59 A. Cannizzo, A. M. Blanco-Rodríguez, A. El Nahhas, J. Šebera, S. Záliš, A. Vlček and M. Chergui, *J. Am. Chem. Soc.*, 2008, **130**, 8967–8974.

60 D. M. Dattelbaum, K. M. Omberg, J. R. Schoonover, R. L. Martin, T. J. Meyer, *Inorg. Chem.*, 2002, **41**(23), 6071–6079.

61 A. M. Blanco Rodríguez, A. Gabrielsson, M. Motevalli, P. Matousek, M. Towrie and J. Sebera, S. Záliš, A. Vlček, 2005, **109**(23), 5016–5025.

62 R. Fernández-Terán and P. Hamm, *J. Chem. Phys.*, 2020, **153**, 154706.

Chapter 5. Perturbation of the vibrational energy transfer pathways in Pt(II) donor-bridge-acceptor complexes with isotopic substitution

---

Abstract

The vibrational dynamics of four Pt(II) *trans*-acetylide donor-bridge-acceptor (donor = phenylene-methylene-phenothiazine (PTZ), acceptor = naphthalene monoimide (NAP), bridge = *trans*-bis(tributylphosphine)-Pt(II)-bis(acetylide)) complexes, where the two acetylide groups have been systematically isotopically labelled with carbon-13, have been studied by Fourier transform two-dimensional infrared spectroscopy, assisted by density functional theory calculations. The acetylide vibrational modes, which have been previously shown to modulate the rate of electronic charge separation, were found to relax to the vibrational ground state by multiple pathways following IR excitation. The initial inhomogeneity of the acetylide 2DIR peak pairs was found to be small, as shown by the small nodal plane gradient at t_2 = 0 ps. The rate of spectral diffusion was site specific, where accelerated rates of spectral diffusion were found for the ^{13}C labelled acetylide modes and the NAP bound acetylide. In all complexes, the acceptor bound acetylide undergoes a transfer of vibrational population from the optically prepared ν_1(NAP-CC) state to an energy accepting mode 8 cm^{-1} lower in frequency, tentatively characterised as an anharmonic combination mode. Isotopic labelling of only one of the acetylide groups results in vibrational decoupling, where the $\nu(^{13}C^{13}C)$ stretching vibration is shifted to lower frequency by 80 cm^{-1}. It is shown herein that as a result of this decoupling, vibrational energy does not propagate through low-frequency modes from the NAP ligand to the PTZ ligand, consistent with previous observations of a ‘vibrational bottleneck’ in transition metal complexes. However, vibrational population transfer pathways between the high-frequency modes were found which overcome the vibrational energy transfer barrier presented by the $Pt(PBu_3)_2$ centre.

5.1. Introduction

The redistribution of vibrational energy is a fundamental process, one which underlies the electronic and chemical dynamics of many functional compounds. In recent years it has been proposed and demonstrated that molecular vibrations can play a pivotal role in determining the efficiency and rate of electron transfer in the condensed phase.[1–3] Selective perturbation and control of photochemical processes with molecular vibrations is an exciting prospect for novel catalytic systems where the required energy is supplied from sunlight, as the key photophysical step in such artificial photosynthetic reactions is the formation of a charge separated state following an electron transfer (ET) process.

ET is common in photochemistry, and underpins the fields of solar energy generation, artificial photosynthesis, light harvesting, and photocatalysis. The efficiency of current photocatalytic systems is hindered by the formation of unproductive excited states, such as low-energy triplets. Therefore, control of electron transfer processes would prove invaluable in the design of catalytic systems which effectively use sunlight as an energy source. However, such control requires a deep understanding of the underlying electronic and vibrational relaxation dynamics. It has been found that molecular vibrations can have a large influence on the excited state relaxation of transition metal complexes. One key example of this is the influence of vibrational-electronic (vibronic) coherences on the excited state dynamics of photosynthetic pigment LHCII and the common 'RuN3' dye. A second example is the demonstrated ability of mode-specific infrared (IR) excitation to modify the excited state dynamics of light harvesting complexes, which allows for control of photophysical and photochemical processes.[4] For example, control of electron transfer with IR excitation (IR control) has been recently demonstrated for organic hydrogen bonded donor-bridge-acceptor species,[5] a Re(I) tricarbonyl complex,[6] as well as Pt(II) bis-acetylide complexes. In the case of a Pt(II) *trans*-acetylide bearing a naphthalene monoimide (NAP) electron acceptor and phenyl-methylene-phenothiazine electron donor (PTZ), IR excitation of the acetylide stretching vibration resulted in 100% deactivation of the charge separation pathway, with a commensurate increase in the yield in the NAP localised triplet intraligand (^{3}IL) state.[7–9] It has been proposed that effective IR control requires the precursor state, which forms the charge-separated state (CSS), to decay on a similar timescale to the vibrational lifetime. In addition, such control processes require the difference in energy between the initial state and the product states should be similar to the vibrational frequency.[10] Therefore, an understanding of the underlying vibrational dynamics of the donor-bridge-acceptor complexes is crucial in the design of future complexes for effective IR control of electron transfer.

It has also been demonstrated that it is possible to use IR excitation to direct the electron transfer process in a molecular 'fork' complex, [Pt(4,4′-$(CO_2Et)_2$-2,2′-bipyridyl)($C{\equiv}C$-Ph-$PTZ)_2$], a complex with two electronically indistinguishable donor ligands. Here, one of the bridging acetylide groups was isotopically labelled with carbon-13. In this case selective electron transfer was achieved by suppressing the electron transfer from the donor ligand perturbed by IR excitation of either the ^{12}C or ^{13}C acetylide stretching mode. The isotopic substitution resulted in a large frequency separation between the decoupled acetylide stretching vibrations, allowing for selective IR excitation.[11] Two-dimensional infrared spectroscopy (2DIR) revealed that there was no significant coupling interactions between the carbon-12 and carbon-13 labelled ligands. It has also been demonstrated that in such Pt(II) donor-bridge-acceptor complexes, it is only the acetylide vibrational modes which can modulate the formation of the charge separated state.

This work aims to build on previous studies of Pt(II) donor-bridge acceptor complexes by further developing our understanding of the vibrational energy transfer processes which have been shown to influence electron transfer. To this end, four complexes have been prepared with the structure NAP-$^{x}C{\equiv}^{x}C$-Pt(PBu_3)$_2$-$^{y}C{\equiv}^{y}C$-PTZ ('NAP' = naphthalene monoimide, 'PTZ' = Ph-CH_2-phenothiazine), where the acetylide ligands have been isotopically labelled with carbon-13 (Figure 5.1). The resulting four complexes were studied by time domain 2DIR spectroscopy to build a model for vibrational energy redistribution within the donor-bridge-acceptor system.

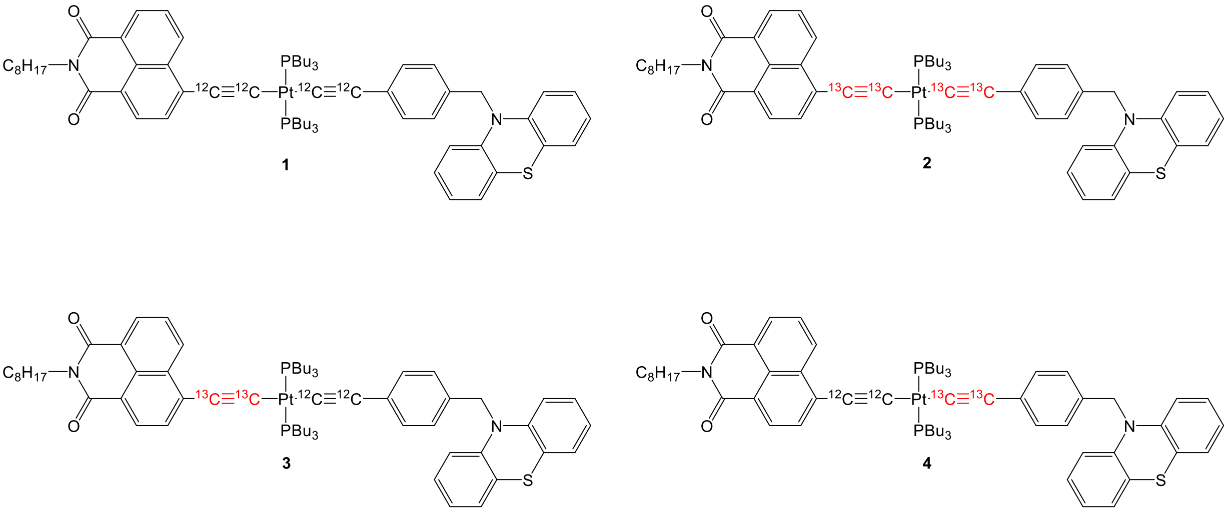

*Figure 5.1 – Chemical structures of complexes **1** – **4**, ^{13}C atoms are labelled in red.*

5.2. Experimental

The synthesis and characterisation of complex **1** has been reported previously.[7] The synthesis and characterisation of complexes **2-4** was carried out by Dr. Andrew Sadler.[12] For all 2DIR data collections, the analyte complex was dissolved in spectroscopic grade dichloromethane (DCM, Sigma-Aldrich). FTIR spectra were recorded in dichloromethane (DCM) with a Perkin-Elmer Spectrum One instrument set to a resolution of 2 cm^{-1}, utilising CaF_2 IR transmission cells.

Time domain 2DIR for complexes **1** – **4** was recorded with the LIFEtime instrument at the Central Laser Facility.[13] Dual synchronised 100 kHz Yb:KGW amplifiers (6 W Pharos SP, 15 W Pharos, Light Conversion) were used to produce 1064 nm light pulses. The 6 W 1064 output was used to pump two OPAs (Orpheus-One, Light Conversion) generating two independently tuneable probe pulses. The dual probe OPA outputs were collimated to a waist of 5-7 mm. The probe spot size at the sample was 50 – 75 μm. The 15 W amplifier pumps an OPA (Orpheus-HP) which is used to generate tuneable IR_{pump} pulses. The pump OPA output is collimated to a 4 mm waist and then passes through a commercially available 100 kHz acousto-optic pulse shaper (PhaseTech Spectroscopy). The pump spot size at the sample was *ca.* 100 μm. The relative IR_{pump} and IR_{probe} polarisation was parallel for all time domain 2DIR experiments. A 4-frame phase cycle was used to suppress unwanted scatter and transient absorption background signals.[14] The population time delay (t_2) was varied with an optical delay stage. Samples were held in CaF_2 Harrick cells. The 2DIR experiment was set up with a 22 fs step size for the t_1 delays, which were scanned up to 4.0 ps. The four-frame phase cycle was setup with the following pump-pump phases: 0,0; 0,π; π,π; π,0.

Data Processing

Prior to Fourier transformation, the TD:2DIR data were zero padded by a factor of two and apodised with a window function. After Fourier transformation a Savitzky-Golay filter was applied to the 2DIR data to smooth the pump axis. If necessary, a scaling factor was applied to the pump axis to correct for small discrepancies between the 2DIR excitation frequencies and the FTIR absorption spectrum. Kinetic traces and pump/probe slices of the TD:2DIR contour maps were extracted with custom LabVIEW software (courtesy of Dr. P. M. Donaldson, RAL, STFC). Spectral diffusion analysis was performed in custom made software available online (developed by Sebastion Gorgon). Anharmonic shifts were obtained through deconvolution of the 2DIR peak pairs with pseudo-Voigt profiles in OriginPro. Exponential fitting of kinetic trace and FFCF data was performed in OriginPro. Global Lifetime Analysis was performed in either OPTIMUS or Glotaran[15,16]. Lifetime Density Analysis was performed in OPTIMUS.[15]

5.3. Results and Discussion

Ground state vibrational absorption spectra

IR spectra of the electronic ground state of complexes **1** – **4** were recorded in DCM at room temperature (Figure 5.2), where vibrational modes of the acetylide bridge were observed in the 1950 – 2150 cm^{-1} region. In **1** and **2**, the symmetry of the bridge results in two acetylide group vibrations – an antisymmetric ($\nu(CC)_a$) and a symmetric ($\nu(CC)_s$) stretching mode. Due to its greater transition dipole moment (Δμ), the $\nu(CC)_a$ absorbance band was significantly more intense than $\nu(CC)_s$. The $\nu(CC)_a$ modes in **1** and **2** have a frequency difference of *ca.* 81 cm^{-1}, consistent with reduced mass analysis for the $^{12}C \rightarrow {}^{13}C$ substitution (Appendix E). Asymmetric isotopic substitution of the bridge leads to a breakdown of the acetylide group vibration; we no longer observe the $\nu(CC)_a$

or ν(CC)$_s$ group vibrations and instead see localised modes corresponding to the individual acetylide groups.

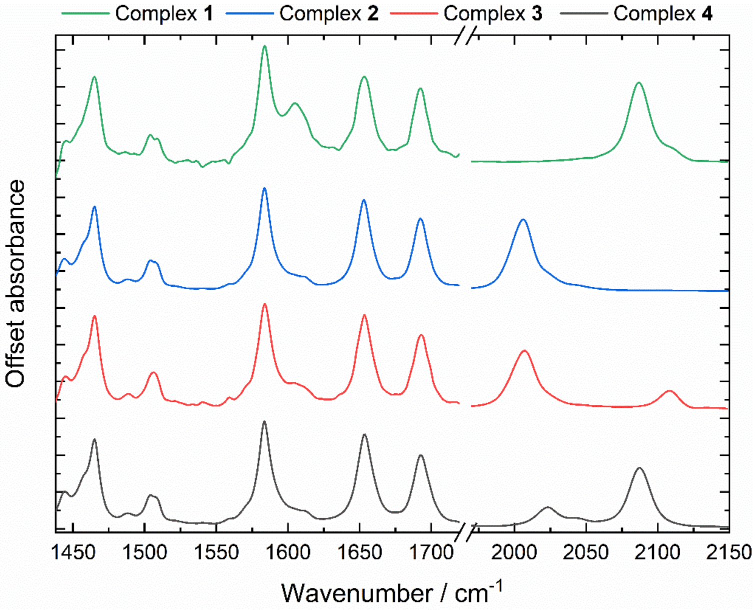

Figure 5.2 – Offset ground state FTIR spectra of complexes ***1*** *–* ***4*** *in the 1440 – 2150 cm^{-1} region, recorded in DCM within a CaF$_2$ solution cell. Spectral deconvolution of the ground state FTIR spectra is presented in Appendix E, fig. E1.*

Alongside the acetylide stretching vibrations, additional low-intensity modes were observed in the 1950 – 2150 cm^{-1} region. These were modelled with pseudo-Voigt profiles to deconvolute the IR spectra (Appendix E, Fig. E1). Three absorption bands were found for both **1** and **2**, corresponding to ν(CC)$_a$, ν(CC)$_s$, and a weaker uncharacterised absorption band. In **3**, six bands were fit to the IR spectrum, where three corresponded to the NAP-acetylide (2006, 2027, 2047 cm^{-1}), and three to the PTZ-acetylide (2068, 2092, 2108 cm^{-1}). Within the margin of error, the IR spectrum of **3** was a superposition of the IR spectra of **1** and **2**. This implied that the isolated ν(NAP-CC) and ν(CC-PTZ) modes in **3** were partially delocalised and had a similar character to the delocalised group vibrations observed in **1** and **2**. This was consistent with visualisation of the harmonic vibrational modes obtained through DFT calculations (See below). Five pseudo-Voigt profiles were required to model the IR spectrum of **4**. The relative intensity of the mode at 2045 cm^{-1} was significantly larger in **4**, compared to **3**. This mode is assigned as a combination band of a [-Ph-CH$_2$-PTZ] ligand mode and the $^{13}C^{13}C$ acetylide stretching vibration. The increased intensity is the product of an accidental Fermi resonance, where two modes with similar frequencies undergo quantum mechanical mixing.[11,17,18] As a result, the intensity of the fundamental ν($^{13}C^{13}C$) mode was decreased, and the intensity of the ν($^{13}C^{13}C$/Ph) mode was increased. A second effect of this Fermi resonance is an increased separation between the ν($^{13}C^{13}C$/Ph) and ν($^{13}C^{13}C$) modes. The intensity of the ground state absorption bands is a measure of the oscillator strength of the vibrational mode. In **3**, the strongest band was the ν($^{13}C^{13}C$)

mode, a result of the strong electronic coupling of the acetylide with the NAP group. The electronic coupling within the [CC-Ph-CH_2-PTZ] ligand is weaker, as the conjugation is disrupted by the aliphatic CH_2 group and tertiary nitrogen atom – limiting delocalisation of the acetylide triple bond and reducing the oscillator strength of the ν(CC-PTZ) vibration compared to the ν(NAP-CC) mode.

Vibrational modes of the [-Ph-CH_2-PTZ] and NAP ligands were observed in the 1450 – 1750 cm^{-1} region of the FTIR spectrum, the three most prominent vibrational absorption bands of the NAP ligand were found in all spectra at 1583, 1653, and 1692 cm^{-1}, corresponding to the aromatic stretching mode of the naphthalene ring (ν(NAP-Ar)), antisymmetric C=O stretching mode ($\nu(CO)_a$), and symmetric C=O stretching modes ($\nu(CO)_s$), respectively. Vibrational modes of the PTZ ligand were also observed in this region. The oscillator strength of these modes was significantly lower than the vibrations of the NAP ligand, hence accurate assignment of these vibrations from the FTIR spectrum is challenging.

The ground state IR spectra of **1** – **4** were modelled by DFT calculations under the harmonic oscillator approximation. The calculated spectra show the acetylide vibrations of **1** and **2** were indeed asymmetric and symmetric combination modes of the two acetylide stretching vibrations. The asymmetric mode was primarily localised on [NAP-CC-] with a weaker contribution from [-CC-Ph-CH_2-PTZ]. Whereas the symmetric mode was primarily localised on the [-CC-Ph-CH_2-PTZ] acetylide. The calculations predict an 83 cm^{-1} difference between the $\nu(^{12}C^{12}C)_a$ and $\nu(^{13}C^{13}C)_a$ vibrational modes, consistent with the experimental data. Calculated vibrational transitions for the ν(NAP-Ar), $\nu(CO)_a$, and $\nu(CO)_s$ modes were found at the expected frequencies. Additional low oscillator strength modes found in this region were also characterised. A combination mode of the phenothiazine and phenyl groups was found at 1607 cm^{-1}, as well as other combination vibrations of the PTZ, CH_2, and Ph groups (1473 cm^{-1}), and the PTZ and CH_2 groups (1446 cm^{-1}). Additional aromatic vibrations of the naphthalene monoimide group (1338, 1397, 1432, 1463, 1583, and 1510 cm^{-1}) were also assigned.

The calculated vibrational modes for **3** and **4** show that isotopic substitution of a single acetylide group did not fully decouple the two groups, where the vibrations had a weak contribution from the other acetylide. The $\nu(^{12}C^{12}C)$ and $\nu(^{13}C^{13}C)$ frequency separation in **3** was greater than the separation of $\nu(^{12}C^{12}C)_a$ and $\nu(^{13}C^{13}C)_a$ in **1** and **2**, with a value of 107 cm^{-1}. This increase was a result of the different local environments for the [NAP-CC] and [CC-Ph-CH_2-PTZ] acetylide groups. In **4**, the separation between acetylide modes was smaller, 64 cm^{-1}, a result of the accidental Fermi resonance between $\nu(^{13}C^{13}C)$ and the $^{13}C^{13}C$/Ph anharmonic combination mode. Upon application of appropriate scaling factors (Appendix E, Table E1-E4), the calculated IR spectra were consistent with the experimental data.

Solvation dynamics of the acetylide vibrational excited states

To determine how the acetylide modes interact with the surrounding functional groups and solvent molecules at ultrafast timescales, the rate of spectral diffusion was investigated. Immediately after population of the ν_1 level by the two laser pulses, at a population time (pump – probe delay time, t_2) of 0 ps, the 2DIR signal was elongated along the diagonal line. This was a result of excitation of a subset of the microstates which comprise the ground state IR spectral lineshape. As the population time increased the 2DIR lineshape changed from elliptical to circular. This spectral diffusion process was attributed to homogeneous broadening of the 2DIR lineshape as the excited molecules re-sample their available geometries and solvent-complex configurations after excitation. At these early delay times, the 2DIR line shape was dependent on the pump frequency. This correlation became weaker until the process was complete, after this point the 2DIR line shape no longer had any dependence on the initial pump frequency.

At short population times, the acetylide diagonal peak pairs in **1** and **2** were indeed elongated along the diagonal axis. As t_2 increased, the lineshape of the peak pair changed from elliptical to circular, concomitant with decreasing gradient of the nodal plane between the positive and negative absorption bands. The initial inhomogeneity of the acetylide vibrational excited states was small, evidenced by the small nodal line tilt angle at $t_2 = 0$ ps. The rate of spectral diffusion in **1** and **2** was modelled with the Centre Line Slope (CLS) method, which estimates the Frequency Fluctuation Correlation Function (FFCF) by plotting the change in centre line slope of the transient and bleach bands over time (Eq. 5.1). The CLS decay traces are available in Appendix E, fig. E4. This method relies on the assumption that the frequency fluctuations of the $\nu_{0\text{-}1}$ and $\nu_{1\text{-}2}$ transitions are strongly correlated, which is acceptable provided the anharmonic shift is small.[14,19,20] The FFCF describes the time-dependent interactions of a vibrational mode with its local environment, where exponential fitting of the estimated FFCF provides the rate of spectral diffusion ($\Delta\omega^2$ – fluctuation amplitude, τ_c – correlation time).

$$FFCF = \langle \delta\omega(t)\delta\omega(0) \rangle = \Delta\omega^2 * e^{-\frac{t}{\tau_c}} \quad \text{(Eq. 5.1)}$$

The amplitude of the acetylide frequency fluctuations ($\Delta\omega^2$) was small, hence the FFCF decay for the acetylide modes approaches the homogeneous limit where the frequency fluctuations are very small or fast. This results in motional narrowing, leading to 2DIR lineshapes which have largely Lorentzian character. These fast fluctuations mean we observe an average of the molecular frequency distribution. Spectral deconvolution of the 2DIR cross-sections with pseudo-Voigt profiles showed that the lineshapes were largely Lorentzian, with a small Gaussian contribution. This Gaussian component demonstrated that the homogeneous limit had not been reached, and the frequency fluctuation rate is between the homogeneous (ultrafast fluctuation) and inhomogeneous (static frequency distribution) limits. Such behaviour is typical for vibrational modes in the condensed phase, where diffusive correlation times from 0.5 – 2 ps are expected for spectral - 149 -iffusion.[14]

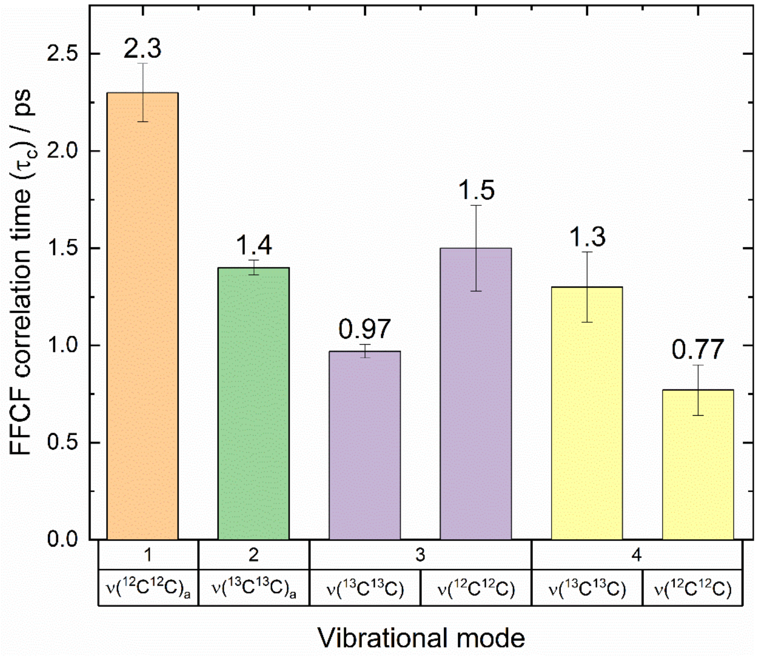

Figure 5.3 – Frequency fluctuation correlation times obtained by monoexponential fitting of the change in centre line slope with increasing population time for the acetylide stretching vibrations of ***1** – **4**. The error bars are calculated from the exponential fit of the estimated FFCF. The FFCF curves and amplitudes are provided in Appendix E, fig. E4, E5.*

The FFCFs for the $\nu(CC)_a$ peak pair of **1** and **2** both started below 1.0 at 0 ps, indicating that some ultrafast inertial spectral diffusion had taken place within the instrument response function (IRF) period, which has a FWHM of approximately 200 fs. Inertial spectral diffusion is characterised as an ultrafast solvation resulting from random motion in the first solvation shell, which occurs on a 100 – 200 fs timescale.[21] Due to the IRF convolution, only diffusive time constants could be obtained from the data.

It was found that the diffusive time constant for **1** was greater than **2** by a factor of 1.6. The suggested explanation for the increase in spectral diffusion rate between **1** and **2** is the change in vibrational frequency of the $\nu(CC)_a$ mode. However, further investigation is required to fully understand the effect of isotopic substitution on the rate of spectral diffusion. An increased rate of spectral diffusion following isotopic substitution was also found in **3**, where the $^{13}C^{13}C$ acetylide had a 1.5x greater spectral diffusion rate compared to the $^{12}C^{12}C$ acetylide. However, this was not the case in **4**, where the $^{13}C^{13}C$ acetylide spectral diffusion rate was 1.7x less than the $^{12}C^{12}C$ acetylide (Figure 5.2). The difference in the spectral diffusion rate between the partially decoupled acetylide groups within the same complex shows that the frequency fluctuations of the $\nu(^{12}C^{12}C)$ and $\nu(^{13}C^{13}C)$ vibrations are uncorrelated, a result of the vibrational decoupling of the two modes. This is also evidenced by a lack of an oscillating signal imprinted onto the FFCF, which indicates very strong coupling of the two vibrations.[21,22]

It is possible that the site-specific rate of frequency fluctuation observed for the acetylide modes in **3** and **4** was a product of the local electronic environment, where proximity to the NAP ligand resulted in increased spectral diffusion rates. It has been reported previously that the electrostatic environment around a vibrating group does influence the rate of spectral diffusion, as shown by the effect of solvent nucleophilicity on the rate of spectral diffusion in both metal carbonyl [Re(R_2-bpy)$(CO)_3$Cl] complexes and small molecule silanes.[23–25] Furthermore, spectral diffusion is not only a product of solvent geometry fluctuation; changes in the molecular geometry of the complex also contribute to these dynamics.[26] The proposal that the different electrostatic environments for the NAP-CC and CC-PTZ acetylides result in different spectral diffusion rates is further supported by spectral diffusion studies comparing the electronic ground and excited states of [Re(R_2-bpy)$(CO)_3$Cl], which have suggested that that the permanent dipole moment of the electronic state under study has an influence on the spectral diffusion rate, where it was shown that the rate of spectral diffusion is slower when the permanent dipole moment is smaller.[23,27] This is consistent with our observations for **3**, where more strongly polarised NAP-acetylide undergoes faster frequency fluctuations than the less polarised PTZ-acetylide. In **4**, it is the PTZ-acetylide which undergoes faster spectral diffusion, it is proposed that this results of the strong coupling between the acetylide and [-Ph-CH_2-PTZ] groups introduced by the accidental Fermi resonance.

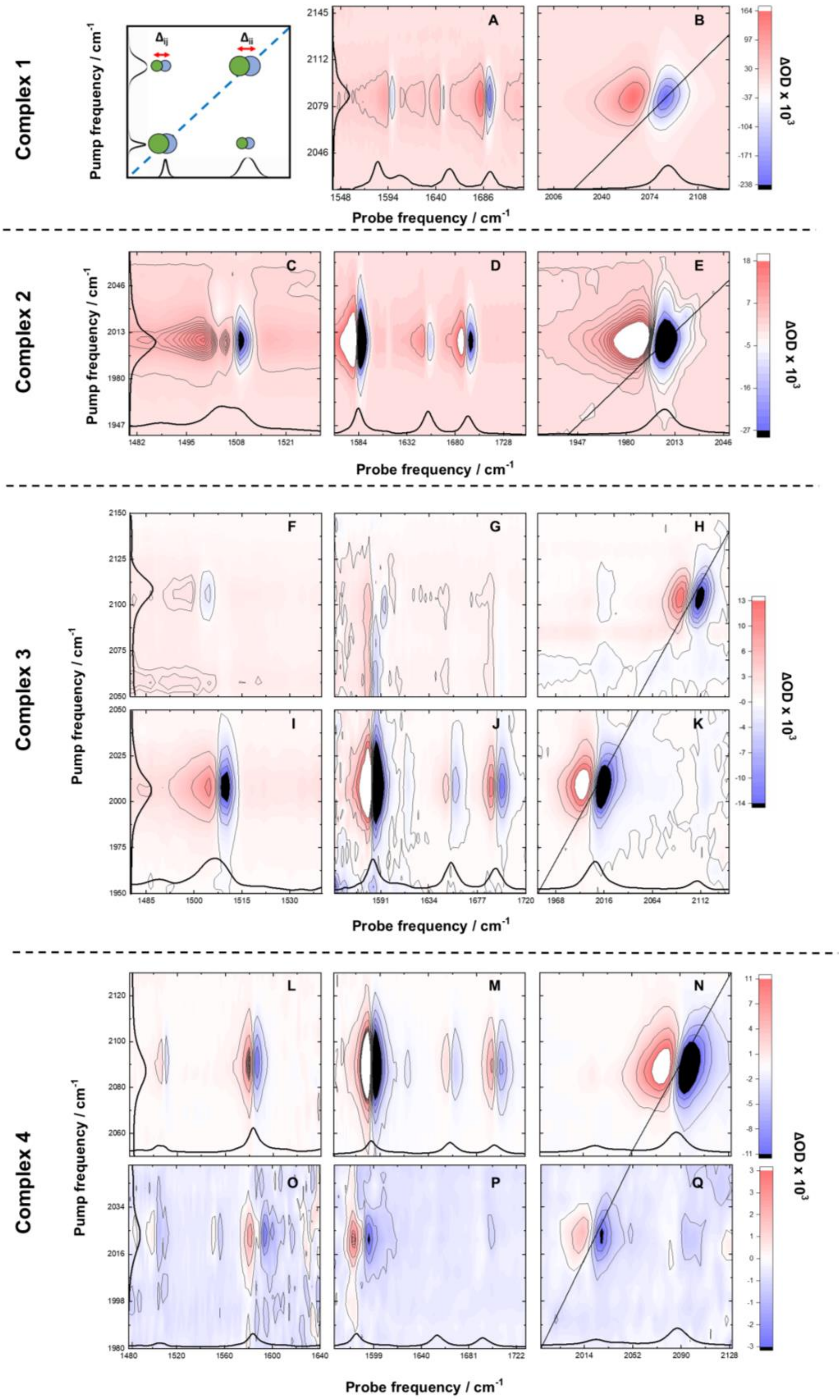

Figure 5.4 – 2DIR contour maps of complexes ***1*** *(A,B),* ***2*** *(C,D,E),* ***3*** *(F,G,H,I,J,K), and* ***4*** *(L,M,N,O,P,Q) recorded at a 2 ps population time following broadband (100 cm^{-1}) IR excitation centred at 2010 or 2080 cm^{-1}. The pump – probe polarisation was parallel for all datasets. The ground state FTIR spectra are superimposed over the 2DIR contour maps along the pump and probe axes. The diagonal line is superimposed over the pumped acetylide stretching mode. An example contour map is shown in the top left of the figure.*

Dynamic changes in the acetylide excited state absorption frequency

In **1** – **4**, the self-responses of the ν(CC) modes were the most prominent features in the 1920 – 2050 cm^{-1} region. Smaller peaks were also observed, which correspond to off-diagonal peak pairs of the coupled acetylide modes. For example, in **1** and **2**, the bleach of the ν(CC)$_s$ mode as well as off-diagonal peak pairs which form from the strong ν(CC)$_a$/ν(CC)$_s$ coupling interactions were observed. These off-diagonal peaks were observable at population times as short as 500 fs. The interaction between the ν(CC)$_a$ and ν(CC)$_s$ modes is assigned as both mechanical and anharmonic coupling mechanisms, where the motion of the acetylides following excitation of the ν(CC)$_a$ mode results in strong perturbation of the ν(CC)$_s$ mode. The ν(CC)$_s$ diagonal peak pair, and the ν(CC)$_a$/ν(CC)$_s$ off-diagonal peak pairs are overlapped with the intense ν(CC)$_a$ peak pair, hence reliable kinetic information on these coupling interactions could not be obtained.

The peak pairs corresponding to the acetylide stretching vibrations in **1** – **4** undergo dynamic changes in anharmonic shift (Δ) as the population time increases (Figure 5.5 A – F). For example, the apparent diagonal anharmonicity (Δ_{ii}) of the ν(CC)$_a$ modes in **1** and **2** was found to decrease from the initial values of 26 and 21 cm^{-1} by 5 cm^{-1} between 2.5 – 10 ps. This decrease occurred with a 1.7 ± 0.06 ps time constant for **1** and 1.4 ± 0.03 ps time constant for **2**. Similar dynamics have been observed previously in lead iodide perovskites,[28,29] transition metal complexes,[30] and organic compounds such as acetylproline-NH$_2$ and hexakis(trimethylsilylethynyl)benzene (HTEB).[31,32]

In **1** – **4**, a blue shift in the excited state absorption (ESA) frequency by 8 cm^{-1} is the cause of the apparent decrease in Δ_{ii}. This results from an energy transfer from the initially populated ν$_1$(CC) level to a lower energy mode with a small frequency separation. This energy accepting mode can also be excited to ν$_2$(CC) by the probe pulse (Figure 5.5 I). As the calculated harmonic IR spectrum does not predict any transitions other than the fundamental ν(CC)$_a$ and ν(CC)$_s$ vibrations, the energy accepting mode results from the anharmonicity of the vibrational potential energy surface, hence, is most likely a combination or overtone mode. It was found that the increase in ESA frequency only takes place when the vibrationally excited acetylide is directly connected to the naphthalene ring. Therefore, the energy accepting mode is likely associated with the NAP ligand (Figure 7.4), hence this vibrational level has been characterised as ν$_1$(CC/NAP).

To further characterise the ν$_1$(CC/NAP) state, antidiagonal cross-sections of the 2DIR data were studied to observe the off-diagonal ν$_{0\text{-}1}$(CC/NAP) bleaches using a previously described method.[32,33]. The antidiagonal spectra were first normalised to the maximum of the excited ν$_1$(CC) bleach, and then the $t_2 = 0$ spectrum was then subtracted from all subsequent spectra (Figure 5.5 G,H). In **1**, the resulting [norm. ΔOD(t_2) – norm. ΔOD($t_2 = 0$)] spectra reveal initial grow in of two new bands on the high and low frequency sides of the fundamental $\nu_{0\text{-}1}$(CC) bleach. These are off-diagonal bleaches which form following population of the ν_1(CC/NAP) mode. The assignment of these bands as off-diagonal signals is confirmed by their equal frequency separation from the fundamental band, which is consistent with the magnitude of the shift in the ESA frequency (8 cm^{-1}). The high frequency band (2093 cm^{-1}) continues to grow in intensity until 5.5 ps, at which point the energy transfer is complete. The low frequency band (2077 cm^{-1}) has more complex dynamics; after initial grow in of the bleach, the measured signal intensity becomes increasingly negative at $t_2 > 3$ ps. This occurs due to the grow in of the new absorption band corresponding to the transition from ν_1(CC/NAP) to $\nu_2(\text{CC})_a$, which overlaps with the antidiagonal line.

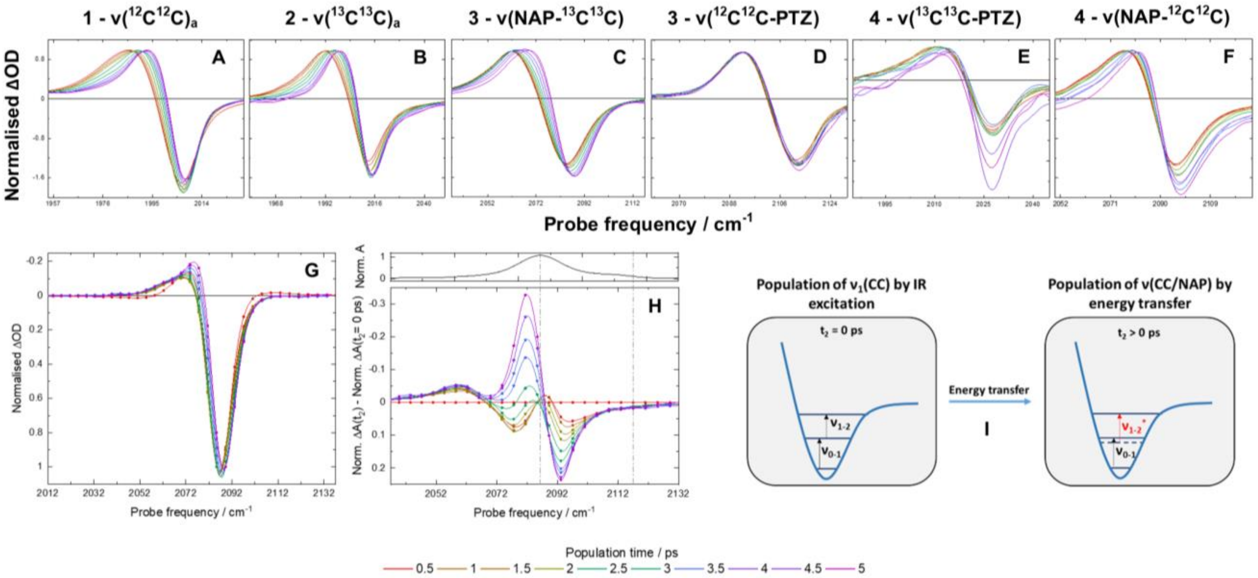

*Figure 5.5 – A,B,C,D,E,F: Dynamic shifts in the excited state absorption frequency for the acetylide stretching vibrations in complexes 1 – 4. G: Normalised antidiagonal cross-sections of the 2DIR spectrum of **1**, intersecting the $\nu_{0\text{-}1}(^{12}C^{12}C)_a$ band. H: Antidiagonal difference spectra obtained by subtraction of the normalised antidiagonal cross section at $t_2 = 0$ from the subsequent population times for **1**. I: Proposed mechanism accounting for the shift in excited state absorption of the acetylide groups adjacent to the NAP ligand. Population times for all graphs are shown below the data. Note that normalisation of the data to the ground state bleach causes excited state absorption bands to be negative and ground state bleach bands to be positive.*

After 10 ps, the intensity of the 2093 cm^{-1} band begins to decrease as the mode relaxes to the ground state. These observations are very similar to those reported previously in the study of HTEB and tricyanomethanide.[32,33] A small band was observed at 2121 cm^{-1} (35 cm^{-1} shift from fundamental $\nu_{0\text{-}1}$ transition), which corresponds to the $\nu_{0\text{-}1}(\text{CC})_s$ off-diagonal bleach. The grow-in and subsequent decay of the of the ν_1(CC/NAP) state was analysed by Lifetime Density Analysis (LDA) to provide estimates of the grow in and decay of the state. It was found that the ν_1(CC/NAP) off-diagonal bleaches grow in with a 810 fs time constant, corresponding to the population transfer from $\nu_1(\text{CC})_a$

to ν_1(CC/NAP), which then then relaxes to low-frequency modes of the bridge with a 2.3 ps time constant.

In **2**, the [norm. ΔOD(t_2) – norm. ΔOD(t_2 = 0 ps)] spectra for the antidiagonal cross-section recorded at the $\nu_{0\text{-}1}$(^{13}C^{13}C) peak centre were similar to **1**. Three observable off-diagonal bleaches formed at small population times, corresponding to the ν_1(CC/NAP) and ν(CC)$_s$ off-diagonal bands. In **2**, the ν(CC)$_s$ cross-peak was more intense than what was observed in **1**, this was attributed to stronger coupling between ν(CC)$_a$ and ν(CC)$_s$. At later population times, an additional off-diagonal band grows in at 2010 cm^{-1} which was not detected in **1**. This band is shifted 5 cm^{-1} higher frequency that $\nu_{0\text{-}1}$(CC)$_a$, and likely corresponds to a second ν_1(^{13}C^{13}C/NAP) mode. The off-diagonal modes in **2** relax to low-frequency modes with a time constant of 3.1 ps.

In **3**, after excitation of the ν(NAP-^{13}C^{13}C) mode, the initial ESA frequency of 1991 cm^{-1} increased by 8 cm^{-1} to 1999 cm^{-1}. The [norm. ΔOD(t_2) – norm. ΔOD(t_2 = 0)] data revealed the formation of off-diagonal peaks at early delay times, corresponding to ν_1(^{13}C^{13}C/NAP). The population transfer time constant could not be reliably obtained by LDA due to the low signal: noise ratio. Therefore, the time constant was modelled by exponential fitting of the frequency shift, which revealed a time constant of 2.2 ± 0.066 ps, similar to the LDA modelled time constants for the analogous processes in **1** and **2**. The ESA frequency of the ν(^{12}C^{12}C-PTZ) self-response did not significantly change from its initial value of 2092 cm^{-1}. In **4**, no significant shift in ESA frequency was observed following excitation of the ν(^{13}C^{13}C-PTZ) mode, whilst the ν(NAP-^{12}C^{12}C) ESA band did undergo a blue shift. As with **3**, it was not possible to obtain a time constant for this process by LDA of the [Norm. ΔOD(t_0) – Norm.(ΔOD(t_2 = 0 ps)] data due to the low signal: noise ratio. Exponential fitting of the ESA shift provided a time constant of 2.8 ± 0.27 ps.

Vibrational relaxation dynamics of the acetylide excited state

In **1**, the ν_1(CC)$_a$ mode does not only relax to ν_1(CC/NAP), it also undergoes IVR to low-frequency modes of the bridge and ν_1(CC)$_s$ mode. The estimated time constants for these energy transfers were obtained by LDA, and were 850 fs and 650 fs, respectively. This was significantly faster than IVR from ν_1(CC/NAP) to low-frequency modes (τ = 2.3 ps). After IVR was complete and the vibrational energy was transferred from the high frequency ν_1(CC)$_a$, ν_1(CC)$_s$, and ν_1(CC/NAP) modes to the low-frequency modes, the remaining acetylide peak pair intensity decays with a time constant of 17 ps. This was associated with VET from low-frequency modes of the acetylide bridge to the continuum of low-frequency solvent modes. The relaxation of the ν_1(CC)$_a$ state by IVR in **2** to low-frequency modes takes place faster, with a 580 fs time constant. After the relaxation to low-frequency modes is complete, the residual peak pair intensity decays with a VET time constant of 8.6 ps.

Excitation of the ν(NAP-^{13}C^{13}C) mode in **3** resulted in similar dynamics to **1** and **2**. The initial ν$_1$(^{13}C^{13}C) state was found to decay to low frequency modes with a time constant of 811 fs. This was followed by a slower VET process which occurs with a time constant of 15 ps. An off-diagonal peak pair associated with the ν(^{12}C^{12}C) acetylide mode was detected at early time delays (100 fs), which suggests that the two acetylide vibrations were not fully decoupled. As the grow-in took place on the ultrafast timescale, the initial coupling mechanism was assigned as anharmonic or dipole-dipole coupling. The low intensity of the off-diagonal modes indicated the two acetylide groups are largely decoupled, showing that vibrational energy transfer across the Pt(II) centre is inhibited. However, unlike the previously reported isotopically labelled *cis*-Pt acetylide complexes, the two acetylide modes are still able to interact through ultrafast coupling interactions.[11] This was also consistent with the partial decoupling observed in the calculated harmonic vibrational modes. No secondary grow in or changes in Δ_{ij} were found, indicating that after initial perturbation of the ν(^{12}C^{12}C-PTZ) mode, no further coupling interactions between the acetylide groups take place. This is consistent with previous proposals that a heavy metal centre between two localised vibrations inhibits coupling between them, where the metal centre acts as a 'vibrational bottleneck'. For example, it has been found that the transition metal centre in [Re(4,4′-CO$_2$Et)-2,2′-bipyridyl)(CO)$_3$Cl], [Ru(4,4′-CO$_2$Et)-2,2′-bipyridyl)$_2$(NCS)$_2$] and [Re(4,4′-CO$_2$Et)-2,2′-bipyridyl)$_2$(CO)$_3$Cl] inhibits vibrational energy transport between modes separated by the metal centre.[30,34] The off-diagonal ν(^{12}C^{12}C-PTZ) peak pair decays by VET with a time constant of 13 ps. Considering these results, the two acetylide vibrations are characterised as 'partially decoupled', where they may interact through ultrafast coupling mechanisms, but cannot transfer vibrational energy through the Pt centre *via* low-frequency modes.

Excitation of ν(^{12}C^{12}C-PTZ) in **3** resulted in two detectable peak pairs in the 1920 – 2140 cm^{-1} spectral region, assigned as the diagonal ν(^{12}C^{12}C-PTZ) peak pair and off-diagonal ν(NAP-^{13}C^{13}C) peak pair. The initially excited ν$_1$(^{12}C^{12}C) state decays by population transfer to the ν(^{13}C^{13}C) mode (see below), IVR to low-frequency modes (τ = 250 fs), as well as VET to the solvent (τ = 16 ps). The VET time constant of the off-diagonal ν(^{13}C^{13}C) mode to the solvent was found to be 23 ps. The discrepancy in the VET time constants for ν(^{12}C^{12}C-PTZ) and ν(NAP-^{13}C^{13}C) further supports the proposal that thermal equilibration of the low-frequency modes on either side of the Pt(II) centre is inhibited by a vibrational bottleneck, where the two acetylide ligands undergo independent VET processes.

In **4** the ν$_1$(NAP-^{12}C^{12}C) mode relaxes by IVR with a time constant of 1.0 ps, followed by VET with a time constant of 27 ps. The relaxation rate of the ν$_1$(^{13}C^{13}C) excited state was found to be significantly faster in **4** compared to **3**. This increased IVR rate was a result of the strong coupling of the ν$_1$(^{13}C^{13}C) fundamental stretching vibration with the ν$_1$(^{13}C^{13}C/Ph) combination mode. Here the

Fermi resonance acts as an ultrafast vibrational energy transfer pathway from the $\nu_1(^{13}C^{13}C)$ level to the vibrational modes of the [-Ph-CH_2-PTZ] group,[35] as shown by the increased rate of off-diagonal signal formation ($\tau = 660$ fs) of the Ph/PTZ modes compared to $\nu_1(^{12}C^{12}C)$ excitation in **3** ($\tau = 1.0$ ps).

Vibrational population transfer between acetylide groups

In **3** and **4**, the asymmetric isotopic substitution introduces new vibrational energy transfer pathways between the partially decoupled acetylide groups (Figure 5.7). As discussed in the previous section, $\nu(^{12}C^{12}C)$ or $\nu(^{13}C^{13}C)$ excitation results in a strong diagonal peak pair corresponding to the pumped mode, as well as low intensity off-diagonal peak pair corresponding to the non-resonant mode.

The off-diagonal anharmonic shift (Δ_{ij}) is a measure of the coupling strength between the pumped mode and the coupled off-diagonal mode. In transition metal complexes it is common that off-diagonal modes are only weakly perturbed by ultrafast coupling or IVR, leading to observation of a distorted $\nu_{0\text{–}1}$ absorption band. The diagonal anharmonic shift (Δ_{ii}) is larger than Δ_{ij} due to population of the ν_1 level, where we observe the $\nu_{1\text{–}2}$ transition. Therefore, it is expected that Δ_{ij} should be smaller than Δ_{ii} for the acetylide modes. This was not always the case in **3** and **4**, where vibrational excitation of ν(CC-PTZ) resulted in a ν(NAP-CC) off-diagonal peak pair with the same anharmonic shift as if it was directly excited (Figure 5.6). This suggests that the non-resonant ν_1(CC-NAP) energy level was populated, and the observed cross-peak was not purely formed as a result of dipole-dipole or anharmonic coupling. Instead, it is proposed that a population transfer from ν_1(CC-PTZ) → ν_1(NAP-CC) takes place following vibrational excitation of the PTZ-acetylide.

Conversely, the off-diagonal peak pair of the ν(CC-PTZ) mode following excitation of the NAP-acetylide was significantly smaller than the diagonal anharmonic shift of the ν(CC-PTZ) peak pair. This suggests that the reverse NAP → PTZ population transfer does not take place. This difference in the population transfer pathways is also reflected in the relative peak pair intensities of the diagonal and off-diagonal modes – the off-diagonal ν(CC-PTZ) peak pair is significantly weaker than the off-diagonal ν(NAP-CC) peak pair.

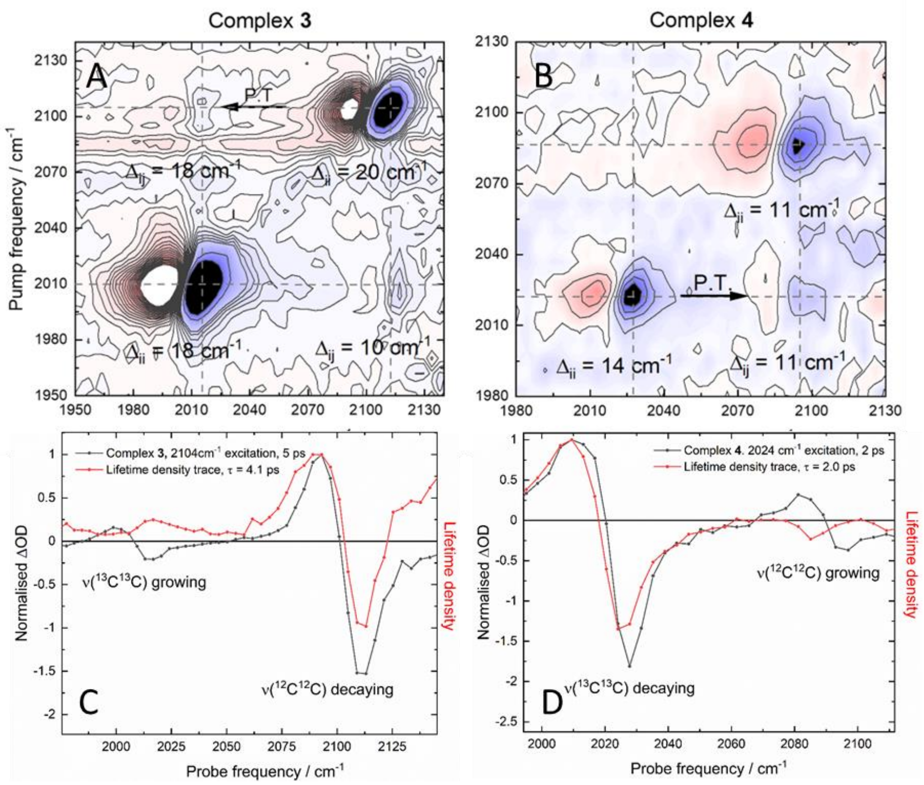

Figure 5.6 – A,B) 2DIR contour maps of the acetylide region of ***3*** *and* ***4****, overlaid with the diagonal and off-diagonal anharmonic shifts for the ν($^{12}C^{12}C$) and ν($^{13}C^{13}C$) peak pairs. The 2DIR data has been scaled to emphasise the off-diagonal peak pairs (****3****: −10-10 ΔmOD,* ***4****: −1-1 ΔmOD.) P.T. = ν(CC-PTZ) → ν(NAP-CC) population transfer. C,D) Lifetime density traces for the PTZ → NAP population transfer process (red) overlaid with cross-sections of the 2DIR contour map along the probe axis at the frequencies shown on the graph.*

This population transfer was further evidenced by a decrease in the diagonal/off-diagonal peak pair intensity ratio as the population time increased (Appendix E, fig. E7). This decrease corresponds to the transfer of vibrational population from the pumped mode to the non-resonant acetylide.[32] An exponential decrease in the ν(CC-PTZ)/ν(NAP-CC) intensity ratio was found for **3** and **4**. The rate of this ratio decrease was modelled by exponential fitting, yielding time constants of 5.1 ± 0.21 ps for **3** and 1.1 ± 0.0077 ps for **4**. These time constants provide an estimate for the rate of the ν(CC-PTZ) → ν(NAP-CC) population transfer. An exponential decrease in the diagonal ν(NAP-CC)/off-diagonal ν(CC-PTZ) intensity ratio was also found for both **3** and **4**, which occurs on the sub-picosecond timescale. Whilst this is potentially indicative of a ν(NAP-CC) → ν(CC-PTZ) population transfer, these ratio changes are convoluted with the IRF and may be a result of the different IVR decay rates of the ν(NAP-CC) and ν(CC-PTZ) modes. Therefore, it cannot be definitively stated if this population transfer is feasible from these ratio changes.

To confirm that the observed anharmonicities and peak pair ratio dynamics do correspond to population transfers, the 2DIR data were modelled with LDA. In **3**, an exponential component was found with a time constant of 4.1 ps which corresponded to decay of the ν($^{12}C^{12}C$) peak pair synchronously with the growth of the ν(^{13}C^{13}C) peak pair, providing further evidence of a ν(CC-PTZ) → ν(NAP-CC) vibrational population transfer (Figure 5.6). The effect of this population transfer on the kinetic traces was found to result in the decay of the off-diagonal mode entering a plateau in the 1.5 – 5 ps time window (Figure 5.7). This indicated that the ν_1(CC-NAP) energy level is being continuously populated during these population times, halting the decay of the peak pair. Similarly, in **4** LDA was able to isolate the ν(CC-PTZ) → ν(NAP-CC) population transfer process, where the ν(^{12}C^{12}C) peak pair growth and the ν(^{13}C^{13}C) peak pair decay occurred simultaneously with a time constant of 2.0 ps. Lifetime density traces were not found which corroborate any ν(NAP-CC) → ν(CC-PTZ) population transfer processes in **3** or **4**. Similarly, the kinetic traces of the off-diagonal ν(CC-PTZ) modes do not exhibit a plateau region which would indicate they are being populated during their vibrational relaxation.

The population transfer requires that the ν(CC-PTZ) and ν(NAP-CC) modes are mutually coupled to a low frequency bath mode. Typically, this will be a vibrational mode of the solvent. In the endothermic ν(^{13}C^{13}C) → ν(^{12}C^{12}C) transition (**4**), the thermally populated solvent modes ($k_bT \approx 200$ cm^{-1}) provide the energy required (*ca.* 60 – 100 cm^{-1}) for the energetically uphill transfer. Conversely, in the reverse exothermic population transfer (**3**), the solvent bath modes accept the excess vibrational energy. The partial delocalisation of the ν(^{12}C^{12}C) and ν(^{13}C^{13}C) modes observed in the DFT calculations may also play a role in facilitating the vibrational population transfer, as each vibration involves motion of the same four carbon atoms. It has been shown previously that spatial overlap of the interacting modes is an important factor in vibrational energy transfer.[38,39]

It has been suggested previously that electronic coupling has an effect on the vibrational relaxation dynamics of coordination compounds.[40] Therefore, it is tentatively proposed that the observed PTZ → NAP directional preference for the population transfer is a result of the electronic coupling of the acetylide groups with the NAP and [Ph-CH$_2$-PTZ] ligands. The electronic structure of the NAP-CC ligand is significantly different to the CC-Ph-CH$_2$-PTZ ligand. Firstly, the NAP acceptor is electron deficient, whilst the PTZ donor is electron rich. Secondly, the C≡C bond in the acceptor is conjugated with both the naphthalene ring and diimide groups, whereas in the donor ligand the π-system is broken by the aliphatic methylene group, and the acetylide is only conjugated with the phenyl ring. These differences in electronic environment may prevent the NAP-CC mode from effectively transferring population across the Pt(II) centre. It is also possible that the rapid ν(CC) → ν(CC/NAP) transfer prevents the NAP-acetylide from taking part in a ν(NAP-CC) → ν(CC-PTZ) population transfer.

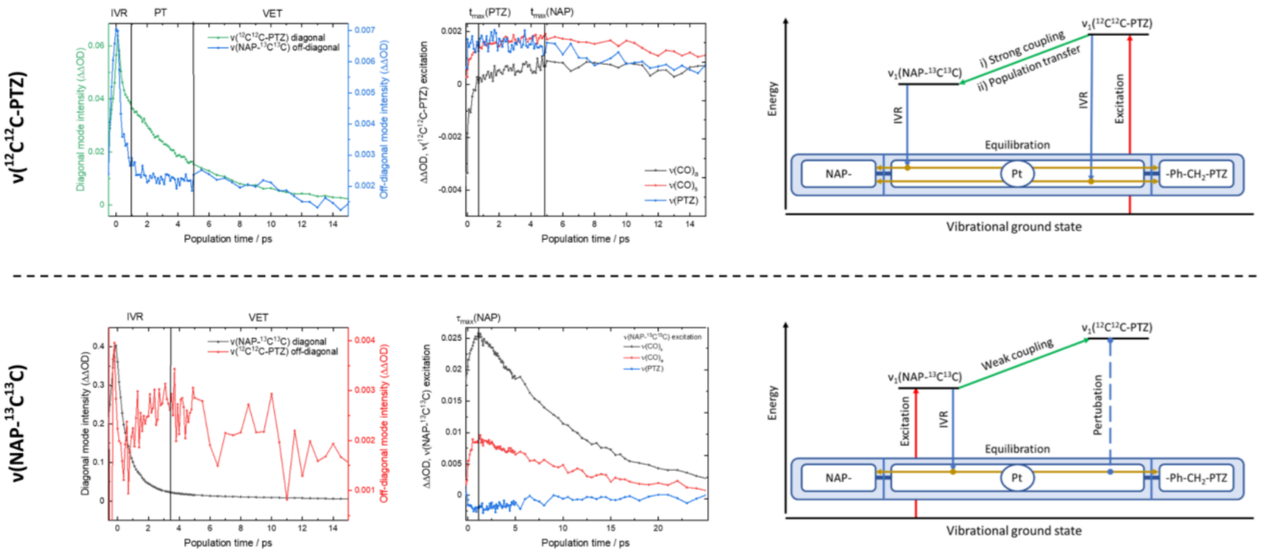

*Figure 5.7 – Kinetic traces and proposed energy level diagrams for vibrational energy redistribution of the acetylide bridge following excitation of the ν(NAP-$^{13}C^{13}C$) and ν($^{12}C^{12}C$-PTZ) vibrations of complex **3**, assigned on the basis of the kinetic traces and Lifetime Density Analysis data. Arrows on the diagram correspond to excitation (red), population transfer/IVR (blue), ultrafast mechanical, dipole-dipole, and anharmonic coupling (green), perturbation of vibrational modes by IVR through low-frequency modes (blue-dash), and vibrational energy transfer to the solvent (orange). The continuum of low frequency modes associated with the IVR process is represented by the blue box.*

Vibrational energy transfer from the acetylide bridge to the ligands

Broadband vibrational excitation of the ν(CC)$_a$ and ν(CC)$_s$ modes in **1** and **2** resulted in the formation of off-diagonal peak pairs in the 1550 – 1710 cm^{-1} region, indicating the acetylide vibrations are coupled to the ligand modes (Figure 5.4A). The most intense off-diagonal peak pairs corresponded to the ν(NAP-Ar), ν(CO)$_s$, and ν(CO)$_a$ modes. These peaks grow in with an initial ultrafast component, as well as a slower component on the picosecond timescale. The ultrafast grow-in, which results in detectable signal at small population times (t_2 < 100 fs) was a result of mechanical, anharmonic and dipole-dipole coupling interactions. The picosecond time constant was ascribed to IVR through low frequency modes from the acetylide bridge. In both **1** and **2**, the peak pair intensity of ν(CO)$_s$ was greater than ν(CO)$_a$, indicating stronger coupling between the acetylide and ν(CO)$_s$ (also shown by the larger value of Δ_{ij} for ν(CO)$_s$). This was potentially a result of the relative orientations of the transition dipole moments for the ν(CO)$_a$ and ν(CO)$_s$ modes, where the ν(CO)$_s$ transition dipole moment is parallel with the transition dipole moment of ν(CC)$_a$. Whereas, the transition dipole moment of the ν(CO)$_a$ is perpendicular to ν(CC)$_a$. Therefore, the ν(CO)$_s$ vibration will have stronger dipole-dipole coupling interaction with ν(CC)$_a$ compared to ν(CO)$_a$/ν(CC)$_a$ (Figure 5.8). The relative peak pair intensities also had a dependence on the isotopic substitution, in **2** the ν(CO)$_s$ peak pair was the most intense, whilst in **1** it was the ν(NAP-Ar) mode. This suggests that isotopic substitution changes the coupling strength between the NAP-acetylide and the naphthalene monoimide groups. However, it is not possible to identify why this occurs from the 2DIR data, and additional DFT calculations of the anharmonic vibrational modes are likely required to further understand the vibrational coupling interactions between these modes.

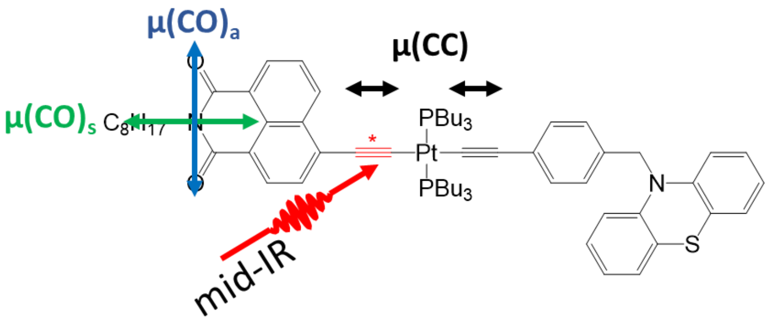

Figure 5.8 – Relative orientations of the transition dipole moments for ν(NAP-^{13}C^{13}C), ν(CO)$_a$ and ν(CO)$_s$ vibrational modes in complex ***3****.*

In **1**, after ultrafast signal formation, the ν(NAP-Ar) off-diagonal peak pair intensity increases with a 1.9 ps time constant. The ν(CO)$_s$ and ν(CO)$_a$ modes also have a second grow in, slower than ν(NAP-Ar), which occurred with a time constant of 2.8 ps. The slower grow in of the CO vibrations is a result of the increased spatial separation from the ν(CC)$_a$ mode. These time constants are consistent with a through-bond IVR process.[41] After IVR is complete, the off-diagonal signals decay with a time constant of 11 ps, ascribed to VET to the solvent, which returns the complex to its vibrational ground state. The off-diagonal signals attributed to the [-Ph-CH$_2$-PTZ] ligand were significantly weaker than the off-diagonal modes of the NAP ligand in **1** and **2**, suggesting that the ν(CC)$_a$ mode was primarily localised on the NAP-acetylide with only a small contribution from the PTZ-acetylide, consistent with the calculated harmonic vibrations.

In **2**, the isotopic substitution resulted in an increase in the ν(CC)$_a$ relaxation rate, indicating stronger coupling between ν(CC)$_a$ and the low-frequency modes within the bridge. As a result, the ν(NAP-Ar) grow-in time constant was less in **2** compared to **1**. The ν(NAP-Ar) peak pair intensity was decreased as a result of isotopic substitution, which suggests the ν(CC)$_a$/ν(NAP-Ar) ultrafast coupling strength is weaker in **2** compared to **1**. These differences were attributed to the 80 cm^{-1} decrease in vibrational frequency. For **1** and **2**, it was not possible to obtain reliable grow in rates for the NAP modes following ν(CC)$_s$ mode due to the small frequency separation between the symmetric and antisymmetric acetylide vibrations.

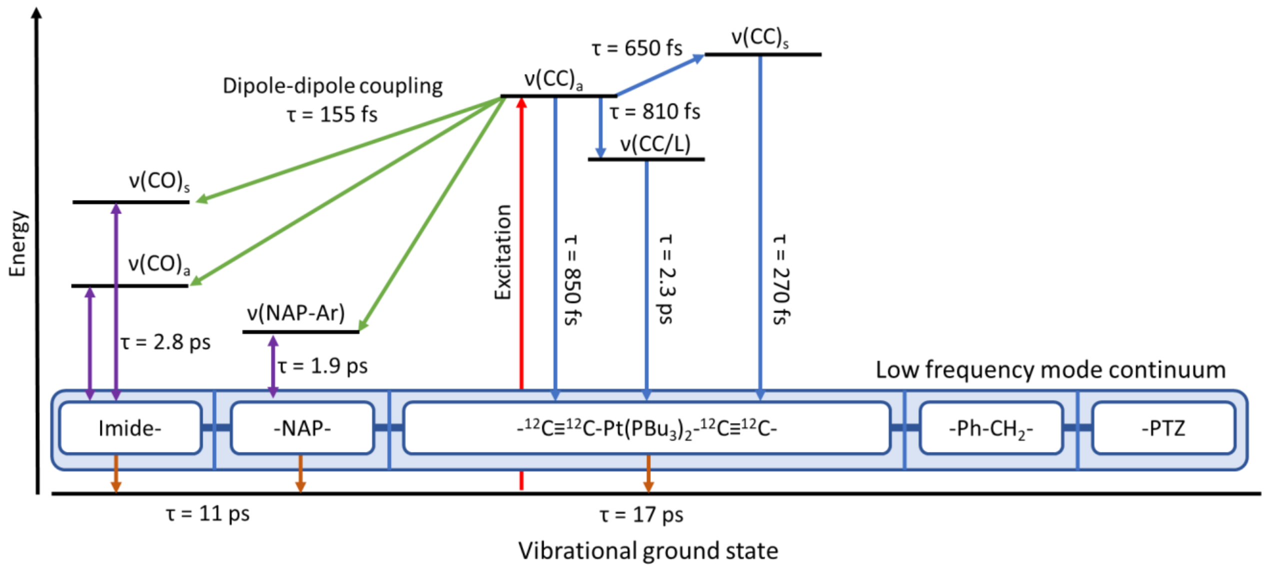

Figure 5.9 – Proposed energy level diagram for vibrational energy redistribution following excitation of the $\nu(CC)_a$ *vibration of complex* ***1****, assigned on the basis of Lifetime Density Analysis data. Arrows on the diagram correspond to excitation (red), population transfer (blue), ultrafast mechanical, dipole-dipole, and anharmonic coupling (green), perturbation of vibrational modes by IVR (purple), and vibrational energy transfer to the solvent (orange). The continuum of low frequency modes associated with the IVR process is represented by the blue box. For complexes* ***2-4****, see Appendix E, fig. E12-E15*

Complex 3

As with **1** and **2**, the off-diagonal signals corresponding to the $\nu(CO)_s$, $\nu(CO)_a$, and ν(NAP-Ar) modes had an ultrafast grow-in, resulting in observable peak pairs by 100 fs (Figure 5.10). This was attributed to mechanical coupling between the $\nu(^{13}C^{13}C)$ and ν(NAP-Ar) mode, as well as dipole-dipole coupling between $\nu(^{13}C^{13}C)$ and the carbonyl modes. The off-diagonal peak pairs have a second, slower grow in which occurs with a time constant of 2.2 ps, which is assigned as IVR from the bridge. The off-diagonal peak pairs then decay by VET to solvent modes with a time constant of 9.6 ps. Off-diagonal peak pairs corresponding to vibrations of the [-Ph-CH_2-PTZ] ligand were also detected, but with very low intensities.

Excitation of the $\nu(^{12}C^{12}C\text{-PTZ})$ mode resulted in a significantly different 2DIR spectrum in the 1550 – 1300 cm^{-1} region compared to $\nu(\text{NAP-}^{13}C^{13}C)$ excitation, where the intensity of the [-Ph-CH_2-PTZ] ligand modes was significantly higher (Figure 5.10). These modes have ground state vibrational frequencies of 1504, 1574, 1602, and 1497 cm^{-1}. The [Ph-CH_2-PTZ] off-diagonal peak pairs were observed following excitation of $\nu(^{12}C^{12}C\text{-PTZ})$ at time delays as short as 100 fs. This shows that the $\nu(^{12}C^{12}C)$ and PTZ modes also have ultrafast mechanical, anharmonic and dipole-dipole coupling interactions. These modes have a secondary grow in with a time constant of 1.0 ps, ascribed as bridge to ligand IVR. These off-diagonal signals then decay with a 9.6 ps time constant as the [-Ph-CH$_2$-PTZ] relaxes by VET to the solvent.

Additionally, it was found that that excitation of the ν(^{12}C^{12}C-PTZ) mode results in the formation of strong off-diagonal signals associated with the NAP ligand whilst excitation of ν(NAP-^{13}C^{13}C) only results in very weak off-diagonal signals for the [-Ph-CH$_2$-PTZ] ligand. This observation is further evidence of vibrational decoupling, where vibrational energy cannot propagate across the Pt(II) centre through the low-frequency modes. This hinders off-diagonal signal formation of the [-Ph-CH$_2$-PTZ] modes following ν(NAP-^{13}C^{13}C) excitation.

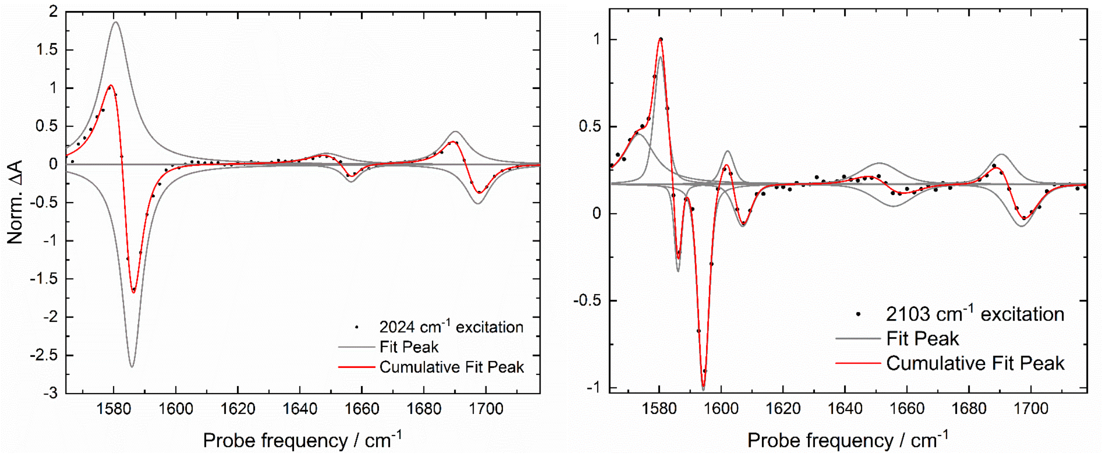

Figure 5.10 – 2DIR spectra of ***3*** *in DCM following excitation of either the ν(NAP-^{13}C^{13}C) or ν(^{12}C^{12}C-PTZ) acetylide vibrations in the off-diagonal 1550 – 1760 cm^{-1} region, demonstrating the difference in off-diagonal signal intensity upon excitation of each acetylide mode.*

The decoupling effect also would also result in weak off-diagonal signal formation for the NAP modes following ν(^{12}C^{12}C-PTZ) excitation. However, the population transfer from ν$_1$(^{12}C^{12}C-PTZ) → ν$_1$(NAP-^{13}C^{13}C) bypasses the vibrational energy transfer barrier imposed by the heavy-metal centre. Thus, after ν$_1$(^{12}C^{12}C-PTZ) excitation, the off-diagonal signals associated with the ν(NAP-Ar) and ν(CO)$_s$ vibrations were observable from 500 fs, and the ν(CO)$_a$ peak pair was observable from 2.0 ps. The relative peak pair intensities of the ν(NAP-Ar) and ν(CO)$_s$, and ν(CO)$_a$ modes were similar to what was observed following direct ν(^{13}C^{13}C-NAP) excitation. The secondary grow in of the ν(NAP-Ar), ν(CO)$_a$, and ν(CO)$_s$ off-diagonal peak pairs was found to occur with a time constant of 2.1 ps, similar to the IVR time constants in **1** and **2**. The off-diagonal NAP signals decay with a time constant of 20 ps.

Complex 4

The dynamics of the NAP ligand modes were similar in **4** to **1** – **3**, the off-diagonal signals of the NAP ligand had an initial ultrafast grow in, attributed to ultrafast anharmonic, mechanical, and dipole-dipole coupling from the ν(NAP-^{12}C^{12}C) mode to the ligand modes. The secondary grow in of the ν(NAP-Ar), $\nu(CO)_a$, and $\nu(CO)_s$ modes occurs with a time constant of 1.1 ps, similar to the IVR dynamics of **1** – **3**. The NAP modes relax to the ground state with a time constant of 11 ps. Similar to **3**, the off-diagonal signals of the [-Ph-CH$_2$-PTZ] group were very weak, providing further evidence of vibrational decoupling.

Due to the Fermi resonance, the ν(CC) and [-Ph-CH$_2$-PTZ] modes are more strongly coupled in **4** compared to **3**. This resulted in an increased rate of off-diagonal signal formation, where the [-Ph-CH$_2$-PTZ] modes are at their maximum intensity by the first measured population time of 100 fs. The [-Ph-CH$_2$-PTZ] modes relax to the vibrational ground state by VET, with a time constant of 8.6 ps. Due to the $\nu(^{13}C^{13}C\text{-PTZ}) \rightarrow \nu(^{12}C^{12}C\text{-NAP})$ population transfer, off-diagonal peak pairs of the NAP vibrational modes also were detected, which form following relaxation of the populated $\nu_1(\text{NAP-}^{12}C^{12}C)$ energy level. The grow in rate (τ = 1.5 ps) of the ν(NAP-Ar), $\nu(CO)_a$, and $\nu(CO)_s$ modes were very similar to direct excitation of $\nu(\text{NAP-}^{12}C^{12}C)$. These modes decay with a VET time constant of 10 ps.

2DIR spectra in the 1320 – 1420 cm^{-1} region

Time domain 2DIR data in the 1320 – 1420 cm^{-1} region were also recorded following excitation of the acetylide modes (Figure 5.11). In this region the spectra are highly convoluted due to the large number of vibrational absorption bands in this region. The 2DIR peak pairs in this region are only detectable following excitation of an acetylide group which is covalently bound to the NAP ligand. This is consistent with the characterisation of the harmonic normal modes, which show that the absorption bands in this region correspond only to vibrations of the NAP ligand. Additionally, this lends further support to the proposal that the Pt(II) centre acts as a vibrational bottleneck, decoupling the dynamics of the [NAP-CC-] and [CC-Ph-CH$_2$-PTZ] ligands.

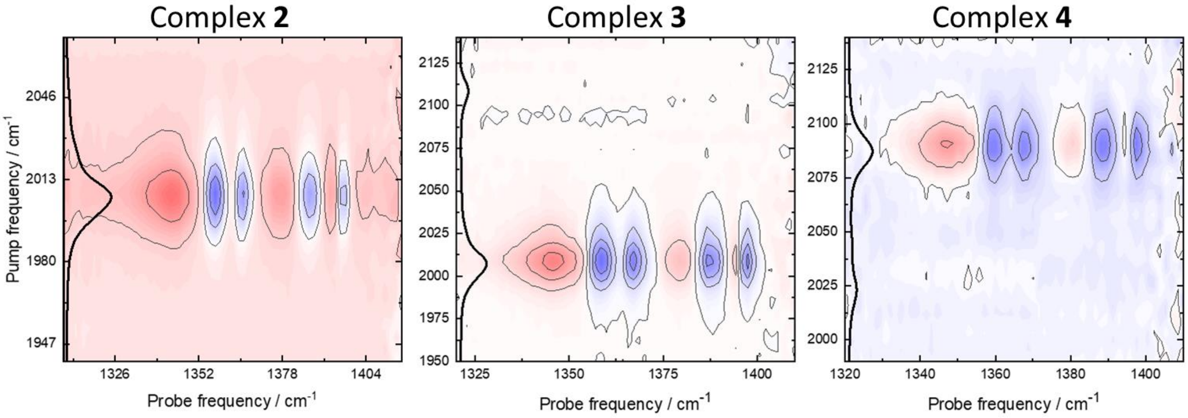

*Figure 5.11 – 2DIR data in the 1320 – 1420 cm^{-1} region of the probe axis. The FTIR absorption spectrum is overlaid over the excitation frequency axis. The broadband pump was centred at 2010 cm^{-1} for **2** and **3**, and 2080 cm^{-1} for **4**. Analogous data was not recorded for **1**.*

In **2**, the off-diagonal NAP modes in this region grow in with a single time constant of 155 fs. Similar to the higher frequency ν(NAP-Ar), ν(CO)$_a$, and ν(CO)$_s$ modes, there was a secondary grow in on a 2 ps timescale, but this LDA component had a very low amplitude. This suggests these modes are primarily coupled with ν(CC)$_a$ by ultrafast coupling mechanisms, such as anharmonic, dipole-dipole, and mechanical coupling, and that IVR through low-frequency modes only weakly perturbs these modes. The NAP modes in this region decay by VET to the solvent with a time constant of 12 ps. In **3**, the NAP modes grow in with a time constant of 195 fs, as with **2**, the IVR component is very weak compared to the higher frequency (NAP-Ar), ν(CO)$_a$, and ν(CO)$_s$ vibrations. The VET time constant was 10 ps. In **4**, the grow in time constant was 171 fs, followed by a VET time constant of 10 ps. As with **2** and **3**, the IVR component in this region had a very weak amplitude.

5.4. Conclusions

Four Pt(II) *trans*-acetylide donor-bridge-acceptor complexes have been studied by 2DIR spectroscopy to determine the effect of isotopic substitution on their vibrational dynamics. This is an important field of study, as these acetylide modes have been shown to alter the rate of electron transfer in these D-B-A complexes. The FTIR spectra reveal the effect of isotopic substitution on the [-CC-Pt(PBu$_3$)$_2$-CC-] bridge, where carbon-13 labelling of both acetylide groups results in an 80 cm^{-1} decrease in the vibrational frequency of the acetylide vibrations. Labelling of only one acetylide group partially decouples these group vibrations, resulting in largely localised ν(^{12}C^{12}C) and ν(^{13}C^{13}C) modes with only weak contributions from the other acetylide group. If the carbon-13 labelled acetylide is adjacent to the [-Ph-CH$_2$-PTZ] group, a Fermi resonance is introduced in the vibrational ground state, resulting in intensity sharing between the ν(^{13}C^{13}C-PTZ) stretching vibration and a combination mode. The oscillator strength of the localised acetylide transitions was found to be dependent on the electronic coupling of the acetylide group with the adjacent ligand, where proximity to the NAP ligand resulted in more intense absorption bands. In future, these relative oscillator strengths could potentially be used to further characterise the TRIR spectra of the excited state following 400 nm excitation.

2DIR experiments were used to show the large influence isotopic substitution has on the vibrational dynamics of the D-B-A complex. In all complexes, the initial inhomogeneity of the vibrational excited state lineshapes was found to be small, and the rate of spectral diffusion following IR excitation was dependent on the local molecular environment. An increased rate of spectral diffusion was found in acetylide groups which are in resonance with the NAP π-system, tentatively ascribed to the strong electronic coupling of the acetylide with the NAP moiety.

Acetylide groups adjacent to the NAP ligand were found to undergo population transfer to a second mode 8 cm^{-1} lower in frequency, tentatively assigned as an anharmonic combination or overtone mode; ν(CC/NAP). This leads to a decrease in the apparent anharmonic shift of the acetylide peak pair as the ESA band shifts to higher frequency during this transition. The vibrational frequency of the second mode in all complexes was ν(CC/NAP) = ν(NAP-CC) – 8 cm^{-1}.

Asymmetric isotopic substitution of the complex was found to decouple the dynamics of the low-frequency modes within the bridge, where vibrational energy propagation by IVR was inhibited by the Pt(II) centre, which acts as a 'vibrational bottleneck'. It has been demonstrated herein that this vibrational energy barrier is overcome by solvent assisted population transfer between the high frequency acetylide stretching vibrations. The population transfer pathways were evidenced by the off-diagonal anharmonicities and relaxation dynamics of the $\nu(^{12}C^{12}C)$ and $\nu(^{13}C^{13}C)$ modes, which indicate a directional preference for the ν(CC-PTZ) → ν(NAP-CC) transfer. Evidence for the reverse ν(NAP-CC) → ν(CC-PTZ) transfer was not found. The directional selectivity is proposed to be a result of the different electronic coupling strengths within the [NAP-CC-] and [-CC-Ph-CH_2-PTZ] ligands. Time constants for these processes were obtained by Lifetime Density Analysis and were found to range from 1 – 5 ps. The population transfer results in delayed relaxation of the off-diagonal ν(NAP-CC) peak pair, where a plateau in the kinetic trace was observed due to re-population of the $\nu = 1$ energy level.

Excitation of the $\nu(^{12}C^{12}C)$ or $\nu(^{13}C^{13}C)$ modes within an asymmetrically labelled acetylide bridge was found to result in ultrafast formation of off-diagonal signals of the ligand modes. This was a result of ultrafast coupling interactions between the acetylide bridge and the ligands, such as mechanical, anharmonic, or dipole-dipole interactions. Following relaxation of the $\nu_1(^{12}C^{12}C)$ or $\nu_1(^{13}C^{13}C)$ excited state to low-frequency modes, vibrational energy propagates from the bridge to the terminal ends of the complex, resulting in a secondary grow-in of the ligand off-diagonal peak pairs on the picosecond timescale. After vibrational energy redistribution is complete, the complex relaxes to the equilibrium ground state by vibrational energy transfer from the low-frequency modes of the complex to the solvent, which occurs with time constants from 10 – 30 ps.

This work adds to a growing body of research into the fundamental vibrational dynamics of coordination complexes. A detailed understanding of these dynamics is required for the future development of transition metal complexes as photoactive components in artificial photosynthesis. Here it is demonstrated how vibrational energy transfer can be inhibited by the heavy-metal centre in a donor-bridge-acceptor assembly, as well as how two mutually coupled high frequency modes can circumvent this insulating effect by vibrational population transfer. These D-B-A complexes provide new insights into vibrational energy redistribution from high-frequency vibrations which have been shown to modulate electron transfer. The results of this work will be used in future studies to understand the role of vibrational energy redistribution in the metal-to-ligand charge transfer and charge separated electronic excited states – with the aim of identifying the vibrational modes which can interact with the electron transfer reaction coordinate. Ideally, this information will aid in the design of new D-B-A complexes where electron transfer is promoted by vibrational excitation.

References

1 Z. Ma, P. Antoniou, P. Zhang, S. S. Skourtis and D. N. Beratan, *J. Chem. Theory Comput.*, 2018, **14**, 4818–4832.

2 C. Bohne, Q. Pan, P. Ceroni, K. Börjesson, J. Rohacova, F. Lewis, A. Vlcek, D. M. Bassani, F. Würthner, A. Sartorel, A. P. de Silva, D. Nocera, F. Scandola, C. Lemon, C. Allain, G. W. Brudvig, S. Marchesan, V. Sundstrom, S. Campagna, S. W. Sheehan, P.-A. Plötz, F. Monti, J. M. Kelly, E. Gibson, M. Maneiro, A. Harriman, A. Ruggi, E. Galoppini, R. Thummel, J. Weinstein, J. Vos, O. Ishitani, D. Gust and A. Díaz-Moscoso, *Faraday Discuss.*, 2015, **185**, 187–217.

3 S. Valianti and S. S. Skourtis, *Mol. Phys.*, 2019, **117**, 2618–2631.

4 I. V. Rubtsov, *Nature Chem.*, 2015, **7**, 683–684.

5 Z. Lin, C. M. Lawrence, D. Xiao, V. V. Kireev, S. S. Skourtis, J. L. Sessler, D. N. Beratan and I. V. Rubtsov, *J. Am. Chem. Soc.*, 2009, **131**, 18060–18062.

6 Y. Yue, T. Grusenmeyer, Z. Ma, P. Zhang, R. H. Schmehl, D. N. Beratan and I. V. Rubtsov, *Dalton Trans.*, 2015, **44**, 8609–8616.

7 P. A. Scattergood, M. Delor, I. V. Sazanovich, O. V. Bouganov, S. A. Tikhomirov, A. S. Stasheuski, A. W. Parker, G. M. Greetham, M. Towrie, E. S. Davies, A. J. H. M. H. M. Meijer and J. A. Weinstein, *Dalton Trans.*, 2014, **43**, 17677–17693.

8 M. Delor, P. A. Scattergood, I. V. Sazanovich, A. W. Parker, G. M. Greetham, A. J. H. M. Meijer, M. Towrie and J. A. Weinstein, *Science*, 2014, **346**, 1492–1495.

9 M. Delor, T. Keane, P. A. Scattergood, I. V. Sazanovich, G. M. Greetham, M. Towrie, A. J. H. M. Meijer and J. A. Weinstein, *Nature Chem.*, 2015, **7**, 689–695.

10 P. A. Scattergood, M. Delor, I. V. Sazanovich, M. Towrie and J. A. Weinstein, *Faraday Discuss.*, 2015, **185**, 69–86.

11 M. Delor, S. A. Archer, T. Keane, A. J. H. M. H. M. Meijer, I. V. Sazanovich, G. M. Greetham, M. Towrie and J. A. Weinstein, *Nature Chem.*, 2017, **9**, 1099–1104.

12 A. J. Sadler, The University of Sheffield, 2018.

13 P. M. Donaldson, G. M. Greetham, D. J. Shaw, A. W. Parker and M. Towrie, *J. Phys. Chem. A*, 2018, **122**, 780–787.

14 P. Hamm and M. Zanni, *Concepts and Methods of 2D Infrared Spectroscopy*, Cambridge University Press, Cambridge, 2011.

15 C. Slavov, H. Hartmann and J. Wachtveitl, *Anal. Chem.*, 2015, **87**, 2328–2336.

16 J. J. Snellenburg, S. P. Laptenok, R. Seger, K. M. Mullen and I. H. M. van Stokkum, *J. Stat. Softw.*, 2012, **49**, 1–22.

17 S. A. Archer, T. Keane, M. Delor, A. J. H. M. Meijer and J. A. Weinstein, *Inorg. Chem.*, 2016,

55, 8251–8253.

18 J. S. Lipkin, R. Song, E. E. Fenlon and S. H. Brewer, *J. Phys. Chem. Lett.*, 2011, **2**, 1672–1676.

19 S. T. Roberts, J. J. Loparo and A. Tokmakoff, *J. Chem. Phys.*, 2006, **125**, 084502.

20 K. Lazonder, M. S. Pshenichnikov and D. A. Wiersma, *Opt. Lett.*, 2006, **31**, 3354.

21 W. P. de Boeij, M. S. Pshenichnikov and D. A. Wiersma, *J. Phys. Chem.*, 1996, **100**, 11806–11823.

22 T. L. C. Jansen, D. Cringus and M. S. Pshenichnikov, *J. Phys. Chem. A*, 2009, **113**, 6260–6265.

23 L. M. Kiefer and K. J. Kubarych, *J. Phys. Chem. A*, 2015, **119**, 959–965.

24 C. M. Olson, A. Grofe, C. J. Huber, I. C. Spector, J. Gao and A. M. Massari, *J. Chem. Phys.*, 2017, **147**, 124302.

25 L. M. Kiefer, J. T. King and K. J. Kubarych, *J. Phys. Chem. A*, 2014, **118**, 9853–9860.

26 L. M. Kiefer and K. J. Kubarych, *Coord. Chem. Rev.*, 2018, **372**, 153–178.

27 L. M. Kiefer, J. T. King and K. J. Kubarych, *Acc. Chem. Res.*, 2015, **48**, 1123–1130.

28 V. C. A. A. Taylor, D. Tiwari, M. Duchi, P. M. Donaldson, I. P. Clark, D. J. Fermin and T. A. A. A. Oliver, *J. Phys. Chem. Lett.*, 2018, **9**, 895–901.

29 A. A. Bakulin, O. Selig, H. J. Bakker, Y. L. A. A. Rezus, C. Müller, T. Glaser, R. Lovrincic, Z. Sun, Z. Chen, A. Walsh, J. M. Frost, T. L. C. C. Jansen, C. Mu, T. Glaser, R. Lovrincic, Z. Sun, Z. Chen, A. Walsh, J. M. Frost and T. L. C. C. Jansen, *J. Phys. Chem. Lett.*, 2015, **6**, 3663–3669.

30 M. Fedoseeva, M. Delor, S. C. Parker, I. V. Sazanovich, M. Towrie, A. W. Parker and J. A. Weinstein, *Phys. Chem. Chem. Phys.*, 2015, **17**, 1688–1696.

31 I. V. Rubtsov and R. M. Hochstrasser, *J. Phys. Chem. B*, 2002, **106**, 9165–9171.

32 Y. Wu, P. Yu, Y. Chen, J. Zhao, H. Liu, Y. Li and J. Wang, *J. Phys. Chem. Lett.*, 2019, **10**, 1402–1410.

33 D. G. Kuroda, P. K. Singh and R. M. Hochstrasser, *J. Phys. Chem. B*, 2013, **117**, 4354–4364.

34 M. Delor, I. V. Sazanovich, M. Towrie, S. J. Spall, T. Keane, A. J. Blake, C. Wilson, A. J. H. M. Meijer and J. A. Weinstein, *J. Phys. Chem. B*, 2014, **118**, 11781–11791.

35 L. P. DeFlores, Z. Ganim, S. F. Ackley, H. S. Chung and A. Tokmakoff, *J. Phys. Chem. B*, 2006, **110**, 18973–18980.

36 S. Park and M. Ji, *ChemPhysChem*, 2011, **12**, 799–805.

37 H. J. B. Marroux and A. J. Orr-Ewing, *J. Phys. Chem. B*, 2016, **120**, 4125–4130.

38 V. M. Kasyanenko, Z. Lin, G. I. Rubtsov, J. P. Donahue and I. V. Rubtsov, *J. Chem. Phys.*, 2009, **131**, 154508.

39 J. C. Phys, R. Bloem, A. G. Dijkstra, C. Jansen, J. Knoester, T. L. C. Jansen and J. Knoester, *J. Chem. Phys.*, 2008, **129**, 055101.

40 V. M. Kasyanenko, S. L. Tesar, G. I. Rubtsov, A. L. Burin and I. V. Rubtsov, *J. Phys. Chem. B*, 2011, **115**, 11063–11073.

41 I. V. Rubtsov and A. L. Burin, *J. Chem. Phys.*, 2019, **150**, 020901.

Chapter 6. Conclusions

Artificial photosynthesis is a promising emergent technology that could enable us to efficiently convert CO_2, a waste greenhouse gas, into useful industrial feedstocks or solar fuels as replacements to the environmentally damaging and rapidly depleting fossil fuels. To achieve this, stable complexes which efficiently harvest visible light, transfer electrons to a catalytic centre, and then perform CO_2 reduction catalysis are required. This undertaking requires a strong understanding of the underlying excited state dynamics, electrochemical processes, and catalytic mechanisms, which this thesis contributes to. Through further development of this field, new photochemical and electrochemical systems will arise that convert CO_2 and H_2O to combustible fuels, allowing for the creation of true carbon neutral energy sources.

The objective of this thesis was to build on our existing knowledge of how the structure of the light harvesting and CO_2 reducing components of an artificial photosynthetic system can affect its capability to perform catalytic reactions. This has been achieved through a combined approach including electrochemical and catalytic studies, as well as ultrafast time-resolved spectroscopy. As stated in the introduction, the aims of this thesis were summarised as five research questions, the outcomes of which are given below.

1) How does the catalytic activity of a Re or Mn Lehn-type catalyst change if dimerisation is inhibited by introduction of sterically hindering groups?

The introduction of sterically hindering groups to the 6,6′-positions of the bipyridyl ring in a $[M(L_2)(CO)_3X]$ (M/X = Mn/Br, Re/Cl) complex was found to significantly alter the catalytic activity of the Mn(I) and Re(I) catalysts. The selected sterically hindering group was a tertiary amide; N-(p-hexylphenyl)-N-ethyl-amide. The introduction of these groups created significant steric bulk around the coordination centre. In the Mn(I) complex, this prevented dimerisation of the $[Mn(L_2)(CO)_3]^{\cdot -}$ complex, a key intermediate in the formation of the active CO_2 reduction catalyst. The prevention of Mn-Mn dimer formation significantly reduced the electrochemical potential required to form the active catalyst when compared to non-sterically hindered complexes. This was in addition to the electron withdrawing effect of the amide groups, which further reduced the reduction potential. The estimated $\log(TOF_{max})$ was larger than previously reported catalysts under the same catalytic conditions, a result of the decreased potential required for active catalyst formation. The Mn(I) catalyst was stable under electrolysis, which resulted in the formation of CO as the reduction product. Furthermore, the catalyst was photosensitised with an earth-abundant chromophore, tetraphenylporphyrin zinc(II), which also resulted in the production of CO.

A decreased second reduction potential was also found for the Re(I) complex, which results from the electron withdrawing effect of the amide groups. The Re(I) catalyst was found to be inactive for photochemical CO_2 reduction, a result of the short excited state lifetime, preventing diffusion controlled electron transfer. Time resolved studies of the Re(I) complex in the UV-vis and IR spectral regions following 400 nm excitation could not ascertain the origin of the reduction in excited state lifetime.

Overall, the introduction of sterically hindering groups significantly improved the performance of the Mn(I) catalyst for CO_2 reduction. As a result, $[Mn(HPEAB)(CO)_3Br]$ is a promising compound for application in artificial photosynthetic systems which utilise only Earth-abundant elements. The Re(I) complex, which does not have the advantage of Earth-abundance, may also be useful in future research. However, the photochemical inactivity of the complex does limit its relevance for further development of artificial photosynthesis.

2) Can we introduce new functionality to Mn Lehn-type catalysts without affecting their ability to perform electro- or photochemical CO_2 reduction?

Through analysis of a Mn(I) catalyst functionalised with $Et_2O_3PCH_2$- groups, it was found that the inductive effect of an electron withdrawing substituent can be decoupled from an aromatic diimine ligand through the introduction of a CH_2 spacer group. This was evidenced through comparison of the phosphonate functionalised complex with $[Mn(dmbpy)(CO)_3Br]$, where both of these species have very similar spectroscopic and electrochemical properties. The electrochemical catalytic performance, quantified with $\log(TOF_{max})$, of the phosphonate catalyst was greater than the previously reported dmbpy catalyst, but at the cost of a higher overpotential. However, the difference was small, showing that that the phosphonate ester group was successfully introduced without affecting the capacity of the Mn(I) complex to reduce CO_2.

The phosphonate ester groups imparted water solubility onto the Mn(I) catalyst, allowing for photocatalytic CO_2 reduction in aqueous solution when combined with a water-soluble porphyrin. This was the first photochemical CO_2 reduction with a $[Mn(L_2)(CO)_3Br]$ catalyst which operates photochemically in aqueous solution under red-light irradiation, which represents a significant achievement for the development of catalytic systems with minimal environmental impact. The choice of irradiation wavelength was critical here, as higher energy wavelengths would have resulted in photolysis of the Mn(I) catalyst. Whilst the rate of CO production was slow when compared to many other CO_2 reducing systems, which was attributed to inefficient electron transfer from the porphyrin photosensitiser, the catalyst was recyclable upon re-purging the reaction mixture with CO_2.

As such, this system may be useful for potential applications of CO which require small volumes, but continuous supply.

In the specific case of electrochemical CO_2 reduction with [Mn(phos-bpy)$(CO)_3$Br], the introduction of the CH_2 spacer is potentially a disadvantage, where use of 4,4′-ethylphosphonato-2,2′-bipyridyl as the diimine ligand instead would likely result in an increase in catalytic performance through reduction of the required reduction potential for active catalyst formation. However, in future, this decoupling effect may be useful when applied to functional groups that are very electron withdrawing or donating, where the inductive effect is sufficiently strong to deactivate the catalytic activity. Furthermore, the introduction of methylene spacer groups could allow for the development of CO_2 reduction catalysts which have dual functionality. For example, a sterically hindering amide in the 6,6′-positions with a decoupled water-solubilising group in the 4,4′-positions could allow for the development of more effective molecular catalysts. Furthermore, as the CH_2 spacer electronically decoupled the new functional group and the bipyridyl ring, its incorporation into an Mn(I) complex prevented red-shifting of the MLCT / XLCT absorption band of the complex. This increases the available range of photosensitisers that can be used without leading to photolysis of the catalyst.

3) How effective are earth-abundant Zn porphyrin complexes at photosensitising Mn Lehn-type catalysts in aqueous and organic solution?

Two Zn(II) porphyrin complexes have been utilised as photosensitisers in this thesis, tetraphenylporphyrin zinc(II) and tetra(N-methyl-4-pyridyl)porphyrin zinc(II) tetrachloride. These complexes, which are able to absorb light at 625 nm, could photosensitise Mn(I) catalysts in organic and aqueous solution – allowing for CO_2 to CO reduction to take place. However, in the case of [Mn(HPEAB)$(CO)_3$Br] and ZnTPP the driving force for intermolecular electron transfer was found to be weak. Therefore, in catalysts which are more electron rich or more difficult to reduce, the porphyrin photosensitisers may not be able to participate in the required electron transfers. Furthermore, [ZnTMPyP]Cl_4 was found to be unstable under catalytic conditions, where it was photoreduced in the presence of a sacrificial donor under 625 nm irradiation. This propensity to undergo photoreduction demonstrates a further disadvantage of porphyrin photosensitisers. Whilst porphyrin complexes are useful photosensitisers in lab-scale catalytic studies, in an idealised artificial photosynthetic system, which utilises Mn(I) catalysts, a more stable photosensitiser is likely required. Therefore, the development of novel photosensitisers which are only comprised of Earth-abundant elements, can harvest wavelengths where the Mn(I) catalyst does not absorb, and are able to effectively photoreduce the catalyst will likely be a required avenue of future research in artificial photosynthesis.

4) Is there a link between the structure of a [Re(L_2)($CO)_3$Cl] CO_2 reduction catalyst and its excited state and vibrational dynamics?

The excited state dynamics of three Re(I) CO_2 reduction catalysts have been studied by time-resolved infrared spectroscopy. 400 nm excitation of [Re(HPEAB)($CO)_3$Cl] resulted in formation of a triplet MLCT/XLCT state, which forms by intersystem crossing from the MLCT/XLCT singlet state. The triplet state vibrationally cools, and then relaxes to the ground state with a 2 ns time constant. The transient IR spectrum of the thermally equilibrated ^{3}MLCT/XLCT state was significantly different to previously reported complexes, which was attributed to reduced solvent-induced line broadening. Vibrational excitation of the symmetric CO stretching vibration in the electronic ground and excited states resulted in very similar dynamics to previously reported Re(I) complexes. This suggests that the origin of the fast non-radiative decay of the ^{3}MLCT/XLCT excited state does not also affect the vibrational relaxation mechanism of the complex.

Replacement of the bipyridyl ligand with a red-light harvesting bis(mesitylimino)acenaphthene ligand resulted in significant changes to the visible light absorption spectrum. Three types of charge transfer transition were found, corresponding to MLCT/XLCT, ILCT, and MLCT. 400 nm excitation was found to produce a highly excited MLCT singlet state, which rapidly decays to the lowest energy singlet excited state, characterised as ^{1}MLCT/XLCT with the aid of DFT calculations. Immediately after intersystem crossing, a single triplet excited state was detected in [Re(mesBIAN)($CO)_3$Cl]. Whilst the complex was vibrationally hot, this triplet was able to internally convert to a second triplet state 979 cm^{-1} higher in energy. Tentatively, this was proposed to be an equilibrium process, which results in a distribution of excited state population that favours T_2 over T_1. After vibrational cooling was complete, this internal conversion process halted, and the two triplet states decayed independently to the ground state with a convoluted time constant of 2.9 ns. This demonstrated the importance of molecular vibrations in mediating the interconversion of excited state species. In the azide substituted complex, [Re(4-mesBIAN-N_3)($CO)_3$Cl], similar dynamics were observed. However, the convoluted transient absorption envelope prevented accurate characterisation of the triplet states formed following 400 nm excitation as well as their dynamics on the picosecond timescale.

In the electronic ground state, the vibrational dynamics of the carbonyl group vibrations were very similar to previously reported Re(I) complexes. The vibrational coupling strength between the aromatic modes of the mesBIAN ligand and the CO ligands was also analysed and found to be weak. Substitution of the mesBIAN ligand with an azide group was found to significantly promote vibrational energy transfer from the aromatic ligand to the carbonyl groups. This was attributed to a direct transfer of vibrational population from the excited azide antisymmetric stretching vibration to the carbonyl modes. The coupling from the CO ligands to the N_3 group was found to be weak, as the complex was not sufficiently excited to complete the endothermic $\nu(CO) \rightarrow \nu_{as}(N_3)$ population transfer.

For both mesBIAN-R complexes, preliminary studies were carried out on vibrational energy redistribution in the triplet excited states present 500 ps after 400 nm excitation. The excited state 2DIR data suggested that excitation of the triplet state(s) with an IR pulse opens an internal conversion pathway between triplets of similar energy, allowing for re-equilibration of the excited state population between the first and second triplet excited states. This further demonstrated the important role molecular vibrations can have in artificial photosynthetic systems.

Whilst progress has been made on understanding the link between structural modification and excited state dynamics of the Re(I) complexes, this study has significant potential for further development. For example, the chemistry of the bipyridyl diimine ligand is very well developed, hence there are many other complexes with the general structure $[Re(R_2\text{-bpy})(CO)_3Cl]$ which could be studied by time-resolved spectroscopy to understand how different functional groups can influence the dynamics of the complex following visible light excitation. In time, this may allow for connections to be made between the molecular structure and the capacity of the complex to perform photochemical CO_2 reduction.

The mesBIAN complexes also present an excellent opportunity for future research, where our understanding of the excited state dynamics of the Re(I) complex would significantly benefit from additional time-resolved spectroscopy experiments. For example, the use of red-light (*ca*. 600 nm) excitation pulses could allow for new insights into the dynamics of red-light harvesting photosensitisers. Furthermore, the vibrational dynamics of the functionalised mesBIAN ligand have significant potential for further experiments. For example, studies could be conducted where the azide group is replaced with an ester, or other vibrational reporting group to further study the vibrational population transfer pathway reported herein. In particular, a functional group with a strong vibrational oscillator strength could allow for study of this energy transfer in the electronic excited state, which was not possible with the azide group. Finally, the observed ability of vibrational excitation to induce internal conversion between triplet states in the $[Re(mesBIAN)(CO)_3Cl]$ complexes is highly intriguing, and further experiments should be done in future to determine if this does take place, and how the process can be used to control the formation of different triplet excited states within $[Re(L_2)(CO)_3Cl]$ complexes. A suggested analyte complex for future study was $[Re(4\text{-mesBIAN-}CO_2Et)(CO)_3Cl]$. This complex would be interesting as the ester functional group is an excellent reporter for vibrational spectroscopy, this could allow for perturbation of this mode in the electronic excited state. Furthermore, as the ester vibration is at lower frequencies than the carbonyl ligand modes, it would provide an interesting comparison to the vibrational dynamics observed in the azide complex.

5) How do the coupling interactions between high-frequency acetylide vibrations affect the redistribution of vibrational energy in a Pt(II) donor-bridge-acceptor complex?

2DIR spectroscopy has been used to interrogate the fundamental vibrational dynamics of four Pt(II) *trans*-acetylide donor-bridge-acceptor complexes. The mechanism of vibrational energy redistribution following excitation of the acetylide groups was found to take place by transfer from the high frequency modes to other coupled high frequency modes, as well as IVR to low-frequency modes of the complex. The vibrational dynamics were modified by labelling the acetylide groups with carbon-13. Contrary to expectations, single-site isotopic substitution did not fully decouple the vibrational dynamics of the two ligands. Instead, vibrational population transfer from the PTZ-acetylide to the NAP-acetylide takes place – this strong coupling interaction bypasses the vibrational energy bottleneck imposed by the Pt(II) centre. However, this coupling was much weaker if the NAP-acetylide was first vibrationally excited, revealing a dependence of the vibrational dynamics on which of the partially decoupled modes was initially excited. These dynamics demonstrate how vibrational coupling interactions between functional groups can be perturbed by isotopic substitution, and how 2DIR spectroscopy can be applied to reveal how two ‘partially decoupled’ modes interact with one another through anharmonic perturbation of the potential energy surface as well as vibrational population transfer.

The charge separation dynamics of the Pt(II) donor-bridge-acceptor complexes studied in chapter 4 can be influenced by mode-specific IR excitation. However, the mechanism of this effect is not yet fully understood. This study of the electronic ground state lays the foundation for future experiments, where this work could be further developed with excited state 2DIR, to determine if the same partial decoupling of the acetylide modes also occurs in the electronic excited state. Furthermore, the effect of IR excitation of each decoupled acetylide mode on the charge separation process can be determined, with the aim of identifying which acetylide vibration is more closely related to the ‘IR-control’ effect. This could lead to the design of new donor-bridge-acceptor complexes where the charge separation pathway can be selected for over non-productive excited state relaxation mechanisms, which would be important for the development of efficient systems for photochemical artificial photosynthesis.

Appendix A – List of abbreviations, symbols, and units

Abbreviations

2DIR	Two-dimensional infrared
A	Absorbance
A	Arrhenius pre-exponential term
ADP	Adenosine diphosphate
ATP	Adenosine triphosphate
BIH	1*H*-benzoimidazole
bpy	2,2′-bipyridine
bpy-acid	4,4′-biscarboxy-2,2′-bipyridine
bpy-ester	4,4′-bis(ethoxy-ester)-2,2′-bipyridine
c	Concentration
Cat	Catalyst
CLF	Central Laser Facility
CSS	Charge-separated state
CT	Charge transfer
CV	Cyclic voltammetry
d	doublet
DAS	Decay associated spectrum
D-B-A	Donor-bridge-acceptor
DCM	Dichloromethane
DFT	Density functional theory
dmbpy	4,4′-dimethyl-2,2′-bipyridine
DMF	Dimethylformamide
DMSO	dimethylsulphoxide
e^-	Electron
$E^{1/2}$	Electrochemical half-potential
EAS	Evolution associated spectrum
E_{ox}	Oxidation potential
$E_{p,a}$	Anodic peak potential
$E_{p,c}$	Cathodic peak potential
eq	Equivalents
E_{red}	Reduction potential
ES	Electrospray

ES-2DIR	Excited state state two-dimensional infrared
ET	Electron transfer
Et	Ethyl
Fc	Ferrocene
Fc$^+$	Ferrocenium
FD	Frequency domain
FFCF	Frequency-frequency correlation function
fs	Femtosecond
FTIR	Fourier transform infrared
GLA	Global lifetime analysis
GS-2DIR	Ground state two-dimensional infrared
GTA	Global target analysis
Hex	Hexyl
HOMO	Highest occupied molecular orbital
HPEAB	6,6′-{N-(4-hexylphenyl)-N(ethyl)-amido}-2,2′-bipyridine
I	Intensity (of light) / Current (Electrical)
IC	Internal conversion
ILCT	Intraligand charge transfer
^{i}Pr	Isopropyl
IR	Infrared
IR-SEC	Infrared-spectroelectrochemistry
ISC	Intersystem crossing
IVR	Intramolecular vibrational redistribution
J	Coupling Constant (NMR) / Joule (Energy)
k	Rate constant
K	Equilibrium constant
l	Path length
Laser	Light Amplification by Stimulated Emission of Radiation
LDA	Lifetime density analysis
LF	Low frequency mode
LLCT	Ligand to ligand charge transfer
LMCT	Ligand to metal charge transfer
LUMO	Lowest unnocupied molecular orbital
m	multiplet
M	Molecule
Me	Methyl

MeCN	Acetonitrile
mesBIAN	Bis(mesitylimino)acenaphthene
mes-bpy	6,6′-mesityl-2,2′-bipyridine
MLCT	Metal-to-ligand charge transfer
M_r	Relative molecular mass
MS	Mass spectrometry
$NADP^+$	Nicotinamide adenine dinucleotide phosphate
NADPH	Reduced nicotinamide adenine dinucleotide phosphate
NAP	1,8-napthalene monoimide
NHE	Normal hydrogen electrode
NMR	Nuclear Magnetic Resonance
Oct	Octyl
OD	Optical density
Phen	1,10′-phenanthroline
Phos-bpy	4,4′-bis(Ethoxyesterphosphonato-methylene)-2,2′-bipyridine
PPy	Phenylpyridine
PS	Photosensitiser
PSI	Photosystem I
PSII	Photosystem II
PT	Population transfer
PTZ	Phenothiazine
Q	Quencher
r.t.	Room temperature
RAL	Rutherford Appleton Laboratory
Redox	Reduction-oxidation
RuBisCO	Ribulose-1,5-bisphosphate carboxylase/oxygenase
s	singlet (NMR)
S_0	Singlet ground state
SCE	Standard calomel electrode
SD	Sacrificial donor
S_n	Singlet excited state
STFC	Science and Technologies Facilities Council
t	triplet
T	Transmittance
t_1	Time delay between 1st and 2nd pump pulses in TD-2DIR
t_2	Time delay between and 2nd pump pulse and the probe pulse in TD-2DIR

t_3	Time delay between and the probe pulse and detection of the emitted signal field in TD-2DIR
TA	Transient absorption
^{t}Bu	Tertiary butyl
TD	Time domain
TEA	Triethylamine
TEOA	Triethanolamine
Terpy	Terpyridyl
TFA	Trifluoroacetic acid
THF	Tetrahydrofuran
TLC	Thin-layer chromatography
TMPyP	Tetra(N-methyl-4-pyridyl)porphyrin
TMS	Trimethylsilyl
T_n	Triplet excited state
TOF	Time of flight
TOF	Turnover frequency
TOF_0	Turnover frequency at zero overpotential
TOF_{max}	Highest turnover frequency at optimum overpotential
TON	Turnover number
TPP	Tetraphenylporphyrin
TRIR	Time resolved infrared
UV	Ultraviolet
UV-vis	Ultraviolet-visible
VET	Intermolecular vibrational energy transfer
XLCT	Halide to ligand charge transfer
ΔA	Differential absorbance
$\Delta G^‡$	Gibbs energy of activation
ΔG_{et}	Gibbs energy of electron transfer

Symbols

$\tilde{v}$	Wavenumber
Δ	Anharmonicity
δ	Chemical shift
Δ_{ii}	Diagonal anharmonicity
Δ_{ij}	Off-diagonal anharmonicity
ΔmOD	10^{-3} x differential optical density

ΔOD	Differential optical density
$h\nu$	A photon
η	Overpotential
λ	Wavelength
ν	Vibrational frequency
ε	Molar extinction coefficient
ξ	Electrical permittivity of vacuum
$\sigma(\nu)$	Absorption cross section
τ	Time constant
φ	Wavefunction

Units

°C	Degrees centigrade
µs	Microsecond
A	Amperes
cm	Centimetre
dm	Decimetre
eV	Electron volts
g	Gram
Hz	Hertz (s^{-1})
K	Kelvin
kHz	Kilohertz
L	Litre
mg	Milligram
mJ	Millijoule
mL	Millilitre
mol	Number of moles
ms	Millisecond
mW	Milliwatt
nm	Nanometre
ns	Nanosecond
ppm	Parts per million
ps	Picosecond
s	Second
V	Volts
W	Watt

Appendix B – Experimental supporting information for chapter 2

Part I: Additional experimental data

UV-vis spectra

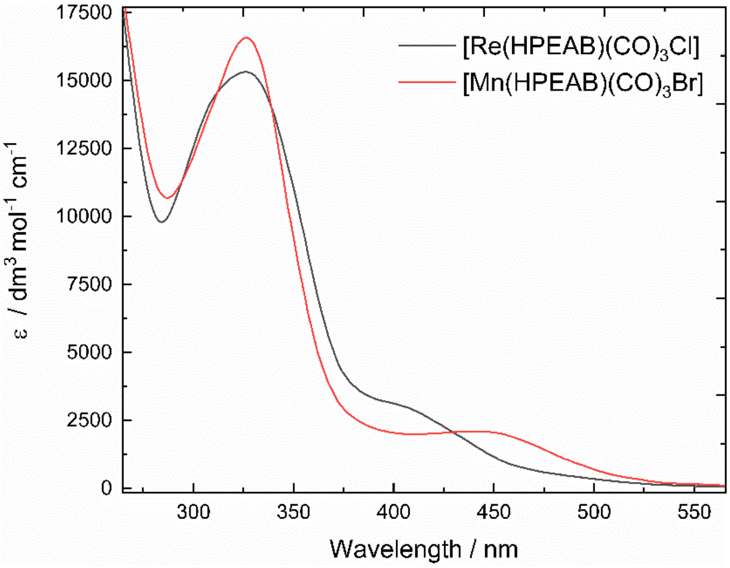

Figure B1 – UV-vis absorption spectra of [Re(HPEAB)(CO)$_3$Cl] and [Mn(HPEAB)(CO)$_3$Br] in dichloromethane, as stated on the graph.

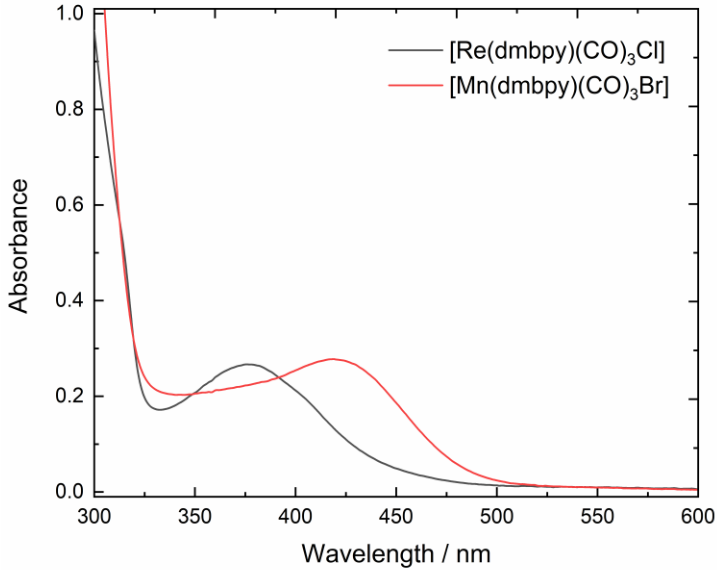

Figure B2 – UV-vis absorption spectra of [Re(dmbpy)(CO)$_3$Cl] and [Mn(dmbpy)(CO)$_3$Br] in dichloromethane, as stated on the graph.

FT-IR spectra

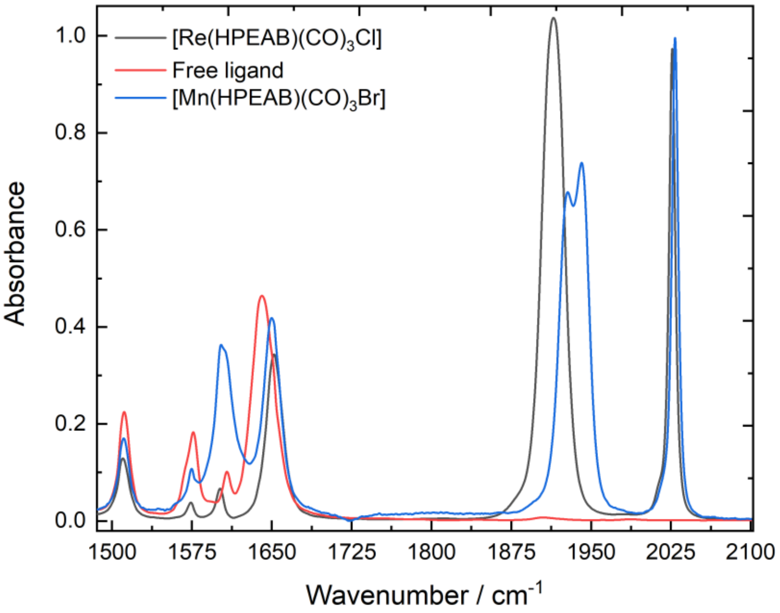

Figure B3 – FT-IR absorption spectra of [Re(HPEAB)(CO)$_3$Cl] and [Mn(HPEAB)(CO)$_3$Br] in dichloromethane, as stated on the graph (Free ligand = 6,6'-{N-(4-hexylphenyl)-N(ethyl)-amido}-2,2'-bipyridine)

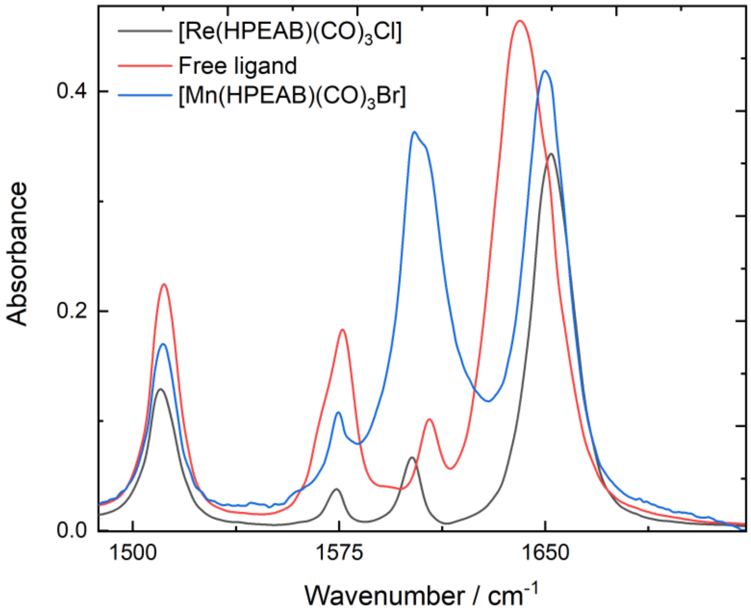

Figure B4 – FT-IR absorption spectra of [Re(HPEAB)(CO)$_3$Cl] and [Mn(HPEAB)(CO)$_3$Br] in dichloromethane, as stated on the graph, focussing on the ligand-centred vibrational modes (Free ligand = 6,6'-{N-(4-hexylphenyl)-N(ethyl)-amido}-2,2'-bipyridine).

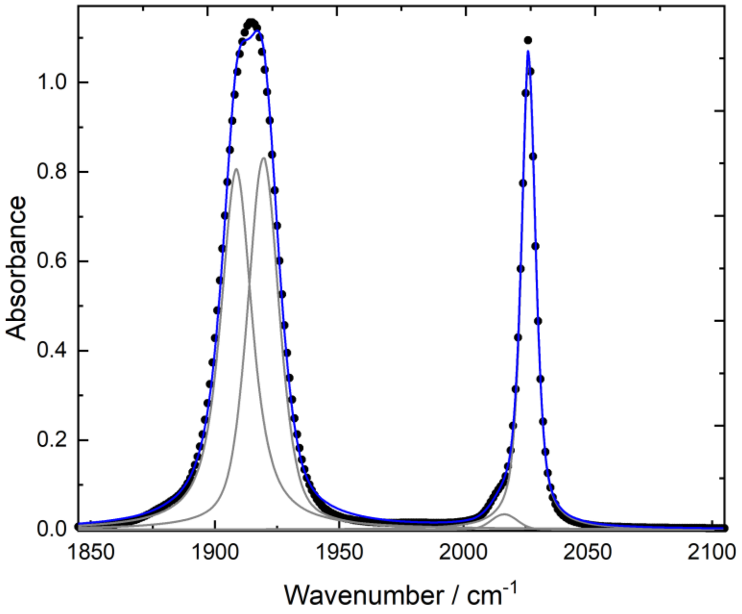

Figure B5 – FT-IR spectrum of [Re(HPEAB)(CO)$_3$Cl] in dichloromethane (dots) in the 1850-2100 cm^{-1} region, deconvoluted by fitting of pseudo-Voigt profiles (grey), to produce the model spectrum (blue).

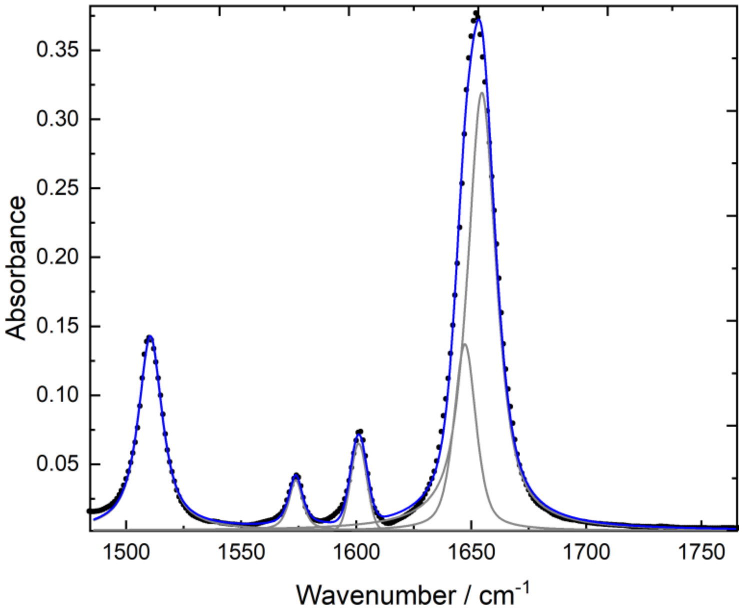

Figure B6 – FT-IR spectrum of [Re(HPEAB)(CO)$_3$Cl] in dichloromethane (dots) in the 1475-1780 cm^{-1} region, deconvoluted by fitting of pseudo-Voigt profiles (grey), to produce the model spectrum (blue).

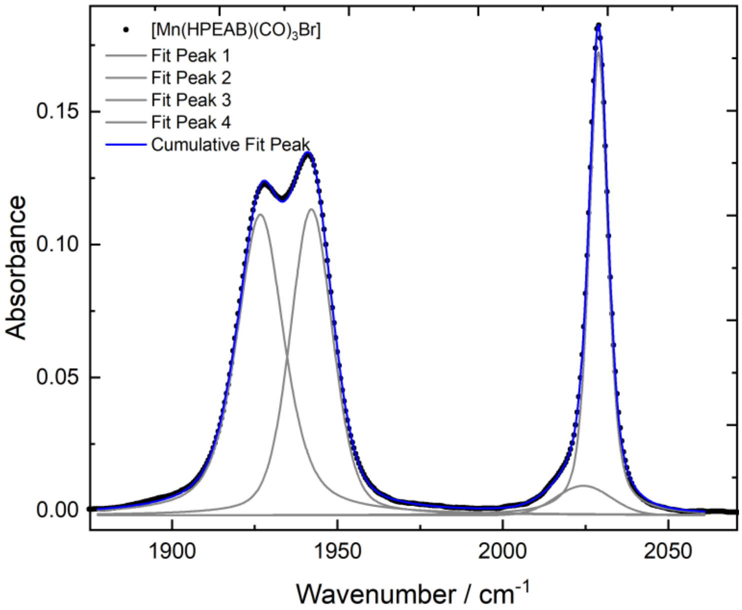

Figure B7 – FT-IR spectrum of [Mn(HPEAB)(CO)3Br] in dichloromethane (dots) in the 1875-2075 cm^{-1} region, deconvoluted by fitting of pseudo-Voigt profiles (grey), to produce the model spectrum (blue).

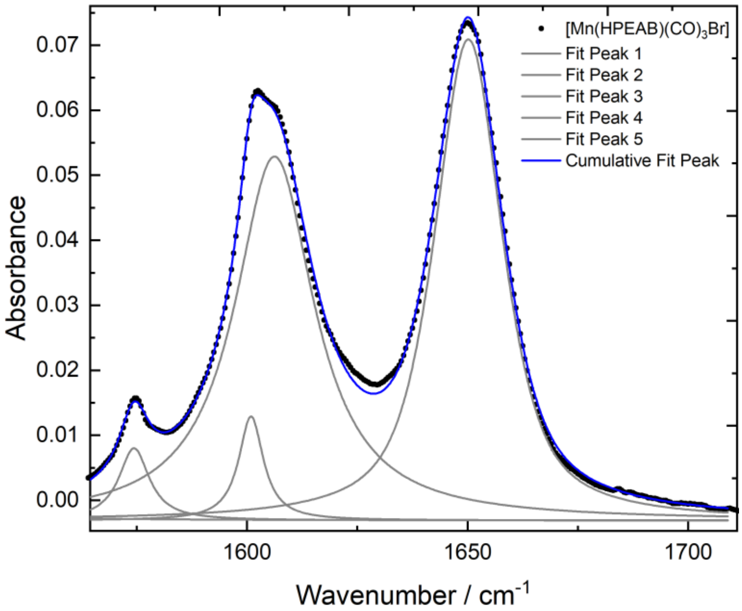

Figure B8 – FT-IR spectrum of [Mn(HPEAB)(CO)3Br] in dichloromethane (dots) in the 1525-1725 cm^{-1} region, deconvoluted by fitting of pseudo-Voigt profiles (grey), to produce the model spectrum (blue).

Equation B1: The pseudo-Voigt(1) function utilised to deconvolute the UV-vis, FTIR, and 2DIR spectra throughout chapters 2 – 5.

$$y = y_0 + A\left[m_u \frac{2}{\pi}\frac{w}{4(x-x_c)^2+w^2} + (1-m_u)\frac{\sqrt{4ln2}}{\sqrt{\pi}w}e^{-\frac{4\ln}{w^2}(x-x_c)^2}\right] \qquad \text{Eq. B1}$$

NMR spectra

Analysis of NMR spectral data

^{1}H NMR spectra (B9-B15) revealed changes in the proton environments of the ligand following complexation of the diimine to the [M(CO)$_5$(X)] starting material. For example, in the free ligand the ethyl groups show the expected triplet-quartet for the CH$_3$CH$_2$ two-spin system. However, upon complexation the quartet was split into two multiplets of equal intensity. This change to an A$_3$MX-type spectrum shows that the protons in the methylene group were no longer equivalent. The suggested explanation for this observation is the planar chirality of the complexes, which renders the CH$_2$ protons diastereotopic because of the limited rotation between the planes of the bipyridyl and phenyl rings. The CH$_2$ multiplet-multiplet separation in the Re complex was 0.33 ppm, compared to 0.06 ppm in the Mn complex. The smaller coupling constant could indicate faster interconversion between diastereoisomers, a result of reduced steric hindrance with the smaller metal centre.

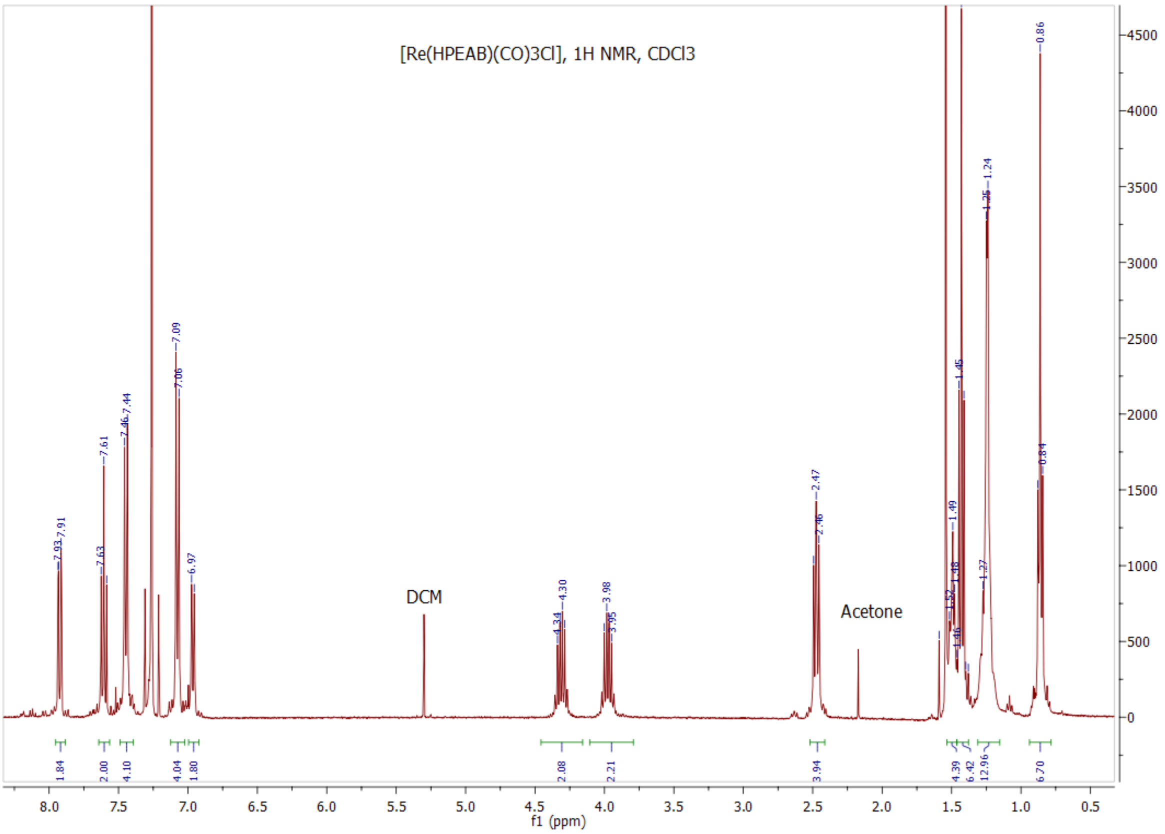

Figure B9 – ^{1}H NMR spectrum of [Re(HPEAB)(CO)$_3$Cl] (400 MHz, CDCl$_3$).

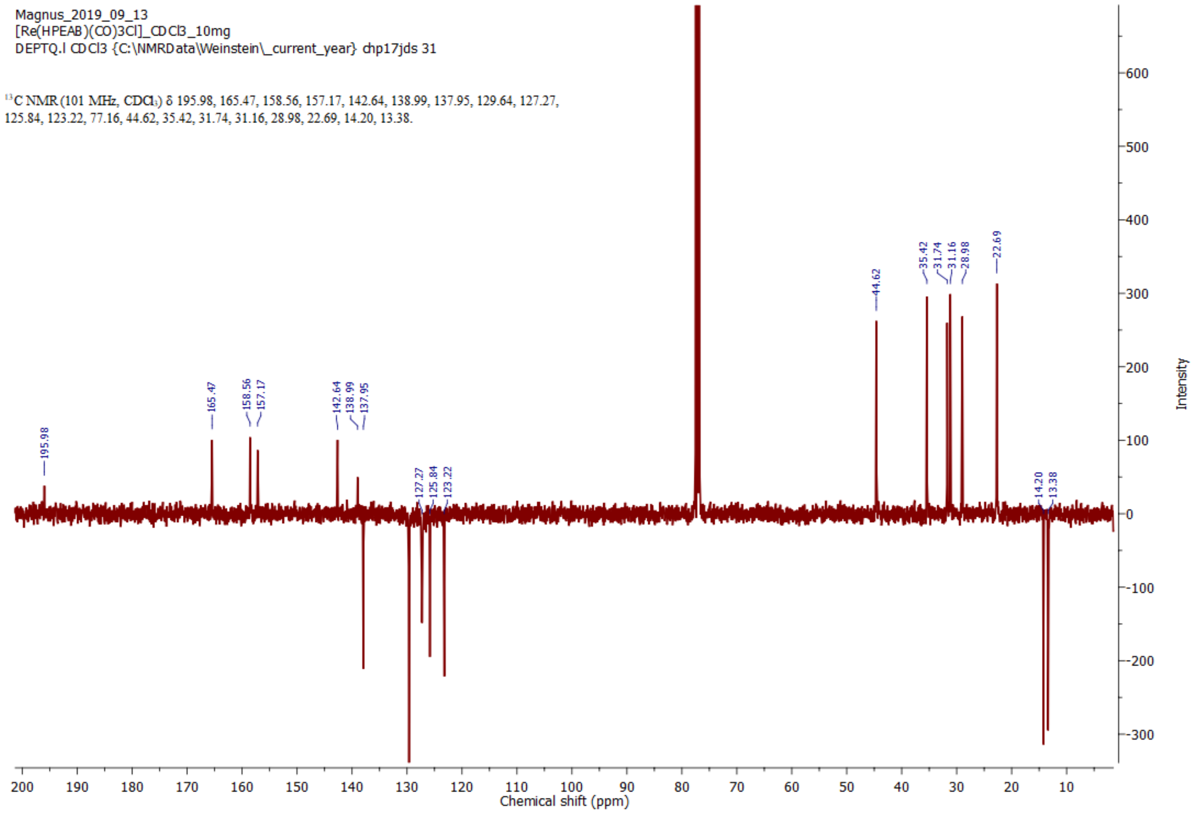

^{13}C NMR (101 MHz, $CDCl_3$) δ 195.98, 165.47, 158.56, 157.17, 142.64, 138.99, 137.95, 129.64, 127.27, 125.84, 123.22, 77.16, 44.62, 35.42, 31.74, 31.16, 28.98, 22.69, 14.20, 13.38.

Figure B10 – ^{13}C NMR spectrum of [Re(HPEAB)(CO)$_3$Cl] (400 MHz, $CDCl_3$).

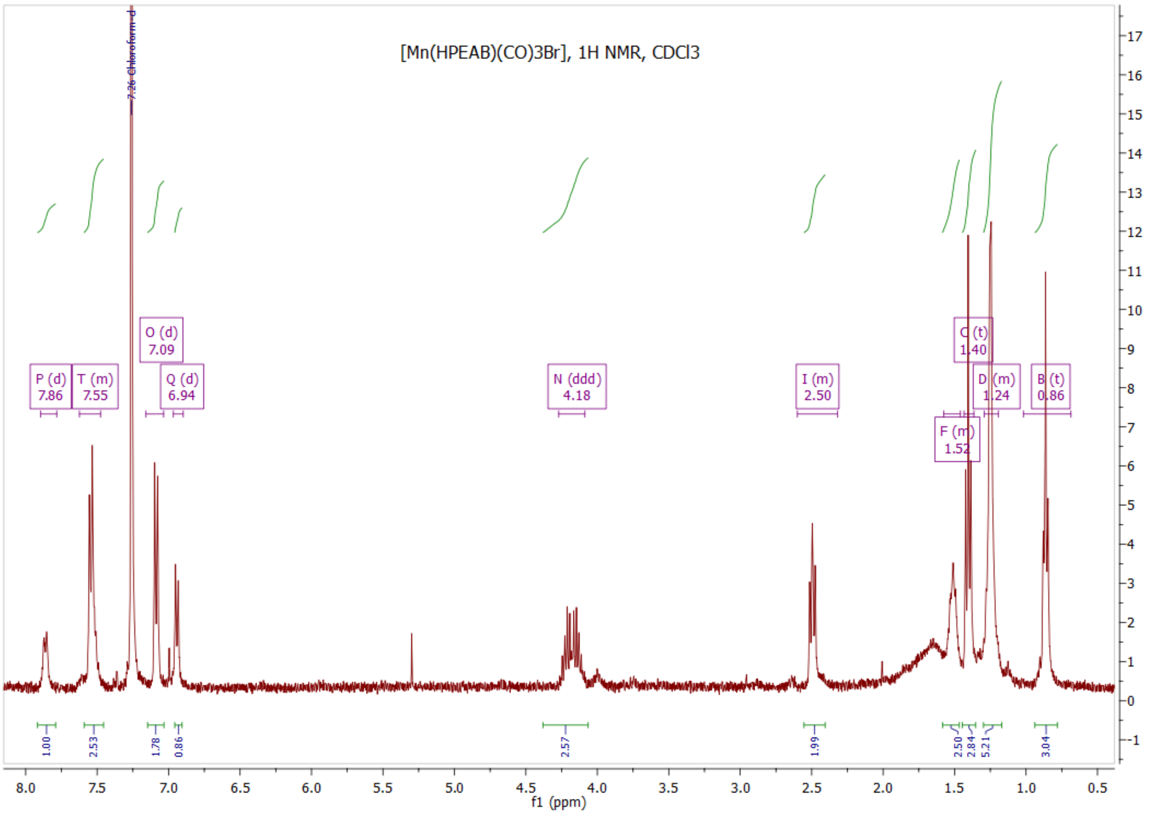

Figure B11 – ^{1}H NMR spectrum of [Mn(HPEAB)(CO)$_3$Br] (400 MHz, $CDCl_3$).

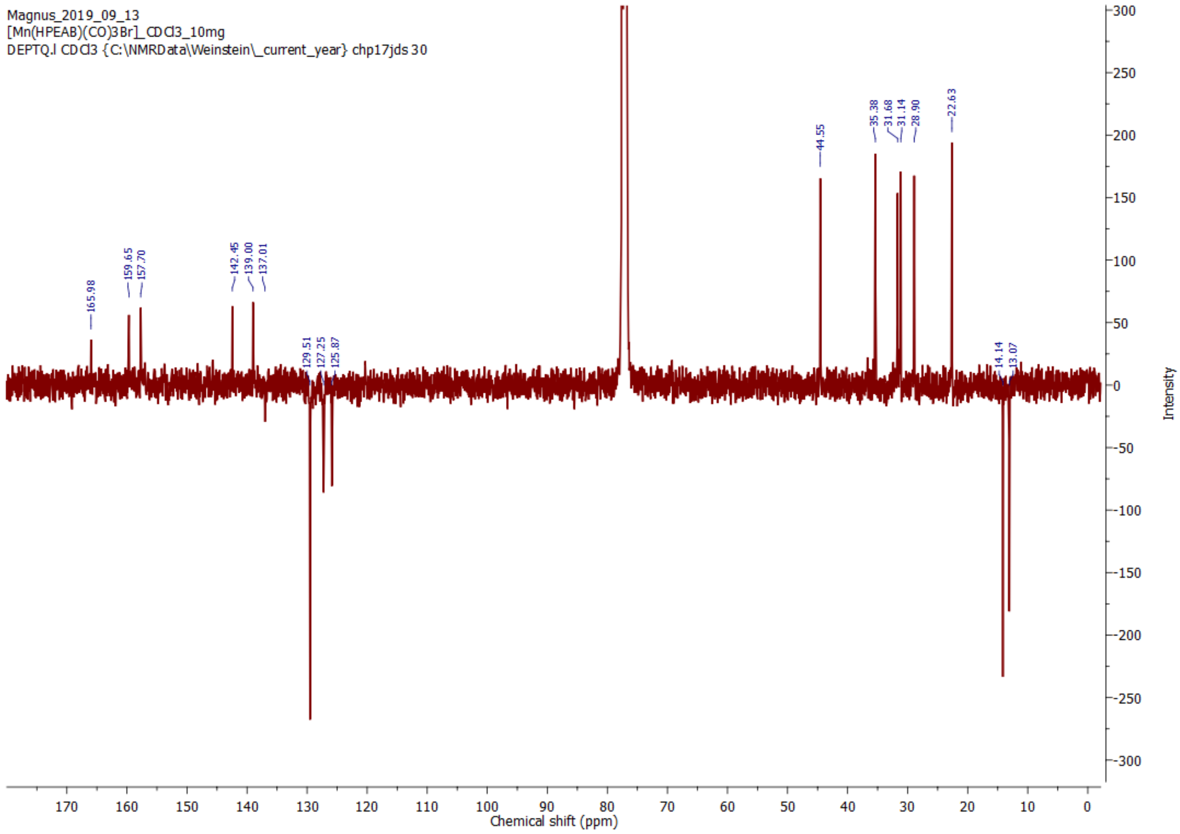

Figure B12 – ^{13}C NMR spectrum of [Mn(HPEAB)(CO)$_3$Br] (400 MHz, CDCl$_3$).

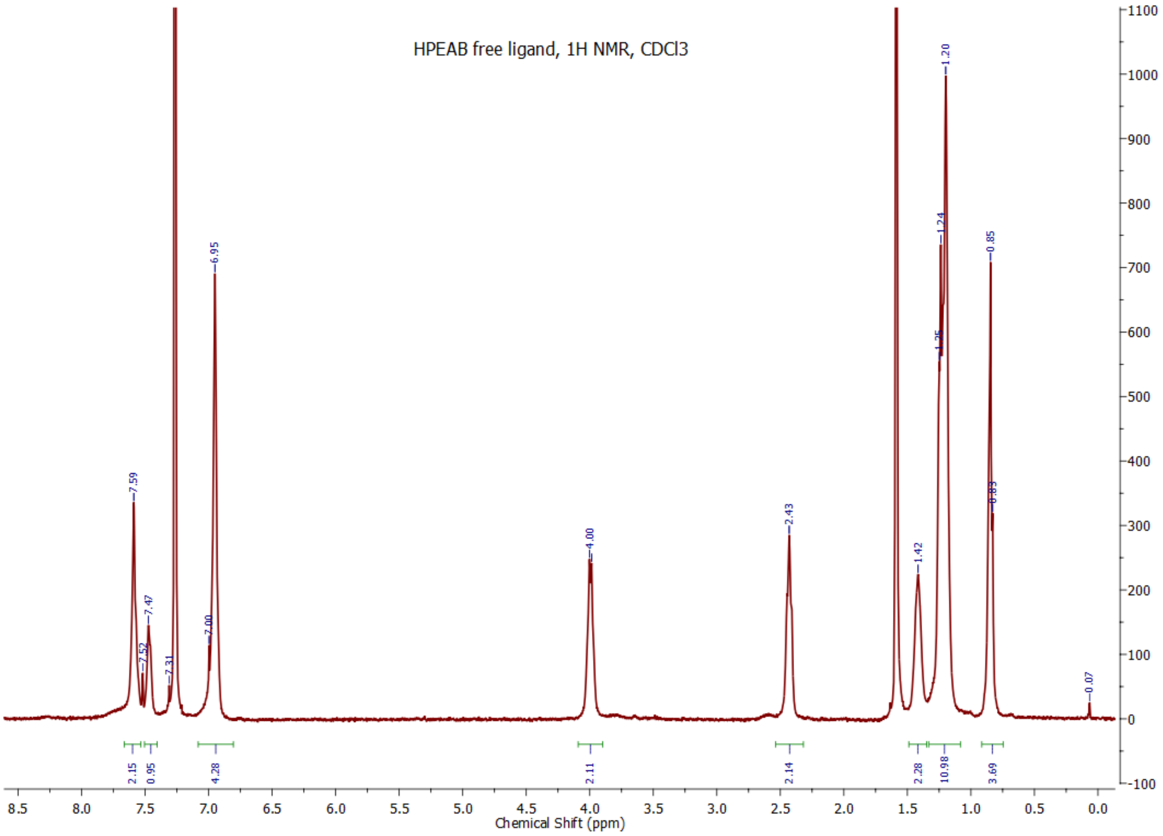

Figure B13 – ^{1}H NMR spectrum of 6,6′-{N-(4-hexylphenyl)-N(ethyl)-amido}-2,2′-bipyridine (HPEAB) (400 MHz, CDCl$_3$).

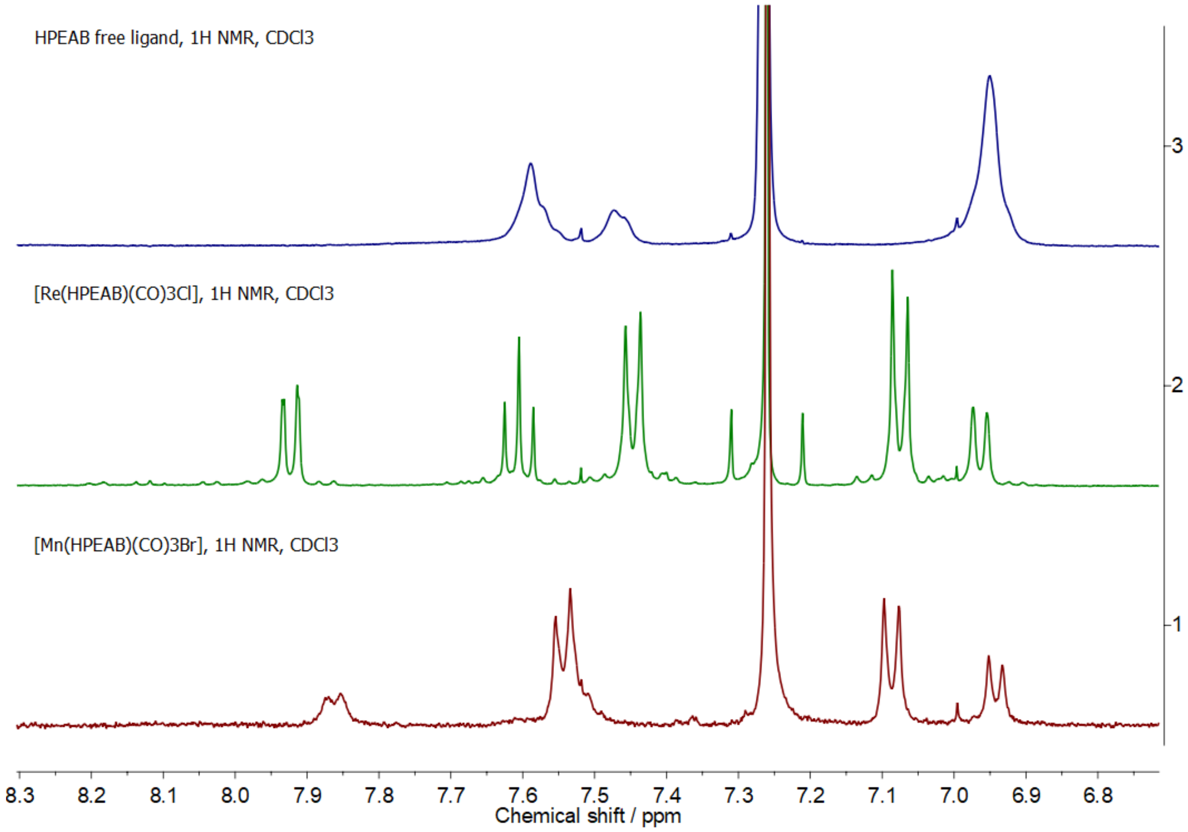

Figure B14 – Overlaid ^{1}H NMR spectra of HPEAB, [Re(HPEAB)(CO)$_3$Cl], and [Mn(HPEAB)(CO)$_3$Br] (400 MHz, CDCl$_3$) showing the differences in the aromatic proton environments (6.8-8.3 ppm).

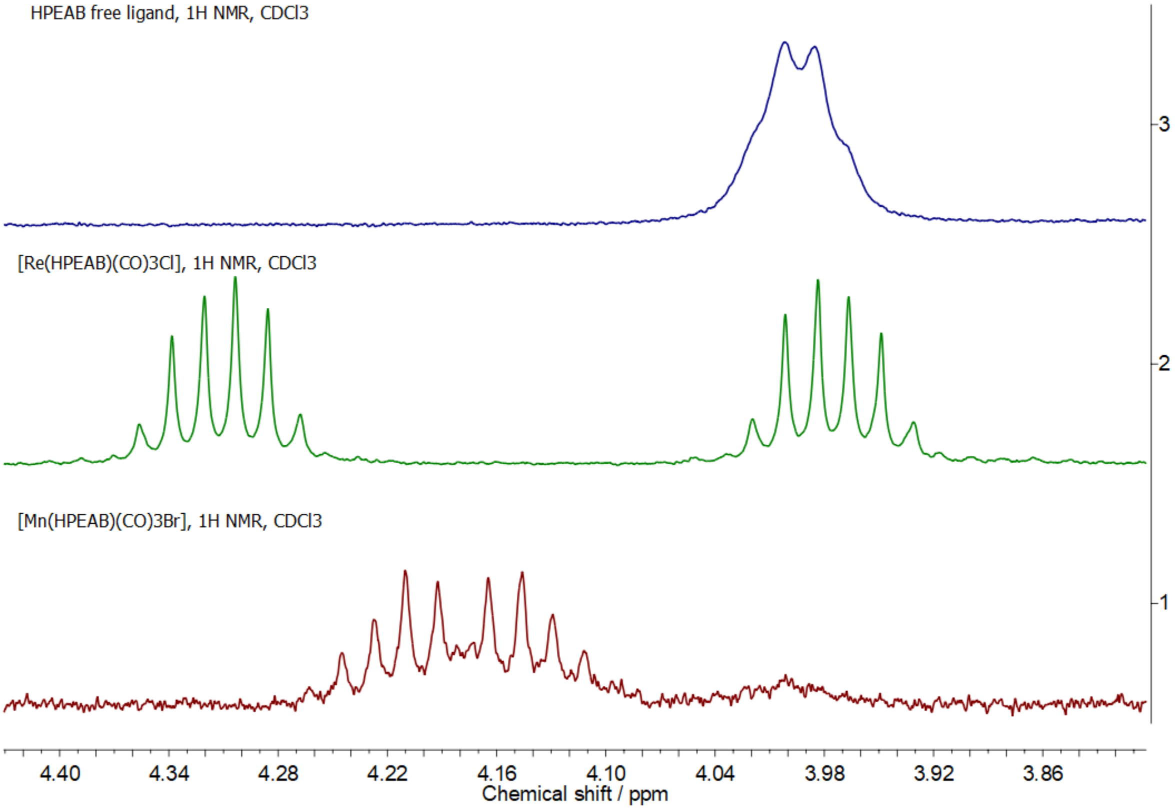

Figure B15 – Overlaid ^{1}H NMR spectra of HPEAB, [Re(HPEAB)(CO)$_3$Cl], and [Mn(HPEAB)(CO)$_3$Br] (400 MHz, CDCl$_3$) showing the differences in the ethyl proton environments upon the amide group (3.8-4.4 ppm).

Elemental analysis reports

[Re(HPEAB)(CO)3Cl]

Molecular formula: $C_{43}H_{50}ClN_4O_5Re$
Carbon (Expected value: 55.86%): Found: 55.60%
Hydrogen (Expected value: 5.45%): Found: 5.39%
Nitrogen (Expected value: 6.06%): Found: 6.04%
Chlorine (Expected value: 3.83%): Found: 3.69%

[Mn(HPEAB)(CO)$_3$Br]

Molecular formula: $C_{43}H_{50}BrMnN_4O_5$

Carbon (Expected value: 61.65%): Found: 61.06%

Hydrogen (Expected value: 6.02%): Found: 5.81%

Nitrogen (Expected value: 6.69%): Found: 6.64%

Bromine (Expected value: 9.54%): Found: 10.09%

Photochemical degradation

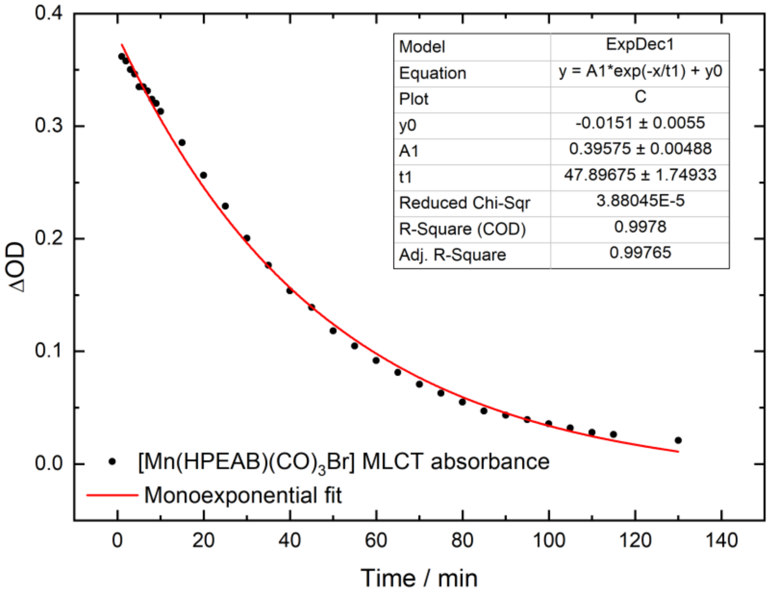

Figure B16 – Kinetic trace for the change in optical density at the MLCT maxima of [Mn(HPEAB)(CO)$_3$Br] during irradiation with a xenon arc lamp (dots), and monoexponential fit of the data used to estimate the time constant of photodecomposition (red).

Cyclic voltammetry

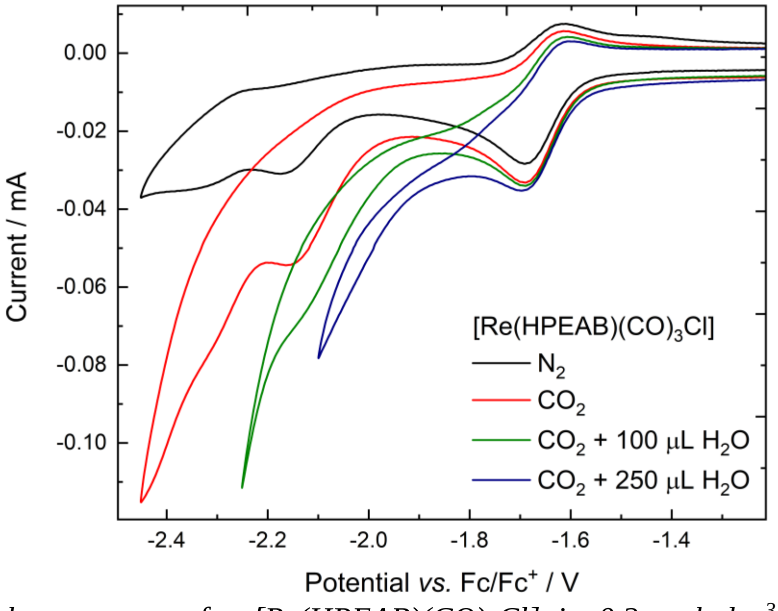

Figure B17 – Cyclic voltammograms for [Re(HPEAB)(CO)$_3$Cl] in 0.2 mol dm^{-3} [NBu$_4$][PF$_6$] supporting electrolyte at a scan rate of 100 mV s^{-1} under various conditions, as stated on the graph.

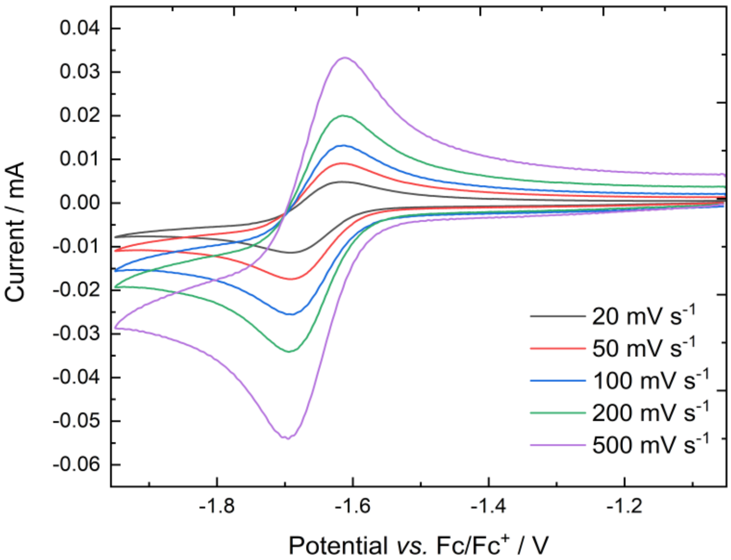

Figure B18 – Cyclic voltammograms of the first reduction of [Re(HPEAB)(CO)$_3$Cl] under N$_2$ atmosphere at multiple scan rates, as stated on the graph.

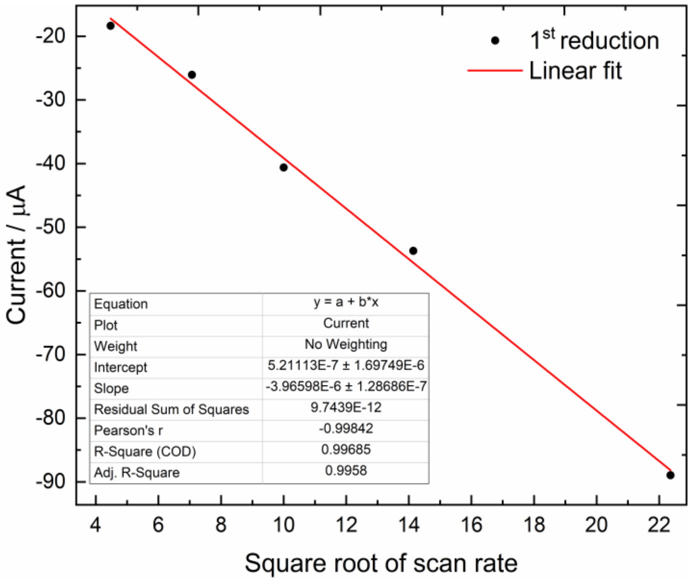

Equation	y = a + b*x
Plot	Current
Weight	No Weighting
Intercept	5.21113E-7 ± 1.69749E-6
Slope	-3.96598E-6 ± 1.28686E-7
Residual Sum of Squares	9.7439E-12
Pearson's r	-0.99842
R-Square (COD)	0.99685
Adj. R-Square	0.9958

Figure B19 – Relationship between the total current of the first reduction couple and the square root of the scan rate for [Re(HPEAB)(CO)$_3$Cl].

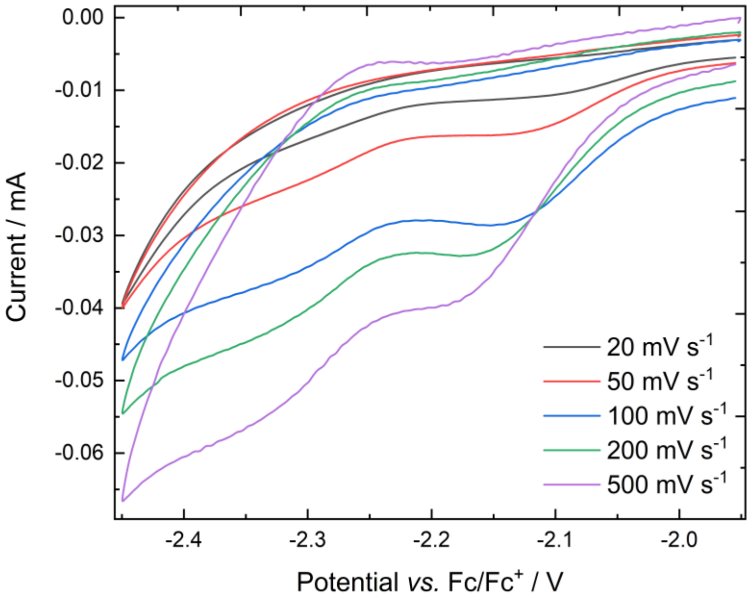

Figure B20 – Cyclic voltammograms of the second reduction of [Re(HPEAB)(CO)$_3$Cl] under N$_2$ atmosphere at multiple scan rates, as stated on the graph.

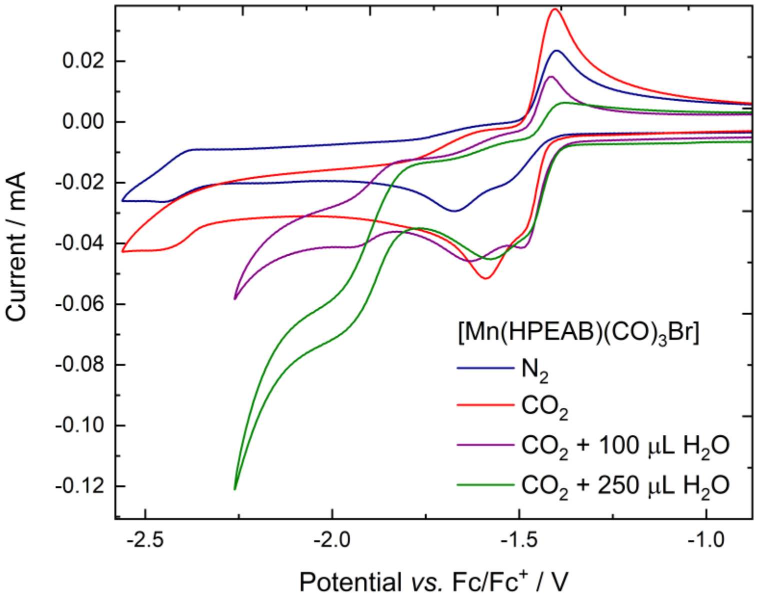

Figure B22 – Cyclic voltammograms for [Mn(HPEAB)(CO)$_3$Br] in 0.2 mol dm^{-3} [NBu$_4$][PF$_6$] supporting electrolyte at a scan rate of 100 mV s^{-1} under various conditions, as stated on the graph.

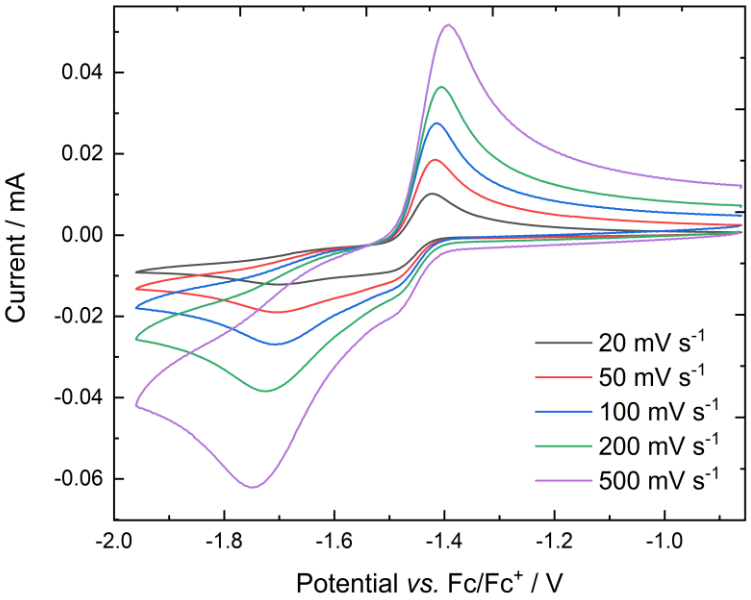

Figure B23 – Cyclic voltammograms of the first and second reduction processes of [Mn(HPEAB)(CO)$_3$*Br] under N*$_2$ *atmosphere at multiple scan rates. Scan rate analysis was not possible due to the significant overlap between redox processes preventing an accurate measure of total current for the redox peak pairs.*

Foot of the wave analysis method

As it was not possible to increase the CV scan rate to a point at which substrate diffusion was rate limiting, the electrochemical performance of the catalysts was estimated by foot-of-the-wave analysis, the methodology of which has been described previously.[1-3] This was done by fit of the onset of catalytic current in four steps:

a) Replotting the cyclic voltammogram with the following equation, where i_p^0 corresponds to the current of the second reduction in inert conditions, F is the Faraday constant, R is the gas constant, T is the temperature, E is the applied voltage, and E_0 is the potential corresponding to the midpoint of the grow-in of the catalytic current.

$$\frac{i}{i_p^0} = \left[1 + e^{\left(\frac{F}{RT}(E-E_0)\right)}\right]^{-1}$$

Equation B – Relationship between $\frac{i}{i_p^0}$ *and* $E - E_0$ *used for the re-plotting of the cyclic voltammetry data to show the onset of catalytic activity.*

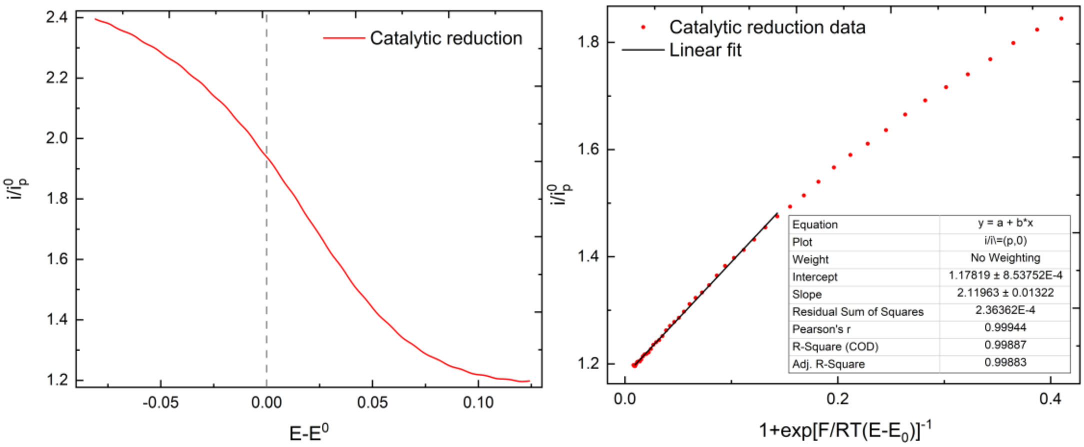

Figure B24 – Cyclic voltammogram for the onset of catalytic activity (left) and linear fit of the onset region (right).

b) The resultant plot will contain a linear region, which then deviates from linearity as $E-E^0$ increases. The gradient of the linear region allows for calculation of the rate constant of catalytic turnover (k_r), where f = F/RT, m is the gradient, n’ is the number of electrons involved in the catalytic process, and C is the initial concentration of catalyst.

$$k_r = \frac{fv\left(\frac{m}{2.24}\right)^2}{n'C_{cat}^0}$$

Equation B2 – Relationship between the observed rate of reaction for the catalytic process and the gradient of the linear foot-of-the wave plot.

c) The turnover frequency can then be calculated using the observed rate constant. TOF is the turnover frequency, E_r^0 is the standard potential for the catalytic reaction, E_{cat}^0 is the standard potential for the reduction of the catalyst.

$$TOF_0 = k_r C_{cat}^0 e^{\left(-f\left(E_r^0 - E_{cat}^0\right)\right)}$$

Equation B3 – Formula for calculation of the observed turnover frequency at zero overpotential.

d) The turnover frequency is a function of the catalytic overpotential (η), and a plot of TOF against overpotential results in a Tafel plot, used for comparing catalytic performance.

$$TOF = \frac{k_r}{1 + e^{\left(f\left(E_r^0 - E_{cat}^0 - \eta\right)\right)}}$$

Equation B4 – Relationship between the turnover frequency and the applied overpotential.

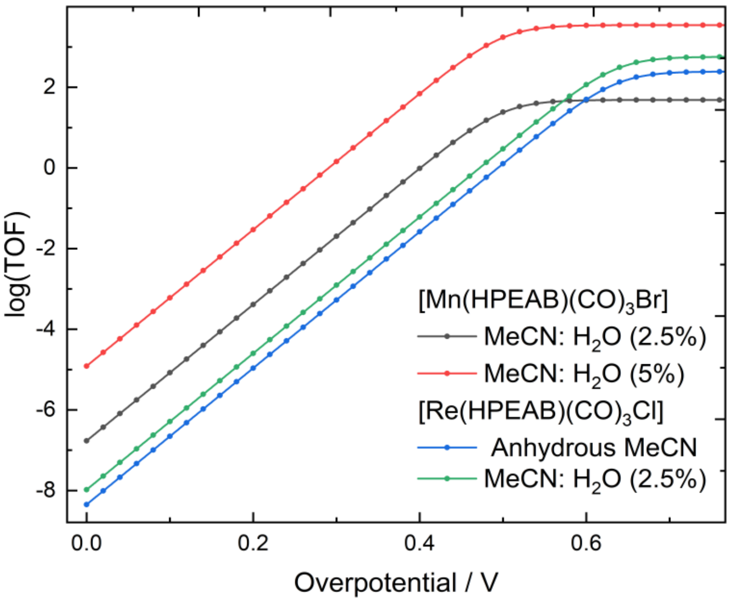

Figure B25 – Catalytic Tafel plots for electrochemical CO_2 reduction with [Re(HPEAB)$(CO)_3$Cl] or [Mn(HPEAB)$(CO)_3$Br] under various conditions, as shown on the graph.

Transient absorption spectroscopy

Transient absorption spectra were analysed by global lifetime analysis in Glotaran.[1] A two component sequential model resulted in the most plausible model for the excited state dynamics. The proposed kinetic model involves intersystem crossing from the singlet to the triplet MLCT, after vibrational cooling of the ^{3}MLCT, it then decays to the ground state with a time constant of 3.44 ns. For further elucidation of the dynamics, TRIR spectroscopy is required.

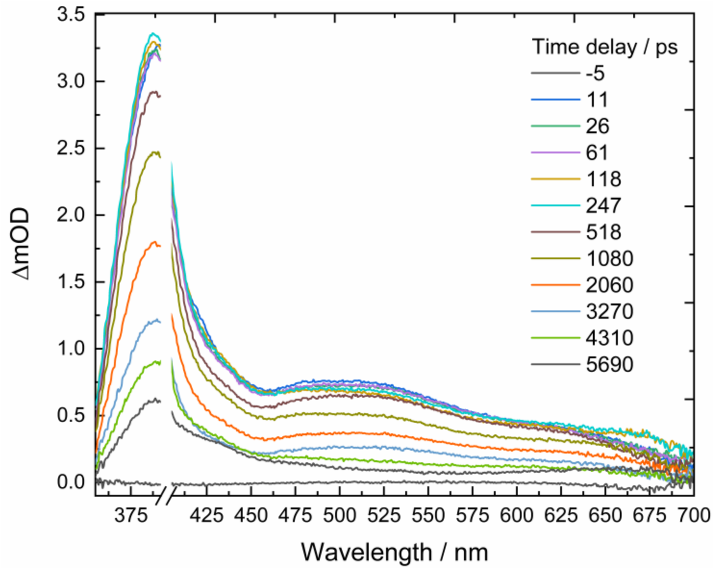

Figure B26 – Transient absorption difference spectra of [Re(HPEAB)$(CO)_3$Cl] following 400 nm excitation at various pump – probe time delays (shown in picoseconds), as stated on the graph. The spectral region from 395-405 nm has been removed due to scattered light from the pump pulse.

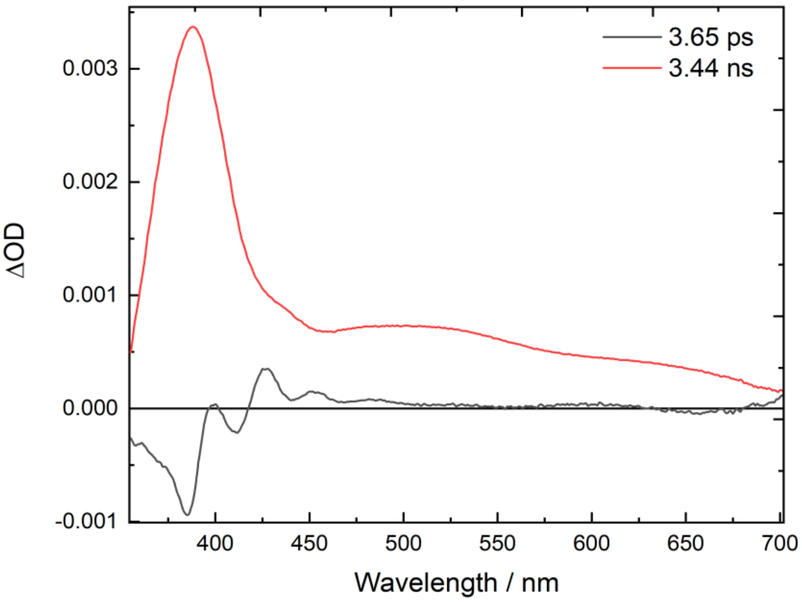

Figure B27 – Decay associated spectra resulting from global lifetime analysis of the transient absorption data. A two component sequential kinetic model was used, where the optimised lifetimes were 3.65 ps and 3.44 ns.

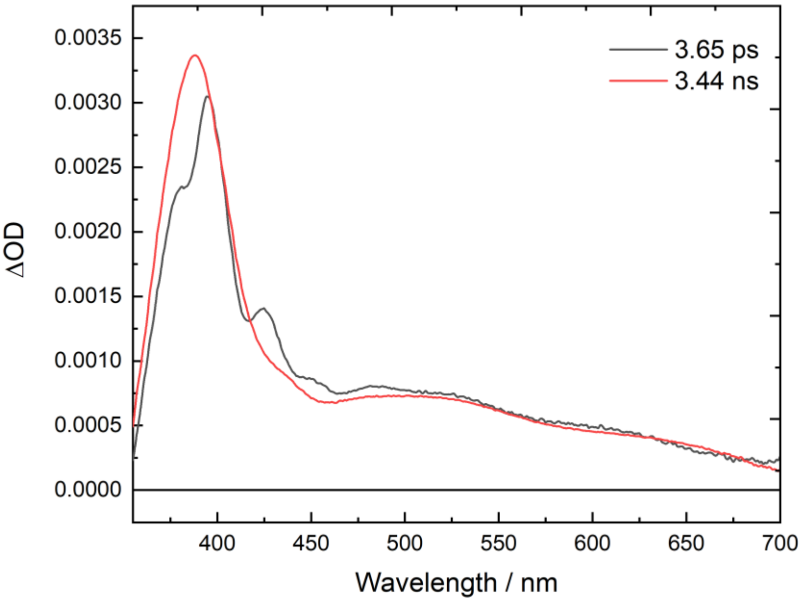

Figure B28 – Evolution associated spectra resulting from global lifetime analysis of the transient absorption data. A two-component sequential kinetic model was used, where the optimised lifetimes were 3.65 ps and 3.44 ns.

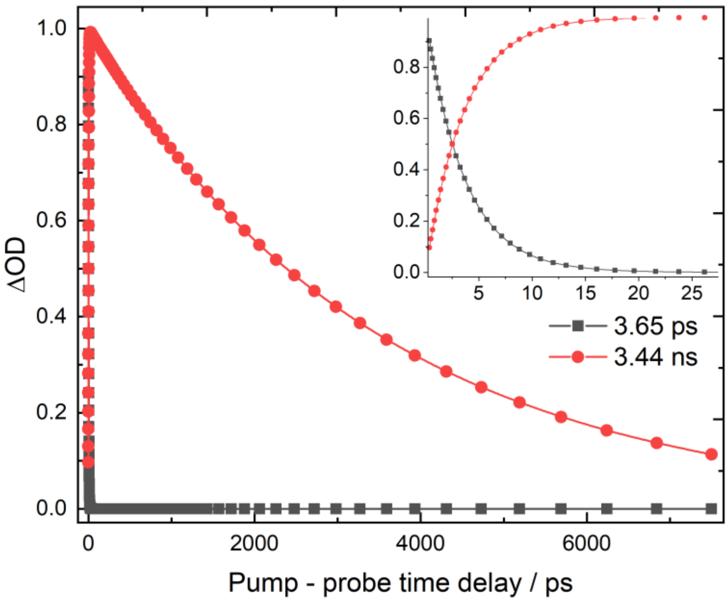

Figure B29 – Model kinetic traces representing the decay of the first and second component of the sequential kinetic model. The inset is a magnified graph focussing on the first 25 ps of the data.

Estimation of the Gibbs energy of electron transfer

The thermodynamic favourability of the photosensitisation of [Mn(HPEAB)(CO)$_3$Br] by ZnTPP in the presence of triethylamine sacrificial donor was estimated with the Rehm-Weller equation.

$$\Delta G_{et} = E^{\frac{1}{2}}\left(\frac{D}{D^{+}}\right) - E^{\frac{1}{2}}\left(\frac{A}{A^{-}}\right) - E_{00} - \frac{e^{2}}{\varepsilon d}$$

Equation B5 – Rehm-Weller equation for estimation of the Gibbs energy of electron transfer (ΔG_{et}) [D – electron donor, A – electron acceptor, $E^{1/2}$ – electrochemical half-wave potential, E_{00} – Excited/ground state energy difference, $\frac{e^2}{\varepsilon d}$ – coulombic term for electrostatic interaction].

The redox potentials of [Mn(HPEAB)(CO)$_3$Br] were measured by cyclic voltammetry, and the E_{00} value for ZnTPP following 625 nm excitation was estimated by emission spectroscopy as 2.07 eV. Literature values for the redox potential of NEt$_3$ (+1.07 V vs. Fc/Fc$^+$) oxidation, ZnTPP oxidation (+0.29 V vs. Fc/Fc$^+$), and ZnTPP reduction (-1.85 V vs. Fc/Fc$^+$).[2,3]

Reductive quenching

It was found that the reductive quenching mechanism was not feasible, as the initial reduction of ZnTPP by triethylamine was thermodynamically unfavourable.

i) $ZnTPP + hv \rightarrow [ZnTPP]^{*}$

ii) $[ZnTPP]^{*} + NEt_3 \rightarrow [ZnTPP]^{-} + {NEt_3}^{+}$

ii) $\Delta G_{et} \;=\; 1.07\,V - -1.85\,V - \;2.07\,eV \;=\; 0.85\,V$

Equation B6 – Estimation of the Gibbs energy of electron transfer for the reduction of the ZnTPP triplet state by triethylamine.

Oxidative quenching

The oxidative quenching of [Mn(HPEAB)(CO)$_3$Br] to form the active catalyst, [Mn(HPEAB)(CO)$_3$]$^-$ was estimated to be thermodynamically favourable.

i) $ZnTPP + hv \rightarrow [ZnTPP]^*$

ii) $[ZnTPP]^* + [Mn(HPEAB)(CO)_3Br] \rightarrow [ZnTPP]^+ + [Mn(HPEAB)(CO)_3Br]^-$

iii) $[ZnTPP]^* + [Mn(HPEAB)(CO)_3] \rightarrow [ZnTPP]^+ + [Mn(HPEAB)(CO)_3]^-$

ii) $\Delta G_{et} = 0.29\,V - -1.48\,V - 2.07\,eV = -0.30\,V$

iii) $\Delta G_{et} = 0.29\,V - -1.74\,V - 2.07\,eV = -0.04\,V$

Equation B7 – Estimation of ΔG_{et} *for the photoinduced electron transfer processes required for formation of* $[Mn(HPEAB)(CO)_3]^-$ *by photosensitisation.*

Estimation of the ΔG_{et} required for the two-electron reduction needed for turnover of the catalytic cycle showed that this process was thermodynamically unfavourable. Therefore, turnover of the catalytic cycle was not possible, resulting in a low TON_{CO}.

$$\Delta G_{et} = 0.29\,V - -1.90\,V - 2.07\,eV = 0.12\,V$$

Equation B8 – Estimation of ΔG_{et} *for the electron transfer required for turnover of the catalytic cycle.*

IR-spectroelectrochemical data analysis

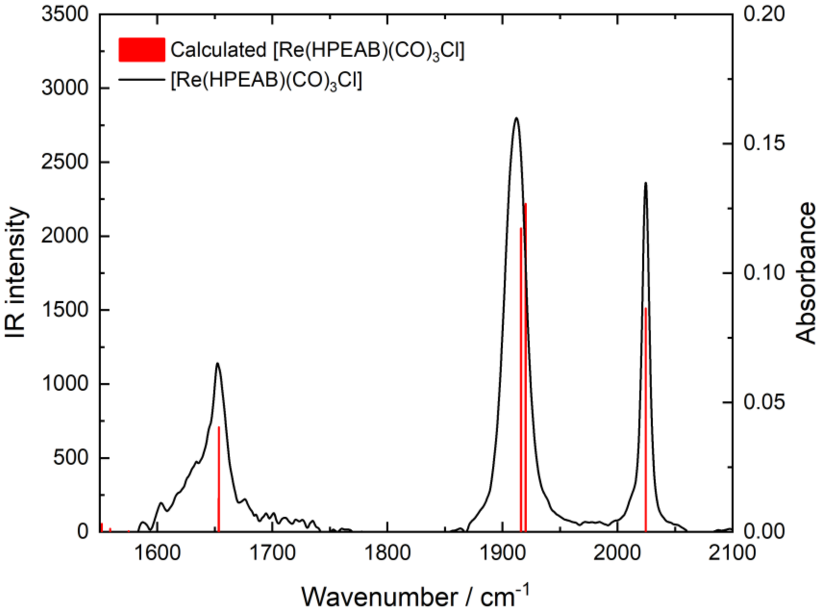

Figure B30 – Assignment of absorption bands observed prior to in situ electrolysis of $[Re(HPEAB)(CO)_3Cl]$ *in anhydrous acetonitrile under argon atmosphere. The bars correspond to calculated vibrational frequencies obtained by DFT, black line corresponds to the experimental spectrum.*

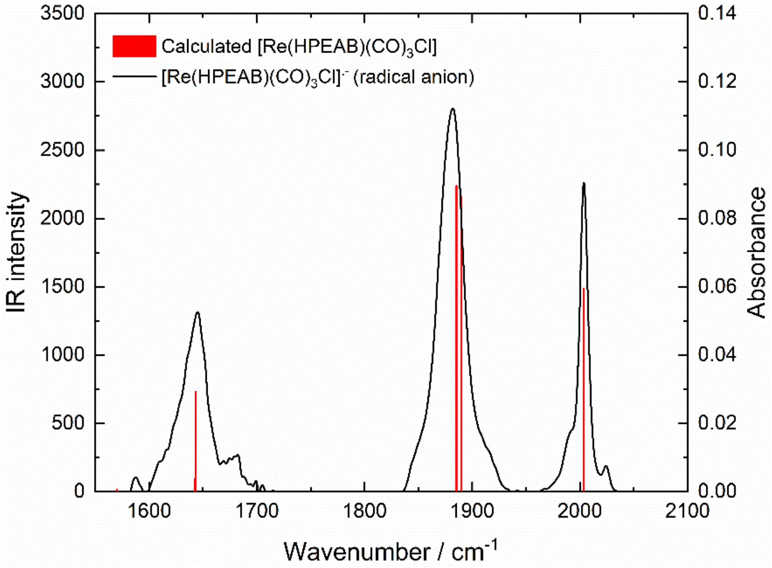

Figure B31 – Assignment of absorption bands observed during in situ electrolysis of [Re(HPEAB)(CO)$_3$Cl] in anhydrous acetonitrile under argon atmosphere at the first reduction potential. The bars correspond to calculated vibrational frequencies obtained by DFT as shown on the graph, the black line corresponds to the experimental spectrum.

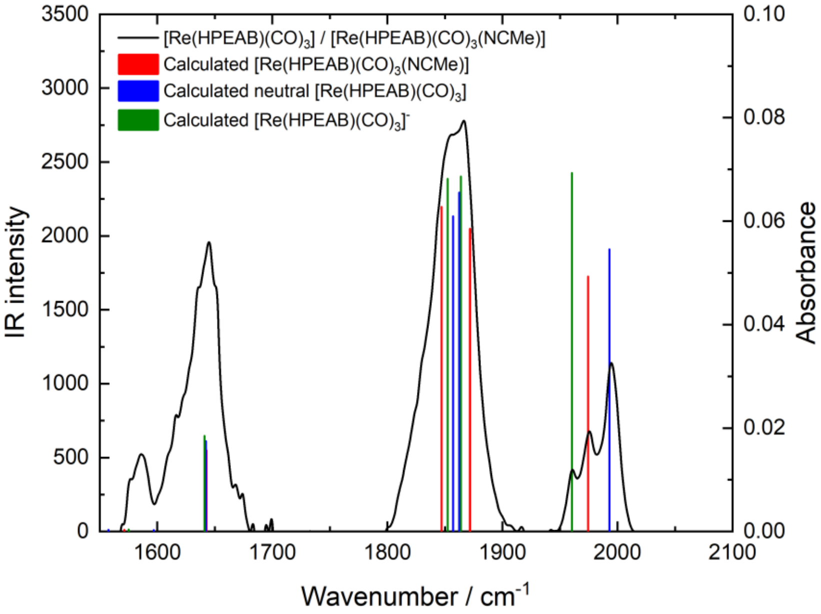

Figure B32 – Assignment of absorption bands observed during in situ electrolysis of [Re(HPEAB)(CO)$_3$Cl] in anhydrous acetonitrile under argon atmosphere at the second reduction potential. The bars correspond to calculated vibrational frequencies obtained by DFT as shown on the graph, the black line corresponds to the experimental spectrum.

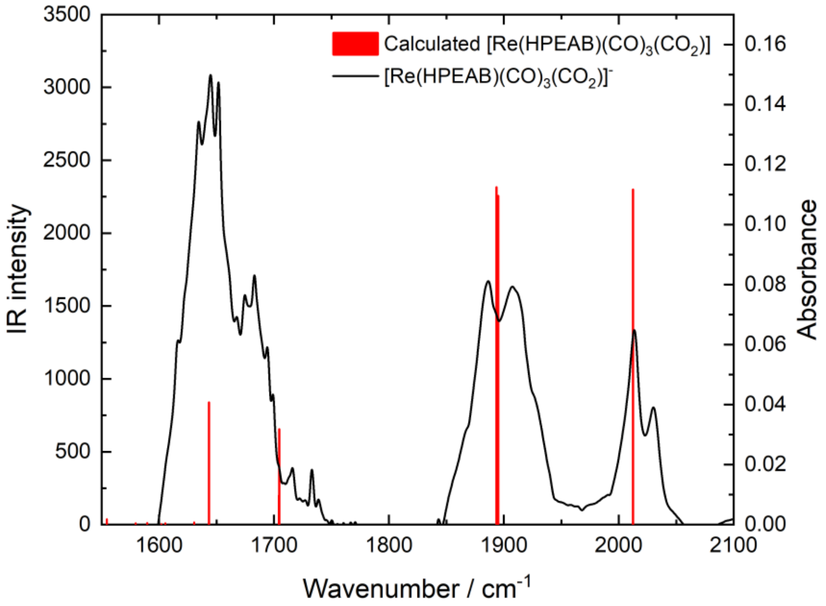

Figure B33 – Assignment of absorption bands observed during in situ electrolysis of [Re(HPEAB)(CO)$_3$Cl] in anhydrous acetonitrile under CO_2 atmosphere at the second reduction potential. The bars correspond to calculated vibrational frequencies obtained by DFT as shown on the graph, the black line corresponds to the experimental spectrum.

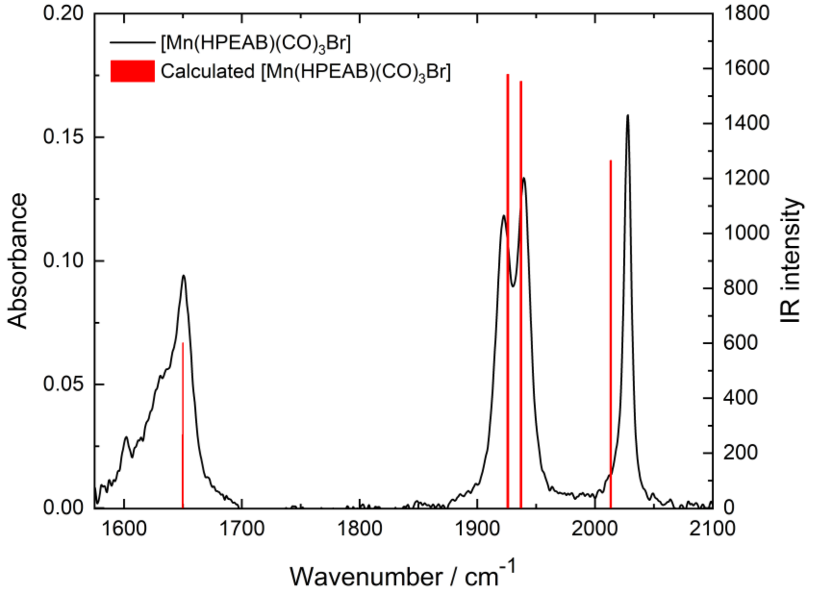

Figure B34 – Assignment of absorption bands observed prior to in situ electrolysis of [Mn(HPEAB)(CO)$_3$Br] in anhydrous acetonitrile under argon atmosphere. The bars correspond to calculated vibrational frequencies obtained by DFT, the black line corresponds to the experimental spectrum.

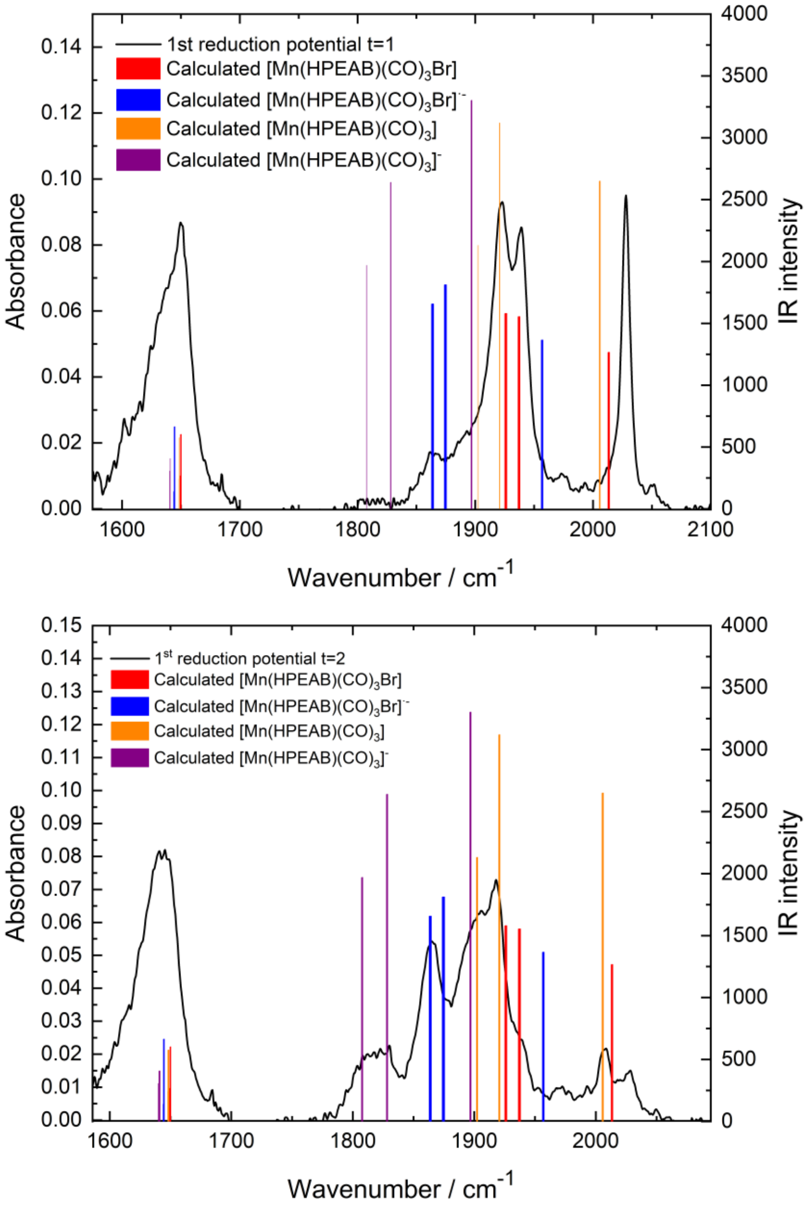

Figure B35 – Assignment of absorption bands observed during in situ electrolysis of [Mn(HPEAB)(CO)$_3$Br] in anhydrous acetonitrile under argon atmosphere at the first reduction potential. The bars correspond to calculated vibrational frequencies obtained by DFT as shown on the graph, the black line corresponds to the experimental spectrum (t=1 – 2 minutes after electrolysis start; t=2 – 30 minutes after electrolysis start).

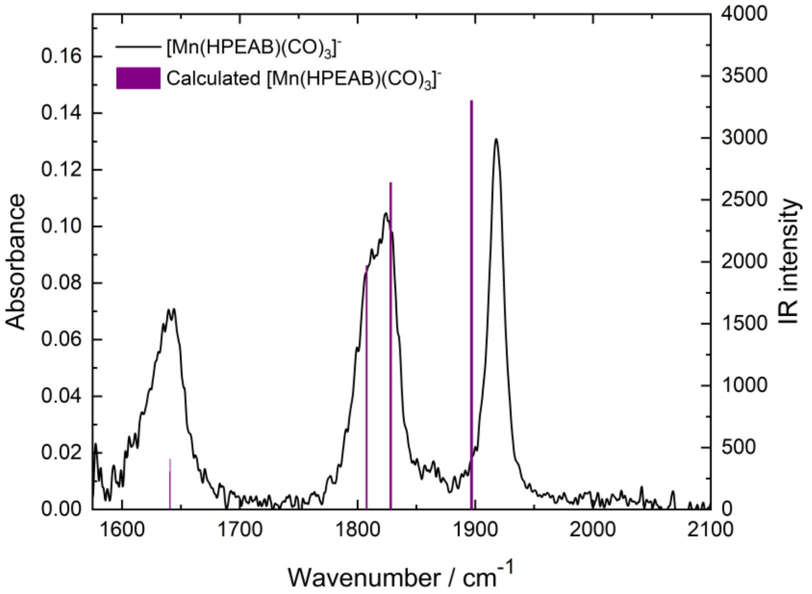

Figure B36 – Assignment of absorption bands observed during in situ electrolysis of [Mn(HPEAB)(CO)$_3$Br] in anhydrous acetonitrile under argon atmosphere at the second reduction potential. The bars correspond to calculated vibrational frequencies obtained by DFT as shown on the graph, the black line corresponds to the experimental spectrum.

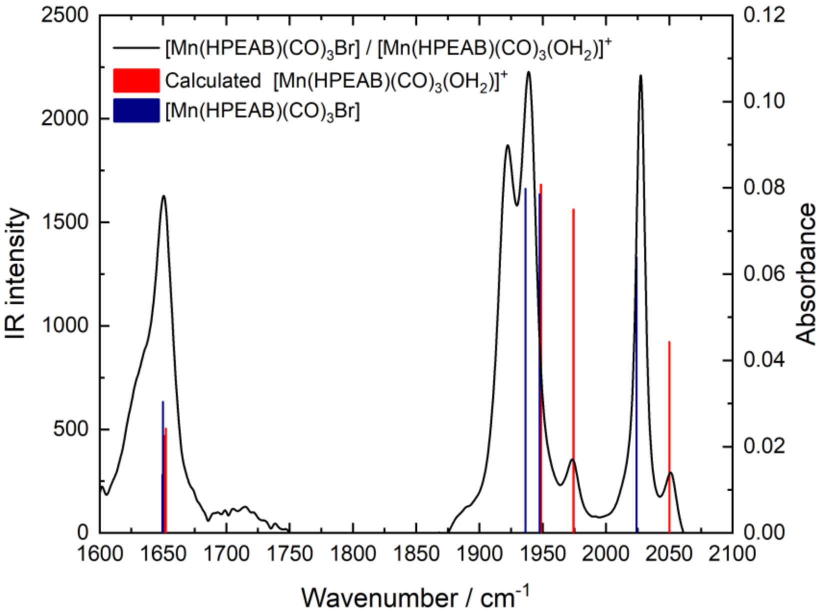

Figure B37 – Assignment of absorption bands observed during in situ electrolysis of [Mn(HPEAB)(CO)$_3$Br] in acetonitrile under argon atmosphere at the first reduction potential. Hydrolysis of the first reduction product was observed due to trace water present in the solvent. The bars correspond to calculated vibrational frequencies obtained by DFT as shown on the graph, the black line corresponds to the experimental spectrum.

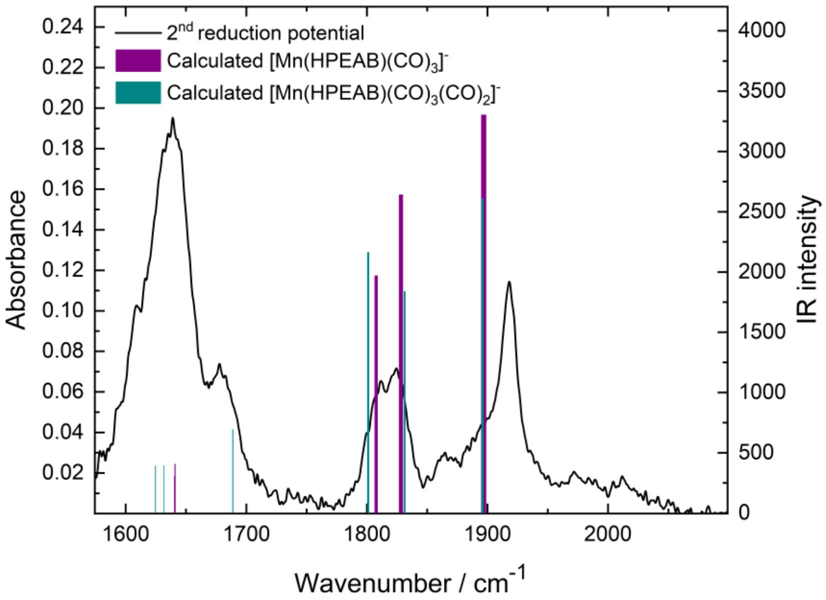

Figure B38 – Assignment of absorption bands observed during in situ electrolysis of [Mn(HPEAB)(CO)$_3$Br] in anhydrous acetonitrile under CO$_2$ atmosphere at the second reduction potential. The strong signal observed at 1605 cm^{-1} was due to the presence of water. The bars correspond to calculated vibrational frequencies obtained by DFT as shown on the graph, the black line corresponds to the experimental spectrum.

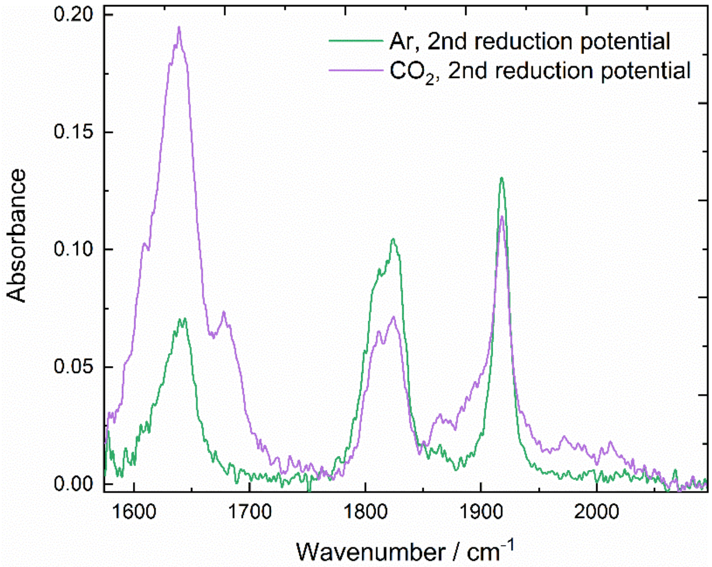

Figure B39 – Overlaid experimental IR-SEC spectra for the product formed following two-electron reduction of [Mn(HPEAB)(CO)$_3$Br] under argon or CO$_2$ atmospheres, as shown on the graph.

Anharmonic scaling factors

Table B1 – Correction factors applied to vibrational frequencies obtained through DFT calculations, used to account for the anharmonicity of the vibrational potential energy surface.

Species	**Anharmonic scaling factors**	
	$\tilde{\nu}$ < 1700 cm^{-1}	**$\tilde{\nu}$ > 1700 cm^{-1}**
[Re(HPEAB)(CO)$_3$Cl]	0.927	0.948
[Re(HPEAB)(CO)$_3$Cl]$^-$	0.924	0.948
[Re(HPEAB)(CO)$_3$]	0.925	0.940
[Re(HPEAB)(CO)$_3$(NCMe)]	0.925	0.925
[Re(HPEAB)(CO)$_3$]$^-$	0.960	0.969
[Re(HPEAB)(CO)$_3$(CO$_2$)]$^-$	0.928	0.951
[Mn(HPEAB)(CO)$_3$Br]	0.925	0.935
[Mn(HPEAB)(CO)$_3$Br]$^-$	0.925	0.918
[Mn(HPEAB)(CO)$_3$Br]	0.925	0.960
[Mn(HPEAB)(CO)$_3$(OH$_2$)]$^+$	0.928	0.939
[Mn(HPEAB)(CO)$_3$]$^-$	0.925	0.930
[Mn(HPEAB)(CO)$_3$(CO$_2$)]$^-$	0.918	0.915

Catalytic studies

Plot of %CO vs time for controlled potential electrolysis of [Re(HPEAB)(CO)$_3$Cl] compared to [Re(dmbpy)(CO)$_3$Cl] reference

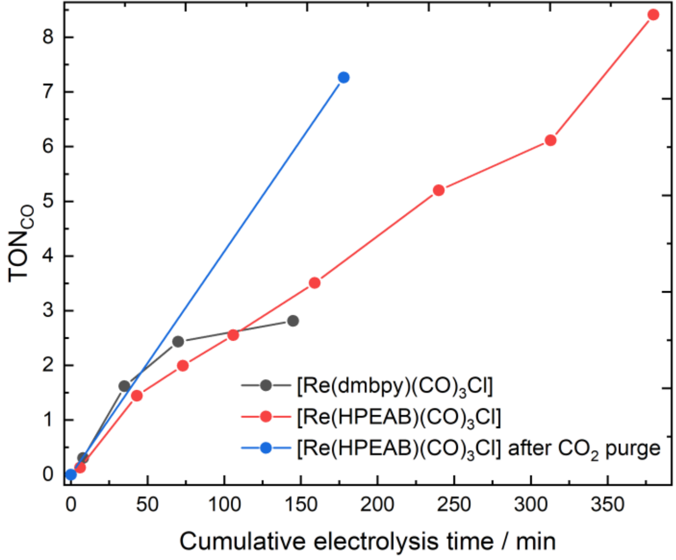

Figure B40 – Turnover number-time profile for carbon monoxide produced by [Re(dmbpy)(CO)$_3$Cl] (grey) and [Re(HPEAB)(CO)$_3$Cl] (red) during controlled potential electrolysis at -1.9 V vs. an Ag wire pseudoreference electrode. Also shown is the catalytic performance of [Re(HPEAB)(CO)$_3$Cl] after re-bubbling the solution with CO$_2$ (blue).

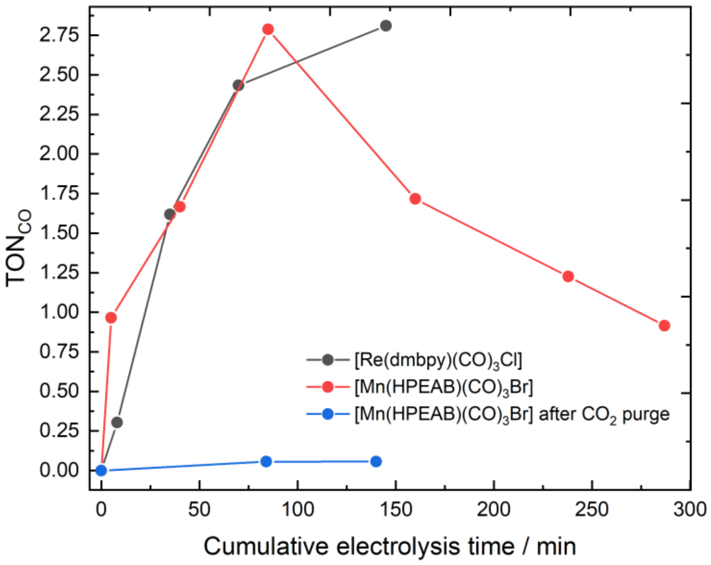

Figure B41 – Turnover number-time profile for carbon monoxide produced by [Re(dmbpy)(CO)$_3$Cl] (grey) and [Mn(HPEAB)(CO)$_3$Br] (red) during controlled potential electrolysis at -1.9 V vs. an Ag wire pseudoreference electrode. Also shown is the catalytic performance of [Mn(HPEAB)(CO)$_3$Br] after re-bubbling the solution with CO$_2$ (blue).

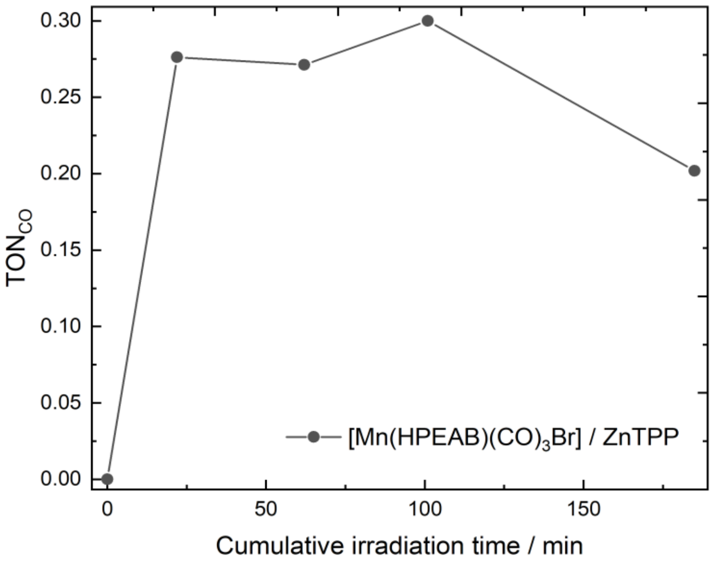

Figure B42 – Turnover number-time profile for carbon monoxide produced by [Mn(HPEAB)(CO)$_3$Br] following photosensitisation by tetraphenylporphyrin zinc(II) under 625 nm irradiation in the presence of triethylamine sacrificial donor.

References

1. C. Costentin, M. Robert and J.-M. M. Savéant, *Chem. Soc. Rev.*, 2013, **42**, 2423–2436.

2. C. Costentin, J. Savøant and J.-M. Savéant, *ChemElectroChem*, 2014, **1**, 1226–1236.

3. C. Costentin, S. Drouet, M. Robert, J. Save and J. M. Savéant, *J. Am. Chem. Soc.*, 2012, **134**, 11235–11242.

Appendix C – Experimental supporting information for chapter 3

Part 1: Materials and Methods

All preparative procedures were carried out using standard techniques. All commercially available reagents were laboratory grade and used as received unless otherwise stated. Dry solvents were obtained from the Grubbs dry solvent service at the University of Sheffield. Air sensitive reactions were carried out under argon delivered through a vacuum-gas manifold at a relative pressure of 0.1 bar. Vacuum was established with a mineral oil sealed rotary vane pump, the ultimate vacuum achievable was 8×10^{-2} mbar.

Gas chromatography

Detection of gaseous products was done using gas chromatography. The gas analysis was performed with a Perkin-Elmer Autosystem XL gas chromatograph equipped with a thermal conductivity detector (TCD). The TCD compared the thermal conductivities of the reference gas (He) with the carrier gas (H_2 for CO detection, N_2 for hydrogen detection) and analyte. The separation column was a Restek RT-M porous layer sieve (5 Å). The column was 30 m long with a diameter of 0.53 mm. The chromatograph method file was designed to achieve maximum separation between the carbon monoxide products and trace nitrogen remaining in the samples. The method file was set-up with the following parameters:

Injection volume: 100 μL

Starting temperature: 30 °C

TCD temperature: 100 °C

Carrier gas: hydrogen

Carrier gas flow rate: 5 cm^3 min^{-1}

Temperature ramp: Hold at 30 °C for three minutes. Then increase the oven temperature by 10 °C min^{-1} until the oven reaches 100 °C. Hold at 100 °C for one minute.

Preparation of tetra(N-methyl-4-pyridyl)porphyrin zinc (II) tetrachloride

This complex was prepared according to a literature procedure.[1]

Preparation of dimethylphenylbenzimidazoline (BIH)

This compound was prepared according to a literature procedure.[2]

Preparation of 4,4'-bis(diethoxymethylphosphonato)-2,2'-bipyridine

This ligand was prepared according to a modified literature procedure.[3]

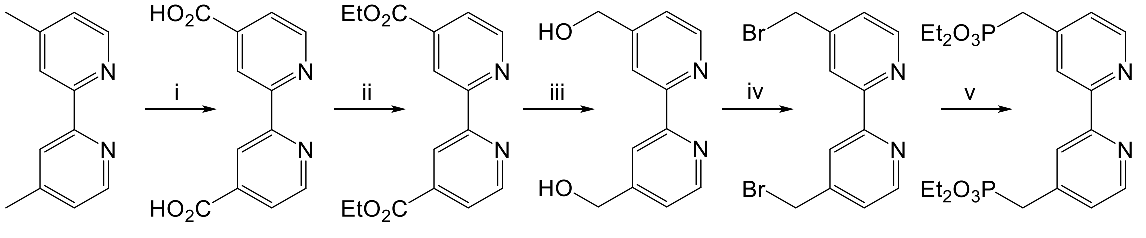

i) $K_2Cr_2O_7/H_2SO_4$ (85%), ii) EtOH-H_2SO_4 (90%), iii) $NaBH_4$-EtOH (81%), iv) HBr-H_2SO_4 (85%), v) $P(OEt)_3$ (80%)

4,4’-dicarboxy-2,2′-bipyridine

4,4′-dimethyl-2,2′-bipyridine (2.5 g 13.5 mmol) was dissolved in of 98% H_2SO_4 (100 cm^{-3}). To this solution, potassium dichromate (12 g) was added in portions whilst stirring, ensuring the temperature remained between 40-80°C. The reaction mixture was then cooled in an ice bath, and the resulting precipitate isolated by vacuum filtration. The precipitate was then refluxed for 16 h in 50% HNO_3 (50 cm^3), then poured over ice and subsequently diluted to with water (400 cm^3) and left to warm to room temperature. The resulting white precipitate was then filtered off, washed with water and acetone and dried under a vacuum to yield the product (2.29 g, 91%).

^{1}H NMR (400 MHz, d^6-DMSO) δ 8.93 (dd, J = 4.9, 0.7 Hz, 2H), 8.87 – 8.83 (m, 2H), 7.92 (dd, J = 4.9, 1.6 Hz, 2H).

4,4′-bis(ethoxyester)-2,2′-bipyridine

4,4′-dicarboxy-2,2′-bipyridine (1.05 g, 4.12 mmol) was suspended in ethanol (40 cm^3) then 98% H_2SO_4 (2 cm^3) was added. The mixture was refluxed at 85 °C under inert atmosphere for 24 hours to give a pale pink solution. Removal of the solvent under reduced pressure left a pale pink oil, which was mixed with water (20 cm^3) and extracted with chloroform (3 x 50 cm^3). The combined organic fractions were dried over anhydrous $MgSO_4$. The mixture was then filtered, and the volume reduced under reduced pressure to approximately 20 cm^3. Addition of methanol (20 cm^3) resulted in formation of a pale pink precipitate, which was isolated by vacuum filtration and then dried under high vacuum to yield the product (964 mg, 76%).

^{1}H NMR (400 MHz, $CDCl_3$) δ 8.97 (s, 2H), 8.89 (d, *J* = 4.9 Hz, 2H), 7.94 (dd, *J* = 5.0, 1.6 Hz, 2H), 4.48 (q, *J* = 7.1 Hz, 4H), 1.47 (t, *J* = 9.2, 5.0 Hz, 6H).

4,4′-bis(hydroxymethyl)-2,2′-bipyridine

4,4′-bis(ethoxyester)-2,2′-bipyridine (750 mg, 2.4 mmol) was suspended in ethanol (50 cm^3) followed by the addition of sodium borohydride (2 g, 53 mmol). The mixture was refluxed at 65 °C under inert atmosphere for 3 hours. A gel was observed forming on the surface of the reaction mixture after approximately 1 hour, which was dissolved by addition of additional ethanol (25 cm^3). After cooling to room temperature, a saturated aqueous solution of NH_4Cl (100 cm^3) was added to the mixture and stirred for 15 min. The ethanol was removed under reduced pressure and the resulting white solid was dissolved in the minimum volume of water (*ca.* 150 cm^3). The solution was extracted with ethyl acetate (5 x 50 cm^3), then the combined organic fractions were dried over anhydrous $MgSO_4$. The solvent was removed under reduced pressure, yielding the product as a pale pink solid (306 mg, 50%).

^{1}H NMR (400 MHz, d^6-DMSO) δ 8.60 (δ, *J* = 4.9 Hz, 2H), 8.39 (s, 2H), 7.40 – 7.34 (m, 2H), 5.56 (t, *J* = 5.8 Hz, 2H), 4.63 (d, *J* = 5.8 Hz, 4H).

4,4′-bis(bromomethyl)-2,2′-bipyridine

4,4′-bis(hydroxymethyl)-2,2′-bipyridine (674 mg, 3.12 mmol) was dissolved in 48% HBr (40 cm^3) and 98% H_2SO_4 (14 cm^3). The resulting fuming orange solution was refluxed at 100 °C for 18 hours. Upon cooling to room temperature, the mixture was neutralized with a saturated aqueous solution of NaOH (*ca.* 200 cm^3). The resulting white precipitate was isolated by vacuum filtration, washed with water (300 cm^3), and then left to dry. The solid was then dissolved in chloroform (40 cm^3), dried over anhydrous $MgSO_4$ and filtered. The solvent was removed under reduced pressure, yielding the product as a white solid (842 mg, 79%).

^{1}H NMR (400 MHz, $CDCl_3$) δ 8.70 (d, *J* = 5.0 Hz, 2H), 8.46 (d, *J* = 1.2 Hz, 2H), 7.39 (dd, *J* = 5.0, 1.8 Hz, 2H), 4.51 (s, 4H).

4,4′-bis(methyl-diethoxyphosphonato)-2,2′-bipyridine

A solution of diethyl phosphite (15 cm^3) in chloroform (10 ^{3}) was purged with N_2 for 30 min. This mixture was transferred to a flask containing 4,4′-bis(bromomethyl)-2,2′-bipyridine (842 mg, 2.46

mmol) and subsequently refluxed at 85 °C for 6 hours. The reaction mixture was allowed to cool to room temperature, and then the solvent and excess diethyl phosphite were removed under reduced pressure to yield the crude product as a pale pink solid. The crude product was purified by column chromatography (SiO_2, 80:20 ethyl acetate: methanol) to yield the purified product as a pale yellow oil. The oil was left overnight, resulting in crystallisation of the product as an off-white solid (942 mg, 64%).

^{1}H NMR (250 MHz, $CDCl_3$) δ 8.60 (d, *J* = 5.0 Hz, 2H), 8.33 (s, 2H), 7.42 – 7.28 (m, 2H), 4.07 (dq, *J* = 8.1, 7.1 Hz, 8H), 3.23 (d, *J* = 22.2 Hz, 4H), 1.27 (t, *J* = 7.1 Hz, 12H). ^{31}P NMR (101 MHz, $CDCl_3$) δ 24.30 (s). MS (ESI, +ve): *m/z* 457.2 (MH^+).

Part 2: Additional characterisation data for [Mn($\{Et_2O_3PCH_2\}_2$bpy)$(CO)_3$(Br)]

UV-vis spectroscopy

Visible absorption spectroscopy of the manganese complex shows successful coordination of the bipyridyl ligand to the complex, as evidenced by the π–π* and MLCT electronic absorption bands. The UV-vis spectrum showed that it would be possible to irradiate the CO_2 reducing systems at 625 nm with no light absorption from the catalyst. Therefore, photolysis could be prevented through the use of porphyrins as photosensitisers.

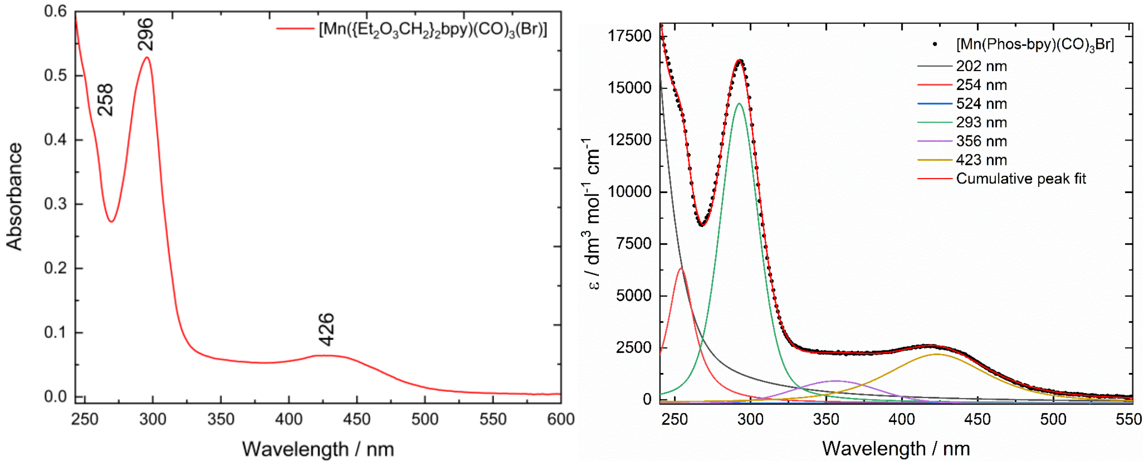

Figure C1 – UV-vis absorption spectra of [Mn(phos-bpy)$(CO)_3$Br] in dichloromethane, the pseudo-Voigt profiles used to deconvolute the absorption spectrum are shown on the right.

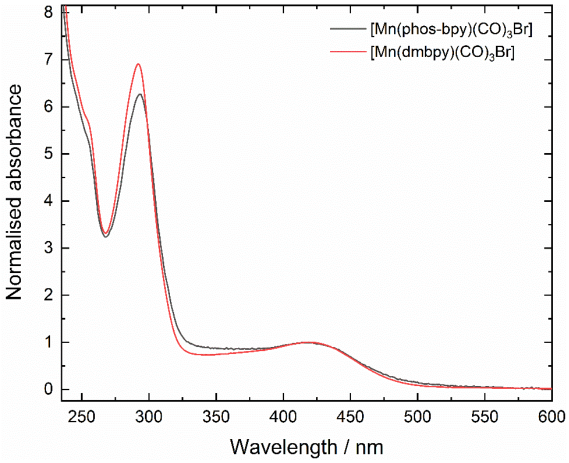

Figure C2 – UV-vis spectra of [Mn(phos-bpy)$(CO)_3$Br] and [Mn(dmbpy)$(CO)_3$Br] in dichloromethane, normalised to the MLCT/XLCT maxima.

FT-IR spectroscopy

FT-IR spectra of the analyte complex in DCM provide evidence for the proposed structure. It was possible to identify vibrational modes attributed to the CO, CH and PO bond vibrations.

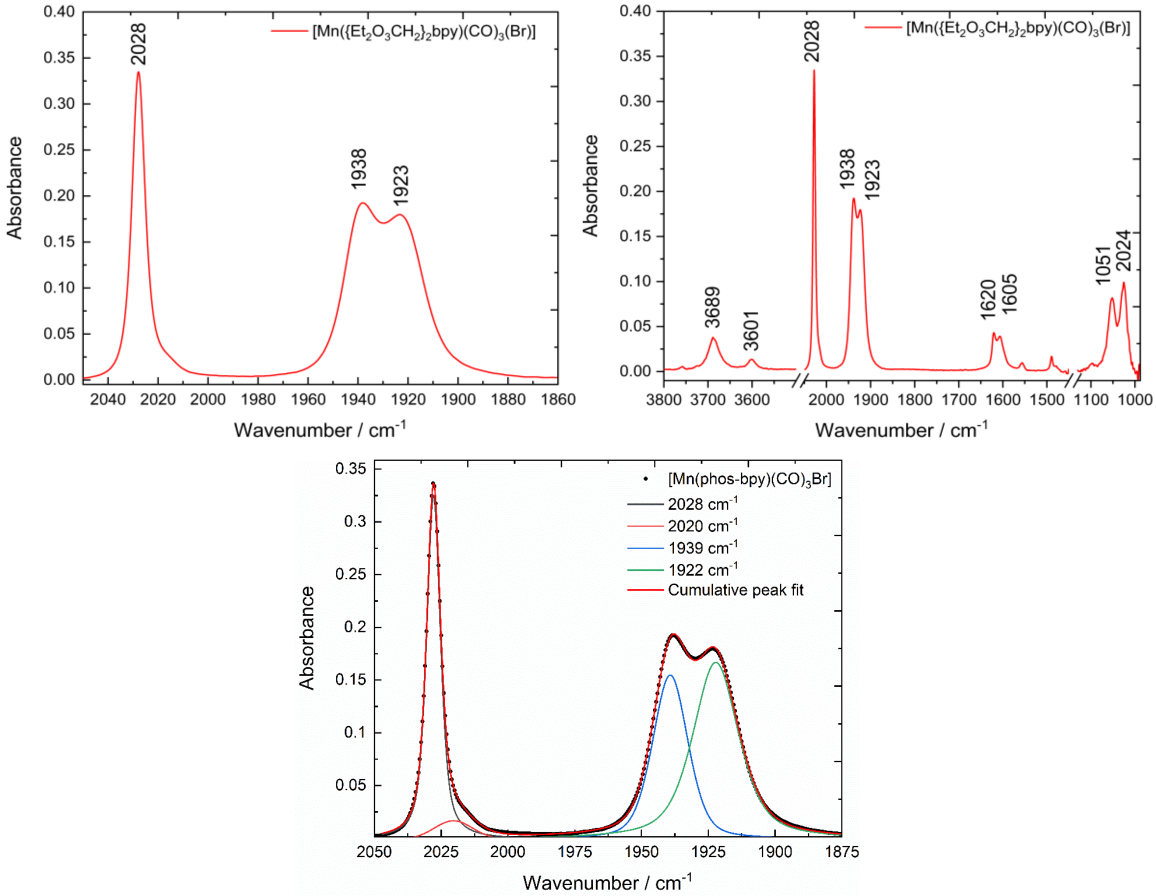

Figure C3 – IR absorption spectra of [Mn(phos-bpy)(CO)$_3$Br] in dichloromethane, the pseudo-Voigt profiles used to deconvolute the carbonyl group vibrations are shown at the bottom.

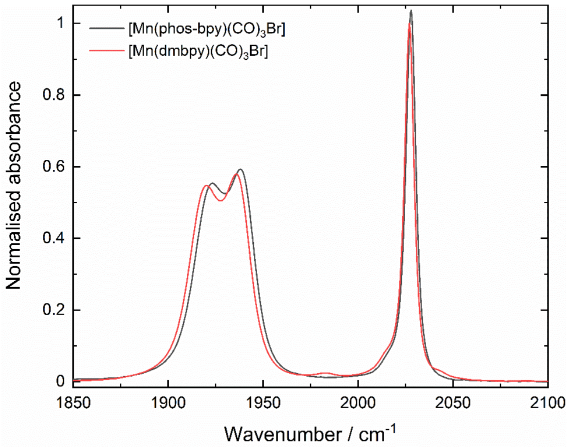

Figure C4 – IR spectra of [Mn(phos-bpy)(CO)$_3$Br] and [Mn(dmbpy)(CO)$_3$Br] in dichloromethane, normalised to the a'(1) maxima.

^{1}H NMR:

^{1}H-NMR was consistent with the proposed structure, showing three resonances for the bipyridyl environments, and three alkyl environments for the methylene and ethyl moieties.

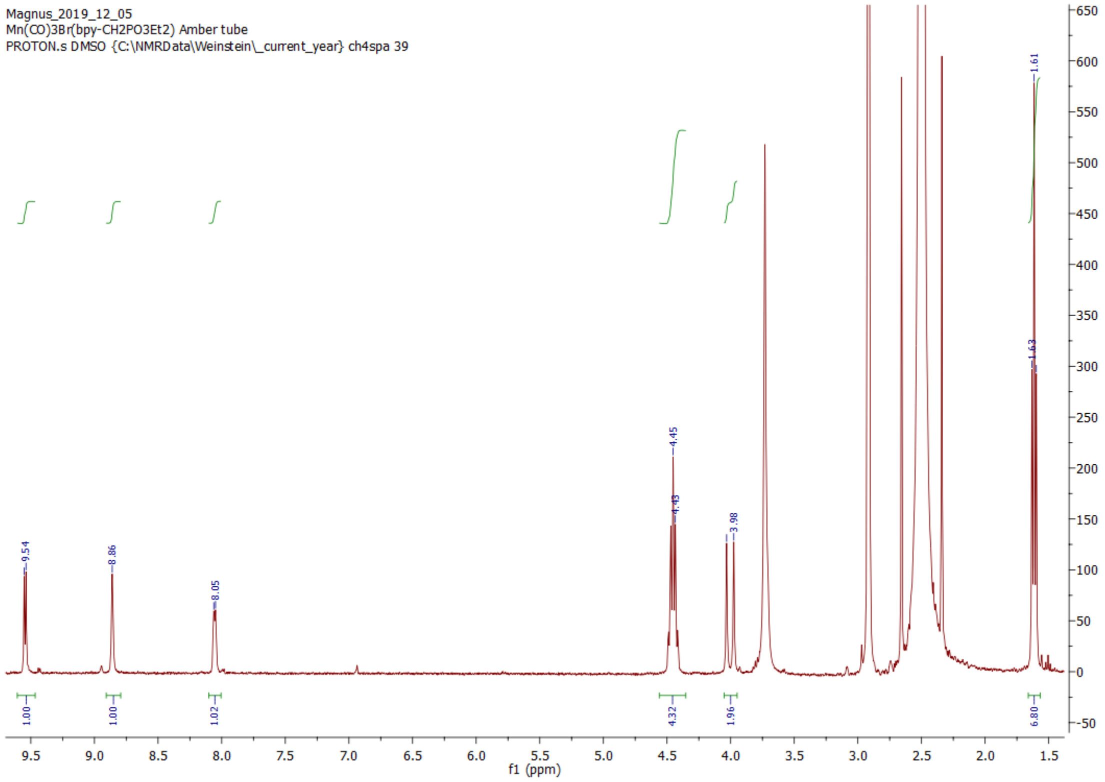

Figure C5 – ^{1}H NMR spectrum of [Mn(phos-bpy)(CO)$_3$Br] in d^{6}-dimethylsulphoxide.

^{13}C NMR:

The methylene group in this complex appears as a doublet due to the coupling between the ^{31}P and ^{13}C nuclei. The small peak at δ=31 is the *C*H$_3$ resonance of acetone. All other signals are attributed to the analyte complex, not all quaternary carbons were observed.

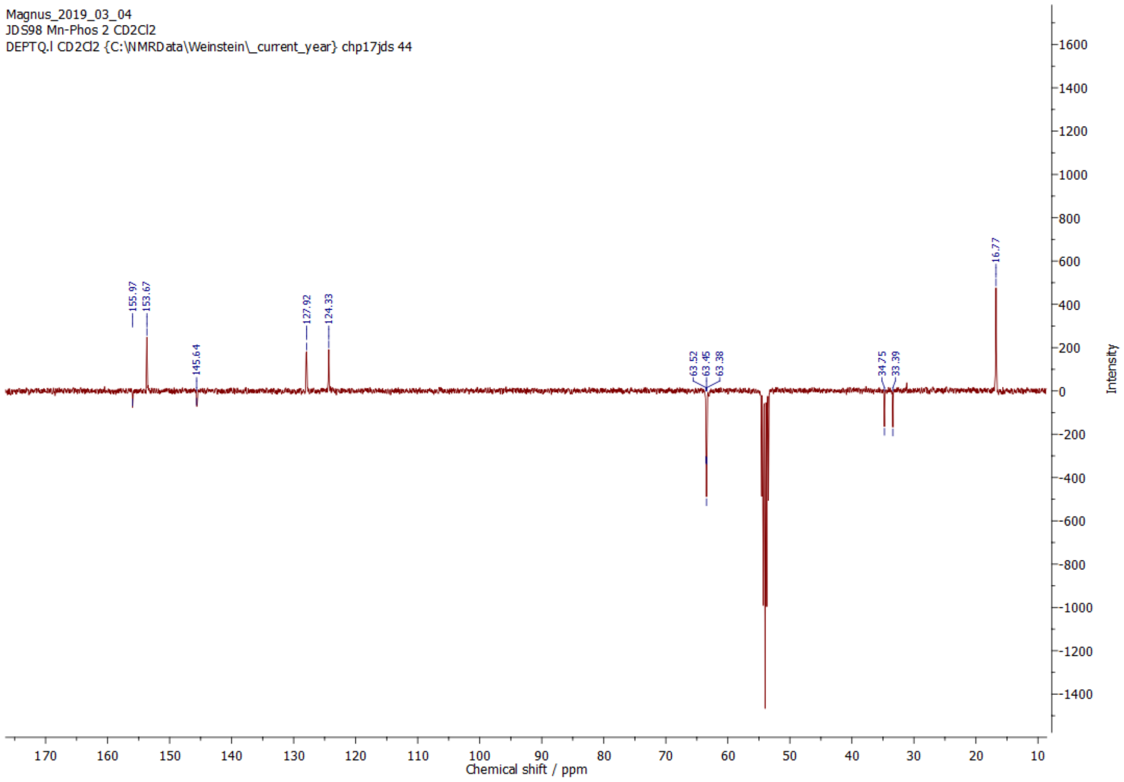

Figure C6 – ^{13}C{^{1}H} NMR spectrum of [Mn(phos-bpy)(CO)$_3$Br] in d^{2}-dichloromethane.

^{31}P NMR

A single resonance was observed in the proton decoupled ^{31}P spectrum. The resonance appears to be a singlet with a small shoulder. This was likely due to convolution with a doublet resulting from ^{31}P-^{13}C coupling. The doublet is much less intense than the singlet peak due to the low abundance of ^{13}C compared to ^{31}P.

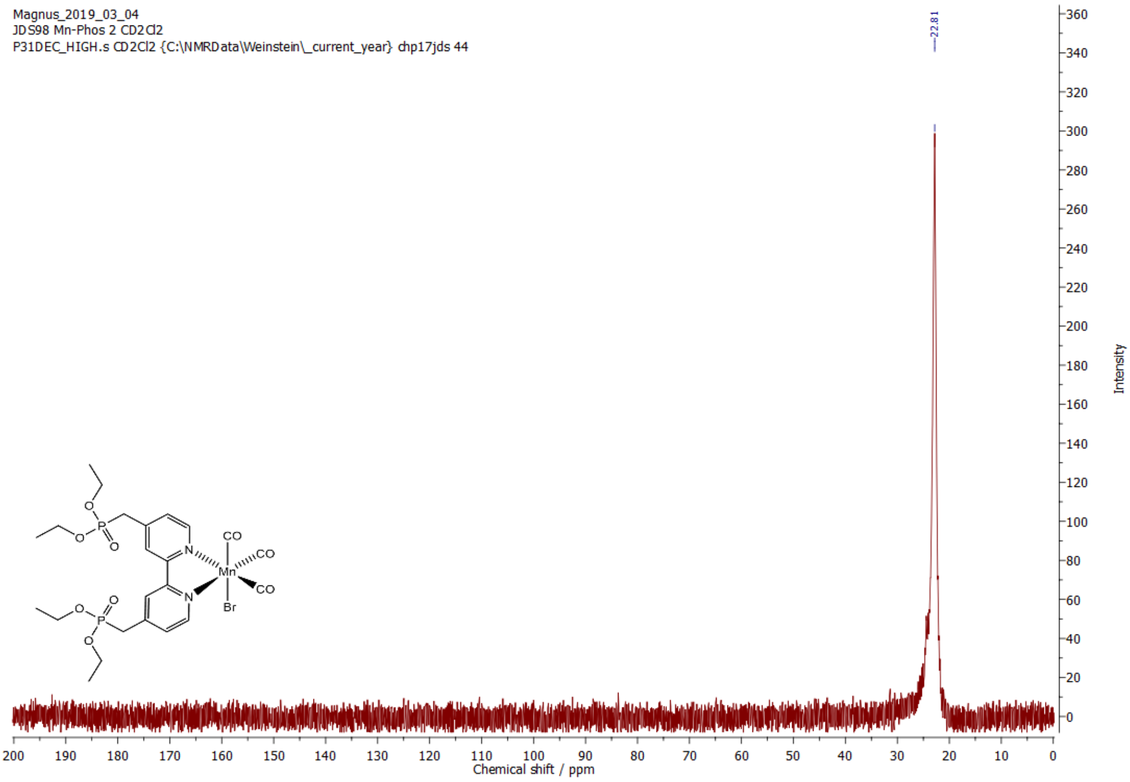

Figure C7 – ^{31}P NMR spectrum of [Mn(phos-bpy)(CO)$_3$Br] in d^2-dichloromethane.

Mass spectrum

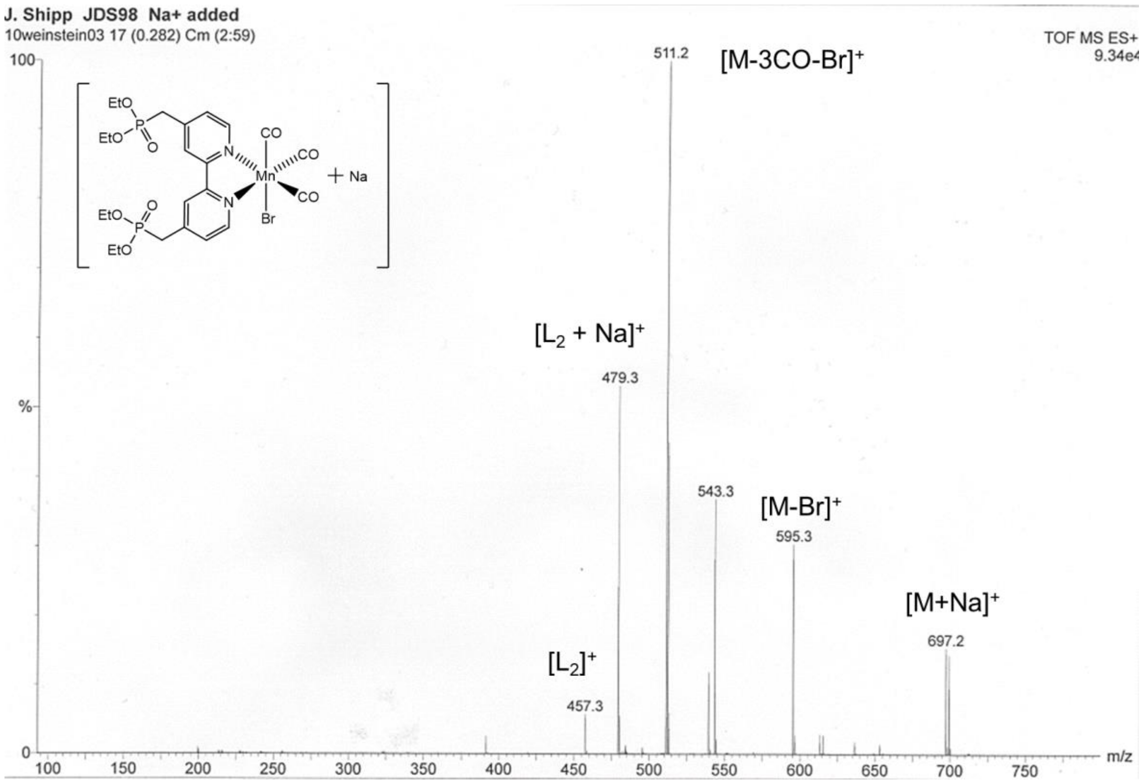

Figure C8 – Positive electrospray ionisation mass spectrum of [Mn(phos-bpy)(CO)$_3$Br], loaded by direct insertion with addition of sodium

Part 3: Additional electrochemical data

[Mn(phos-bpy)(CO)$_3$Br] – 1st oxidation

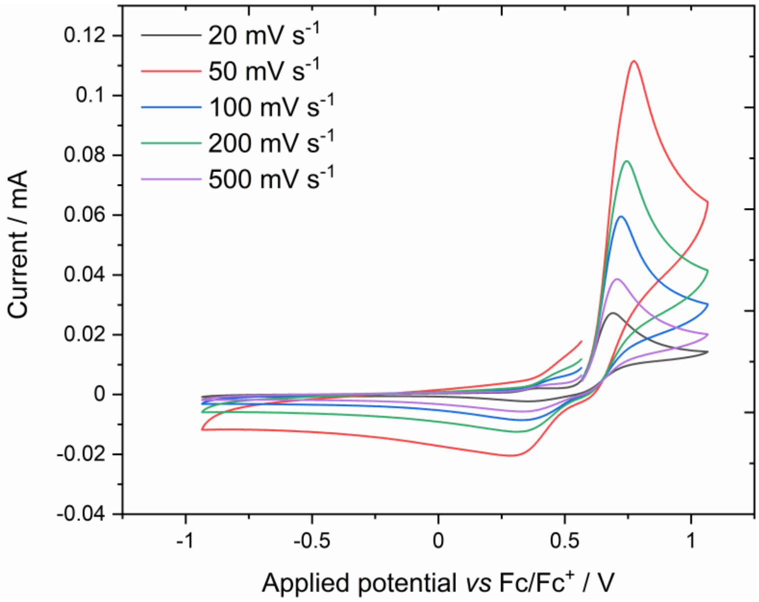

Figure C9 – Cyclic voltammograms of the 1st oxidation of [Mn(phos-bpy)(CO)$_3$Br] in anhydrous acetonitrile, under N_2 atmosphere at various scan rates, as shown on the graph.

[Mn(phos-bpy)(CO)$_3$Br] – 1st reduction

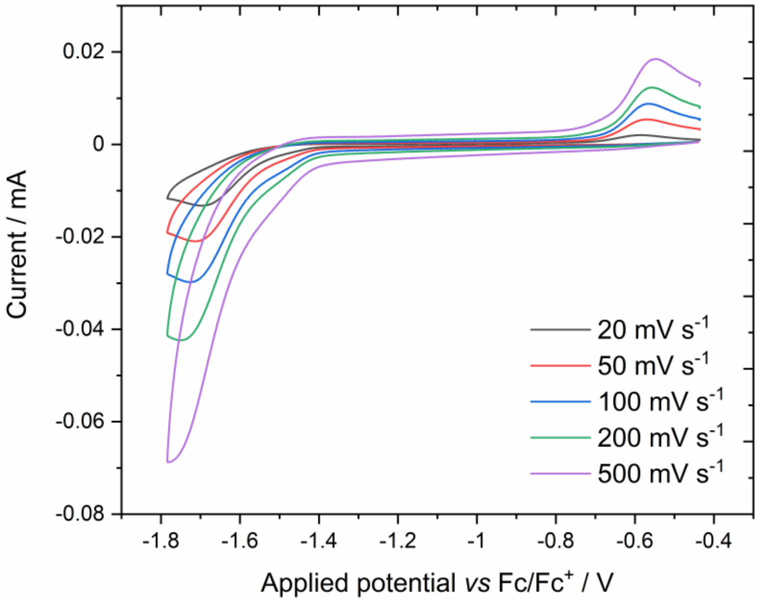

Figure C10 – Cyclic voltammograms of the 1st reduction of [Mn(phos-bpy)(CO)$_3$Br] in anhydrous acetonitrile, under N$_2$ atmosphere at various scan rates, as shown on the graph.

[Mn(phos-bpy)(CO)$_3$Br] – 2nd reduction

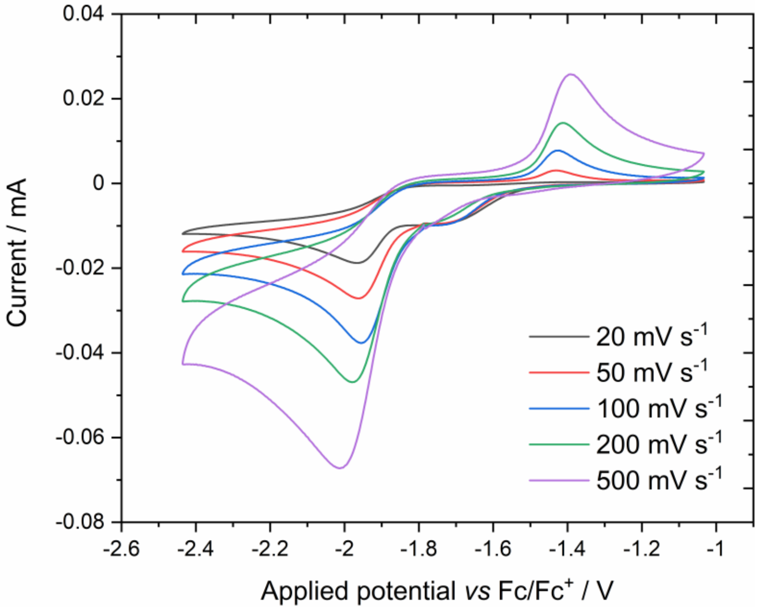

Figure C11 – Cyclic voltammograms of the 2nd reduction of [Mn(phos-bpy)(CO)$_3$Br] in anhydrous acetonitrile, under N$_2$ atmosphere at various scan rates, as shown on the graph.

[Mn(phos-bpy)(CO)$_3$Br] – 3rd reduction

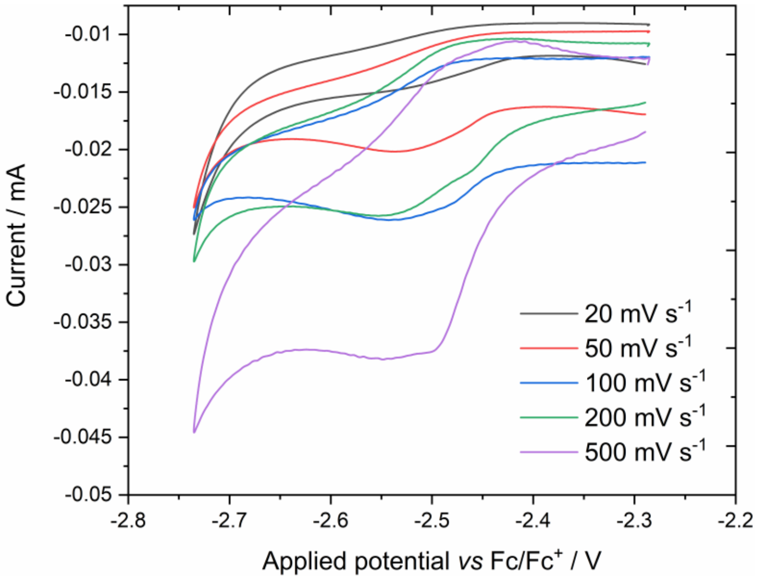

Figure C12 – Cyclic voltammograms of the 3rd reduction of [Mn(phos-bpy)(CO)$_3$Br] in anhydrous acetonitrile, under N_2 atmosphere at various scan rates, as shown on the graph.

[Mn(phos-bpy)(CO)$_3$Br] – Plots of peak current against square root of the scan rate

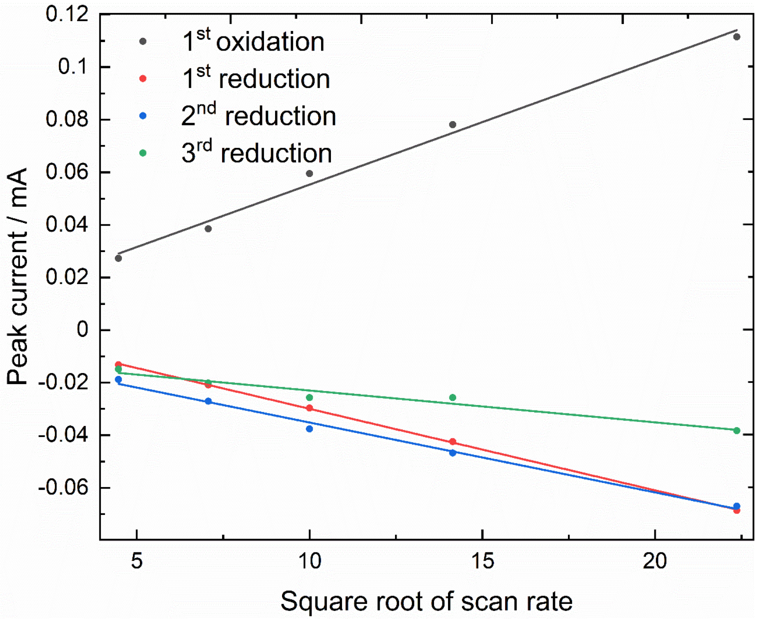

Figure C13 – Relationship between the total peak current of the redox couple against the square root of the scan rate for the four electrochemical processes of [Mn(phos-bpy)(CO)$_3$Br], recorded in anhydrous acetonitrile under N_2 atmosphere. The lines are linear fits of the data.

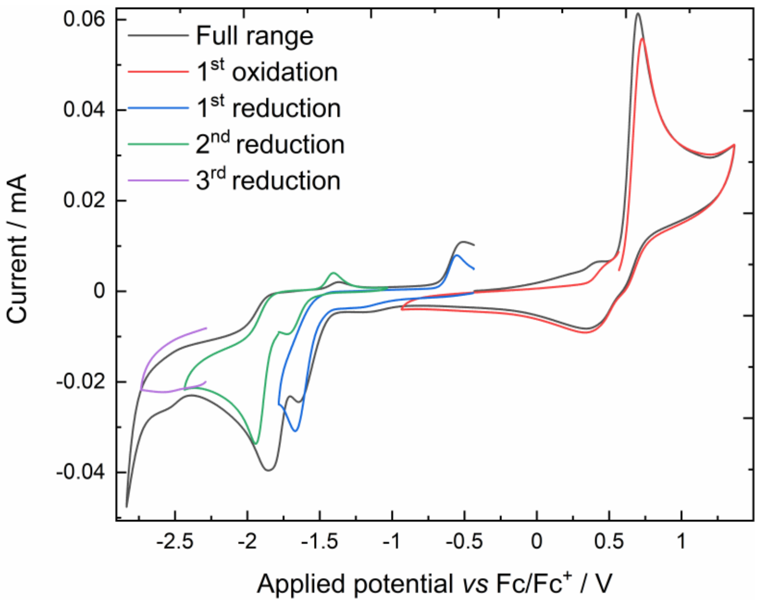

Figure C14 – Cyclic voltammogram of [Mn(phos-bpy)(CO)$_3$Br] in anhydrous acetonitrile under CO$_2$ atmosphere, also shown are isolations of the individual redox processes, as stated on the graph.

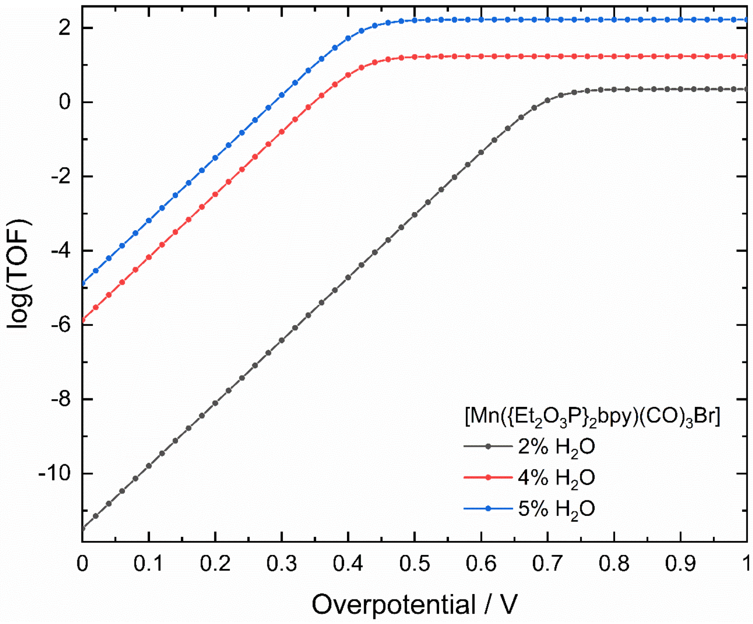

Figure C15 – Catalytic Tafel plots for electrochemical CO$_2$ reduction with [Mn(phos-bpy)(CO)$_3$Br] in the presence of different water concentrations, as shown on the graph.

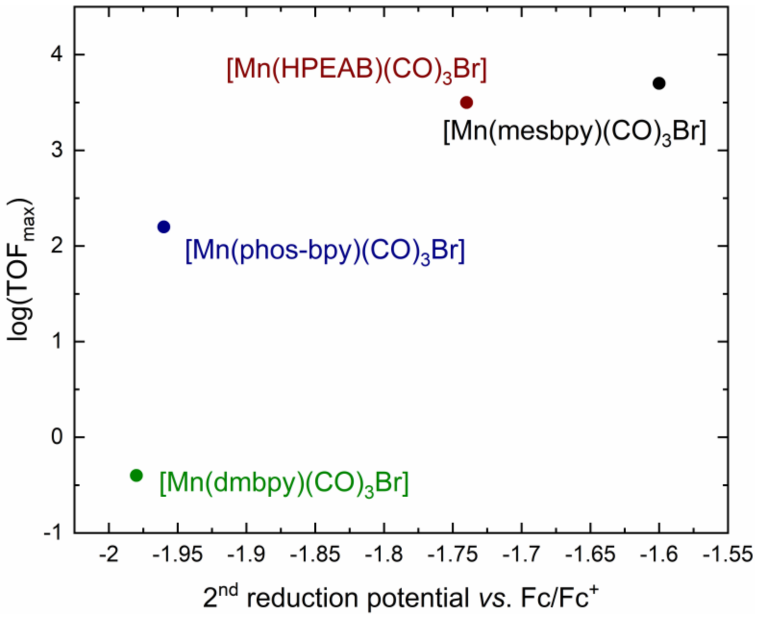

Figure C16 – A plot of 2nd reduction potential against log(TOF$_{max}$) for four different CO_2 reduction catalysts in 5% H_2O: MeCN for [Mn(dmbpy)(CO)$_3$Br], [Mn(phos-bpy)(CO)$_3$Br], and [Mn(HPEAB)(CO)$_3$Br]. [Mn(mesbpy)(CO)$_3$Br] was studied in MeCN with 0.3 mol dm^{-3} trifluoroacetic acid.

Part 4: Additional photocatalytic data

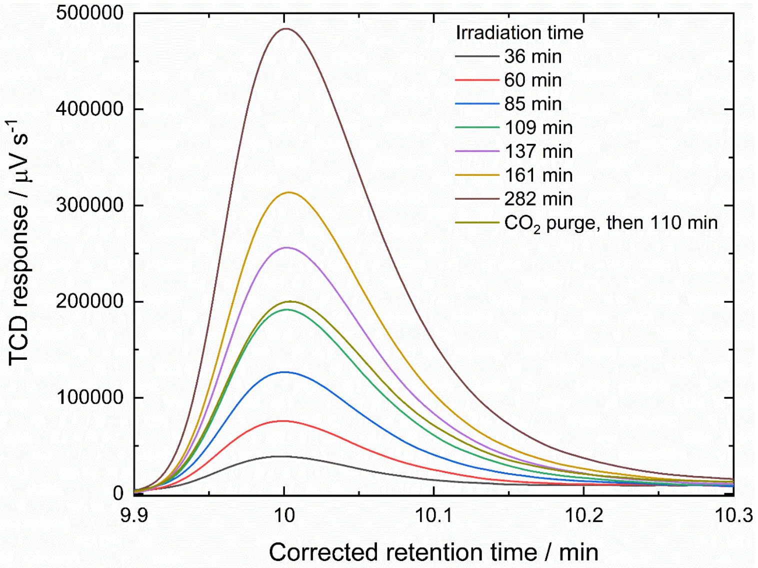

*Figure C17 – Gas chromatograms of the reaction mixture headspace during photocatalytic CO_2 reduction with **1**, **2**, and ascorbic acid in aqueous solution under 625 nm irradiation.*

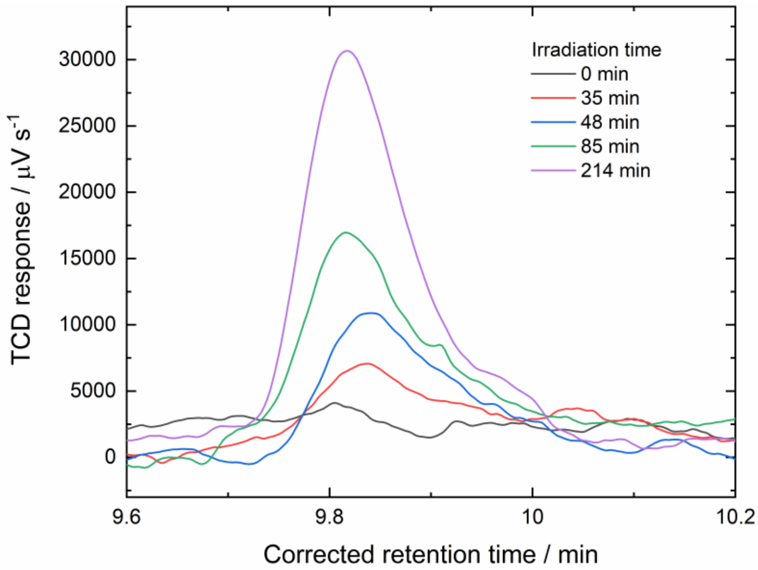

Figure C18 – Gas chromatography traces for the photocatalytic control experiment, where [Mn(phos-bpy)(CO)$_3$Br] and ascorbic acid were dissolved in aqueous solution and irradiated with 625 nm light.

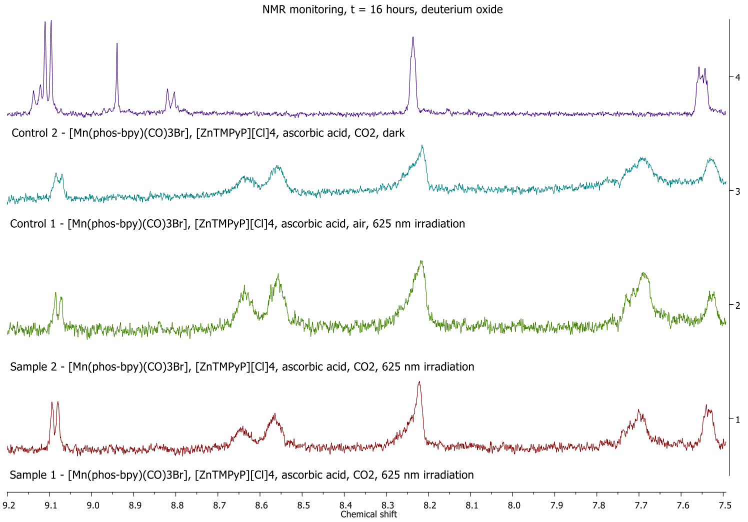

Figure C19 – ^1H NMR spectra of [Mn(phos-bpy)(CO)$_3$Br], [ZnTMPyP][Cl]$_4$, and ascorbic acid in D_2O under various conditions, recorded 16 hours after sample preparation.

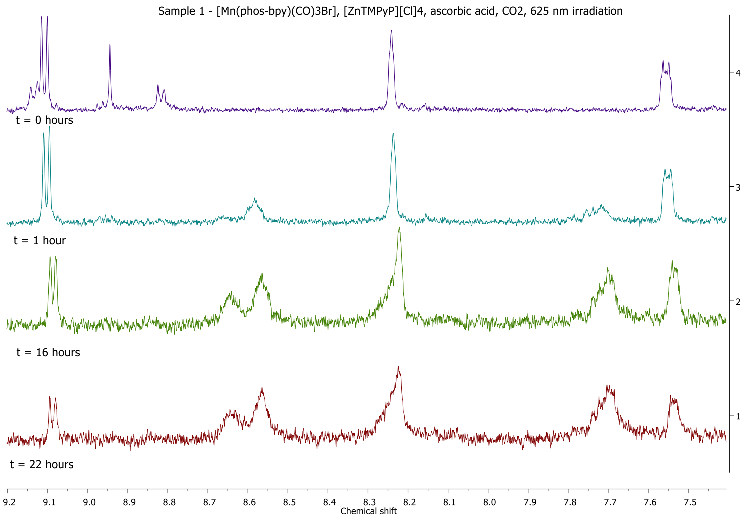

Figure C20 – ^{1}H NMR spectra of [Mn(phos-bpy)(CO)$_3$Br], [ZnTMPyP][Cl]$_4$, and ascorbic acid in D$_2$O under ^{12}CO$_2$ atmosphere after at different irradiation times, as stated on the graph.

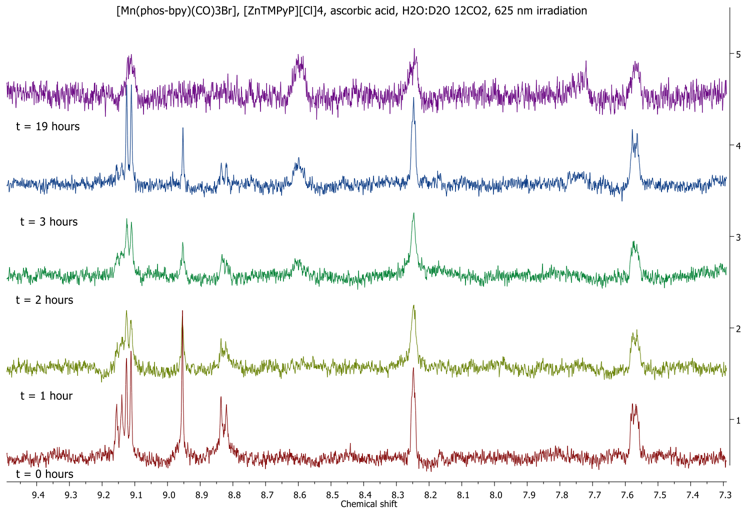

Figure C21 – ^{1}H NMR spectra of [Mn(phos-bpy)(CO)$_3$Br], [ZnTMPyP][Cl]$_4$, and ascorbic acid in 90:10 H$_2$O:D$_2$O under ^{12}CO$_2$ atmosphere after at different irradiation times, as stated on the graph.

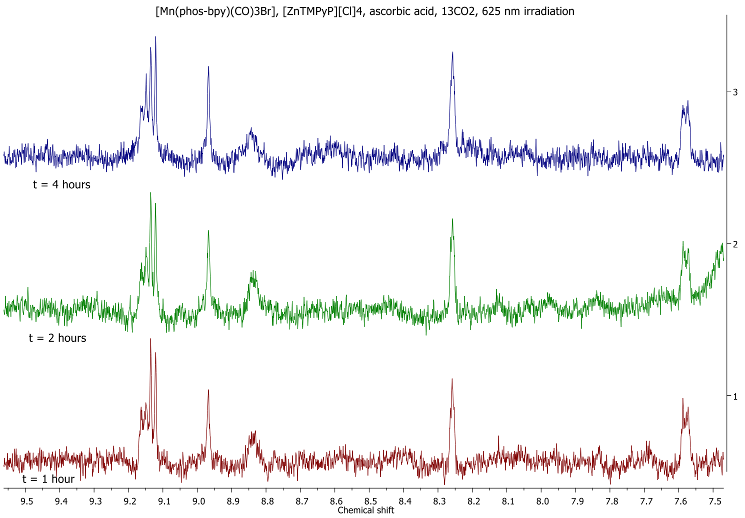

Figure C22 – ^{1}H NMR spectra of [Mn(phos-bpy)(CO)$_3$Br], [ZnTMPyP][Cl]$_4$, and ascorbic acid in 90:10 H_2O:D_2O under $^{13}CO_2$ atmosphere after at different irradiation times, as stated on the graph.

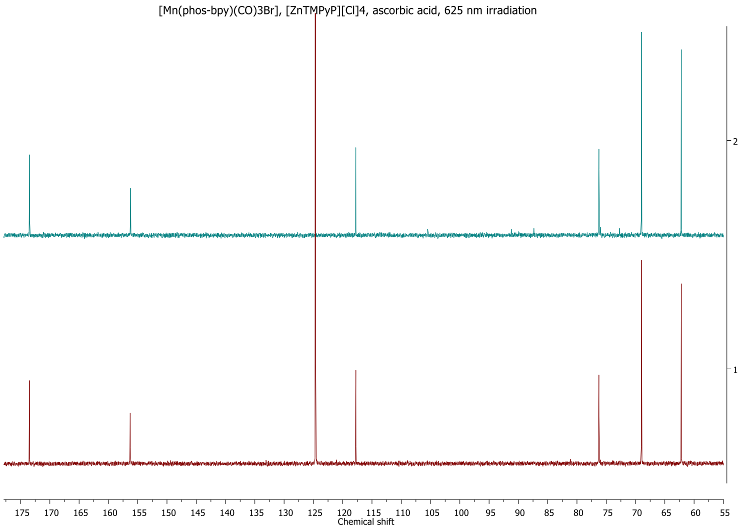

Figure C23 – ^{13}C{^{1}H} NMR spectra of [Mn(phos-bpy)(CO)$_3$Br], [ZnTMPyP][Cl]$_4$, and ascorbic acid in 90:10 H_2O:D_2O under 3 hours of 625 nm irradiation. Top: Sample prepared without CO_2 purge. Bottom: Sample purged with $^{13}CO_2$. The $^{13}CO_2$ resonance was observed at 124 ppm.

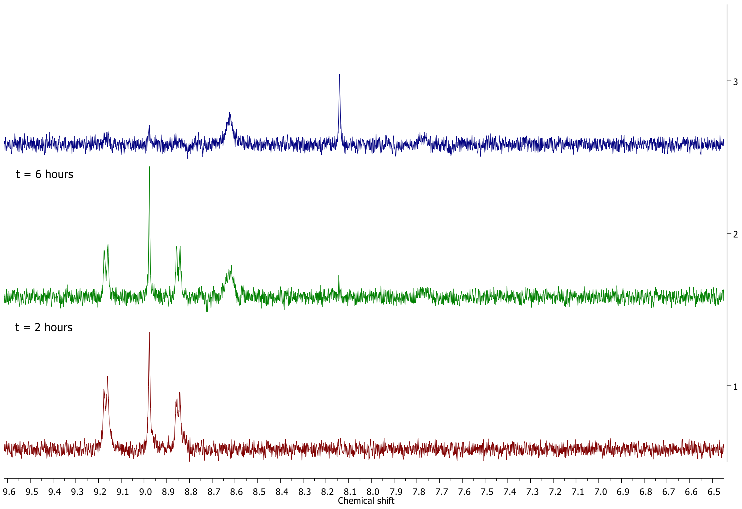

Figure C25 – ^{1}H NMR spectra of [ZnTMPyP][Cl]$_4$ and ascorbic acid in D_2O at different irradiation times, as stated on the graphs

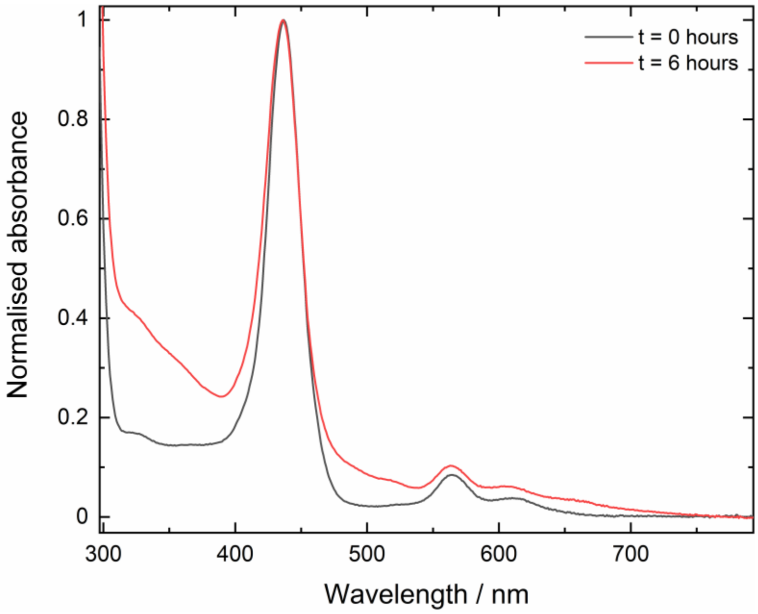

Figure C26 – UV-vis absorption spectra of [ZnTMPyP][Cl]$_4$ and ascorbic acid in D_2O at different irradiation times, as stated on the graph.

X-Ray crystallographic data

1 was crystallised by diffusion of Et_2O vapour into a solution of the complex in dichloromethane (DCM) to yield yellow crystals of the complex. The studied crystal with dimensions 0.5 x 0.5 x 0.4 mm was found to be triclinic with the P-1 space group. The unit cell contained two molecules of **1**, and no solvent co-crystallised with the complex. The complex formed the expected facial isomer, consistent with previously reported [Mn(L_2)(CO)$_3$(X)] complexes. In the unit cell, the two molecules are offset and rotated 180° from one another, with the axial plane of the Mn centre pointed toward the bipyridyl π-system of the other complex. This geometry minimised the steric interaction of the four phosphonate ester groups by separating them by the largest possible distance.

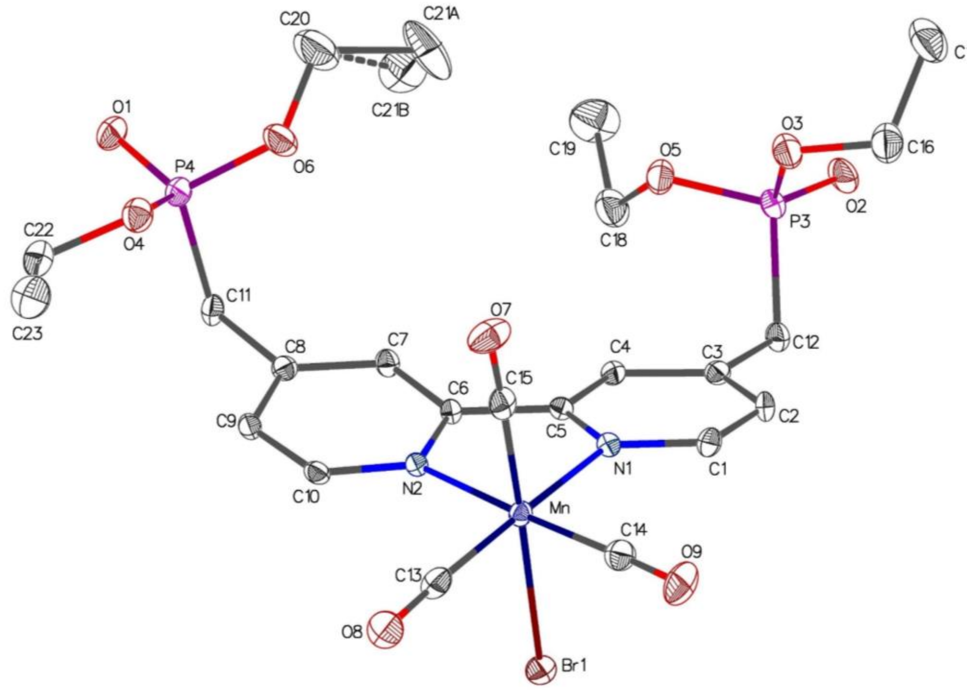

Figure C27 - Molecular structure and unit cell of the [Mn(4,4'-{Et$_2$*PO*$_3$*CH*$_2$*}-2,2'-bipyridyl)(CO)*$_3$*Br] crystal, measured by single crystal X-ray diffraction, thermal ellipsoids are drawn at the 50% probability level. Bond distances and angles are provided in the appendix C.*

Appendix D – Experimental supporting information for chapter 4

Part I

1. DFT calculations

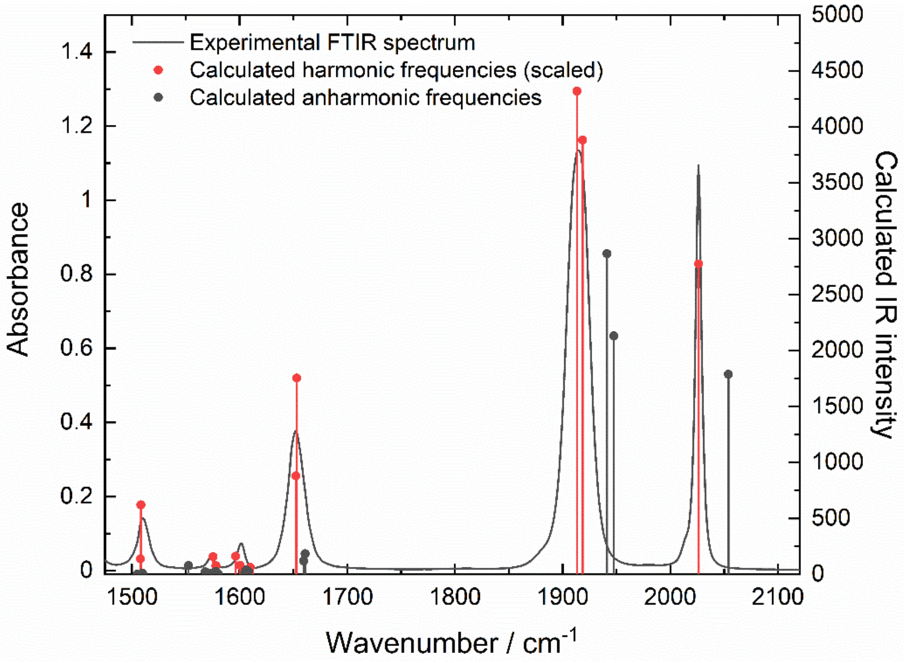

Figure D1 – Calculated harmonic and anharmonic frequencies for [Re(HPEAB)(CO)$_3$Cl] in DCM (dots), overlaid with the experimental FTIR spectrum. The harmonic frequencies at ν < 1800 were scaled by a factor of 0.9775, and the frequencies at ν > were scaled by a factor of 0.9725.

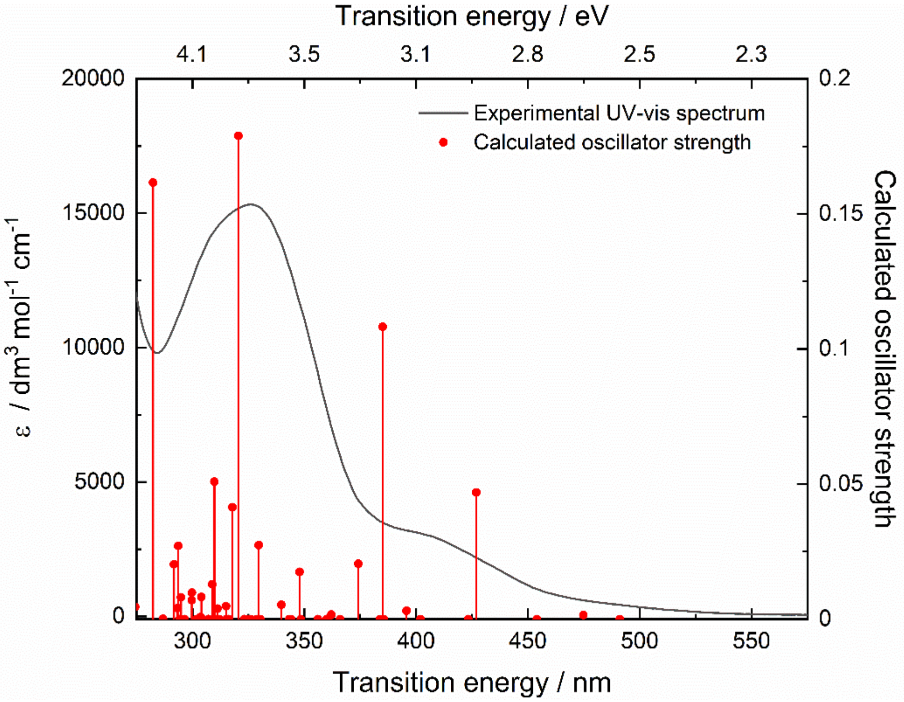

Figure D2 – Calculated electronic transition energies (dots) overlaid with the experimental UV-vis absorption spectrum of [Re(HPEAB)(CO)$_3$Cl] in DCM. The energy axis is given in both nanometres and electron volts.

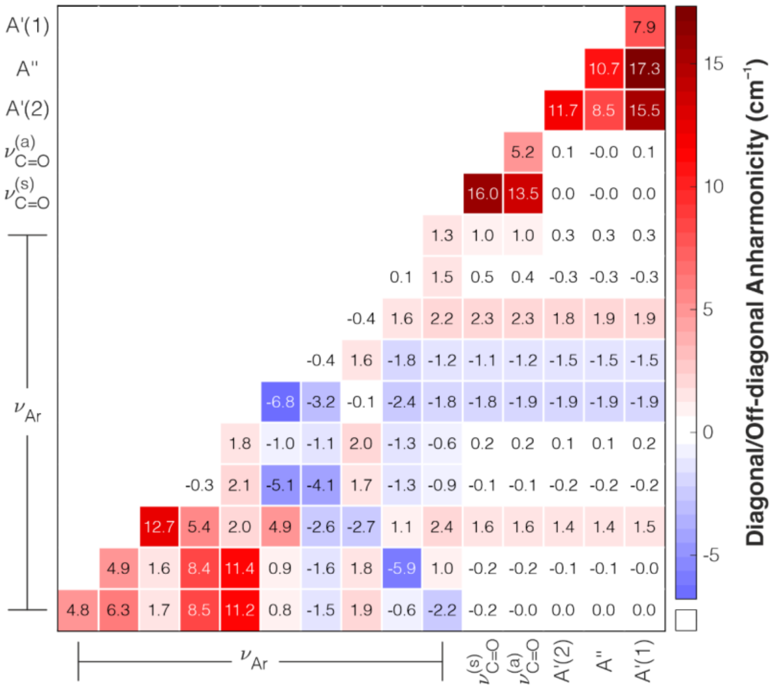

	ν_{Ar}										$\nu^{(s)}_{C=O}$	$\nu^{(a)}_{C=O}$	A'(2)	A''	A'(1)
A'(1)															7.9
A''														10.7	17.3
A'(2)													11.7	8.5	15.5
$\nu^{(a)}_{C=O}$												5.2	0.1	-0.0	0.1
$\nu^{(s)}_{C=O}$											16.0	13.5	0.0	-0.0	0.0
ν_{Ar}										1.3	1.0	1.0	0.3	0.3	0.3
									0.1	1.5	0.5	0.4	-0.3	-0.3	-0.3
								-0.4	1.6	2.2	2.3	2.3	1.8	1.9	1.9
							-0.4	1.6	-1.8	-1.2	-1.1	-1.2	-1.5	-1.5	-1.5
						-6.8	-3.2	-0.1	-2.4	-1.8	-1.8	-1.9	-1.9	-1.9	-1.9
					1.8	-1.0	-1.1	2.0	-1.3	-0.6	0.2	0.2	0.1	0.1	0.2
				-0.3	2.1	-5.1	-4.1	1.7	-1.3	-0.9	-0.1	-0.1	-0.2	-0.2	-0.2
			12.7	5.4	2.0	4.9	-2.6	-2.7	1.1	2.4	1.6	1.6	1.4	1.4	1.5
		4.9	1.6	8.4	11.4	0.9	-1.6	1.8	-5.9	1.0	-0.2	-0.2	-0.1	-0.1	-0.0
	4.8	6.3	1.7	8.5	11.2	0.8	-1.5	1.9	-0.6	-2.2	-0.2	-0.0	0.0	0.0	0.0

Figure D3 – Anharmonic coupling constants between vibrational modes obtained by DFT calculations.

2. Global lifetime analysis for TRIR of [Re(HPEAB)(CO)$_3$Cl]

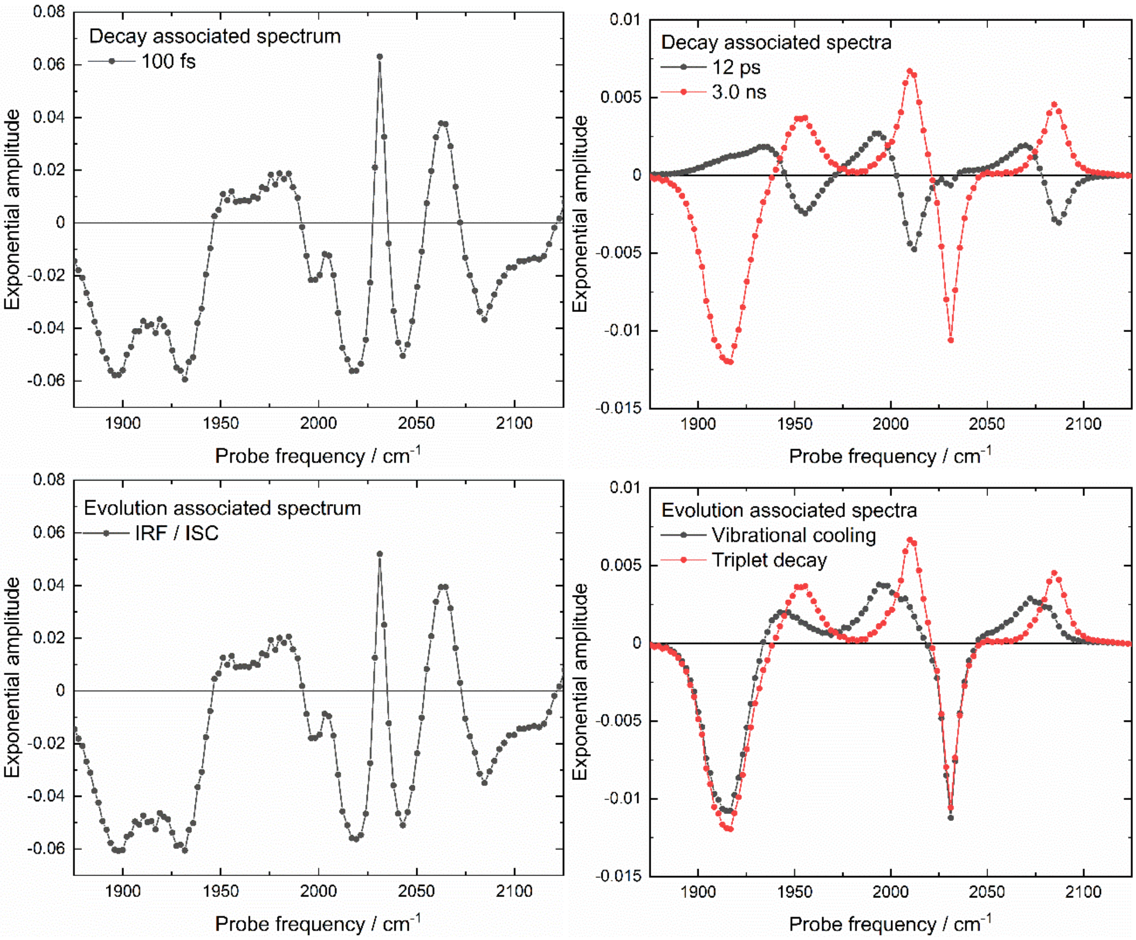

Figure D4 – Decay associated and evolution associated spectra for the three-component sequential global lifetime analysis model used to determine the rate of excited state relaxation of [Re(HPEAB)(CO)$_3$Cl].

3. Lifetime density analysis

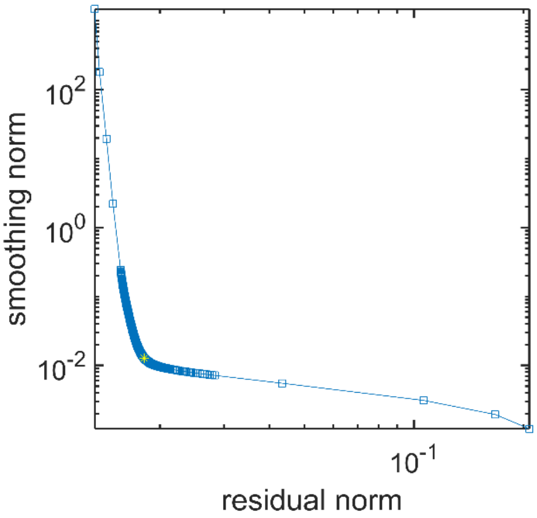

Figure D5 – 'L-curve' obtained from Lifetime Density Analysis of the [Re(HPEAB)(CO)$_3$Cl] TRIR spectra in the 1975 – 2125 cm^{-1} region following 400 nm excitation. The yellow star shows the selected regularisation parameter used in the data analysis, which had a value of 0.57962.

4. Processing of kinetic traces from 2DIR data

The kinetic traces displayed in the main text were acquired through subtraction of the bleach intensity in ΔA from the transient intensity in ΔA. The resulting data represents the grow in and decay of the 2DIR peak pair, where the y-axis unit is in ΔΔA (or ΔΔOD). This procedure minimises noise in the kinetic data by accounting for fluctuation of the spectral baseline during the delay time scan. The kinetic traces of the a″, a′(2), and a′(1) peak pairs, and the resulting ΔΔOD traces are shown below. In the analysis of the kinetic data, both the raw and (transient – bleach) traces were studied to ensure no undesirable changes to the grow in or decay time constants was introduced.

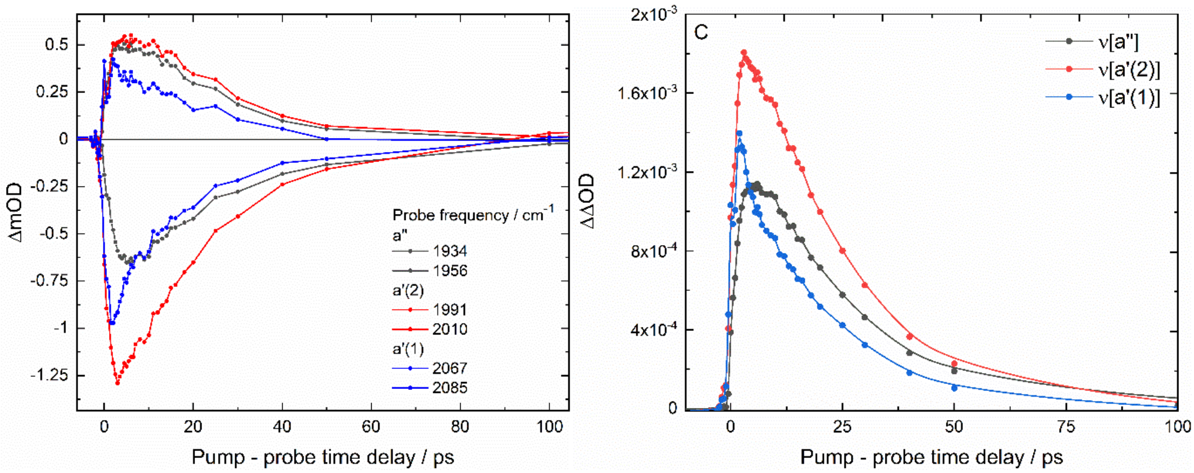

Figure D6 – Comparison of the raw and (transient – bleach) kinetic data for the high-frequency a", a'(2), and a'(1) peak pairs observed in the excited state 2DIR spectra of [Re(HPEAB)(CO)$_3$Cl].

5. Emission spectroscopy data

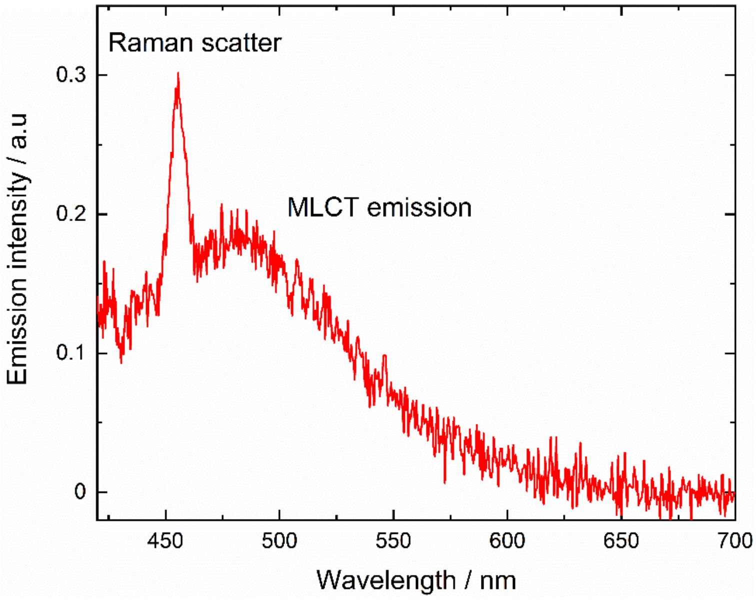

Figure D7 – Steady-state emission spectrum of a 1.1x10^{-5} mol dm^{-3} [Re(HPEAB)(CO)$_3$Cl] in DCM following 400 nm excitation. The integration time was set to 1 second, the emission and excitation slits were set to 2.5 mm.

6. Summary of peak positions, anharmonic shifts, and time constants for 2DIR data

Table D1 – Characterisation data for the 2DIR peak pairs of [Re(HPEAB)(CO)$_3$Cl] in the ground state and ^{3}MLCT excited states following either excitation of the ν[a′(1)] or ν(C=O) vibrational modes.

Pump ν / cm^{-1}	**Mode**	**Transient ν / cm^{-1}**	**Bleach ν / cm^{-1}**	**Maximum peak pair area / mOD**	**Δ_{ii} / cm^{-1}**	**Δ_{ij} / cm^{-1}**	**Grow in time constant / ps**	**Decay time constant / ps**	**t_{max} / ps**
	Ground state								
2026	ν[C=O]	1621	1633	0.37	/	12	3.6	42	15
	ν[a′(1)]	2009	2018	162	15	/	/	16	2.0
	ν[a′(1) / CM]	2002	2018	/	/	8.9	/	1.5, 38	2.0
	ν[a″]	1886	1910	177	/	16	/	1.9, 39	2.0
	ν[a′(2)]								
1651	ν[C=O]	1609	1624	2.3	17	/	/	2.6	0.5
	ν[a′(1)]	2013	2020	0.87	/	6.7	5.3	22	9
	ν[a′(1) / CM]	2002	2020	/	/	18	5.1	20	9
	ν[a″]	1891	1914	0.18	/	22	3.7	21	8
	ν[a′(2)]								
	^{3}MLCT state								
2061	ν[C=O]	/	/	/	/	/	/	/	/
	ν[a′(1)]	2070	2085	1.39	17	/	/	1.6, 24	2
	ν[a″]	1931	1956	1.1	/	22	/	30	6
	ν[a′(2)]	1991	2010	1.8	/	18	/	30	3
1626	ν[C=O]	/	1622	0.09	/	/	/	/	1
	ν[a′(1)]	/	/	/	/	/	/	/	/
	ν[a″]	/	/	/	/	/	/	/	/
	ν[a′(2)]	/	/	/	/	/	/	/	/

Part II

Additional FTIR spectra

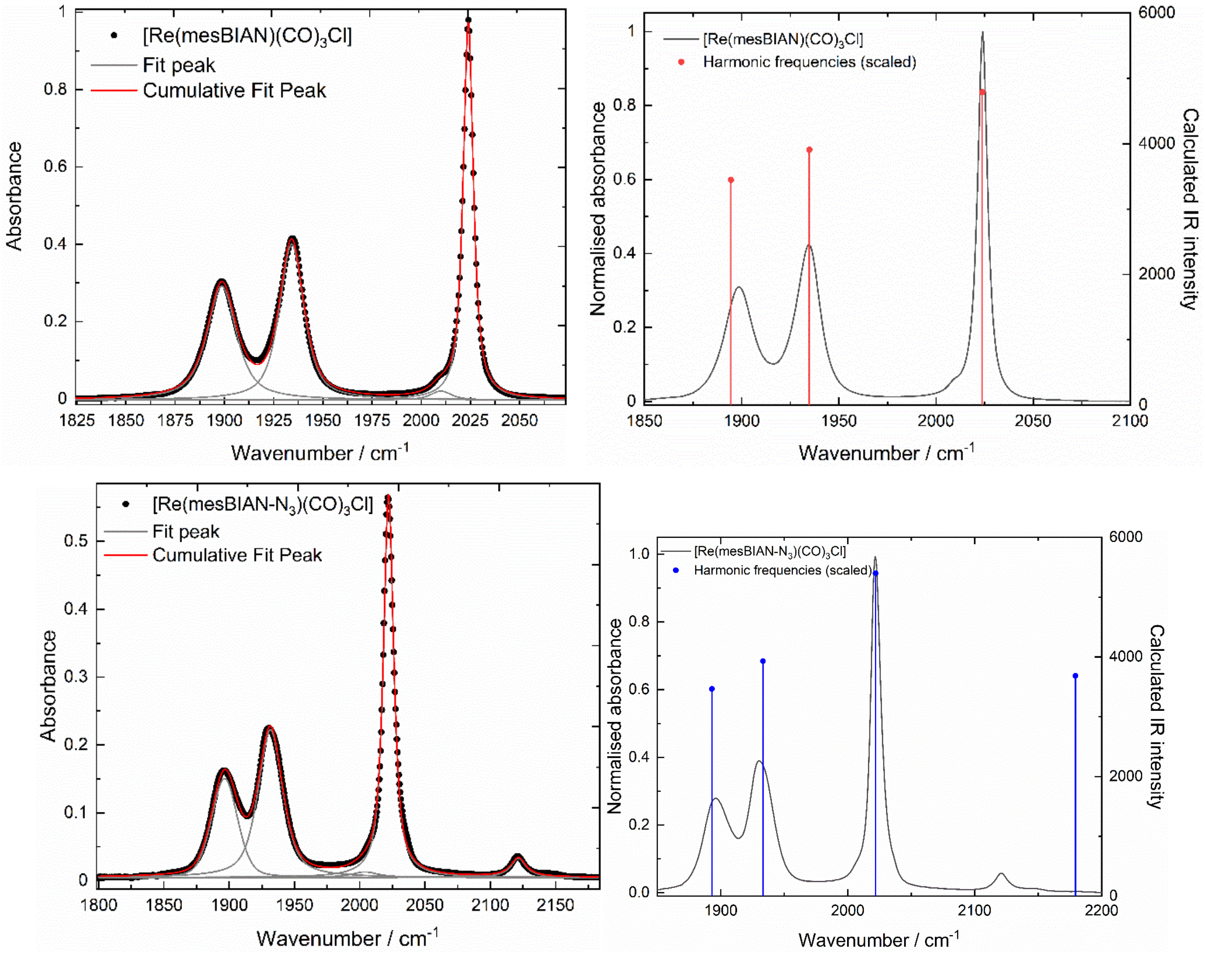

Figure D8 – FTIR spectra of [Re(mesBIAN)(CO)$_3$Cl] and [Re(mesBIAN-N$_3$)(CO)$_3$Cl], deconvoluted with pseudo-Voigt profiles (left column) or overlaid with the scaled harmonic IR frequencies obtained from DFT calculations. The harmonic scaling factor for the mesBIAN complex was 0.9718. The harmonic scaling factor for the mesBIAN-N$_3$ complex was 0.9715.

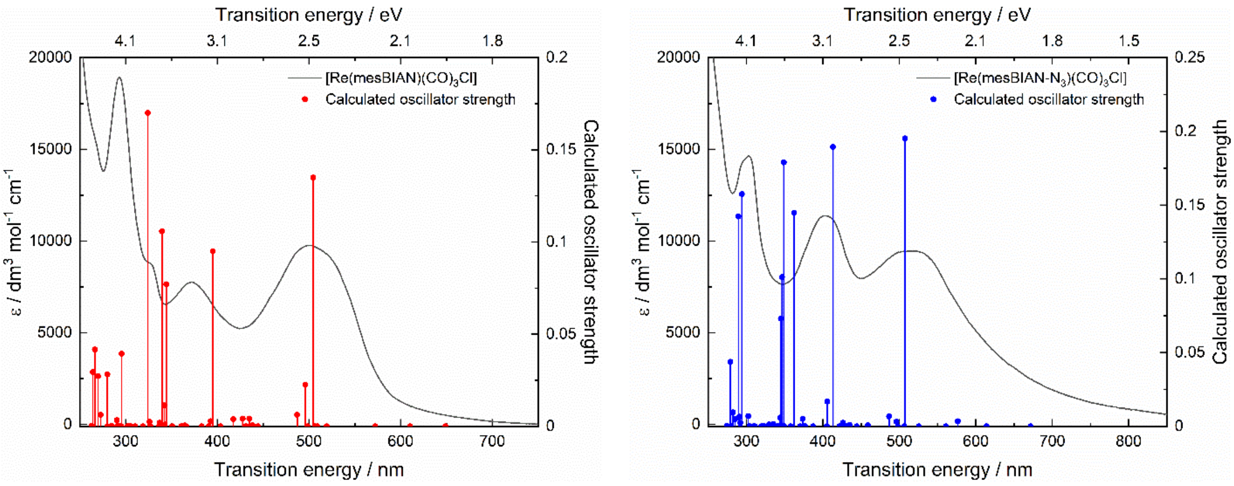

Figure D9 – Calculated electronic transition energies for [Re(mesBIAN)(CO)$_3$Cl] and [Re(mesBIAN-N$_3$)(CO)$_3$Cl], obtained from TD-DFT calculations (dots), overlaid with the experimental UV-vis absorption spectra.

Additional TRIR data for [Re(mesBIAN)(CO)$_3$Cl]

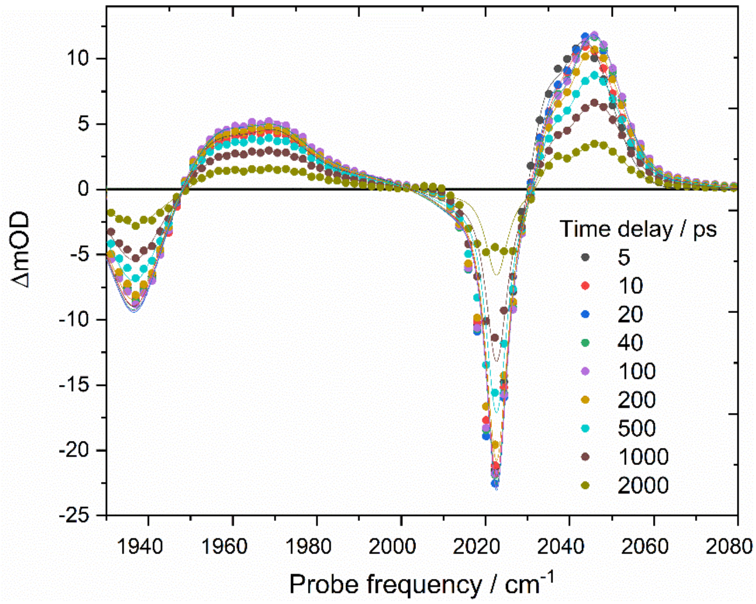

Figure D10 – Experimental TRIR spectra of [Re(mesBIAN)(CO)$_3$Cl] (dots), overlaid with the cumulative peak fit data from deconvolution of the spectra with ten pseudo-Voigt profiles.

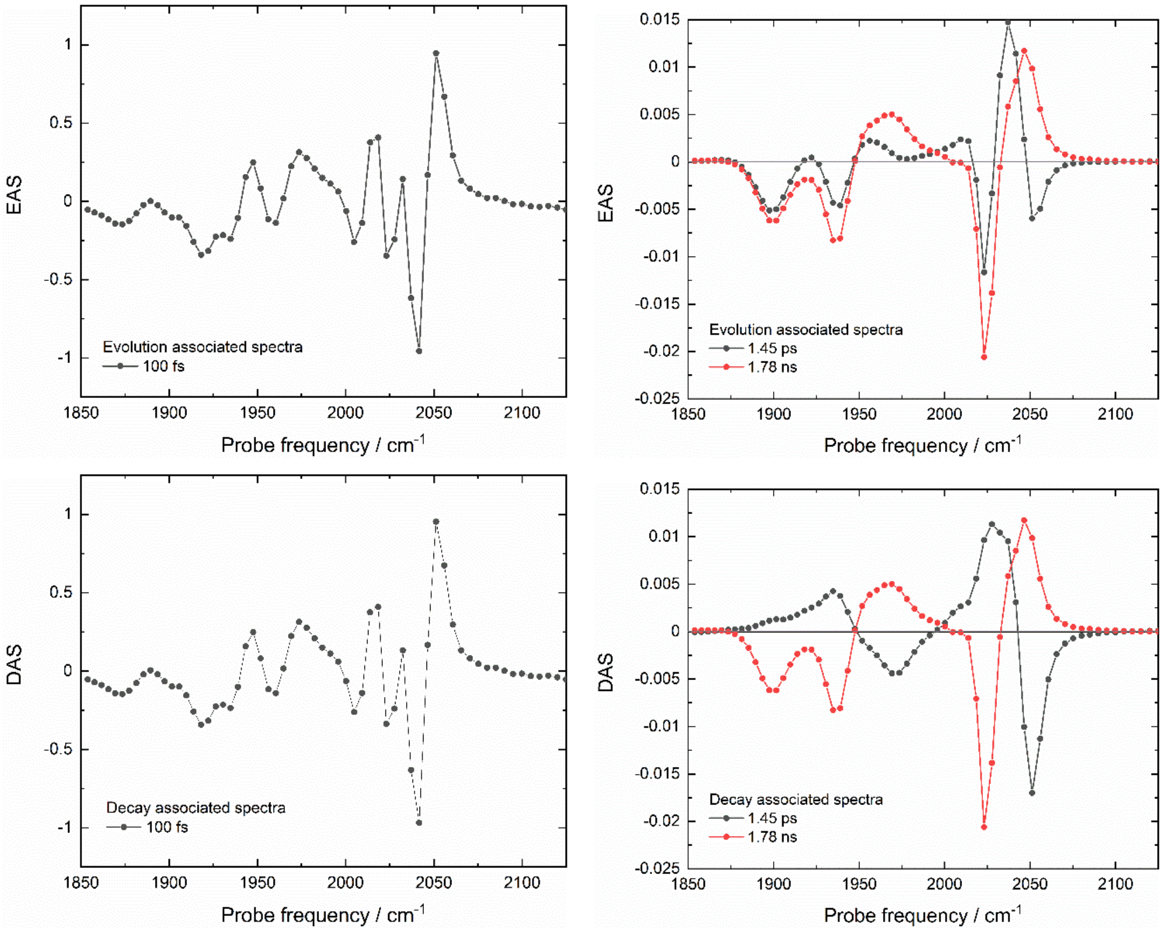

Figure D11 – Decay and evolution associated spectra for the 3-component sequential global lifetime analysis of [Re(mesBIAN)(CO)$_3$Cl].

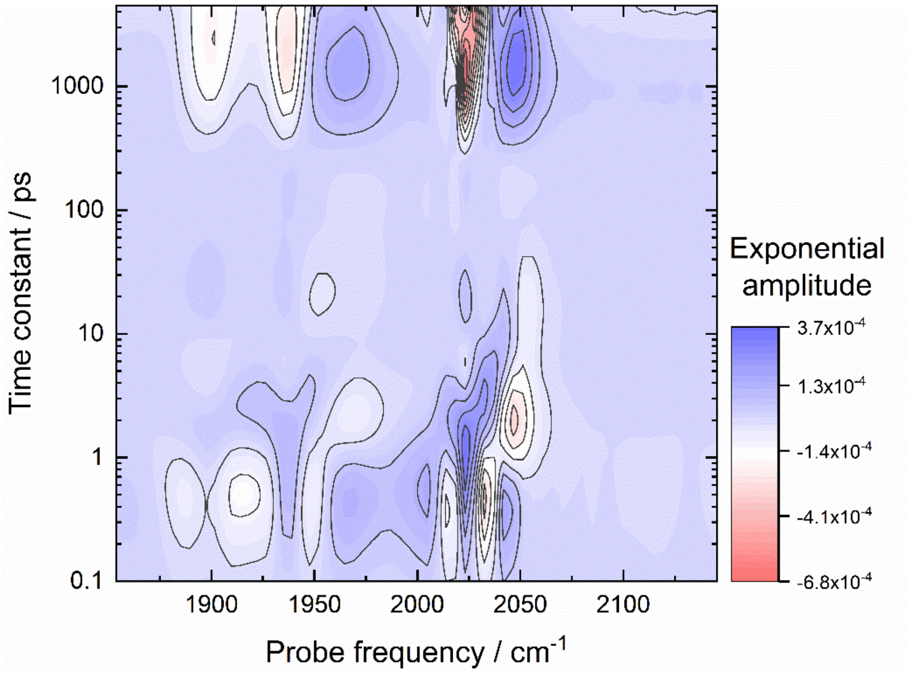

Figure D12 – Lifetime density map for a fit of 200-time constants between 0.1 and 4500 ps to the TRIR data of [Re(mesBIAN)(CO)$_3$Cl]. The regularisation factor for this data was 0.72125.

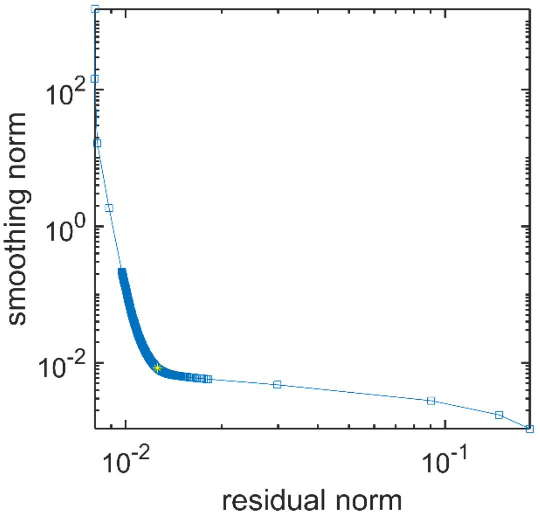

Figure D13 – 'L-curve' obtained from Lifetime Density Analysis of [Re(mesBIAN)(CO)$_3$Cl]. The yellow star shows the selected regularisation parameter used in the data analysis, which had a value of 0.57962.

Additional TRIR data for [Re(4-mesBIAN-N$_3$)(CO)$_3$Cl]

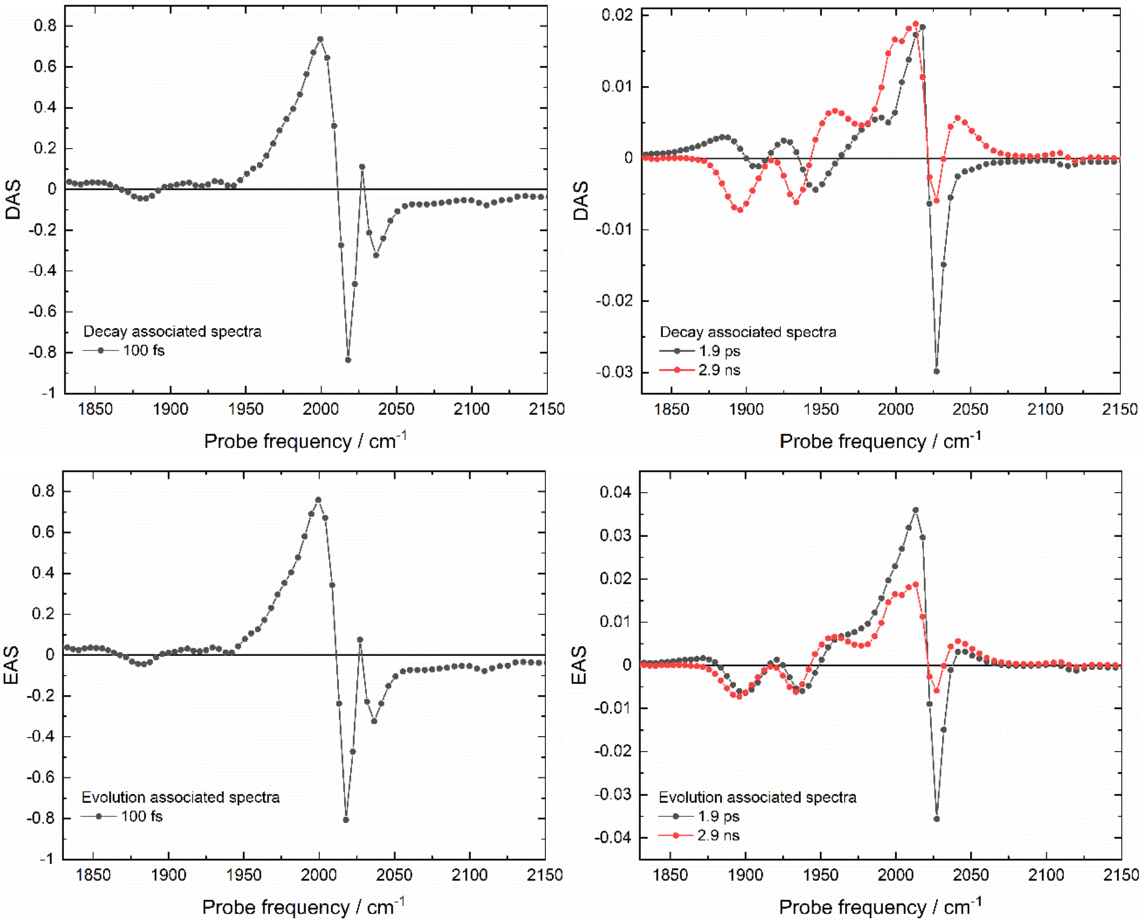

Figure D14 – Decay and evolution associated spectra for the 3-component sequential global lifetime analysis of [Re(4-mesBIAN-N$_3$)(CO)$_3$Cl].

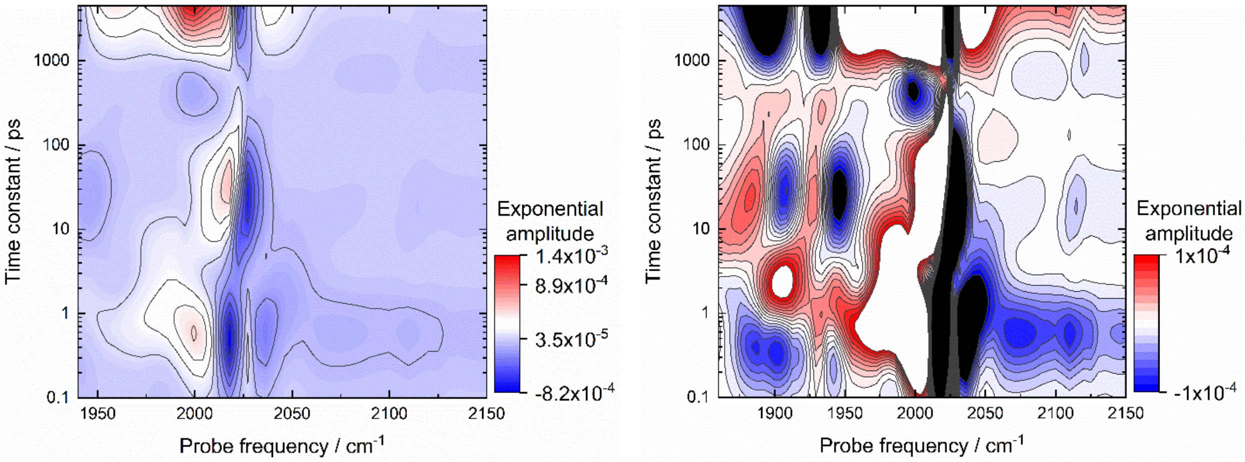

Figure D14 – Lifetime density analysis data following a fit of 200 time constants evenly distributed from 0.1 – 4500 ps for the TRIR data of [Re(4-mesBIAN-N$_3$)(CO)$_3$Cl].The regularisation parameter for this LDA was 1.1887.

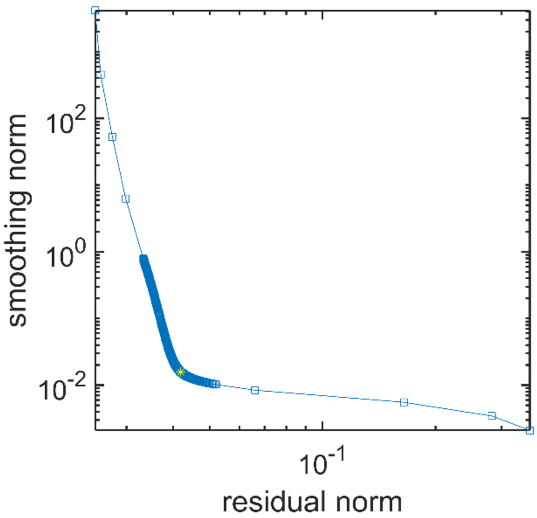

Figure D15 – 'L-curve' for the Lifetime density analysis of [Re(4-mesBIAN-N$_3$)(CO)$_3$Cl], the yellow star indicates the selected regularisation parameter of 1.1887.

Additional 2DIR spectra

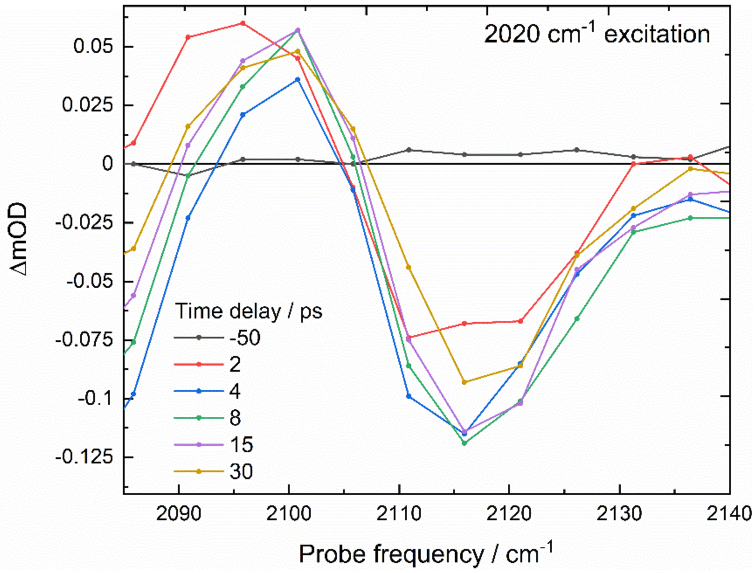

Figure D16 – Ground state 2DIR spectra of [Re(4-mesBIAN-N$_3$)(CO)$_3$Cl] in the 2085 – 2140 cm^{-1} region, showing the low intensity ν_{as}(N$_3$) off-diagonal peak pair formed following excitation of the a'(1) mode at 2026 cm^{-1}

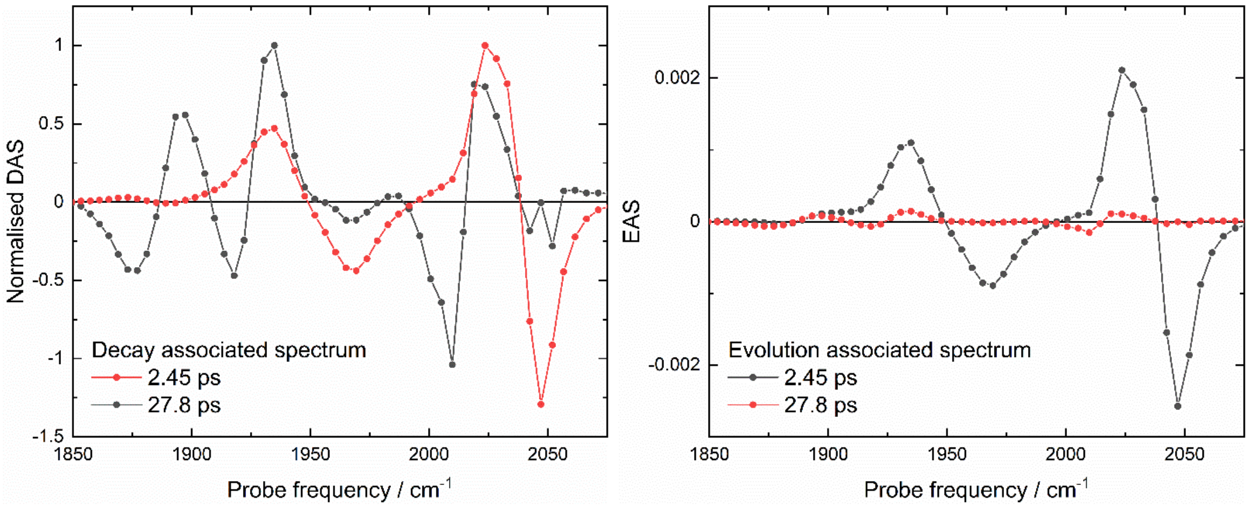

Figure D17 – Decay associated spectra and evolution associated spectra for the two-component sequential global analysis model of the excited state 2DIR data recorded for [Re(mesBIAN)(CO)$_3$Cl]. For clarity, the DAS have been normalised to the most intense positive band.

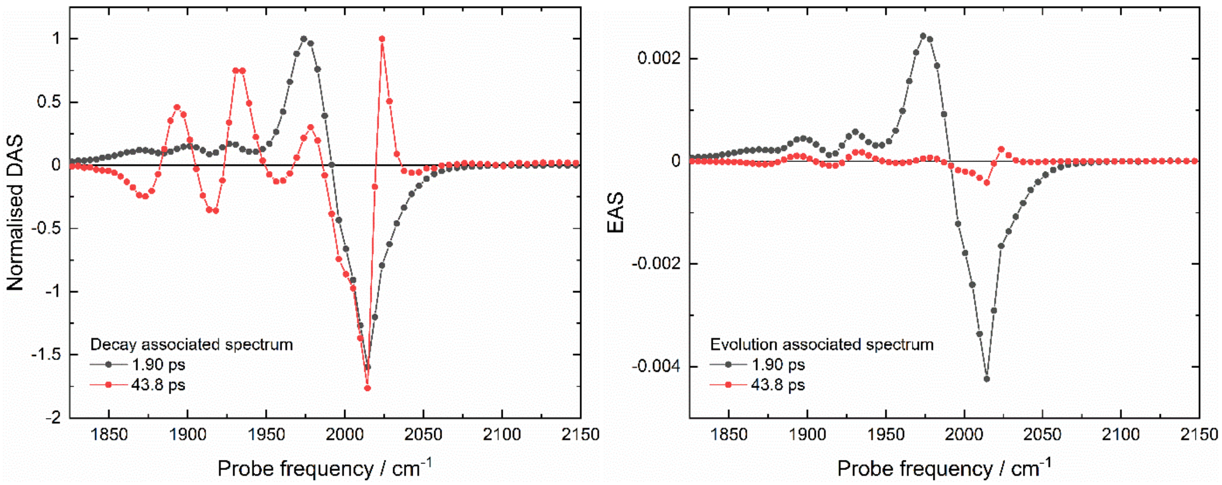

Figure D18 – Decay associated spectra and evolution associated spectra for the two-component sequential global analysis model of the excited state 2DIR data recorded for [Re(4-mesBIAN-N$_3$)(CO)$_3$Cl]. For clarity, the DAS have been normalised to the most intense positive band.

Appendix E – Experimental supporting information for chapter 5

---

1. Ground state FTIR spectral analysis

1.1 Reduced mass analysis for 1 and 2

The effect of $^{12}C \rightarrow {}^{13}C$ isotopic substitution on the acetylide stretching vibrational frequency was estimated with reduced mass analysis. This calculation accurately reproduced the observed shift in vibrational frequency.

Hooke's Law:

$$\nu = \frac{1}{2\pi c}\sqrt{\frac{k}{\mu}}$$

Reduced mass formula:

$$\mu = \frac{m_1 \cdot m_2}{m_1 + m_2}$$

$$m_1 = m_2 = 12\ gmol^{-1}$$

$$m_3 = m_4 = 13\ g\ mol^{-1}$$

For $^{12}C{\equiv}^{12}C$ acetylide:

$$\mu = \frac{12\ gmol^{-1} \cdot 12\ gmol^{-1}}{12\ gmol^{-1} + 12\ gmol^{-1}} = 6.0\ g\ mol^{-1} = 3.9 \cdot 10^{24}\ g$$

$$k_{12C\equiv 12C} = \mu(2\pi c\nu)^2 = 1.89\ \cdot 10^{11}\ cm^{-1}$$

For $^{13}C{\equiv}^{13}C$ acetylide:

$$\mu = \frac{13\ gmol^{-1} \cdot 13\ gmol^{-1}}{13\ gmol^{-1} + 13\ gmol^{-1}} = 6.5\ g\ mol^{-1} = 3.6 \cdot 10^{24}\ g$$

$$\nu_{13C\equiv 13\mathrm{C}} = \frac{1}{2\pi c}\sqrt{\frac{k}{\mu}} = 2005\ cm^{-1}$$

Calculated vibrational frequency shift of ν(CC)a upon $^{12}C \rightarrow {}^{13}C$ isotopic substitution:

$$\nu_{12C\equiv 12\mathrm{C}} - \nu_{13C\equiv 13\mathrm{C}} = 82\ cm^{-1}$$

Experimental vibrational frequency shift of ν(CC)a upon $^{12}C \rightarrow {}^{13}C$ isotopic substitution:

$$2007\ cm^{-1} - 2087\ cm^{-1} = 81\ cm^{-1}$$

Observed shift in vibrational frequency is consistent with expected change.

1.2 Spectral deconvolution

The normalised ground state FTIR spectra of complexes **1-4** in the 1975 – 2125 cm^{-1} region were deconvoluted by fitting of pseudo-Voigt profiles to the experimental data, as discussed in the main text.

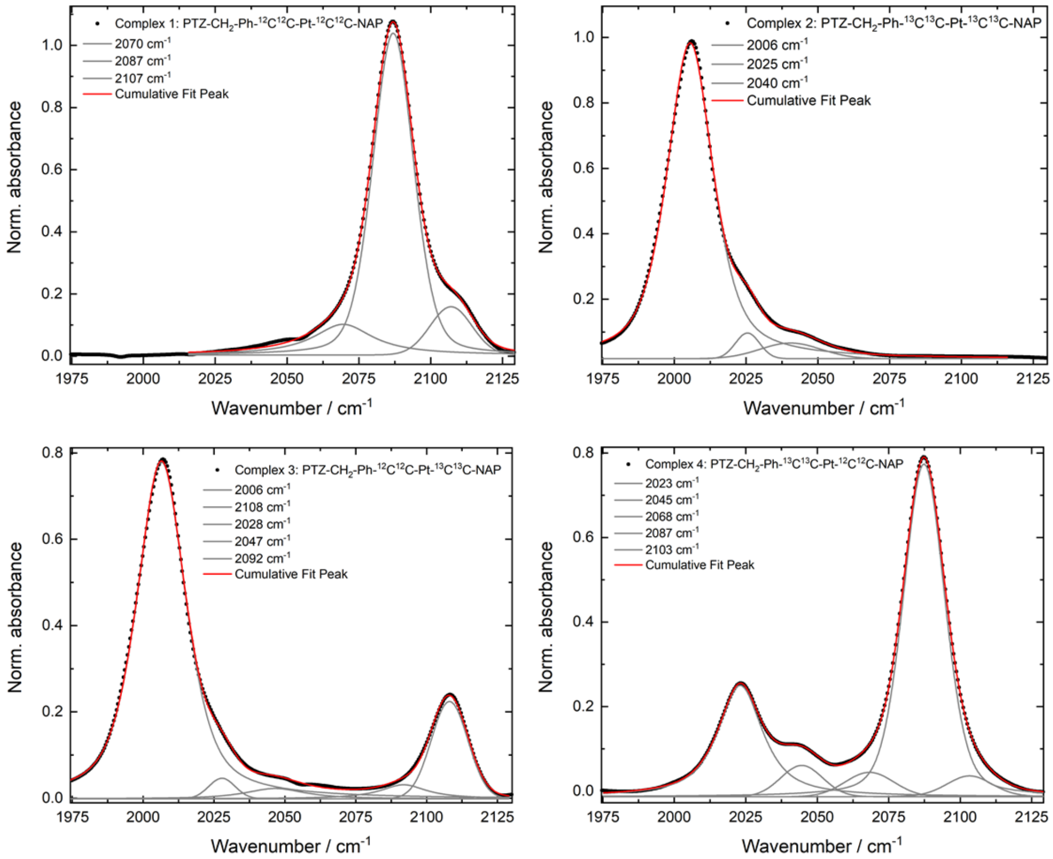

*Figure E1 – Deconvoluted ground state FTIR spectra for complexes **1** – **4** using pseudo-Voigt curves.*

1.3 Frequency scaled harmonic IR spectra

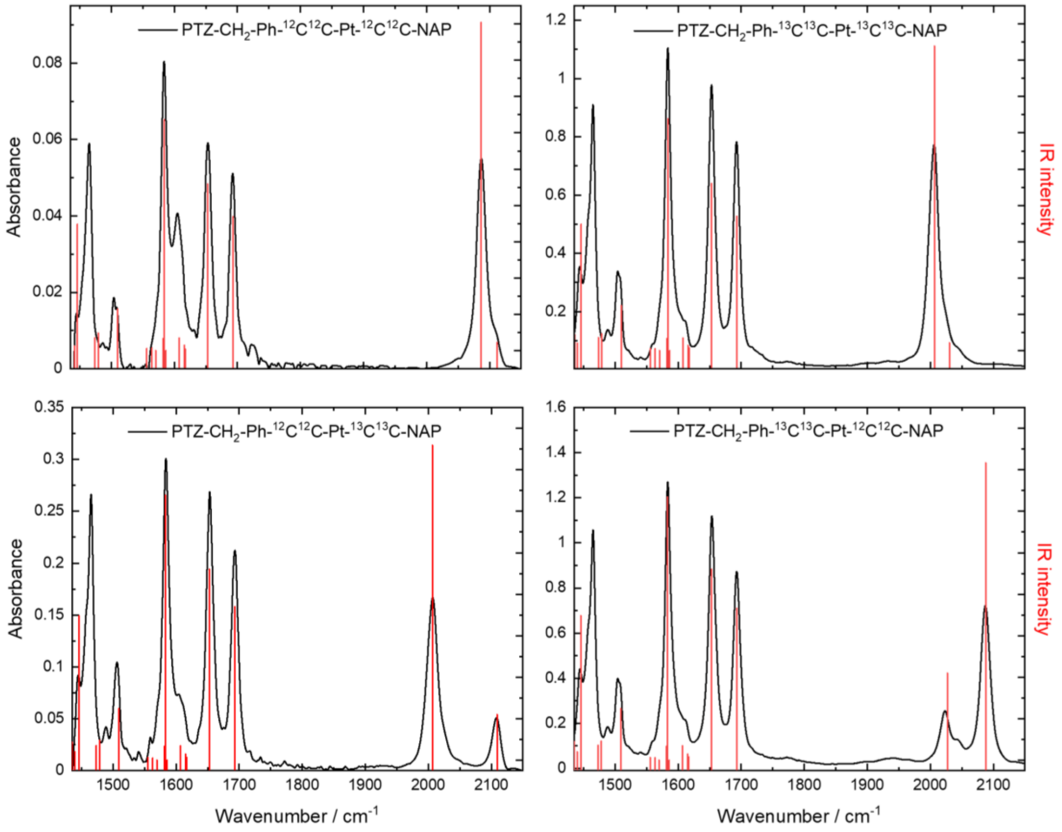

*Figure E2 – Calculated harmonic IR spectra for the electronic ground state of complexes **1-4**, overlaid with the experimental IR spectra recorded in dichloromethane solution within a CaF$_2$ solution cell. The harmonic frequencies have been scaled to match the frequencies of the experimental data.*

1.4 Normal mode characterisation and anharmonic scaling factors

The harmonic normal modes were characterised by visualising them in Gaussian. Scaling factors were applied to the harmonic frequencies to minimise the discrepancy between the calculated normal modes and the experimental IR frequencies. The normal modes were scaled with a single factor, with the exception of ν(CO)$_a$ and ν(CO)$_s$, which were scaled separately.

*Table E1 – Calculated harmonic frequencies, assignments, scaled anharmonic frequencies and anharmonic scaling factors for complex **1**.*

Name	**Description**	**Harmonic frequency / cm^{-1}**	**Scaled anharmonic frequency / cm^{-1}**	**Anharmonic scaling factor**
ν(NAP/CO-1)	Combination of naphthalene aromatic vibration and symmetric carbonyl mode	1337	1277	0.955
ν(NAP/CO-2)	Combination of naphthalene aromatic vibration and symmetric carbonyl mode	1398	1335	0.955
ν(NAP-1)	Naphthalene aromatic vibration	1434	1370	0.955
ν(NAP-2)	Naphthalene aromatic vibration	1460	1394	0.955

ν(PTZ/CH$_2$)	Combination mode of phenothiazine and methylene groups	1514	1446	0.955
ν(PTZ/CH$_2$/Ph)	Combination mode of phenothiazine, methylene, and phenylene groups	1543	1473	0.955
ν(NAP/CO-3)	Naphthalene aromatic vibration with weak contribution from carbonyl modes	1581	1510	0.955
ν(NAP-Ar)	Highest frequency / most intense naphthalene aromatic vibration	1658	1584	0.955
ν(PTZ/CH$_2$/Ph)	Combination mode of phenothiazine, methylene, and phenylene groups	1683	1607	0.955
ν(CO)$_a$	Antisymmetric carbonyl vibration of diimine group	1767	1652	0.935
ν(CO)$_s$	Symmetric carbonyl vibration of diimine group	1810	1693	0.935
ν(CC)$_a$	Antisymmetric acetylide group vibration, primarily localised on NAP-acetylide	2185	2086	0.955
ν(CC)$_s$	Symmetric acetylide group vibration, primarily localised on PTZ-acetylide	2211	2112	0.955

*Table E2 – Calculated harmonic frequencies, assignments, scaled anharmonic frequencies and anharmonic scaling factors for complex **2**.*

Name	**Description**	**Harmonic frequency / cm^{-1}**	**Scaled anharmonic frequency / cm^{-1}**	**Anharmonic scaling factor**
ν(NAP/CO-1)	Combination of naphthalene aromatic vibration and symmetric carbonyl mode	1338	1278	0.955
ν(NAP/CO-2)	Combination of naphthalene aromatic vibration and symmetric carbonyl mode	1397	1334	0.955
ν(NAP-1)	Naphthalene aromatic vibration	1432	1368	0.955
ν(NAP-2)	Naphthalene aromatic vibration	1463	1397	0.955
ν(PTZ/CH$_2$)	Combination mode of phenothiazine and methylene groups	1514	1446	0.955
ν(PTZ/CH$_2$/Ph)	Combination mode of phenothiazine, methylene, and phenylene groups	1543	1474	0.955
ν(NAP/CO-3)	Naphthalene aromatic vibration with weak contribution from carbonyl modes	1580	1510	0.955
ν(NAP-Ar)	Highest frequency / most intense naphthalene aromatic vibration	1658	1584	0.955
ν(PTZ/CH$_2$/Ph)	Combination mode of phenothiazine, methylene, and phenylene groups	1683	1607	0.955
ν(CO)$_a$	Antisymmetric carbonyl vibration of diimine group	1767	1653	0.935
ν(CO)$_s$	Symmetric carbonyl vibration of diimine group	1810	1693	0.935
ν(CC)$_a$	Antisymmetric acetylide group vibration, primarily localised on NAP-acetylide	2101	2006	0.955
ν(CC)$_s$	Symmetric acetylide group vibration, primarily localised on PTZ-acetylide	2126	2030	0.955

Table E3 – Calculated harmonic frequencies, assignments, scaled anharmonic frequencies and anharmonic scaling factors for complex ***3****.*

Name	**Description**	**Harmonic frequency / cm^{-1}**	**Scaled anharmonic frequency / cm^{-1}**	**Anharmonic scaling factor**
ν(NAP/CO-1)	Combination of naphthalene aromatic vibration and symmetric carbonyl mode	1338	1277	0.9545
ν(NAP/CO-2)	Combination of naphthalene aromatic vibration and symmetric carbonyl mode	1397	1334	0.9545
ν(NAP-1)	Naphthalene aromatic vibration	1432	1367	0.9545
ν(NAP-2)	Naphthalene aromatic vibration	1462	1396	0.9545
ν(PTZ/CH_2)	Combination mode of phenothiazine and methylene groups	1514	1445	0.9545
ν(PTZ/CH_2/Ph)	Combination mode of phenothiazine, methylene, and phenylene groups	1543	1473	0.9545
ν(NAP/CO-3)	Naphthalene aromatic vibration with weak contribution from carbonyl modes	1580	1509	0.9545
ν(NAP-Ar)	Highest frequency / most intense naphthalene aromatic vibration	1661	1586	0.9545
ν(PTZ/CH_2/Ph)	Combination mode of phenothiazine, methylene, and phenylene groups	1683	1607	0.9545
ν$(CO)_a$	Antisymmetric carbonyl vibration of diimine group	1767	1653	0.935
ν$(CO)_s$	Symmetric carbonyl vibration of diimine group	1810	1693	0.935
ν(NAP-$^{13}C^{13}C$)	Partially delocalised carbon-13 labelled acetylide mode on the NAP ligand, with weak contribution from the carbon-12 PTZ-acetylide	2102	2007	0.9545
ν($^{12}C^{12}C$-PTZ)	Partially delocalised carbon-13 labelled acetylide mode on the PTZ ligand, with weak contribution from the carbon-13 NAP-acetylide	2209	2109	0.9545

Table E4 – Calculated harmonic frequencies, assignments, scaled anharmonic frequencies and anharmonic scaling factors for complex ***4****.*

Name	**Description**	**Harmonic frequency / cm^{-1}**	**Scaled anharmonic frequency / cm^{-1}**	**Anharmonic scaling factor**
ν(NAP/CO-1)	Combination of naphthalene aromatic vibration and symmetric carbonyl mode	1338	1277	0.9545
ν(NAP/CO-2)	Combination of naphthalene aromatic vibration and symmetric carbonyl mode	1397	1334	0.9545
ν(NAP-1)	Naphthalene aromatic vibration	1432	1367	0.9545
ν(NAP-2)	Naphthalene aromatic vibration	1463	1396	0.9545
ν(PTZ/CH_2)	Combination mode of phenothiazine and methylene groups	1514	1445	0.9545

ν(PTZ/CH$_2$/Ph)	Combination mode of phenothiazine, methylene, and phenylene groups	1543	1473	0.9545
ν(NAP/CO-3)	Naphthalene aromatic vibration with weak contribution from carbonyl modes	1580	1509	0.9545
ν(NAP-Ar)	Highest frequency / most intense naphthalene aromatic vibration	1658	1583	0.9545
ν(PTZ/CH$_2$/Ph)	Combination mode of phenothiazine, methylene, and phenylene groups	1683	1607	0.9545
ν(CO)$_a$	Antisymmetric carbonyl vibration of diimine group	1767	1653	0.935
ν(CO)$_s$	Symmetric carbonyl vibration of diimine group	1810	1693	0.935
ν(^{13}C^{13}C-PTZ)	Partially delocalised carbon-13 labelled acetylide mode on the PTZ ligand, with weak contribution from the carbon-12 NAP-acetylide	2123	2027	0.9545
ν(NAP-^{12}C^{12}C)	Partially delocalised carbon-13 labelled acetylide mode on the NAP ligand, with weak contribution from the carbon-13 PTZ-acetylide	2187	2087	0.9545

2. Deconvolution of contour map cross-sections

Cross-sections of the 2DIR data were deconvoluted with *pseudo*-Voigt profiles to allow for anharmonic shift determination and assignment of the convoluted 2DIR lineshapes. Assignment of the deconvoluted bands was done using the calculated normal modes. However, the calculated modes could not account for every peak pair in the 2DIR spectrum. Several of the peak pairs which were strongest following ν(CC-PTZ) excitation were not accounted for by the harmonic calculations. Therefore, these transitions are likely weak anharmonic combination modes of the aromatic phenothiazine and phenylene groups.

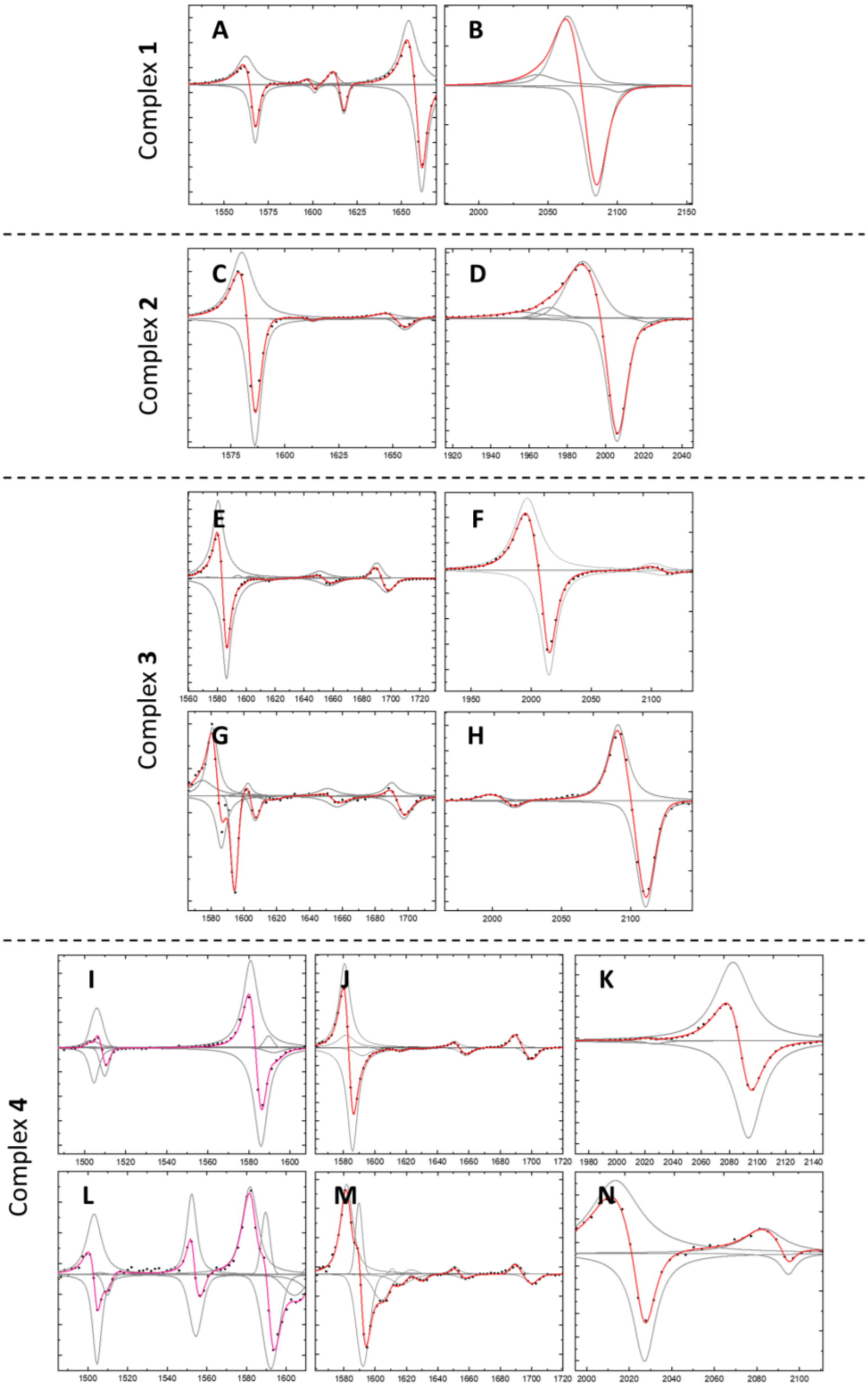

Figure E3 – Cross-sections of the time domain 2DIR spectra at a 2 ps population time, deconvoluted with pseudo-Voigt profiles

Table E5 – Assignment of the deconvoluted 2DIR modes, modes with imprecise characterisation have been labelled as either 'NAP mode' or 'PTZ mode'

Plot (Figure E11)	**Pump Frequency / cm^{-1}**	**Deconvoluted peak centre frequency / cm^{-1}**	**Assignment**
A	2086	1562	ν_{1-2}(NAP-Ar)
		1568	ν_{0-1}(NAP-Ar)
		1597	ν_{1-2}(PTZ/CH_2/Ph)
		1601	ν_{0-1}(PTZ/CH_2/Ph)
		1611	$\nu_{1-2}(\mathrm{CO})_a$
		1618	$\nu_{0-1}(\mathrm{CO})_a$
		1654	$\nu_{1-2}(\mathrm{CO})_s$
		1662	$\nu_{0-1}(\mathrm{CO})_s$
B	2086	2043	Anharmonic overtone
		2064	$\nu_{1-2}(\mathrm{CC})_a$
		2084	$\nu_{0-1}(\mathrm{CC})_a$
		2101	$\nu_{0-1}(\mathrm{CC})_s$
C	2008	1580	ν_{1-2}(NAP-Ar)
		1586	ν_{0-1}(NAP-Ar)
		1608	ν_{1-2}(PTZ/CH_2/Ph)
		1613	ν_{0-1}(PTZ/CH_2/Ph)
		1647	$\nu_{1-2}(\mathrm{CO})_a$
		1656	$\nu_{0-1}(\mathrm{CO})_a$
		1687	$\nu_{1-2}(\mathrm{CO})_s$
		1695	$\nu_{0-1}(\mathrm{CO})_s$
D	2008	1956	Anharmonic overtone
		1971	Anharmonic overtone
		1988	$\nu_{1-2}(\mathrm{CC})_a$
		2006	$\nu_{0-1}(\mathrm{CC})_a$
		2023	$\nu_{0-1}(\mathrm{CC})_s$
E	2008	1573	ν_{1-2}(PTZ)
		1581	ν_{1-2}(NAP-Ar)
		1586	ν_{0-1}(NAP-Ar)
		1594	PTZ mode
		1602	ν_{1-2}(PTZ/CH_2/Ph)
		1607	ν_{0-1}(PTZ/CH_2/Ph)
		1615	ν_{0-1}(PTZ)
		1651	$\nu_{1-2}(\mathrm{CO})_a$
		1657	$\nu_{0-1}(\mathrm{CO})_a$
		1690	$\nu_{1-2}(\mathrm{CO})_s$
		1697	$\nu_{0-1}(\mathrm{CO})_s$
F	2012	1997	ν_{1-2}(NAP-^{13}C^{13}C)
		2015	ν_{0-1}(NAP-^{13}C^{13}C)

		2101	$\nu_{1-2}(^{12}\mathrm{C}^{12}\mathrm{C\text{-}PTZ})$
		2111	$\nu_{0-1}(^{12}\mathrm{C}^{12}\mathrm{C\text{-}PTZ})$
G	2103	1575	PTZ mode
		1581	ν_{1-2}(NAP-Ar)
		1586	ν_{0-1}(NAP-Ar)
		1594	PTZ mode
		1602	$\nu_{1-2}(\mathrm{PTZ/CH_2/Ph})$
		1607	$\nu_{0-1}(\mathrm{PTZ/CH_2/Ph})$
		1617	PTZ mode
		1651	$\nu_{1-2}(\mathrm{CO})_a$
		1657	$\nu_{0-1}(\mathrm{CO})_a$
		1690	$\nu_{1-2}(\mathrm{CO})_s$
		1698	$\nu_{0-1}(\mathrm{CO})_s$
H	2104	1998	$\nu_{1-2}(\mathrm{NAP\text{-}}^{13}\mathrm{C}^{13}\mathrm{C})$
		2016	$\nu_{0-1}(\mathrm{NAP\text{-}}^{13}\mathrm{C}^{13}\mathrm{C})$
		2091	$\nu_{1-2}(^{12}\mathrm{C}^{12}\mathrm{C\text{-}PTZ})$
		2112	$\nu_{0-1}(^{12}\mathrm{C}^{12}\mathrm{C\text{-}PTZ})$
I	2091	1503	NAP mode
		1505	NAP mode
		1506	ν_{1-2}(NAP/CO-3)
		1510	ν_{0-1}(NAP/CO-3)
		1582	ν_{1-2}(NAP-Ar)
		1586	PTZ mode
		1590	ν_{1-2}(PTZ)
		1592	ν_{0-1}(PTZ)
J	2091	1582	ν_{1-2}(NAP-Ar)
		1586	ν_{0-1}(NAP-Ar)
		1590	PTZ mode
		1592	PTZ mode
		1604	PTZ mode
		1611	PTZ mode
		1617	PTZ mode
		1624	PTZ mode
		1629	PTZ mode
		1651	$\nu_{1-2}(\mathrm{CO})_a$
		1658	$\nu_{0-1}(\mathrm{CO})_a$
		1689	$\nu_{1-2}(\mathrm{CO})_s$
		1700	$\nu_{0-1}(\mathrm{CO})_s$
K	2091	2024	$\nu_{1-2}(^{13}\mathrm{C}^{13}\mathrm{C\text{-}PTZ})$
		2027	$\nu_{0-1}(^{13}\mathrm{C}^{13}\mathrm{C\text{-}PTZ})$
		2083	$\nu_{1-2}(\mathrm{NAP\text{-}}^{12}\mathrm{C}^{12}\mathrm{C})$
		2094	$\nu_{0-1}(\mathrm{NAP\text{-}}^{12}\mathrm{C}^{12}\mathrm{C})$

L	2026	1503	NAP mode
		1505	NAP mode
		1506	ν_{1-2}(NAP/CO-3)
		1510	ν_{0-1}(NAP/CO-3)
		1552	PTZ mode
		1554	PTZ mode
		1581	ν_{1-2}(NAP-Ar)
		1590	PTZ mode
		1592	ν_{0-1}(NAP-Ar)
		1604	PTZ mode
M	2026	1581	ν_{1-2}(NAP-Ar)
		1582	PTZ mode
		1590	PTZ mode
		1592	ν_{0-1}(NAP-Ar)
		1604	PTZ mode
		1611	PTZ mode
		1617	PTZ mode
		1624	PTZ mode
		1629	PTZ mode
		1651	PTZ mode
		1658	$\nu_{0-1}(CO)_a$
		1689	$\nu_{1-2}(CO)_s$
		1700	$\nu_{0-1}(CO)_s$
N	2024	2013	ν_{1-2}(^{13}C^{13}C-PTZ)
		2027	ν_{0-1}(^{13}C^{13}C-PTZ)
		2083	ν_{1-2}(NAP-^{12}C^{12}C)
		2095	ν_{0-1}(NAP-^{12}C^{12}C)

3. Spectral diffusion analysis

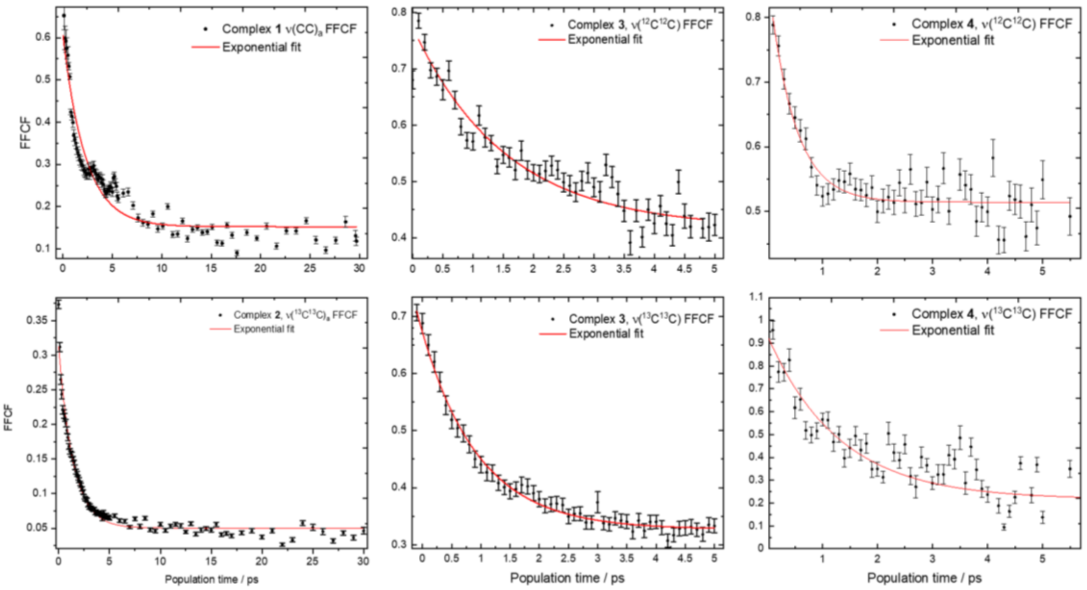

Figure E4 – Estimated frequency-frequency correlation functions, calculated using the nodal line slope method by fitting of 2D gaussian peaks to the 2DIR data at each population time. The error bars are calculated from the uncertainty in the fit of each 2D gaussian.

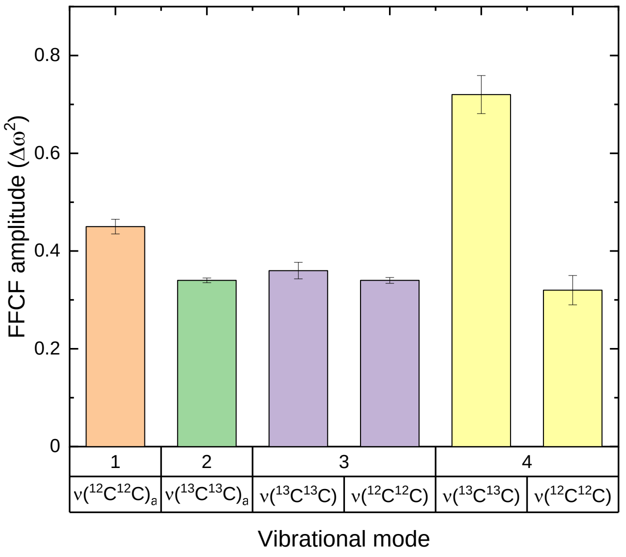

Figure E5 – Amplitudes obtained by exponential fitting of the estimated FFCF curves obtained with the centre line slope method. The error bars are calculated from the exponential fit.

4. Dynamic changes in acetylide excited state absorption frequency

Antidiagonal spectra difference spectra (y = Norm. t_2 – Norm. t_0)

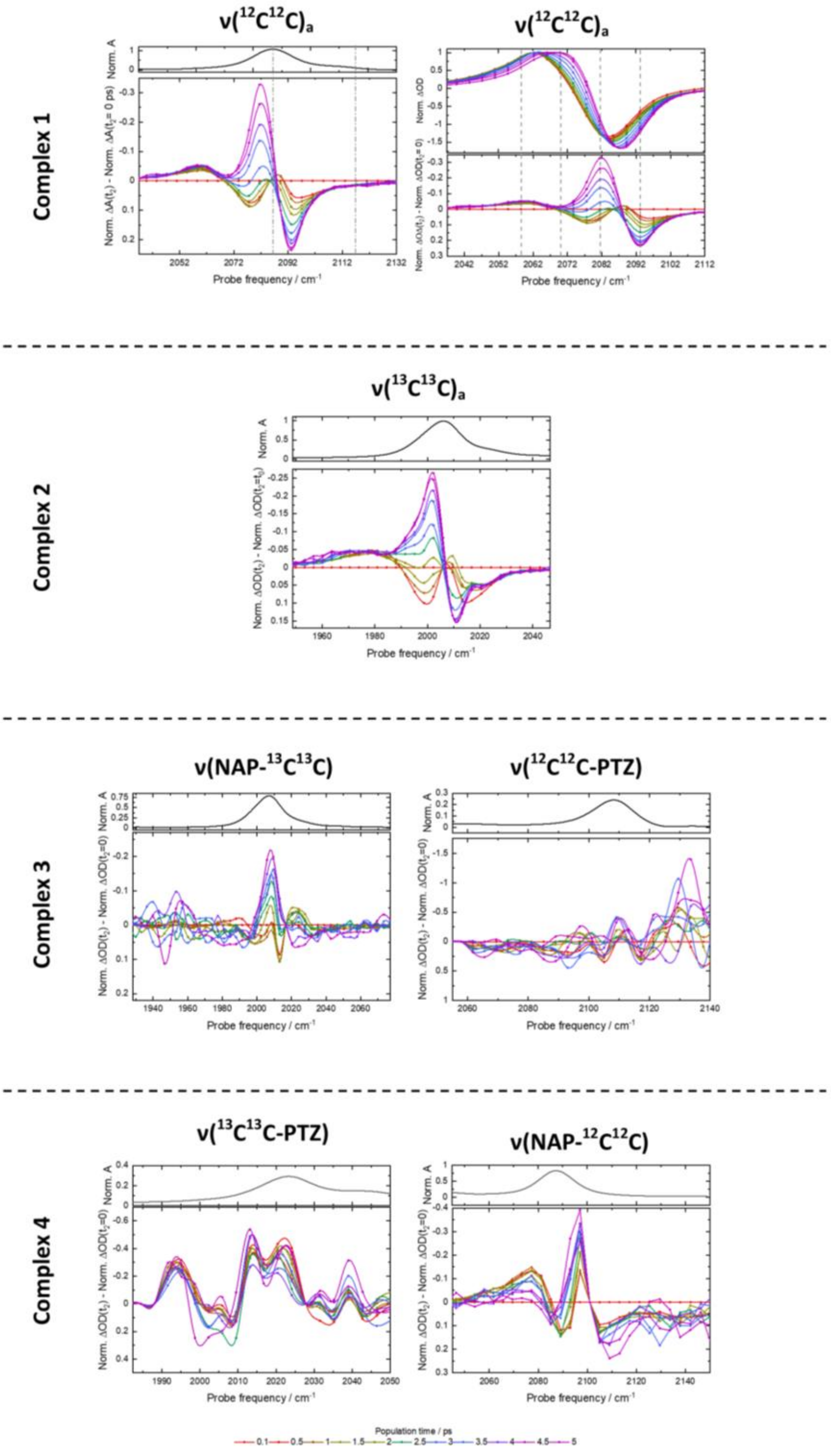

*Figure E6 – Normalised antidiagonal ΔOD(t_2) – ΔOD(t_2=0 ps) spectra for the diagonal acetylide peak pairs in complexes **1-4**. The antidiagonal cross-sections displayed intersect the maxima of the ground state bleach.*

5. Peak intensity ratio changes for acetylide transient absorption bands

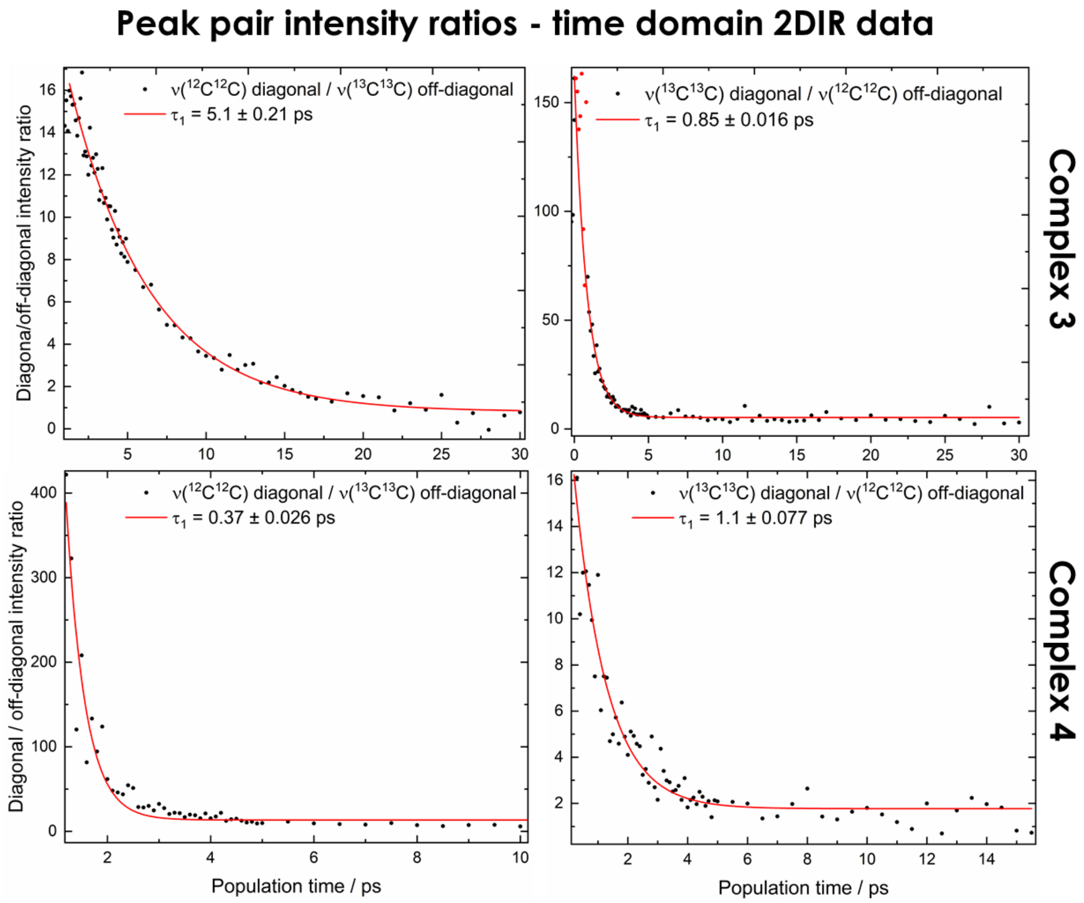

*Figure E7 – Changes in the ratio of diagonal and off-diagonal peak pair intensity for the ν(^{12}C^{12}C) or ν(^{13}C^{13}C) modes of **3** and **4**. The change in this ratio has been fit with a monoexponential decay profile.*

6. Lifetime density analysis data

Lifetime density analysis was used to estimate the time constants for the vibrational relaxation steps in complexes **1-4**. Prior to LDA, the 2DIR cross-sections at a particular excitation frequency were combined to allow for simultaneous analysis of the diagonal peak pair and all off-diagonal peak pairs. The reported time constants in the main text corresponded to the maxima of the grow in or decay components of each peak pair. Each LDA trace is analogous to a decay associated spectrum for a particular time constant in Global Lifetime Analysis. However, unlike GLA, the LDA results are not hindered by the limitations of a sequential or simultaneous model. The regularisation parameter for each LDA calculation was set to the 'corner' of the L-curve generated during the fitting algorithm, as described previously.

The LDA traces corresponding to photophysical processes in the proposed model of the vibrational dynamics of **1** – **4** are shown below. These traces correspond to the photophysical processes shown in the energy level diagrams for the vibrational dynamics.

Complex 1

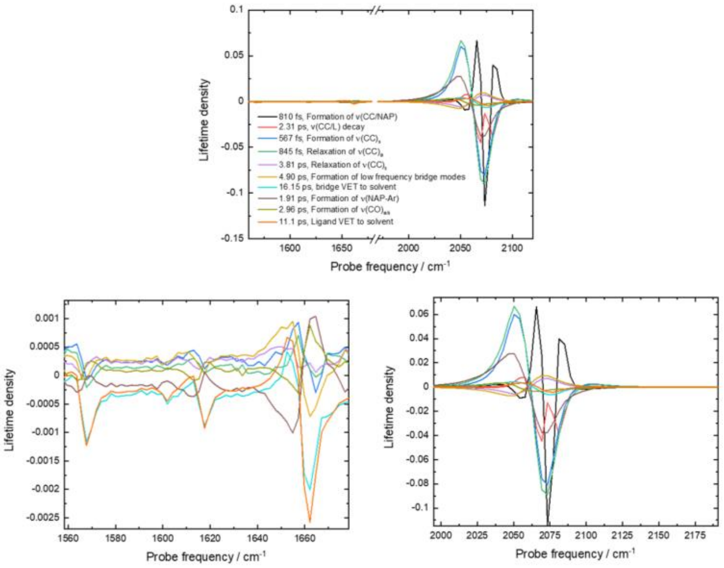

*Figure E8 – Lifetime density traces for **1**, obtained by LDA of the combined 2DIR cross sections at 2086 cm^{-1} excitation*

Complex 2

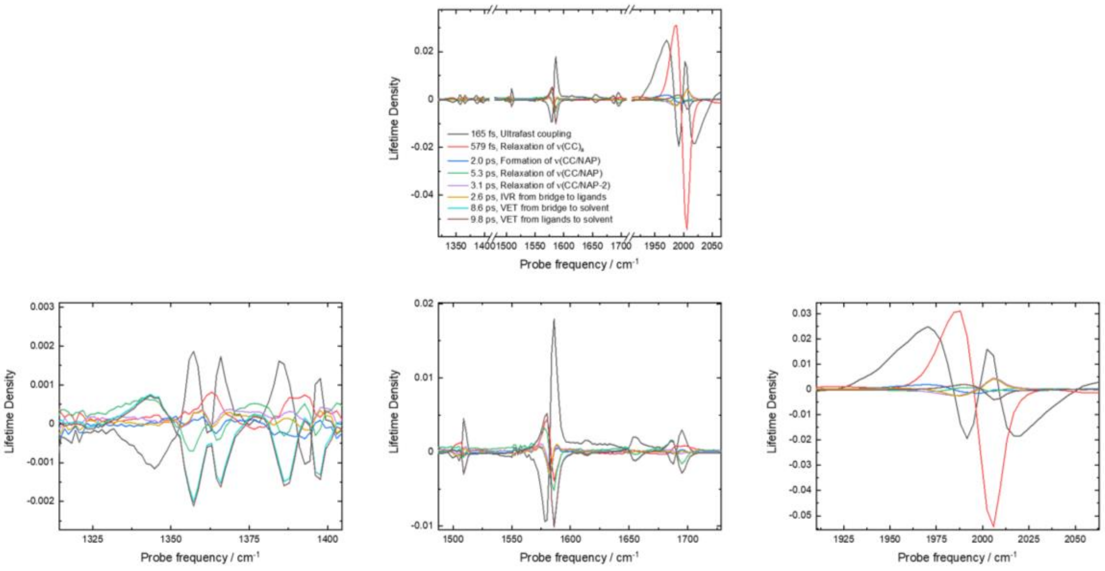

*Figure E9 – Lifetime density traces for **2**, obtained by LDA of the combined 2DIR cross sections at 2008 cm^{-1} excitation*

Complex 3

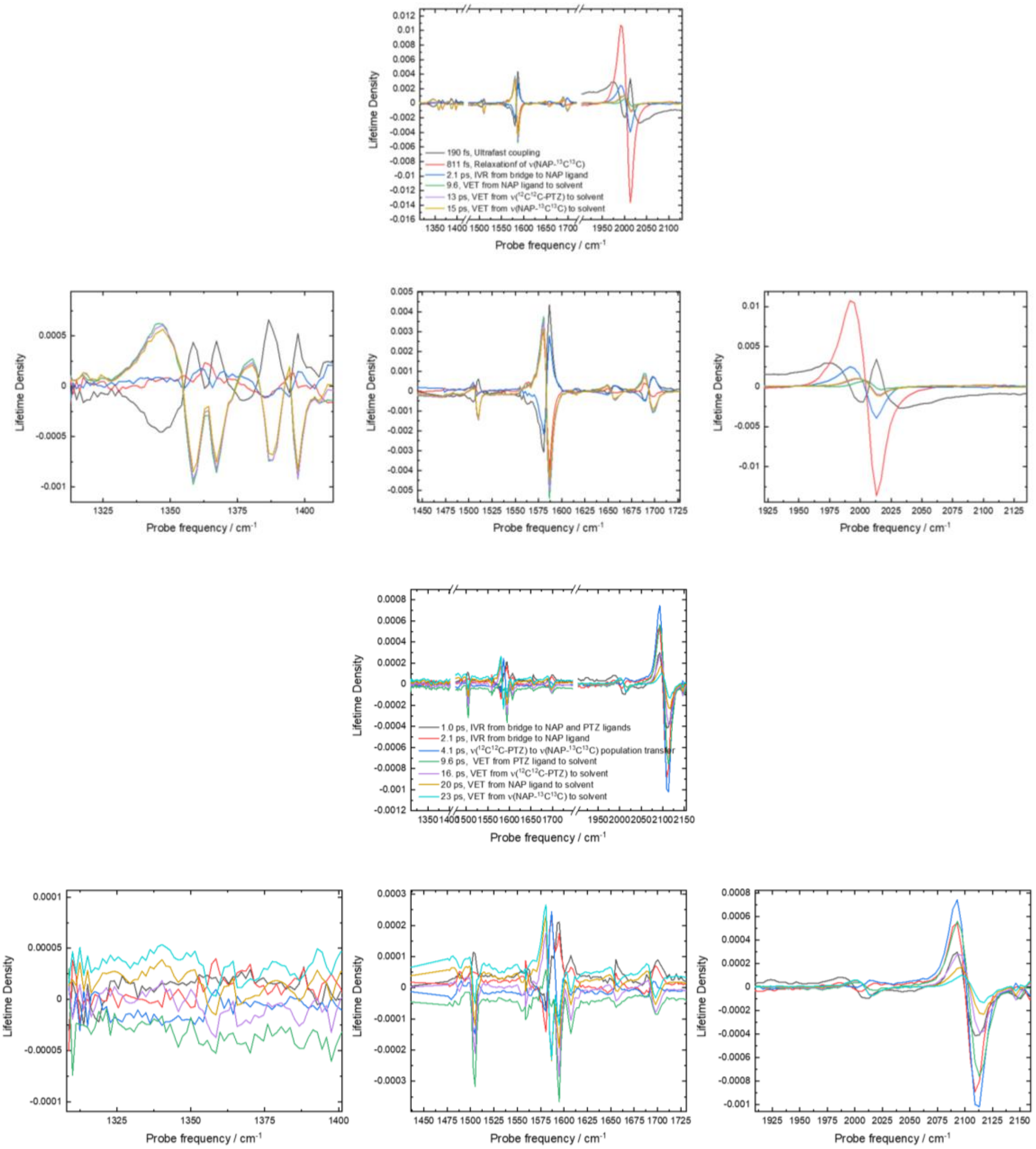

*Figure E10 – Lifetime density traces for **3**, obtained by LDA of the combined 2DIR cross sections at 2012 (top group) and 2108 cm^{-1} (bottom group) excitation.*

Complex 4

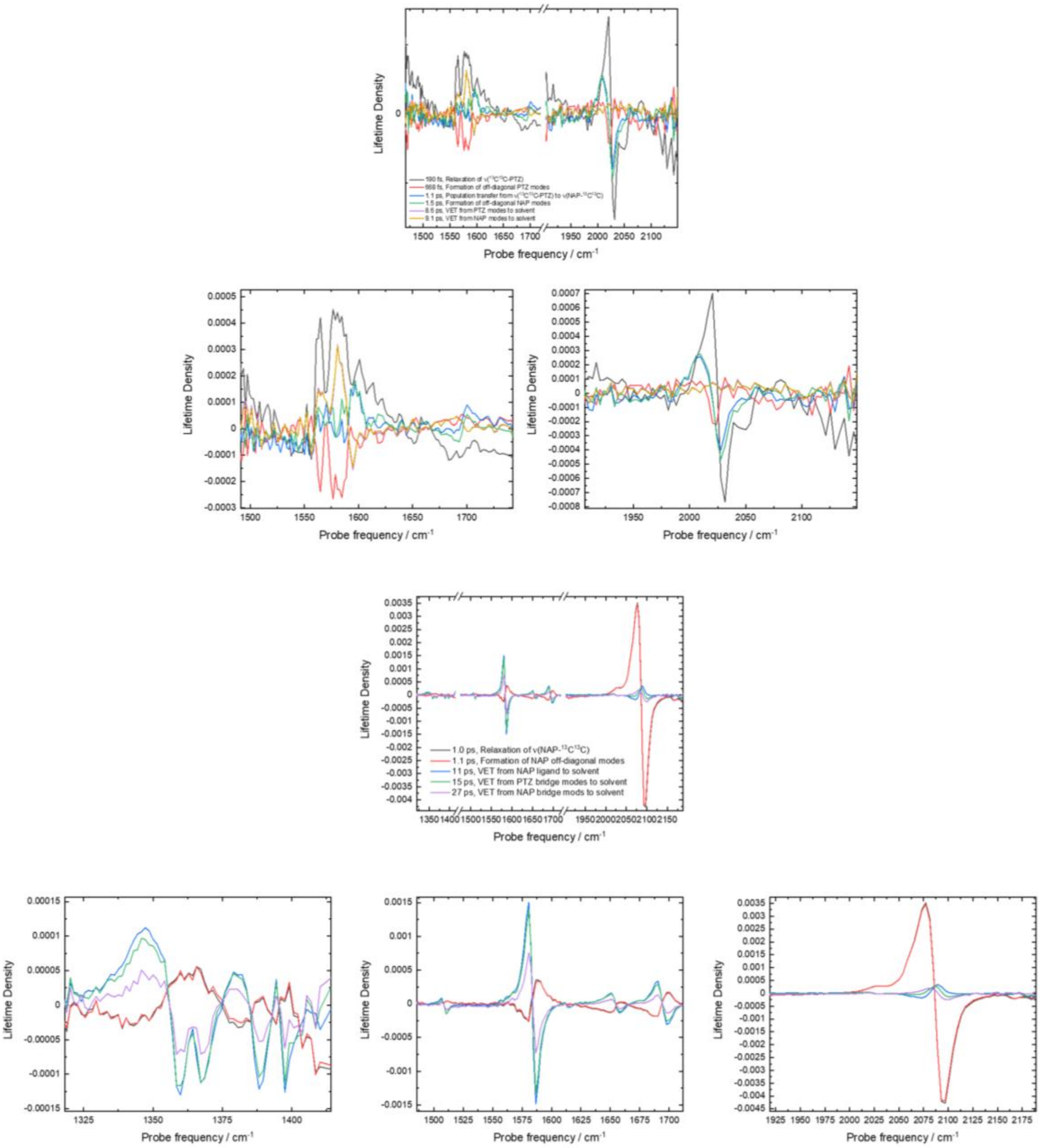

*Figure E11 – Lifetime density traces for **4**, obtained by LDA of the combined 2DIR cross sections at 2024 (top group) and 2091 cm^{-1} (bottom group) excitation.*

7. Proposed photophysical mechanisms and energy level diagrams

Complex 1

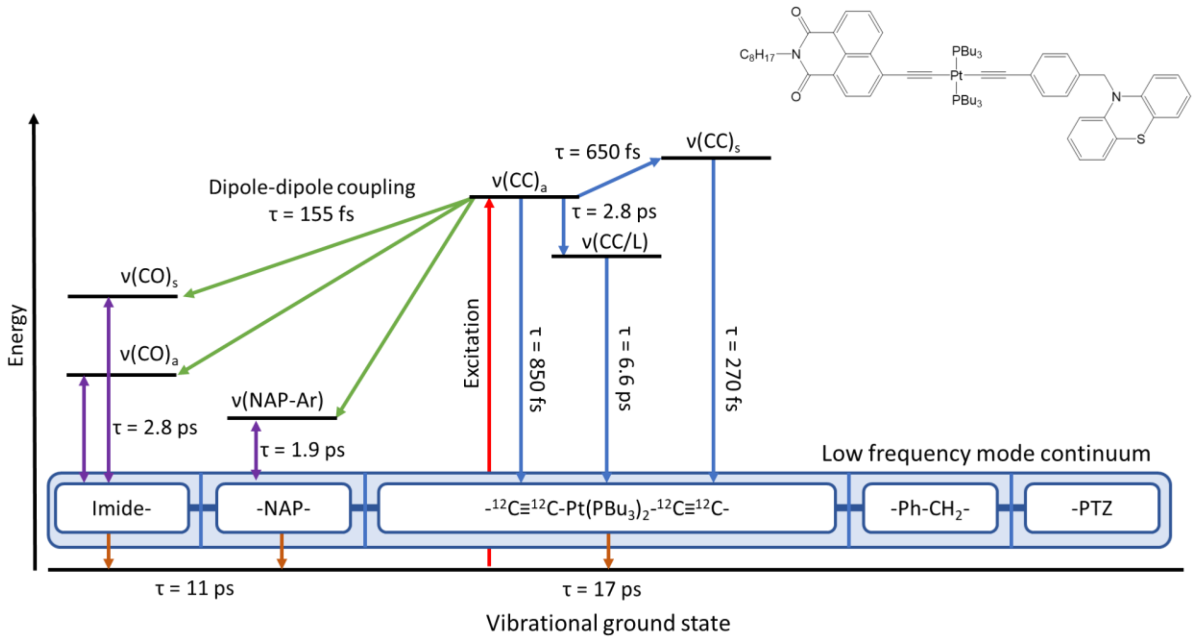

Figure E12– Proposed energy level diagram for vibrational energy redistribution following excitation of the $\nu(CC)_a$ vibration of complex **1**, *assigned on the basis of Lifetime Density Analysis data. Arrows on the diagram correspond to excitation (red), population transfer (blue), ultrafast mechanical, dipole-dipole, and anharmonic coupling (green), perturbation of vibrational modes by IVR (purple), and vibrational energy transfer to the solvent (orange). The continuum of low frequency modes associated with the IVR process is represented by the blue box.*

Complex 2

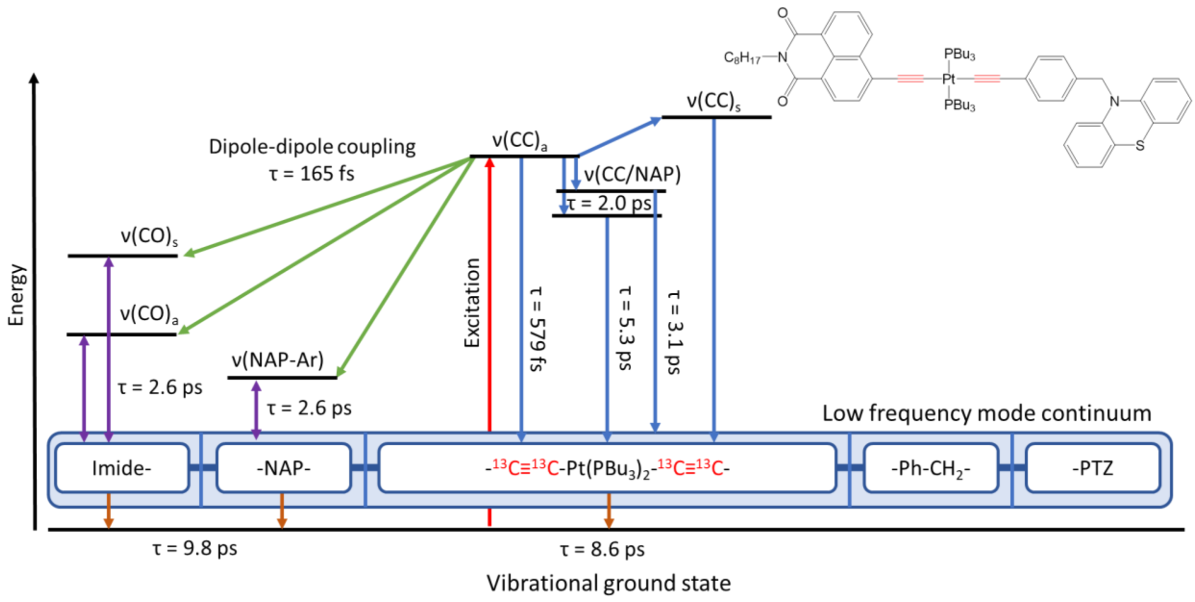

Figure E13 – Proposed energy level diagram for vibrational energy redistribution following excitation of the $\nu(CC)_a$ *vibration of complex* ***2****, assigned on the basis of Lifetime Density Analysis data. Arrows on the diagram correspond to excitation (red), population transfer (blue), ultrafast mechanical, dipole-dipole, and anharmonic coupling (green), perturbation of vibrational modes by IVR (purple), and vibrational energy transfer to the solvent (orange). The continuum of low frequency modes associated with the IVR process is represented by the blue box.*

Complex 3

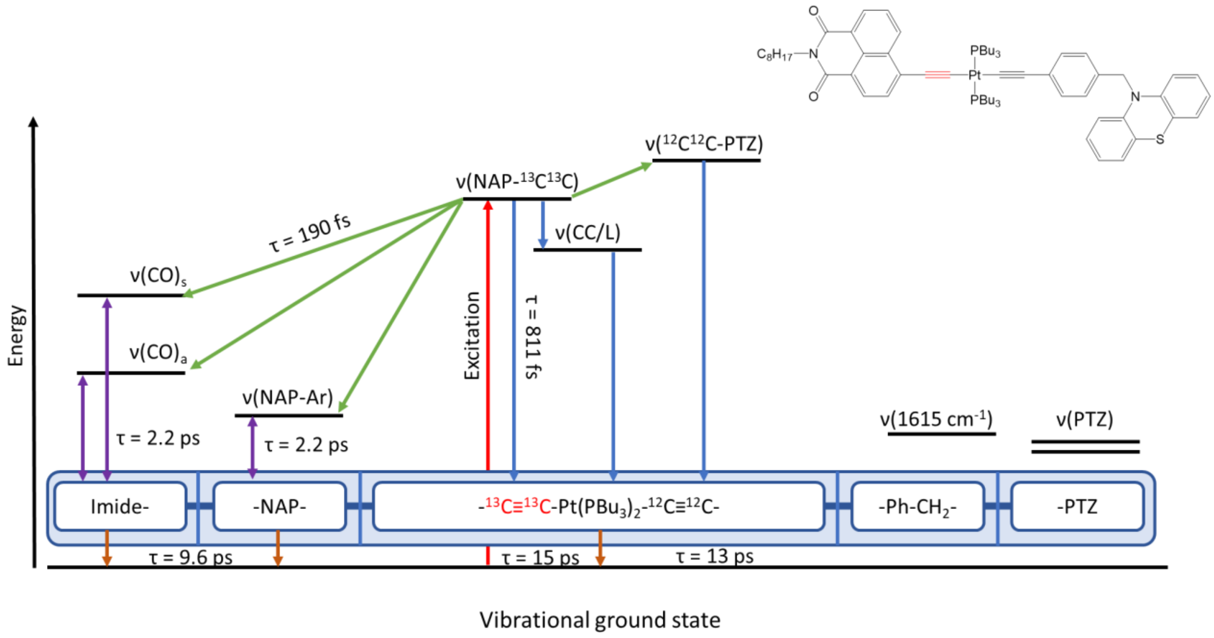

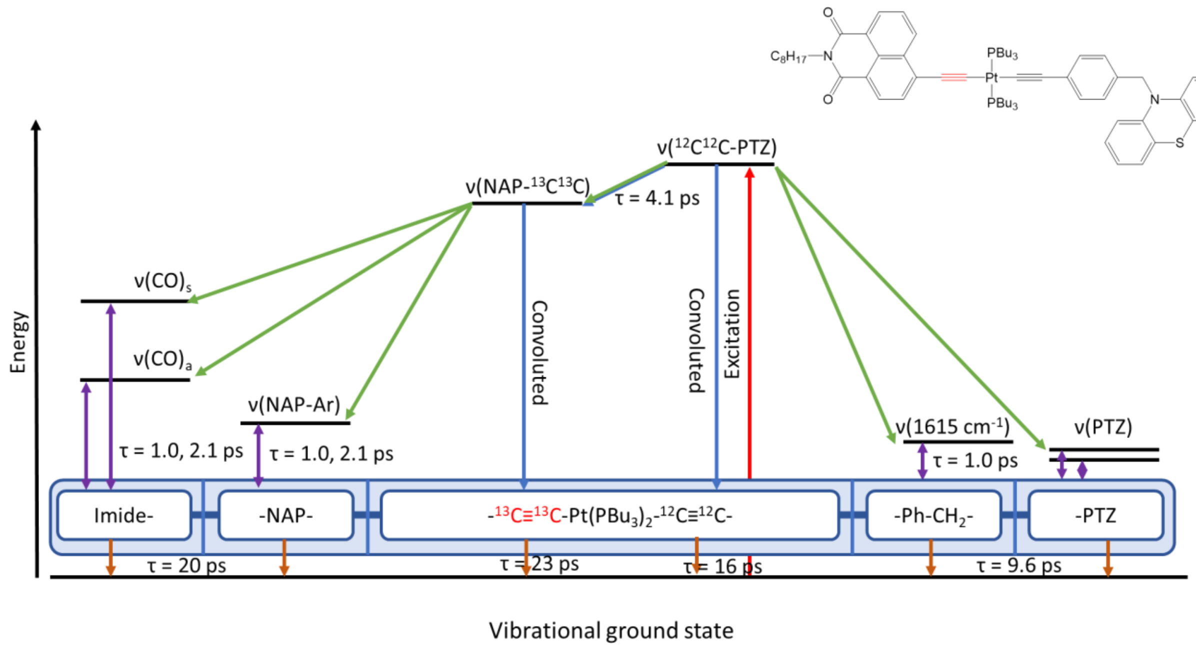

*Figure E14 – Proposed energy level diagrams for vibrational energy redistribution following excitation of the ν(CC)$_a$ vibration of complex **3**, assigned on the basis of Lifetime Density Analysis data. Arrows on the diagram correspond to excitation (red), population transfer (blue), ultrafast mechanical, dipole-dipole, and anharmonic coupling (green), perturbation of vibrational modes by IVR (purple), and vibrational energy transfer to the solvent (orange). The continuum of low frequency modes associated with the IVR process is represented by the blue box.*

Complex 4

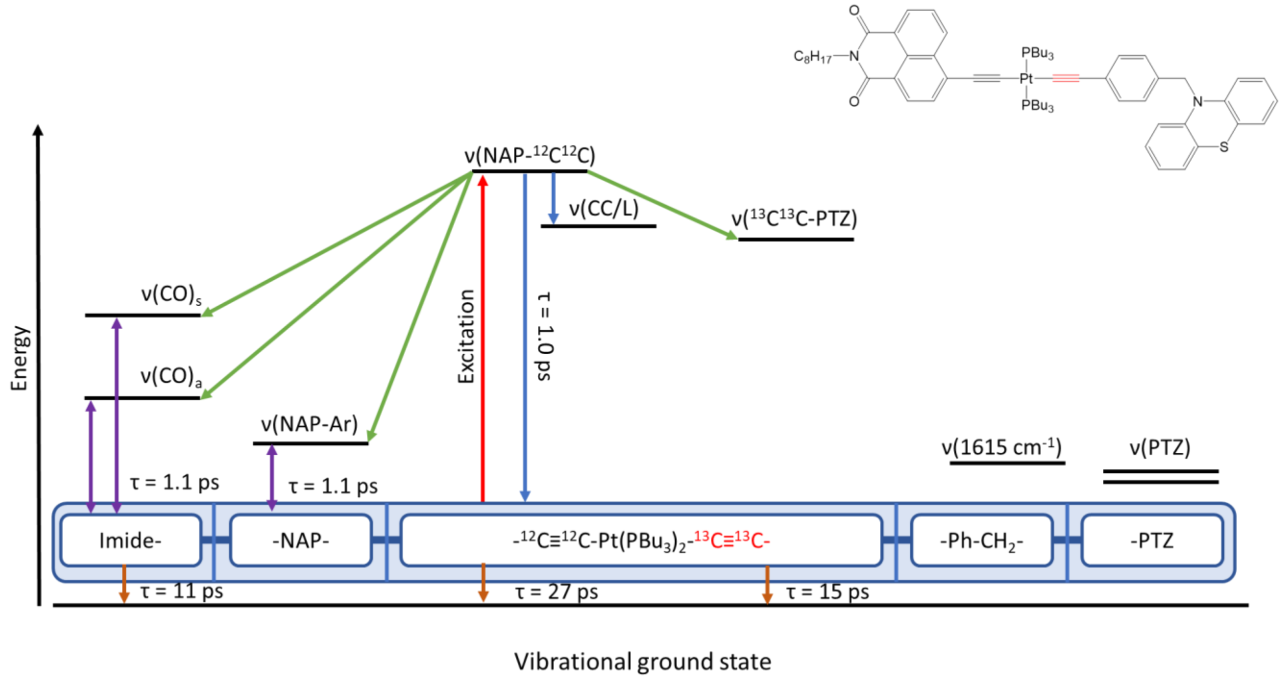

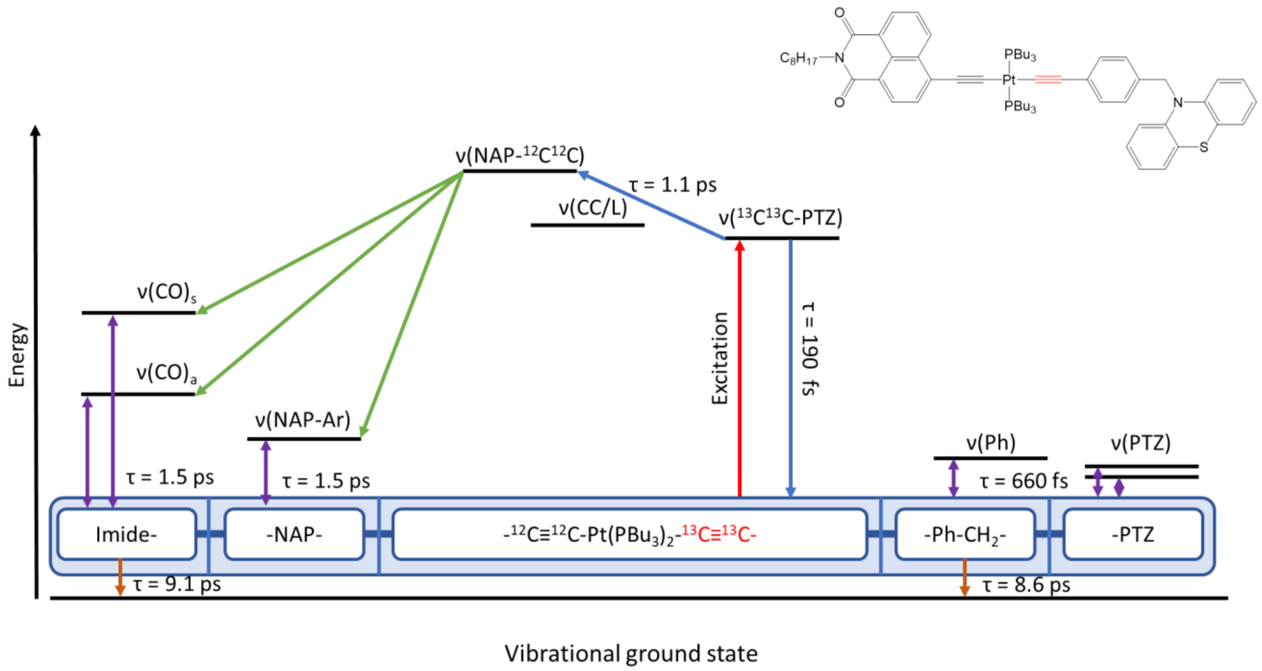

Figure E15 – Proposed energy level diagram for vibrational energy redistribution following excitation of the v(CC)$_a$ vibration of complex ***4****, assigned on the basis of Lifetime Density Analysis data. Arrows on the diagram correspond to excitation (red), population transfer (blue), ultrafast mechanical, dipole-dipole, and anharmonic coupling (green), perturbation of vibrational modes by IVR (purple), and vibrational energy transfer to the solvent (orange). The continuum of low frequency modes associated with the IVR process is represented by the blue box.*